DISTRIBUTED-ROUGHNESS EFFECTS ON STABILITY AND TRANSITION IN SWEPT-WING BOUNDARY LAYERS

Annual Technical Report for:

NASA-LANGLEY COOPERATIVE AGREEMENT # NCC-1-194

National Aeronautics and Space Administration
Flow Modeling and Control Branch, M-S 170
Attention: M. Walsh and J.R. Dagenhart
NASA-Langley Research Center
Hampton, VA. 23681

and

THE BOEING COMPANY CONTRACT #ZA0078

The Boeing Company
P.O. Box 3707, Mail Stop 67-IM
Attention: S. Stanford and J.D. Crouch
2810 160th Ave. S.E.
Seattle, WA. 98124-2207

DURING 5/17/96-12/31/96

Submitted by

RUBEN B. CARRILLO, JR.
MARK S. REIBERT
WILLIAM S. SARIC (Principal Investigator)

Mechanical and Aerospace Engineering
Arizona State University
Tempe, AZ 85287-6106

Janice D. Bennett, Director
Office of Research Creative Activity
(602) 965-8239

ABSTRACT

Boundary-layer stability experiments are conducted in the Arizona State University Unsteady Wind Tunnel on a 45° swept airfoil. The pressure distribution and test conditions are designed to suppress Tollmien-Schlichting disturbances and provide crossflow-dominated transition. The surface of the airfoil is finely polished to a near mirror finish. Under these conditions, submicron surface irregularities cause the naturally occurring stationary crossflow waves to grow to nonuniform amplitudes. Spanwise-uniform stationary crossflow disturbances are generated through careful control of the initial conditions with full-span arrays of micron-high roughness elements near the attachment line. Detailed hot-wire measurements are taken to document the stationary crossflow structure and determine growth rates for the total and individual-mode disturbances. Naphthalene flow visualization provides transition location information. Roughness spacing and roughness height are varied to examine the effects on transition location and all amplified wavelengths. The measurements show that roughness spacings that do not contain harmonics equal to the most unstable wavelength as computed by linear stability theory effectively suppress the most unstable mode. Under certain conditions, subcritical roughness spacing delays transition past that of the corresponding smooth surface.

TABLE OF CONTENTS

		Page
LIST OF TABLES		viii
LIST OF FIGURES		ix
NOMENCLATURE		xxvii
1	INTRODUCTION	1
	1.1 Background and Motivation	1
	1.1.1 Boundary-Layer Transition	2
	1.1.2 Transition Prediction	3
	1.2 Swept-Wing Flows and Crossflow Instability	4
	1.3 Review of Recent Research	6
	1.3.1 Experimental Investigations	7
	1.3.2 Theoretical Investigations	9
	1.4 Experimental Objectives	11
	1.5 Outline	12
2	EXPERIMENTAL FACILITY	13
	2.1 Unsteady Wind Tunnel	13
	2.2 Traverse and Sting	15
	2.3 Computer Systems	16
	2.4 Instrumentation	18
3	EXPERIMENTAL DESIGN	21
	3.1 Swept-Wing Model	21
	3.1.1 Airfoil	21
	3.1.2 Test Section	22
	3.2 Test Conditions	23

Page

3.2.1 Angle of Attack 23

3.2.2 Reynolds Number 24

3.2.3 Roughness Configuration 24

3.3 Coordinate System Definitions 27

3.4 Linear Stability Calculations 28

4 EXPERIMENTAL TECHNIQUES 31

4.1 Hot-Wire Signal Processing 31

4.1.1 Velocity Calibration 32

4.1.2 Temperature Compensation 32

4.2 Wind-Tunnel Speed Control 34

4.3 Flow Visualization 34

4.4 Disturbance Measurement Techniques 35

4.4.1 Boundary-Layer Scans 35

4.4.2 Constant-Y Scans 37

5 RESULTS 41

5.1 Overview 41

5.2 Basic State 42

5.2.1 Cp Distribution 43

5.2.2 Boundary-Layer Profiles 44

5.3 Natural Surface Roughness—Data Set $\mathcal{A}$ 45

5.3.1 Flow Visualization 45

5.3.2 Special Considerations 46

5.3.3 Total Disturbance Amplitude Measurements 47

5.3.4 Individual-Mode Disturbance Amplitude Measurements 50

5.4 [6|18] Roughness—Data Set $\mathcal{B}$ 52

Page

5.4.1 Total Disturbance Amplitude Measurements 53

5.4.2 Individual-Mode Disturbance Amplitude Measurements 54

5.5 [12|18] and [18|18] Roughness—Data Sets $\mathcal{C}$ and $\mathcal{D}$ 55

5.5.1 Total Disturbance Amplitude Measurements 56

5.5.2 Individual-Mode Disturbance Amplitude Measurements 57

5.6 [6|8] Roughness—Data Set $\mathcal{E}$ 58

5.6.1 Flow Visualization 58

5.6.2 Total Disturbance Amplitude Measurements 60

5.6.3 Individual-Mode Disturbance Amplitude Measurements 61

5.6.4 Theoretical Comparison 62

5.7 [48|8] Roughness—Data Set $\mathcal{F}$ 63

5.7.1 Total Disturbance Amplitude Measurements 63

5.7.2 Individual-Mode Disturbance Amplitude Measurements 64

6 CONCLUSIONS 65

6.1 Specific Results 65

6.1.1 Basic State 65

6.1.2 Natural Surface Roughness 65

6.1.3 Distributed Artificial Roughness 66

6.2 Summary 68

REFERENCES 69

LIST OF TABLES

Table		Page
2.1	Traverse system specifications.	16
3.1	Roughness Re_k values at $x/c = 0.023$ and $Re_c = 2.4 \times 10^6$.	26
3.2	Boundary-layer hot-wire probe rotation angles.	28
5.1	Experimental data sets.	42
5.2	Approximate transition location as determined from naphthalene flow visualization.	46
5.3	Total and individual-mode disturbance amplitudes at $x/c = 0.45$ for $Re_c = 2.4 \times 10^6$ and $[k\|18]$ roughness.	58

LIST OF FIGURES

Figure		Page
2.1	Plan view of the ASU Unsteady Wind Tunnel.	75
2.2	Elevation view of the ASU Unsteady Wind Tunnel.	76
2.3	Side view of traverse carriage.	77
2.4	Front view of traverse carriage.	78
2.5	Plan view of hot-wire sting.	79
3.1	Unswept NLF(2)-0415 airfoil and C_p distribution for $\alpha = 0°$ and $\delta_F = 0°$ in free air.	80
3.2	Test-section floor and ceiling liners with NLF(2)-0415 airfoil at $\alpha = -4°$.	81
3.3	Unswept NLF(2)-0415 airfoil and upper-surface C_p distribution for $\alpha = -4°$ and $\delta_F = 0°$ in free air.	82
3.4	Profilometer measurement of NLF(2)-0415 surface roughness.	83
3.5	Schematic swept-wing plan view showing coordinate systems and curved inviscid streamline.	84
3.6	Schematic swept-wing cross section showing coordinate systems.	85
3.7	Schematic of typical swept-wing boundary-layer profile showing tangential, crossflow, and total velocity profiles.	86
3.8	Hot-wire sting showing the necessary probe rotations to align the boundary-layer wire with the airfoil surface.	87
3.9	Linear theory N-factors for stationary crossflow disturbances. $Re_c = 2.4 \times 10^6$.	88
4.1	Typical hot-wire velocity calibration.	89
4.2	Typical hot-wire temperature compensation.	90
4.3	Wind tunnel speed-control program.	91
4.4	Typical boundary-layer profile scan.	92
4.5	Typical spanwise traverse-alignment scan.	93

Figure Page

4.6 Typical spanwise four-sweep constant-Y scan. 94

5.1 Comparison of experimental and theoretical pressure coefficients for $Re_c = 1.6 \times 10^6$. 95

5.2 Comparison of experimental and theoretical pressure coefficients for $Re_c = 2.4 \times 10^6$. 96

5.3 Comparison of experimental and theoretical pressure coefficients for $Re_c = 3.2 \times 10^6$. 97

5.4 Pressure distribution dependence upon Reynolds number for upper ports. 98

5.5 Pressure distribution dependence upon Reynolds number for lower ports. 99

5.6 Comparison of average C_p distribution with past experiment and theory for $Re_c = 1.6 \times 10^6$. 100

5.7 Comparison of average C_p distribution with past experiment and theory for $Re_c = 2.4 \times 10^6$. 101

5.8 Comparison of average C_p distribution with past experiment and theory for $Re_c = 3.2 \times 10^6$. 102

5.9 Spanwise array of 100 boundary-layer scans covering 99 mm in span at $x/c = 0.20$. $Re_c = 1.6 \times 10^6$, no artificial roughness. 103

5.10 Comparison of experimental spanwise-average boundary-layer profiles at $x/c = 0.20$. $Re_c = 1.6 \times 10^6$, no artificial roughness. 104

5.11 Naphthalene flow visualization for $Re_c = 2.4 \times 10^6$ and no artificial roughness. 105

5.12 Naphthalene flow visualization for $Re_c = 2.6 \times 10^6$ and no artificial roughness. 106

5.13 Naphthalene flow visualization for $Re_c = 2.8 \times 10^6$ and no artificial roughness. 107

5.14 Normalized boundary-layer velocity contours at $x/c = 0.60$. $Re_c = 2.4 \times 10^6$, no artificial roughness. 108

5.15 Spanwise array of 100 boundary-layer profiles spaced 1 mm apart in span at $x/c = 0.60$. $Re_c = 2.4 \times 10^6$, no artificial roughness. 109

5.16 Spanwise array of 100 disturbance profiles spaced 1 mm apart in span at $x/c = 0.60$. $Re_c = 2.4 \times 10^6$, no artificial roughness. 110

Figure Page

5.17 Normalized disturbance velocity contours at $x/c = 0.60$. $Re_c = 2.4 \times 10^6$, no artificial roughness. 111

5.18 Stationary crossflow mode shape at $x/c = 0.60$. $Re_c = 2.4 \times 10^6$, no artificial roughness. 112

5.19 Normalized boundary-layer velocity contours at $x/c = 0.05$. $Re_c = 2.4 \times 10^6$, no artificial roughness. 113

5.20 Normalized boundary-layer velocity contours at $x/c = 0.10$. $Re_c = 2.4 \times 10^6$, no artificial roughness. 114

5.21 Normalized boundary-layer velocity contours at $x/c = 0.15$. $Re_c = 2.4 \times 10^6$, no artificial roughness. 115

5.22 Normalized boundary-layer velocity contours at $x/c = 0.20$. $Re_c = 2.4 \times 10^6$, no artificial roughness. 116

5.23 Normalized boundary-layer velocity contours at $x/c = 0.25$. $Re_c = 2.4 \times 10^6$, no artificial roughness. 117

5.24 Normalized boundary-layer velocity contours at $x/c = 0.30$. $Re_c = 2.4 \times 10^6$, no artificial roughness. 118

5.25 Normalized boundary-layer velocity contours at $x/c = 0.35$. $Re_c = 2.4 \times 10^6$, no artificial roughness. 119

5.26 Normalized boundary-layer velocity contours at $x/c = 0.40$. $Re_c = 2.4 \times 10^6$, no artificial roughness. 120

5.27 Normalized boundary-layer velocity contours at $x/c = 0.45$. $Re_c = 2.4 \times 10^6$, no artificial roughness. 121

5.28 Normalized boundary-layer velocity contours at $x/c = 0.50$. $Re_c = 2.4 \times 10^6$, no artificial roughness. 122

5.29 Normalized boundary-layer velocity contours at $x/c = 0.55$. $Re_c = 2.4 \times 10^6$, no artificial roughness. 123

5.30 Spanwise array of 100 boundary-layer profiles spaced 1 mm apart in span at $x/c = 0.05$. $Re_c = 2.4 \times 10^6$, no artificial roughness. 124

5.31 Spanwise array of 100 boundary-layer profiles spaced 1 mm apart in span at $x/c = 0.10$. $Re_c = 2.4 \times 10^6$, no artificial roughness. 125

Figure Page

5.32 Spanwise array of 100 boundary-layer profiles spaced 1 mm apart in span at $x/c = 0.15$. $Re_c = 2.4 \times 10^6$, no artificial roughness. 126

5.33 Spanwise array of 100 boundary-layer profiles spaced 1 mm apart in span at $x/c = 0.20$. $Re_c = 2.4 \times 10^6$, no artificial roughness. 127

5.34 Spanwise array of 100 boundary-layer profiles spaced 1 mm apart in span at $x/c = 0.25$. $Re_c = 2.4 \times 10^6$, no artificial roughness. 128

5.35 Spanwise array of 100 boundary-layer profiles spaced 1 mm apart in span at $x/c = 0.30$. $Re_c = 2.4 \times 10^6$, no artificial roughness. 129

5.36 Spanwise array of 100 boundary-layer profiles spaced 1 mm apart in span at $x/c = 0.35$. $Re_c = 2.4 \times 10^6$, no artificial roughness. 130

5.37 Spanwise array of 100 boundary-layer profiles spaced 1 mm apart in span at $x/c = 0.40$. $Re_c = 2.4 \times 10^6$, no artificial roughness. 131

5.38 Spanwise array of 100 boundary-layer profiles spaced 1 mm apart in span at $x/c = 0.45$. $Re_c = 2.4 \times 10^6$, no artificial roughness. 132

5.39 Spanwise array of 100 boundary-layer profiles spaced 1 mm apart in span at $x/c = 0.50$. $Re_c = 2.4 \times 10^6$, no artificial roughness. 133

5.40 Spanwise array of 100 boundary-layer profiles spaced 1 mm apart in span at $x/c = 0.55$. $Re_c = 2.4 \times 10^6$, no artificial roughness. 134

5.41 Spanwise array of 100 disturbance profiles spaced 1 mm apart in span at $x/c = 0.05$. $Re_c = 2.4 \times 10^6$, no artificial roughness. 135

5.42 Spanwise array of 100 disturbance profiles spaced 1 mm apart in span at $x/c = 0.10$. $Re_c = 2.4 \times 10^6$, no artificial roughness. 136

5.43 Spanwise array of 100 disturbance profiles spaced 1 mm apart in span at $x/c = 0.15$. $Re_c = 2.4 \times 10^6$, no artificial roughness. 137

5.44 Spanwise array of 100 disturbance profiles spaced 1 mm apart in span at $x/c = 0.20$. $Re_c = 2.4 \times 10^6$, no artificial roughness. 138

5.45 Spanwise array of 100 disturbance profiles spaced 1 mm apart in span at $x/c = 0.25$. $Re_c = 2.4 \times 10^6$, no artificial roughness. 139

5.46 Spanwise array of 100 disturbance profiles spaced 1 mm apart in span at $x/c = 0.30$. $Re_c = 2.4 \times 10^6$, no artificial roughness. 140

Figure Page

5.47 Spanwise array of 100 disturbance profiles spaced 1 mm apart in span at $x/c = 0.35$. $Re_c = 2.4 \times 10^6$, no artificial roughness. 141

5.48 Spanwise array of 100 disturbance profiles spaced 1 mm apart in span at $x/c = 0.40$. $Re_c = 2.4 \times 10^6$, no artificial roughness. 142

5.49 Spanwise array of 100 disturbance profiles spaced 1 mm apart in span at $x/c = 0.45$. $Re_c = 2.4 \times 10^6$, no artificial roughness. 143

5.50 Spanwise array of 100 disturbance profiles spaced 1 mm apart in span at $x/c = 0.50$. $Re_c = 2.4 \times 10^6$, no artificial roughness. 144

5.51 Spanwise array of 100 disturbance profiles spaced 1 mm apart in span at $x/c = 0.55$. $Re_c = 2.4 \times 10^6$, no artificial roughness. 145

5.52 Stationary crossflow mode shapes for $Re_c = 2.4 \times 10^6$ and no artificial roughness. 146

5.53 Total disturbance amplitude and relative N-factor for $Re_c = 2.4 \times 10^6$ and no artificial roughness. 147

5.54 Spanwise hot-wire scan at $x/c = 0.25$ and $Y = 0.70$ mm. $Re_c = 2.4 \times 10^6$, no artificial roughness. 148

5.55 Spanwise hot-wire scan at $x/c = 0.30$ and $Y = 0.85$ mm. $Re_c = 2.4 \times 10^6$, no artificial roughness. 149

5.56 Spanwise hot-wire scan at $x/c = 0.35$ and $Y = 1.1$ mm. $Re_c = 2.4 \times 10^6$, no artificial roughness. 150

5.57 Spanwise hot-wire scan at $x/c = 0.40$ and $Y = 1.15$ mm. $Re_c = 2.4 \times 10^6$, no artificial roughness. 151

5.58 Spanwise hot-wire scan at $x/c = 0.45$ and $Y = 1.15$ mm. $Re_c = 2.4 \times 10^6$, no artificial roughness. 152

5.59 Spanwise hot-wire scan at $x/c = 0.50$ and $Y = 1.1$ mm. $Re_c = 2.4 \times 10^6$, no artificial roughness. 153

5.60 Spanwise hot-wire scan at $x/c = 0.55$ and $Y = 1.05$ mm. $Re_c = 2.4 \times 10^6$, no artificial roughness. 154

5.61 Power spectral density of constant-Y scan at $x/c = 0.25$ and $Y = 0.70$ mm. $Re_c = 2.4 \times 10^6$, no artificial roughness. 155

Figure Page

5.62 Power spectral density of constant-Y scan at $x/c = 0.30$ and $Y = 0.85$ mm. $Re_c = 2.4 \times 10^6$, no artificial roughness. 156

5.63 Power spectral density of constant-Y scan at $x/c = 0.35$ and $Y = 1.1$ mm. $Re_c = 2.4 \times 10^6$, no artificial roughness. 157

5.64 Power spectral density of constant-Y scan at $x/c = 0.40$ and $Y = 1.15$ mm. $Re_c = 2.4 \times 10^6$, no artificial roughness. 158

5.65 Power spectral density of constant-Y scan at $x/c = 0.45$ and $Y = 1.15$ mm. $Re_c = 2.4 \times 10^6$, no artificial roughness. 159

5.66 Power spectral density of constant-Y scan at $x/c = 0.50$ and $Y = 1.1$ mm. $Re_c = 2.4 \times 10^6$, no artificial roughness. 160

5.67 Power spectral density of constant-Y scan at $x/c = 0.55$ and $Y = 1.05$ mm. $Re_c = 2.4 \times 10^6$, no artificial roughness. 161

5.68 Single-mode disturbance amplitude and N-factors. $Re_c = 2.4 \times 10^6$, no artificial roughness. 162

5.69 Total and single-mode disturbance amplitude and N-factors. $Re_c = 2.4 \times 10^6$, no artificial roughness. 163

5.70 Normalized boundary-layer velocity contours at $x/c = 0.05$. $Re_c = 2.4 \times 10^6$, [6|18] roughness. 164

5.71 Normalized boundary-layer velocity contours at $x/c = 0.10$. $Re_c = 2.4 \times 10^6$, [6|18] roughness. 165

5.72 Normalized boundary-layer velocity contours at $x/c = 0.15$. $Re_c = 2.4 \times 10^6$, [6|18] roughness. 166

5.73 Normalized boundary-layer velocity contours at $x/c = 0.20$. $Re_c = 2.4 \times 10^6$, [6|18] roughness. 167

5.74 Normalized boundary-layer velocity contours at $x/c = 0.25$. $Re_c = 2.4 \times 10^6$, [6|18] roughness. 168

5.75 Normalized boundary-layer velocity contours at $x/c = 0.30$. $Re_c = 2.4 \times 10^6$, [6|18] roughness. 169

5.76 Normalized boundary-layer velocity contours at $x/c = 0.35$. $Re_c = 2.4 \times 10^6$, [6|18] roughness. 170

Figure Page

5.77 Normalized boundary-layer velocity contours at $x/c = 0.40$. $Re_c = 2.4 \times 10^6$, [6|18] roughness. 171

5.78 Normalized boundary-layer velocity contours at $x/c = 0.45$. $Re_c = 2.4 \times 10^6$, [6|18] roughness. 172

5.79 Spanwise array of 100 boundary-layer profiles spaced 1 mm apart in span at $x/c = 0.05$. $Re_c = 2.4 \times 10^6$, [6|18] roughness. 173

5.80 Spanwise array of 100 boundary-layer profiles spaced 1 mm apart in span at $x/c = 0.10$. $Re_c = 2.4 \times 10^6$, [6|18] roughness. 174

5.81 Spanwise array of 100 boundary-layer profiles spaced 1 mm apart in span at $x/c = 0.15$. $Re_c = 2.4 \times 10^6$, [6|18] roughness. 175

5.82 Spanwise array of 100 boundary-layer profiles spaced 1 mm apart in span at $x/c = 0.20$. $Re_c = 2.4 \times 10^6$, [6|18] roughness. 176

5.83 Spanwise array of 100 boundary-layer profiles spaced 1 mm apart in span at $x/c = 0.25$. $Re_c = 2.4 \times 10^6$, [6|18] roughness. 177

5.84 Spanwise array of 100 boundary-layer profiles spaced 1 mm apart in span at $x/c = 0.30$. $Re_c = 2.4 \times 10^6$, [6|18] roughness. 178

5.85 Spanwise array of 100 boundary-layer profiles spaced 1 mm apart in span at $x/c = 0.35$. $Re_c = 2.4 \times 10^6$, [6|18] roughness. 179

5.86 Spanwise array of 100 boundary-layer profiles spaced 1 mm apart in span at $x/c = 0.40$. $Re_c = 2.4 \times 10^6$, [6|18] roughness. 180

5.87 Spanwise array of 100 boundary-layer profiles spaced 1 mm apart in span at $x/c = 0.45$. $Re_c = 2.4 \times 10^6$, [6|18] roughness. 181

5.88 Spanwise array of 100 disturbance profiles spaced 1 mm apart in span at $x/c = 0.05$. $Re_c = 2.4 \times 10^6$, [6|18] roughness. 182

5.89 Spanwise array of 100 disturbance profiles spaced 1 mm apart in span at $x/c = 0.10$. $Re_c = 2.4 \times 10^6$, [6|18] roughness. 183

5.90 Spanwise array of 100 disturbance profiles spaced 1 mm apart in span at $x/c = 0.15$. $Re_c = 2.4 \times 10^6$, [6|18] roughness. 184

5.91 Spanwise array of 100 disturbance profiles spaced 1 mm apart in span at $x/c = 0.20$. $Re_c = 2.4 \times 10^6$, [6|18] roughness. 185

Figure Page

5.92 Spanwise array of 100 disturbance profiles spaced 1 mm apart in span at $x/c = 0.25$. $Re_c = 2.4 \times 10^6$, [6|18] roughness. 186

5.93 Spanwise array of 100 disturbance profiles spaced 1 mm apart in span at $x/c = 0.30$. $Re_c = 2.4 \times 10^6$, [6|18] roughness. 187

5.94 Spanwise array of 100 disturbance profiles spaced 1 mm apart in span at $x/c = 0.35$. $Re_c = 2.4 \times 10^6$, [6|18] roughness. 188

5.95 Spanwise array of 100 disturbance profiles spaced 1 mm apart in span at $x/c = 0.40$. $Re_c = 2.4 \times 10^6$, [6|18] roughness. 189

5.96 Spanwise array of 100 disturbance profiles spaced 1 mm apart in span at $x/c = 0.45$. $Re_c = 2.4 \times 10^6$, [6|18] roughness. 190

5.97 Normalized disturbance velocity contours at $x/c = 0.45$. $Re_c = 2.4 \times 10^6$, [6|18] roughness. 191

5.98 Stationary crossflow mode shapes for $Re_c = 2.4 \times 10^6$ and [6|18] roughness. 192

5.99 Total disturbance amplitude and relative N-factor for $Re_c = 2.4 \times 10^6$ and [6|18] roughness. 193

5.100 Spanwise hot-wire scan at $x/c = 0.10$ and $Y = 0.60$ mm. $Re_c = 2.4 \times 10^6$, [6|18] roughness. 194

5.101 Spanwise hot-wire scan at $x/c = 0.15$ and $Y = 0.75$ mm. $Re_c = 2.4 \times 10^6$, [6|18] roughness. 195

5.102 Spanwise hot-wire scan at $x/c = 0.20$ and $Y = 0.90$ mm. $Re_c = 2.4 \times 10^6$, [6|18] roughness. 196

5.103 Spanwise hot-wire scan at $x/c = 0.25$ and $Y = 0.95$ mm. $Re_c = 2.4 \times 10^6$, [6|18] roughness. 197

5.104 Spanwise hot-wire scan at $x/c = 0.30$ and $Y = 0.95$ mm. $Re_c = 2.4 \times 10^6$, [6|18] roughness. 198

5.105 Spanwise hot-wire scan at $x/c = 0.35$ and $Y = 0.85$ mm. $Re_c = 2.4 \times 10^6$, [6|18] roughness. 199

5.106 Spanwise hot-wire scan at $x/c = 0.40$ and $Y = 0.85$ mm. $Re_c = 2.4 \times 10^6$, [6|18] roughness. 200

5.107 Spanwise hot-wire scan at $x/c = 0.45$ and $Y = 0.85$ mm. $Re_c = 2.4 \times 10^6$, [6|18] roughness. 201

Figure Page

5.108 Power spectral density of constant-Y scan at $x/c = 0.10$ and $Y = 0.60$ mm. $Re_c = 2.4 \times 10^6$, [6|18] roughness. 202

5.109 Power spectral density of constant-Y scan at $x/c = 0.15$ and $Y = 0.75$ mm. $Re_c = 2.4 \times 10^6$, [6|18] roughness. 203

5.110 Power spectral density of constant-Y scan at $x/c = 0.20$ and $Y = 0.90$ mm. $Re_c = 2.4 \times 10^6$, [6|18] roughness. 204

5.111 Power spectral density of constant-Y scan at $x/c = 0.25$ and $Y = 0.95$ mm. $Re_c = 2.4 \times 10^6$, [6|18] roughness. 205

5.112 Power spectral density of constant-Y scan at $x/c = 0.30$ and $Y = 0.95$ mm. $Re_c = 2.4 \times 10^6$, [6|18] roughness. 206

5.113 Power spectral density of constant-Y scan at $x/c = 0.35$ and $Y = 0.85$ mm. $Re_c = 2.4 \times 10^6$, [6|18] roughness. 207

5.114 Power spectral density of constant-Y scan at $x/c = 0.40$ and $Y = 0.85$ mm. $Re_c = 2.4 \times 10^6$, [6|18] roughness. 208

5.115 Power spectral density of constant-Y scan at $x/c = 0.45$ and $Y = 0.85$ mm. $Re_c = 2.4 \times 10^6$, [6|18] roughness. 209

5.116 Single-mode disturbance amplitude and N-factors. $Re_c = 2.4 \times 10^6$, [6|18] roughness. 210

5.117 Total and single-mode disturbance amplitude and N-factors. $Re_c = 2.4 \times 10^6$, [6|18] roughness. 211

5.118 Normalized boundary-layer velocity contours at $x/c = 0.45$. $Re_c = 2.4 \times 10^6$, [12|18] roughness. 212

5.119 Spanwise array of 100 boundary-layer profiles spaced 1 mm apart in span at $x/c = 0.45$. $Re_c = 2.4 \times 10^6$, [12|18] roughness. 213

5.120 Spanwise array of 100 disturbance profiles spaced 1 mm apart in span at $x/c = 0.45$. $Re_c = 2.4 \times 10^6$, [12|18] roughness. 214

5.121 Stationary crossflow mode shape at $x/c = 0.45$. $Re_c = 2.4 \times 10^6$, [12|18] roughness. 215

5.122 Spanwise hot-wire scan at $x/c = 0.45$ and $Y = 0.80$ mm. $Re_c = 2.4 \times 10^6$, [12|18] roughness. 216

Figure Page

5.123 Power spectral density of constant-Y scan at $x/c = 0.45$ and $Y = 0.80$ mm. $Re_c = 2.4 \times 10^6$, [12|18] roughness. 217

5.124 Normalized boundary-layer velocity contours at $x/c = 0.45$. $Re_c = 2.4 \times 10^6$, [18|18] roughness. 218

5.125 Spanwise array of 100 boundary-layer profiles spaced 1 mm apart in span at $x/c = 0.45$. $Re_c = 2.4 \times 10^6$, [18|18] roughness. 219

5.126 Spanwise array of 100 disturbance profiles spaced 1 mm apart in span at $x/c = 0.45$. $Re_c = 2.4 \times 10^6$, [18|18] roughness. 220

5.127 Stationary crossflow mode shape at $x/c = 0.45$. $Re_c = 2.4 \times 10^6$, [18|18] roughness. 221

5.128 Spanwise hot-wire scan at $x/c = 0.45$ and $Y = 0.80$ mm. $Re_c = 2.4 \times 10^6$, [18|18] roughness. 222

5.129 Power spectral density of constant-Y scan at $x/c = 0.45$ and $Y = 0.80$ mm. $Re_c = 2.4 \times 10^6$, [18|18] roughness. 223

5.130 Stationary crossflow mode shapes at $x/c = 0.45$ for $Re_c = 2.4 \times 10^6$ and [k|18] roughness. 224

5.131 Naphthalene flow visualization for $Re_c = 2.4 \times 10^6$, [6|8] roughness. . . 225

5.132 Naphthalene flow visualization for $Re_c = 2.6 \times 10^6$, [6|8] roughness. . . 226

5.133 Naphthalene flow visualization for $Re_c = 2.8 \times 10^6$, [6|8] roughness. . . 227

5.134 Normalized boundary-layer velocity contours at $x/c = 0.05$. $Re_c = 2.4 \times 10^6$, [6|8] roughness. 228

5.135 Normalized boundary-layer velocity contours at $x/c = 0.10$. $Re_c = 2.4 \times 10^6$, [6|8] roughness. 229

5.136 Normalized boundary-layer velocity contours at $x/c = 0.15$. $Re_c = 2.4 \times 10^6$, [6|8] roughness. 230

5.137 Normalized boundary-layer velocity contours at $x/c = 0.20$. $Re_c = 2.4 \times 10^6$, [6|8] roughness. 231

5.138 Normalized boundary-layer velocity contours at $x/c = 0.25$. $Re_c = 2.4 \times 10^6$, [6|8] roughness. 232

5.139 Normalized boundary-layer velocity contours at $x/c = 0.30$. $Re_c = 2.4 \times 10^6$, [6|8] roughness. 233

Figure Page

5.140 Normalized boundary-layer velocity contours at $x/c = 0.35$. $Re_c = 2.4 \times 10^6$, [6|8] roughness. 234

5.141 Normalized boundary-layer velocity contours at $x/c = 0.40$. $Re_c = 2.4 \times 10^6$, [6|8] roughness. 235

5.142 Normalized boundary-layer velocity contours at $x/c = 0.45$. $Re_c = 2.4 \times 10^6$, [6|8] roughness. 236

5.143 Normalized boundary-layer velocity contours at $x/c = 0.50$. $Re_c = 2.4 \times 10^6$, [6|8] roughness. 237

5.144 Normalized boundary-layer velocity contours at $x/c = 0.55$. $Re_c = 2.4 \times 10^6$, [6|8] roughness. 238

5.145 Normalized boundary-layer velocity contours at $x/c = 0.60$. $Re_c = 2.4 \times 10^6$, [6|8] roughness. 239

5.146 Spanwise array of 100 boundary-layer profiles spaced 1 mm apart in span at $x/c = 0.05$. $Re_c = 2.4 \times 10^6$, [6|8] roughness. 240

5.147 Spanwise array of 100 boundary-layer profiles spaced 1 mm apart in span at $x/c = 0.10$. $Re_c = 2.4 \times 10^6$, [6|8] roughness. 241

5.148 Spanwise array of 100 boundary-layer profiles spaced 1 mm apart in span at $x/c = 0.15$. $Re_c = 2.4 \times 10^6$, [6|8] roughness. 242

5.149 Spanwise array of 100 boundary-layer profiles spaced 1 mm apart in span at $x/c = 0.20$. $Re_c = 2.4 \times 10^6$, [6|8] roughness. 243

5.150 Spanwise array of 100 boundary-layer profiles spaced 1 mm apart in span at $x/c = 0.25$. $Re_c = 2.4 \times 10^6$, [6|8] roughness. 244

5.151 Spanwise array of 100 boundary-layer profiles spaced 1 mm apart in span at $x/c = 0.30$. $Re_c = 2.4 \times 10^6$, [6|8] roughness. 245

5.152 Spanwise array of 100 boundary-layer profiles spaced 1 mm apart in span at $x/c = 0.35$. $Re_c = 2.4 \times 10^6$, [6|8] roughness. 246

5.153 Spanwise array of 100 boundary-layer profiles spaced 1 mm apart in span at $x/c = 0.40$. $Re_c = 2.4 \times 10^6$, [6|8] roughness. 247

5.154 Spanwise array of 100 boundary-layer profiles spaced 1 mm apart in span at $x/c = 0.45$. $Re_c = 2.4 \times 10^6$, [6|8] roughness. 248

Figure Page

5.155 Spanwise array of 100 boundary-layer profiles spaced 1 mm apart in span at $x/c = 0.50$. $Re_c = 2.4 \times 10^6$, [6|8] roughness. 249

5.156 Spanwise array of 100 boundary-layer profiles spaced 1 mm apart in span at $x/c = 0.55$. $Re_c = 2.4 \times 10^6$, [6|8] roughness. 250

5.157 Spanwise array of 100 boundary-layer profiles spaced 1 mm apart in span at $x/c = 0.60$. $Re_c = 2.4 \times 10^6$, [6|8] roughness. 251

5.158 Spanwise array of 100 disturbance profiles spaced 1 mm apart in span at $x/c = 0.05$. $Re_c = 2.4 \times 10^6$, [6|8] roughness. 252

5.159 Spanwise array of 100 disturbance profiles spaced 1 mm apart in span at $x/c = 0.10$. $Re_c = 2.4 \times 10^6$, [6|8] roughness. 253

5.160 Spanwise array of 100 disturbance profiles spaced 1 mm apart in span at $x/c = 0.15$. $Re_c = 2.4 \times 10^6$, [6|8] roughness. 254

5.161 Spanwise array of 100 disturbance profiles spaced 1 mm apart in span at $x/c = 0.20$. $Re_c = 2.4 \times 10^6$, [6|8] roughness. 255

5.162 Spanwise array of 100 disturbance profiles spaced 1 mm apart in span at $x/c = 0.25$. $Re_c = 2.4 \times 10^6$, [6|8] roughness. 256

5.163 Spanwise array of 100 disturbance profiles spaced 1 mm apart in span at $x/c = 0.30$. $Re_c = 2.4 \times 10^6$, [6|8] roughness. 257

5.164 Spanwise array of 100 disturbance profiles spaced 1 mm apart in span at $x/c = 0.35$. $Re_c = 2.4 \times 10^6$, [6|8] roughness. 258

5.165 Spanwise array of 100 disturbance profiles spaced 1 mm apart in span at $x/c = 0.40$. $Re_c = 2.4 \times 10^6$, [6|8] roughness. 259

5.166 Spanwise array of 100 disturbance profiles spaced 1 mm apart in span at $x/c = 0.45$. $Re_c = 2.4 \times 10^6$, [6|8] roughness. 260

5.167 Spanwise array of 100 disturbance profiles spaced 1 mm apart in span at $x/c = 0.50$. $Re_c = 2.4 \times 10^6$, [6|8] roughness. 261

5.168 Spanwise array of 100 disturbance profiles spaced 1 mm apart in span at $x/c = 0.55$. $Re_c = 2.4 \times 10^6$, [6|8] roughness. 262

5.169 Spanwise array of 100 disturbance profiles spaced 1 mm apart in span at $x/c = 0.60$. $Re_c = 2.4 \times 10^6$, [6|8] roughness. 263

5.170 Stationary crossflow mode shapes for $Re_c = 2.4 \times 10^6$ and [6|8] roughness. 264

Figure Page

5.171 Total disturbance amplitude and relative N-factor for $Re_c = 2.4 \times 10^6$ and [6|8] roughness. 265

5.172 Spanwise hot-wire scan at $x/c = 0.10$ and $Y = 0.60$ mm. $Re_c = 2.4 \times 10^6$, [6|8] roughness. 266

5.173 Spanwise hot-wire scan at $x/c = 0.15$ and $Y = 0.80$ mm. $Re_c = 2.4 \times 10^6$, [6|8] roughness. 267

5.174 Spanwise hot-wire scan at $x/c = 0.20$ and $Y = 0.90$ mm. $Re_c = 2.4 \times 10^6$, [6|8] roughness. 268

5.175 Spanwise hot-wire scan at $x/c = 0.25$ and $Y = 0.90$ mm. $Re_c = 2.4 \times 10^6$, [6|8] roughness. 269

5.176 Spanwise hot-wire scan at $x/c = 0.30$ and $Y = 0.85$ mm. $Re_c = 2.4 \times 10^6$, [6|8] roughness. 270

5.177 Spanwise hot-wire scan at $x/c = 0.35$ and $Y = 0.90$ mm. $Re_c = 2.4 \times 10^6$, [6|8] roughness. 271

5.178 Spanwise hot-wire scan at $x/c = 0.40$ and $Y = 0.90$ mm. $Re_c = 2.4 \times 10^6$, [6|8] roughness. 272

5.179 Spanwise hot-wire scan at $x/c = 0.45$ and $Y = 1.0$ mm. $Re_c = 2.4 \times 10^6$, [6|8] roughness. 273

5.180 Spanwise hot-wire scan at $x/c = 0.50$ and $Y = 0.90$ mm. $Re_c = 2.4 \times 10^6$, [6|8] roughness. 274

5.181 Spanwise hot-wire scan at $x/c = 0.55$ and $Y = 1.0$ mm. $Re_c = 2.4 \times 10^6$, [6|8] roughness. 275

5.182 Spanwise hot-wire scan at $x/c = 0.60$ and $Y = 1.0$ mm. $Re_c = 2.4 \times 10^6$, [6|8] roughness. 276

5.183 Power spectral density of constant-Y scan at $x/c = 0.10$ and $Y = 0.60$ mm. $Re_c = 2.4 \times 10^6$, [6|8] roughness. 277

5.184 Power spectral density of constant-Y scan at $x/c = 0.15$ and $Y = 0.80$ mm. $Re_c = 2.4 \times 10^6$, [6|8] roughness. 278

5.185 Power spectral density of constant-Y scan at $x/c = 0.20$ and $Y = 0.90$ mm. $Re_c = 2.4 \times 10^6$, [6|8] roughness. 279

Figure Page

5.186 Power spectral density of constant-Y scan at $x/c = 0.25$ and $Y =$ 0.90 mm. $Re_c = 2.4 \times 10^6$, [6|8] roughness. 280

5.187 Power spectral density of constant-Y scan at $x/c = 0.30$ and $Y =$ 0.85 mm. $Re_c = 2.4 \times 10^6$, [6|8] roughness. 281

5.188 Power spectral density of constant-Y scan at $x/c = 0.35$ and $Y =$ 0.90 mm. $Re_c = 2.4 \times 10^6$, [6|8] roughness. 282

5.189 Power spectral density of constant-Y scan at $x/c = 0.40$ and $Y =$ 0.90 mm. $Re_c = 2.4 \times 10^6$, [6|8] roughness. 283

5.190 Power spectral density of constant-Y scan at $x/c = 0.45$ and $Y =$ 1.0 mm. $Re_c = 2.4 \times 10^6$, [6|8] roughness. 284

5.191 Power spectral density of constant-Y scan at $x/c = 0.50$ and $Y =$ 0.90 mm. $Re_c = 2.4 \times 10^6$, [6|8] roughness. 285

5.192 Power spectral density of constant-Y scan at $x/c = 0.55$ and $Y =$ 1.0 mm. $Re_c = 2.4 \times 10^6$, [6|8] roughness. 286

5.193 Power spectral density of constant-Y scan at $x/c = 0.60$ and $Y =$ 1.0 mm. $Re_c = 2.4 \times 10^6$, [6|8] roughness. 287

5.194 Single-mode disturbance amplitude and N-factors. $Re_c = 2.4 \times 10^6$, [6|8] roughness. 288

5.195 Total and single-mode disturbance amplitude and N-factors. $Re_c =$ 2.4×10^6, [6|8] roughness. 289

5.196 Comparison of experimental and theoretical total disturbance amplification factor N for $Re_c = 2.4 \times 10^6$ and [6|8] roughness. 290

5.197 Normalized boundary-layer velocity contours at $x/c = 0.05$. $Re_c =$ 2.4×10^6, [48|8] roughness. 291

5.198 Normalized boundary-layer velocity contours at $x/c = 0.10$. $Re_c =$ 2.4×10^6, [48|8] roughness. 292

5.199 Normalized boundary-layer velocity contours at $x/c = 0.15$. $Re_c =$ 2.4×10^6, [48|8] roughness. 293

5.200 Normalized boundary-layer velocity contours at $x/c = 0.20$. $Re_c =$ 2.4×10^6, [48|8] roughness. 294

Figure Page

5.201 Normalized boundary-layer velocity contours at $x/c = 0.25$. $Re_c = 2.4 \times 10^6$, [48|8] roughness. 295

5.202 Normalized boundary-layer velocity contours at $x/c = 0.30$. $Re_c = 2.4 \times 10^6$, [48|8] roughness. 296

5.203 Normalized boundary-layer velocity contours at $x/c = 0.35$. $Re_c = 2.4 \times 10^6$, [48|8] roughness. 297

5.204 Normalized boundary-layer velocity contours at $x/c = 0.40$. $Re_c = 2.4 \times 10^6$, [48|8] roughness. 298

5.205 Normalized boundary-layer velocity contours at $x/c = 0.45$. $Re_c = 2.4 \times 10^6$, [48|8] roughness. 299

5.206 Normalized boundary-layer velocity contours at $x/c = 0.50$. $Re_c = 2.4 \times 10^6$, [48|8] roughness. 300

5.207 Normalized boundary-layer velocity contours at $x/c = 0.55$. $Re_c = 2.4 \times 10^6$, [48|8] roughness. 301

5.208 Spanwise array of 100 boundary-layer profiles spaced 1 mm apart in span at $x/c = 0.05$. $Re_c = 2.4 \times 10^6$, [48|8] roughness. 302

5.209 Spanwise array of 100 boundary-layer profiles spaced 1 mm apart in span at $x/c = 0.10$. $Re_c = 2.4 \times 10^6$, [48|8] roughness. 303

5.210 Spanwise array of 100 boundary-layer profiles spaced 1 mm apart in span at $x/c = 0.15$. $Re_c = 2.4 \times 10^6$, [48|8] roughness. 304

5.211 Spanwise array of 100 boundary-layer profiles spaced 1 mm apart in span at $x/c = 0.20$. $Re_c = 2.4 \times 10^6$, [48|8] roughness. 305

5.212 Spanwise array of 100 boundary-layer profiles spaced 1 mm apart in span at $x/c = 0.25$. $Re_c = 2.4 \times 10^6$, [48|8] roughness. 306

5.213 Spanwise array of 100 boundary-layer profiles spaced 1 mm apart in span at $x/c = 0.30$. $Re_c = 2.4 \times 10^6$, [48|8] roughness. 307

5.214 Spanwise array of 100 boundary-layer profiles spaced 1 mm apart in span at $x/c = 0.35$. $Re_c = 2.4 \times 10^6$, [48|8] roughness. 308

5.215 Spanwise array of 100 boundary-layer profiles spaced 1 mm apart in span at $x/c = 0.40$. $Re_c = 2.4 \times 10^6$, [48|8] roughness. 309

Figure Page

5.216 Spanwise array of 100 boundary-layer profiles spaced 1 mm apart in span at $x/c = 0.45$. $Re_c = 2.4 \times 10^6$, [48|8] roughness. 310

5.217 Spanwise array of 100 boundary-layer profiles spaced 1 mm apart in span at $x/c = 0.50$. $Re_c = 2.4 \times 10^6$, [48|8] roughness. 311

5.218 Spanwise array of 100 boundary-layer profiles spaced 1 mm apart in span at $x/c = 0.55$. $Re_c = 2.4 \times 10^6$, [48|8] roughness. 312

5.219 Spanwise array of 100 disturbance profiles spaced 1 mm apart in span at $x/c = 0.05$. $Re_c = 2.4 \times 10^6$, [48|8] roughness. 313

5.220 Spanwise array of 100 disturbance profiles spaced 1 mm apart in span at $x/c = 0.10$. $Re_c = 2.4 \times 10^6$, [48|8] roughness. 314

5.221 Spanwise array of 100 disturbance profiles spaced 1 mm apart in span at $x/c = 0.15$. $Re_c = 2.4 \times 10^6$, [48|8] roughness. 315

5.222 Spanwise array of 100 disturbance profiles spaced 1 mm apart in span at $x/c = 0.20$. $Re_c = 2.4 \times 10^6$, [48|8] roughness. 316

5.223 Spanwise array of 100 disturbance profiles spaced 1 mm apart in span at $x/c = 0.25$. $Re_c = 2.4 \times 10^6$, [48|8] roughness. 317

5.224 Spanwise array of 100 disturbance profiles spaced 1 mm apart in span at $x/c = 0.30$. $Re_c = 2.4 \times 10^6$, [48|8] roughness. 318

5.225 Spanwise array of 100 disturbance profiles spaced 1 mm apart in span at $x/c = 0.35$. $Re_c = 2.4 \times 10^6$, [48|8] roughness. 319

5.226 Spanwise array of 100 disturbance profiles spaced 1 mm apart in span at $x/c = 0.40$. $Re_c = 2.4 \times 10^6$, [48|8] roughness. 320

5.227 Spanwise array of 100 disturbance profiles spaced 1 mm apart in span at $x/c = 0.45$. $Re_c = 2.4 \times 10^6$, [48|8] roughness. 321

5.228 Spanwise array of 100 disturbance profiles spaced 1 mm apart in span at $x/c = 0.50$. $Re_c = 2.4 \times 10^6$, [48|8] roughness. 322

5.229 Spanwise array of 100 disturbance profiles spaced 1 mm apart in span at $x/c = 0.55$. $Re_c = 2.4 \times 10^6$, [48|8] roughness. 323

5.230 Stationary crossflow mode shapes for $Re_c = 2.4 \times 10^6$ and [48|8] roughness. 324

5.231 Total disturbance amplitude and relative N-factor for $Re_c = 2.4 \times 10^6$ and [48|8] roughness. 325

Figure Page

5.232 Total disturbance amplitude for $Re_c = 2.4 \times 10^6$ and [k|8] roughness. . 326

5.233 Spanwise hot-wire scan at $x/c = 0.05$ and $Y = 0.45$ mm. $Re_c = 2.4 \times 10^6$, [48|8] roughness. 327

5.234 Spanwise hot-wire scan at $x/c = 0.10$ and $Y = 0.65$ mm. $Re_c = 2.4 \times 10^6$, [48|8] roughness. 328

5.235 Spanwise hot-wire scan at $x/c = 0.15$ and $Y = 0.75$ mm. $Re_c = 2.4 \times 10^6$, [48|8] roughness. 329

5.236 Spanwise hot-wire scan at $x/c = 0.20$ and $Y = 0.75$ mm. $Re_c = 2.4 \times 10^6$, [48|8] roughness. 330

5.237 Spanwise hot-wire scan at $x/c = 0.25$ and $Y = 0.70$ mm. $Re_c = 2.4 \times 10^6$, [48|8] roughness. 331

5.238 Spanwise hot-wire scan at $x/c = 0.30$ and $Y = 0.80$ mm. $Re_c = 2.4 \times 10^6$, [48|8] roughness. 332

5.239 Spanwise hot-wire scan at $x/c = 0.35$ and $Y = 0.90$ mm. $Re_c = 2.4 \times 10^6$, [48|8] roughness. 333

5.240 Spanwise hot-wire scan at $x/c = 0.40$ and $Y = 0.90$ mm. $Re_c = 2.4 \times 10^6$, [48|8] roughness. 334

5.241 Spanwise hot-wire scan at $x/c = 0.45$ and $Y = 1.0$ mm. $Re_c = 2.4 \times 10^6$, [48|8] roughness. 335

5.242 Spanwise hot-wire scan at $x/c = 0.50$ and $Y = 0.90$ mm. $Re_c = 2.4 \times 10^6$, [48|8] roughness. 336

5.243 Spanwise hot-wire scan at $x/c = 0.55$ and $Y = 0.80$ mm. $Re_c = 2.4 \times 10^6$, [48|8] roughness. 337

5.244 Power spectral density of constant-Y scan at $x/c = 0.05$ and $Y = 0.45$ mm. $Re_c = 2.4 \times 10^6$, [48|8] roughness. 338

5.245 Power spectral density of constant-Y scan at $x/c = 0.10$ and $Y = 0.65$ mm. $Re_c = 2.4 \times 10^6$, [48|8] roughness. 339

5.246 Power spectral density of constant-Y scan at $x/c = 0.15$ and $Y = 0.75$ mm. $Re_c = 2.4 \times 10^6$, [48|8] roughness. 340

5.247 Power spectral density of constant-Y scan at $x/c = 0.20$ and $Y = 0.75$ mm. $Re_c = 2.4 \times 10^6$, [48|8] roughness. 341

Figure Page

5.248 Power spectral density of constant-Y scan at $x/c = 0.25$ and $Y = 0.70$ mm. $Re_c = 2.4 \times 10^6$, [48|8] roughness. 342

5.249 Power spectral density of constant-Y scan at $x/c = 0.30$ and $Y = 0.80$ mm. $Re_c = 2.4 \times 10^6$, [48|8] roughness. 343

5.250 Power spectral density of constant-Y scan at $x/c = 0.35$ and $Y = 0.90$ mm. $Re_c = 2.4 \times 10^6$, [48|8] roughness. 344

5.251 Power spectral density of constant-Y scan at $x/c = 0.40$ and $Y = 0.90$ mm. $Re_c = 2.4 \times 10^6$, [48|8] roughness. 345

5.252 Power spectral density of constant-Y scan at $x/c = 0.45$ and $Y = 1.0$ mm. $Re_c = 2.4 \times 10^6$, [48|8] roughness. 346

5.253 Power spectral density of constant-Y scan at $x/c = 0.50$ and $Y = 0.90$ mm. $Re_c = 2.4 \times 10^6$, [48|8] roughness. 347

5.254 Power spectral density of constant-Y scan at $x/c = 0.55$ and $Y = 0.80$ mm. $Re_c = 2.4 \times 10^6$, [48|8] roughness. 348

5.255 Single-mode disturbance amplitude and N-factors. $Re_c = 2.4 \times 10^6$, [48|8] roughness. 349

5.256 Total and single-mode disturbance amplitude and N-factors. $Re_c = 2.4 \times 10^6$, [48|8] roughness. 350

NOMENCLATURE

A	disturbance amplitude
A_o	reference disturbance amplitude
C	= 1.83 m, airfoil streamwise chord
C_p	pressure coefficient
C_{p_2}	unswept pressure coefficient
C_{p_3}	swept pressure coefficient
C_T	hot-wire temperature-compensation coefficient
c	= 1.29 m, airfoil normal chord
E	hot-wire anemometer output voltage
f	frequency [Hz]
f_c	Nyquist critical frequency [Hz]
k	roughness height [m]
M	Mach number; number of FFT averages
m	mode number
N	$= \ln(A/A_o)$, amplification factor; number of samples
p	static pressure [Pa]
p_∞	freestream static pressure [Pa]
Re_c	$= U_\infty C/\nu$, streamwise chord Reynolds number
Re_k	$= U(k)k/\nu$, roughness Reynolds number
Re_θ	$= u_t\theta/\nu$, attachment-line Reynolds number
S	length of a data set; spanwise extent of a hot-wire scan [m]
T	temperature [°C]

U	$= (u^2 + w^2)^{1/2} = U(y)$, total velocity magnitude [m/s]
U_e	boundary-layer edge velocity along X axis [m/s]
U_∞	freestream velocity along X axis [m/s]
u, v, w	velocity components in global (X, Y, Z) coordinates [m/s]
u', v', w'	disturbance velocity components in (X, Y, Z) coordinates [m/s]
u_n, v_n, w_n	velocity components in model-oriented (x, y, z) coordinates [m/s]
u_t, v_t, w_t	velocity components in boundary-layer (x_t, y_t, z_t) coordinates [m/s]
X, Y, Z	global test-section coordinates: X is in the streamwise direction, Y is normal to test-section front wall, Z is unswept spanwise coordinate (positive down)
x, y, z	model-oriented coordinates: x is chordwise (normal to leading edge), y is normal to chord line, z is spanwise (parallel to leading edge)
x_t, y_t, z_t	boundary-layer coordinates: x_t is tangent to inviscid streamline, y_t is normal to model surface, z_t is crossflow direction
α	airfoil angle of attack
β	boundary-layer hot-wire support rotation angle
Δ	change or difference, e.g., ΔT is a temperature difference
Δ_s	sampling interval
Δf	spectral frequency resolution
$\Delta\lambda$	spectral wavelength resolution
δ_F	flap deflection angle
Λ	sweep angle
λ	wavelength [m]
λ_s	$= \lambda_z$
λ_z	wavelength measured in swept span direction [m]

ν	kinematic viscosity [m^2/s]
θ	momentum thickness [m]
ρ	density [kg/m^3]
σ	boundary-layer hot-wire probe rotation angle about longitudinal axis
ξ, ζ, z	body-intrinsic coordinates: ξ is chordwise and tangent to airfoil surface, ζ is normal to airfoil surface, z is spanwise (parallel to leading edge)

CHAPTER 1

Introduction

1.1 Background and Motivation

Boundary-layer transition from laminar to turbulent flow is arguably one of the most important unsolved problems in fluid mechanics. Understanding the processes that influence boundary-layer transition can not only lead to accurate transition prediction, but can eventually lead to techniques for transition control. The practical applications of this are virtually endless. Separation and stall characteristics of airfoils, heat transfer of turbine blades, subsonic and supersonic vehicle performance, and skin-friction drag prediction are just a few of the many engineering problems that rely strongly on the state of the boundary layer. Accurate transition-prediction techniques will allow better modeling of any of these problems. In addition, transition-control techniques can have a profound impact on these types of problems. If laminar flow could be maintained over the wings of a modern transport aircraft, an estimated 25% reduction in fuel consumption would be achieved (Pfenninger 1977; Thomas 1985; Saric 1994b).

In light of the enormous potential gains that could be attained, much research has been focused on boundary-layer stability and transition. Significant advances

have been made in Laminar Flow Control (LFC) projects. Active LFC methods such as wall suction, surface heating in water, and surface cooling in gases, as well as passive methods such as careful shaping of the pressure distribution, can be used to delay transition. Despite these advances and numerous theoretical and experimental studies, no mathematical model exists at this time that can accurately predict the transition Reynolds number for Blasius flow over a flat plate (Saric 1994c).

1.1.1 Boundary-Layer Transition

The complicated process of boundary-layer transition is usually described as occurring in three stages. The first stage, which involves the entrainment of disturbances into the boundary layer, is called *receptivity* (Morkovin 1969). In the receptivity stage, external disturbances such as freestream acoustic and vortical disturbances, surface roughness, and surface vibration enter the boundary layer as small fluctuations of the basic state. This stage is the least understood in the process, but is extremely important because it provides the initial conditions of amplitude, frequency, and phase for the instability waves that eventually lead to transition. The receptivity process is further complicated by factors such as Reynolds number, pressure gradient, sweep, and surface curvature. Although several instability mechanisms may exist in the boundary layer, different combinations of the above factors can lead to very different observed instability modes.

The second stage of the transition process involves the initial growth of the small disturbances in the boundary layer and is modeled by *linear stability theory*. Linearized, unsteady, disturbance equations derived from the nonlinear Navier-Stokes equations are solved to determine the growth of the unstable disturbances. For incompressible, parallel-flow basic states, these equations reduce to the well-known Orr-Sommerfeld equation, which has been used very successfully to model several types of disturbances, including Tollmien-Schlichting (T-S) instabilities. Of the three stages,

this phase has been the focus of most study and is considered to be well understood (Saric 1992b).

The final stage in the transition process occurs when the disturbances grow large enough to interact with each other. Nonlinear interactions can distort the basic-state boundary layer, leading to secondary inflectional instabilities that grow rapidly and lead to transition. Although it is generally believed that transition occurs very quickly once nonlinear interactions develop, Reibert et al. (1996) show evidence of extended regions of nonlinear effects starting well before the onset of transition.

For most cases, this three-stage representation of the transition process is satisfactory. Under some circumstances with very large initial disturbance amplitudes, however, the second phase is bypassed and nonlinear effects and transition occur immediately. This bypass process is not well understood, and is discussed by Morkovin (1969, 1993).

1.1.2 Transition Prediction

Because the second phase of the transition process is the best understood, most transition-prediction schemes are formulated based on linear theory. The most widely used technique is the e^N method developed by Smith and Gamberoni (1956) and van Ingen (1956). In this method, the growth rates computed by the linear stability equations are integrated starting from the neutral stability point to the transition location (determined experimentally) to obtain the amplitude ratio A/A_o. The natural log of this ratio is called the amplification factor N. Detailed reviews of this method are given by Arnal (1984, 1992, 1994), Saric (1992b, 1994c), and Reed et al. (1996). Basically, experimental data and linear stability results are compared to obtain the corresponding N-factor at transition. This transition N-factor can then be used to predict where transition will occur in flow conditions for which experimental data are unavailable.

In general, the e^N method works reasonably well (within some error), for systems with *similar* geometries and disturbance conditions. Blindly applying this method to flows for which no comparative experimental data are available, however, can be outright dangerous (Saric 1994c). Linear theory cannot account for initial conditions, thus the e^N method completely ignores the receptivity process. Plus, this method does not account for any nonlinear interactions. For flows in which these effects are important, such as crossflow-dominated boundary layers, the e^N method fails. For example, Radeztsky et al. (1993a) and Reibert (1996a) show that in swept-wing flows the transition location and corresponding transition N-factor can be changed dramatically if the surface roughness conditions are changed. Reibert et al. (1996) show that nonlinear effects can cause amplitude saturation in swept-wing flows, yielding extended regions of constant N-factor well before transition occurs.

Thus, any generally applicable transition-prediction scheme needs to consider all three stages of the transition process. At this time, however, no such model exists.

1.2 Swept-Wing Flows and Crossflow Instability

This experiment concerns the instability mechanisms found in three-dimensional boundary layers in swept-wing flows. Four types of instabilities have been recognized in these flows: attachment line, streamwise, centrifugal, and crossflow. The attachment-line instability results either from a basic instability of the attachment-line flow or from the propagation of turbulent disturbances along the leading edge, and is typically found on swept wings with a large leading-edge radius (Poll 1979, 1984, 1985; Hall et al. 1984; Hall and Malik 1986). The streamwise instability is associated with the chordwise velocity component and is similar to the familiar T-S instability found in two-dimensional flows. This instability mechanism usually occurs in zero or slightly unfavorable-pressure-gradient regions. Centrifugal instabilities ap-

pear as Görtler vortices and may develop over concave regions of the surface (Floryan and Saric 1982; Floryan 1991; Benmalek and Saric 1994; Saric 1994a). Finally, the crossflow instability results from the combined effects of wing sweep and pressure gradient. Of these four instability mechanisms, any number and any combination may appear in the boundary layer depending upon the discussed influential factors.

The focus of this experiment is the crossflow instability that occurs in strong favorable-pressure-gradient regions of swept wings. This combination of sweep and pressure gradient results in highly curved streamlines, with the inviscid streamlines being first deflected inboard near the leading edge and then outboard in the pressure-recovery region. Because the fluid momentum is lower near the wall, these deflections are greater within the boundary layer. This results in a velocity component within the boundary layer parallel to the surface and perpendicular to the inviscid streamlines. This component of the flow is called the *crossflow* velocity. The crossflow velocity must satisfy the no-slip condition at the wall and asymptotically reach zero at the boundary-layer edge, thus the crossflow profile contains an inflection point. This inflectional profile is subject to a dynamic instability, resulting in unstable co-rotating crossflow vortices aligned roughly in the streamwise direction.

The crossflow instability differs from other instability mechanisms such as the T-S disturbance in that it shows amplification of both stationary and traveling waves. In most crossflow experiments, both types of waves are present, but one usually dominates and controls transition. Linear theory predicts that the traveling disturbances are more highly amplified, however many experiments show dominance of the stationary crossflow waves. Whether the stationary or traveling waves dominate is directly related to the receptivity process. Stationary waves are found to be dominant in low-disturbance environments, while traveling waves dominate transition in high-turbulence environments (Müller and Bippes 1989; Bippes 1990, 1991; Bippes 1991).

Flight conditions are more like the low-disturbance environment, so the stationary waves are considered to be more important. In light of this, the stationary crossflow disturbance is the focus of this experiment.

One of the most interesting features of the stationary waves is that, although the (v', w') disturbances of the waves are typically very weak, experiments show evidence of strong nonlinear effects (Dagenhart et al. 1989, 1990; Bippes and Nitschke-Kowsky 1990; Bippes et al. 1991; Radeztsky et al. 1994; Reibert et al. 1996). Because the stationary waves are fixed with respect to the model and are approximately aligned with the inviscid streamline, the stationary structure "acts" on the same fluid (approximately). The integrated effect of the convection of high-momentum fluid toward the surface where $v' < 0$ and low-momentum fluid away from the surface where $v' > 0$ produces large u' distortions in the streamwise boundary-layer profile. The end result is a significant change of the basic-state flow and corresponding nonlinear effects.

Another interesting feature of the stationary crossflow waves is the development of secondary instabilities. The stationary structure produces strong, spatially varying u' distortions, resulting in an alternating pattern of accelerated, inflected, and decelerated mean boundary-layer profiles. The inflected profiles are subject to a high-frequency secondary instability that grows quickly and leads to local breakdown (Kohama et al. 1991). This local breakdown appears as a saw-toothed transition pattern.

1.3 Review of Recent Research

Significant progress has been made in the understanding of the transition process in three-dimensional boundary layers, but there are still many aspects that are not well understood. Although numerous theoretical efforts have been made to shed light on this subject, there have been relatively few detailed experiments for validation.

The combined effects of complicated geometries, nonlinear interactions, and multiple instability mechanisms has made this a difficult problem to master.

1.3.1 Experimental Investigations

Modern experimental investigations of the crossflow instability mechanism start with Saric and Yeates (1985), Poll (1985), and Michel et al. (1985). Saric and Yeates used a swept flat-plate model with a favorable pressure gradient generated by a wall bump to study crossflow waves. This investigation provided early experimental evidence of nonlinear effects, in that the first superharmonic of the fundamental disturbance was observed. Experiments by Poll (1985) used a cylinder with a variable sweep angle, and Michel et al. (1985) used a high-aspect-ratio swept airfoil to study crossflow.

The DLR experiments in Germany provide many important results concerning the role of receptivity and nonlinear effects in the crossflow problem. These results are found in Nitschke-Kowsky and Bippes (1988), Bippes (1990, 1991), Bippes and Müller (1990), Bippes and Nitschke-Kowsky (1990), Müller (1990), Müller et al. (1990), Bippes et al. (1991), and Deyhle et al. (1993). The most recent results are presented in Lerche and Bippes (1995) and Deyhle and Bippes (1996). In these experiments, as in most crossflow studies, both traveling and stationary crossflow waves are measured. The importance of each type in terms of the transition process is found to be dependent upon the freestream turbulence. In high-turbulence environments, it was found that the traveling waves dominate and control transition, while the stationary disturbances are suppressed. However, in low-turbulence environments, the stationary crossflow waves show large growth rates and dominate transition.

These experiments show that the initial growth rates of the stationary and traveling disturbances agree qualitatively with linear theory. However, a nonlinear saturation is observed at higher amplitudes. The traveling crossflow waves show a spanwise amplitude modulation, indicating nonlinear interactions with the stationary distur-

bance. Another important result of the DLR experiments is that the pattern of stationary vortices is fixed relative to the model. This indicates that the stationary disturbance is sensitive to surface roughness rather than freestream disturbances.

In the swept-wing experiments of Arnal et al. (1984), the stationary crossflow wavelength evolves in the chordwise direction, with longer-wavelength disturbances appearing downstream. In order to accommodate the larger wavelengths, individual vortices merge or vanish. Later crossflow experiments by Arnal's group are presented in Arnal and Juillen (1987) and Arnal et al. (1990).

The experiments at Arizona State University represent a comprehensive study of the stationary crossflow instability. The design of these experiments is reviewed in Saric et al. (1990). A low-aspect-ratio 45°-swept wing is used in a low-turbulence wind tunnel to generate stationary-crossflow-wave-dominated transition. The findings of the original experiments are found in Dagenhart et al. (1989, 1990) and Dagenhart (1992). In these experiments, stationary crossflow growth rates and wavelengths were found to be smaller than predicted by linear theory. In addition, unlike the results of Arnal et al. (1984), a fixed-wavelength vortex pattern is observed.

The sensitivity of stationary crossflow waves to roughness-induced initial conditions is studied by Radeztsky et al. (1993a). In these experiments, a single micron-sized roughness element applied near the leading edge causes early local transition and significantly decreases the transition Reynolds number. Later experiments by Radeztsky et al. (1994) continue the sensitivity study under conditions where natural stationary crossflow amplitudes are not measurable. Spanwise arrays of artificial roughness elements are applied near the leading edge to control the disturbance wavelength. Even under this condition of very weakly amplified waves, agreement with linear theory is not observed. It was initially thought that the large roughness elements ($Re_k \approx 100$) necessary to excite the stationary instability were producing local

nonlinearities and causing the discrepancy from linear theory. Very recent computational results (Haynes and Reed 1996), however, show that the discrepancy is due to the lack of curvature terms in the linear stability analysis.

Later stationary crossflow wave experiments at ASU are presented in Reibert et al. (1996) and Reibert (1996a). This work again studies the sensitivity of stationary crossflow waves to roughness-induced initial conditions, but the swept airfoil is configured as it was for Dagenhart (1992) and significant crossflow is generated even under natural surface roughness conditions. Similar to Radeztsky et al. (1994), spanwise arrays of artificial roughness elements ($Re_k = 0.1$) are used to control the stationary crossflow wavelength and produce uniform crossflow waves. The results show strong nonlinear interactions and amplitude saturation for various roughness spacings and roughness heights. It is interesting that for a fixed roughness spacing, the disturbances tend to grow to a constant saturation amplitude, regardless of the initial roughness height. In addition, nonlinear interactions are observed over extended regions well before the onset of transition.

In other experiments at ASU, Kohama et al. (1991) identified a high-frequency secondary instability that occurs when the boundary layer is dominated by the stationary crossflow disturbance. This instability appears locally where the mean streamwise boundary-layer profile has been inflected by the stationary disturbance. Once present, this secondary instability grows rapidly and leads to local breakdown and transition. Thus, the stationary crossflow wave provides the mechanism that eventually leads to transition in low-turbulence environments.

1.3.2 Theoretical Investigations

The experimental investigations all indicate that traditional linear stability theory is not sufficient to accurately model crossflow-dominated flows. In light of this, significant theoretical and computational efforts have been conducted in recent years to

improve transition prediction. For crossflow-dominated flows, these efforts consider nonparallel effects, streamline and surface curvature, nonlinear effects, and receptivity issues. Radeztsky (1994) provides a general overview of these recent efforts. The most recent advances in stability and transition modeling have been from direct numerical simulations (DNS) and the parabolized stability equations (PSE). These techniques allow more accurate modeling by accounting for nonparallel and nonlinear effects and the subsequent basic-state distortions.

DNS have produced several important results related to the stationary crossflow disturbance. Recent achievements come from Reed and Lin (1987) and Lin (1992), who conducted numerical simulations for swept-wing flows similar to the experiments at ASU. Meyer and Kleiser (1988, 1990) performed numerical simulations to investigate interactions between the stationary and traveling crossflow disturbances. Nonlinear saturation of the stationary disturbances is observed, and comparisons are made with the experiments of Müller and Bippes (1989). More recently, Wintergerste and Kleiser (1995) used DNS to study crossflow-vortex breakdown in the nonlinear final phase of transition.

The PSE show definite promise of being an accurate and extremely efficient method for boundary-layer stability analysis. A detailed description of the PSE is given by Herbert (1994). Basically, the PSE formulation yields an initial-boundary-value problem that can be solved with very efficient marching techniques. Nonparallel effects and nonlinear terms can be retained, allowing accurate modeling of flows where these are important. The PSE, however, do not solve the receptivity problem and rely on specified initial conditions. Recent applications of the PSE come from Wang et al. (1994), who predicted nonlinear amplitude saturation for both the stationary and traveling crossflow disturbances for the swept-wing experiments at ASU. Stuckert et al. (1993), Schrauf et al. (1995), and Haynes and Reed (1996) apply the PSE

to study stability and transition in swept-wing flows. More recently, comparisons between stationary crossflow stability experiments at ASU and nonlinear PSE calculations show excellent agreement (Reibert 1996a; Haynes 1996).

1.4 Experimental Objectives

As revealed in this chapter, initial conditions and nonlinear effects are extremely important in crossflow-dominated flows. Although significant progress has been made (both experimentally and theoretically) in the understanding of this instability mechanism, several questions still remain unanswered. Thus, the goals of this study are (1) to obtain more understanding of the fundamental physics of the stationary crossflow instability in low-turbulence environments, and (2) to contribute to the currently existing experimental database for theoretical code development.

Specifically, this experiment builds upon the earlier study by Reibert (1996a) at the ASU Unsteady Wind Tunnel on the effects of distributed surface roughness on the nonlinear development of stationary crossflow waves. In light of this, the airfoil model and test conditions are selected to match those of the earlier experiment to allow direct comparisons, and detailed measurements are taken to verify the existence of similar conditions. As in the previous experiment, stationary vortices with fixed initial conditions are introduced by applying spanwise arrays of circular roughness elements near the attachment line. In the work of Reibert (1996a), the elements were applied such that the spacing was equal to or a multiple of the most unstable wavelength (according to linear theory) . The focus of this experiment is to study the resulting stationary disturbance growth when the roughness element spacing is not equal to or a multiple of the most amplified wavelength.

The measurement objectives are to provide detailed information about the stationary crossflow disturbance. Boundary-layer velocity measurements will reveal the

structure of the stationary vortices and provide total disturbance mode shapes and amplitudes. Spanwise velocity traces will allow individual crossflow modes to be separated and individually tracked.

1.5 Outline

The following chapters describe the details of the current experiment. Chapter 2 describes the ASU Unsteady Wind Tunnel facility, including discussion about instrumentation and data-acquisition equipment. Design aspects of the experiment and test-condition selection are discussed in chapter 3. Chapter 4 describes the measurement techniques used to acquire and process data, as well as calibration methods and tunnel control. The results of the experiment are presented and discussed in chapter 5. These include basic-state measurements, total and individual-mode stationary-crossflow disturbance amplitudes, and transition location data. Chapter 6 presents the conclusions.

CHAPTER 2

Experimental Facility

2.1 Unsteady Wind Tunnel

This experiment is conducted in the Arizona State University Unsteady Wind Tunnel. This facility is a low-speed, low-turbulence, closed-circuit tunnel which has the ability to generate unsteady flows via a unique double-duct design. The wind tunnel was originally designed and built in 1970 at the National Bureau of Standards (NBS) in Gaithersburg, Maryland by Dr. Philip Klebanoff and calibrated by Dr. James McMichael. In 1984, under the direction of Dr. William Saric, the tunnel was moved to Arizona State University. To improve flow quality and make the tunnel suitable for boundary-layer stability and transition research, significant reconstruction and redesign were conducted. The modified facility became operational in 1987 and is shown in figures 2.1 and 2.2. Saric (1992a) provides a detailed description of the facility, so only key features will be described here.

The Unsteady Wind Tunnel incorporates several design features to produce exceptionally low freestream turbulence levels. The fan section is isolated from the rest of the tunnel by a flexible coupling to reduce transmitted vibrations. Both the motor housing and the test section sit on isolated concrete pads to minimize transmitted vibrations through the building foundation. In addition, the test section and fan are

separated by a sound-insulated wall. Inside the tunnel, steel turning vanes with a 50 mm chord and 40 mm spacing are placed in all four corners. At the beginning of the test leg, the flow passes through a honeycomb wall (item 'b' in figure 2.1) with a 6.35 mm cell size to reduce large-scale disturbances. Immediately following the honeycomb are seven tightly stretched stainless steel screens each separated by 230 mm. The first five screens have an open-area ratio of 0.7, and the last two are seamless with an open-area ratio of 0.65. Following the screens is a 1.6 m long settling chamber where viscosity naturally damps out remaining small-scale disturbances. The contraction cone has a 5.33:1 contraction ratio, and its walls follow a fifth-order polynomial to eliminate curvature discontinuities at the entrance and exit.

The Unsteady Wind Tunnel fan is driven by a 150 hp, variable-speed DC motor. The single-stage axial fan is 1.83 m in diameter and consists of nine adjustable-pitch blades and eleven fixed stators. The motor is controlled by a Mentor II digital DC drive, which is interfaced to the wind-tunnel computer system for automated speed control (discussed later). For this experiment, test-section velocities up to 35 m/s are attainable.

As mentioned earlier, unsteady flows are achieved via a unique double-duct design. Air is diverted from the primary duct (i.e., test section) into the secondary duct by opening a trap door located in the plenum. A vertical array of rotating shutters is located in each duct just upstream of the pressure-recovery region (see figure 2.2). These shutters rotate 90° out of phase, creating up to 100% velocity fluctuations at 25 Hz in the test section, while minimizing unsteady loading on the fan. For steady operation, as in this experiment, the shutters in the primary duct are locked open, and the secondary duct shutters are closed.

The Unsteady Wind Tunnel has two interchangeable 1.4 m × 1.4 m × 5 m test sections that can be mounted on casters for easy movement. As mentioned earlier,

the test section is connected to the rest of the tunnel only with a flexible coupling. Thus, changing experiments simply involves removing this coupling, rolling out the installed test section, and rolling the second one in place. The uninstalled test section is stored in the work area, allowing another experiment to be prepared while one is in the tunnel.

2.2 Traverse and Sting

Hot-wire probes are accurately positioned within the test section by a computer-controlled, three-dimensional traverse system. Figures 2.3 and 2.4 show front and side views of the traverse carriage. This carriage is mounted on two stainless steel Thompson rails for movement in the X (streamwise) direction. All main components of the traverse (drives, leadscrews, rails, and carriage) are mounted outside of the test section. The only component that penetrates into the flow is the instrumentation sting. This is extremely important when conducting stability experiments, as internal traverse components can cause local pressure gradients and global flowfield adjustments that can considerably alter stability measurements (Saric 1990). The instrumentation sting mounts to an aluminum sub-carriage (item 'd' in figures 2.3 and 2.4), which moves in the Y (wall-normal) direction along two guide rails via a high-resolution lead screw and microstepping motor. In the Z (vertical) direction, two microstepping motors, each attached to a vertical lead screw, drive the entire Y carriage along two vertical guide rails (see figure 2.3).

The sting extends into the test section through a slotted plexiglass panel contained within the test-section wall. The slot runs in the streamwise direction, which allows for X moves. A zipper running along the slot automatically opens and closes around the sting whenever an X move occurs, minimizing any flow through the slotted panel. The panel slides vertically within the test-section wall to allow for Z moves. Two

Table 2.1: Traverse system specifications.

Direction	X	Y	Z
Total Travel	1.25 m	100 mm	175 mm
Minimum Step	12 μm	0.7 μm	1.3 μm

microstepping motors and lead screws are coordinated to move the panel when the Y carriage is moved vertically. The entire system is enclosed by an air-tight plexiglass outer wall, which minimizes any transverse loading on the slotted window.

The precision lead screws are all driven by Compumotor microstepping motors, and digital position feedback is provided by 1000-line Renco optical encoders on all axes. A Compumotor four-axis digital motion controller coordinates all traverse movements. Table 2.1 shows the traverse system capabilities.

The instrumentation sting is shown in figure 2.5, and is the same one used in previous swept-wing experiments at the Unsteady Wind Tunnel. The sting consists of two parts: a streamlined carbon-composite section and an aluminum mounting strut. Two Dantec probe mounts are attached to the composite section of the sting for simultaneous freestream and boundary-layer measurements. The boundary-layer probe holder rotates about the Z axis to allow for accurate positioning of the hot wire in the thin boundary layer.

2.3 Computer Systems

Automation of tunnel control and measurement procedures is considered standard practice at the Unsteady Wind Tunnel. Many tasks (tunnel control, hot-wire calibration, data acquisition, etc.) are standardized. This improves the overall operational efficiency at the facility and minimizes any subjectivity introduced by the researcher. Several computers are available for these tasks and oversee wind-tunnel operations.

A Sun SPARCstation 20 serves as the primary data-acquisition and tunnel-control

computer. This workstation has two 60 MHz SuperSPARC+ processors, each rated at 167 MIPS and 36.6 MFLOPS, and 64 MB of RAM. The system consists of a 20 inch monitor with 1152 × 900 resolution, a 3.15 GB hard drive, and a 5 GB tape drive. A National Instruments GPIB interface (model GPIB-SPRC-B) is installed for communication with external data-acquisition equipment. The SPARCstation runs the Solaris version 2.4 operating system, which provides a multiuser, multitasking environment. This is ideally suited for the facility as it allows simultaneous operation of tunnel control, data acquisition, analysis, and program development.

A PC compatible ACT486 with a 50 MHz 80486DX processor serves as a back-up data-acquisition computer. This system has 20 MB of RAM, a 17 inch monitor with 1024 × 768 resolution, a 425 MB hard disk, and a 2 GB tape drive. This machine is also equipped with a National Instruments model AT-GPIB/TNT GPIB interface. The PC runs the Santa Cruz Operation's Open Desktop Server System version 2.0, which provides a multiuser, multitasking UNIX environment.

Additional workstation capabilities are provided by a DECstation 5000, which uses a 25 MHz R3000 processor. This unit is equipped with 16 MB of RAM, a 19 inch grayscale monitor, 2.43 GB of hard-drive space, and a 100 MB tape drive. The DECstation runs the Ultrix operating system, Digital's UNIX based on BSD.

General-purpose computing is done on a Macintosh Quadra 650, which runs on a 33 MHz MC68040 processor and has 24 MB of RAM. The system includes a 17 inch display with 832 × 624 resolution, a 230 MB hard drive, and an 8 GB tape drive. The Quadra runs System 7.5.5 of the Macintosh OS. Several applications are installed, including word-processing, drafting, and spreadsheet software.

Printed output is provided by two printers dedicated to the wind tunnel. High-quality grayscale output comes from a Hewlett-Packard HP4M 600 dpi PostScript laser printer. In addition, a Hewlett-Packard 1200C/PS 300 dpi PostScript inkjet

printer provides color output.

2.4 Instrumentation

Pressure and temperature measurements near the test section entrance are used to determine freestream flow conditions. A 10 torr MKS model 698A differential pressure transducer connected to a Pitot-static tube measures dynamic pressure. The test-section static pressure is measured by a 1000 torr absolute pressure transducer (MKS model 390HA) connected to the static side of the Pitot-static tube. The differential and absolute pressure transducers are connected to MKS 670 and MKS 270B signal conditioners, respectively, which each provide visual pressure readouts as well as analog output signals. These analog signals are wired into the data-acquisition system. In addition, the MKS 670 is remotely accessible via a GPIB interface. A second differential pressure transducer and a third signal conditioner (MKS models 398HD and 270B) are available for miscellaneous differential pressure measurements. A thin-film RTD measures the test-section temperature, and its calibrated analog output is sent to the data-acquisition system.

Accurate freestream and boundary-layer velocity measurements are provided by hot-wire anemometry. Two Dantec 55M01 constant-temperature anemometers using 55M10 CTA standard bridges each operate a Dantec 55P15 boundary-layer probe. Each hot-wire probe uses a 5 μm platinum-plated tungsten wire, which is welded across two probe tines separated by 1.25 mm. The tines are offset 3 mm from the probe axis to facilitate measurements within the thin boundary layer. The probes mount into standard 4 mm probe supports which are attached to the instrumentation sting.

AC signals are conditioned with a two-channel Stewart model VBF44 filter. Each channel provides several filter-response options for optimal filtering in the time or

frequency domain with cutoffs ranging from 1 Hz to 250 kHz. Pre- and post-filter gains provide up to 70 dB total gain for each channel. Remote operation of the filter is available via a RS-232 interface.

Analog voltage signals are digitized with two IOtech ADC488/8SA analog-to-digital (A/D) converters. Each unit provides 16-bit A/D conversion and simultaneous sample-and-hold capability for up to eight differential input channels. When connected in a master/slave configuration, the two units provide for up to 16 channels of simultaneous A/D conversion. Each channel has an independently programmable voltage range, which varies from ± 1 to ± 10 volts. Sampling rates are discretely variable from 0.2 Hz to 100 kHz. A GPIB interface provides for high-speed communication with the data-acquisition computer.

CHAPTER 3

Experimental Design

The chapter explains the design and setup used in this experiment. A description of the test model and its configuration within the test section is given. The test conditions are discussed and selected.

3.1 Swept-Wing Model

3.1.1 Airfoil

This experiment uses the existing NLF(2)-0415 airfoil (Somers and Horstmann 1985), which has been used at the Unsteady Wind Tunnel in several previous swept-wing experiments (Dagenhart et al. 1989, 1990; Saric et al. 1990; Kohama et al. 1991; Radeztsky et al. 1993a, 1994; Reibert et al. 1996). This airfoil is actually designed for laminar flow in an unswept configuration for application on general aviation aircraft. Through careful shaping of the airfoil surface, the favorable pressure gradient extends back to $x/c = 0.71$ and is designed to naturally maintain laminar flow as long as possible by minimizing growth of the Tollmien-Schlichting (T-S) instability. Figure 3.1 shows the airfoil shape and design pressure distribution at 0° angle of attack.

In this and past experiments at ASU, the airfoil is swept 45°, creating a nearly ideal situation for studying the crossflow and/or T-S instabilities in three-dimensional boundary layers. The small leading-edge radius of the NLF(2)-0415 eliminates the

attachment-line instability mechanism for the moderate Reynolds number range of the Unsteady Wind Tunnel. For $Re_c = 2.4 \times 10^6$ and $\alpha = -4°$, the attachment-line Reynolds number $Re_\theta = 44$. In addition, the Görtler instability is not present because there are no concave regions on the upper surface of the model. At small positive angles of attack, the upper surface pressure distribution is flat or slightly decelerated, creating strong growth of T-S disturbances. At $\alpha = 0°$, the weakly favorable pressure gradient back to $x/c = 0.71$ yields both slightly amplified crossflow and T-S waves. At small negative angles of attack, the pressure gradient is even more favorable, creating strong crossflow while suppressing growth of the T-S instability. Additional control over the pressure distribution is available from a 20%-chord trailing-edge flap with a $\pm 20°$ maximum deflection angle. A detailed review of the operating range of the NLF(2)-0415 is given by Dagenhart (1992).

3.1.2 Test Section

The NLF(2)-0415 model is installed vertically in a test section dedicated to this experiment and is supported by a shaft and thrust bearing. The shaft axis runs parallel to the leading edge and is located at $x/c = 0.25$. The thrust bearing is mounted to the test-section floor located 610 mm from the front wall and 760 mm from the back wall. This off-center placement keeps the model away from the symmetry plane, which is good experimental practice. This shaft and thrust bearing combination allows the angle of attack of the airfoil to be rotated about the 1/4-chord line from $-4°$ to $+4°$ in $1°$ increments.

One of the goals of this experiment is to provide a detailed experimental database for theoretical code development. Because the model is not small compared to the test section, wall-interference effects cannot be ignored. Therefore, any computation must account for the four test-section walls if meaningful comparisons are to be made. Unfortunately, the effects of the floor and ceiling dramatically complicate

computational efforts because they prevent the use of a spanwise-invariant flowfield assumption. Spanwise invariance of the flowfield is attainable if the swept wing is infinite in span. An infinite-span airfoil not only allows the use of significantly more efficient computational techniques, but it also creates a benchmark configuration for crossflow-instability experiments.

To simulate an infinite span, test-section floor and ceiling end liners are installed that follow the inviscid streamlines for an infinite-span airfoil. The liners used in this experiment are the same ones used by Dagenhart (1992) and Reibert (1996a) for previous studies at $\alpha = -4°$. Figure 3.2 shows the NLF(2)-0415 airfoil and end liners for this configuration.

The thickness of the end liners at the test-section entrance necessitates the addition of liners in the contraction cone. These liners begin at the inflection point of the contraction-cone walls, and follow a 5th-order polynomial to eliminate curvature discontinuities. With the addition of these liners, the contraction ratio changes from 5.33:1 to 6.55:1.

3.2 Test Conditions

As mentioned in chapter 1, this study builds upon the experimental results of Reibert et al. (1996). As a result, several of the test conditions (angle of attack and Reynolds number) are kept the same as those of the previous experiment so that direct comparisons can be made. For those that are changed (roughness configuration), the selected test conditions are based upon questions raised from the previous results.

3.2.1 Angle of Attack

The focus of this experiment is to study the crossflow instability, therefore the angle of attack is set to $-4°$. At $\alpha = -4°$, the C_p distribution (figure 3.3) shows a favorable

pressure gradient from the attachment line to $x/c = 0.71$. Under these conditions, the boundary layer is subcritical to T-S disturbances, leaving transition dominated by the stationary crossflow instability. Early experiments by Dagenhart et al. (1989, 1990) and Kohama et al. (1991), as well as the more recent experiments of Reibert et al. (1996) confirm this.

3.2.2 Reynolds Number

Several factors must be taken into account when selecting a test Reynolds number. If the Reynolds number is too high, wind-tunnel heating effects can be a problem and, more importantly, the transition location will be too far forward to do a detailed study of the disturbance growth. If the Reynolds number is too low, the disturbance growth rates will not be large enough to generate significant crossflow. In this experiment, the chord Reynolds number is selected to be $Re_c = 2.4 \times 10^6$. This represents a good tradeoff between the above factors in that significant growth rates are achieved while minimizing heating effects and extending the laminar-flow region. $Re_c = 2.4 \times 10^6$ is the baseline Reynolds number used by Reibert (1996a).

3.2.3 Roughness Configuration

The primary goal of this experiment is to study the effects of roughness-induced initial conditions on the growth of the *stationary* crossflow disturbances. As mentioned in section 2.1, the Unsteady Wind Tunnel has very low freestream turbulence levels. This minimizes the effects of the *traveling* crossflow waves, which are influenced by freestream disturbances (Bippes and Müller 1990; Müller 1990; Bippes 1991; Deyhle and Bippes 1996). The stationary crossflow waves, on the other hand, are strongly influenced by surface roughness near the attachment line (Radeztsky et al. 1993a, 1994). Therefore, to do an accurate study of the stationary structure, it is critical that the surface-roughness distribution be carefully defined and controlled.

The NLF(2)-0415 airfoil's aluminum surface is finely polished to a near mirror finish. Profilometer measurement of the surface finish (figure 3.4) in the mid-chord region show typical roughness levels of 0.12 μm rms, while near the attachment line, the surface has levels of about 0.25 μm rms. This extremely smooth finish provides ideal conditions for studying roughness-induced stationary crossflow waves.

Initial conditions are carefully controlled by applying roughness elements near the attachment line following the techniques of Radeztsky et al. (1993a) and Reibert et al. (1996). To maintain spanwise invariance, the roughness elements are applied in full-span arrays at $x/c = 0.023$. This chord location maximizes the effects of the roughness and is near the neutral point of the stationary crossflow instability (Radeztsky et al. 1993a). The spanwise spacing of the roughness elements fixes the wavelength of the fundamental crossflow disturbance, allowing the study of different fundamental wavelengths as well as any interactions between the fundamental and harmonic disturbances. In this study, two different roughness spacings are used: 18 mm and 8 mm. The 18 mm spacing is selected because it does not have a harmonic with a 12 mm wavelength, which is most unstable in the absence of artificial roughness according to linear theory. The 8 mm spacing allows the study of the effects of a subcritical ($\lambda_z < 12$ mm) roughness spacing on the stationary crossflow disturbance.

Two different types of roughness elements are used in this experiment. The first type are circular rub-down dots produced by Geographics found on Geotype Geosenior #GS-104 and Geotype Geomini #39 transfer sheets. The dots used have a diameter of 3.7 mm and produce a roughness height of 6 μm when applied to the airfoil surface. This type of dot is stackable for producing larger roughness heights up to a practical limit of 3 to 4 layers. As the number of layers is increased, it becomes exceedingly difficult to maintain a clean, well-defined roughness edge. In this experiment, up to three roughness elements are stacked to produce roughness heights up to

Table 3.1: Roughness Re_k values at $x/c = 0.023$ and $Re_c = 2.4 \times 10^6$.

Roughness Configuration			Re_k
Type	Layers	k [μm]	
rub-down	1	6	0.11
rub-down	2	12	0.45
rub-down	3	18	1.0
die-cut tape	1	48	7.0

$k = 18$ μm. The second type of roughness element are in-house die-cut circular dots made from 3M #850 industrial polyester tape. These dots are 3.7 mm in diameter and yield a roughness height of 48 μm when applied to the surface.

Roughness heights are measured with respect to the boundary layer in terms of a roughness Reynolds number, defined by

$$Re_k = \frac{U(k)k}{\nu}, \tag{3.1}$$

where k is the roughness height (dimensional) and $U(k)$ is the boundary-layer velocity at the top of the element. The boundary layer is too thin for a direct measurement at $x/c = 0.023$, therefore the Re_k values are determined using theoretical boundary-layer solutions. Table 3.1 summarizes the Re_k values for the roughness configurations used in this experiment. If the Re_k values are too large, the roughness elements can trip the boundary layer or produce a local turbulent wedge due to an instability of the wake behind the element (von Doenhoff and Braslow 1961; Juillen and Arnal 1990). For the roughness configurations of this experiment, the Re_k values are well below the Braslow limit for three-dimensional roughness.

3.3 Coordinate System Definitions

If any comparisons between theoretical predictions and experimental results are to be made accurately, a clear understanding of the coordinate systems involved is necessary. Figures 3.5 and 3.6 show the typical coordinate systems involved when dealing with swept-wing flows. In both figures, the freestream flow is from left to right. The (X, Y, Z) axes represent the global test-section coordinate system. X is in the streamwise direction, Y is normal to the test-section front wall, and Z is in the vertical direction positive down (right-handed system). The velocity components in this global coordinate system are (u, v, w). In the model-oriented coordinate system (x, y, z), x is normal to the leading edge, y is normal to the chord line, and z is parallel to the leading edge. The velocity components in this system are (u_n, v_n, w_n). The boundary-layer coordinate system (x_t, y_t, z_t) is aligned with the inviscid streamline. In this system, x_t is tangent to the inviscid streamline, y_t is normal to the airfoil surface, and z_t is normal to the inviscid streamline positive in the right-handed sense. In this coordinate system, velocity components are denoted by (u_t, v_t, w_t). The z_t coordinate and w_t velocity component are defined as the crossflow direction and crossflow velocity, respectively. A typical swept-wing boundary layer is shown in figure 3.7, highlighting the boundary-layer coordinate system. The tangential and crossflow velocity components combine to produce a twisted three-dimensional profile. Note that for positive sweep angle Λ (see figure 3.5), the crossflow velocity component is negative up to the pressure minimum. A fourth coordinate system, often used in computation studies, is the body-intrinsic system (ξ, ζ, z). In this system, ξ is tangent to the airfoil surface and normal to the leading edge, ζ is normal to the surface $(\zeta = y_t)$, and z, again, is along the swept span parallel to the leading edge.

Due to practical traverse limits, the hot-wire scans performed in this experiment are done in the (Y, z) plane. Two probe rotations are required to get the boundary-

Table 3.2: Boundary-layer hot-wire probe rotation angles.

x/c	β [°]	σ [°]	x/c	β [°]	σ [°]
0.05	30	16	0.35	12	6
0.10	25	12	0.40	10	6
0.15	20	10	0.45	10	5
0.20	18	9	0.50	8	4
0.25	15	8	0.55	5	3
0.30	15	7	0.60	5	2

layer hot wire close to and aligned with the model. These rotations are shown in figure 3.8. The entire boundary-layer probe support is first rotated by an angle β around the Z axis to prevent the back of the support from hitting the wing as the hot-wire is moved within the boundary layer . Then, the hot-wire probe is rotated about its own longitudinal axis by an angle σ to get the element parallel with the surface. Table 3.2 summarizes the necessary probe rotations at the chord locations where measurements are taken. Once rotated, the hot wire measures the total velocity normal to the element. Thus, any computation must transform the results to this frame if accurate comparisons are to be made.

3.4 Linear Stability Calculations

Although it has been reiterated that nonlinear effects are important in crossflow-dominated swept-wing flows, linear stability theory can still provide valuable insight into the relative growth between modes, as well as information about the most unstable modes. Linear stability calculations are computed for stationary crossflow disturbances at the test Reynolds number using an updated version of Haynes' stability code (Haynes and Reed 1996). The updated code includes surface curvature effects. Figure 3.9 shows the N-factor curves for several spanwise wavelengths at $Re_c = 2.4 \times 10^6$. Short wavelength disturbances grow rapidly at small x/c and then

decay, while longer wavelength modes decay initially and are then amplified downstream. The modes with the largest N-factors downstream have median wavelengths, which show strong growth early but still remain unstable at larger x/c.

CHAPTER 4

Experimental Techniques

Accurate boundary-layer stability measurements require carefully designed experimental procedures. A clear understanding of both the stability problem and the principles behind the measurement hardware is necessary to determine which factors may affect the results. This chapter explains the measurement techniques used in the present experiment.

4.1 Hot-Wire Signal Processing

Central to quantifying the stationary crossflow disturbance are velocity measurements taken within the boundary layer via hot-wire anemometry. Hot-wire signal analysis is a complex subject, and several calibration and signal-processing techniques have been developed over the years. Typically these techniques rely on a particular physical model of the heat-transfer characteristics of a hot wire. Rather than adopt a certain physical model, the approach taken at the Unsteady Wind Tunnel is to focus on computer-based calibration and analysis. This eliminates the need for any extra analog conditioning equipment (such as linearizers and temperature compensators) at the expense of increased software development.

4.1.1 Velocity Calibration

As explained in section 2.4, each hot wire is connected to a constant-temperature anemometer (CTA). For low-speed flows, the voltage output of a CTA is primarily a function of the fluid velocity and the temperature difference between the fluid and hot-wire element (Perry 1982). If the temperature difference is kept constant, the CTA response is governed by the classic King's Law:

$$U = \left(P + QE^2\right)^2. \tag{4.1}$$

The parameters P and Q are determined from physical aspects of the fluid and hot wire. Perry (1982) shows that simple polynomial calibration is often at least as accurate as sophisticated flow models. In light of this, King's Law is generalized to a simple 4th-order polynomial fit at the Unsteady Wind Tunnel. A 4th-order fit is selected because it matches King's Law to the leading term, and its increased generality over equation 4.1 allows for a more accurate fit of a given data set.

The output of the anemometers is calibrated against the velocity measured by the Pitot-static probe. A series of calibration points are acquired from 1 m/s to 32 m/s, which encompasses the tunnel velocities encountered in this experiment. The entire calibration procedure is completely automated and takes less than 10 minutes to perform. Figure 4.1 shows a typical hot-wire velocity calibration. The 4th-order polynomial fit represents the sampled data exceptionally well.

4.1.2 Temperature Compensation

The Arizona State University UWT does not have a cooling system, hence it is subject to temperature increases from fan-generated and frictional heating. For a typical high-Reynolds-number experiment, it is not uncommon for the tunnel temperature to increase by 20°C over the extent of a single run that takes hours to complete.

As mentioned in the previous section, the CTA output depends upon both fluid velocity and temperature difference, therefore the large temperature changes cannot be ignored. To account for the voltage drift associated with changing test-section temperature, the hot-wire signals are temperature compensated via software.

The compensation technique employed at the Unsteady Wind Tunnel assumes that the square of the CTA voltage varies linearly with temperature for a fixed velocity. The slope of this linear model is the *compensation coefficient* C_T, which is a function of velocity. Reibert (1996a) provides a detailed description of the current technique, which improves upon that of Radeztsky et al. (1993b) to account for the velocity dependence of C_T. In brief, the test-section temperature, Pitot-static velocity, and CTA voltage output are monitored as the tunnel is preheated. The data at several velocities before and after the preheat are used to compute the corresponding compensation coefficient. The speed dependence of the compensation coefficient is modeled with a 2nd-order polynomial least-squares curve fit. Figure 4.2 shows the experimental data and curve fit for a typical hot-wire temperature compensation. As with the velocity calibration, the temperature-compensation technique is completely automated. It is important to note that the compensation-coefficient curves are determined before the hot-wire velocity calibration. This allows the voltage-velocity relationship to be compensated for any temperature changes during the calibration, effectively yielding a constant-temperature hot-wire calibration.

During data acquisition, the acquired test-section temperature and CTA output are used to determine the compensated hot-wire voltage. This compensated voltage is then used in the voltage-velocity relationship determined from the hot-wire calibration. These procedures are automatically implemented at the Unsteady Wind Tunnel via a set of standard programming libraries (Reibert 1996b) that are easily incorporated into any data-acquisition code.

4.2 Wind-Tunnel Speed Control

Wind-tunnel speed control is provided by a custom LabVIEW virtual instrument (figure 4.3) on the Sun SPARCstation data-acquisition computer. This graphical program monitors and displays the test-section temperature, static pressure, dynamic pressure, and fan rpm. The tunnel can be operated to control one of three different parameters: freestream velocity, Reynolds number, or nondimensional frequency. Once the parameter and corresponding value are set, the program continuously adjusts the motor speed as necessary to achieve and maintain the control value. Once the target value is reached within tolerance, the "At Target" indicator turns on and the program measures tunnel conditions and makes updates less frequently (typically every 15 seconds). This frees up the shared A/D system to perform other tasks such as experimental data acquisition. For this experiment, the tunnel is operated to control chord Reynolds number.

4.3 Flow Visualization

Naphthalene flow visualization provides a visual "footprint" of the stationary crossflow waves and transition pattern. The stationary disturbance produces a spanwise modulation of the mean boundary layer, consequently yielding a similar modulation of the surface shear stress. Naphthalene sublimes at a rate proportional to shear stress at room temperature, so it is a good medium for viewing both the vortex pattern and transition (where surface shear stress is high).

The naphthalene is dissolved in 1,1,1-trichloroethane before being applied to the wing, which allows the combined substance to be sprayed onto the surface with a standard compressed-air sprayer. Once applied to the wing, the solvent quickly evaporates, and a thin layer of naphthalene is left on the surface. To avoid any roughness

contamination due to the small thickness of the naphthalene coating, the substance is not sprayed onto the model for $x/c < 0.20$.

Once the naphthalene coating is applied, the tunnel is run up to the desired test condition. As the tunnel runs, areas of high shear stress are indicated by sublimation of the naphthalene, and areas of low shear are where the naphthalene remains. Since the stationary crossflow waves produce a spanwise modulation of the surface shear stress, the vortex pattern appears as streaks of alternating sublimed and remaining naphthalene. In the turbulent region, where the shear stresses are high, the naphthalene sublimes quickly.

4.4 Disturbance Measurement Techniques

Two measurement techniques are used to quantify the stationary crossflow disturbance amplitude. Wall-normal boundary-layer scans yield information about the total disturbance, and constant-Y scans are used to extract spectral information.

4.4.1 Boundary-Layer Scans

A two-dimensional map of the stationary crossflow vortex structure is obtained with a spanwise set of wall-normal boundary-layer scans. Similar to the method used by Reibert (1996a), 100 mean-flow boundary-layer profiles each spaced 1 mm apart in span are acquired. Once the profiles are attained, velocity contours, disturbance profiles, and disturbance mode shapes are created. Total disturbance amplitudes are then computed from the mode-shape profiles.

Before the scan, the boundary-layer (BL) hot-wire probe is adjusted so that the element is parallel to the local surface. The wire is then moved to the boundary-layer edge and the scan is started. Each boundary-layer profile is acquired independently of all others. The BL probe measures the mean velocity within the boundary layer,

and the freestream (FS) probe measures the mean velocity in the external flow at the same chord location. At the start of the scan, the boundary-layer edge velocity U_e and external velocity are acquired, and the ratio between them is recorded. The probes are then moved toward the airfoil surface a specified edge-step distance, and the mean velocities at each probe are measured. At each measurement point, the BL hot-wire velocity is normalized by the instantaneous U_e, which is determined by scaling the FS hot-wire velocity by the edge-to-external-flow velocity ratio. This normalization is necessary since the tunnel velocity changes as the scan progresses due to wind-tunnel heating. The scan continues with subsequent step distances being scaled with u/U_e for finer resolution near the surface. The boundary-layer scan is terminated when u/U_e reaches a specified value, and the airfoil surface location is determined by a straight-line fit through the lower portion of the profile (typically through $u/U_e < 0.30$). The BL probe is then moved to the edge of the boundary layer at the next span location and the whole procedure is repeated starting with the determination of the edge-to-external-flow velocity ratio. Figure 4.4 shows a typical boundary-layer profile acquired with this type of scan.

This boundary-layer scanning technique has both positive and negative aspects. The individual profiles have the advantage of being completely self-aligning, meaning that the surface location can be determined from the measurements. Thus, any slight misalignment between the traverse and model does not introduce significant error. On the downside, however, a full set of profiles takes a considerable amount of time. A typical scan of 100 profiles can take up to 5 hours to complete depending upon the thickness of the boundary layer. Consequently, this type of scan is not useful for extracting spectral information about the disturbance because the number of scans required for good frequency resolution would be prohibitively time consuming.

4.4.2 Constant-Y Scans

Spanwise mean velocity traces taken at a constant height Y above the airfoil surface provide data suitable for accurate spectral analysis. The wavenumber content of the stationary crossflow disturbance can be extracted from the scans yielding individual-mode disturbance amplitudes. These are tracked at various x/c to generate individual-mode growth curves.

Spectral Analysis Issues

An important concern when dealing with discrete experimental data is the appropriate choice of sampling parameters to obtain the desired spectral resolution. For a signal that is a function of time, frequency resolution is typically the important characteristic. In this experiment, however, where the signals are functions of space rather than time, *wavelength* resolution is the important criterion. Of course, spectral techniques are just as applicable to spatially varying signals as they are to time-domain signals, but the translation to the spatial domain will reveal the requirements of the measurement technique.

For a given set of N evenly spaced measurements over a distance S, the sampling interval Δ_s is defined as

$$\Delta_s = \frac{S}{N-1}. \tag{4.2}$$

Mathematically, the sampling frequency $f = 1/\Delta_s$. Thus, in the spatial sense "frequency" is in cycles per unit length (or inverse wavelength). The one-sided power spectrum for this set of data is defined at $N/2+1$ discrete frequencies given by

$$f_k = \frac{k}{N\Delta_s}, \quad k = 0, \ldots, \frac{N}{2}. \tag{4.3}$$

It follows that the frequency resolution is $\Delta f = 1/(N\Delta_s)$, and the Nyquist critical

frequency is $f_c = 1/(2\Delta_s)$. In the spatial sense, the power estimates are at the $N/2+1$ wavelengths

$$\lambda_k = \frac{N\Delta_s}{k}, \quad k = 0, \ldots, \frac{N}{2}, \tag{4.4}$$

giving a wavelength resolution that is not equally spaced in λ and a minimum resolvable wavelength of $\lambda_c = 2\Delta_s$.

Since $\lambda = 1/f$, the wavelength resolution is given by

$$\Delta\lambda = \left|\frac{d\lambda}{df}\right| \Delta f = \frac{\lambda^2}{N\Delta_s} \approx \frac{\lambda^2}{S}. \tag{4.5}$$

The wavelength resolution is a function of λ and increases with the square of the wavelength, meaning that shorter wavelengths are resolved better than longer ones. Increasing the total span S decreases $\Delta\lambda$ for all wavelengths, thus the best wavelength resolution is achieved when the span of the data is maximized. Increasing the number of samples N for a fixed S has no effect on $\Delta\lambda$, rather it decreases the smallest resolvable wavelength.

Scanning Procedures

The sampling parameters S and N for the constant-Y scan are selected based on the previous discussion. For the best attainable wavelength resolution in the spectral domain, the scan covers a span of 240 mm, which is the maximum possible due to traverse constraints. 256 points along the span are acquired, giving a wavelength resolution $\Delta\lambda = 0.6$ mm at $\lambda = 12$ mm. In addition, the spectrum will resolve wavelengths from 1.9 mm to 240 mm. Radeztsky (1994) and Reibert (1996a) successfully used these values for S and N in their experiments to extract individual-mode stationary disturbance amplitudes.

As its name implies, the constant-Y scan relies on measuring mean velocities at

a fixed height in the boundary layer. To maintain a constant height above the airfoil surface as the hot wire moves along the span, provisions are necessary to account for any misalignment between the traverse and the model. This is accomplished by preceding the constant-Y scan with a traverse-alignment scan, which determines the location of the airfoil surface in traverse coordinates.

As discussed in section 4.4.1, traverse/model misalignment is not a major concern for the wall-normal scanning technique because each profile accurately determines the location of the airfoil surface. In light of this, a series of 25 boundary-layer profiles are taken over the 240 mm span, and the surface coordinate is recorded at each span location. The acquired profiles are very detailed near the surface for an accurate fit to zero velocity, but are very coarse high in the boundary layer in order to minimize the scan time. After the surface coordinates are acquired at all span locations, the data are fit with a 4th-order polynomial. This curve fit is then used during the spanwise scan to keep the BL probe at the desired Y height. Figure 4.5 shows the results of a typical traverse-alignment scan.

Once the location of the airfoil surface is determined, the constant-Y scan proceeds. At the beginning of the scan, the BL hot wire is positioned at the edge of the boundary layer. The mean velocities measured by the BL and FS hot wires are acquired, and the boundary-layer-edge-to-external-flow velocity ratio is calculated. The BL probe is then moved down into the boundary layer to the desired Y height above the surface. As with the wall-normal boundary-layer scans, the mean velocity measured by the BL wire is normalized by the instantaneous edge velocity U_e at all points. The scan continues with the probes being moved along the swept span, acquiring 256 points over the 240 mm span. At each point, the traverse-alignment fit is used to make any necessary corrections to maintain the fixed height. Once the scan is completed, the BL probe is moved back to the initial location and the procedure is

repeated three more times for spectral averaging, providing four constant-Y sweeps of 256 points each over the 240 mm span. Figure 4.6 shows a typical constant-Y scan.

Note that the technique described here differs slightly from that of Reibert (1996a), who performed a single constant-Y sweep of 1024 points over the 240 mm span and then demultiplexed the data into 4 sweeps of 256 points each over 240 mm for averaging. In terms of spectral resolution, the two techniques are identical. The current technique will yield slightly more accurate results, especially near the leading edge where Y sensitivity is greatest, basically because the averaging is done with four virtually independent (all four rely on the same traverse-alignment scan) constant-Y sweeps. For each sweep, a separate edge-to-external-flow velocity ratio is determined, whereas in the past technique a single ratio is computed at the start of the scan and is used for all points.

CHAPTER 5

Results

5.1 Overview

The experimental results are presented and discussed in this chapter. The basic state is documented and compared to experimental results of Reibert (1996a) and to theory. Measurements of the stationary crossflow disturbance under natural surface roughness conditions are presented in detail. These data are followed by the results obtained under varying initial surface roughness conditions.

All stationary crossflow amplitude data are acquired using the two hot-wire techniques explained in section 4.4. Table 5.1 summarizes the six data sets examined in this study. The chord Reynolds number is shown in the column labeled Re_c and is fixed at 2.4×10^6 for all cases. Columns k and λ_z show the roughness height and spanwise spacing, respectively, and the last two columns give the type of scan used. A bullet ($\bullet$) in the BL and Span columns indicates wall-normal boundary-layer scans and constant-Y spanwise scans, respectively. Note that both scan types are used for all data sets.

To maintain consistency with Reibert (1996a), the shorthand notation $[k|\lambda_z]$ will be used to unambiguously define the roughness configuration. As outlined in section 3.2.3, the roughness elements are applied in a full-span array at $x/c = 0.023$ for

Table 5.1: Experimental data sets.

Data Set	$Re_c/10^6$	Roughness		Scan Type	
		k [μm]	λ_z [mm]	BL	Span
$\mathcal{A}$	2.4	0	0	•	•
$\mathcal{B}$	2.4	6	18	•	•
$\mathcal{C}$	2.4	12	18	•	•
$\mathcal{D}$	2.4	18	18	•	•
$\mathcal{E}$	2.4	6	8	•	•
$\mathcal{F}$	2.4	48	8	•	•

all cases. Therefore, specifying the roughness height and spacing fully determines the roughness configuration. Thus, [6|18] represents a full-span roughness array with a $k = 6$ μm element height and a $\lambda_z = 18$ mm spanwise spacing. The natural roughness case, data set $\mathcal{A}$, is given the notation [0|0].

When presenting the results for individual-mode disturbance amplitudes, crossflow modes will be designated in the shorthand notation (f, m), where f is the disturbance frequency and m is the mode number. The mode number is defined as the disturbance wavenumber normalized by the wavenumber of the fundamental mode. Thus, $m = 1$ and $m = 2$ indicate the fundamental disturbance and first superharmonic, respectively. The spanwise-invariant disturbance, typically called the "mean-flow distortion" mode, is represented by $(0, 0)$.

5.2 Basic State

Basic-state conditions are determined with pressure measurements and wall-normal boundary-layer scans. Reibert (1996a) documents the basic state for the NLF(2)-0415 at $\alpha = -4°$ case, so the data presented in this section are to verify the existence of similar conditions.

5.2.1 Cp Distribution

The pressure distribution is measured with two rows of pressure ports located near the upper and lower ends of the model. The C_p distributions for $Re_c = 1.6 \times 10^6$, 2.4×10^6, and 3.2×10^6 for both sets of ports are shown in figures 5.1–5.3. Also shown in these figures is the MCARF (Stevens et al. 1971) theoretical C_p distribution. Note that the measured C_p is larger than the MCARF solution for all chord Reynolds numbers. This is consistent with the results of Reibert (1996a), who cites several possible explanations for the differences. The discrepancy between the upper-port measurements and theory is largest in the $0.05 \leq x/c \leq 0.35$ region, which Dagenhart (1992) explains as being the result of the upper liner being too thin in this region. The discrepancy between measured C_p and theory for the lower ports increases as x/c increases. Reibert (1996a) attributes this to the inclined test-section floor, which drops by 50 mm over its length of 4.9 m to approximately account for boundary-layer growth on the test-section walls and airfoil model. The computations do account for the existence of the front and rear test-section walls but do not include any displacement-thickness corrections.

The pressure distributions at the above three Reynolds numbers are plotted together for the upper and lower ports in figures 5.4 and 5.5, showing a slight C_p dependence upon Re_c. This dependence is due to changes in the displacement thickness of the boundary layers, and is not due to compressibility effects since $M < 0.1$ for all test conditions (Reibert 1996a). This result is expected because the drop in the test-section floor is functionally optimal for only one test condition. Overall, the slight Reynolds number dependence is negligible.

Of most importance is the pressure-distribution comparison with the data of Reibert (1996a), since similar basic states will allow direct comparisons between data sets. Figures 5.6–5.8 show the average of the upper- and lower-port C_p distributions, as

well as the results of Reibert (1996a) and theory, for $Re_c = 1.6 \times 10^6$, 2.4×10^6, and 3.2×10^6. Excellent agreement is obtained with the earlier experiments, verifying the existence of a similar global flowfield.

In short, generally good agreement is obtained between the measured and theoretical pressure distribution, especially in terms of the pressure gradient. Excellent agreement is observed between the experimental C_p distributions of this study and those of Reibert (1996a).

5.2.2 Boundary-Layer Profiles

As shown in table 5.1, all stationary-crossflow disturbance measurements are conducted at $Re_c = 2.4 \times 10^6$. It is impossible, however, to measure the basic-state profiles at this chord Reynolds number because large-amplitude stationary crossflow waves are generated even under no artificial roughness conditions. In the absence of artificial roughness, Reibert (1996a) observed nonlinear mean-flow distortions for $Re_c \geq 1.8 \times 10^6$ and, thus, measured the basic-state boundary layers only at $Re_c = 1.6 \times 10^6$.

Specific details of the basic-state boundary layer are obtained using the wall-normal boundary-layer scanning technique explained in section 4.4.1. Figure 5.9 shows 100 profiles at $x/c = 0.20$ each separated by 1 mm in the swept span direction. The profiles show no evidence of stationary crossflow waves and are essentially identical, confirming the success of the test-section liners in producing a spanwise invariant flowfield in the test region of the model. Figure 5.10 shows the spanwise average of the 100 profiles at $x/c = 0.20$ plotted with the average profile measured by Reibert (1996a). The average profile is slightly more accelerated than that of the previous experiment, but excellent agreement overall is obtained between the average profiles.

The exceptional agreement of the spanwise-average profiles at $x/c = 0.20$, as well as the agreement between average C_p distributions, between this and previous

experiments are sufficient to verify the existence of similar flowfields. Reibert (1996a) provides in-depth details and discussion of the basic-state profiles at $Re_c = 1.6 \times 10^6$ at several chord locations.

5.3 Natural Surface Roughness—Data Set $\mathcal{A}$

5.3.1 Flow Visualization

Naphthalene flow visualization (see section 4.3) is used to determine surface shear-stress patterns and transition locations. Figures 5.11, 5.12, and 5.13 show the naphthalene patterns for $Re_c = 2.4 \times 10^6$, 2.6×10^6, and 2.8×10^6, respectively. The photographs show the upper airfoil surface, and the flow is from left to right. Lines of constant chord are marked with a black felt-tip pen on the surface of the model. The white numerals represent the chord location in percent. The stationary crossflow vortices transpose high- and low-momentum fluid within the boundary layer, yielding a spanwise modulation of the surface shear stress. This modulation is clearly indicated as alternating streaks in the naphthalene.

Regions in which the boundary layer is turbulent are indicated by complete sublimation of the naphthalene (dark areas). Note that this does not hold true in the region near the leading edge, where naphthalene is not sprayed to prevent roughness contamination. Transition appears as a series of turbulent wedges, which is characteristic for swept-wing flows. Note that the transition pattern is nonuniform under natural surface roughness conditions. This is consistent with past experiments and is indicative of submicron roughness irregularities near the leading edge.

The transition pattern moves forward along the wing as the chord Reynolds number increases. The nonuniformity of the wedges makes it difficult, however, to quantify the transition location. Adopting the method used by Reibert (1996a), the transition location is defined as the average of the upstream vertices of the turbulent wedges.

Table 5.2: Approximate transition location as determined from naphthalene flow visualization.

Roughness		Transition Location [x/c]		
k [μm]	λ_z [mm]	$Re_c = 2.4 \times 10^6$	$Re_c = 2.6 \times 10^6$	$Re_c = 2.8 \times 10^6$
0	0	0.65	0.60	0.51
6	8	0.80	0.59	0.49
48	8	0.59	0.45	0.32

Using this definition, the approximate transition locations for [0|0] and other roughness configurations are presented in table 5.2. The flow-visualization results of the other roughness cases will be discussed in subsequent sections.

5.3.2 Special Considerations

As mentioned earlier, measurable distortions of the mean boundary layer are generated for $Re_c \geq 1.8 \times 10^6$ in the absence of artificial roughness. Figure 5.14 shows a contour plot of the normalized boundary-layer velocities at $Re_c = 2.4 \times 10^6$ for $x/c = 0.60$. The figure shows the streamwise velocity u/U_e in the (Y, z) plane, with the Y axis magnified 10 times that of z to enhance detail. The mean flow is towards the reader, and the stationary crossflow vortices are turning in the right-handed orientation (counterclockwise). These velocity contours are generated from 100 boundary-layer profiles acquired with the wall-normal scanning technique outlined in section 4.4.1.

The naturally occurring stationary crossflow waves are nonuniform in span even though the airfoil surface is finely polished to a mirror-like finish. This nonuniformity is due to submicron surface irregularities near the leading edge, signifying the extreme sensitivity of this disturbance to roughness-induced initial conditions (Reibert et al. 1996).

Although clearly containing multiple modes, figure 5.14 definitely shows a strong

feature with a spanwise spacing of approximately 12 mm which is about the most amplified wavelength according to linear stability theory. The spanwise nonuniformity indicates nonlinear interactions among many modes, which is typical of earlier experimental investigations (Müller and Bippes 1989; Dagenhart et al. 1989, 1990; Bippes and Nitschke-Kowsky 1990; Bippes et al. 1991; Deyhle et al. 1993).

Reibert (1996a) opted not to do a detailed study of the naturally occurring crossflow waves because the spanwise nonuniformity leads to undesirable side effects. There is definite ambiguity in determining the disturbance amplitude. Dagenhart (1992) measured the disturbance amplitude and growth by acquiring data over a single vortex wavelength and tracking the vortex at all chord locations. With this method, the growth rates will strongly depend upon the vortex chosen, as well as the ability to track the same vortex. In addition, the unknown natural surface roughness conditions make comparisons to theory difficult. Any computation would need to consider the possibly infinite number of modes excited to be appropriate.

5.3.3 Total Disturbance Amplitude Measurements

Although the nonuniformity of the naturally occurring crossflow waves presents definite difficulties, the experimental database would not be complete without some attempt to quantify the disturbance. Rather than attempt to measure the growth rate of a single vortex (Dagenhart 1992), the more objective and consistent technique of acquiring 100 wall-normal profiles over 99 mm in span (see section 4.4.1) is used to determine the total disturbance amplitude.

Figure 5.15 shows the 100 mean boundary-layer profiles used to generate the contours in figure 5.14. The profiles are each separated by 1 mm in span. The dots represent the spanwise average of the profiles, which includes the basic state plus the $(0,0)$ mean-flow distortion mode. Each profile contains about 65 measurement points, with each datum point being the time-averaged velocity over two seconds.

The existence of accelerated, decelerated, and doubly inflected mean profiles just millimeters apart shows the momentum transfer effects of the stationary vortices. The distortion of the spanwise-averaged profile shows the effects of strong nonlinear interactions.

Stationary crossflow disturbance profiles are obtained by subtracting the spanwise-averaged profile from each of the 100 boundary-layer profiles. Figure 5.16 shows the results for the profiles of figure 5.15. The disturbance levels reach a maximum of about 36% near $Y = 1.2$ mm. Smooth phase changes between the profiles indicate the wave-like nature of the stationary structure. The asymmetry of the profiles is due to both the nonuniformity and, more importantly, the rollover seen in figure 5.14. Figure 5.17 shows the disturbance velocity contours generated from the 100 disturbance profiles. Only two contour levels are shown to emphasize regions of velocity surplus and deficit. This plot clearly shows the upwelling and downwelling of low-momentum and high-momentum fluid, respectively, within the boundary layer. Although figure 5.17 accentuates the rollover phenomenon, no extra information is presented that cannot be gathered from the normalized-velocity contours and disturbance profiles. Therefore, disturbance velocity contours will be shown only for select cases.

Total disturbance mode shapes are created by taking a spanwise rms at each Y position of the 100 disturbance profiles. For a spatially varying stationary wave, this is equivalent to computing a time-domain rms for a traveling disturbance. Figure 5.18 shows the mode shape computed from the disturbance profiles of figure 5.16. The rms mode shape reaches a maximum amplitude of 14% at $Y = 1.0$ mm and shows the development of a second lobe high in the boundary layer. This second lobe is indicative of the presence of nonlinear effects and corresponds to the slightly inflectional distortion of the spanwise-average profile of figure 5.15. The reader should definitely understand that the rms mode shape computed in this manner contains all modes.

Under no artificial roughness conditions, the *total* disturbance mode shape consists of a potentially infinite number of modes, as is evident by the richness of spectral content seen in figure 5.14.

The disturbance measurements described above for $x/c = 0.60$ are repeated at 5% chord intervals for $0.05 \leq x/c \leq 0.55$. Figures 5.19–5.29 show the normalized velocity contours at these locations. The mean boundary-layer velocity profiles used to construct the contour plots are shown in figures 5.30–5.40. Figures 5.41–5.51 present the corresponding disturbance profiles. The mode shapes computed from the spanwise rms of the disturbance profiles are shown in figure 5.52 for $0.25 \leq x/c \leq 0.60$. Under natural surface roughness conditions, the disturbance is too weak to measure accurately for $x/c \leq 0.20$. This series of plots clearly shows how the stationary crossflow waves cause distortions of the mean boundary layer.

The mode-shape profiles of figure 5.52 are used to compute amplitudes of the total stationary disturbance. Three methods are used to quantify the disturbance. The first technique uses the maximum of the rms mode shape as the amplitude. The second method uses the average over Y of the mode shape, which is essentially the integral of $|u'|$. The third method computes the rms with respect to Y of the disturbance, which corresponds to the integral of $|u'|^2$. Figure 5.53 shows the amplitude distribution for [0|0] roughness at $Re_c = 2.4 \times 10^6$ for each of the three methods. Also shown in this figure are the corresponding N-factors for each method. The initial amplitude at $x/c = 0.25$ is used as the reference for each N-factor curve. Regardless of the amplitude computation method used, the N-factors collapse nicely onto a single curve. This is typical and is seen by Radeztsky (1994) and Reibert (1996a). The slope of N is the local spatial growth rate, and the approximately constant slope up to $x/c = 0.50$ indicates exponential growth in this region. Past 50% chord, the growth rate decreases slightly, indicating the beginnings of amplitude saturation and strong

nonlinear interactions. It is also at $x/c = 0.50$ where the second lobe is first noticeable in the mode shape in figure 5.52.

5.3.4 Individual-Mode Disturbance Amplitude Measurements

As mentioned earlier, the disturbance amplitudes computed from the wall-normal scans represent the *total* disturbance and include all amplified stationary modes. Individual-mode disturbance amplitudes are obtained using the constant-Y scanning technique outlined in section 4.4.2. The Y-height scanned at each chord location is the location corresponding to the maximum of the total disturbance mode shape. This allows direct comparison between the individual-mode and total disturbance amplitudes.

Figures 5.54–5.60 show the spanwise scans for $0.25 \leq x/c \leq 0.55$. In these figures, the normalized velocity is plotted as a function of swept span (z). The constant-Y scans cover a span of 240 mm, which is the maximum available due to traverse constraints. Note that at each chord location, the spanwise scan consists of four sweeps over the full 240 mm, yielding four traces in each of the constant-Y plots. Each sweep takes approximately 15 minutes. The agreement between each individual sweep for $x/c \geq 0.30$ shows the excellent repeatability of this technique. At $x/c = 0.25$ there is some variance, which is due to the combined effects of small disturbance amplitudes and large du/dY gradients in a thin boundary layer. It is in regions with these characteristics where taking four sweeps provides the most benefits.

Figures 5.54–5.60 clearly show the development of the mean boundary-layer distortion. As seen in the normalized velocity contours, the constant-Y traces are nonuniform in span and show a definite dominant wavelength.

Figures 5.61–5.67 show the corresponding power spectra of the constant-Y scans at $0.25 \leq x/c \leq 0.55$. The power spectral density (PSD) is plotted against spanwise wavelength λ_z (or the equivalent λ_s in the figures). An FFT-based power spectrum

technique with 64-times spectral smoothing through zero padding is used to compute power estimates. Reibert (1996a) successfully used this technique to accurately extract the peaky spectra with sufficient resolution to compute disturbance amplitudes by integrating the PSD.

The spectra for $0.40 \leq x/c \leq 0.55$ are plotted on a consistent scale to accentuate the disturbance growth. For $x/c \leq 0.35$, the power axis is magnified to enhance detail in this region where disturbance amplitudes are small. The power spectra at all chord locations show a definite peak at $\lambda_z = 11.0$ mm, which is approximately the most amplified wavelength according to linear theory. In addition to this peak, there is also significant energy in several broadband regions for $\lambda_z \geq 9.0$ mm. This broadband energy grows with increasing x/c and corresponds to the nonuniformity observed in the constant-Y traces.

The disturbance energy for a single mode is computed by integrating the corresponding peak in the spectrum, where the extent of a peak is defined as the first local minimum on each side. Since there is definitely energy in the 11 mm component (and linear theory approximately predicts this to be the most unstable wavelength), only this mode's amplitudes will be computed. No attempt is made to compute the amplitudes of the more broadband disturbances, but their role in the total disturbance will be apparent.

Figure 5.68 shows the disturbance amplitude and corresponding relative N-factor distribution for [0|0] and $Re_c = 2.4 \times 10^6$. As with the total disturbance amplitude plot (figure 5.53), the dashed lines represent the disturbance amplitude, and the solid lines indicate the amplification factor N. The reference amplitude for the 11 mm component is $x/c = 0.25$, where the disturbance is first detected. The amplitude of the 11 mm wavelength disturbance grows to about 7% at $x/c = 0.55$.

Of more interest is the comparison of the individual-mode amplitude with the total

disturbance amplitude computed from the maximum of the mode shape. Since the constant-Y scans at each chord location are conducted at the height corresponding to the maximum of the mode-shape profile, direct comparisons can be made. Figure 5.69 shows the total and individual-mode amplitude curves, as well as the corresponding N-factors. As expected, the total disturbance amplitude is larger than the 11 mm disturbance amplitude at all x/c, indicating the importance of the energy in the broadband wavelengths. The total disturbance grows to about 10% at $x/c = 0.55$, while the 11 mm component grows to about 7%. Both the total and individual-mode disturbances show the characteristic amplitude saturation. The 11 mm component shows strong saturation starting at $x/c = 0.45$, indicating nonlinear interactions between this and the more broadband disturbances.

The detailed disturbance amplitude measurements provided here for the [0|0] roughness case reiterates the findings of Reibert (1996a). The unknown natural roughness of the airfoil surface makes any comparison with theory unnecessarily difficult. Submicron roughness irregularities in the finely-polished surface yield stationary crossflow waves that are nonuniform in span. Although there is a dominant wavelength that is predictable by linear theory, any stability calculation (linear or nonlinear) that includes only this single mode will fail to characterize the disturbance. An accurate computation would need to take into account the multitude of modes excited by the random surface roughness.

5.4 [6|18] Roughness—Data Set *B*

To generate stationary crossflow waves that are uniform in span and contain a fixed spectral content, artificial surface roughness elements are applied to the airfoil surface as explained in section 3.2.3. These roughness elements provide fixed initial conditions for the stationary vortices. A full-span array of 6 μm high roughness elements spaced

18 mm apart is applied at $x/c = 0.023$. Radeztsky et al. (1993a) shows that this chord location maximizes the effect of the applied roughness.

5.4.1 Total Disturbance Amplitude Measurements

Figures 5.70–5.78 show the normalized velocity contours at $Re_c = 2.4 \times 10^6$. The addition of artificial roughness has moved the first detectable disturbance location to $x/c = 0.10$. Although the spanwise spacing is 18 mm, the series of contour plots show a clear 9 mm structure developing early at $x/c = 0.10$. The first indications of an 18 mm component are observed at $x/c = 0.25$, where every other vortex is slightly larger than the intermediate one. By 45% chord, a definite 18 mm vortex structure exists, as well as some strong harmonic content. Even at $x/c = 0.45$, the small artificial roughness yields boundary-layer distortions that are very uniform and periodic in span.

The boundary-layer profiles from which the contour maps are made are shown in figures 5.79–5.87. The corresponding disturbance profiles are presented in figures 5.88–5.96. As with the no roughness case, the stationary disturbance has dramatically distorted the mean boundary layer. Even the spanwise-average profile is doubly inflected for $x/c \geq 0.30$. Figure 5.97 shows the normalized disturbance velocity contours at $x/c = 0.45$. Again, the disturbance is significantly more uniform in span than that of the no roughness case, highlighting the extreme sensitivity of this stationary disturbance to small leading-edge roughness.

Figure 5.98 presents the total disturbance mode-shape profiles for $0.10 \leq x/c \leq 0.45$. The stationary crossflow disturbance amplitude and corresponding N-factor distribution are computed using the three methods described above and are shown in figure 5.99. The N-factor curves show dramatic amplitude saturation for $x/c \geq 0.25$. At these chord locations, the characteristic second lobe appears in the mode-shape profiles, indicating strong nonlinear effects.

5.4.2 Individual-Mode Disturbance Amplitude Measurements

A full set of spanwise scans are conducted to extract the modal content of the disturbance. Figures 5.100–5.107 show the normalized velocity as a function of span at a fixed height in the boundary layer for $0.10 \leq x/c \leq 0.45$. Again, the height scanned corresponds to the maximum of the total disturbance mode shape at each x/c. The power spectral density computations for these scans are presented in figures 5.108–5.115. Unstable modes are first detected at $x/c = 0.10$. The spectrum at this location (figure 5.108) shows energy in the $(0, 2)$ mode ($\lambda_z = 9$ mm). Although there is a peak evident at $\lambda_z = 18$ mm, its amplitude is very small and close to the noise of the spectrum. Based on a consistent definition of the spectral noise, the 18 mm peak is ignored. It is interesting that the $(0, 2)$ mode contains more energy than the fundamental ($\lambda_z = 18$ mm).

The fundamental mode is not measurable until $x/c = 0.20$ (figure 5.110). Although the fundamental is detected, the first superharmonic at $\lambda_z = 9$ mm still contains most of the disturbance energy. The fundamental disturbance grows rapidly for $0.35 \leq x/c \leq 0.45$, where the $(0, 2)$ mode actually shows some decay. Higher harmonics become unstable for $x/c \geq 0.25$. The spectrum at $x/c = 0.45$ (figure 5.115) shows detectable disturbances for the $(0, 3)$ and $(0, 4)$ modes ($\lambda_z = 6$ mm and 4.5 mm). No amplified subharmonics (wavelength doubling) of the roughness spacing are detected. This is consistent with the findings of Reibert (1996a).

Note that the 12 mm wavelength, which is approximately the most unstable according to linear theory, is not amplified at any x/c. The 18 mm forcing has successfully suppressed the growth of this wavelength disturbance. Reibert (1996a) did not observe this because his roughness spacings were all multiples of 12 mm. Radeztsky (1994) does show this phenomenon, however, his studies were on the NLF(2)-0415 at a different angle of attack ($\alpha = 0°$) with much larger roughness heights (146 μm).

Integrating the peaks in the PSD yields the corresponding disturbance amplitude for each mode. Figure 5.116 shows the individual-mode disturbance amplitude. The $(0,2)$ mode shows exponential growth up to $x/c = 0.25$, at which point the mode begins to saturate. The $(0,2)$ mode reaches a maximum amplitude of 13% at $x/c = 0.40$, after which it decays. It is in this saturation and decay region ($0.35 \leq x/c \leq 0.45$) of the $(0,2)$ mode where the fundamental disturbance shows strong growth. This is also the region of strong nonlinear effects as seen by the growth of the second lobe in the total disturbance mode-shape profiles (figure 5.98).

Also presented in figure 5.116 are the corresponding N-factor distributions. Since the individual modes are first detected at different chord locations with different initial amplitudes, each wavelength N-factor curve is referenced to a different amplitude. Thus, direct comparisons between the value of N are meaningless. Comparisons between the growth *rates*, however, are entirely meaningful.

The total disturbance amplitude and N-factor distribution are shown with the individual-mode amplitudes in figure 5.117. The amplitude of the $(0,2)$ mode ($\lambda_z =$ 9 mm) agrees well with the total disturbance amplitude up to $x/c = 0.30$, indicating the dominance of this harmonic even over the fundamental. For $x/c > 0.30$, the $(0,2)$ mode amplitude drops from the total disturbance and the amplitudes of the fundamental and higher harmonics grow.

5.5 [12|18] and [18|18] Roughness—Data Sets $\mathcal{C}$ and $\mathcal{D}$

Reibert (1996a) observed the interesting feature that, for a fixed roughness spacing of $\lambda_z = 12$ mm, the total disturbance amplitude grew to a constant saturation amplitude even when the roughness height was varied from 6 μm to 48 μm. Although the initial disturbance amplitude increased with larger roughness, the effects downstream relaxed and yielded similar looking mode shape. Data Sets $\mathcal{C}$ and $\mathcal{D}$ provide further

evidence of this characteristic for the $\lambda_z = 18$ mm roughness spacing.

The roughness height in this study is increased from 6 μm to 12 μm and then to 18 μm by stacking the roughness elements. Transition occurs at $x/c \approx 0.50$ for all three roughness heights. Since saturation amplitude comparisons are the primary concern, disturbance amplitude data are acquired only at $x/c = 0.45$. Both the total disturbance and individual-mode disturbance amplitudes will be computed and compared.

5.5.1 Total Disturbance Amplitude Measurements

Figure 5.118 shows the normalized velocity contours for [12|18] roughness at $Re_c = 2.4 \times 10^6$ and $x/c = 0.45$. The 100 boundary-layer profiles used to create these contours are presented in figure 5.119, and the corresponding disturbance profiles are shown in figure 5.120. Figure 5.121 shows the rms mode shape of the total disturbance. As with the velocity contours for the [6|18] roughness at $x/c = 0.45$ (figure 5.78), the velocity contours produced by the [12|18] roughness clearly show the existence of the fundamental ($\lambda_z = 18$ mm), as well as the first superharmonic ($\lambda_z = 9$ mm).

The procedure is repeated for [18|18] roughness initial conditions. The velocity contours, boundary-layer profiles, and disturbance profiles at $x/c = 0.45$ are shown in figures 5.124, 5.125, and 5.126, respectively. Figure 5.127 shows the total disturbance mode shape. The results are similar to those of the [6|18] and [12|18] roughness cases.

The total disturbance mode-shape profiles at $x/c = 0.45$ for the three roughness heights are shown together for comparison in figure 5.130. All three mode shapes show a large second lobe high in the boundary layer, indicating that all three cases are well into the saturation region where nonlinear effects are important. Despite the tripling of the applied surface roughness, the total disturbance amplitude (based on the max of the mode shape) remains approximately constant at 14%. Consistent with the results of Reibert (1996a), there is a redistribution of energy high in the boundary

layer with increasing initial roughness. Increasing from 6 μm to 18 μm roughness has actually increased the disturbance-layer thickness by almost a millimeter.

5.5.2 Individual-Mode Disturbance Amplitude Measurements

As with earlier cases, spectral information is obtained using the constant-Y scanning technique. Figures 5.122 and 5.123 show the spanwise scan and corresponding spectrum for [12|18] roughness at $Re_c = 2.4 \times 10^6$ and $x/c = 0.45$. The spanwise scan and spectrum for [18|18] roughness are presented in figures 5.128 and 5.129, respectively. The spectra for both roughness cases show similar features to the [6|18] case (figure 5.115), with harmonics detectable to the $(0, 4)$ mode. Again, no subharmonics are observed and the 12 mm wavelength is not excited.

Individual peaks are integrated to obtain the individual-mode disturbance amplitudes. Table 5.3 summarizes the amplitudes for the total and individual-mode disturbances at $x/c = 0.45$. As mentioned in the previous section, the total disturbance amplitude remains constant at about 14% with increasing roughness height. There does appears to be some redistribution of energy in the modal content as the initial conditions are increased. It is difficult, however, to make any meaningful conclusions about the effects of the larger roughness on the individual-mode amplitudes. As shown by the [6|18] roughness, forcing at $\lambda_z = 18$ mm actually excites the 9 mm wavelength first, which grows rapidly, saturates, and then *decays*. It is possible that the larger roughness heights yield larger initial amplitudes for the 9 mm component, which would then grow, saturate, and decay sooner than for the [6|18] roughness case. This would explain the smaller $(0, 2)$ mode amplitudes, since the mode would be decaying over a larger distance by the time $x/c = 0.45$ is reached. Of course this is all just speculation, and further study must be done before any definite conclusions can be made.

Table 5.3: Total and individual-mode disturbance amplitudes at $x/c = 0.45$ for $Re_c = 2.4 \times 10^6$ and [k|18] roughness.

Roughness Height	Disturbance Mode Amplitude [%]				
	Total	$\lambda_z = 18$ mm	$\lambda_z = 9$ mm	$\lambda_z = 6$ mm	$\lambda_z = 4.5$ mm
6 μm	14.2	10.1	10.0	3.3	0.9
12 μm	14.8	12.8	8.3	2.7	0.5
18 μm	13.3	11.2	8.0	0.8	0.9

5.6 [6|8] Roughness—Data Set $\mathcal{E}$

Sections 5.4 and 5.5 show the effective suppression of the most unstable wavelength by using a roughness spacing that does not contain superharmonics with wavelengths around 12 mm. In addition, no evidence of subharmonics in this and past experiments by Reibert (1996a) has ever been observed. Linear stability theory predicts that short-wavelength disturbances grow early, saturate, and then decay. Thus, the next logical step is to study the effects of a subcritical roughness spacing ($\lambda_z < 12$ mm).

Both linear stability theory and the 18 mm-spaced roughness experiments presented above show that the 9 mm wavelength is also very unstable. Therefore, it is desirable to space the roughness elements less than 9 mm apart. For this study, the 6 μm-high roughness elements are applied in a full-span array at $x/c = 0.023$ with a spanwise spacing of 8 mm.

5.6.1 Flow Visualization

As for the [0|0] roughness case, surface-shear-stress patterns and transition locations are determined using naphthalene flow visualization (see section 4.3). Figures 5.131, 5.132, and 5.133 show the naphthalene pattern for $Re_c = 2.4 \times 10^6$, $Re_c = 2.6 \times 10^6$, and $Re_c = 2.8 \times 10^6$, respectively. Again, the flow is from left to right, and the leading edge and chord locations are marked.

At $Re_c = 2.4 \times 10^6$ (figure 5.131), the transition pattern is extremely interesting.

The [6|8] roughness has effectively delayed transition *past* the pressure minimum location ($x/c = 0.70$). In fact, transition has been moved back even past the transition location observed under natural surface roughness conditions (figure 5.11). Transition occurs for the [6|8] roughness case at approximately 80% chord, which is the location of the junction between the wing and trailing-edge flap. Thus, it is entirely possible that the junction actually causes transition.

Figure 5.131 shows definite vortex streaks with an 8 mm spacing for $0.30 \leq x/c \leq 0.45$. For $x/c > 0.45$, however, the 8 mm structure "washes out" and the vortex streaks appear at larger spanwise spacings. Although the spacing between streaks becomes larger in general, there is definite spanwise nonuniformity in the spacing. Thus, it is difficult to make any conclusions about the longer wavelengths based solely on the flow visualization. Detailed boundary-layer measurements shed more light on this phenomenon.

For $Re_c = 2.6 \times 10^6$ and [6|8] roughness (figure 5.132), transition occurs at approximately 59% chord, which is comparable to the transition location for the no roughness case (figure 5.12). Vortex streaks spaced at 8 mm are apparent up to about $x/c = 0.45$, at which point the longer wavelength structure appears. Transition again occurs in this region where the longer spanwise spacing dominates.

The transition pattern for [6|8] roughness and $Re_c = 2.8 \times 10^6$ is shown in figure 5.133. At this Reynolds number, transition moves forward to about 50% chord, which is slightly more forward than the location for the corresponding natural roughness case (figure 5.13). As with the $Re_c = 2.4 \times 10^6$ and 2.6×10^6 cases, 8 mm-spaced vortex streaks are observed. For $Re_c = 2.8 \times 10^6$, however, the 8 mm structure extends to $x/c = 0.50$. Transition occurs in this region where the 8 mm structure dominates, and there is no evidence of the longer-wavelength vortex streaks.

In general, the [6|8] roughness shows the ability of subcritical roughness spacing

to delay transition. For $Re_c \leq 2.6 \times 10^6$, the transition location is at least as far back as that induced even by the finely-polished natural surface roughness conditions. Table 5.2 summarizes the approximate transition locations for [6|8] and other roughness configurations.

5.6.2 Total Disturbance Amplitude Measurements

The normalized velocity contours, boundary-layer profiles, and disturbance profiles for $Re_c = 2.4 \times 10^6$ and [6|8] roughness are shown in figures 5.134–5.145, 5.146–5.157, and 5.158–5.169, respectively. The disturbance is first measurable at $x/c = 0.10$, and a very uniform and dominant $\lambda_z = 8$ mm mode develops for $0.10 \leq x/c \leq 0.25$. At $x/c = 0.30$, although the contour plot (figure 5.139) still shows a dominant 8 mm mode, there is noticeable development of some slight nonuniformity. This nonuniformity becomes more dramatic with increasing x/c, and the 8 mm structure fades out in favor of some longer wavelength disturbances. By $x/c = 0.50$, (figure 5.143) the dominance of the fundamental mode ($\lambda_z = 8$ mm) is gone, and at $x/c = 0.60$ (figure 5.145) the fundamental mode is indistinguishable in the velocity contours. This is consistent with the results of the naphthalene flow visualization discussed earlier.

Figure 5.170 shows the rms mode-shape profiles for $0.10 \leq x/c \leq 0.60$. The total disturbance amplitude and corresponding N-factors computed from the mode shapes are presented in figure 5.171. The total disturbance grows rapidly from $0.10 \leq x/c \leq 0.30$, at which point the amplitude saturates and then shows strong decay. At $x/c = 0.30$, the second lobe high in the mode shape is evident, indicating strong nonlinear effects. The amplitude continues to decay for $0.30 \leq x/c \leq 0.45$, At $x/c = 0.45$, the amplitude levels off and then shows a second region of strong growth for $0.50 \leq x/c \leq 0.60$. Reibert (1996a) observed a similar two-stage growth in some of his data, but never experienced such a dramatic amplitude decay before the second growth region.

5.6.3 Individual-Mode Disturbance Amplitude Measurements

The modal content of the stationary vortex structure for [6|8] roughness is determined with spanwise scans and spectral analysis. Figures 5.172–5.182 show the constant-height spanwise scans for $0.10 \leq x/c \leq 0.60$. The corresponding PSD estimates are shown in figures 5.183–5.193. As seen with the normalized velocity contours, the spanwise scans show a very uniform disturbance up to $x/c = 0.25$. The fundamental mode is first detected at $x/c = 0.10$ and grows rapidly to $x/c = 0.30$. The $(0, 2)$ mode becomes measurable at $x/c = 0.20$. For $x/c > 0.30$, nonuniformities develop as longer wavelength modes grow and eventually become dominant. At $x/c = 0.60$, the spectrum (figure 5.193) shows no evidence of the fundamental and $(0, 2)$ modes, rather, the spectrum is dominated by broadband energy contained in longer wavelengths ($\lambda_z \geq 10$ mm). This is similar to the [0|0] roughness results which show nonuniformities due to the excitation of longer wavelength disturbances.

Peaks in the PSD are integrated to obtain disturbance amplitudes for each unstable mode. Figure 5.194 shows the amplitude and N-factor distribution for the fundamental and $(0, 2)$ mode disturbances. The total disturbance amplitude and N-factor curve is added for comparison in figure 5.195. The fundamental mode shows excellent agreement with the total disturbance for $0.10 \leq x/c \leq 0.25$. For $x/c \geq 0.30$, the fundamental amplitude drops dramatically from the total disturbance amplitude. Unlike the results of [6|18] roughness and Reibert (1996a), the total disturbance is *not* completely made up by the fundamental and its superharmonics. In other words, strong growth of the $(0, 2)$ mode is not seen in the region where the fundamental drops from the total disturbance ($0.30 \leq x/c \leq 0.60$). Rather, the continuing growth of the total disturbance occurs because the longer wavelengths become unstable downstream. Note that the longer-wavelength disturbances are broadband and are not subharmonics of the fundamental disturbance.

In short, $Re_c = 2.4 \times 10^6$ and [6|8] roughness delays transition past that of the natural roughness case. Strong early growth of the 8 mm mode effectively suppresses initial growth of the the very unstable 9 mm and 12 mm modes near the leading edge, which linear stability theory predicts to be the region where these modes have the largest growth rates. The fundamental ($\lambda_z = 8$ mm) mode saturates and then decays rapidly. This dramatic decay allows for longer wavelength background disturbances (due to submicron surface irregularities) to become unstable. The growth of these longer-wavelength broadband disturbances eventually leads to transition.

5.6.4 Theoretical Comparison

Figure 5.196 shows a comparison between the total disturbance N-factor and a nonlinear PSE computation from Haynes. The experimental N-factor distribution is computed from the maximum of the mode shape profiles, and is the same as seen in figures 5.171 and 5.195. As discussed in section 1.3.2, the PSE require specified initial conditions. For the nonlinear computations, the necessary initial conditions are determined by matching the total disturbance amplitudes of the computation and experiment at $x/c = 0.10$, where the disturbance is first measurable experimentally.

Good agreement is observed between the theoretical and experimental results. The nonlinear PSE slightly underpredicts the initial strong growth, but it accurately predicts the maximum N reached by the first growth stage and even captures the dramatic amplitude decay. This indicates that the drastic decay is a nonlinear effect, since the linear computations do not predict this feature. The nonlinear PSE does not predict the second growth stage downstream. This is expected because the second growth region is due to longer-wavelength broadband disturbances, and not the fundamental 8 mm or superharmonic disturbances. The nonlinear PSE code initially puts energy into the fundamental wavelength and then superharmonic modes are "turned on" as nonlinear effects cause them to grow above a specified threshold.

Thus, as implemented here, the PSE will not be able to predict the longer wavelength modes downstream.

5.7 [48|8] Roughness—Data Set $\mathcal{F}$

The [6|8] roughness results proved to be very different from any past findings where $\lambda_z \geq 12$ mm roughness spacings were used. For these larger roughness spacings, results of the 18 mm-spaced roughness cases (sections 5.4 and 5.5) and of Reibert (1996a) show that increasing the roughness height has no noticeable effect on the total-disturbance saturation amplitude and little effect on transition location. Naphthalene flow visualization results (see table 5.2), however, show that the average transition location moves forward to $x/c = 0.59$ when the roughness height is increased from 6 μm to 48 μm for the subcritical 8 mm-spaced artificial roughness. Detailed hot-wire measurements for [48|8] roughness and $Re_c = 2.4 \times 10^6$ will shed light onto this interesting result.

5.7.1 Total Disturbance Amplitude Measurements

Figures 5.197–5.207, 5.208–5.218, and 5.219–5.229 show the normalized velocity contours, boundary-layer profiles, and disturbance profiles, respectively. The total disturbance mode-shape profiles are presented in figure 5.230. Figure 5.231 shows the total disturbance amplitude and corresponding N-factor distribution. This series of plots shows trends similar to those of the [6|8] roughness case, with the total disturbance amplitude showing a two-stage growth with an intermediate dramatic decay.

Figure 5.232 shows the amplitude distribution of [48|8] roughness compared with that of [6|8] roughness. The larger surface roughness yields larger initial total disturbance amplitudes. The disturbance is first measurable at $x/c = 0.05$ for [48|8] roughness, but was not detected until $x/c = 0.10$ for [6|8] roughness. The larger

initial amplitude causes saturation to occur sooner at $x/c = 0.25$, rather than at $x/c = 0.30$ for [6|8] roughness. In fact, all of the characteristic features (initial detection, saturation, decay, and regrowth) have been moved forward by 5% chord with the increase in roughness height. [48|8] roughness has also increased the maximum amplitude of the first growth stage from 11% (for [6|8] roughness) to 14%. It is interesting that after the first growth stage, the total disturbance amplitude decays to approximately the same amplitude for both the [6|8] and [48|8] roughness cases. At this point where the longer wavelengths have become unstable, both amplitude curves show similar growth rates.

5.7.2 Individual-Mode Disturbance Amplitude Measurements

Figures 5.233–5.243 and 5.244–5.254 show the constant-Y scans and corresponding PSD estimates, respectively. As with [6|8] roughness, the spectra show dominance of the fundamental ($\lambda_z = 8$ mm) mode early and the development of longer-wavelength modes for $x/c \geq 0.35$. The total disturbance and individual-mode amplitude and N-factor curves are presented in figure 5.256. Similar to the results of [6|8] roughness, the fundamental amplitude agrees well with the total disturbance amplitude for $0.05 \leq x/c \leq 0.15$. For $0.15 \leq x/c \leq 0.35$, the fundamental drops slightly below the total amplitude as the $(0, 2)$ mode shows some growth and then decays. For $x/c > 0.35$, the $(0, 2)$ mode becomes immeasurable and the fundamental drops well below the total disturbance amplitude, signifying strong growth of the longer wavelengths.

CHAPTER 6

Conclusions

6.1 Specific Results

6.1.1 Basic State

This experiment complements the work of Reibert (1996a), so it is important to establish similar flowfields to allow direct data comparisons. Pressure distribution measurements show good agreement with the theoretical C_p distribution of the NLF(2)-0415 airfoil. In addition, excellent agreement is observed between the pressure distribution of this experiment and that of Reibert (1996a), indicating the existence of similar global flowfields.

Wall-normal hot-wire measurements provide specific details of the basic-state boundary layer. The basic-state profiles verify the success of the floor and ceiling test-section liners in producing a spanwise invariant flowfield in the test region of the model. Comparisons with Reibert (1996a) show excellent agreement between the average basic-state profiles, further confirming similar test conditions.

6.1.2 Natural Surface Roughness

In the absence of artificial roughness, the naturally occurring stationary crossflow waves grow to nonuniform amplitudes due to submicron roughness irregularities near

the leading edge. Even under these conditions, nonlinear effects and a jagged transition pattern are observed. Boundary-layer maps and constant-Y scans provide detailed information about the total and individual-mode disturbances. The total disturbance shows strong initial growth followed by a nonlinear amplitude saturation.

Although the crossflow disturbance is nonuniform in span, a definite 11 mm-wavelength component is observed, which is approximately the most unstable mode according to linear theory. In addition to this component, significant broadband disturbance energy is contained in longer wavelengths at all chord locations. The 11 mm disturbance grows and saturates due to nonlinear interactions with the broadband disturbances, at which point the longer-wavelength waves continue to grow.

Overall, the results of the minimum-surface-roughness case indicate the extreme sensitivity of the stationary crossflow disturbance to surface roughness and the importance of nonlinear effects.

6.1.3 Distributed Artificial Roughness

Carefully applied roughness elements near the leading edge provide known initial conditions for the disturbance growth and uniform crossflow waves. The spacing of the roughness elements fixes the fundamental wavelength of the crossflow disturbance.

18 mm Roughness Spacing

The growth of the total disturbance is initially exponential (as described by linear theory), but then shows amplitude saturation downstream. The individual-mode disturbances, once detected, also show initial growth consistent with linear theory followed by nonlinear saturation. Although the roughness spacing is 18 mm, the results clearly show development of the 9 mm harmonic wavelength disturbance first. This indicates that the Fourier decomposition of the roughness distribution is important in the receptivity process, and is consistent with the findings of Reibert (1996a). In

addition, the fundamental 18 mm disturbance doesn't show strong growth until the 9 mm mode saturates, indicating strong nonlinear interactions between individual modes. As with the earlier experiments, no subharmonics (wavelength doubling) are observed.

Increasing the height of the roughness elements does not change the total disturbance amplitude at saturation. Similar mode-shape profiles are observed downstream, with a redistribution of energy high in the boundary layer. This suggests that once the nonlinear effects are large enough to cause amplitude saturation, the energy is redistributed higher in the disturbance layer, leaving the total disturbance amplitude fixed.

In general, the results of the [6|18], [12|18], and [18|18] roughness cases are consistent with those of Reibert (1996a), with one additional discovery. Applying the roughness elements such that the spacing is not a multiple of the most unstable wavelength ($\lambda_z = 12$ mm) effectively suppresses growth of this most unstable mode. The strong growth of the $(0, 2)$ mode ($\lambda_z = 9$ mm) prevents the naturally occurring dominant mode from appearing. This suggests that forcing modes that do not grow strongly (nor have superharmonics that grow strongly) may yield smaller total disturbance growth.

8 mm Roughness Spacing

A subcritical roughness spacing of 8 mm is examined. Under certain conditions, the subcritical spacing effectively delays transition past that of even the natural roughness case. The fundamental disturbance shows initial exponential growth, but then saturates and decays dramatically. The strong initial growth of the subcritical disturbance inhibits growth of the most unstable wavelengths. The dramatic decay allows longer-wavelength background disturbances to grow downstream (as linear theory predicts), which eventually lead to transition.

Unlike earlier results, increasing the roughness height for the subcritical 8 mm spacing moves transition forward. This occurs because the larger roughness heights produce larger initial disturbance amplitudes that saturate and decay sooner than for smaller roughness heights. This earlier decay with larger roughness allows longer-wavelength background disturbances to grow sooner, eventually leading to earlier transition.

The implications of the subcritical-roughness-spacing results are profound. Although some issues must be addressed in terms of appropriate roughness height, subcritically spaced roughness shows promise as an effective passive transition-control technique.

6.2 Summary

This experiment contributes to the understanding of the processes that influence boundary-layer transition in stationary-crossflow-dominated flows. The ability of submicron-high distributed roughness elements applied near the attachment line to dramatically alter the disturbance growth and even delay transition underscores the extreme sensitivity of the stationary crossflow disturbance to roughness. Thus, any accurate transition prediction in swept-wing flows must consider receptivity and nonlinear effects, as well as the initial growth described by linear theory. The data of this experiment add to the existing database for theoretical code development and validation.

REFERENCES

Arnal, D. 1984. Description and prediction of transition in two-dimensional incompressible flow. In *Special Course on Stability and Transition of Laminar Flows*, AGARD R-709.

Arnal, D. 1992. Boundary-layer transition: Prediction, application to drag reduction. In *Special Course on Skin Friction Drag Reduction*, AGARD R-786. Loughton, Essex: Specialised Printing Services Ltd. ISBN 92-835-0661-8.

Arnal, D. 1994. Boundary-layer transition: Predictions based on linear theory. In *Special Course on Progress in Transition Modelling*, AGARD R-793. Loughton, Essex: Specialised Printing Services Ltd. ISBN 92-835-0742-8.

Arnal, D. and J. C. Juillen. 1987. Three-dimensional transition studies at ONERA-CERT. AIAA Paper 87-1335.

Arnal, D., E. Coustols, and J. C. Juillen. 1984. Experimental and theoretical study of transition phenomena on an infinite swept wing. Rech. Aérosp. No. 1984-4.

Arnal, D., G. Casalis, and J. C. Juillen. 1990. Experimental and theoretical analysis of natural transition on infinite swept wing. In *Laminar-Turbulent Transition* (eds. D. Arnal and R. Michel), vol. 3, pp. 311–325. Berlin: Springer-Verlag. ISBN 3-540-52196-8.

Benmalek, A. and W. S. Saric. 1994. Effects of curvature variations on the nonlinear evolution of Goertler vortices. *Phys. Fluids* 3(10):3353–3367.

Bippes, H. 1990. Instability feature appearing on swept wing configurations. In *Laminar-Turbulent Transition* (eds. D. Arnal and R. Michel), vol. 3, pp. 419–430. Berlin: Springer-Verlag. ISBN 3-540-52196-8.

Bippes, H. 1991. Experiments on transition in three-dimensional accelerated boundary-layer flows. In *Proc. R.A.S. Boundary Layer Transition and Control*, Cambridge, U.K.

Bippes, H. and B. Müller. 1990. Disturbance growth in an unstable three-dimensional boundary layer. In *Numerical and Physical Aspects of Aerodynamics Flows IV* (ed. T. Cebeci), pp. 345–358. Berlin: Springer-Verlag. ISBN 3-540-52259-X.

Bippes, H. and P. Nitschke-Kowsky. 1990. Experimental study of instability modes in a three-dimensional boundary layer. *AIAA J.* 28(10):1758–1763.

Bippes, H., B. Müller, and M. Wagner. 1991. Measurements and stability calculations of the disturbance growth in an unstable three-dimensional boundary layer. *Phys. Fluids* 3(10):2371–2377.

Dagenhart, J. R. 1992. *Crossflow Stability and Transition Experiments in a Swept-Wing Flow.* Ph.D. diss., Virginia Polytechnic Institute and State University. Also NASA TM-108650.

Dagenhart, J. R., W. S. Saric, M. C. Mousseux, and J. P. Stack. 1989. Crossflow vortex instability and transition on a 45-degree swept wing. AIAA Paper 89-1892.

Dagenhart, J. R., W. S. Saric, J. A. Hoos, and M. C. Mousseux. 1990. Experiments on swept-wing boundary layers. In *Laminar-Turbulent Transition* (eds. D. Arnal and R. Michel), vol. 3, pp. 369–380. Berlin: Springer-Verlag. ISBN 3-540-52196-8.

Deyhle, H. and H. Bippes. 1996. Disturbance growth in an unstable three-dimensional boundary layer and its dependence on environmental conditions. To appear in *J. Fluid Mech.*

Deyhle, H., G. Höhler, and H. Bippes. 1993. Experimental investigation of instability wave propagation in a 3-D boundary-layer flow. *AIAA J.* 31(4):637–645.

Floryan, J. M. 1991. On the Görtler instability of boundary layers. *Prog. Aerospace Sci.* 28:235–271.

Floryan, J. M. and W. S. Saric. 1982. Stability of Görtler vortices in boundary layers. *AIAA J.* 20(4):316–324.

Hall, P. and M. R. Malik. 1986. On the instability of a three-dimensional attachment-line boundary layer: Weakly nonlinear theory and a numerical approach. *J. Fluid Mech.* 163:257–282.

Hall, P., M. R. Malik, and D. I. A. Poll. 1984. On the stability of an infinite swept attachment-line boundary layer. *Phil. Trans. Roy. Soc. Lon. A* 395:229–245.

Haynes, T. S. 1996. *Nonlinear Stability and Saturation of Crossflow Vortices in Swept-Wing Boundary Layers.* Ph.D. diss., Arizona State University.

Haynes, T. S. and H. L. Reed. 1996. Computations in nonlinear saturation of stationary crossflow vortices in a swept-wing boundary layer. AIAA Paper 96-0182.

Herbert, T. 1994. Parabolized stability equations. In *Special Course on Progress in Transition Modelling*, AGARD R-793. Loughton, Essex: Specialised Printing Services Ltd. ISBN 92-835-0742-8.

Juillen, J. C. and D. Arnal. 1990. Etude expérimentale du déclencement de la transition par rugosités et par ranier sur de bord d'attaque d'une aile en flèche en èncoulement incompressible. Rapport Final 51/5018.35, CERT/ONERA.

Kohama, Y., W. S. Saric, and J. A. Hoos. 1991. A high-frequency secondary instability of crossflow vortices that leads to transition. In *Proc. R.A.S. Boundary Layer Transition and Control*, Cambridge, U.K.

Lerche, T. and H. Bippes. 1995. Experimental investigation of cross-flow instability under the influence of controlled disturbance generation. In *Proc. Colloquium of the Royal Netherlands Academy of Arts and Sciences on Transitional Boundary Layers in Aerodynamics: State-of-the-Art and Future Directions of Research*, Amsterdam. Elsevier.

Lin, R.-S. 1992. *Stationary Crossflow Instability on an Infinite Swept Wing.* Ph.D. diss., Arizona State University.

Meyer, F. and L. Kleiser. 1988. Numerical simulation of the nonlinear evolution of a perturbation in a three-dimensional boundary layer. In *DGLR, Flows with Separation*, pp. 39–40.

Meyer, F. and L. Kleiser. 1990. Numerical simulation of transition due to crossflow instability. In *Laminar-Turbulent Transition* (eds. D. Arnal and R. Michel), vol. 3, pp. 609–619. Berlin: Springer-Verlag. ISBN 3-540-52196-8.

Michel, R., D. Arnal, E. Coustols, and J. C. Juillen. 1985. Experimental and theoretical studies of boundary layer transition on a swept infinite wing. In *Laminar-Turbulent Transition* (ed. V. V. Kozlov), vol. 2, pp. 553–561. Berlin: Springer-Verlag. ISBN 3-540-15250-4.

Morkovin, M. V. 1969. On the many faces of transition. In *Viscous Drag Reduction* (ed. C. S. Wells), pp. 1–31. New York: Plenum.

Morkovin, M. V. 1993. Bypass-transition research: Issues and philosophy. In *Instabilities and Turbulence in Engineering Flows* (eds. D. Ashpis, T. Gatski, and R. Hirsh). Kluwer Academic.

Müller, B. 1990. Experimental study of travelling waves in a three-dimensional boundary layer. In *Laminar-Turbulent Transition* (eds. D. Arnal and R. Michel), vol. 3, pp. 489–498. Berlin: Springer-Verlag. ISBN 3-540-52196-8.

Müller, B. and H. Bippes. 1989. Experimental study of instability modes in a three-dimensional boundary layer. In *Fluid Dynamics of Three-Dimensional Turbulent Shear Flows and Transition*, AGARD CP-438. Loughton, Essex: Specialised Printing Services Ltd. ISBN 92-835-0502-6.

Müller, B., H. Bippes, and F. S. Collier, Jr. 1990. The stability of a three dimensional boundary layer over a swept flat plate. In *Instability and Transition* (eds. M. Y. Hussaini and R. G. Voight), vol. 2, pp. 268–277. New York: Springer-Verlag. ISBN 0-387-97324-9.

Nitschke-Kowsky, P. and H. Bippes. 1988. Instability and transition of a three-dimensional boundary layer on a swept flat plate. *Phys. Fluids* 31(4):786–795.

Perry, A. E. 1982. *Hot-wire Anemometry.* New York: Oxford University Press. ISBN 0-19-856327-2.

Pfenninger, W. 1977. Laminar flow control—laminarization. In *Special Course on Concepts for Drag Reduction*, AGARD R-654.

Poll, D. I. A. 1979. Transition in the infinite swept attachment line boundary layer. *Aeronaut. Q.* 30:607–629.

Poll, D. I. A. 1984. Transition description and prediction in three-dimensional flows. In *Special Course on Stability and Transition of Laminar Flows*, AGARD R-709.

Poll, D. I. A. 1985. Some observations of the transition process on the windward face of a long yawed cylinder. *J. Fluid Mech.* 150:329–356.

Radeztsky, R. H. Jr. 1994. *Growth and Development of Roughness-Induced Stationary Crossflow Vortices.* Ph.D. diss., Arizona State University.

Radeztsky, R. H. Jr., M. S. Reibert, W. S. Saric, and S. Takagi. 1993a. Effect of micron-sized roughness on transition in swept-wing flows. AIAA Paper 93-0076.

Radeztsky, R. H. Jr., M. S. Reibert, and S. Takagi. 1993b. A software solution to temperature-induced hot-wire voltage drift. In *Proc. Third International Symposium on Thermal Anemometry*, vol. 167, pp. 49–55. ASME-FED.

Radeztsky, R. H. Jr., M. S. Reibert, and W. S. Saric. 1994. Development of stationary crossflow vortices on a swept wing. AIAA Paper 94-2373.

Reed, H. L. and R.-S. Lin. 1987. Stability of three-dimensional boundary layers. SAE Paper 87-1857.

Reed, H. L., W. S. Saric, and D. Arnal. 1996. Linear stability theory applied to boundary layers. *Ann. Rev. Fluid Mech.* 28:389–428.

Reibert, M. S. 1996a. *Nonlinear Stability, Saturation, and Transition in Crossflow-Dominated Boundary Layers.* Ph.D. diss., Arizona State University.

Reibert, M. S. 1996b. *Standard C Libraries and Codes: A Guide to Programming at the ASU Unsteady Wind Tunnel.* Arizona State University. Unsteady Wind Tunnel Internal Documentation.

Reibert, M. S., W. S. Saric, R. B. Carrillo, Jr., and K. L. Chapman. 1996. Experiments in nonlinear saturation of stationary crossflow vortices in a swept-wing boundary layer. AIAA Paper 96-0184.

Saric, W. S. 1990. Low-speed experiments: Requirements for stability measurements. In *Instability and Transition* (eds. M. Y. Hussaini and R. G. Voight), vol. 1, pp. 162–174. New York: Springer-Verlag. ISBN 0-387-97323-0.

Saric, W. S. 1992a. The ASU transition research facility. AIAA Paper 92-3910.

Saric, W. S. 1992b. Laminar-turbulent transition: Fundamentals. In *Special Course on Skin Friction Drag Reduction*, AGARD R-786. Loughton, Essex: Specialised Printing Services Ltd. ISBN 92-835-0661-8.

Saric, W. S. 1994a. Görtler vortices. *Ann. Rev. Fluid Mech.* 26:379–409.

Saric, W. S. 1994b. Low-speed boundary-layer transition experiments. In *Aspects of Transition to Turbulence: Experiments, Theory & Computations* (eds. M. Hussaini and T. Corke).

Saric, W. S. 1994c. Physical description of boundary-layer transition: Experimental evidence. In *Special Course on Progress in Transition Modelling*, AGARD R-793. Loughton, Essex: Specialised Printing Services Ltd. ISBN 92-835-0742-8.

Saric, W. S. and L. G. Yeates. 1985. Experiments on the stability of crossflow vortices in swept-wing flows. AIAA Paper 85-0493.

Saric, W. S., J. R. Dagenhart, and M. C. Mousseux. 1990. Experiments in swept-wing transition. In *Numerical and Physical Aspects of Aerodynamics Flows IV* (ed. T. Cebeci), pp. 359–371. Berlin: Springer-Verlag. ISBN 3-540-52259-X.

Schrauf, G., T. Herbert, and G. Stuckert. 1995. Evaluation of transition in flight tests using nonlinear PSE analysis. AIAA Paper 95-1801.

Smith, A. M. O. and N. Gamberoni. 1956. Transition, pressure gradient, and stability theory. ES 26388, Douglas Aircraft Company, El Segundo, California.

Somers, D. M. and K. H. Horstmann. 1985. Design of a medium-speed natural-laminar-flow airfoil for commuter aircraft applications. *DFVLR-IB/29-85/26.*

Stevens, W. A., S. H. Goradia, and J. A. Braden. 1971. A mathematical model for two-dimensional multi-component airfoils in viscous flow. CR-1843, NASA.

Stuckert, G. K., T. Herbert, and V. Esfahanian. 1993. Stability and transition on swept wings. AIAA Paper 93-0078.

Thomas, A. S. W. 1985. Aircraft drag reduction technology—a summary. In *Special Course on Aircraft Drag Prediction and Reduction*, AGARD R-723. Loughton, Essex: Specialised Printing Services Ltd. ISBN 92-835-1507-2.

van Ingen, J. L. 1956. A suggested semi-empirical method for the calculation of the boundary-layer transition region. VTH 71 & 74, Dept. Aero. Eng., Univ. of Techn., Delft, Netherlands.

von Doenhoff, A. E. and A. L. Braslow. 1961. The effect of distributed roughness on laminar flow. In *Boundary-Layer Control* (ed. Lachmann), vol. 2. Pergamon.

Wang, M., T. Herbert, and G. K. Stuckert. 1994. Crossflow-induced transition in compressible swept-wing flows. AIAA Paper 94-2374.

Wintergerste, T. and L. Kleiser. 1995. Direct numerical simulation of transition in a three-dimensional boundary layer. In *Proc. Colloquium of the Royal Netherlands Academy of Arts and Sciences on Transitional Boundary Layers in Aerodynamics: State-of-the-Art and Future Directions of Research*, Amsterdam. Elsevier.

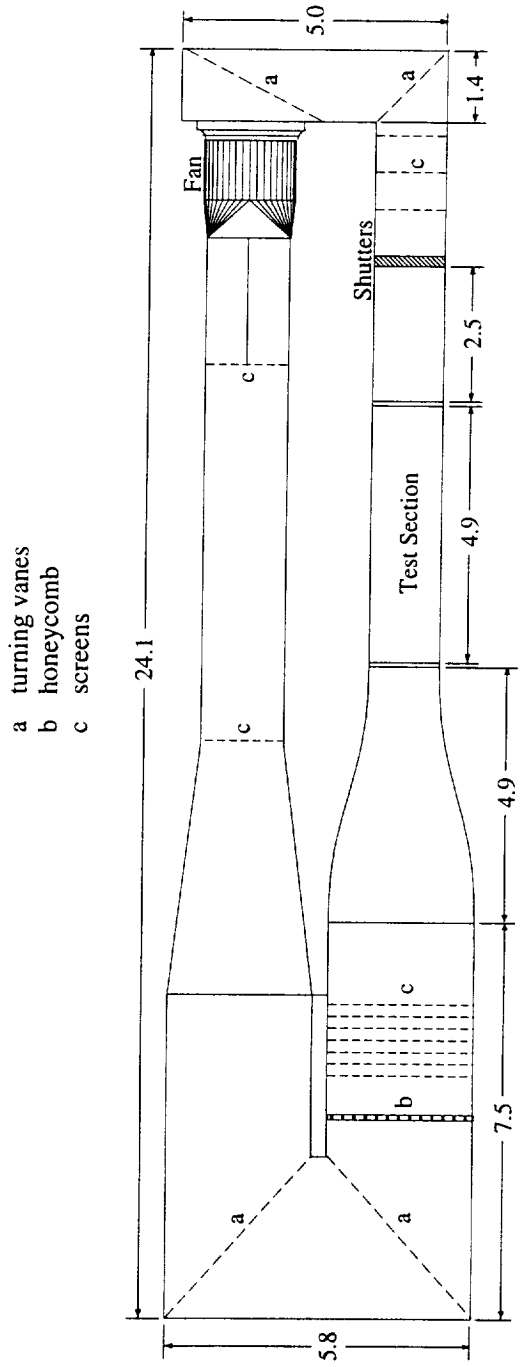

Figure 2.1: Plan view of the ASU Unsteady Wind Tunnel. All dimensions are in meters.

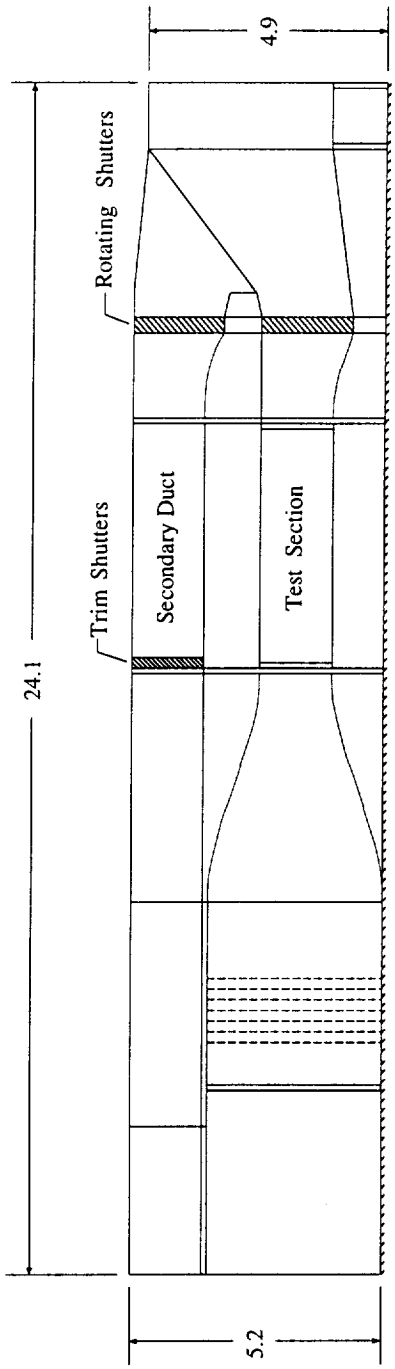

Figure 2.2: Elevation view of the ASU Unsteady Wind Tunnel. All dimensions are in meters.

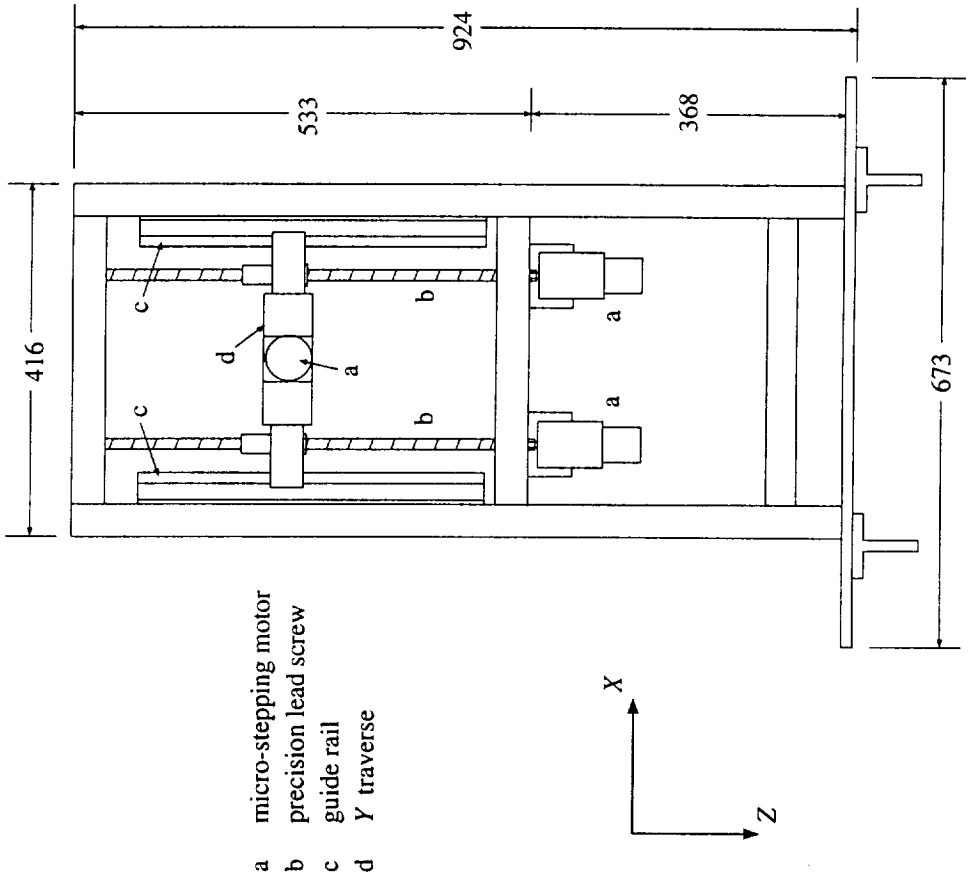

Figure 2.3: Side view of traverse carriage. All dimensions are in millimeters.

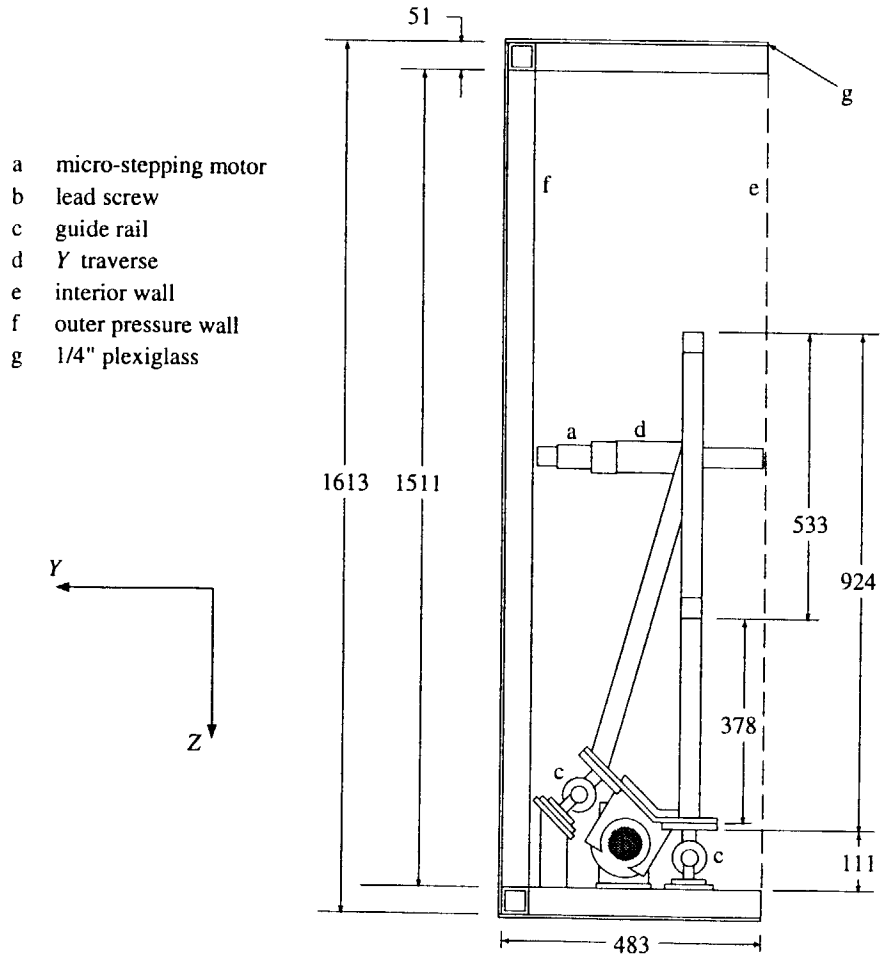

Figure 2.4: Front view of traverse carriage. All dimensions are in millimeters.

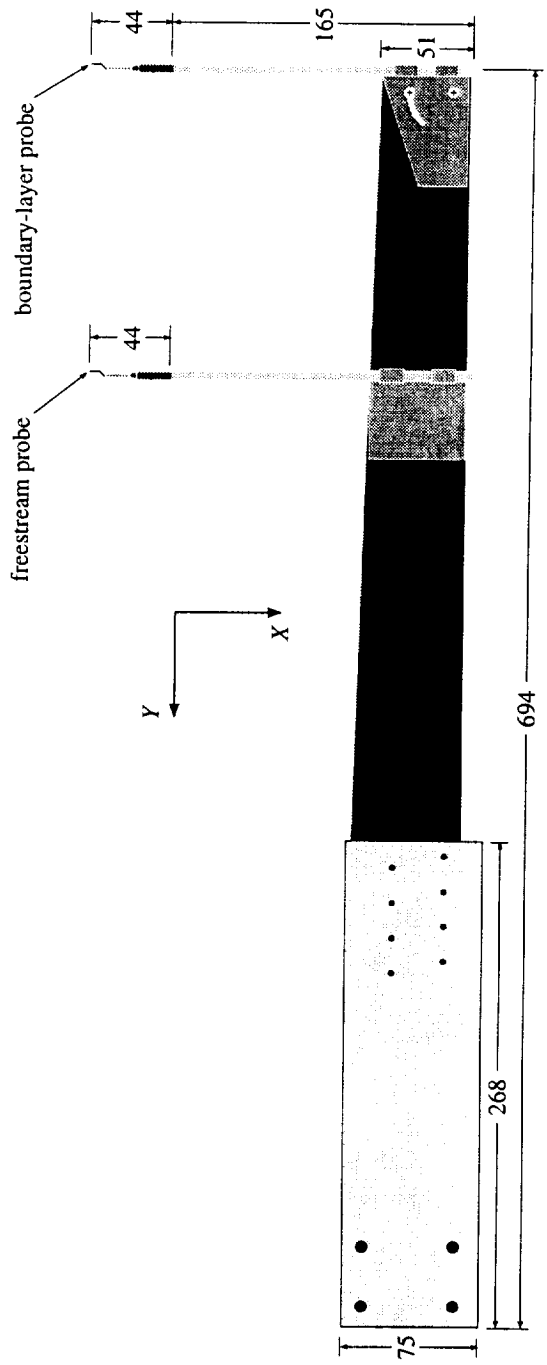

Figure 2.5: Plan view of hot-wire sting. All dimensions are in millimeters.

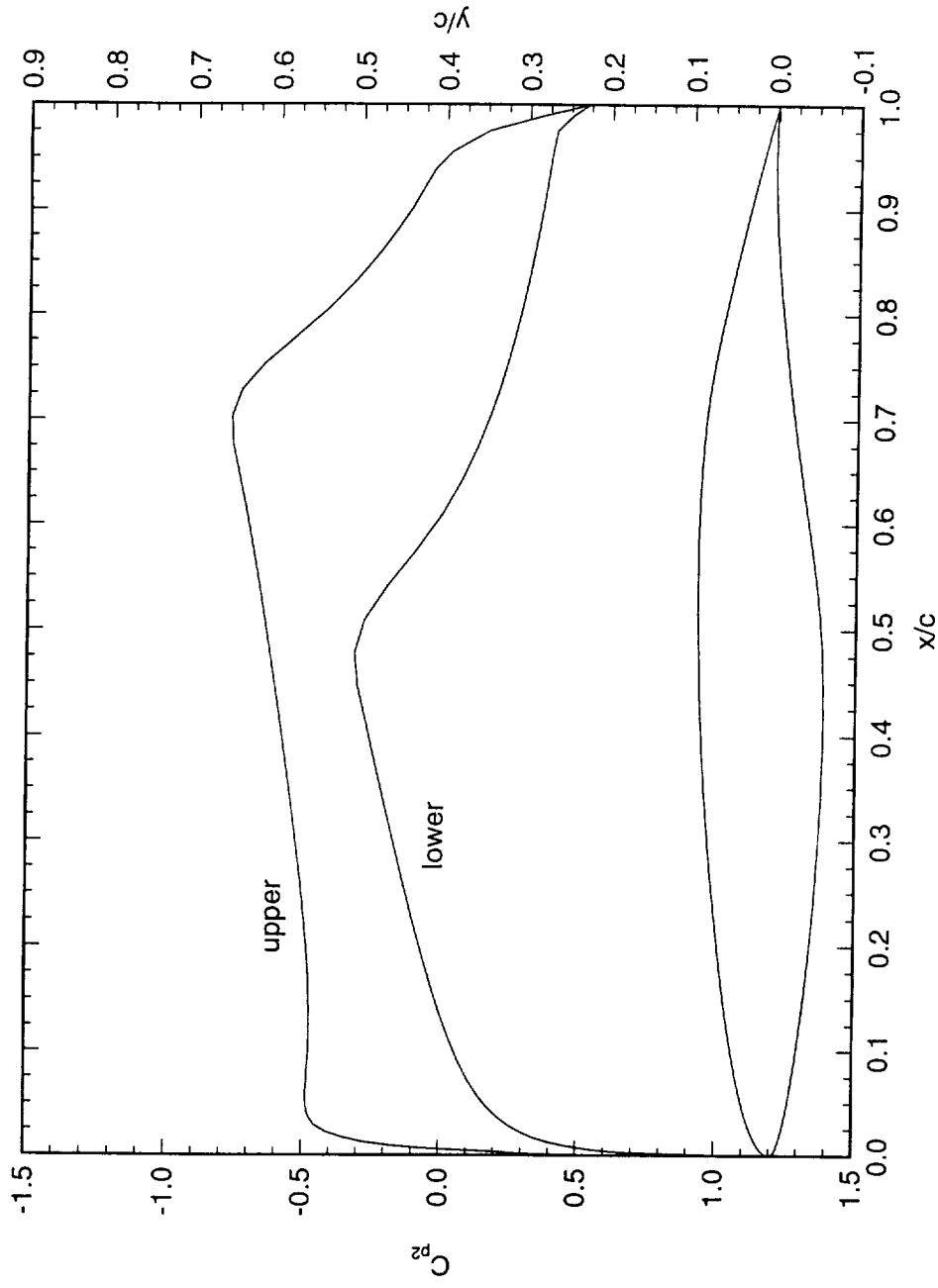

Figure 3.1: Unswept NLF(2)-0415 airfoil and C_p distribution for $\alpha = 0°$ and $\delta_F = 0°$ in free air.

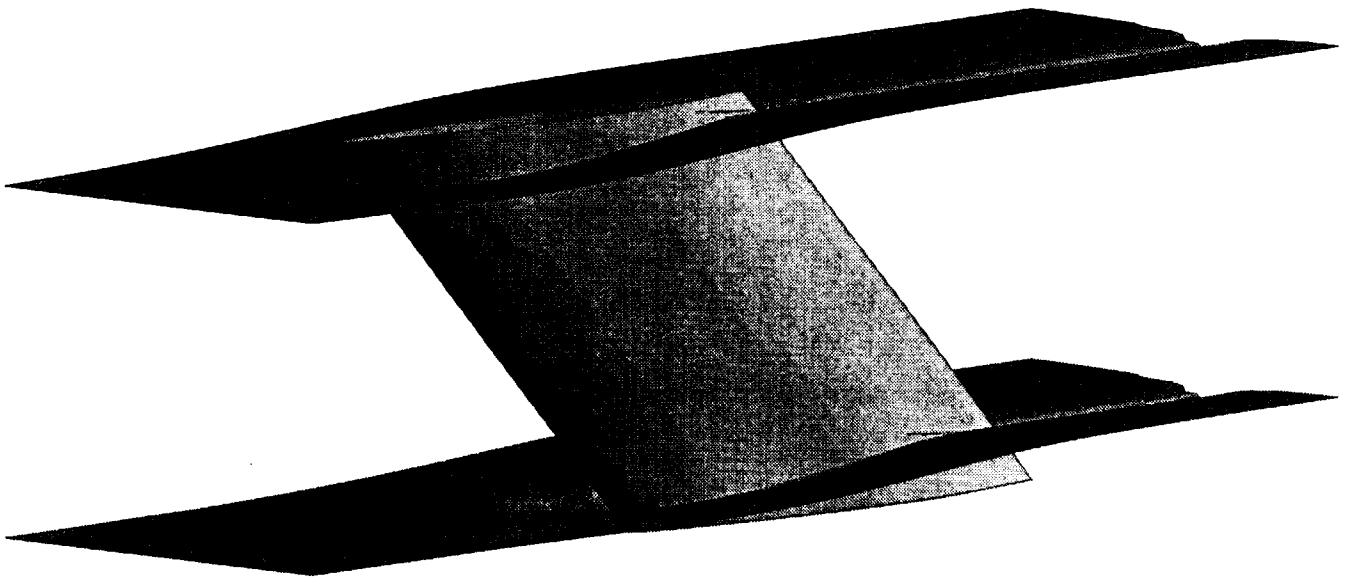

Figure 3.2: Test-section floor and ceiling liners with NLF(2)-0415 airfoil at $\alpha = -4°$.

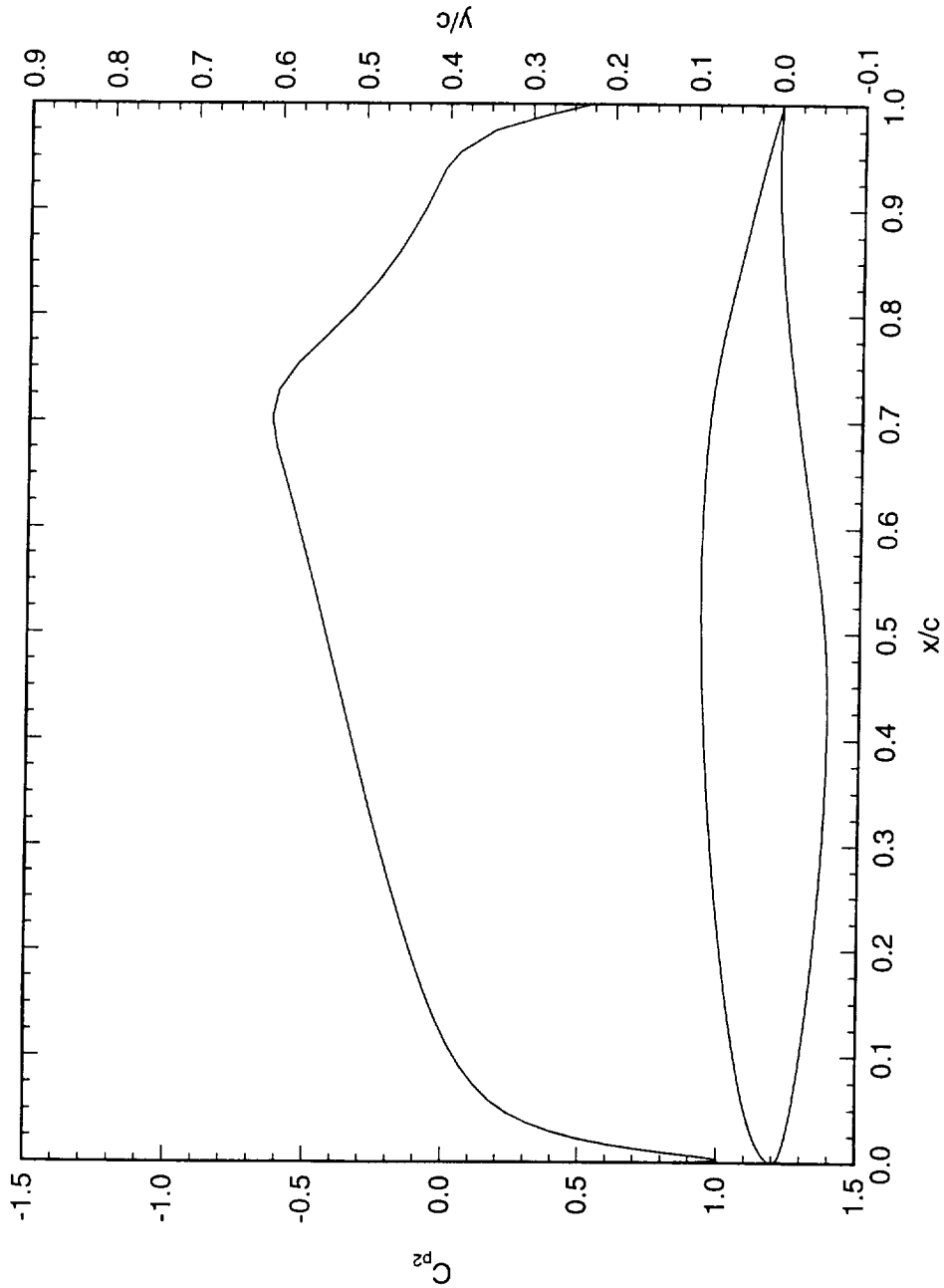

Figure 3.3: Unswept NLF(2)-0415 airfoil and upper-surface C_p distribution for $\alpha = -4°$ and $\delta_F = 0°$ in free air.

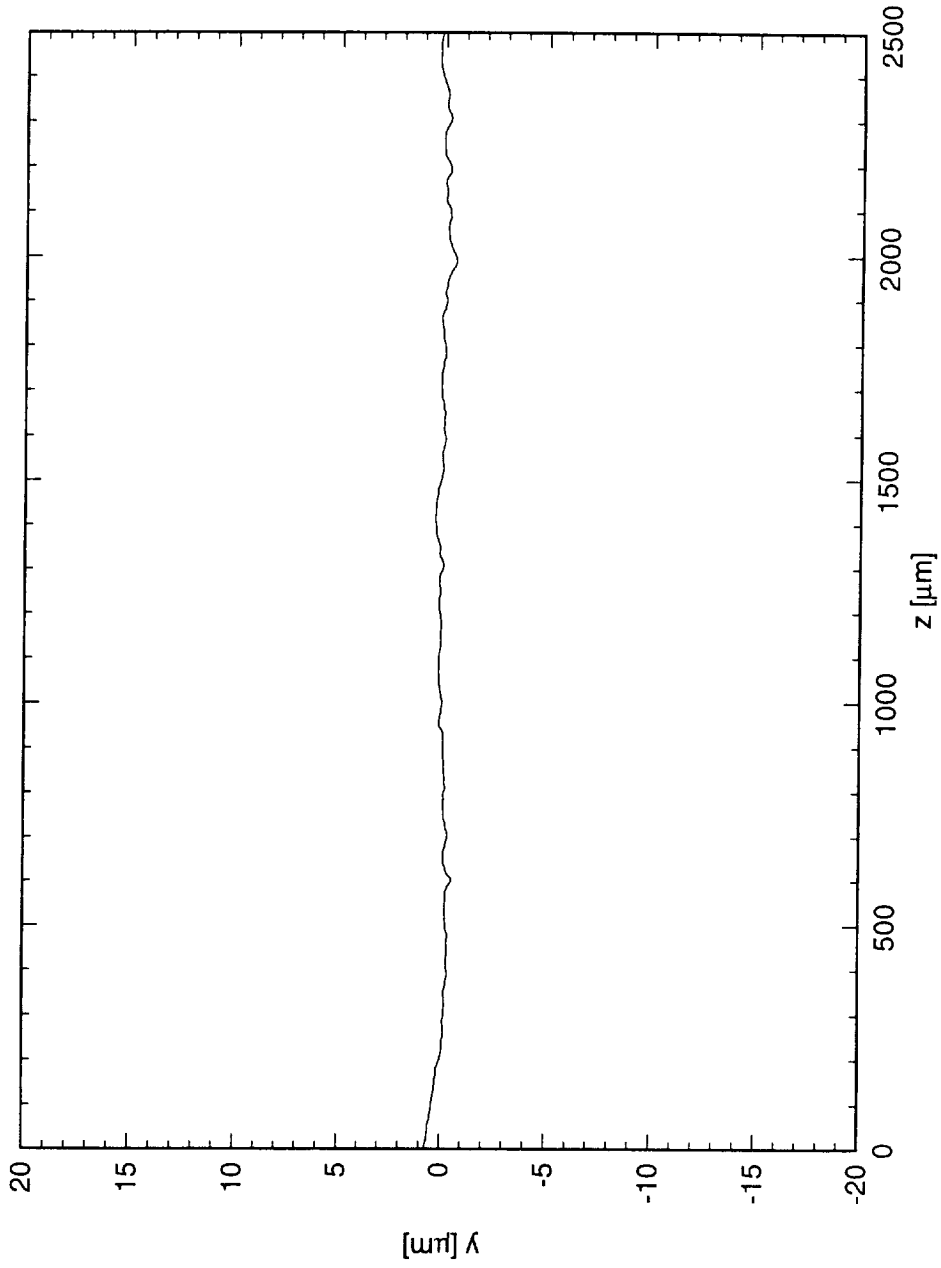

Figure 3.4: Profilometer measurement of NLF(2)-0415 surface roughness. Filtered 20–1500 μm, 0.12 μm rms.

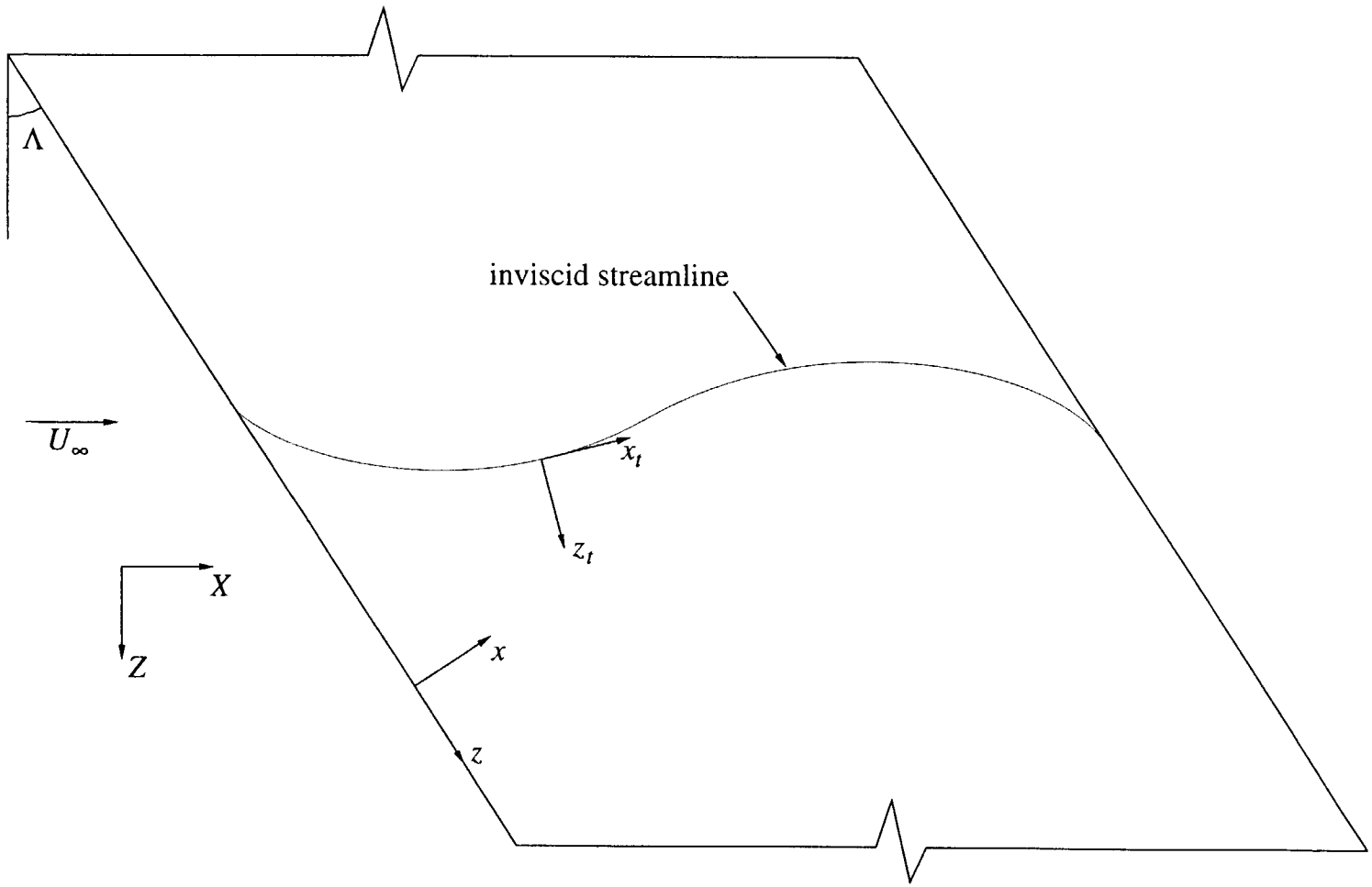

Figure 3.5: Schematic swept-wing plan view showing coordinate systems and curved inviscid streamline.

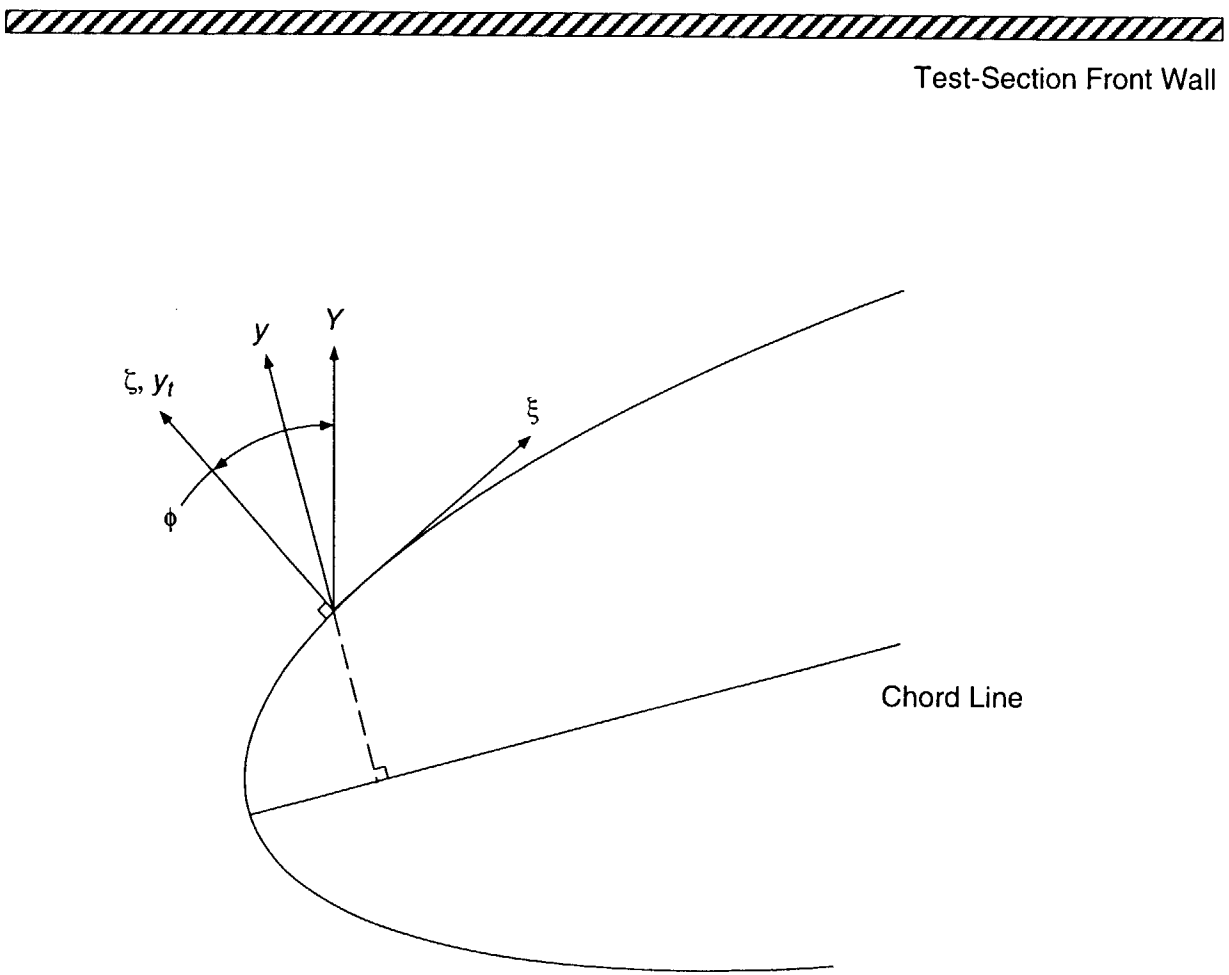

Figure 3.6: Schematic swept-wing cross section showing coordinate systems.

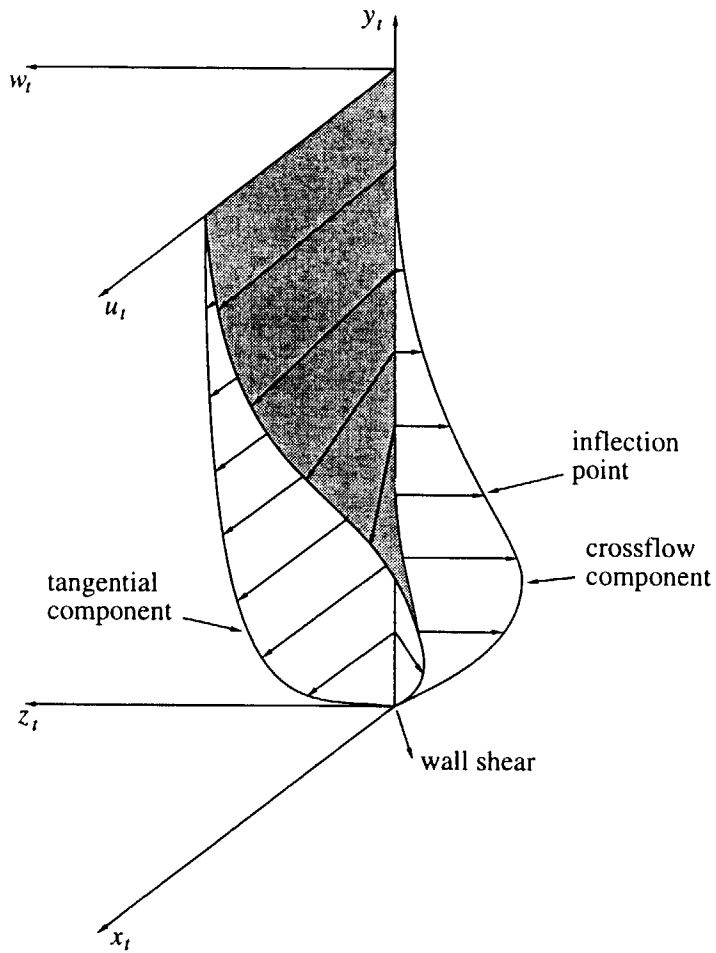

Figure 3.7: Schematic of typical swept-wing boundary-layer profile showing tangential, crossflow, and total velocity profiles.

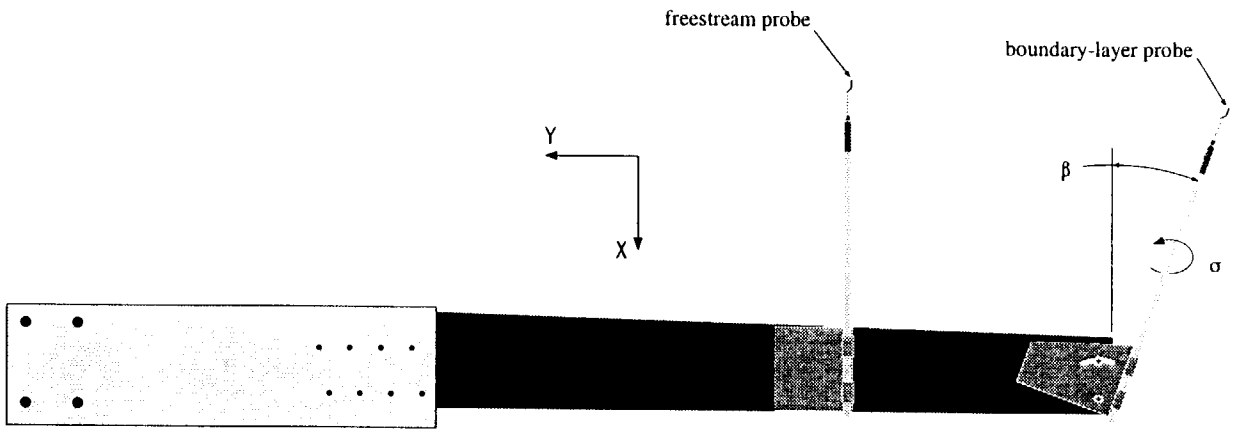

Figure 3.8: Hot-wire sting showing the necessary probe rotations to align the boundary-layer wire with the airfoil surface.

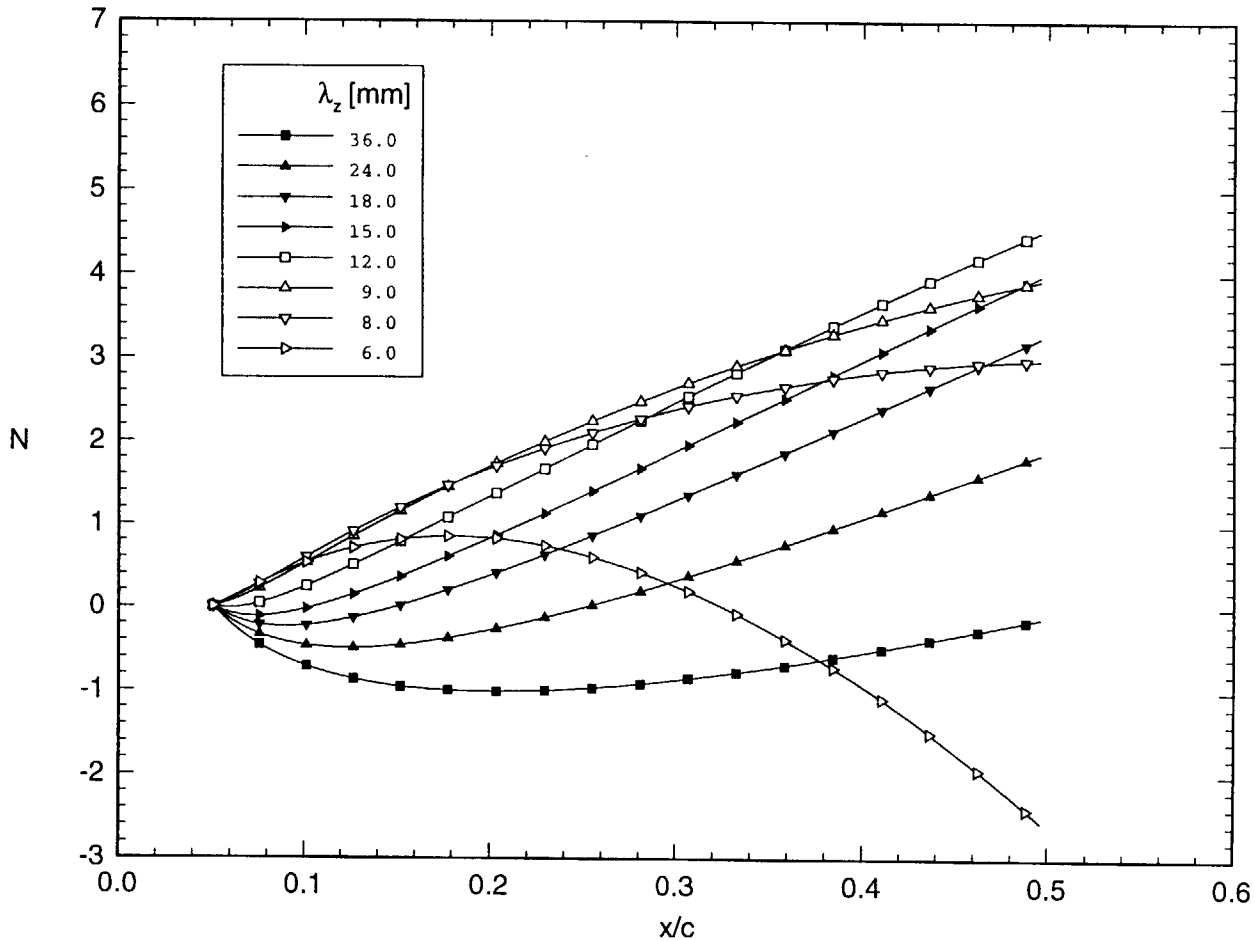

Figure 3.9: Linear theory N-factors for stationary crossflow disturbances. $Re_c = 2.4 \times 10^6$. The reference point for the N-factor calculations is $x/c = 0.05$. The calculations include curvature effects.

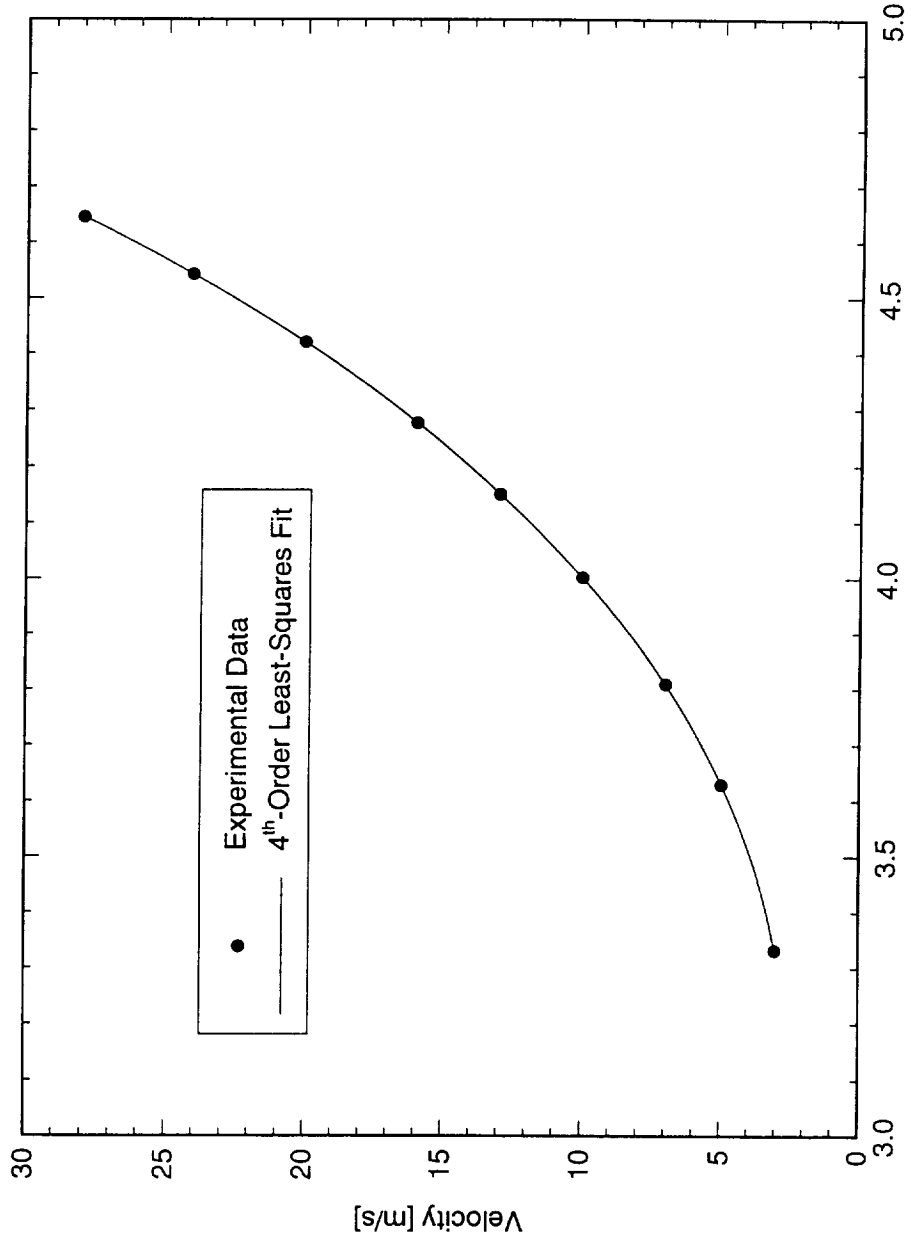

Figure 4.1: Typical hot-wire velocity calibration.

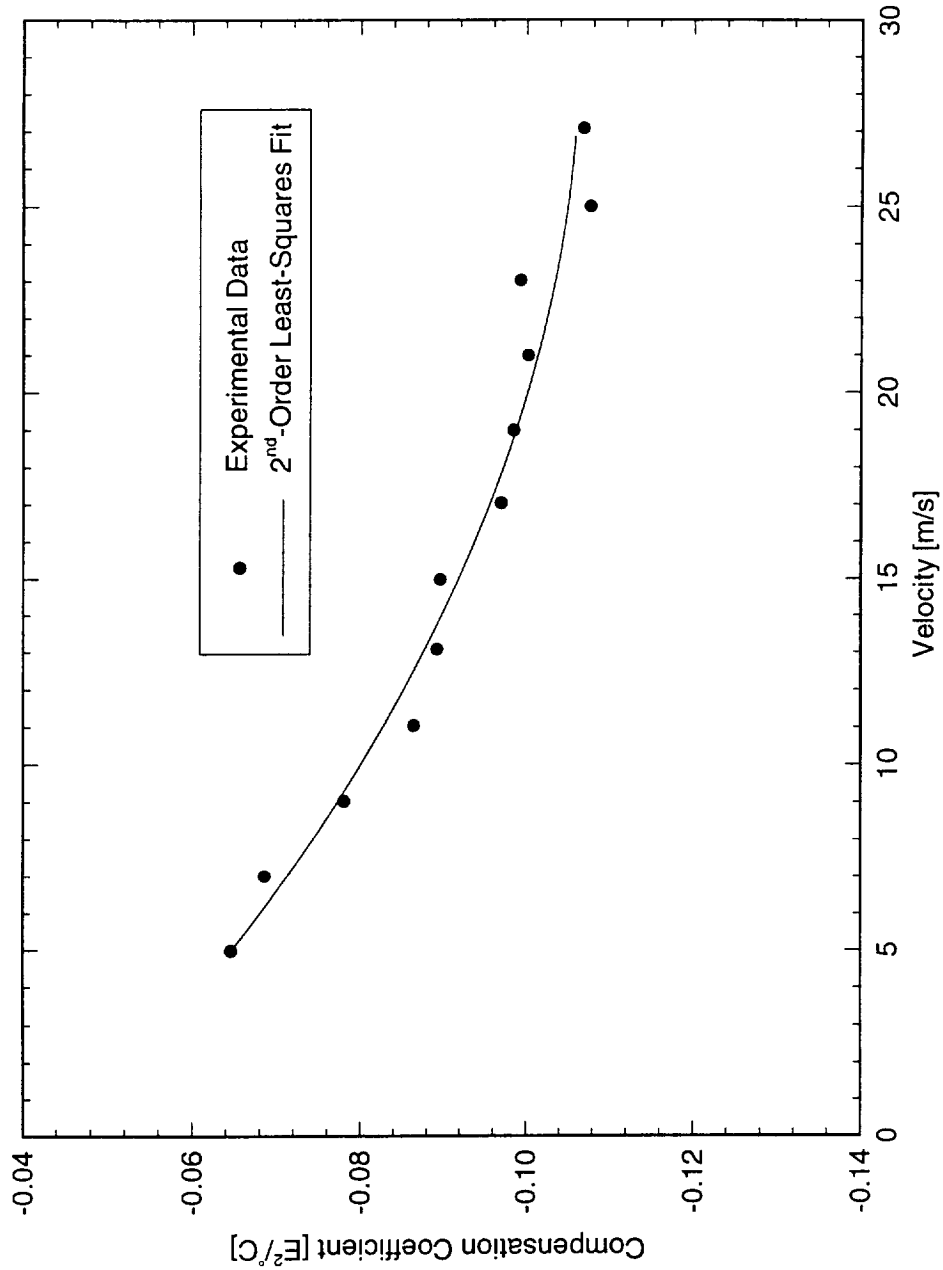

Figure 4.2: Typical hot-wire temperature compensation. The scatter in the data is caused by short sampling times.

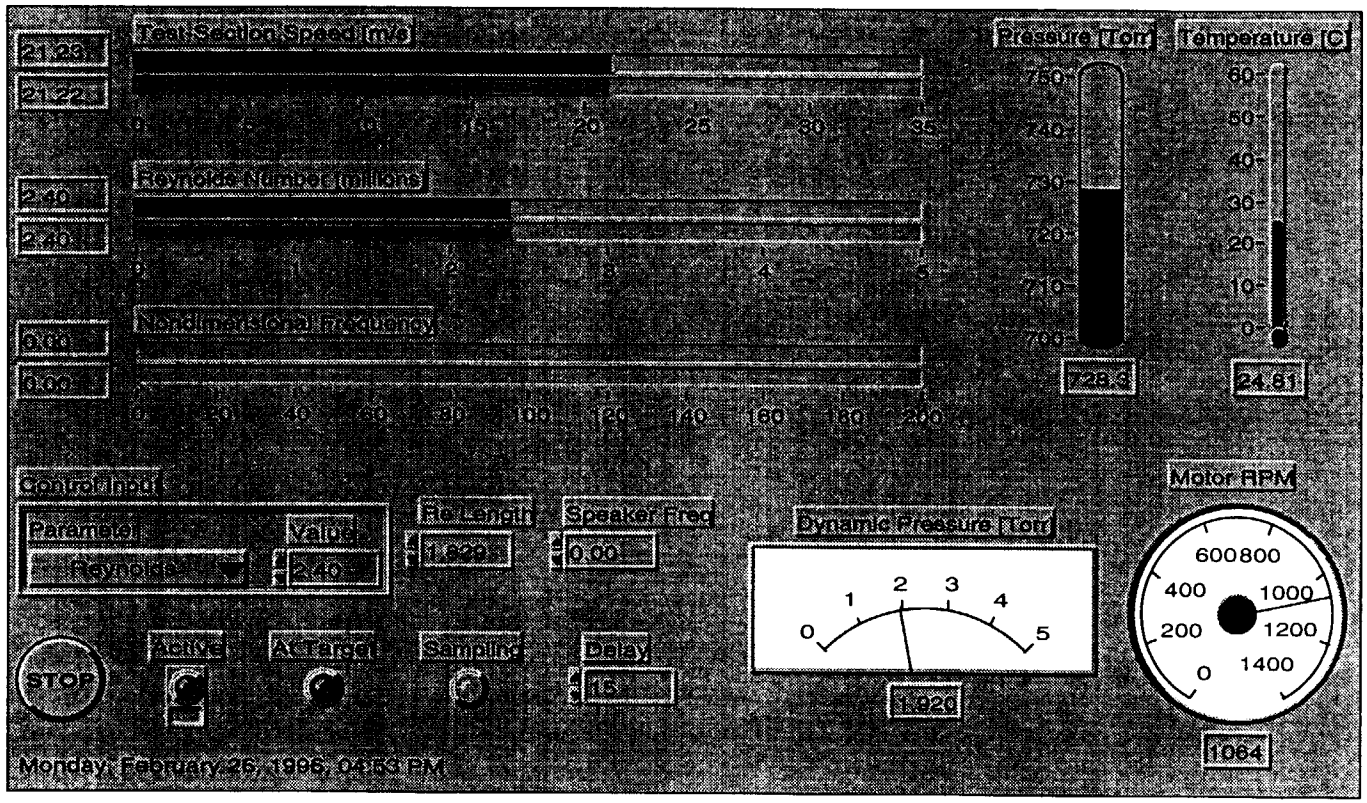

Figure 4.3: Wind tunnel speed-control program. The program monitors several tunnel conditions and adjusts the motor rpm as necessary to maintain the desired control input.

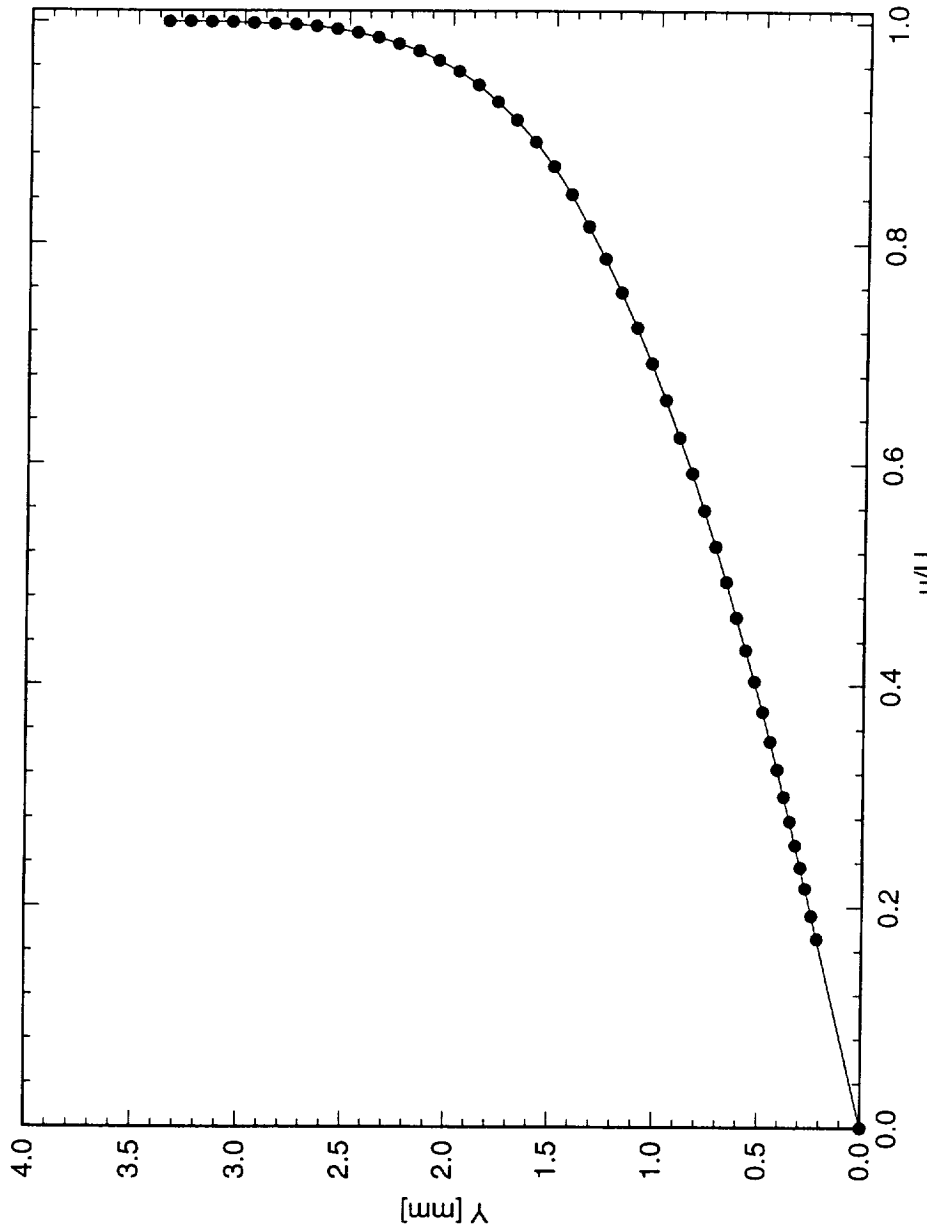

Figure 4.4: Typical boundary-layer profile scan. $Re_c = 1.6 \times 10^6$, $x/c = 0.20$.

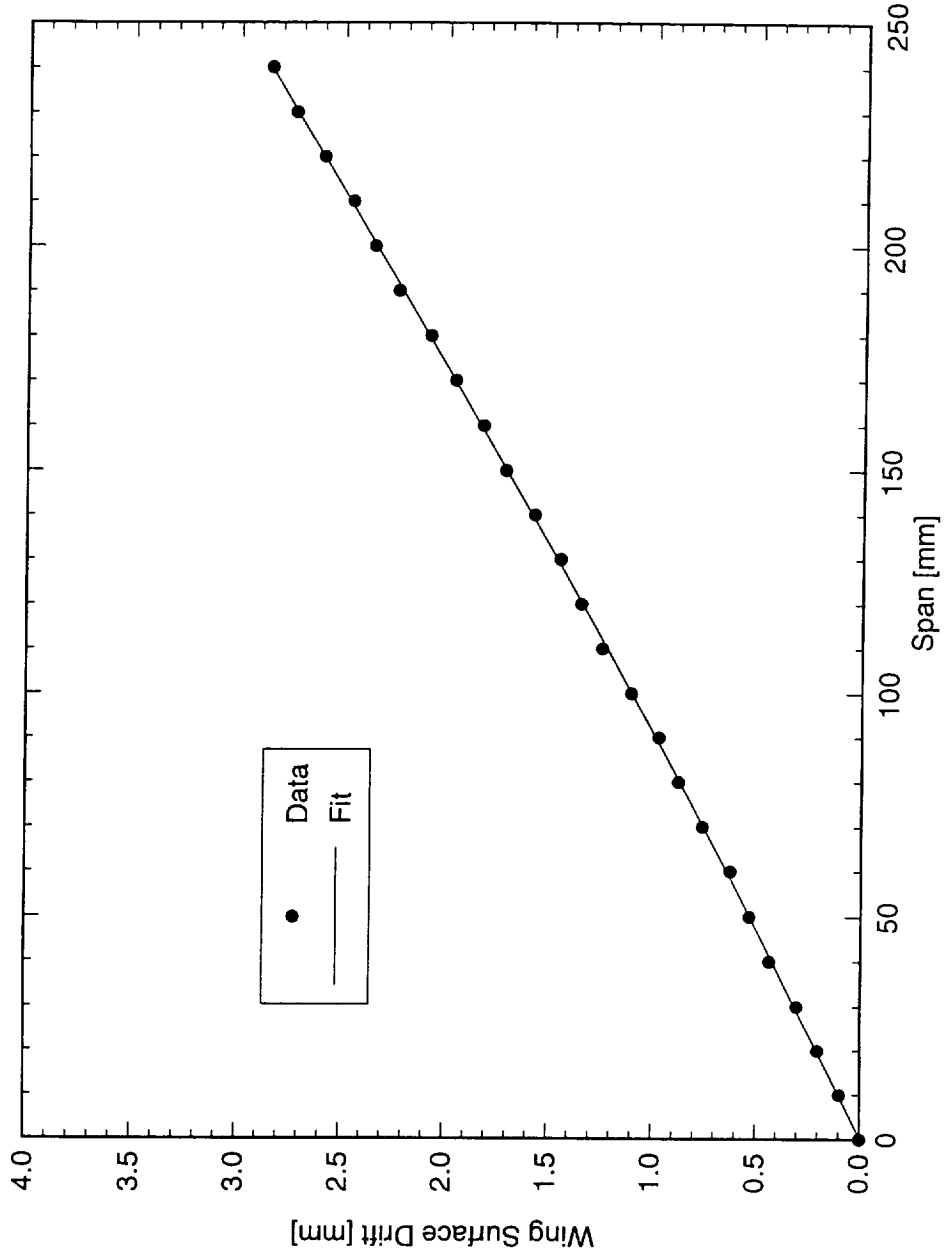

Figure 4.5: Typical spanwise traverse-alignment scan. Model/traverse misalignment is indicated by the apparent surface drift with span. Scan is at $x/c = 0.25$. $Re_c = 2.4 \times 10^6$.

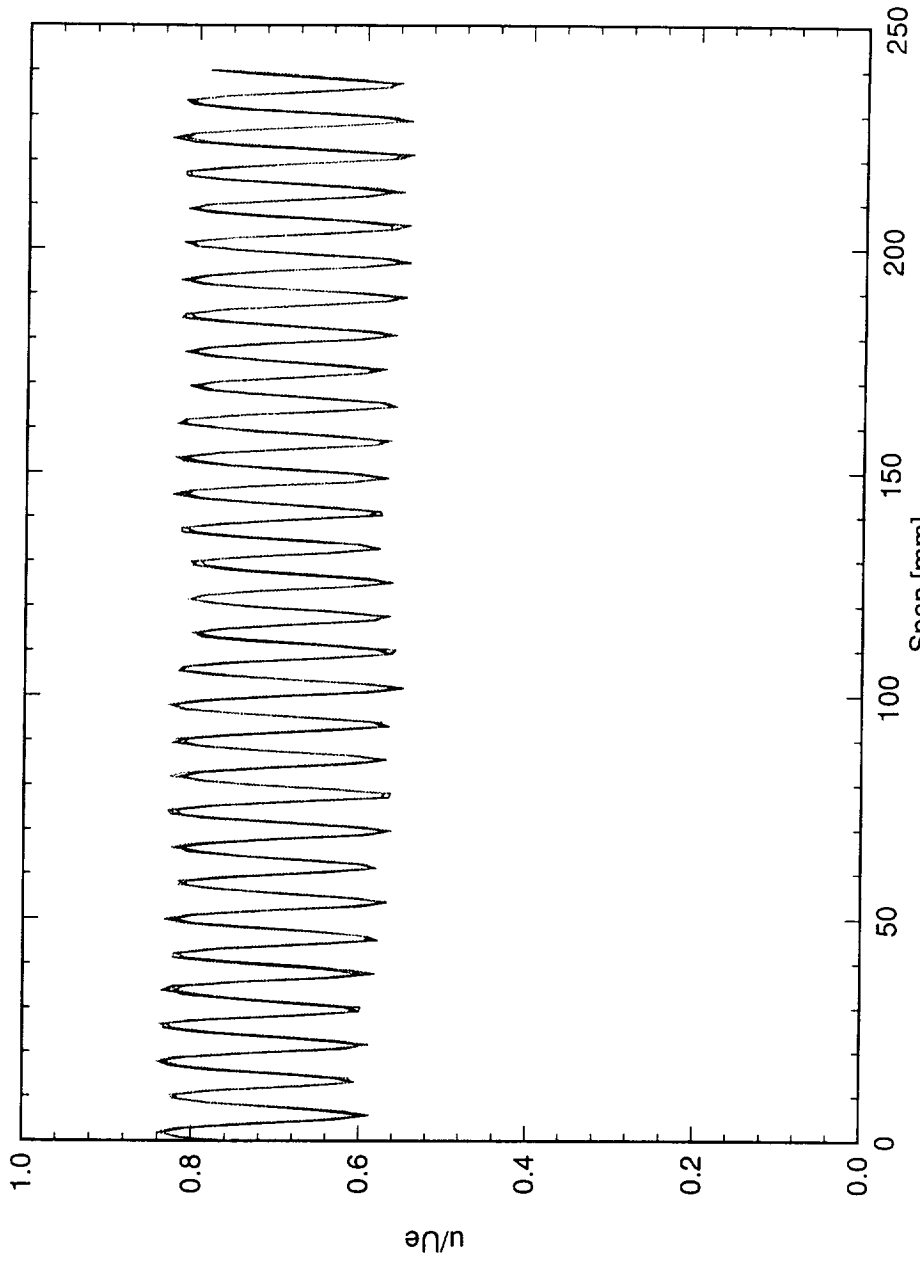

Figure 4.6: Typical spanwise four-sweep constant-Y scan. Each of the four sweeps is shown. A full-span array of 6 μm roughness with 8 mm spacing is applied at $x/c = 0.023$.

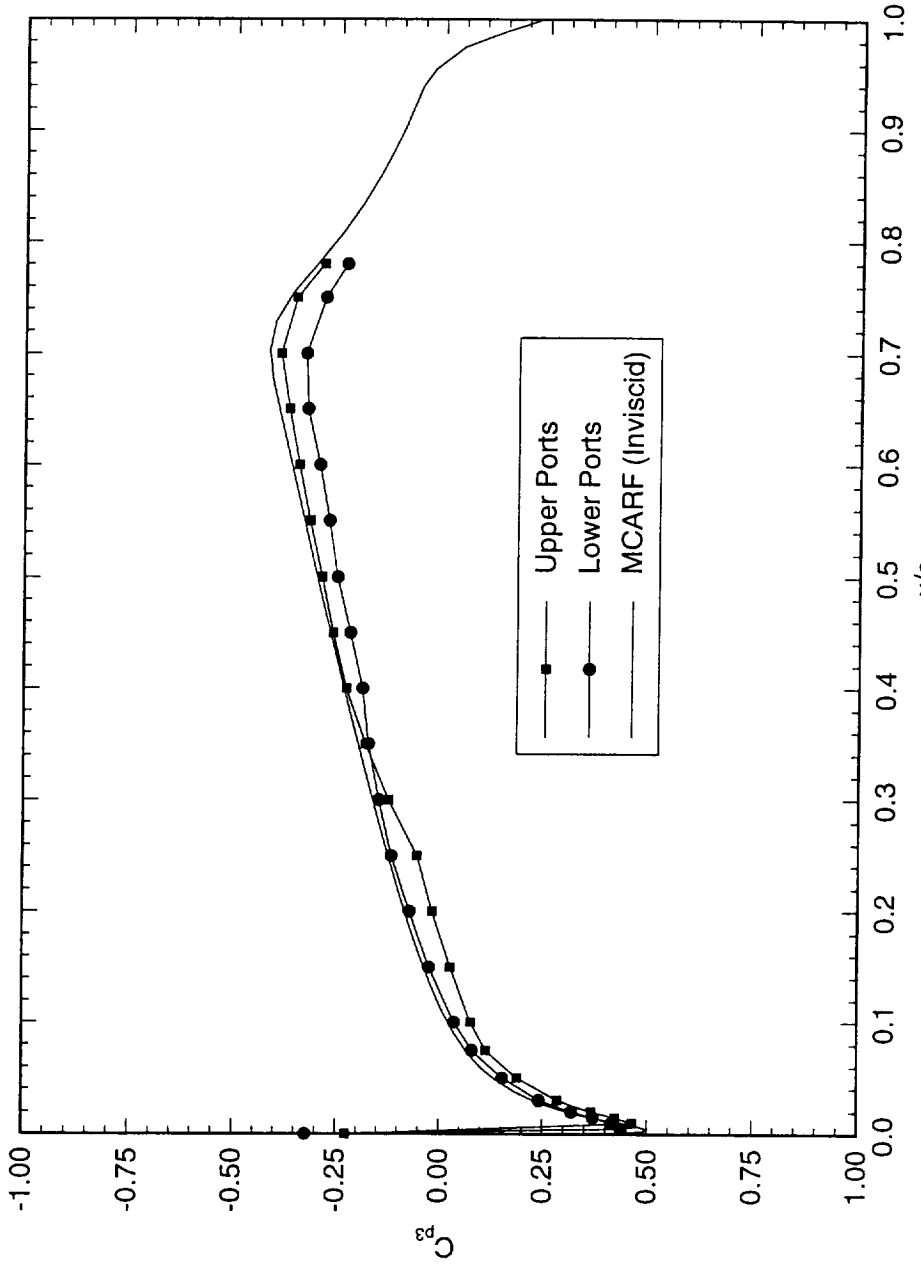

Figure 5.1: Comparison of experimental and theoretical pressure coefficients for $Re_c = 1.6 \times 10^6$.

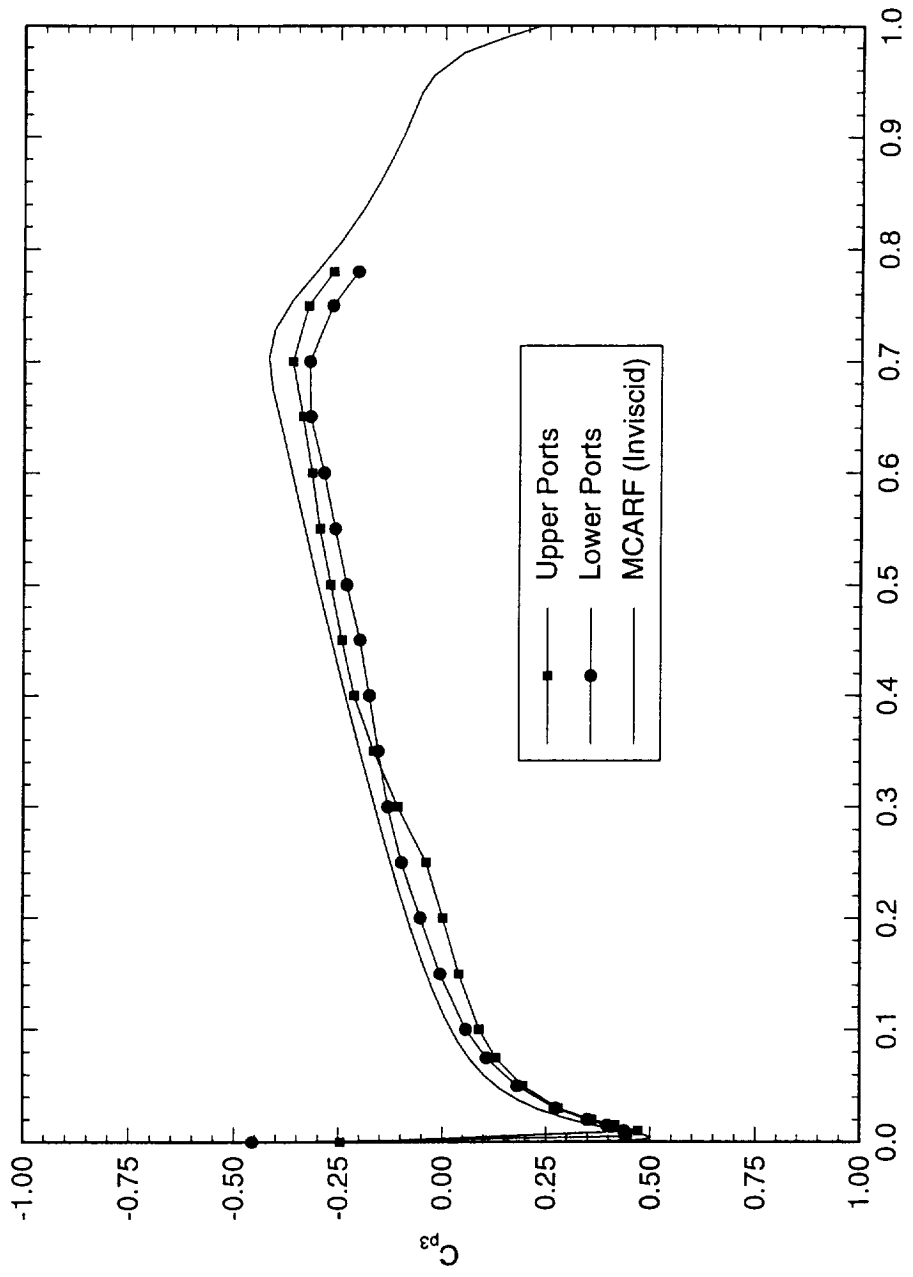

Figure 5.2: Comparison of experimental and theoretical pressure coefficients for $Re_c = 2.4 \times 10^6$.

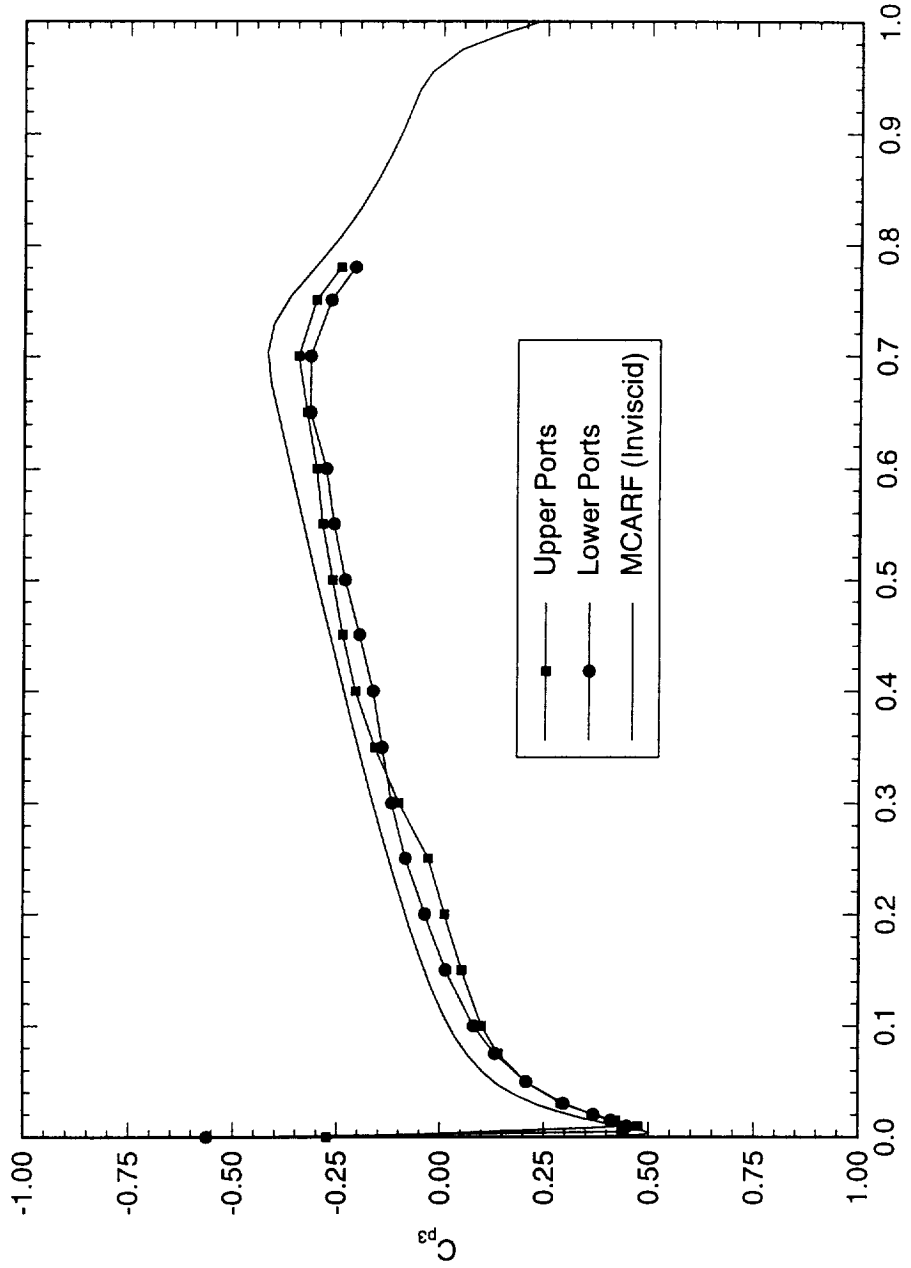

Figure 5.3: Comparison of experimental and theoretical pressure coefficients for $Re_c = 3.2 \times 10^6$.

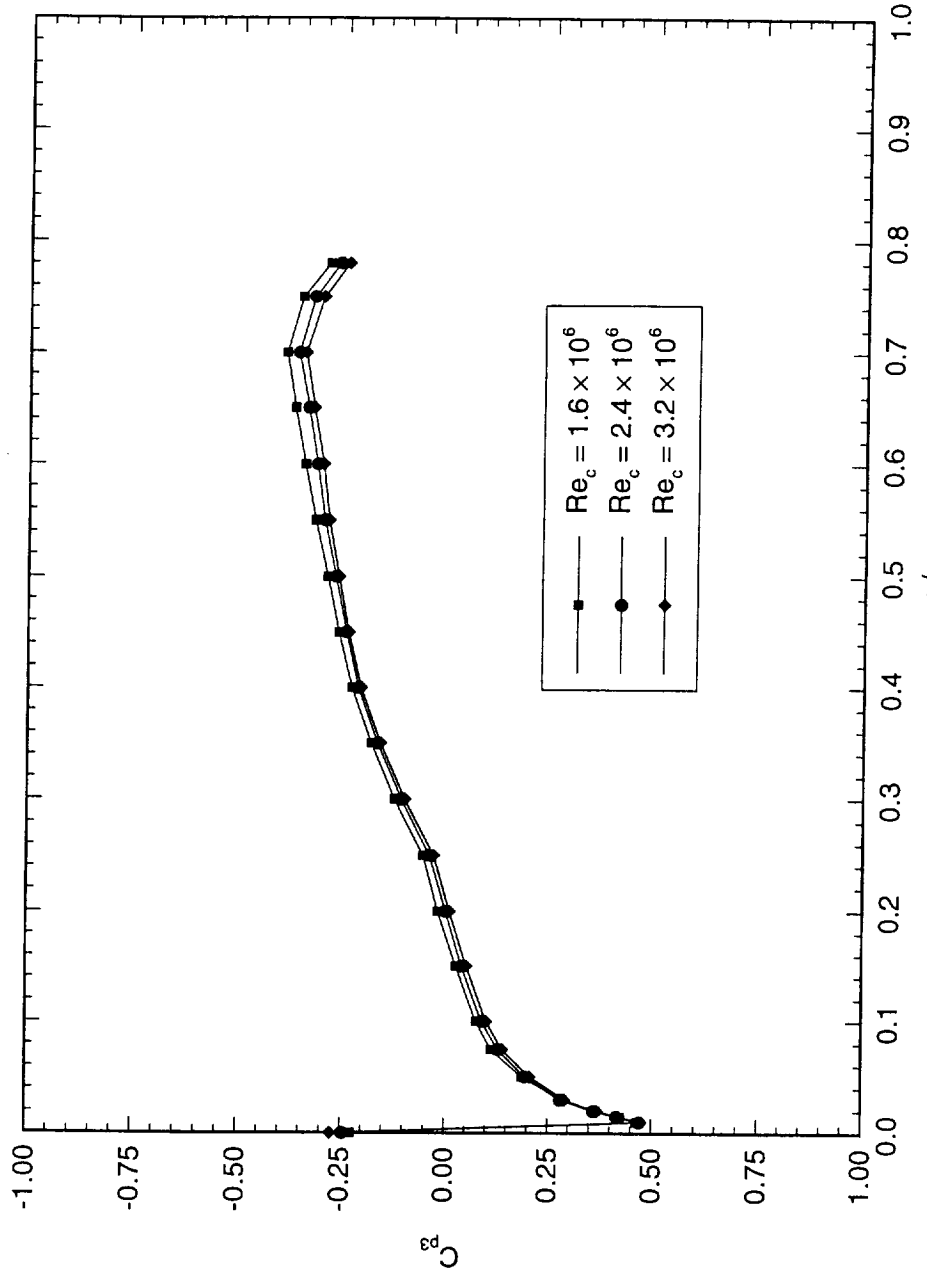

Figure 5.4: Pressure distribution dependence upon Reynolds number for upper ports.

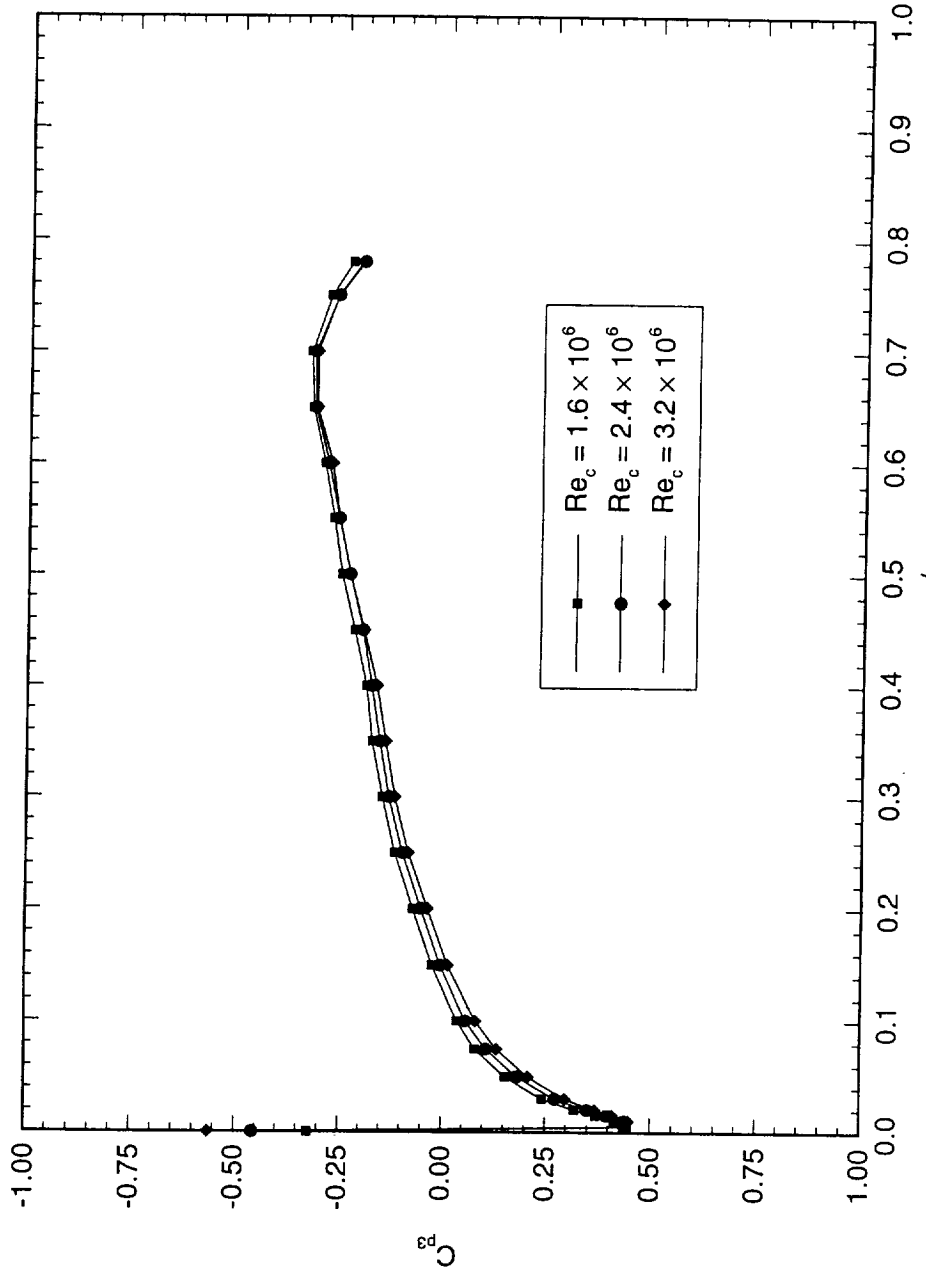

Figure 5.5: Pressure distribution dependence upon Reynolds number for lower ports.

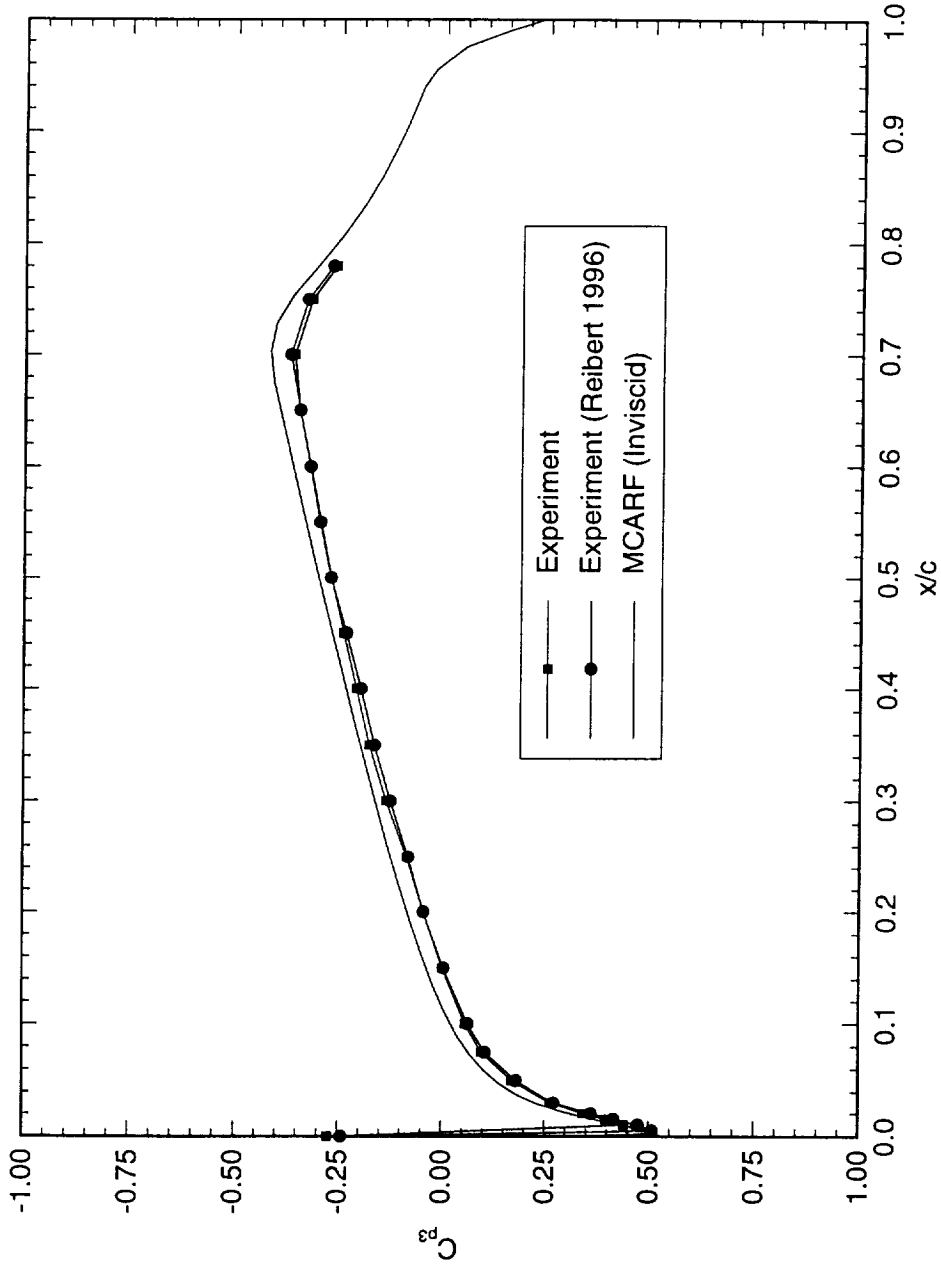

Figure 5.6: Comparison of average C_p distribution with past experiment and theory for $Re_c = 1.6 \times 10^6$.

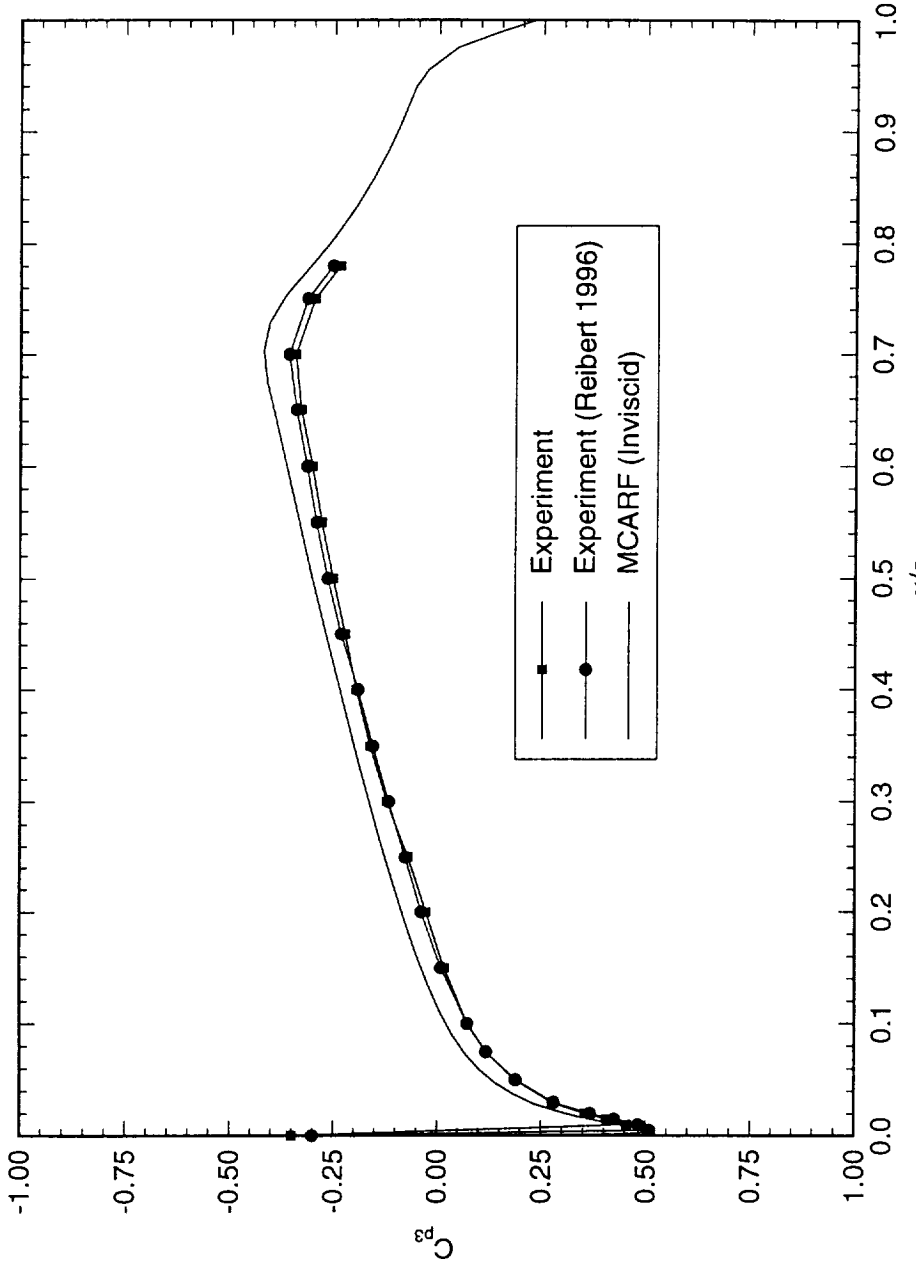

Figure 5.7: Comparison of average C_p distribution with past experiment and theory for $Re_c = 2.4 \times 10^6$.

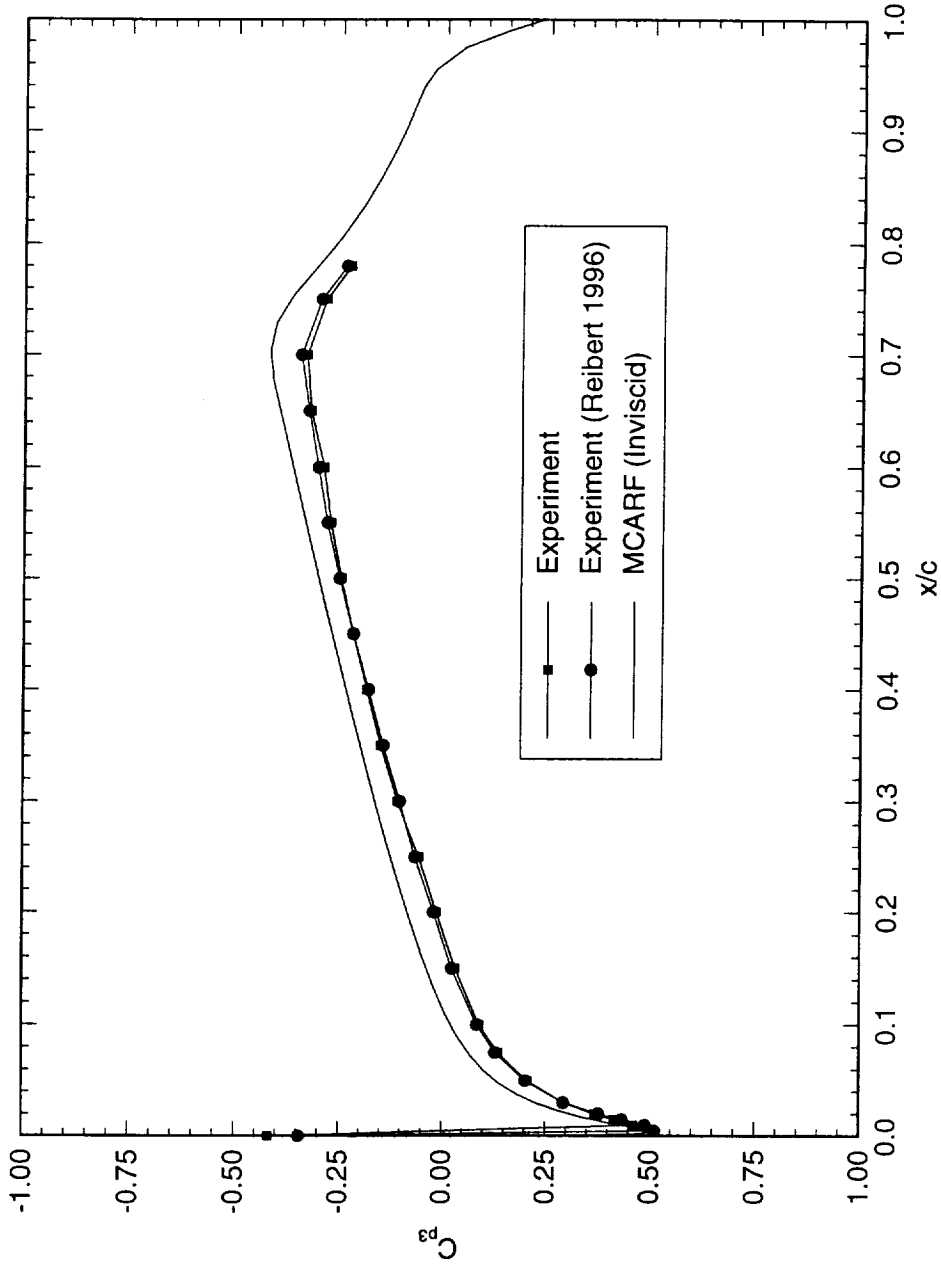

Figure 5.8: Comparison of average C_p distribution with past experiment and theory for $Re_c = 3.2 \times 10^6$.

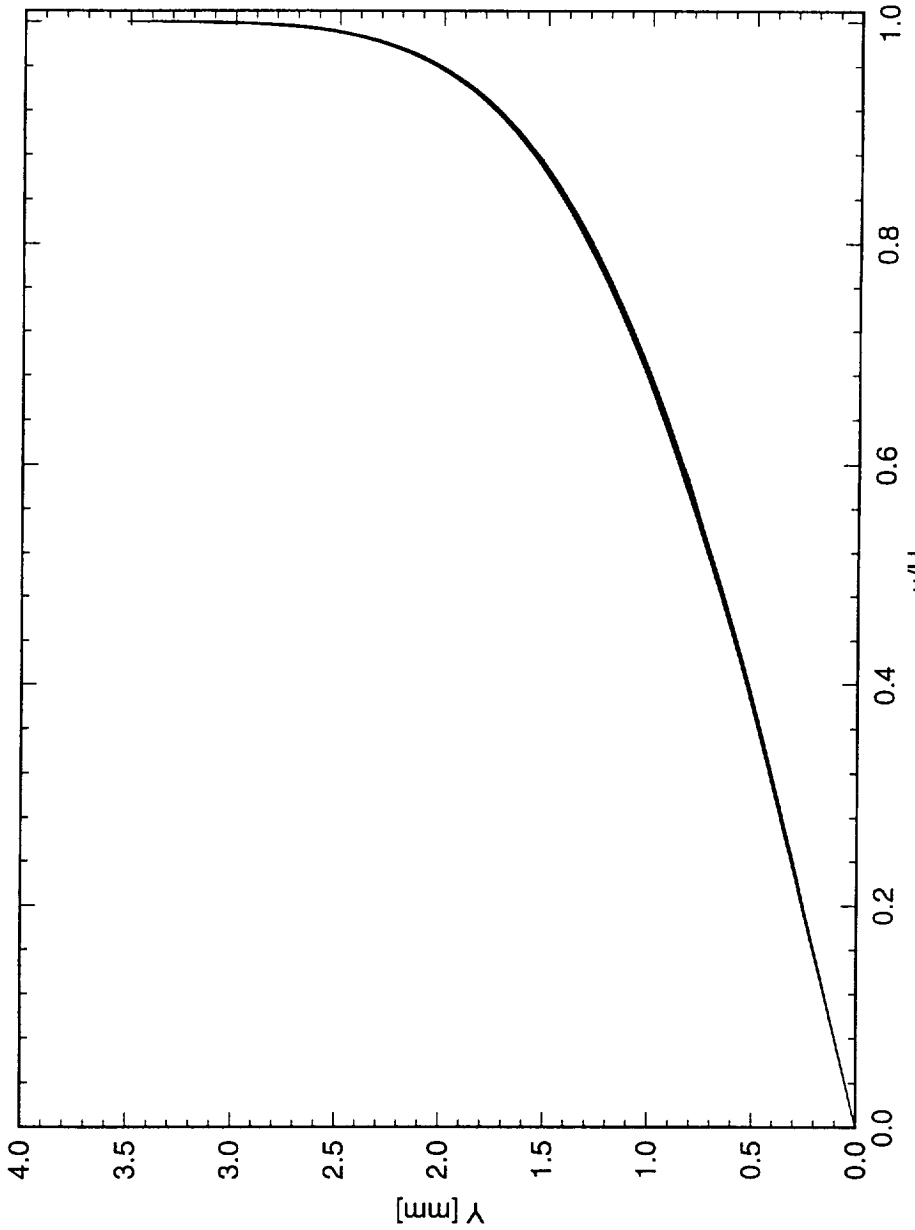

Figure 5.9: Spanwise array of 100 boundary-layer scans covering 99 mm in span at $x/c = 0.20$. $Re_c = 1.6 \times 10^6$, no artificial roughness.

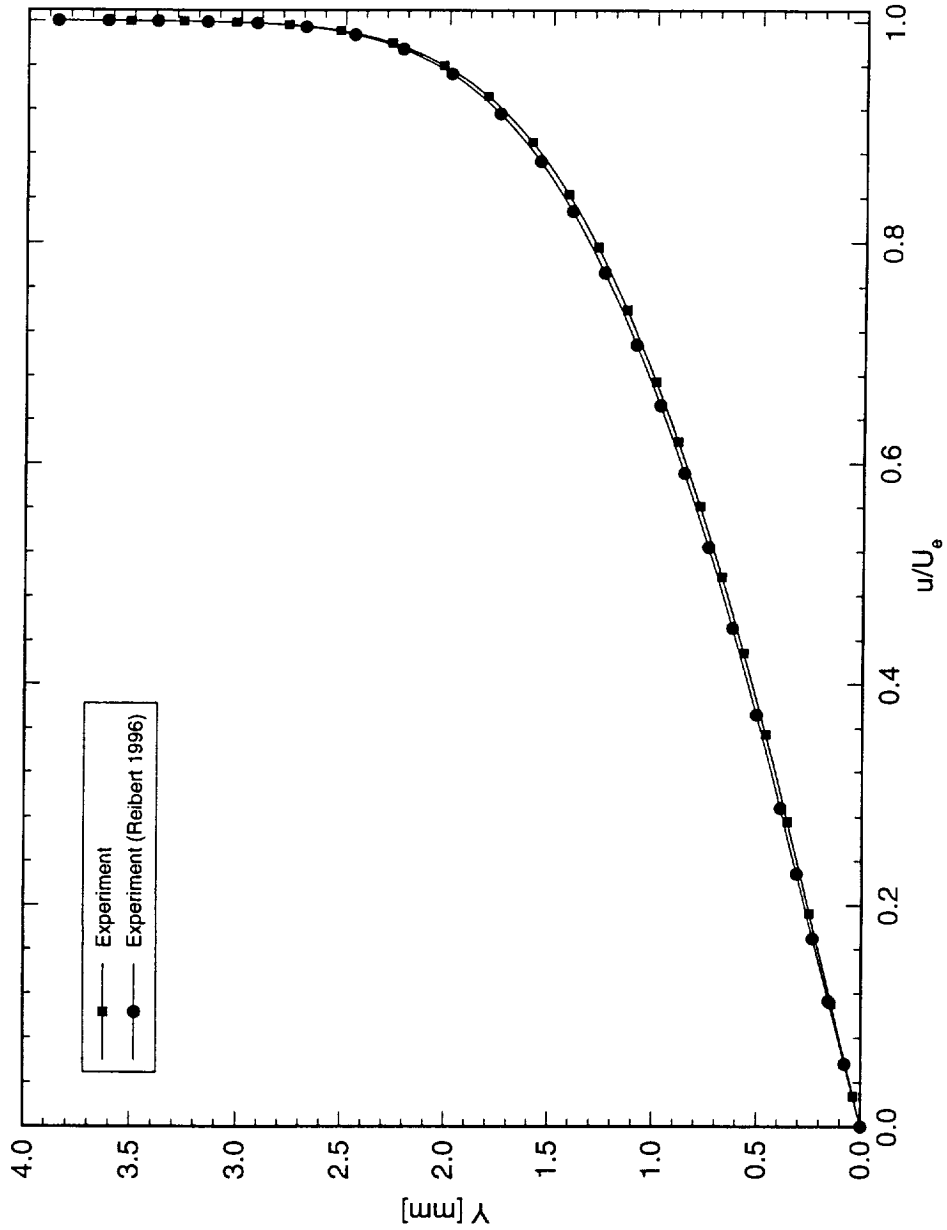

Figure 5.10: Comparison of experimental spanwise-average boundary-layer profiles at $x/c = 0.20$. $Re_c = 1.6 \times 10^6$, no artificial roughness. The symbols are merely identifiers and do not indicate measurement points.

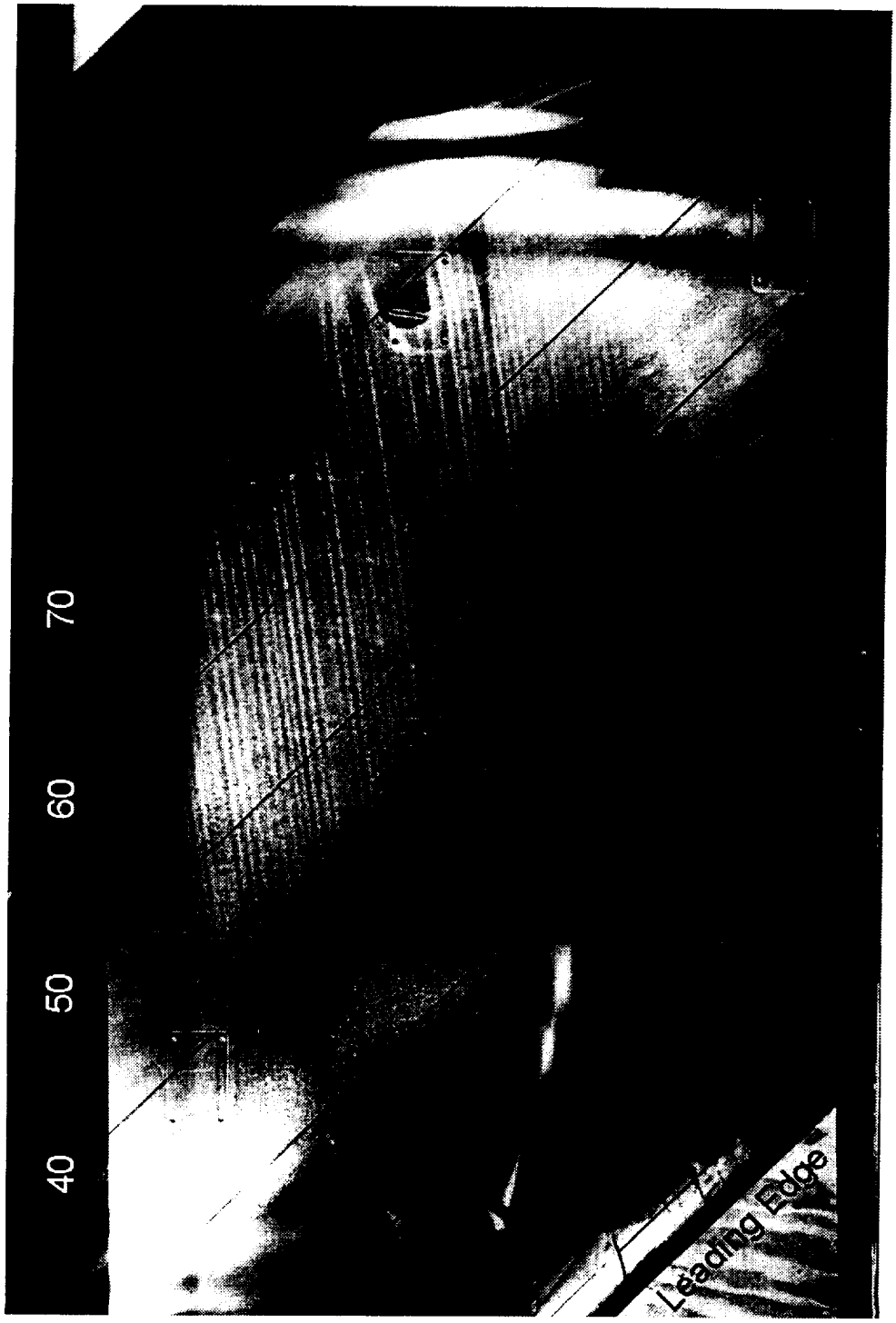

Figure 5.11: Naphthalene flow visualization for $Re_c = 2.4 \times 10^6$ and no artificial roughness.

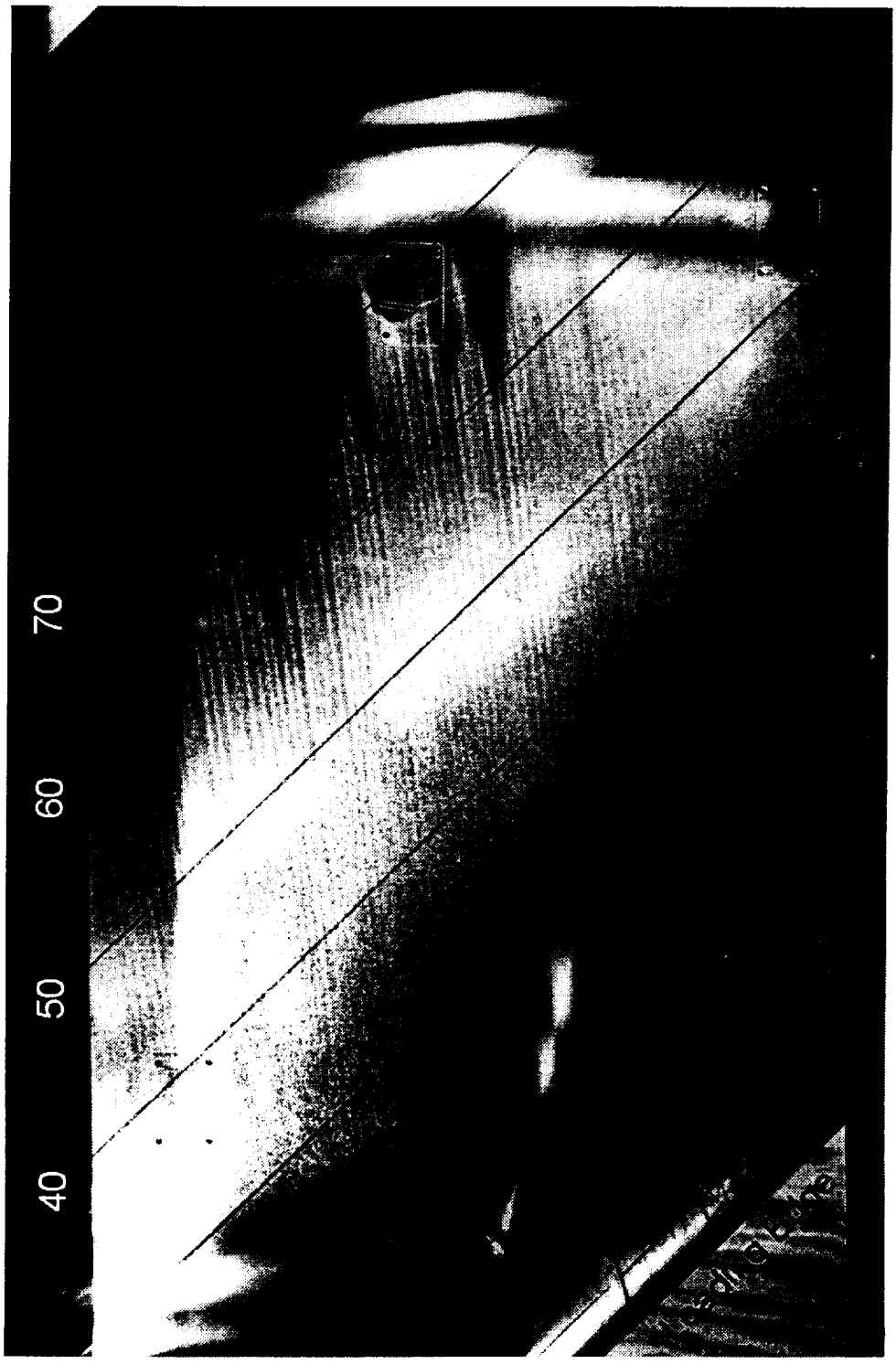

Figure 5.12: Naphthalene flow visualization for $Re_c = 2.6 \times 10^6$ and no artificial roughness.

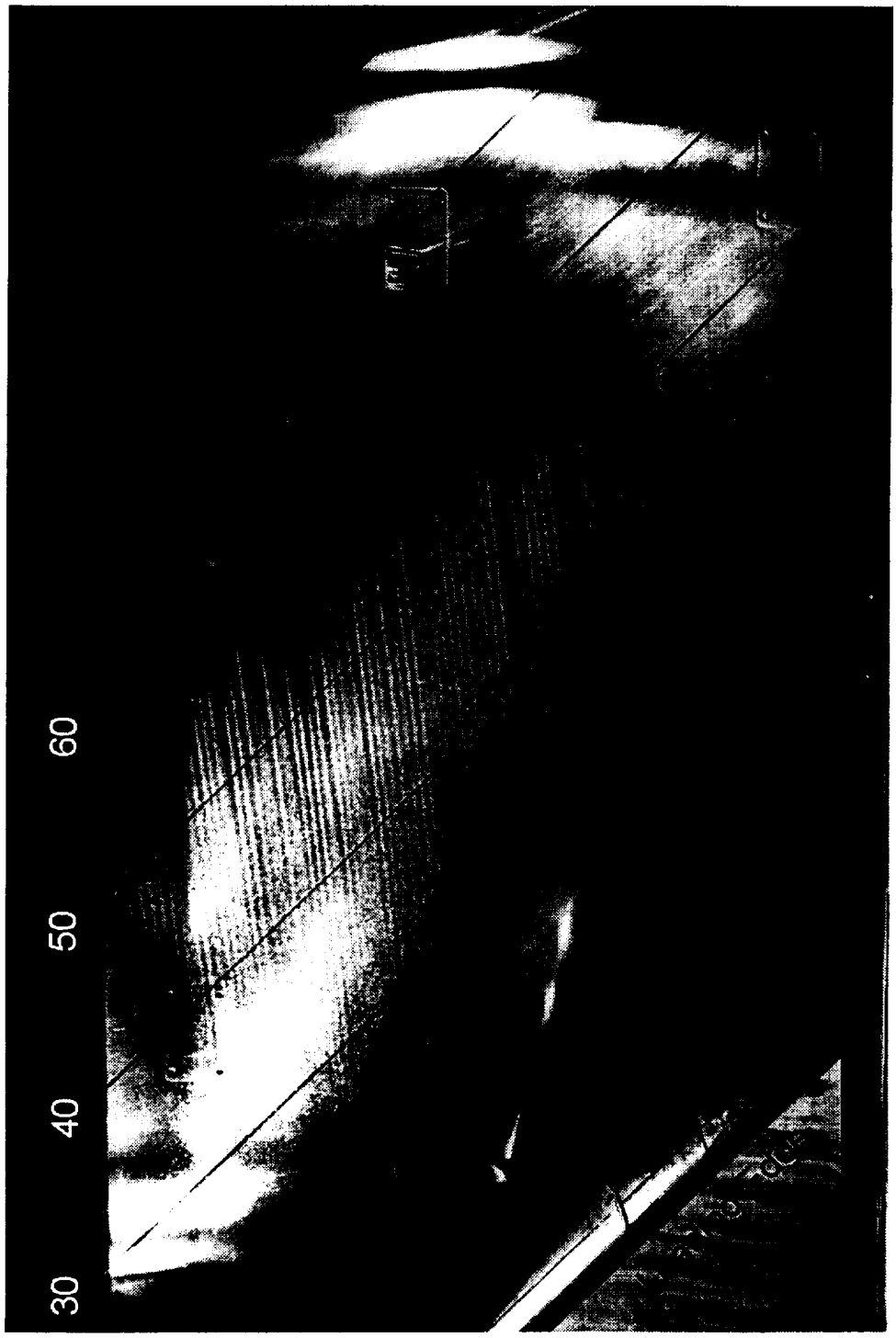

Figure 5.13: Naphthalene flow visualization for $Re_c = 2.8 \times 10^6$ and no artificial roughness.

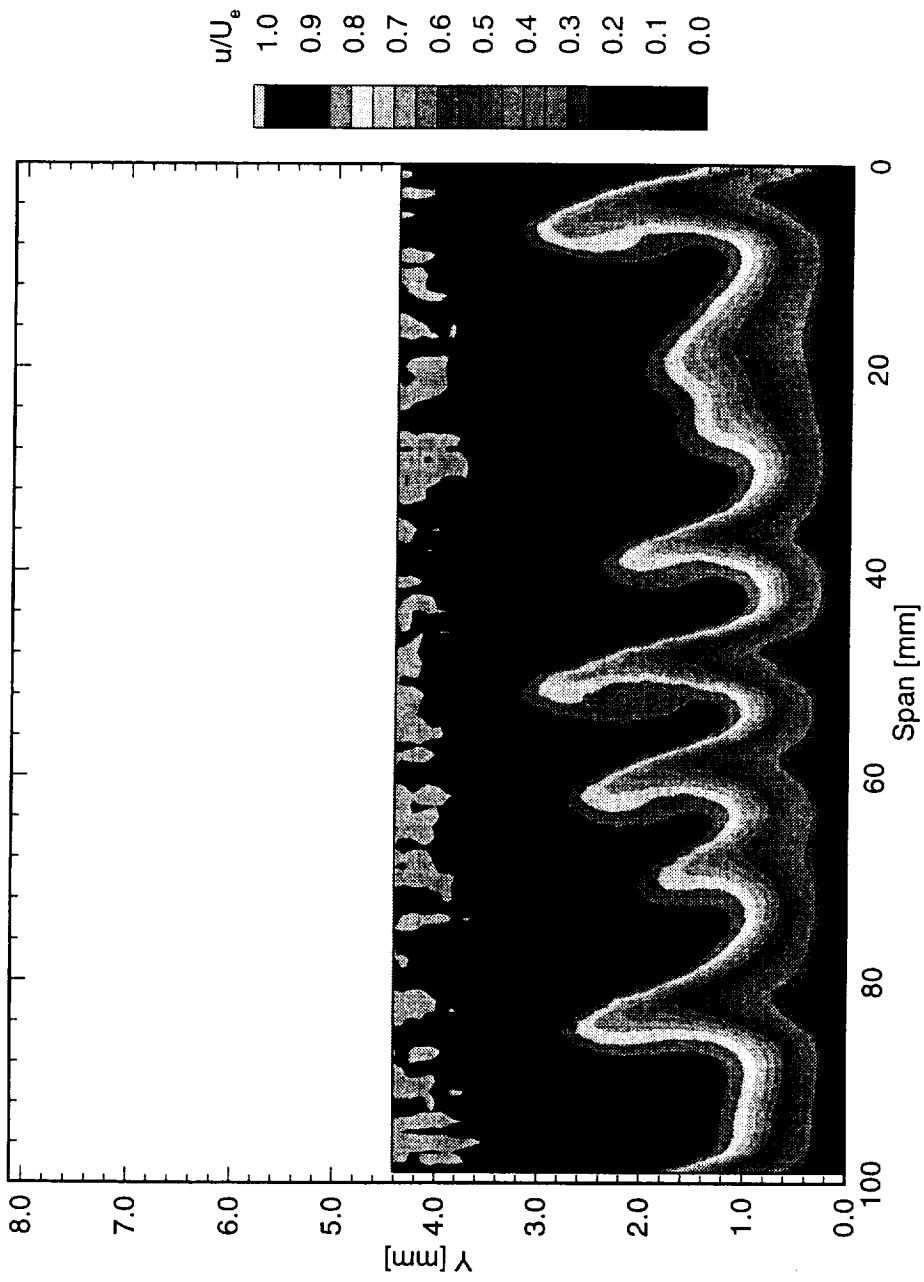

Figure 5.14: Normalized boundary-layer velocity contours at $x/c = 0.60$. $Re_c = 2.4 \times 10^6$, no artificial roughness.

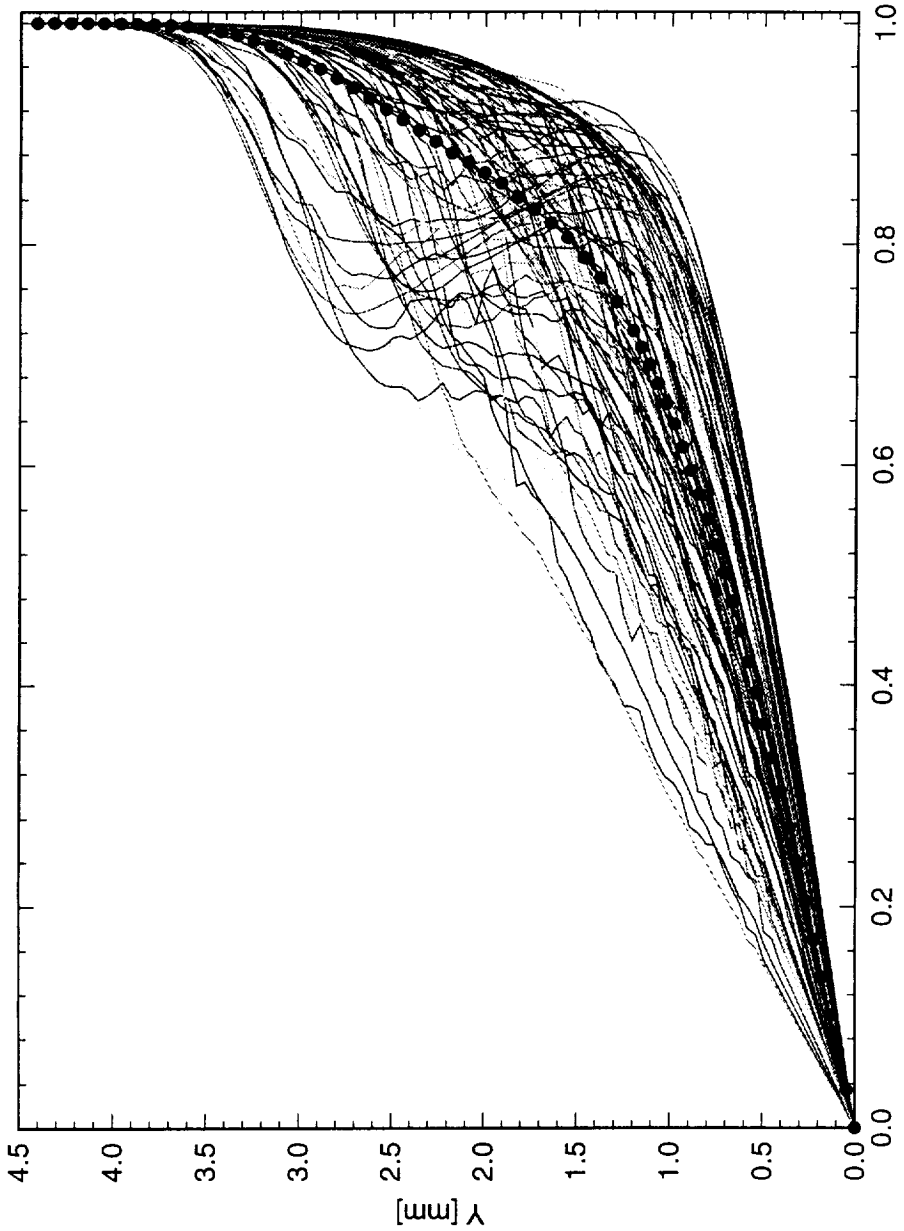

Figure 5.15: Spanwise array of 100 boundary-layer profiles spaced 1 mm apart in span at $x/c = 0.60$. $Re_c = 2.4 \times 10^6$, no artificial roughness. The dots represent the spanwise average of the profiles.

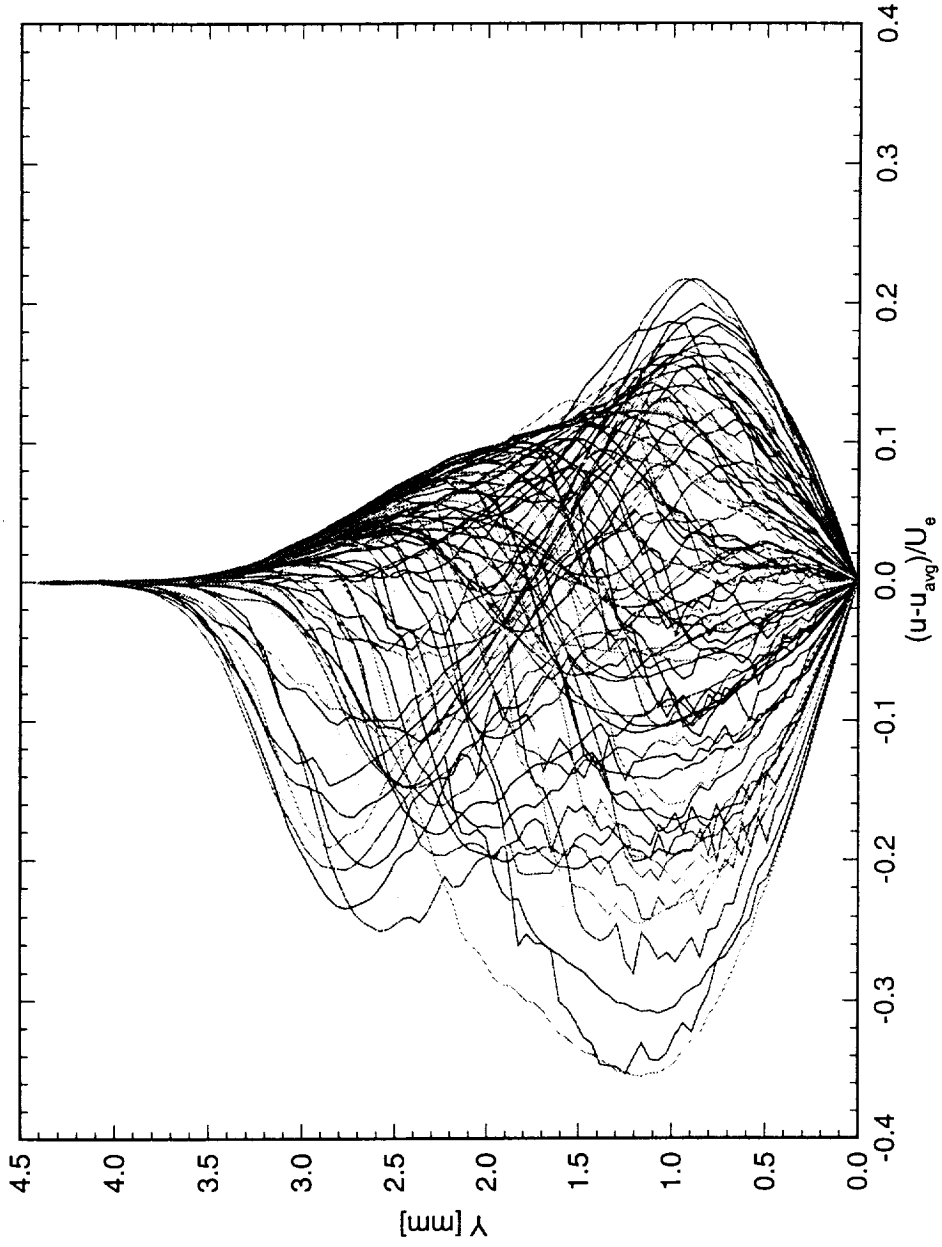

Figure 5.16: Spanwise array of 100 disturbance profiles spaced 1 mm apart in span at $x/c = 0.60$. $Re_c = 2.4 \times 10^6$, no artificial roughness.

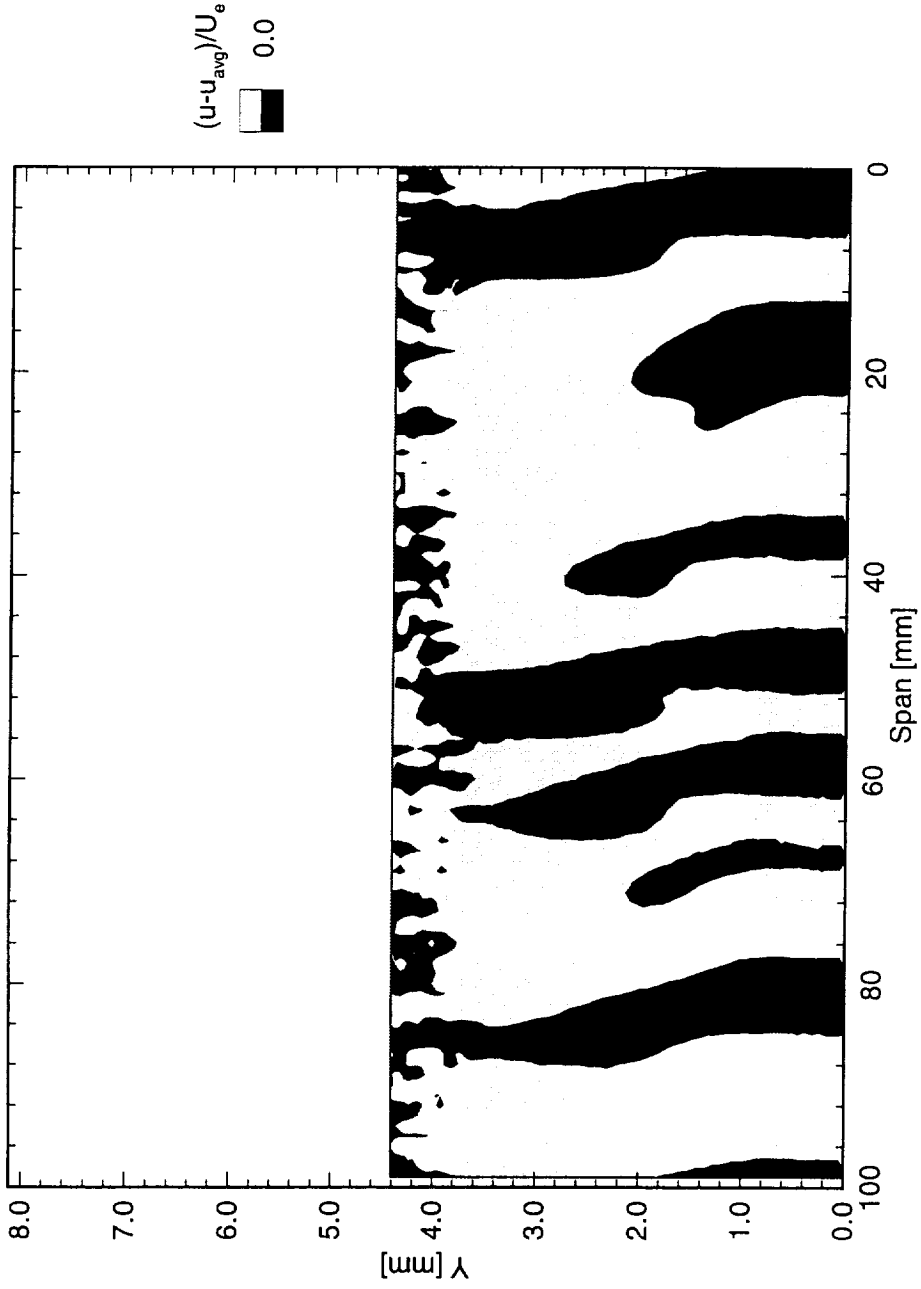

Figure 5.17: Normalized disturbance velocity contours at $x/c = 0.60$. $Re_c = 2.4 \times 10^6$, no artificial roughness.

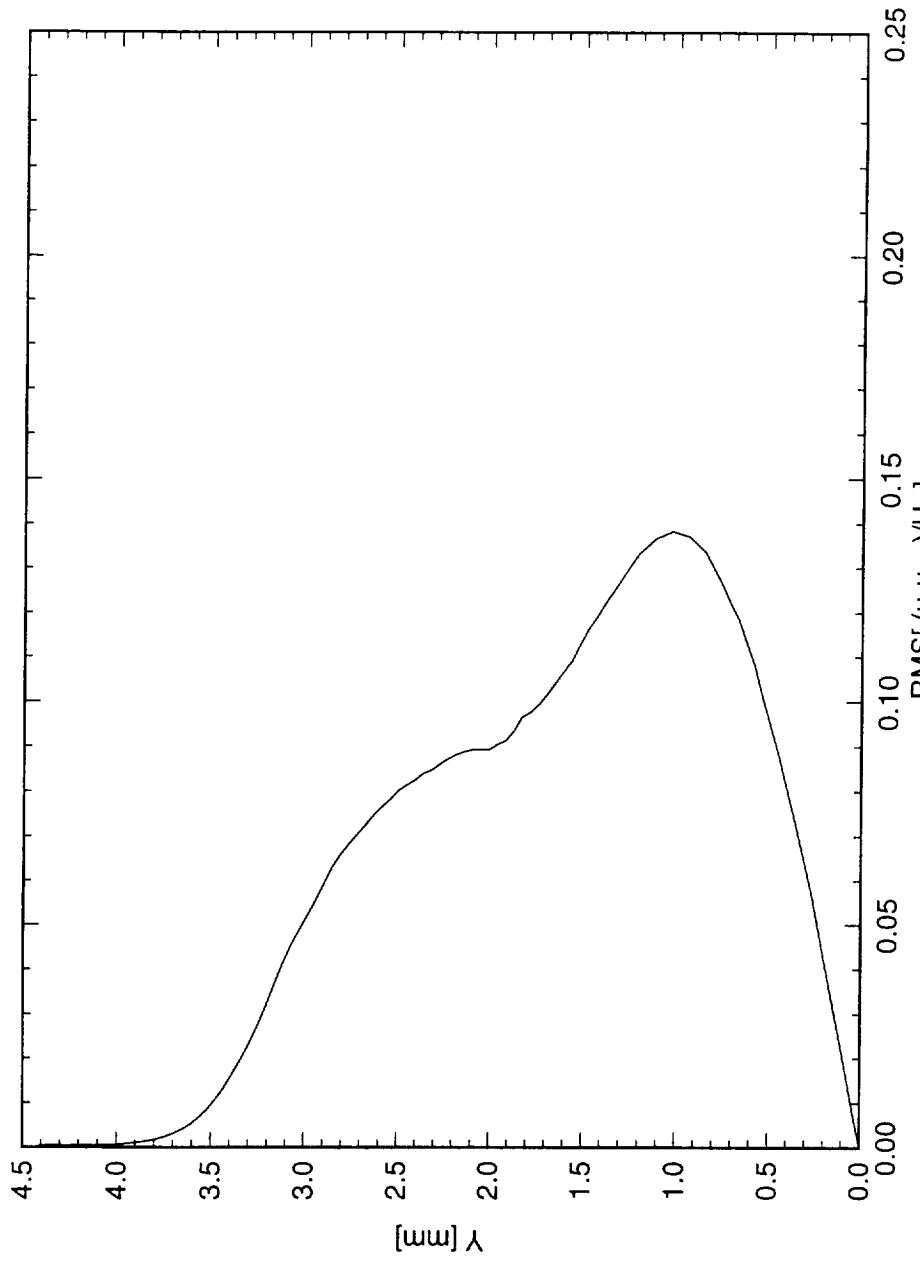

Figure 5.18: Stationary crossflow mode shape at $x/c = 0.60$. $Re_c = 2.4 \times 10^6$, no artificial roughness.

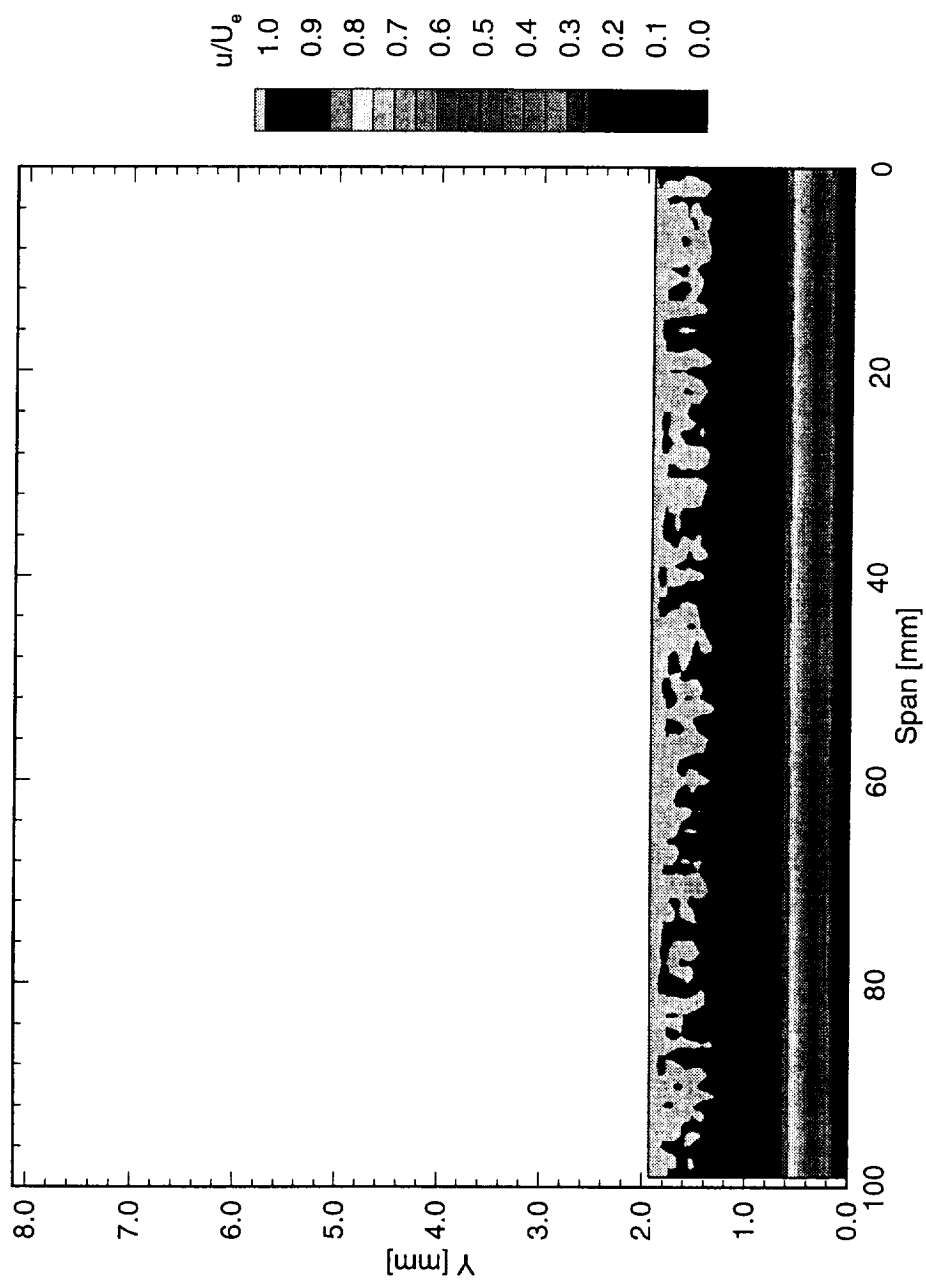

Figure 5.19: Normalized boundary-layer velocity contours at $x/c = 0.05$. $Re_c = 2.4 \times 10^6$, no artificial roughness.

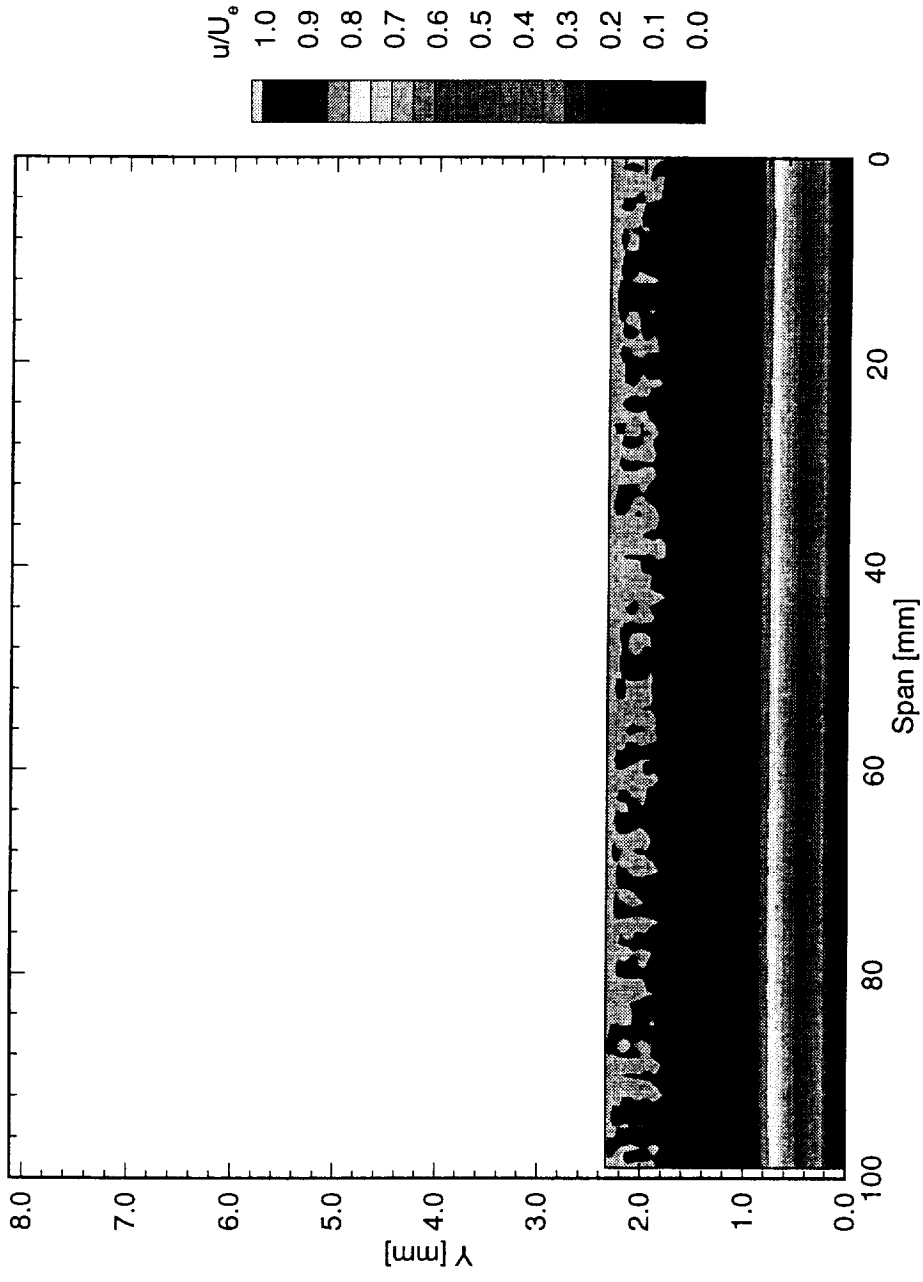

Figure 5.20: Normalized boundary-layer velocity contours at $x/c = 0.10$. $Re_c = 2.4 \times 10^6$, no artificial roughness.

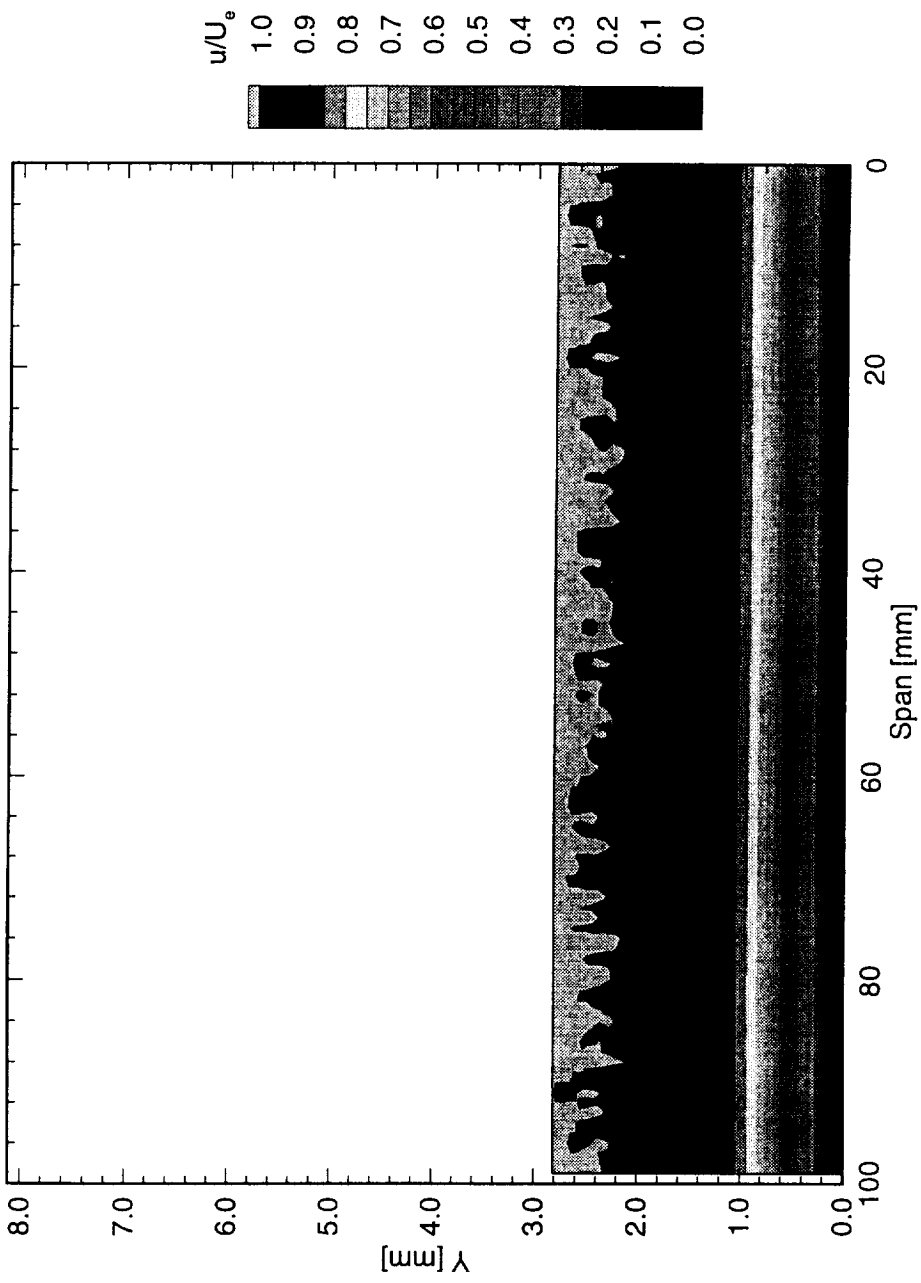

Figure 5.21: Normalized boundary-layer velocity contours at $x/c = 0.15$. $Re_c = 2.4 \times 10^6$, no artificial roughness.

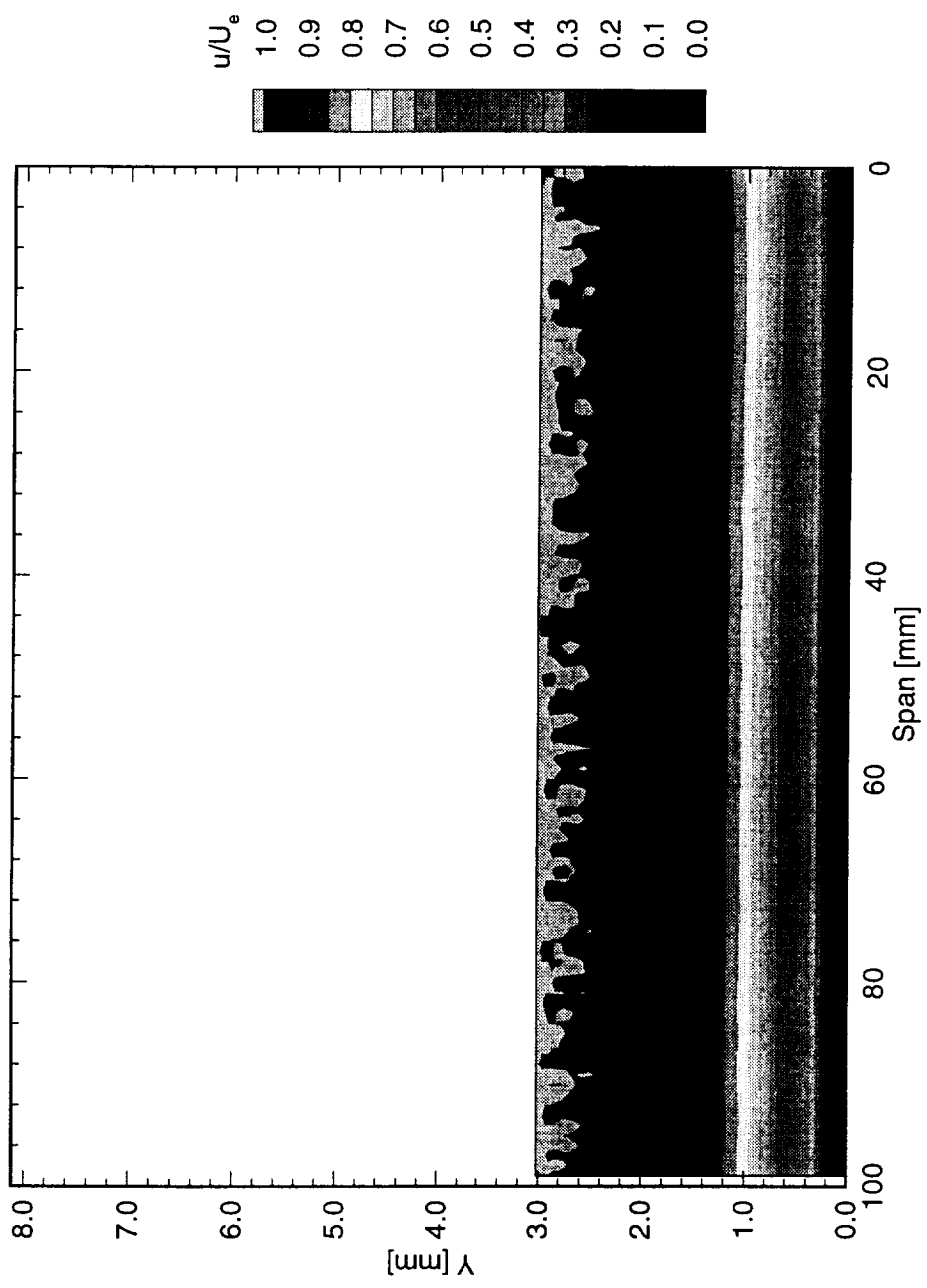

Figure 5.22: Normalized boundary-layer velocity contours at $x/c = 0.20$. $Re_c = 2.4 \times 10^6$, no artificial roughness.

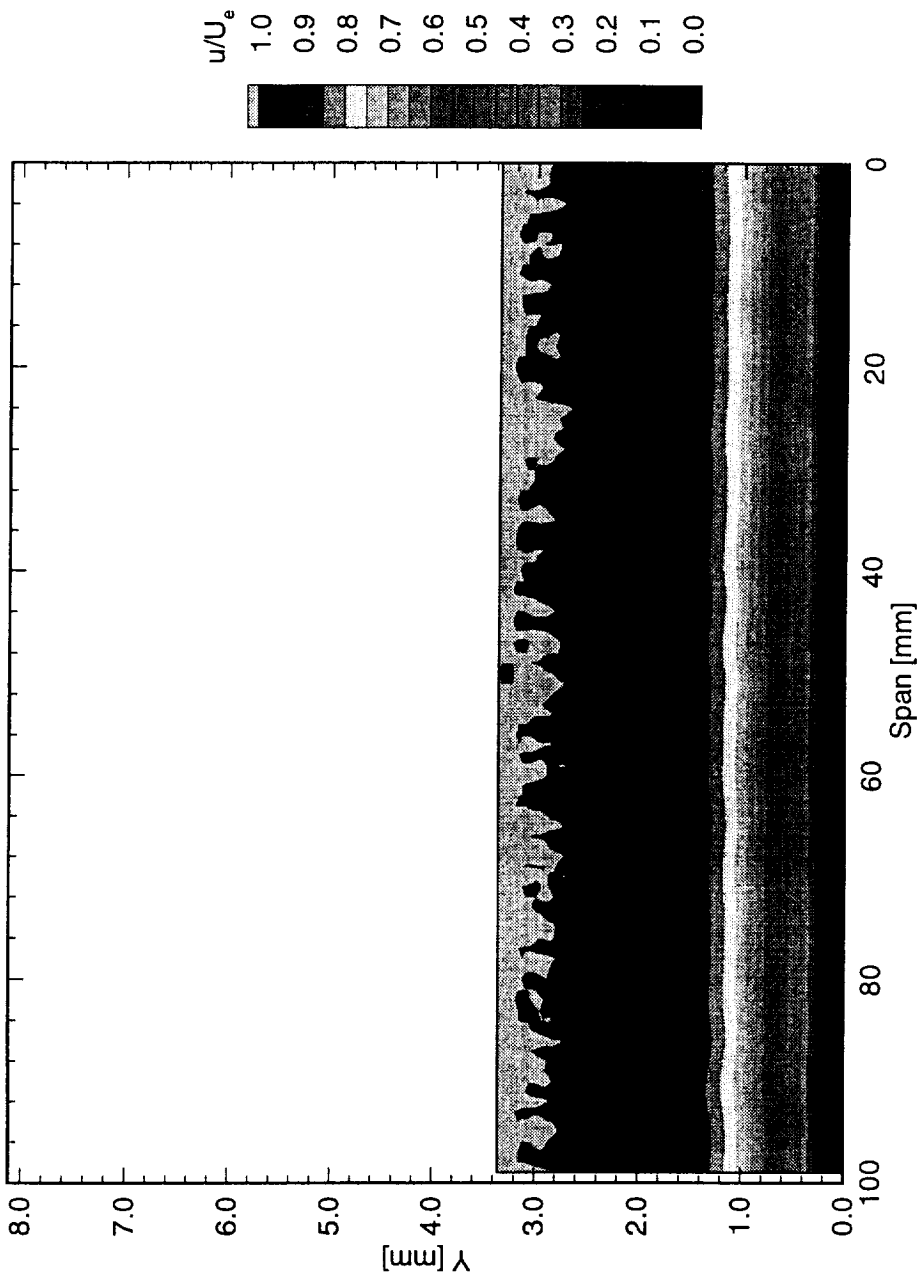

Figure 5.23: Normalized boundary-layer velocity contours at $x/c = 0.25$. $Re_c = 2.4 \times 10^6$, no artificial roughness.

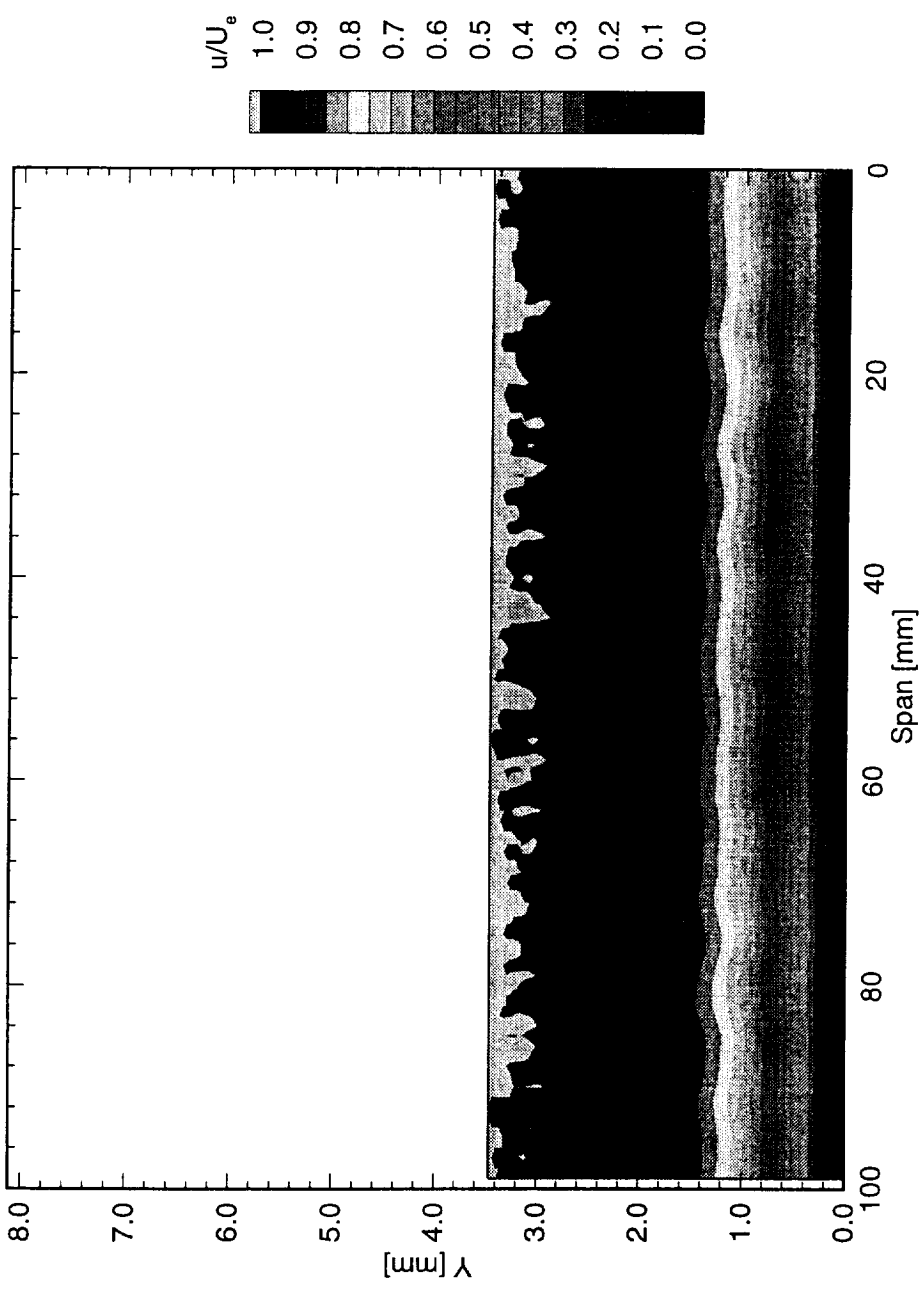

Figure 5.24: Normalized boundary-layer velocity contours at $x/c = 0.30$. $Re_c = 2.4 \times 10^6$, no artificial roughness.

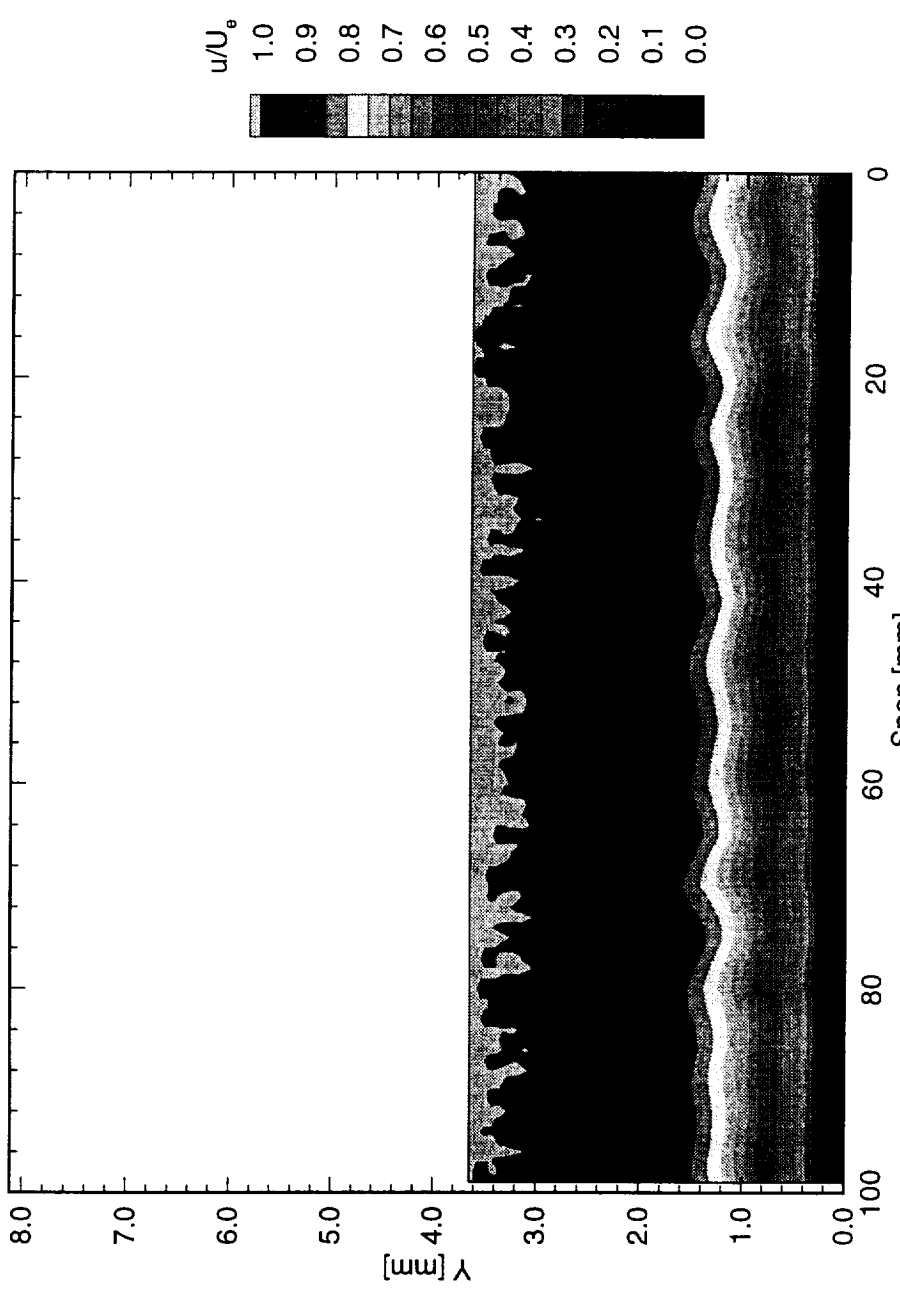

Figure 5.25: Normalized boundary-layer velocity contours at $x/c = 0.35$. $Re_c = 2.4 \times 10^6$, no artificial roughness.

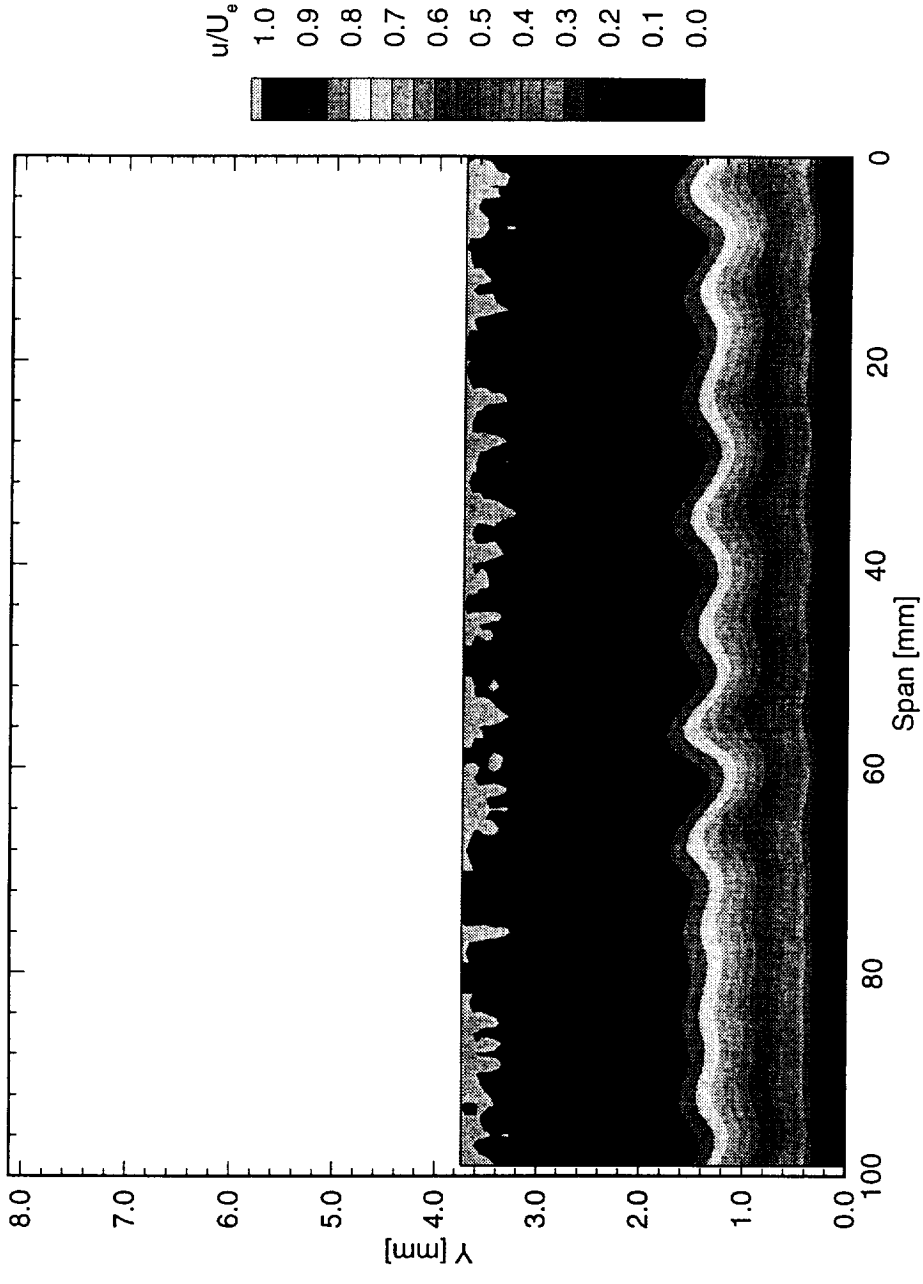

Figure 5.26: Normalized boundary-layer velocity contours at $x/c = 0.40$. $Re_c = 2.4 \times 10^6$, no artificial roughness.

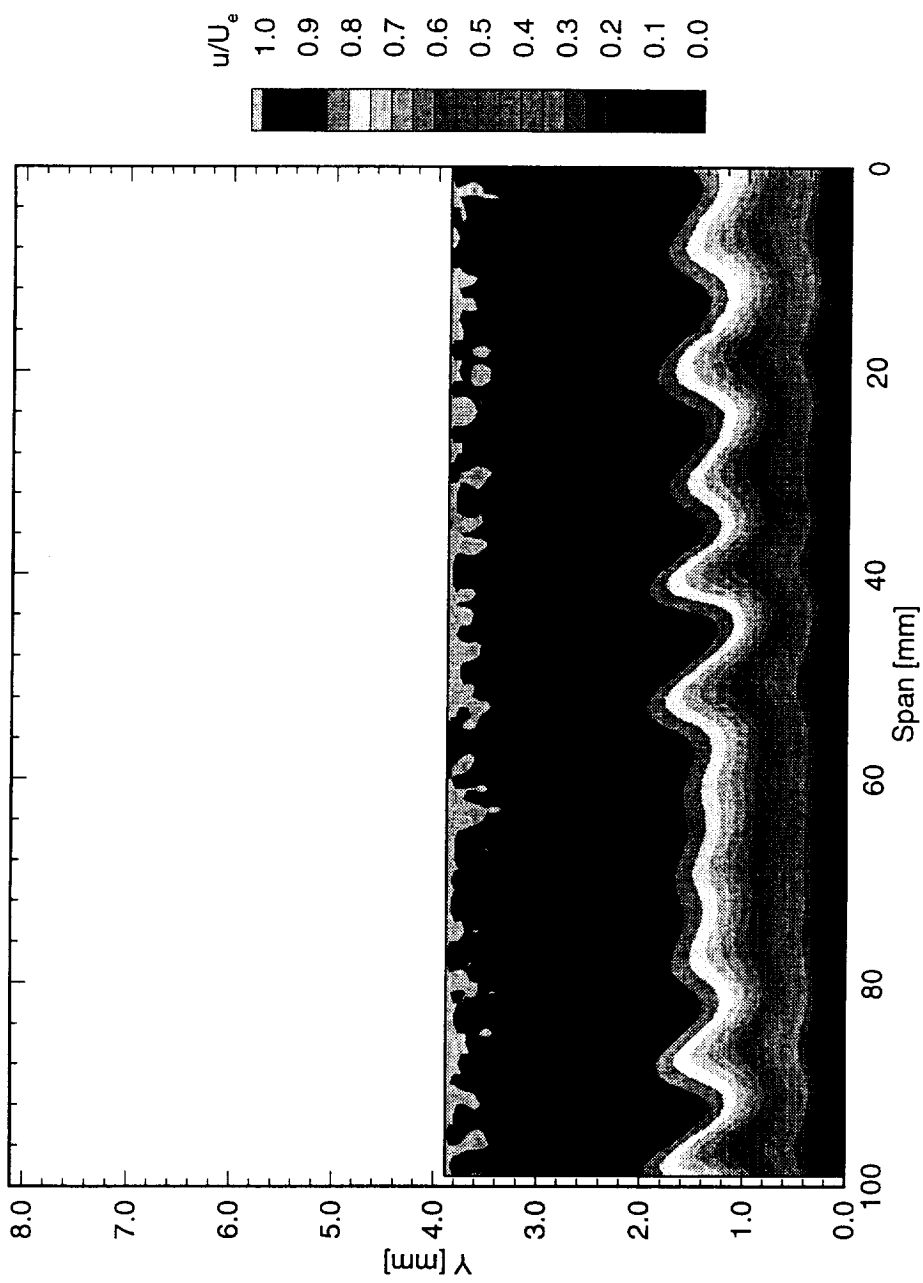

Figure 5.27: Normalized boundary-layer velocity contours at $x/c = 0.45$. $Re_c = 2.4 \times 10^6$, no artificial roughness.

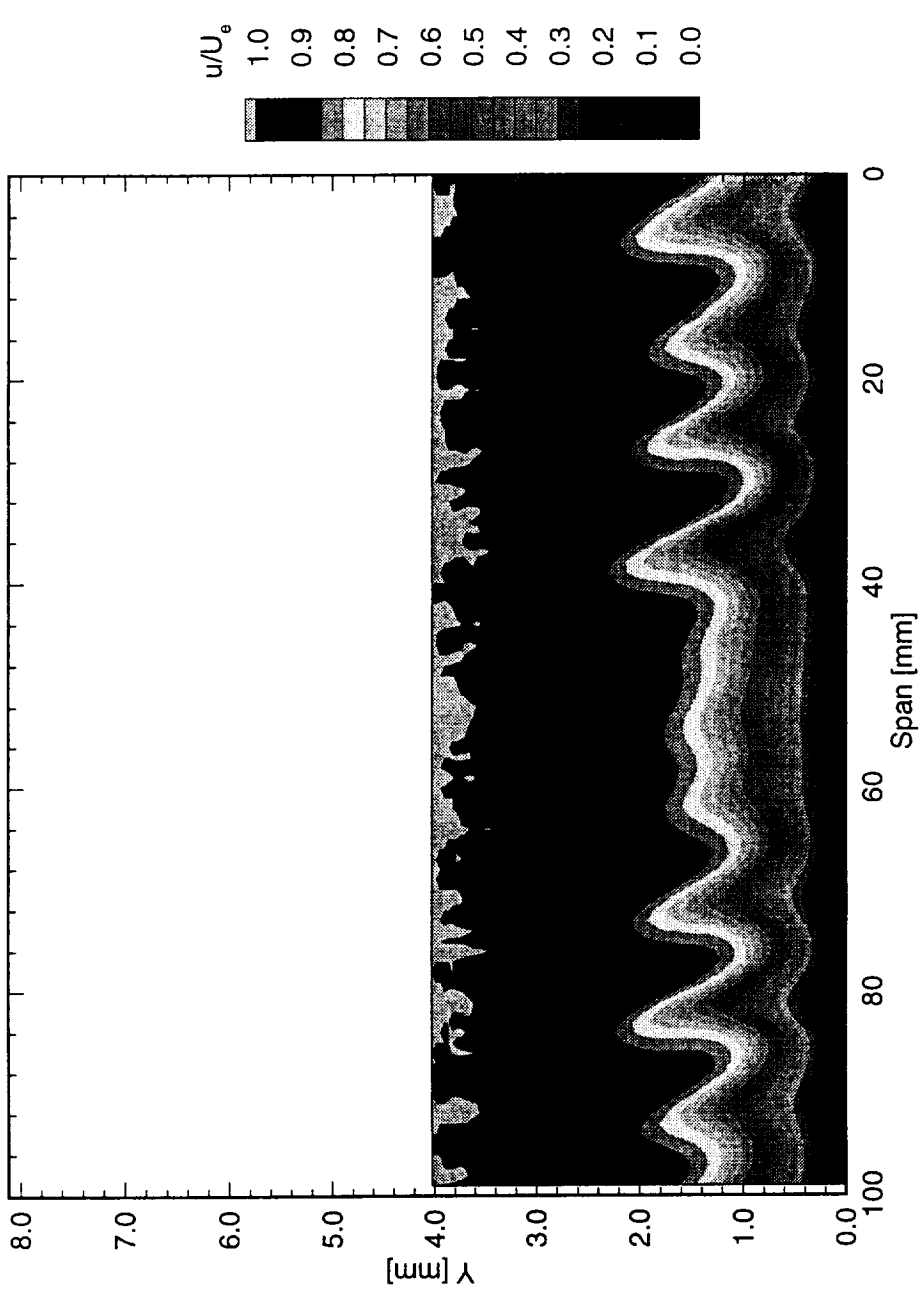

Figure 5.28: Normalized boundary-layer velocity contours at $x/c = 0.50$. $Re_c = 2.4 \times 10^6$, no artificial roughness.

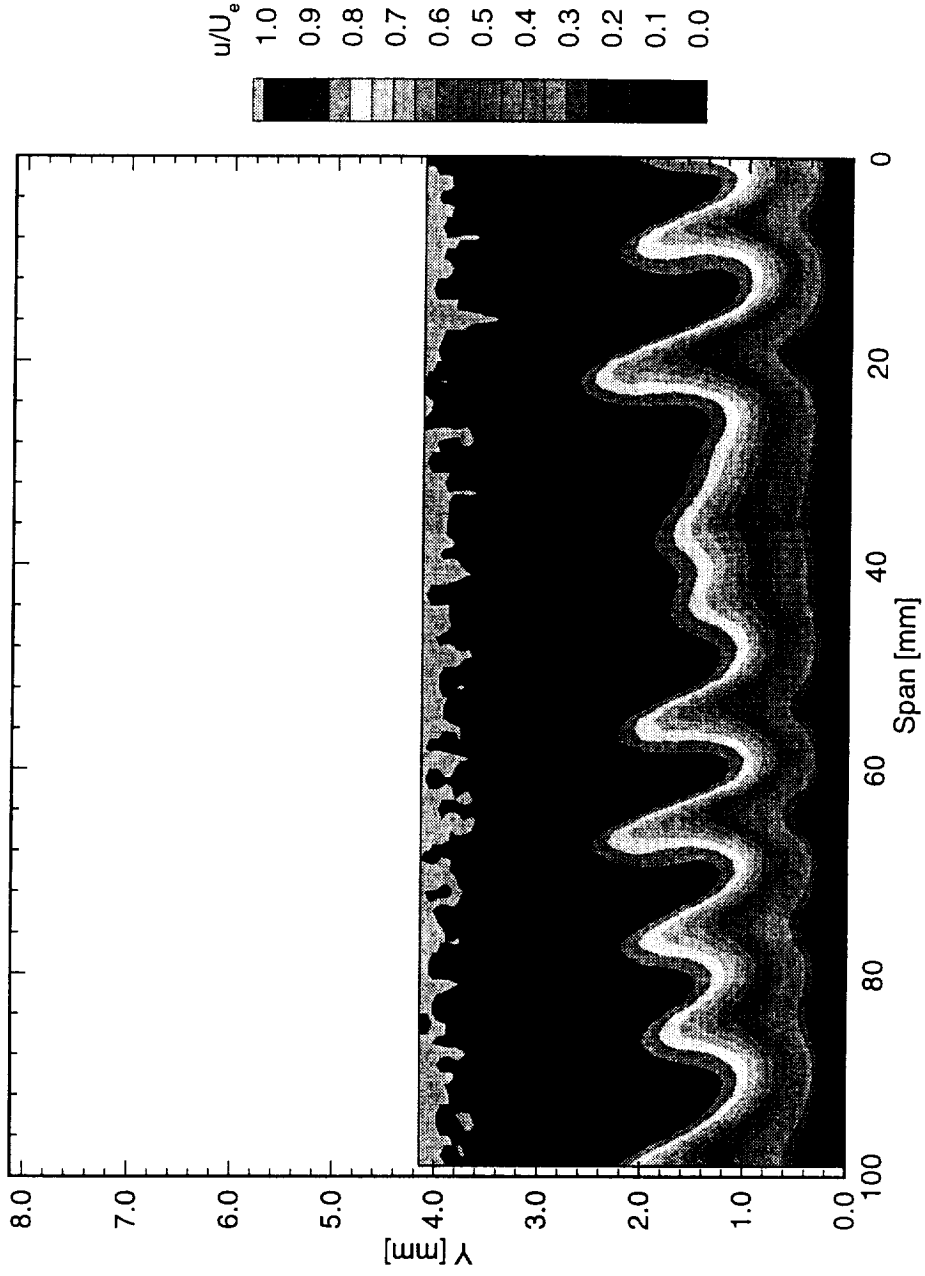

Figure 5.29: Normalized boundary-layer velocity contours at $x/c = 0.55$. $Re_c = 2.4 \times 10^6$, no artificial roughness.

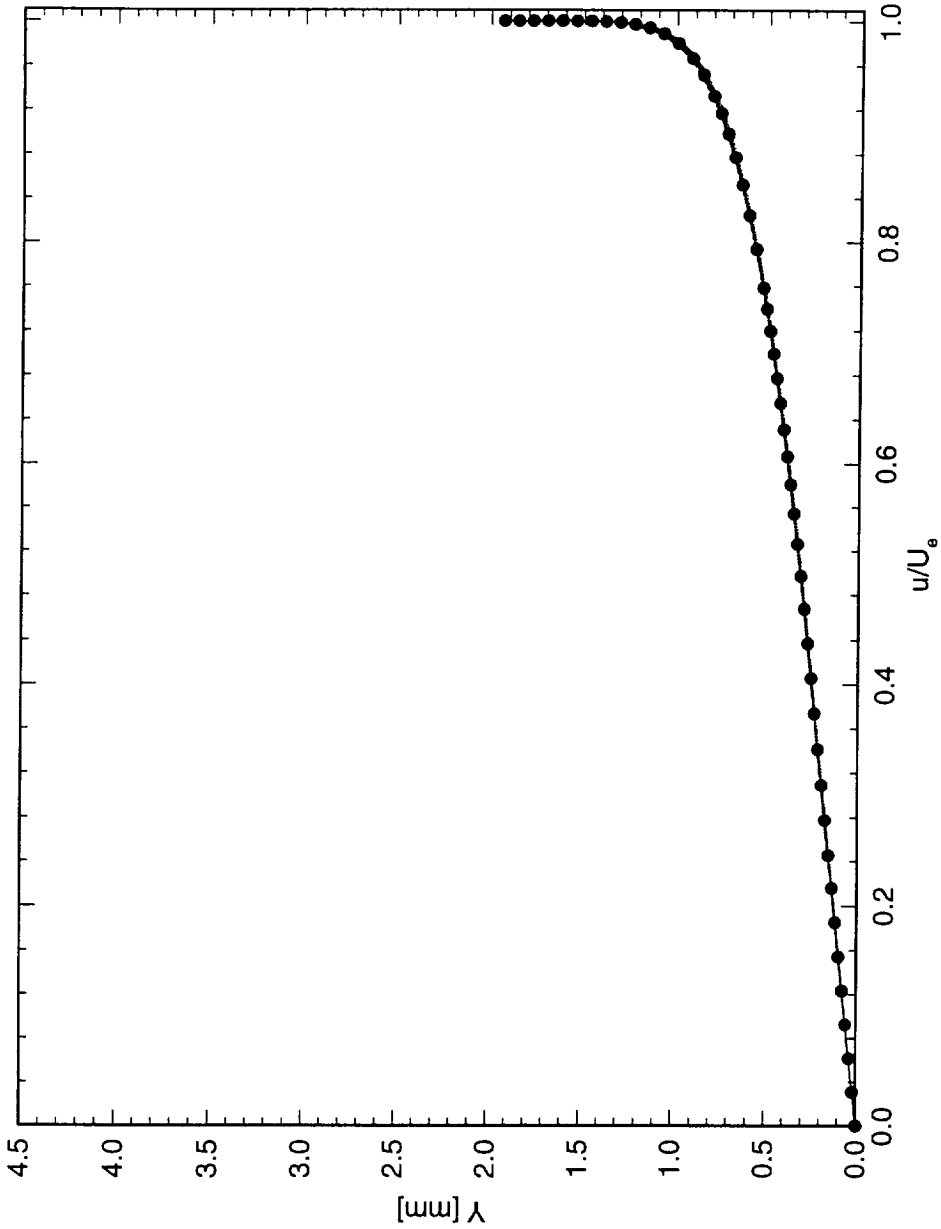

Figure 5.30: Spanwise array of 100 boundary-layer profiles spaced 1 mm apart in span at $x/c = 0.05$. $Re_c = 2.4 \times 10^6$, no artificial roughness. The dots represent the spanwise average of the profiles.

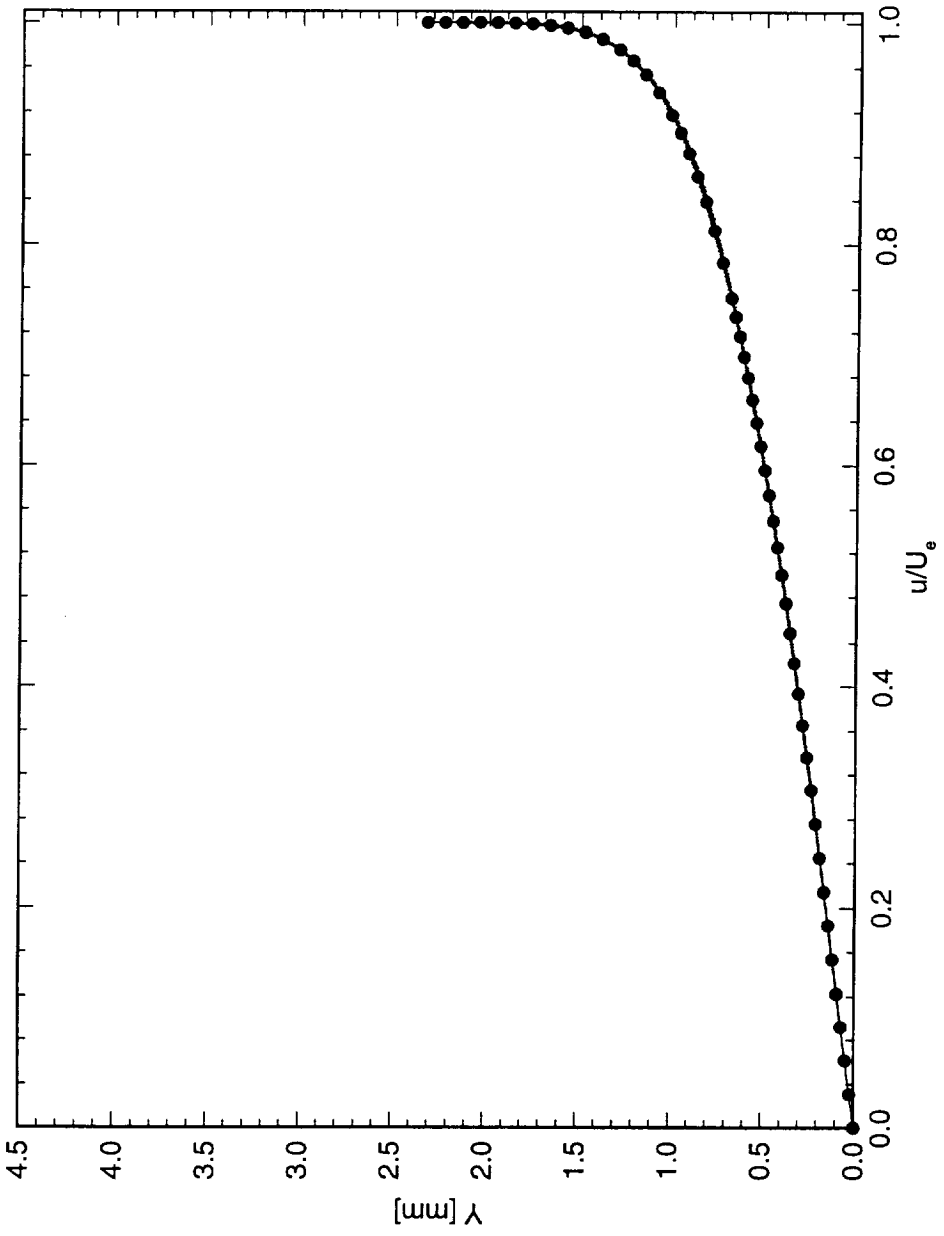

Figure 5.31: Spanwise array of 100 boundary-layer profiles spaced 1 mm apart in span at $x/c = 0.10$. $Re_c = 2.4 \times 10^6$, no artificial roughness. The dots represent the spanwise average of the profiles.

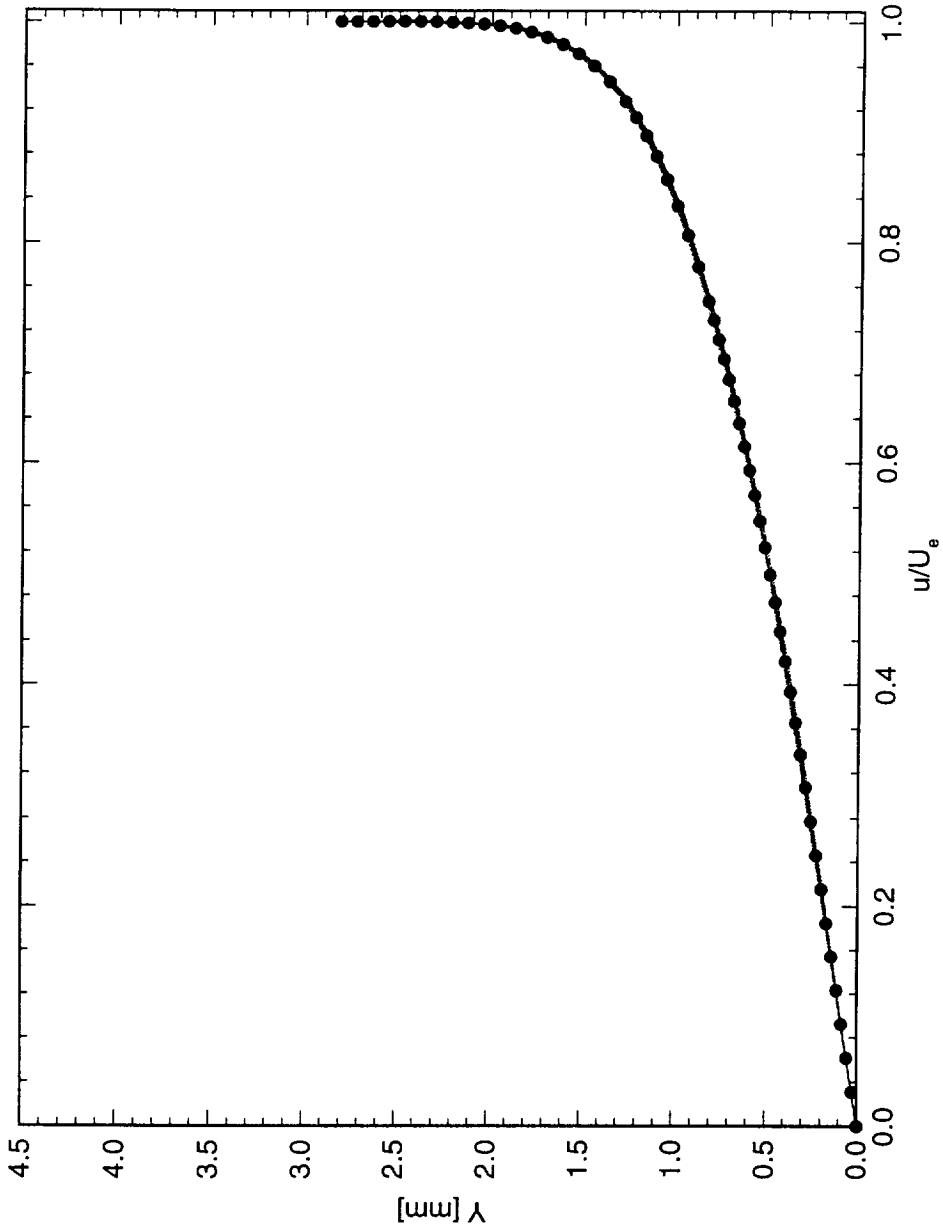

Figure 5.32: Spanwise array of 100 boundary-layer profiles spaced 1 mm apart in span at $x/c = 0.15$. $Re_c = 2.4 \times 10^6$, no artificial roughness. The dots represent the spanwise average of the profiles.

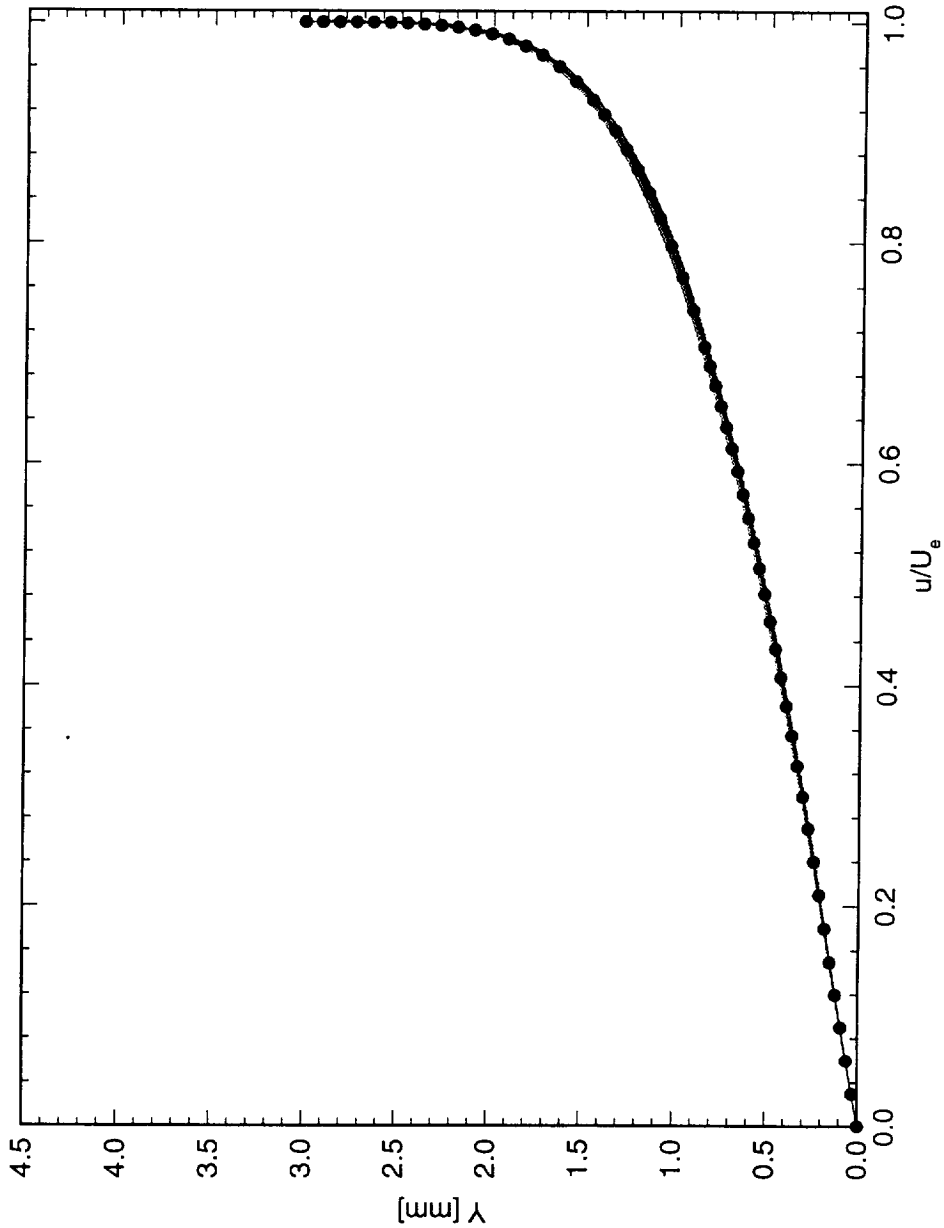

Figure 5.33: Spanwise array of 100 boundary-layer profiles spaced 1 mm apart in span at $x/c = 0.20$. $Re_c = 2.4 \times 10^6$, no artificial roughness. The dots represent the spanwise average of the profiles.

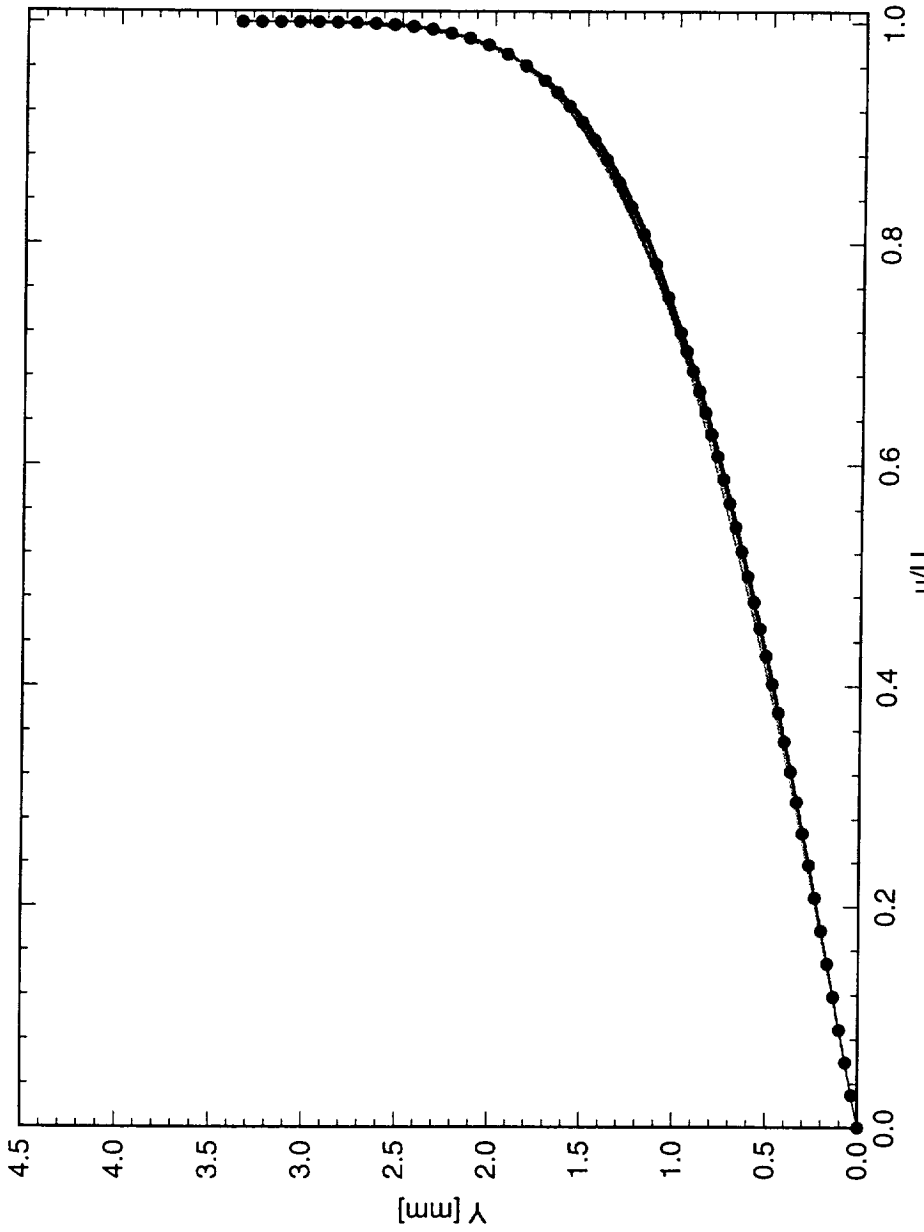

Figure 5.34: Spanwise array of 100 boundary-layer profiles spaced 1 mm apart in span at $x/c = 0.25$. $Re_c = 2.4 \times 10^6$, no artificial roughness. The dots represent the spanwise average of the profiles.

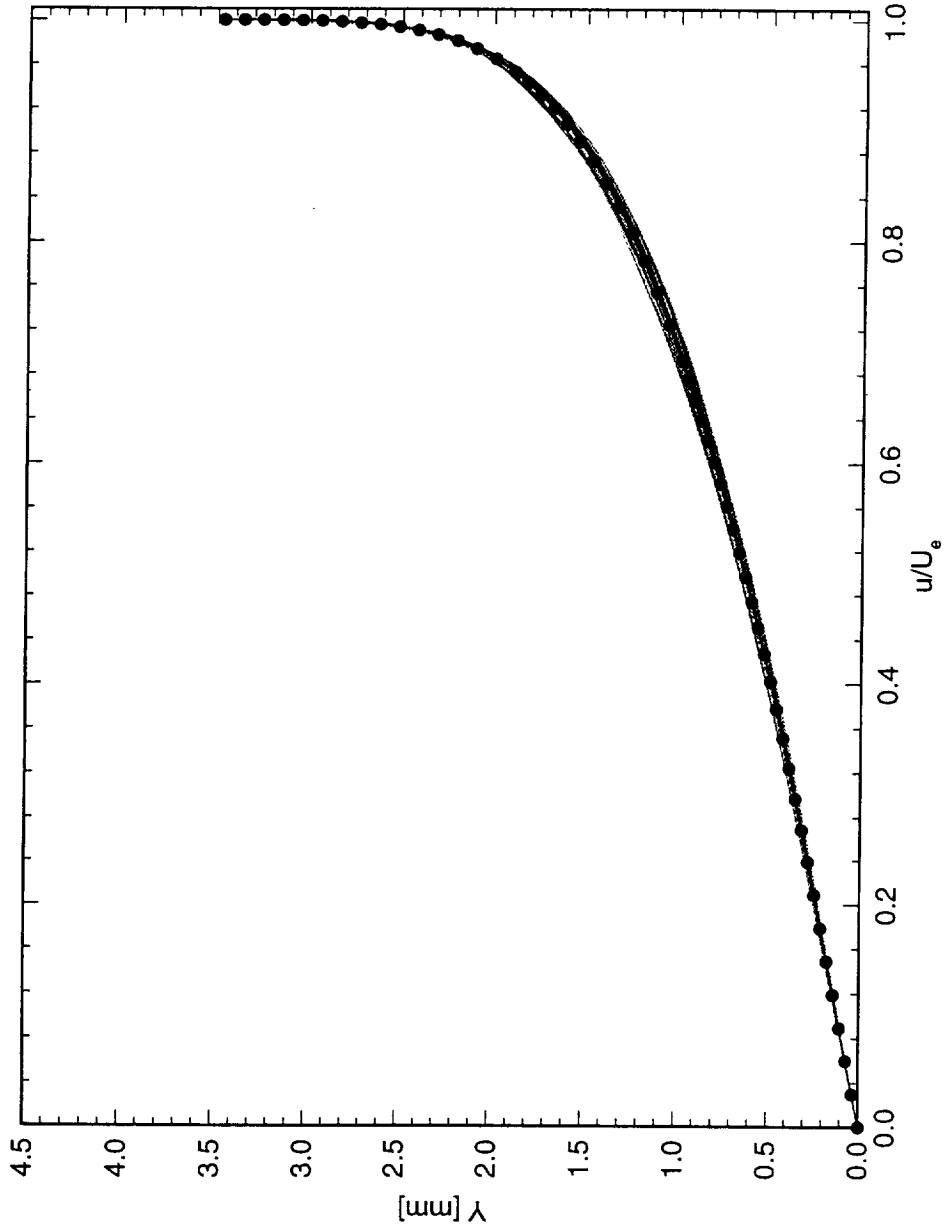

Figure 5.35: Spanwise array of 100 boundary-layer profiles spaced 1 mm apart in span at $x/c = 0.30$. $Re_c = 2.4 \times 10^6$, no artificial roughness. The dots represent the spanwise average of the profiles.

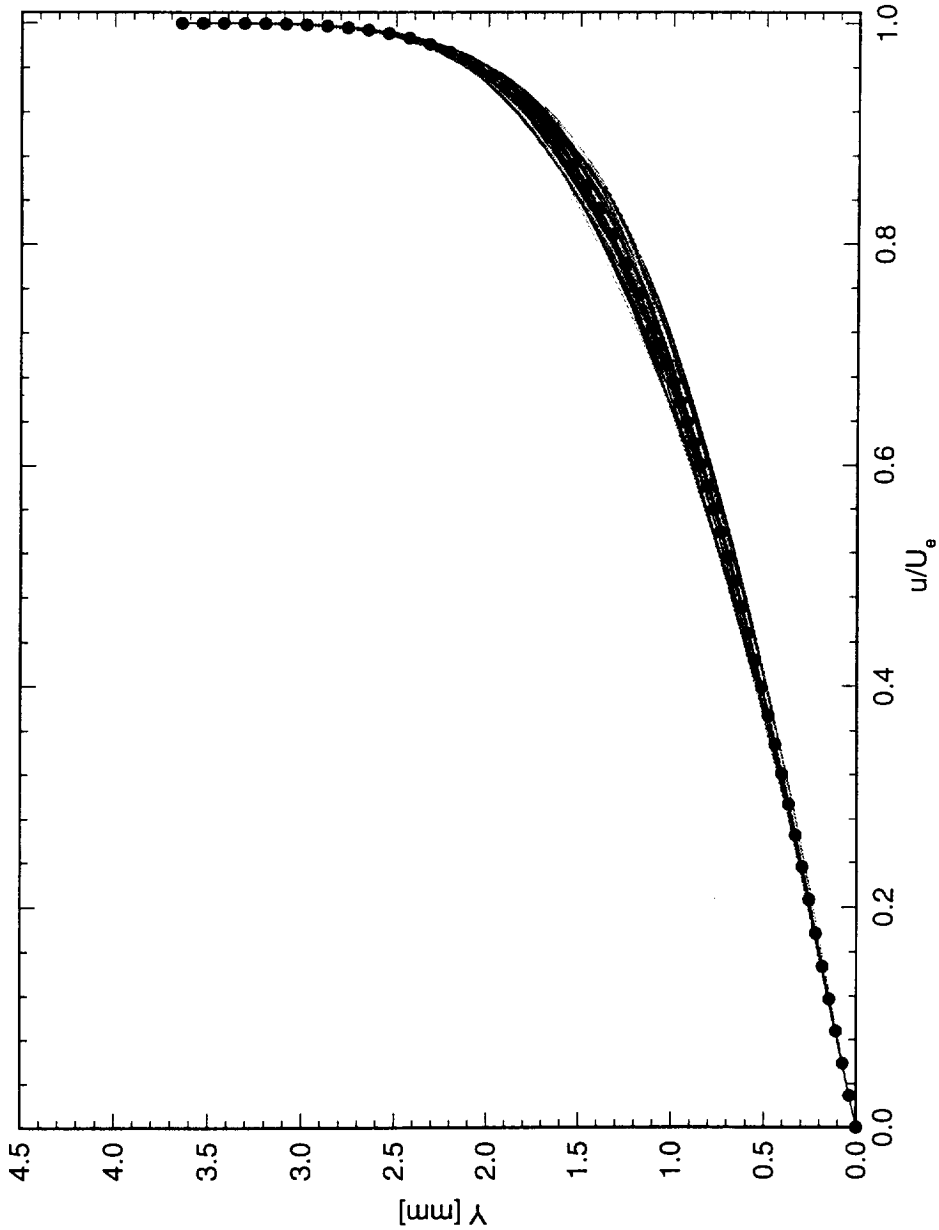

Figure 5.36: Spanwise array of 100 boundary-layer profiles spaced 1 mm apart in span at $x/c = 0.35$. $Re_c = 2.4 \times 10^6$, no artificial roughness. The dots represent the spanwise average of the profiles.

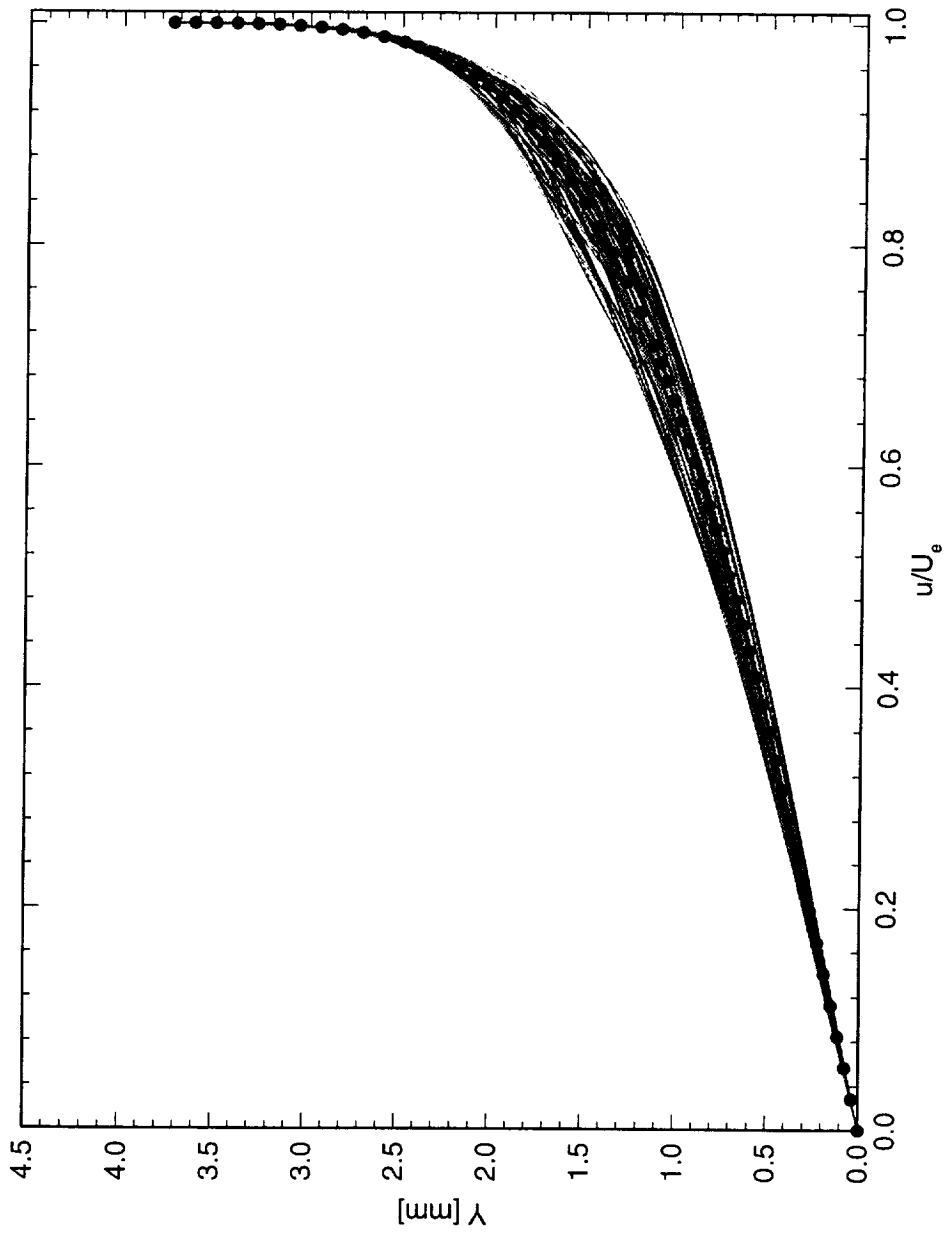

Figure 5.37: Spanwise array of 100 boundary-layer profiles spaced 1 mm apart in span at $x/c = 0.40$. $Re_c = 2.4 \times 10^6$, no artificial roughness. The dots represent the spanwise average of the profiles.

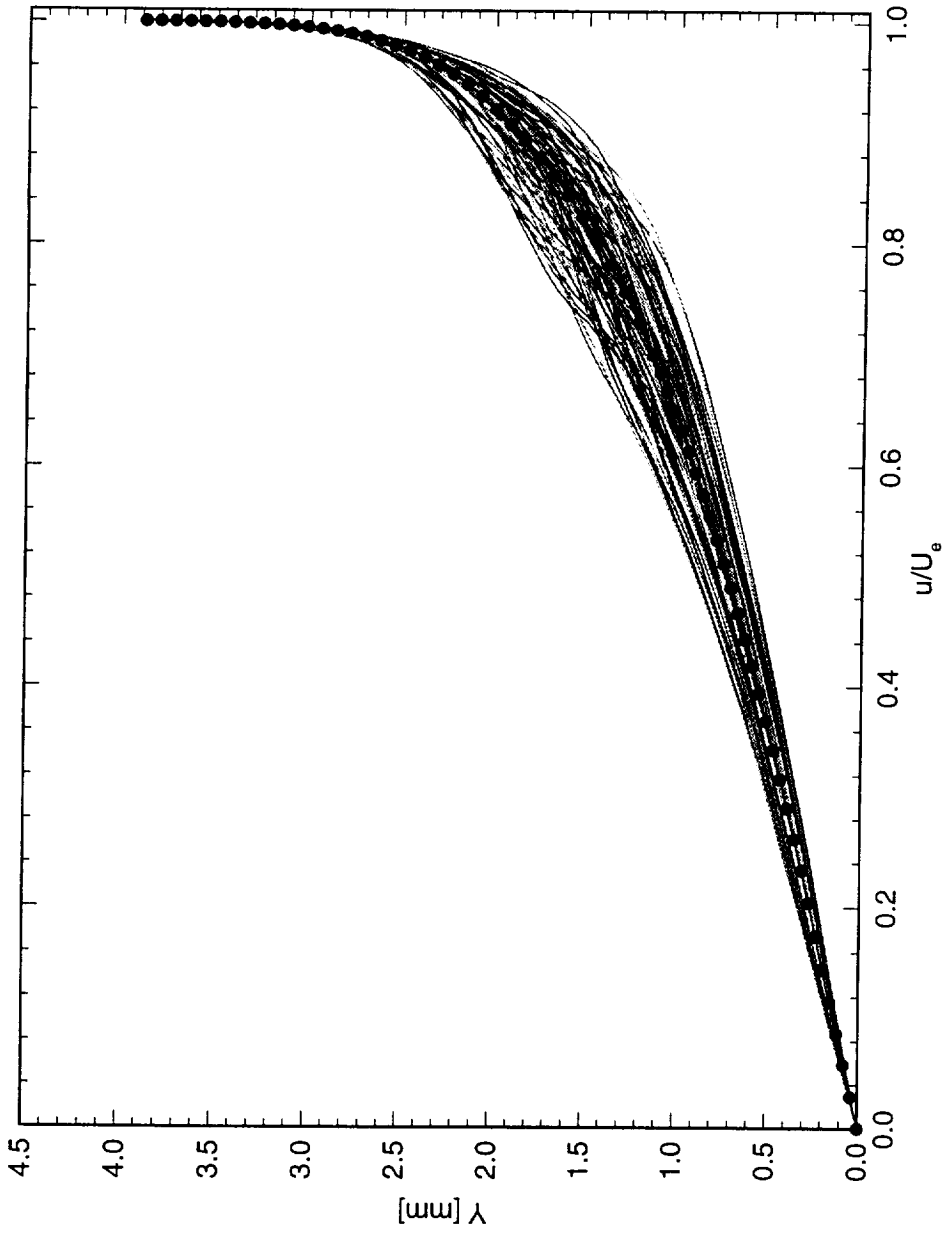

Figure 5.38: Spanwise array of 100 boundary-layer profiles spaced 1 mm apart in span at $x/c = 0.45$. $Re_c = 2.4 \times 10^6$, no artificial roughness. The dots represent the spanwise average of the profiles.

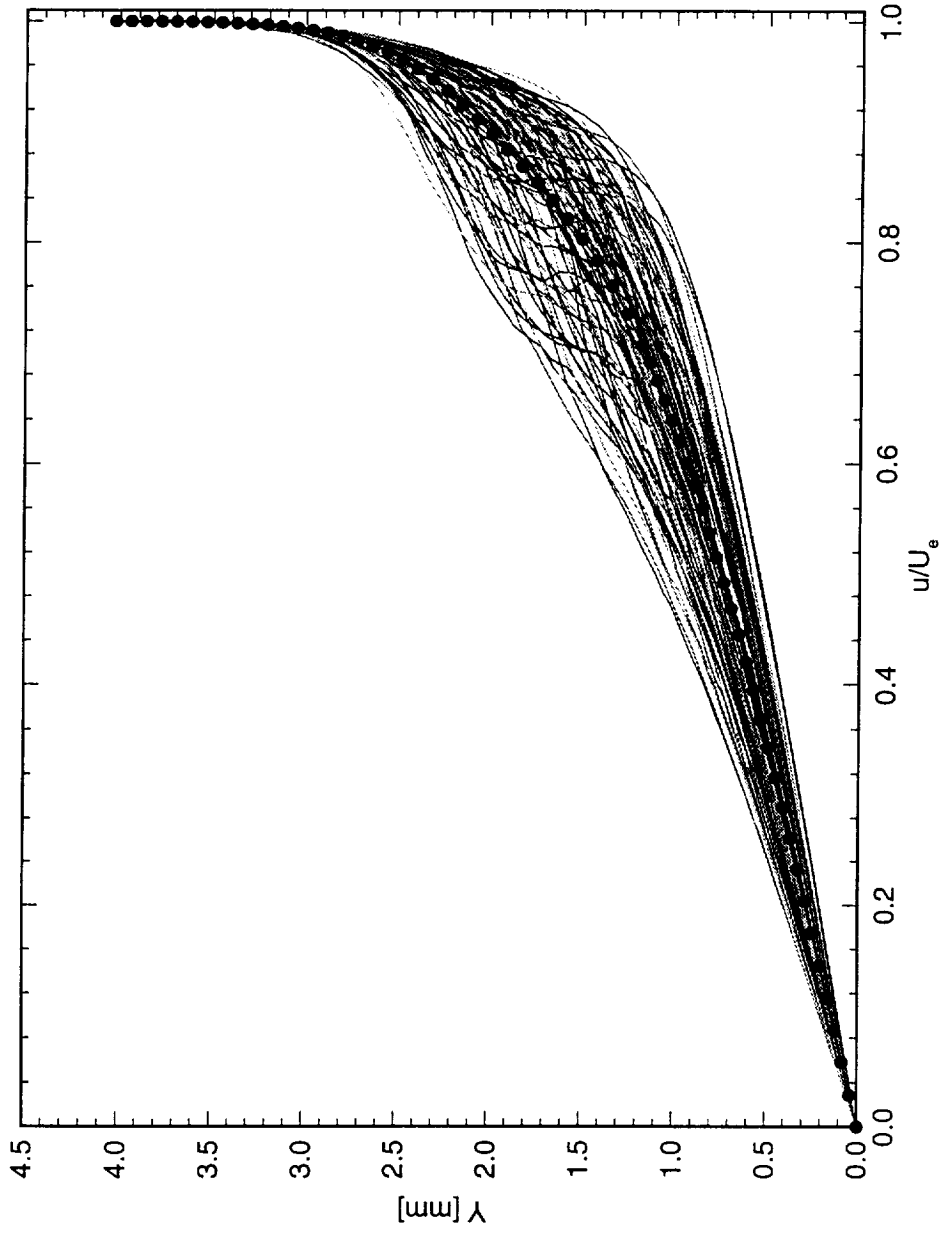

Figure 5.39: Spanwise array of 100 boundary-layer profiles spaced 1 mm apart in span at $x/c = 0.50$. $Re_c = 2.4 \times 10^6$, no artificial roughness. The dots represent the spanwise average of the profiles.

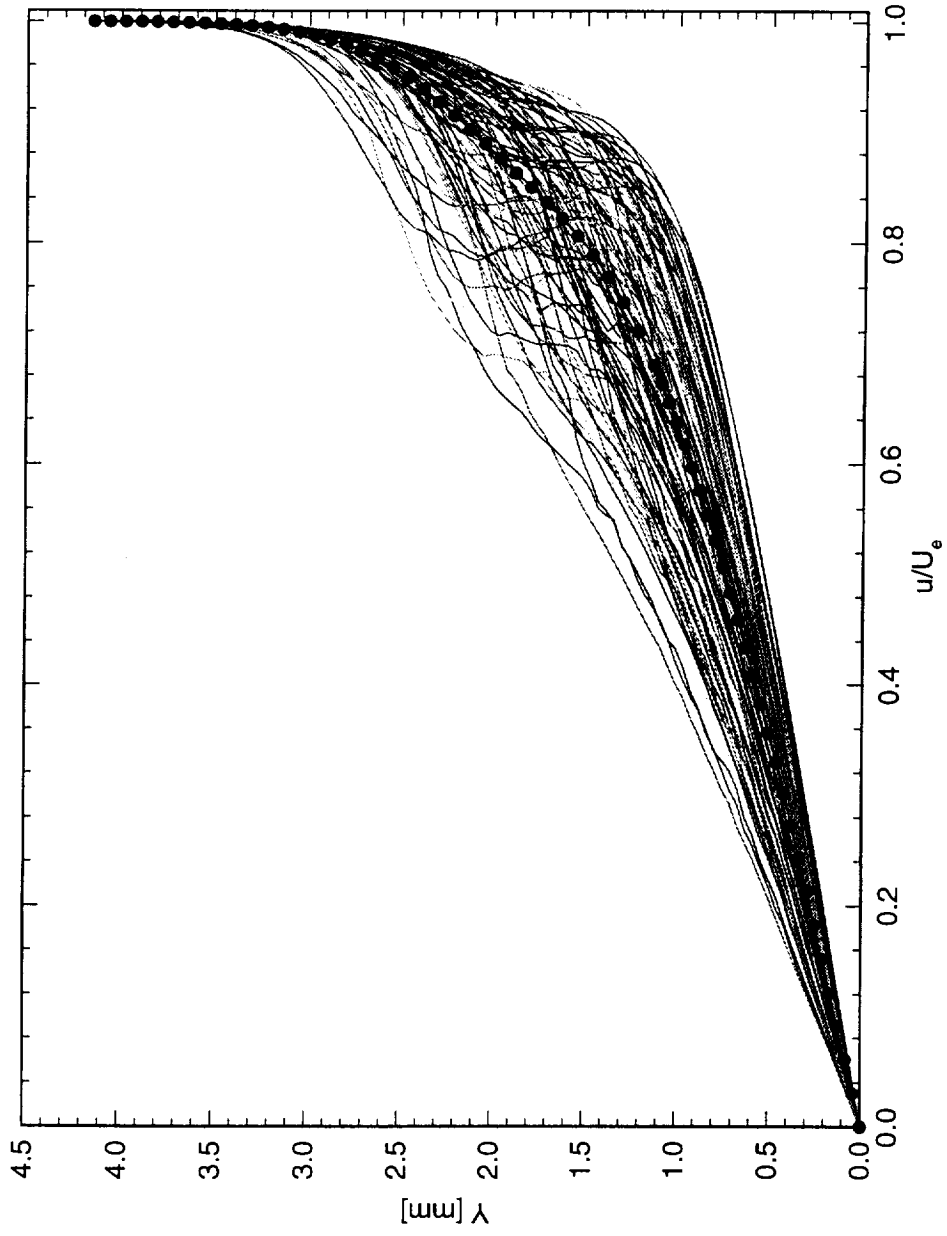

Figure 5.40: Spanwise array of 100 boundary-layer profiles spaced 1 mm apart in span at $x/c = 0.55$. $Re_c = 2.4 \times 10^6$, no artificial roughness. The dots represent the spanwise average of the profiles.

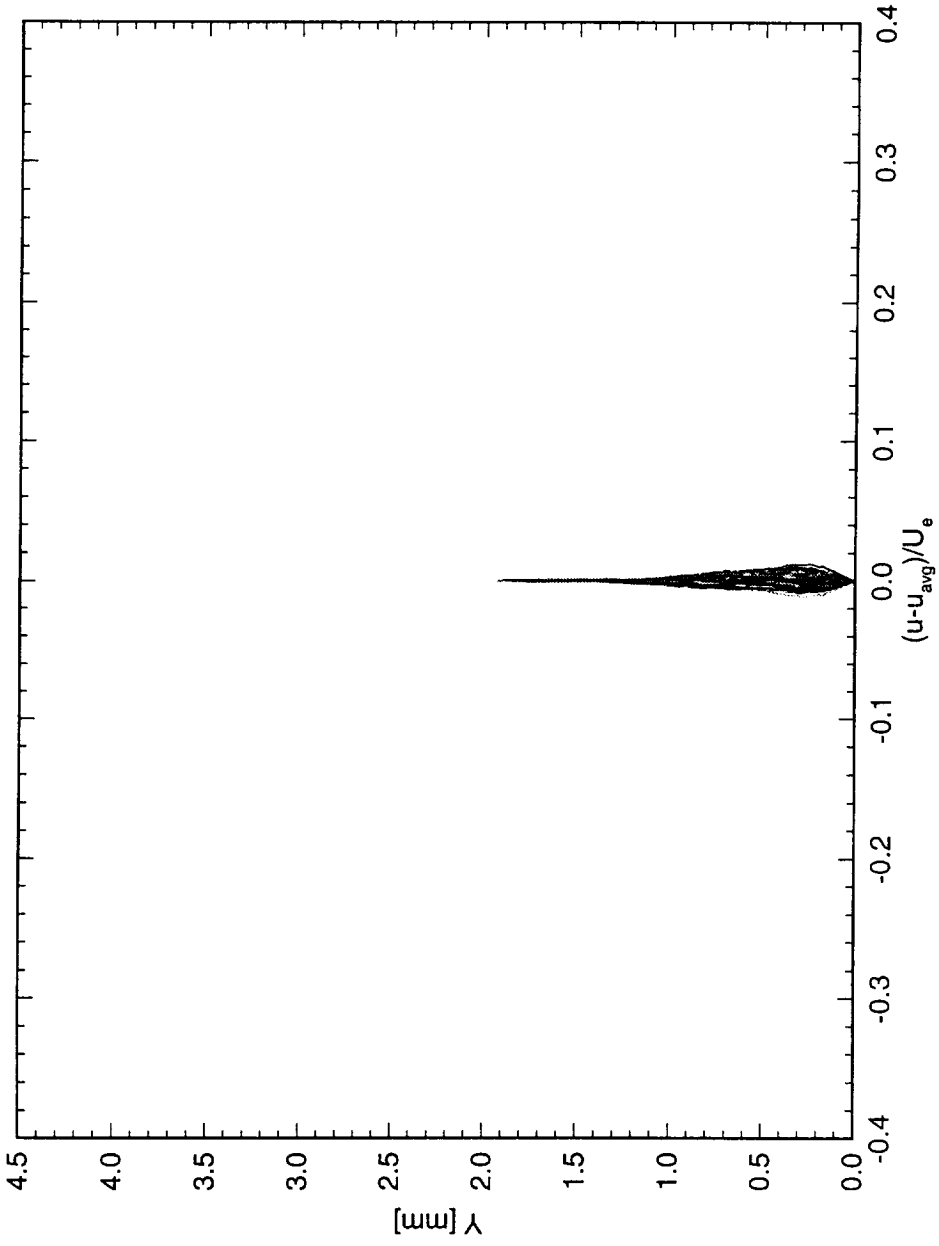

Figure 5.41: Spanwise array of 100 disturbance profiles spaced 1 mm apart in span at $x/c = 0.05$. $Re_c = 2.4 \times 10^6$, no artificial roughness.

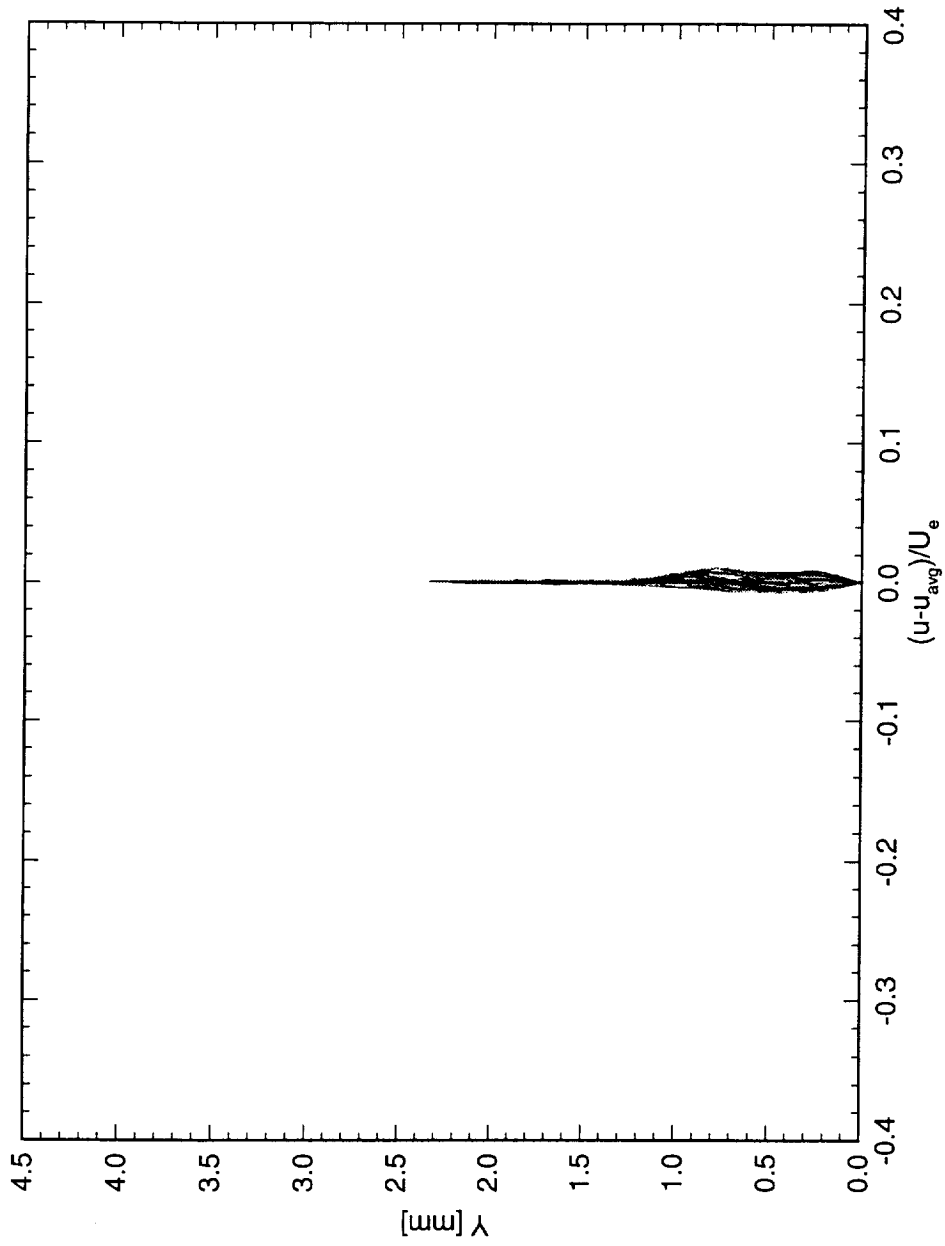

Figure 5.42: Spanwise array of 100 disturbance profiles spaced 1 mm apart in span at $x/c = 0.10$. $Re_c = 2.4 \times 10^6$, no artificial roughness.

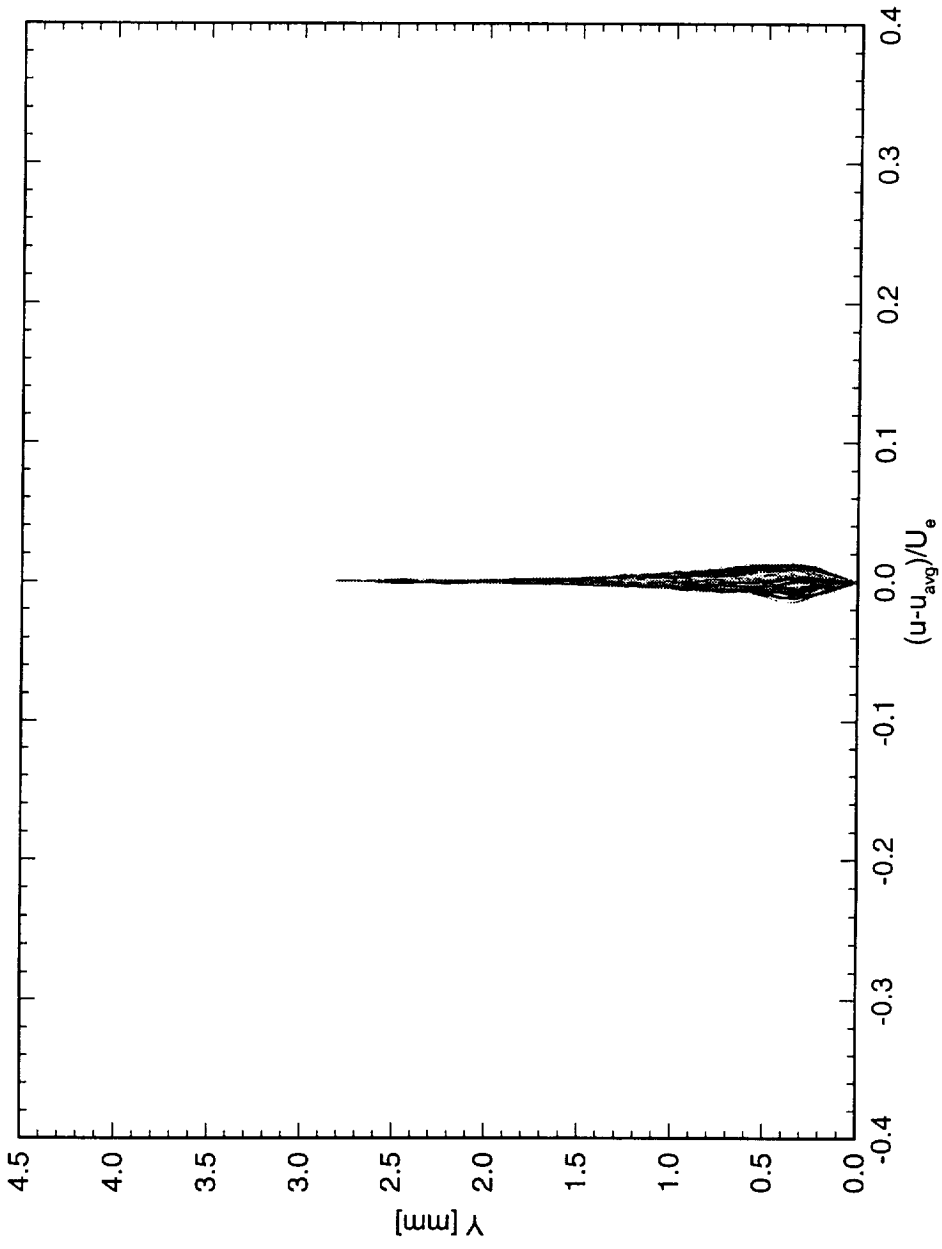

Figure 5.43: Spanwise array of 100 disturbance profiles spaced 1 mm apart in span at $x/c = 0.15$. $Re_c = 2.4 \times 10^6$, no artificial roughness.

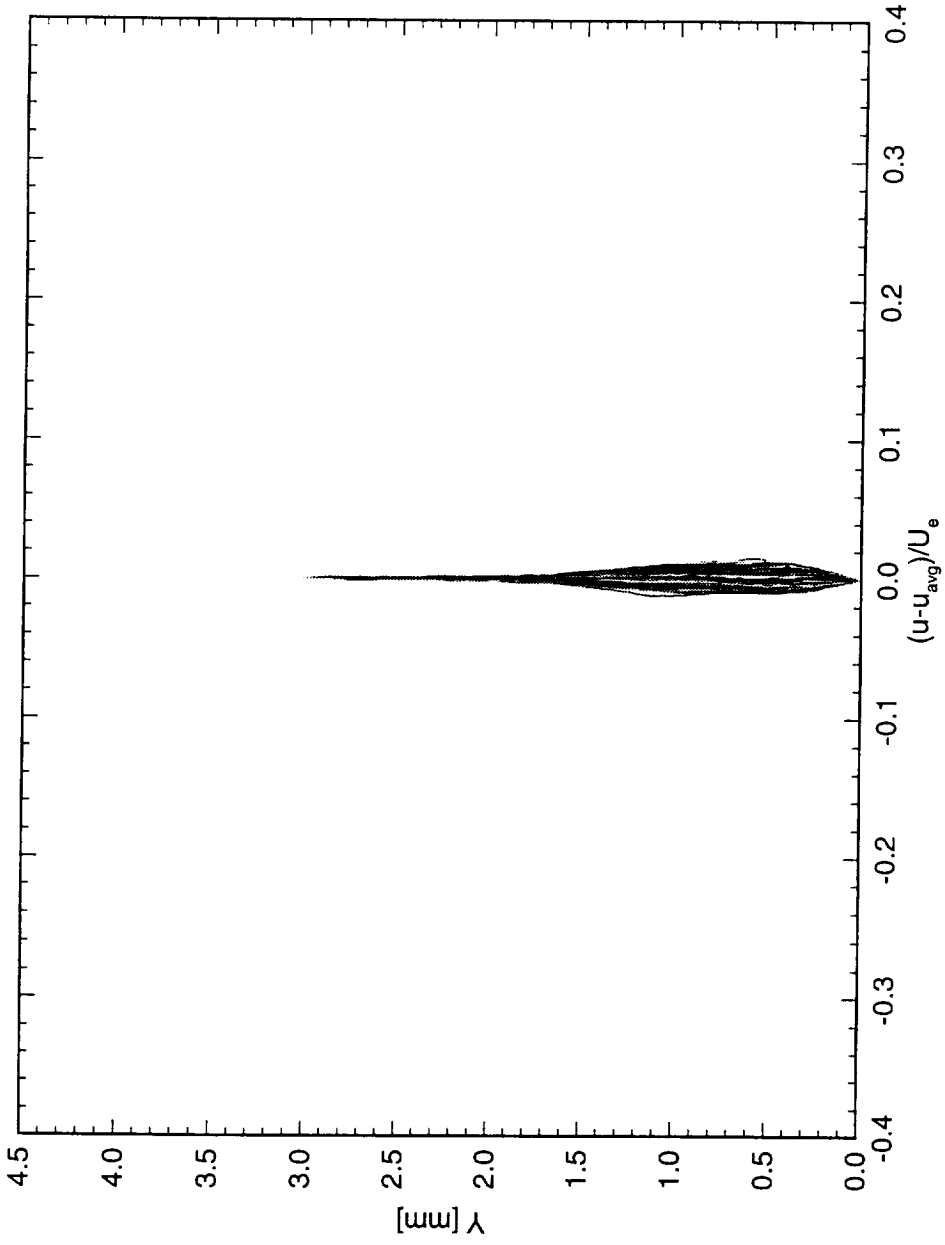

Figure 5.44: Spanwise array of 100 disturbance profiles spaced 1 mm apart in span at $x/c = 0.20$. $Re_c = 2.4 \times 10^6$, no artificial roughness.

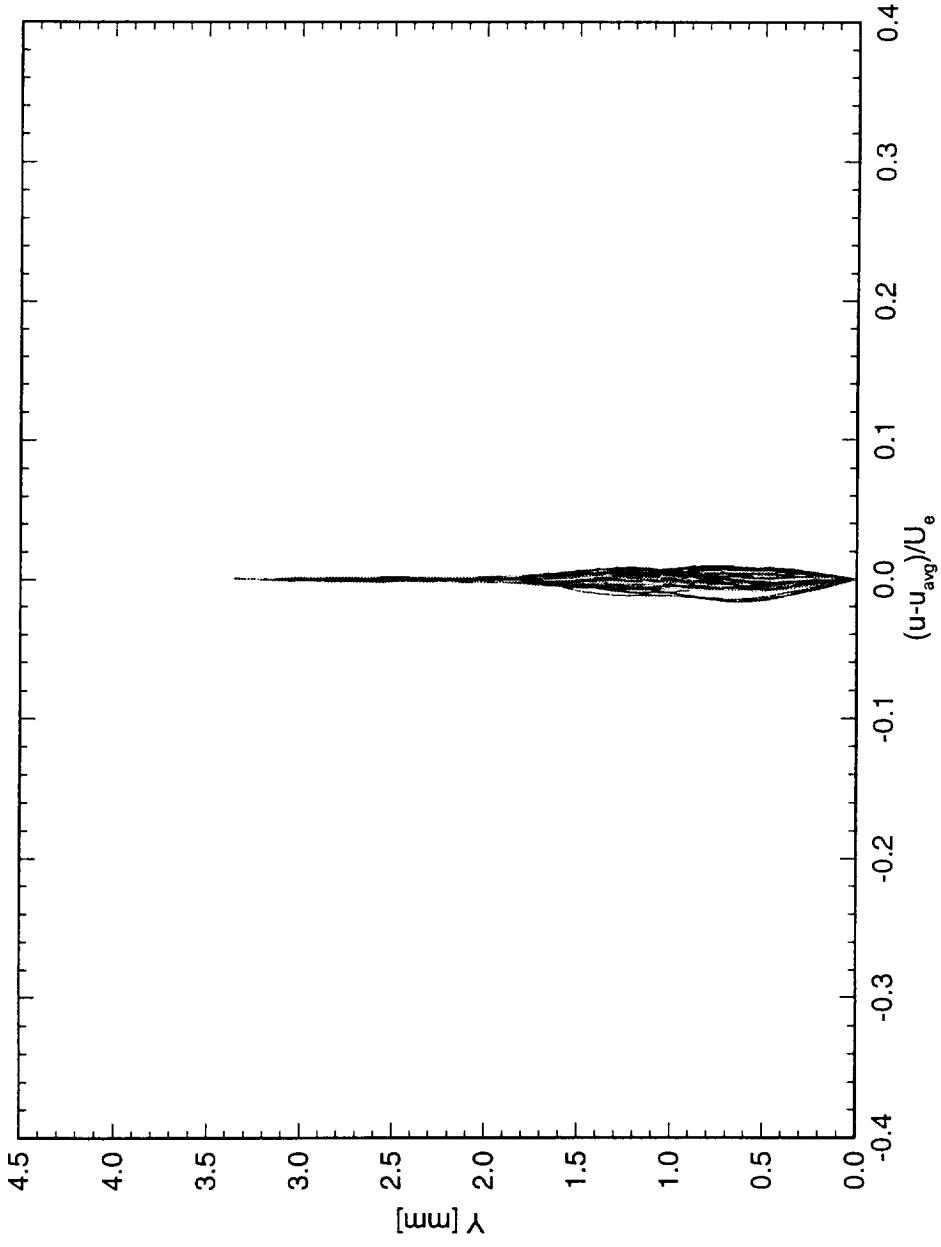

Figure 5.45: Spanwise array of 100 disturbance profiles spaced 1 mm apart in span at $x/c = 0.25$. $Re_c = 2.4 \times 10^6$, no artificial roughness.

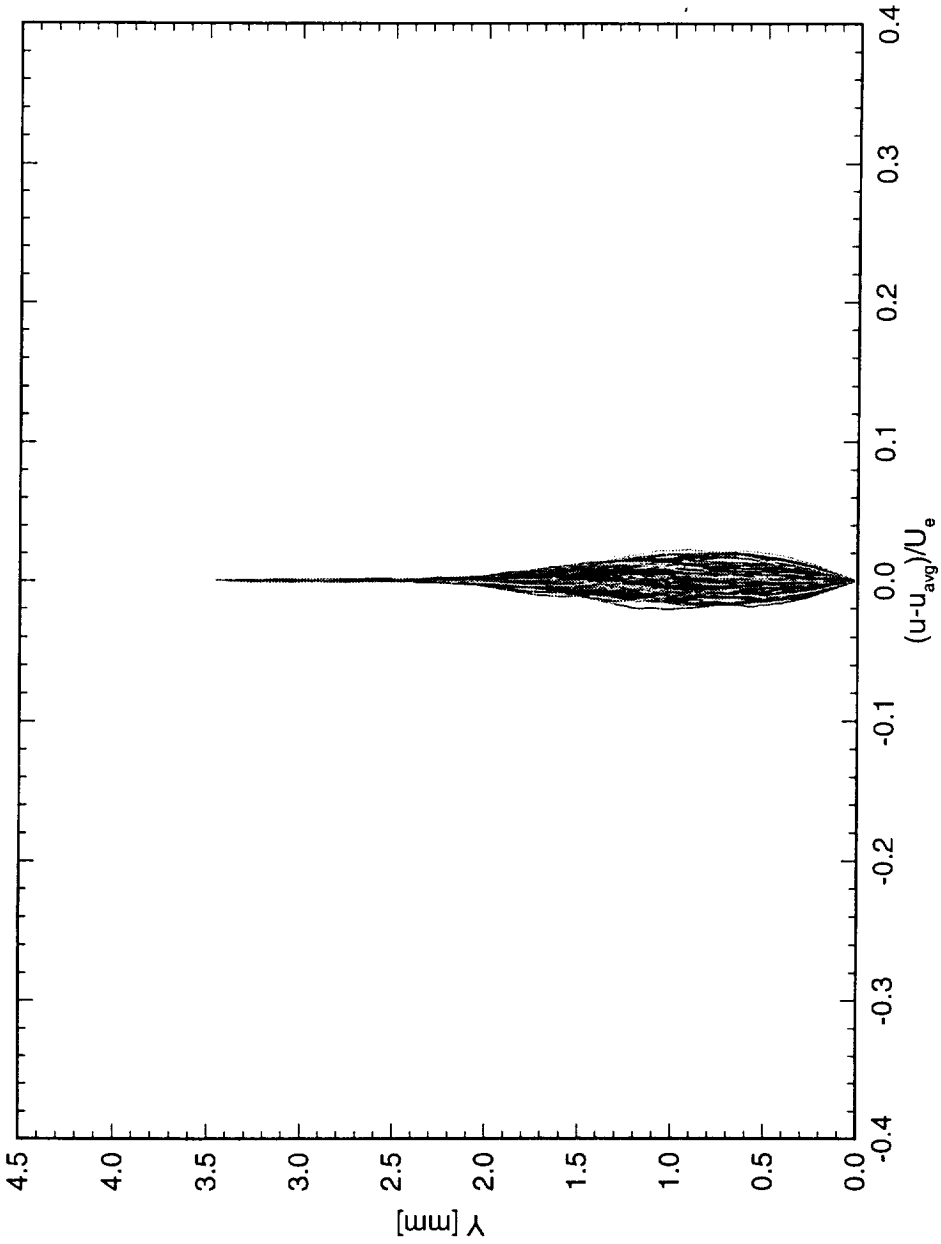

Figure 5.46: Spanwise array of 100 disturbance profiles spaced 1 mm apart in span at $x/c = 0.30$. $Re_c = 2.4 \times 10^6$, no artificial roughness.

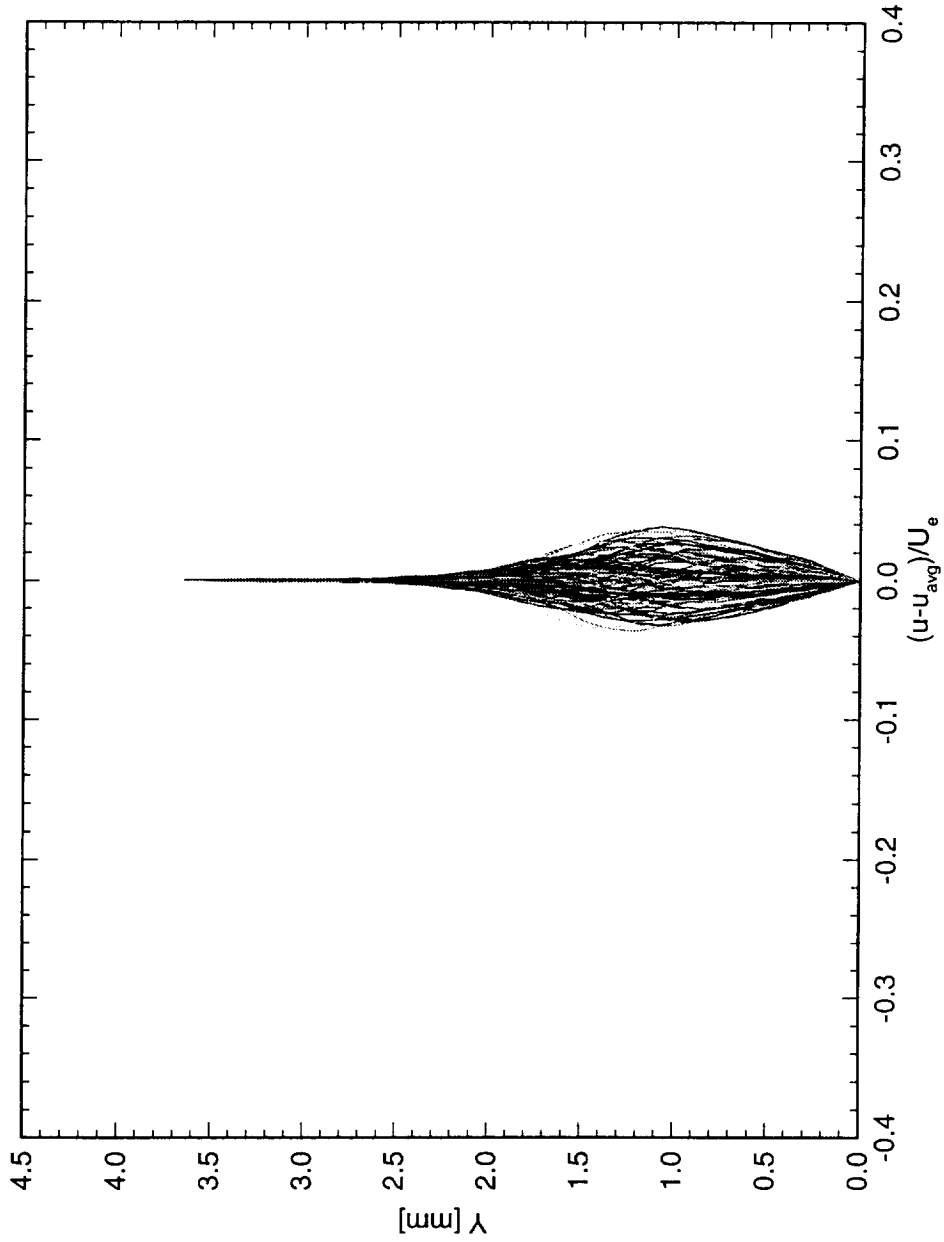

Figure 5.47: Spanwise array of 100 disturbance profiles spaced 1 mm apart in span at $x/c = 0.35$. $Re_c = 2.4 \times 10^6$, no artificial roughness.

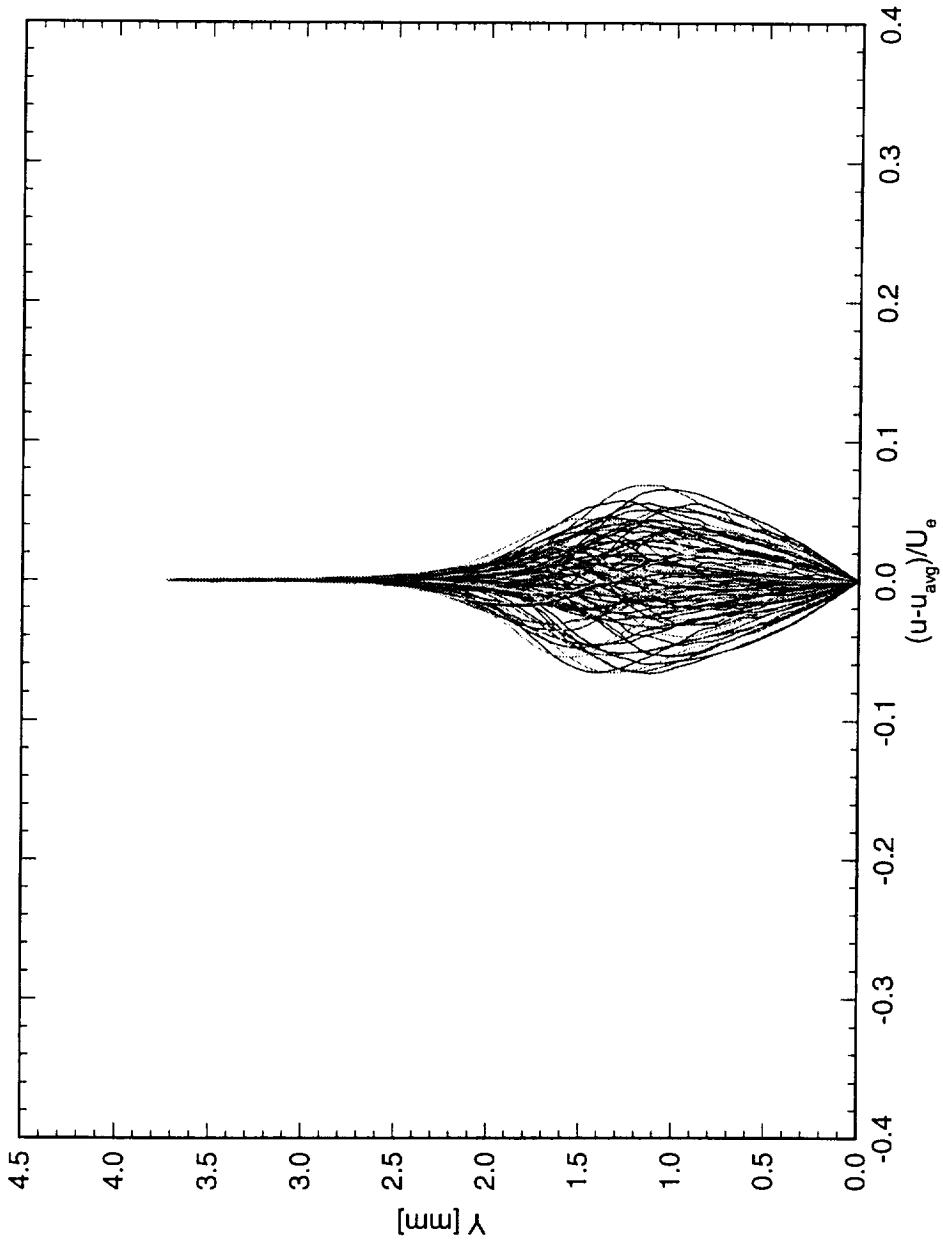

Figure 5.48: Spanwise array of 100 disturbance profiles spaced 1 mm apart in span at $x/c = 0.40$. $Re_c = 2.4 \times 10^6$, no artificial roughness.

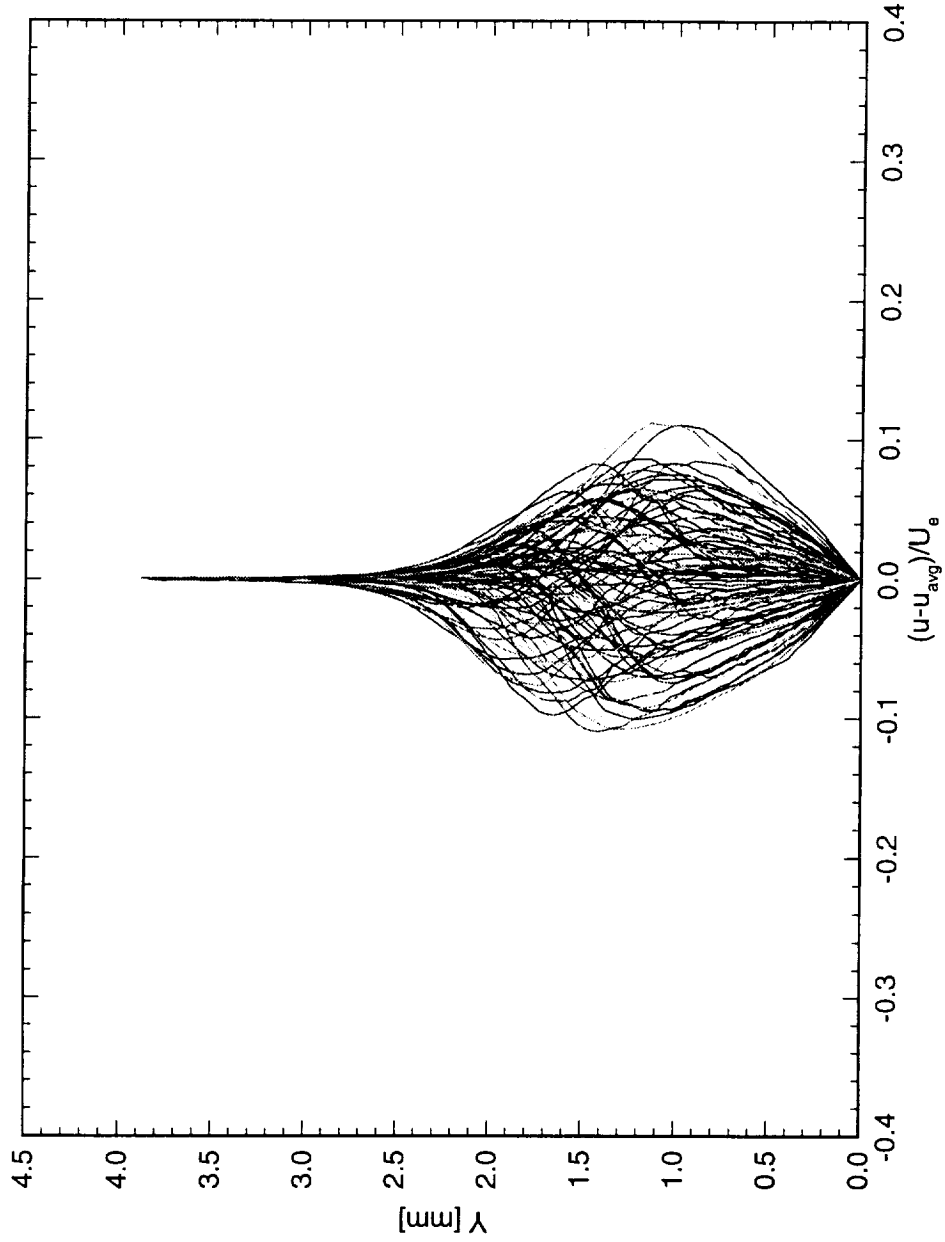

Figure 5.49: Spanwise array of 100 disturbance profiles spaced 1 mm apart in span at $x/c = 0.45$. $Re_c = 2.4 \times 10^6$, no artificial roughness.

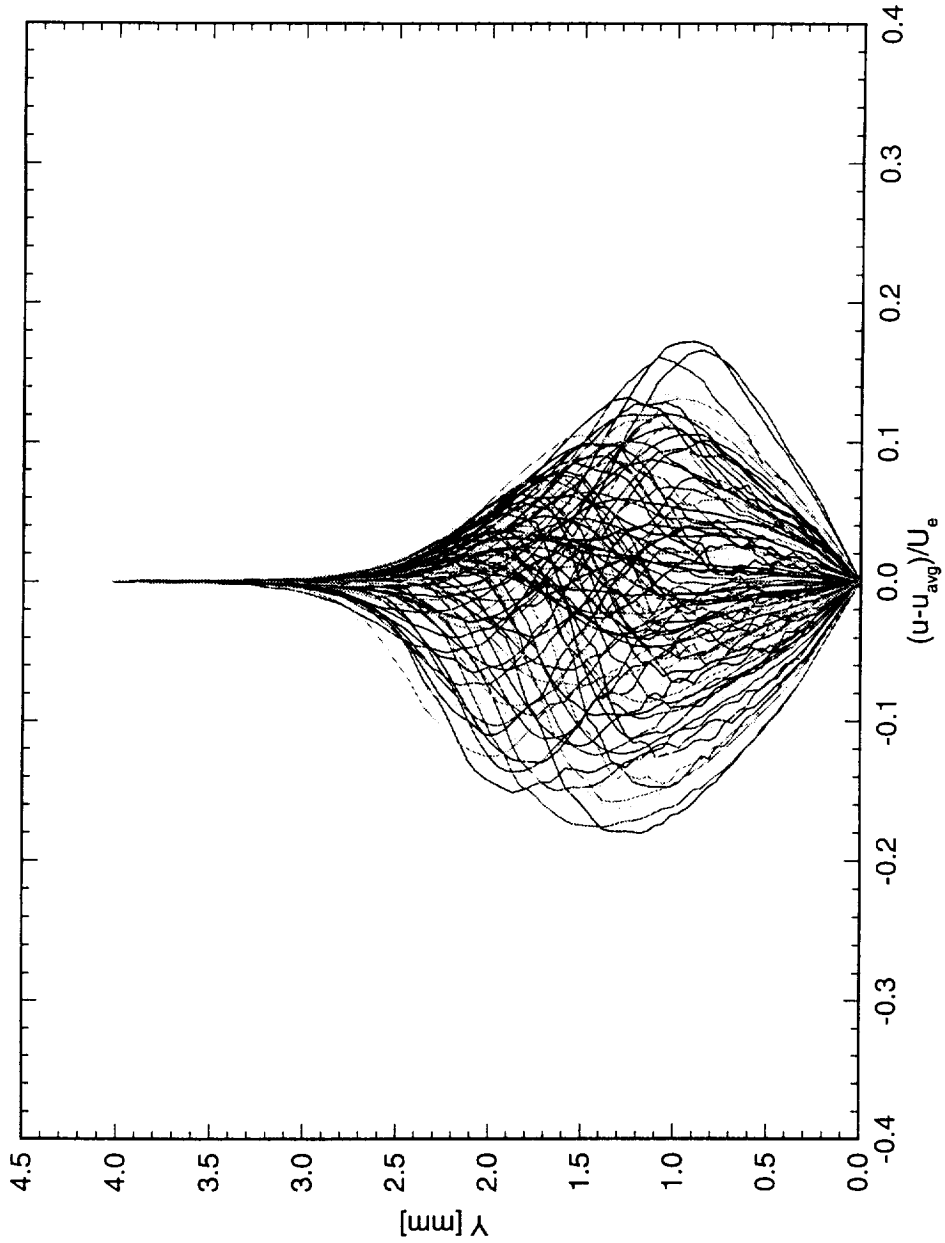

Figure 5.50: Spanwise array of 100 disturbance profiles spaced 1 mm apart in span at $x/c = 0.50$. $Re_c = 2.4 \times 10^6$, no artificial roughness.

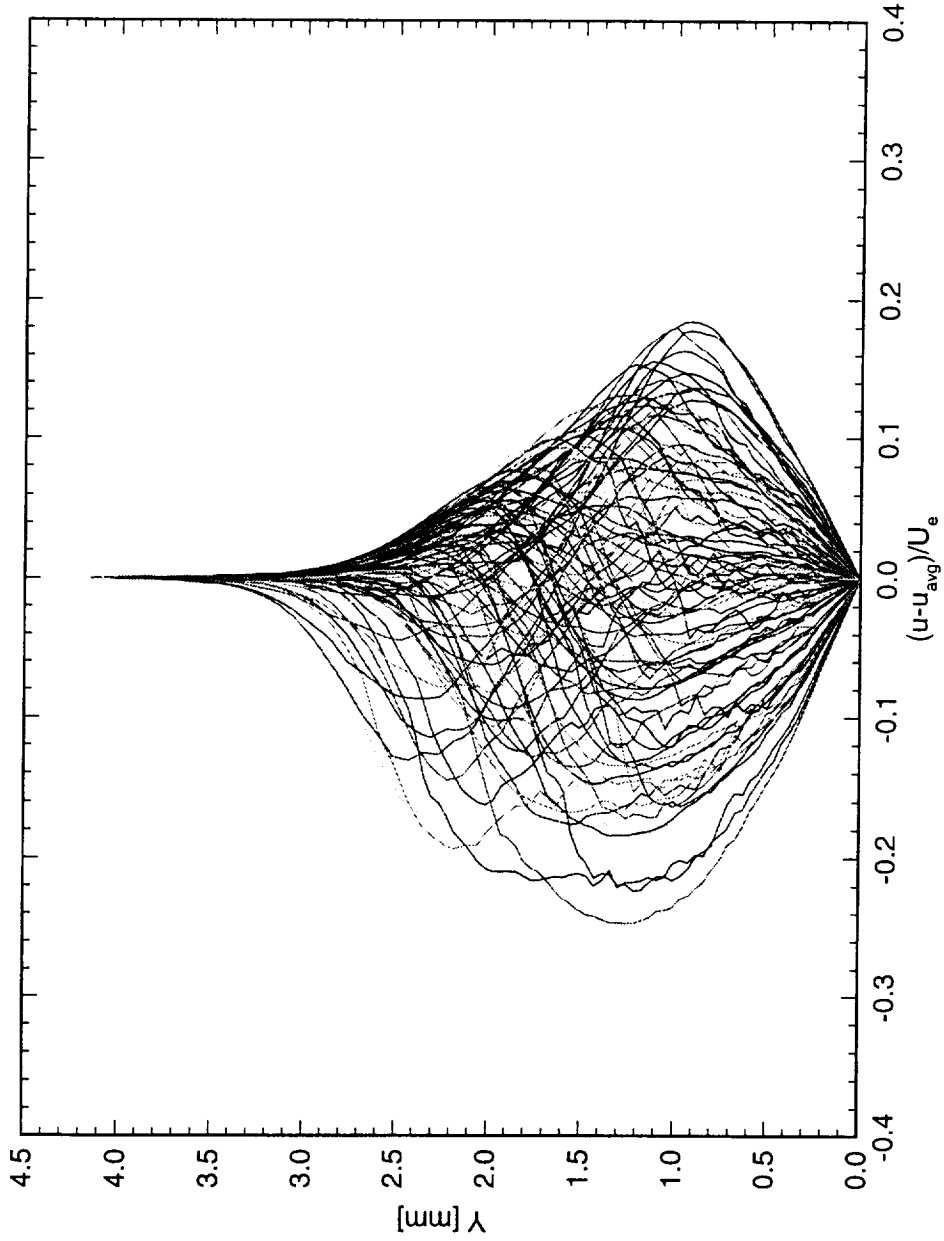

Figure 5.51: Spanwise array of 100 disturbance profiles spaced 1 mm apart in span at $x/c = 0.55$. $Re_c = 2.4 \times 10^6$, no artificial roughness.

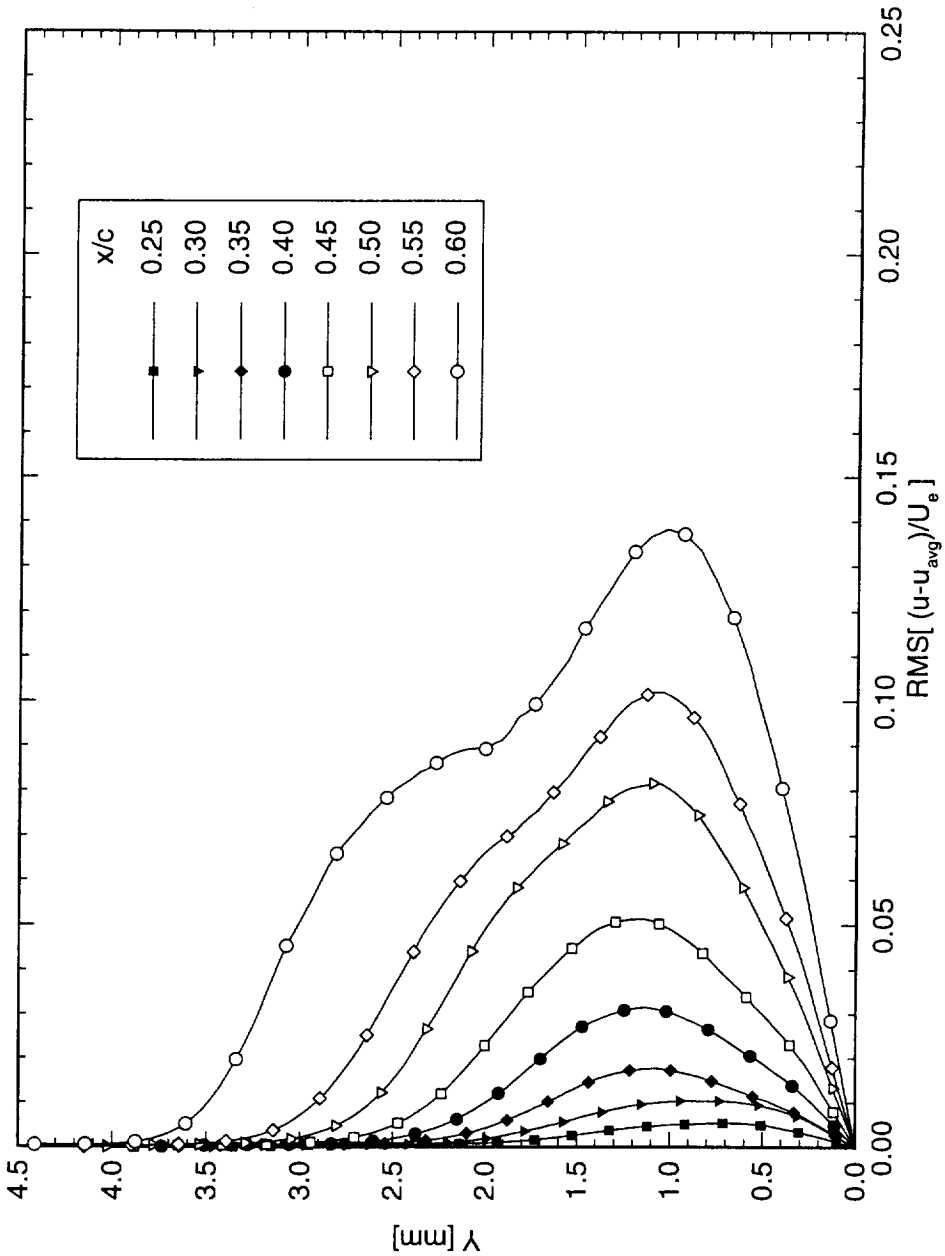

Figure 5.52: Stationary crossflow mode shapes for $Re_c = 2.4 \times 10^6$ and no artificial roughness. The symbols are merely indicators and do not indicate measurement points

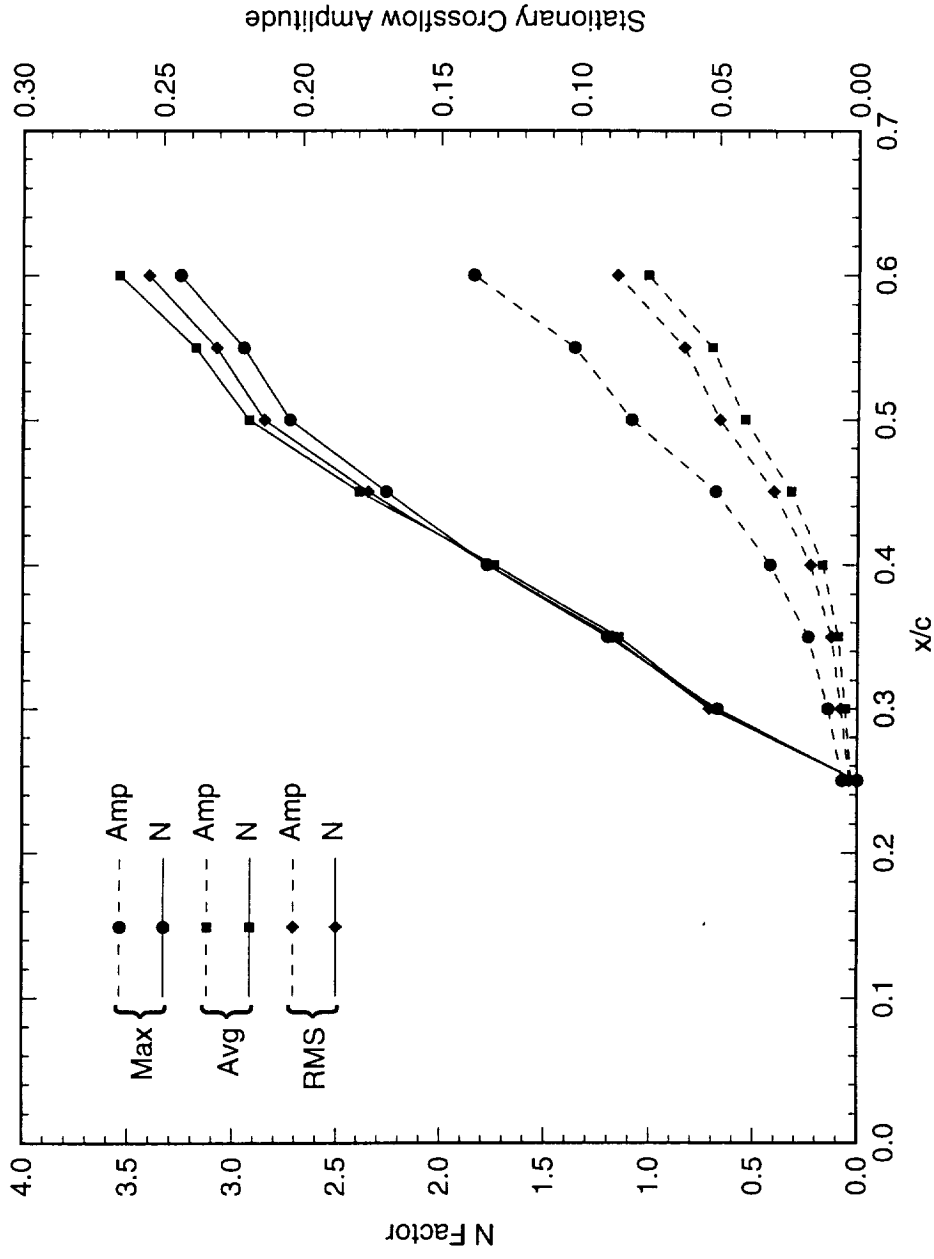

Figure 5.53: Total disturbance amplitude and relative N-factor for $Re_c = 2.4 \times 10^6$ and no artificial roughness. N-factor calculations are relative to $x/c = 0.25$.

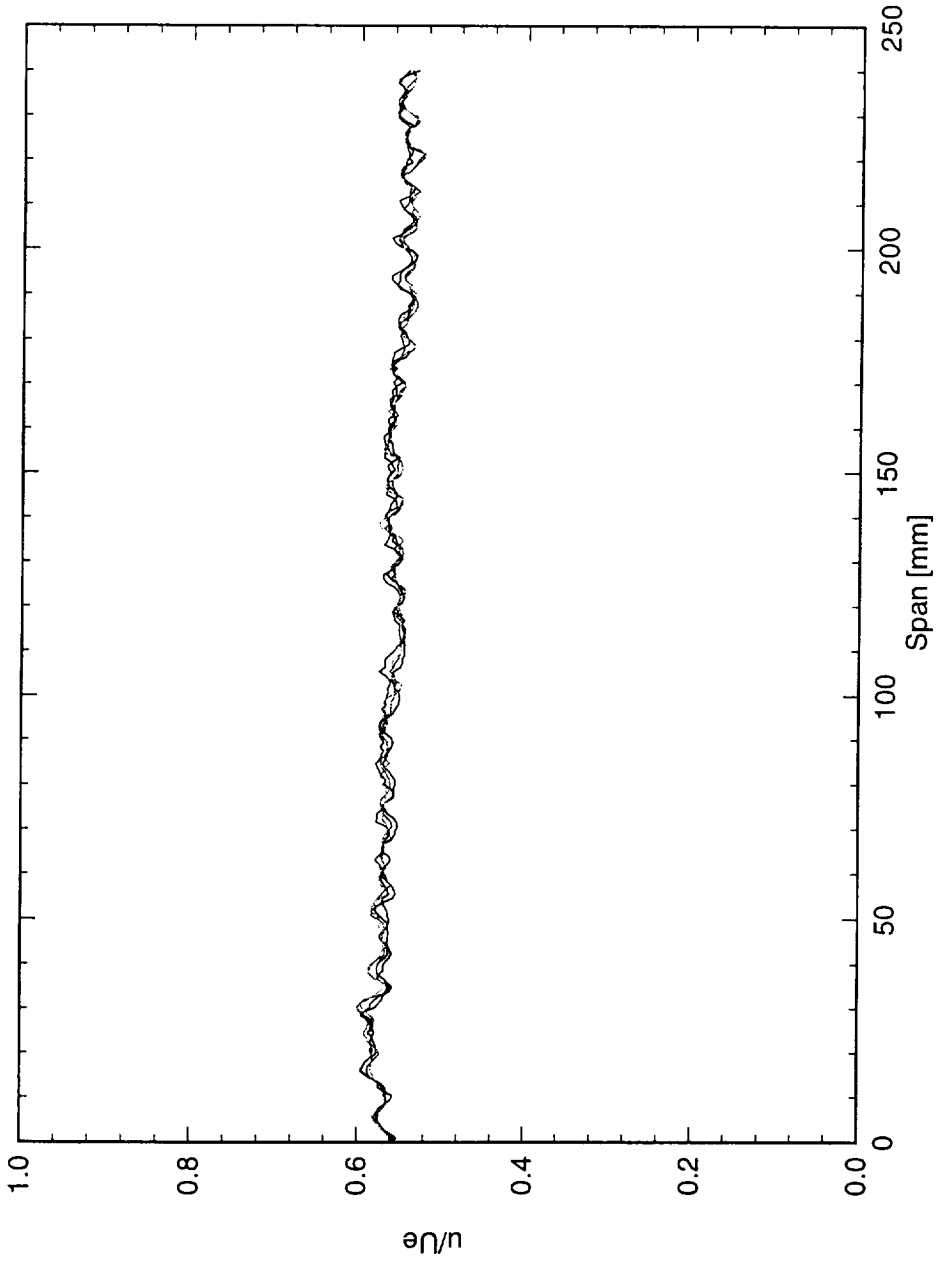

Figure 5.54: Spanwise hot-wire scan at $x/c = 0.25$ and $Y = 0.70$ mm. $Re_c = 2.4 \times 10^6$, no artificial roughness.

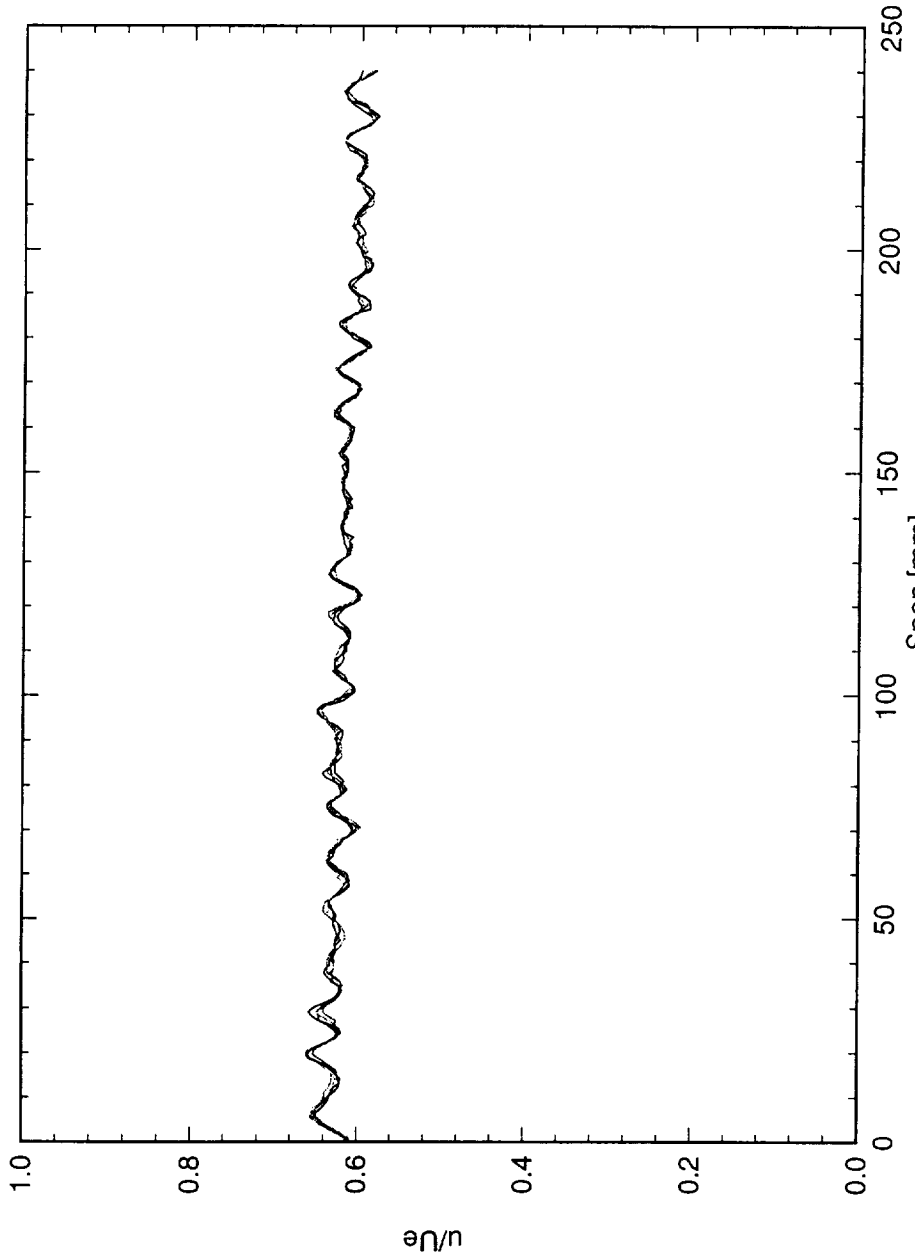

Figure 5.55: Spanwise hot-wire scan at $x/c = 0.30$ and $Y = 0.85$ mm. $Re_c = 2.4 \times 10^6$, no artificial roughness.

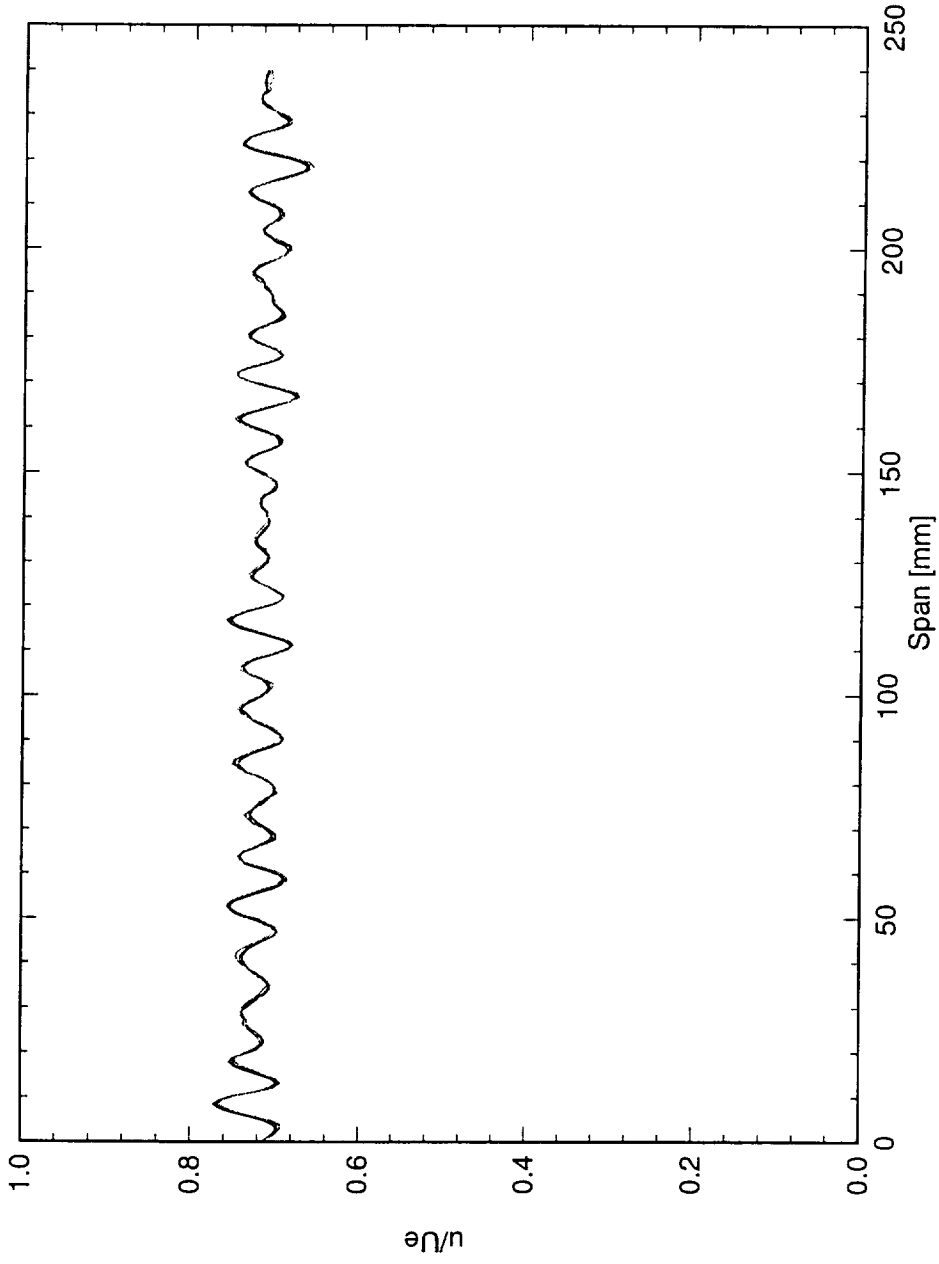

Figure 5.56: Spanwise hot-wire scan at $x/c = 0.35$ and $Y = 1.1$ mm. $Re_c = 2.4 \times 10^6$, no artificial roughness.

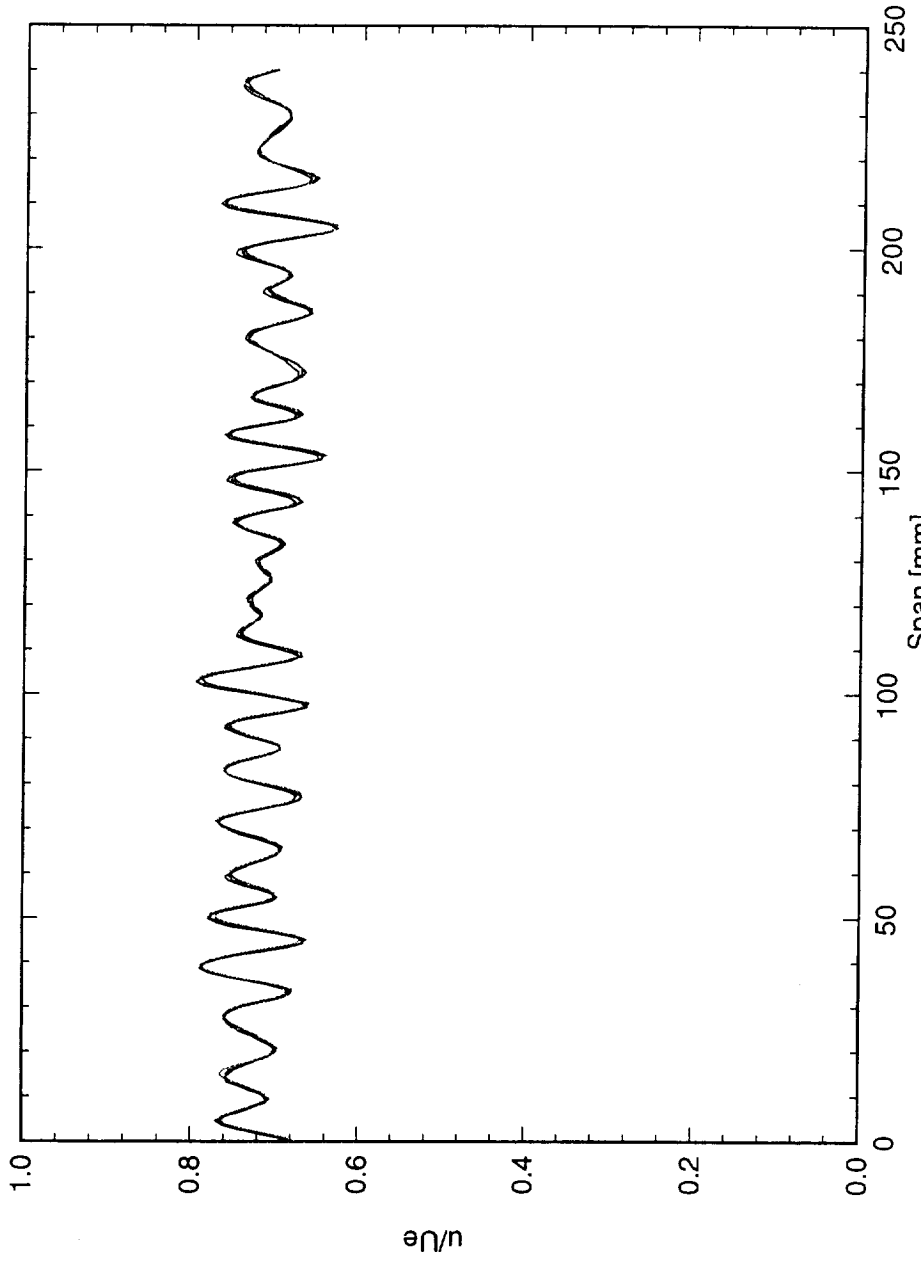

Figure 5.57: Spanwise hot-wire scan at $x/c = 0.40$ and $Y = 1.15$ mm. $Re_c = 2.4 \times 10^6$, no artificial roughness.

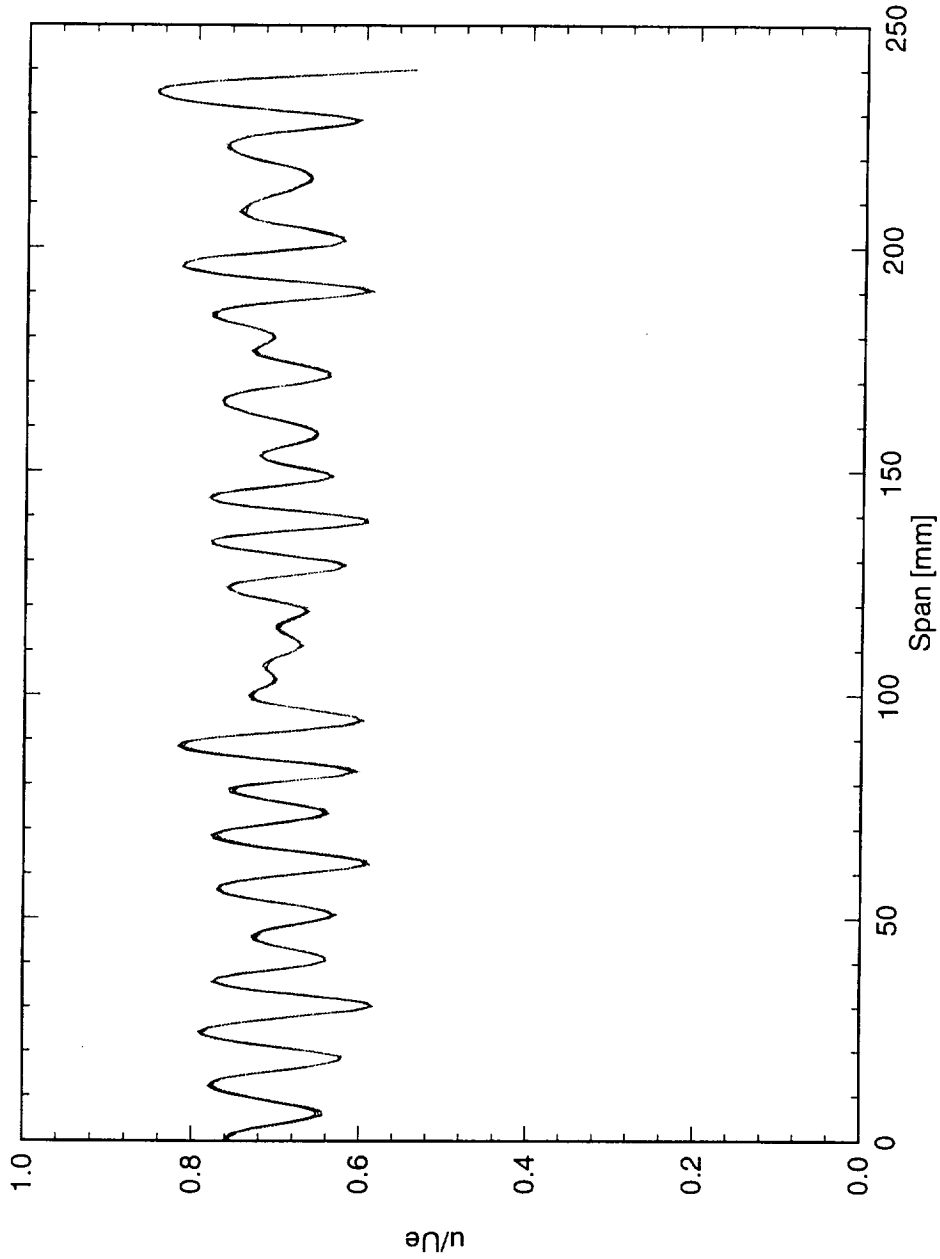

Figure 5.58: Spanwise hot-wire scan at $x/c = 0.45$ and $Y = 1.15$ mm. $Re_c = 2.4 \times 10^6$, no artificial roughness.

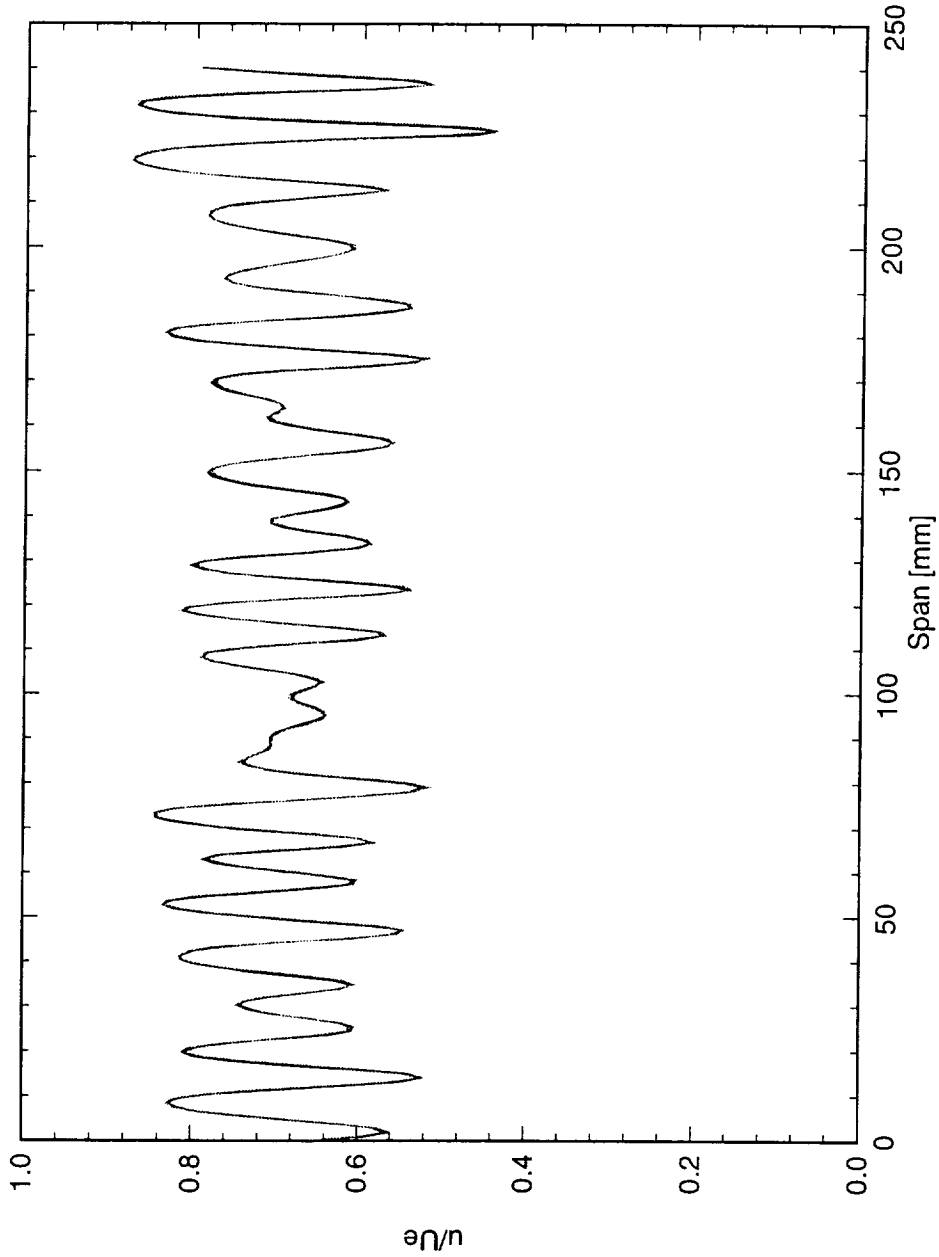

Figure 5.59: Spanwise hot-wire scan at $x/c = 0.50$ and $Y = 1.1$ mm. $Re_c = 2.4 \times 10^6$, no artificial roughness.

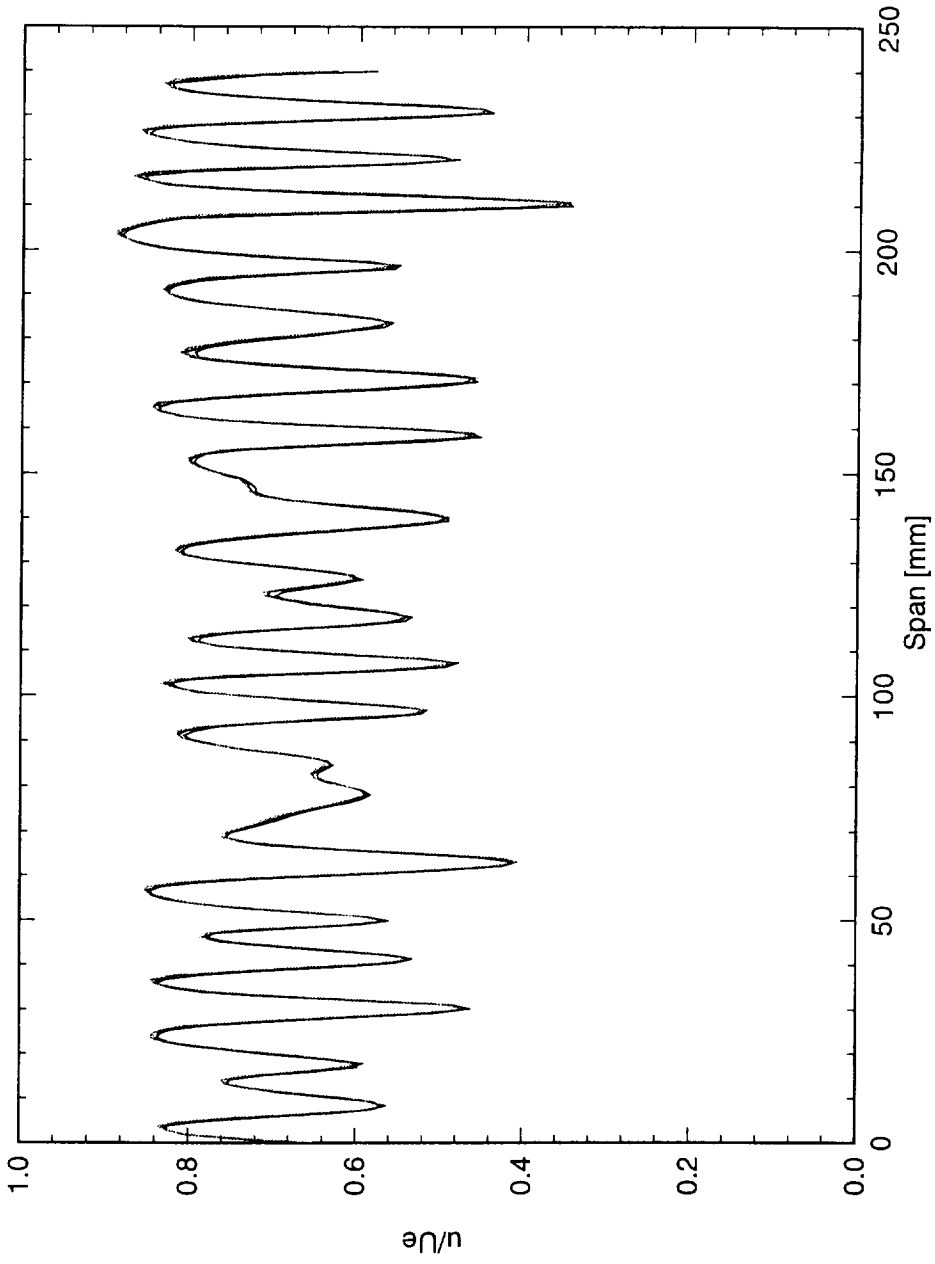

Figure 5.60: Spanwise hot-wire scan at $x/c = 0.55$ and $Y = 1.05$ mm. $Re_c = 2.4 \times 10^6$, no artificial roughness.

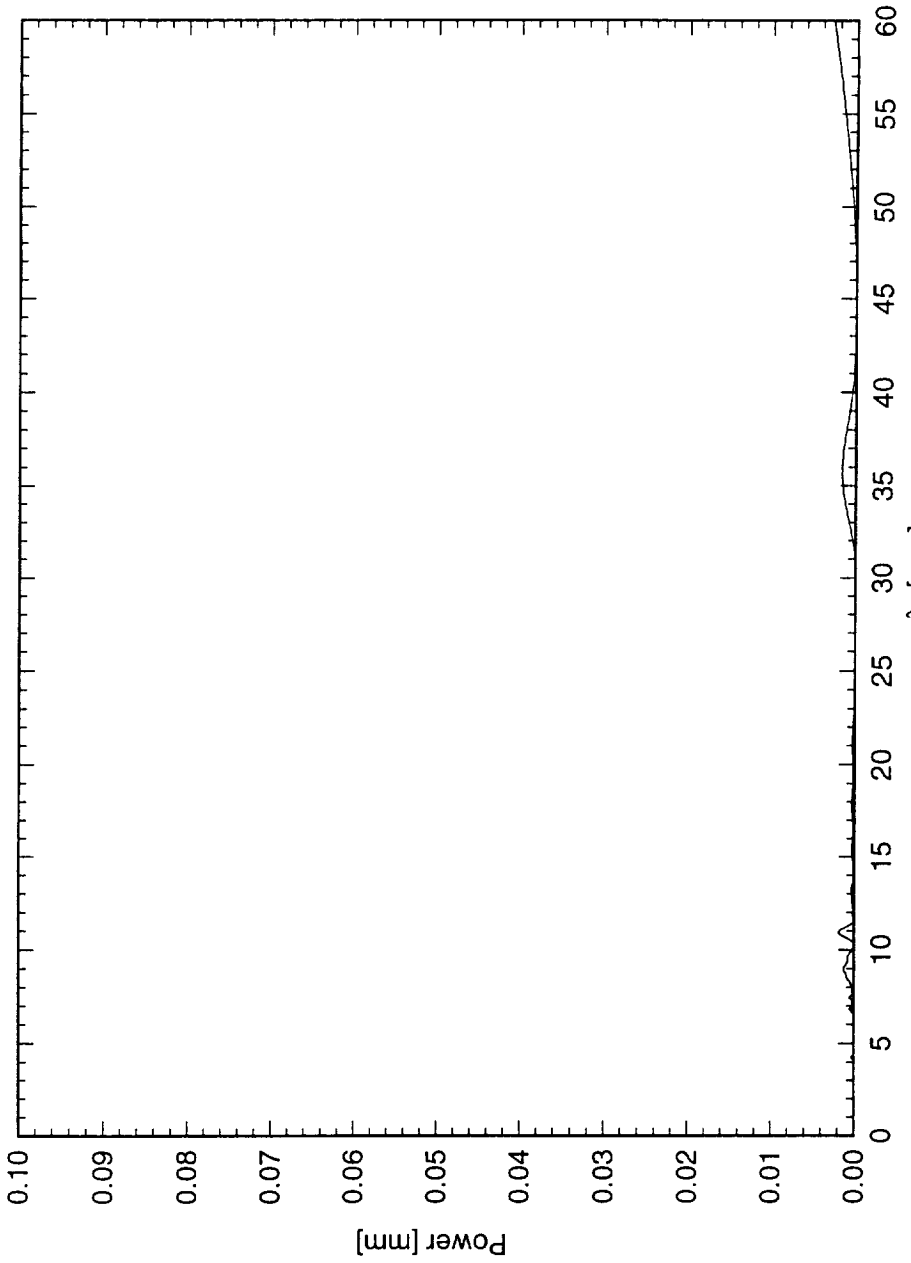

Figure 5.61: Power spectral density of constant-Y scan at $x/c = 0.25$ and $Y = 0.70$ mm. $Re_c = 2.4 \times 10^6$, no artificial roughness.

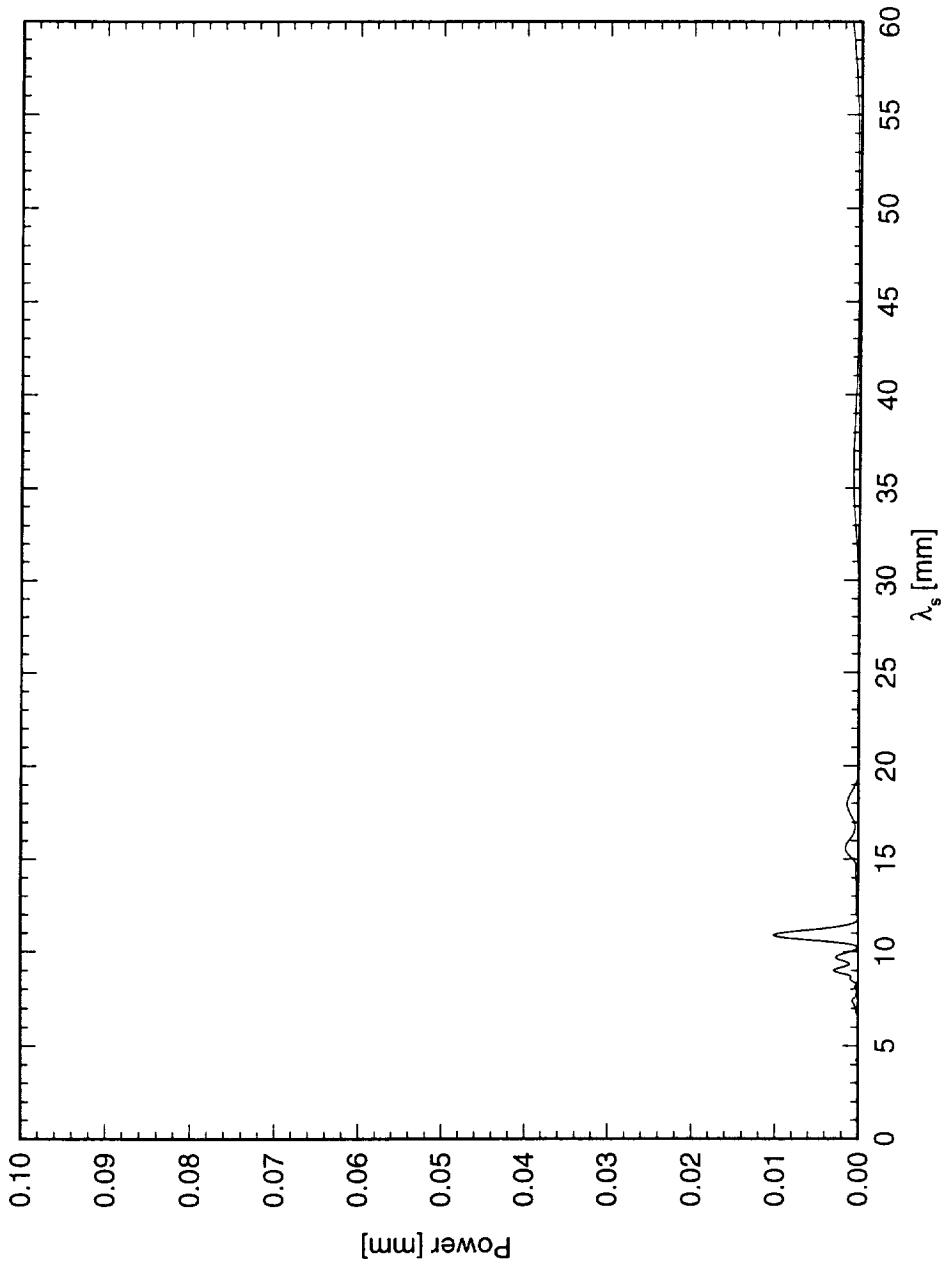

Figure 5.62: Power spectral density of constant-Y scan at $x/c = 0.30$ and $Y = 0.85$ mm. $Re_c = 2.4 \times 10^6$, no artificial roughness.

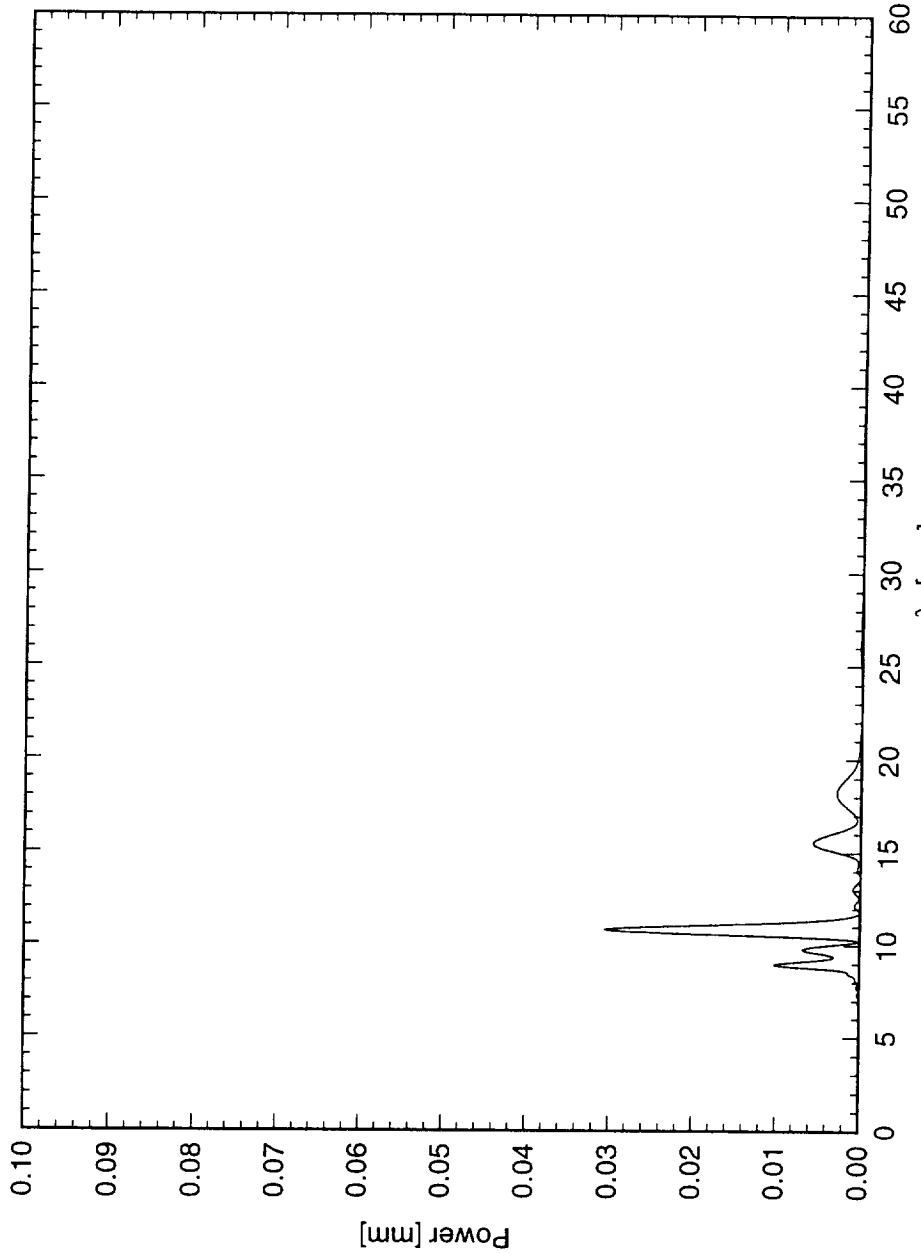

Figure 5.63: Power spectral density of constant-Y scan at $x/c = 0.35$ and $Y = 1.1$ mm. $Re_c = 2.4 \times 10^6$, no artificial roughness.

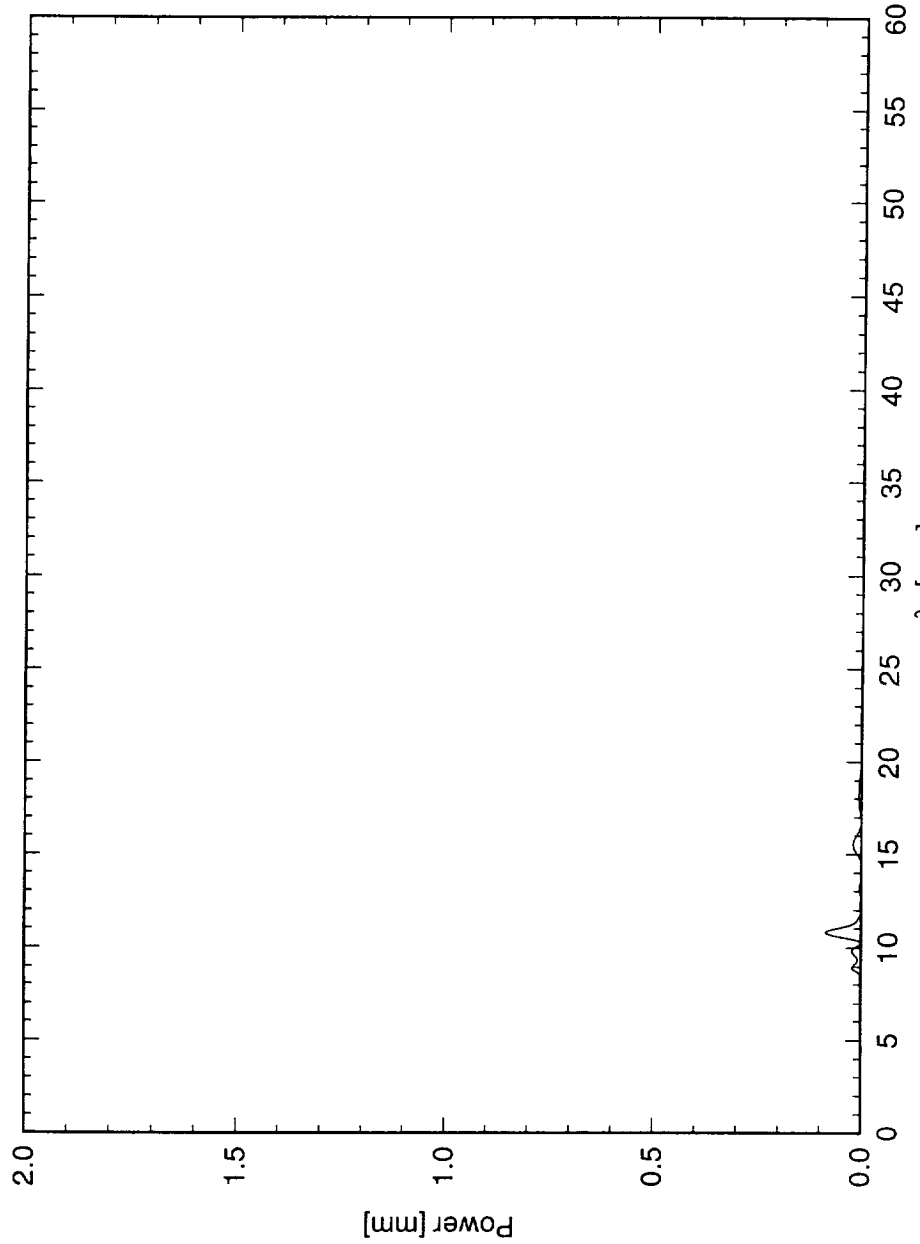

Figure 5.64: Power spectral density of constant-Y scan at $x/c = 0.40$ and $Y = 1.15$ mm. $Re_c = 2.4 \times 10^6$, no artificial roughness.

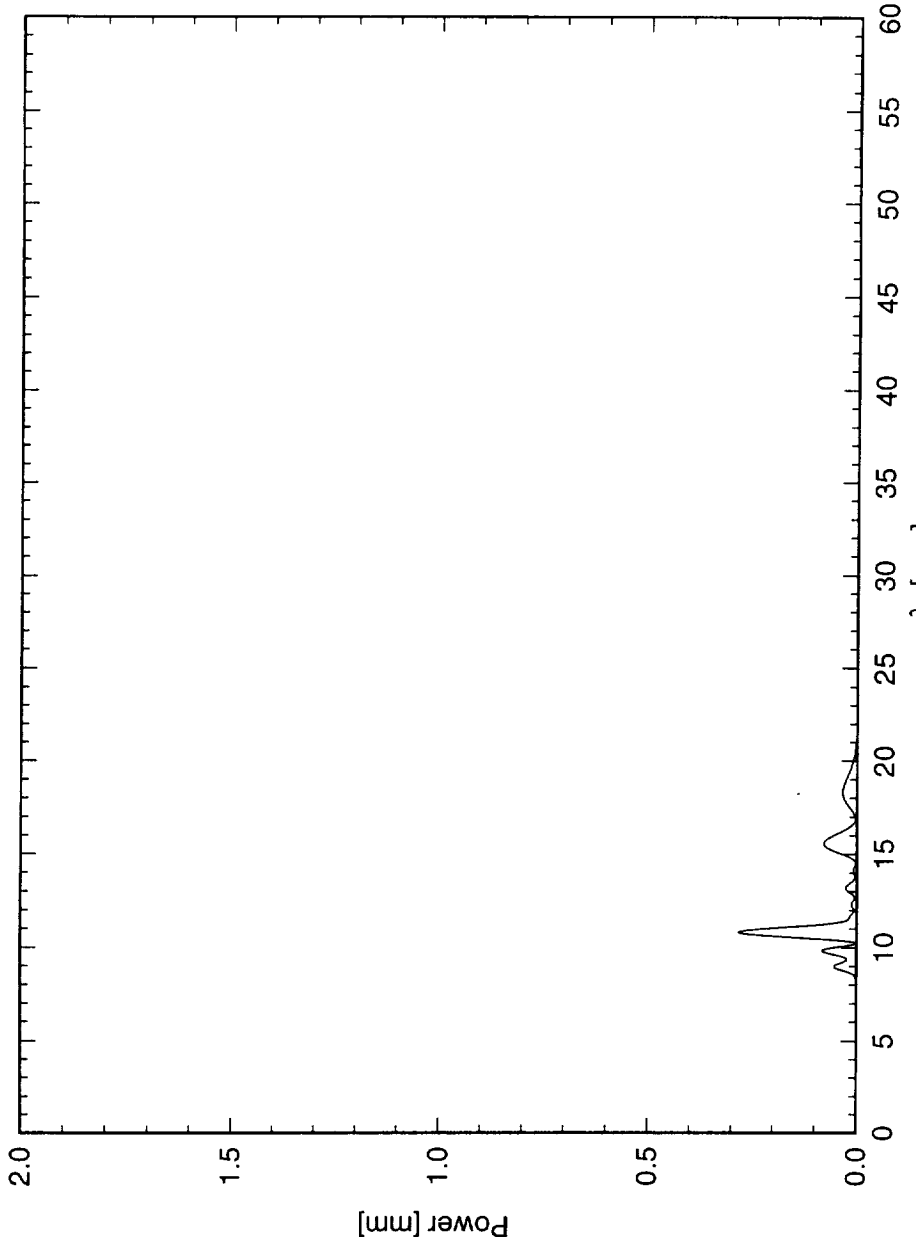

Figure 5.65: Power spectral density of constant-Y scan at $x/c = 0.45$ and $Y = 1.15$ mm. $Re_c = 2.4 \times 10^6$, no artificial roughness.

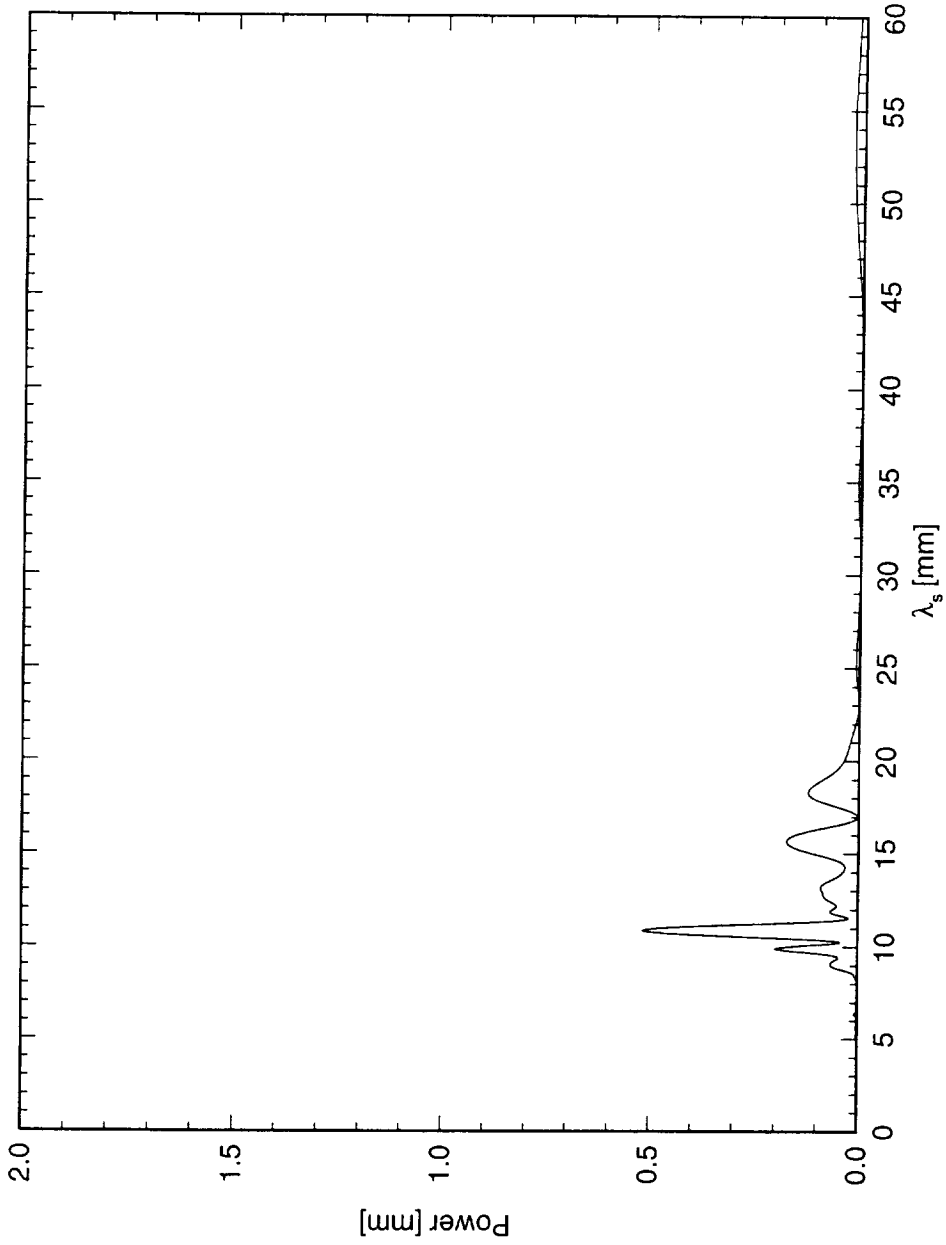

Figure 5.66: Power spectral density of constant-Y scan at $x/c = 0.50$ and $Y = 1.1$ mm. $Re_c = 2.4 \times 10^6$, no artificial roughness.

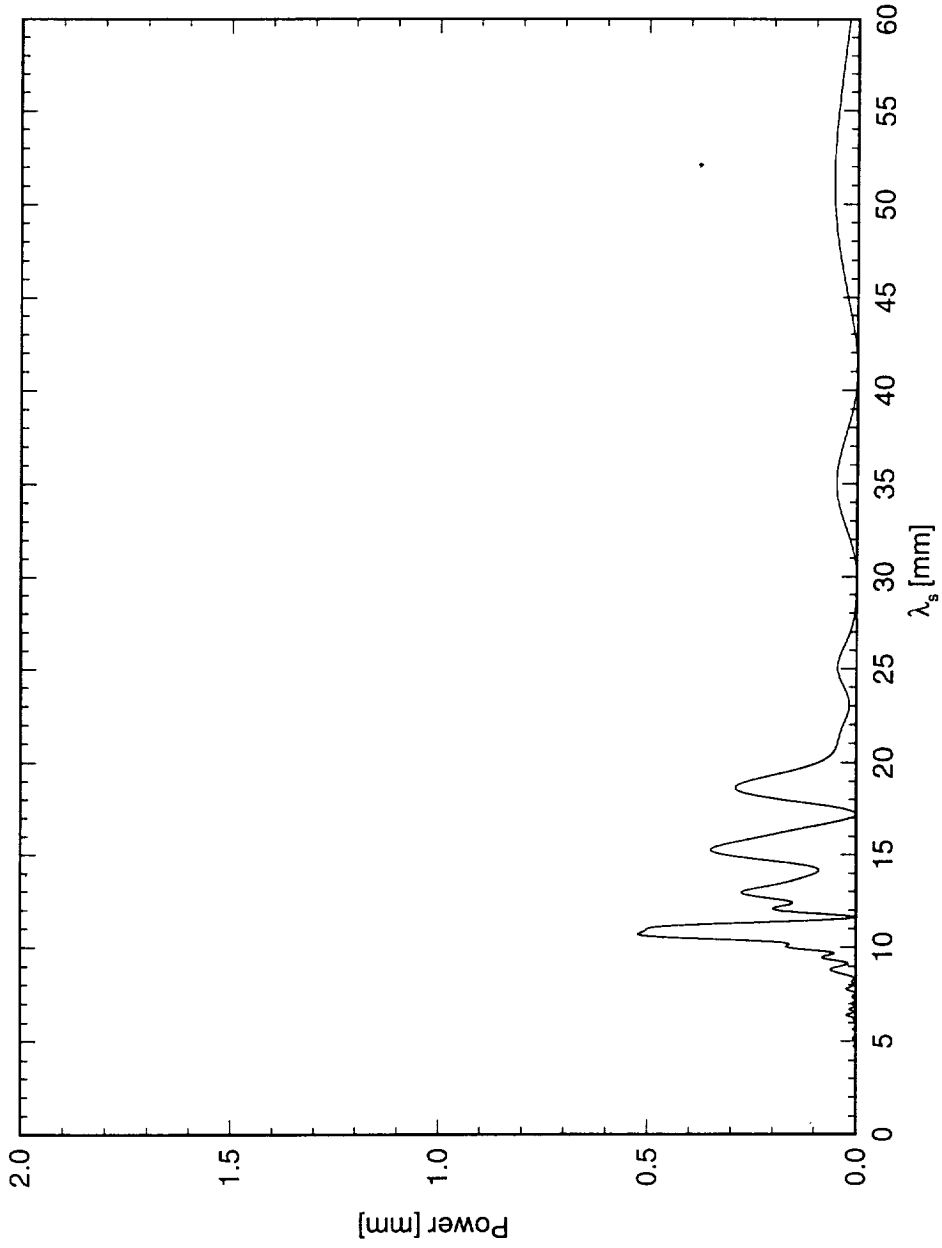

Figure 5.67: Power spectral density of constant-Y scan at $x/c = 0.55$ and $Y = 1.05$ mm. $Re_c = 2.4 \times 10^6$, no artificial roughness.

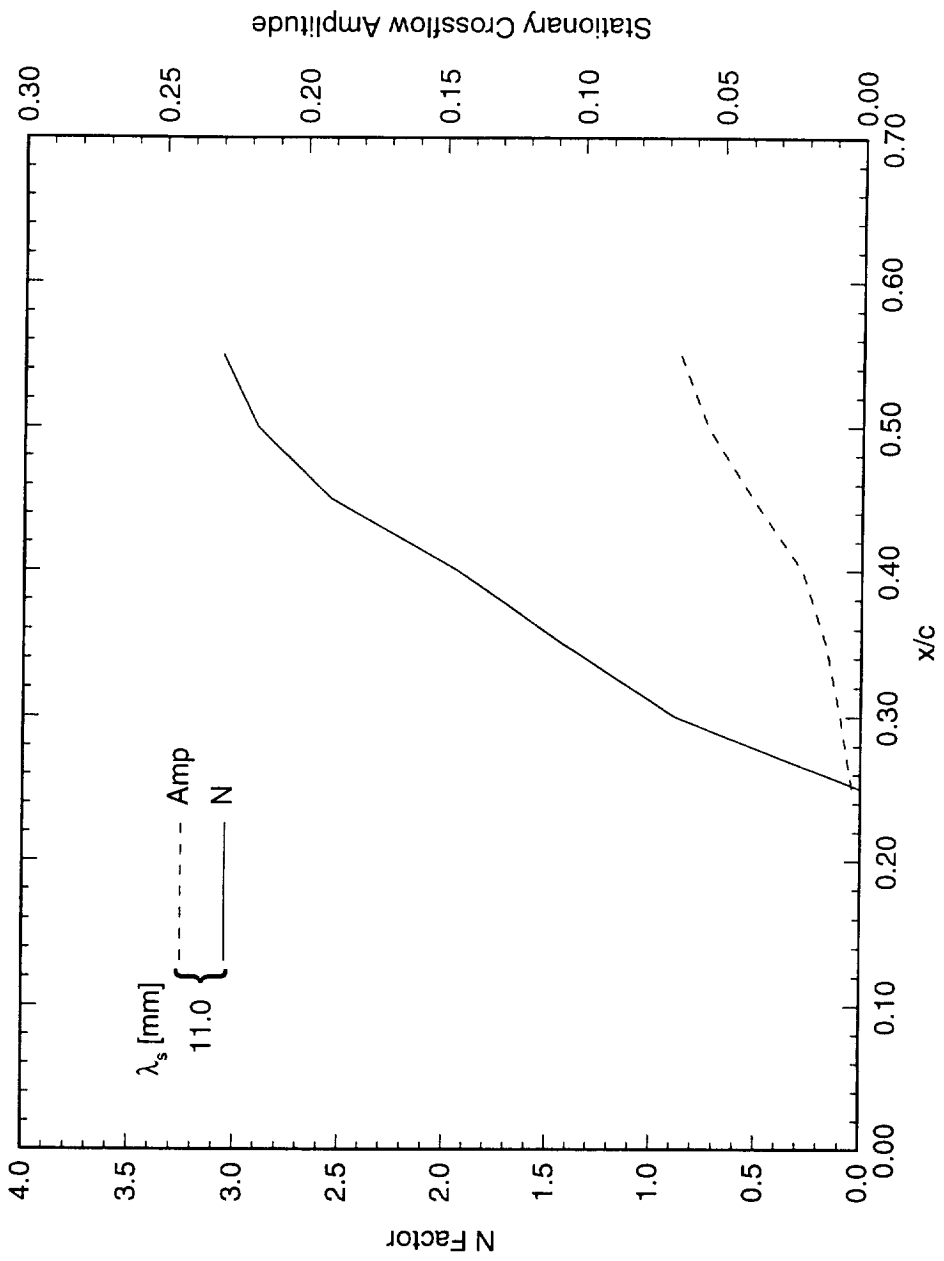

Figure 5.68: Single-mode disturbance amplitude and N-factors. $Re_c = 2.4 \times 10^6$, no artificial roughness. N-factor calculations are relative to $x/c = 0.25$.

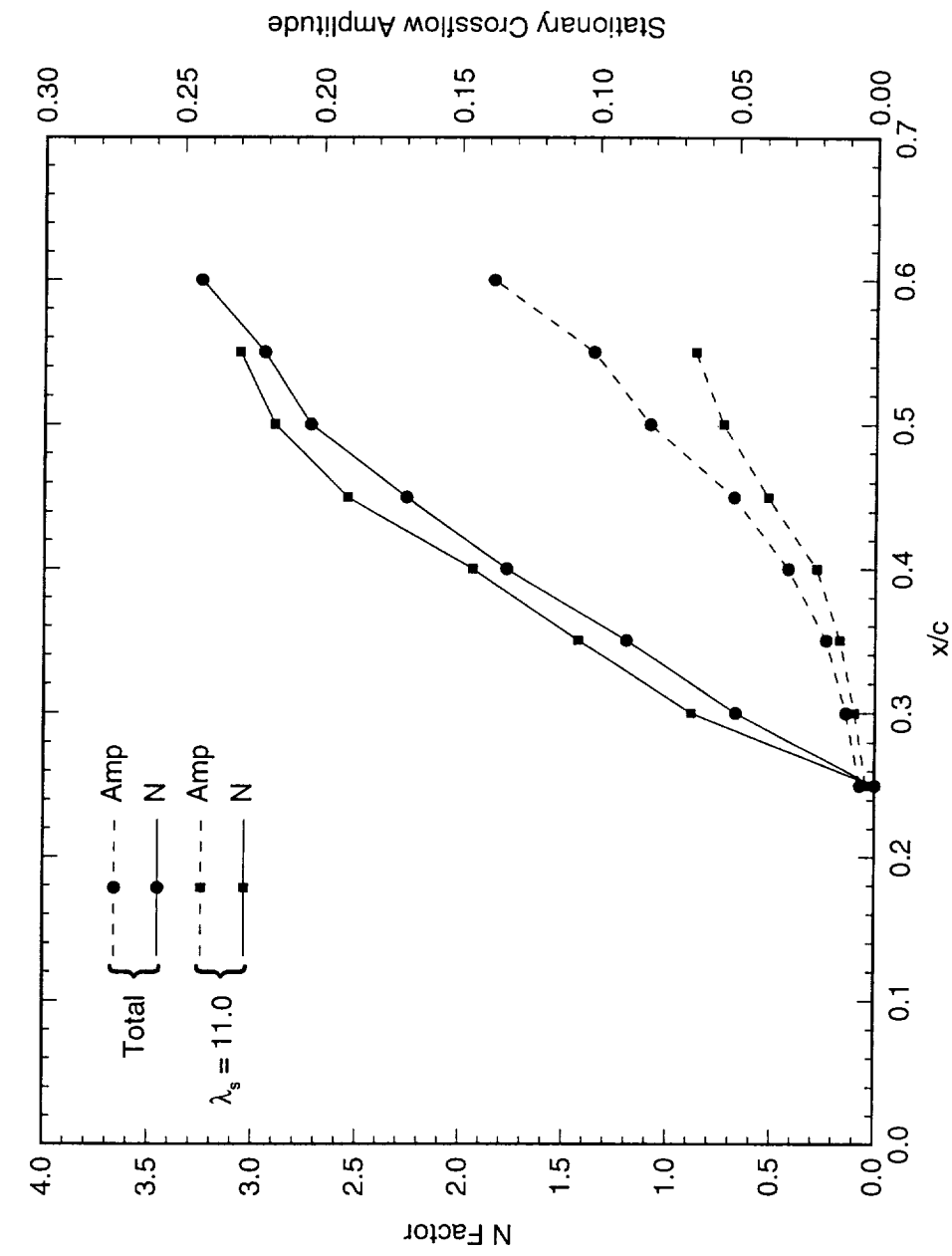

Figure 5.69: Total and single-mode disturbance amplitude and N-factors. $Re_c = 2.4 \times 10^6$, no artificial roughness. N-factor calculations are relative to $x/c = 0.25$.

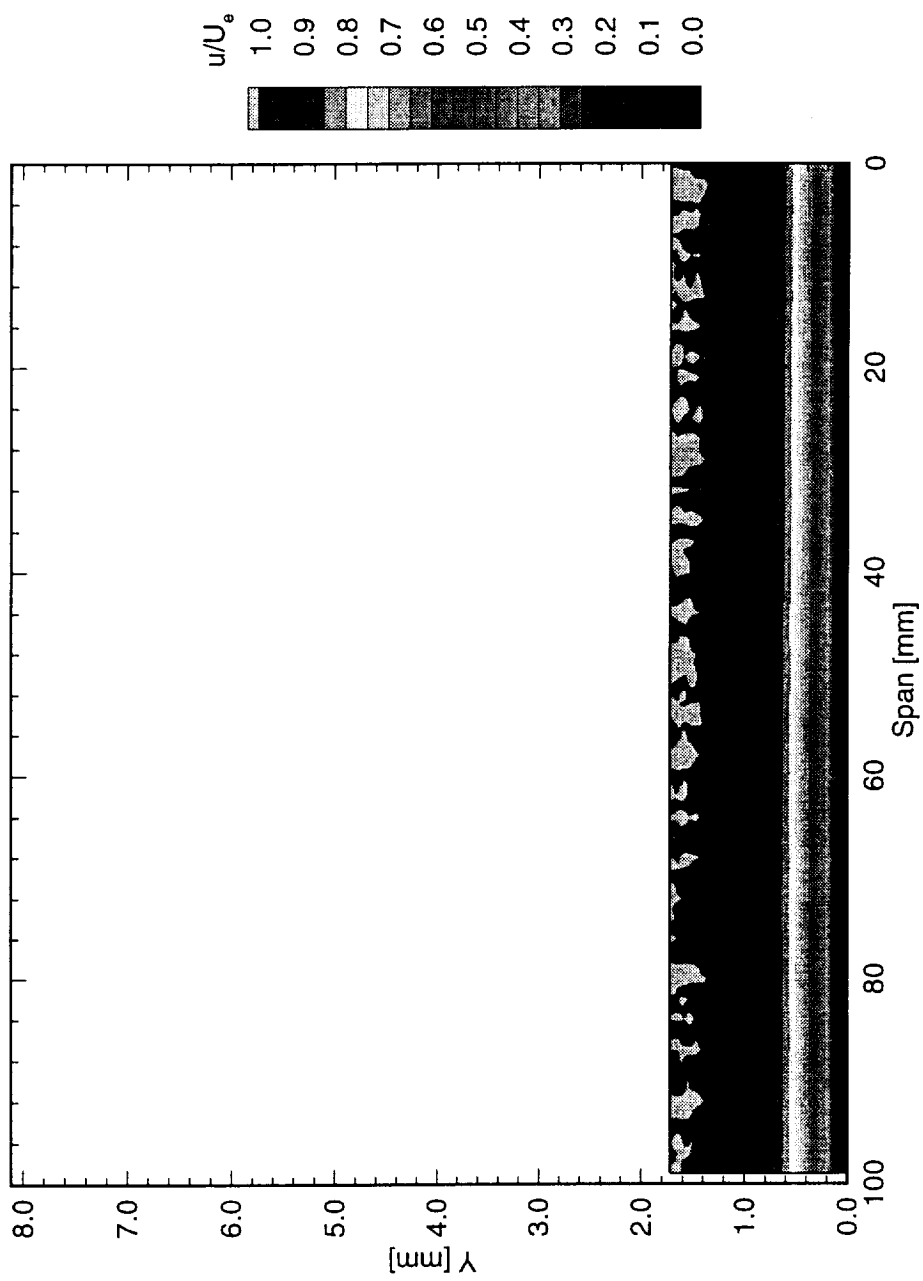

Figure 5.70: Normalized boundary-layer velocity contours at $x/c = 0.05$. $Re_c = 2.4 \times 10^6$, [6|18] roughness.

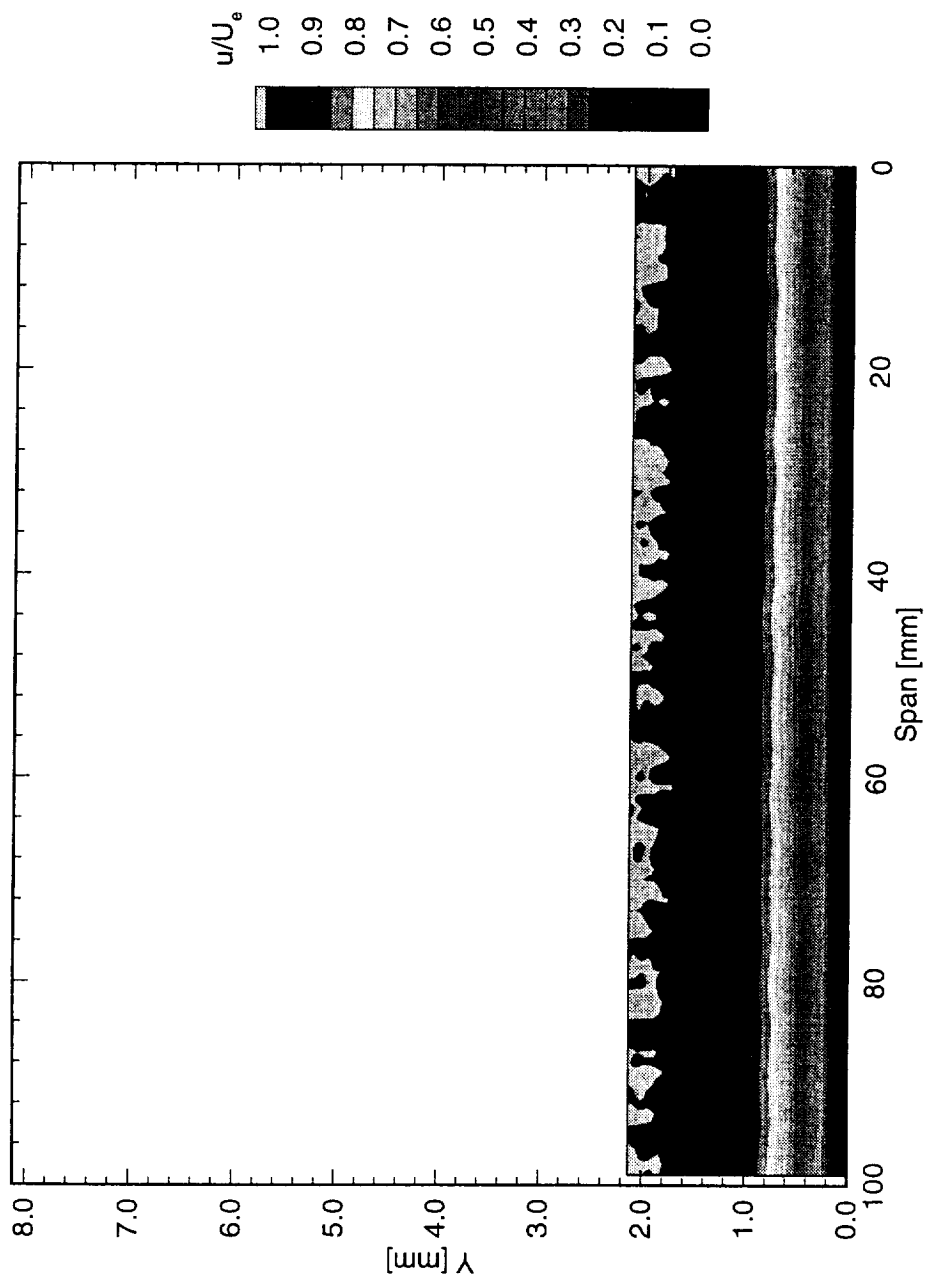

Figure 5.71: Normalized boundary-layer velocity contours at $x/c = 0.10$. $Re_c = 2.4 \times 10^6$, [6|18] roughness.

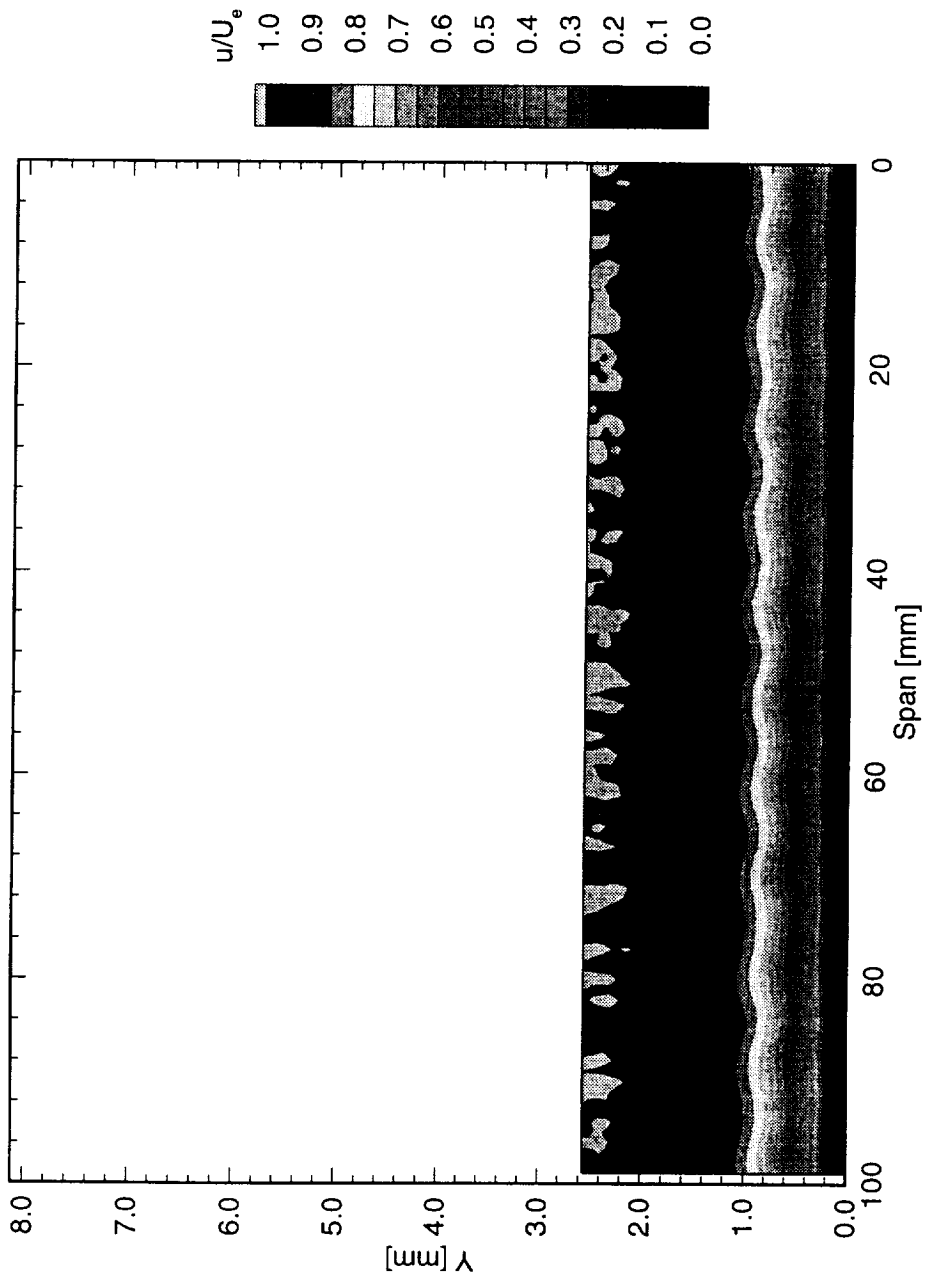

Figure 5.72: Normalized boundary-layer velocity contours at $x/c = 0.15$. $Re_c = 2.4 \times 10^6$, [6|18] roughness.

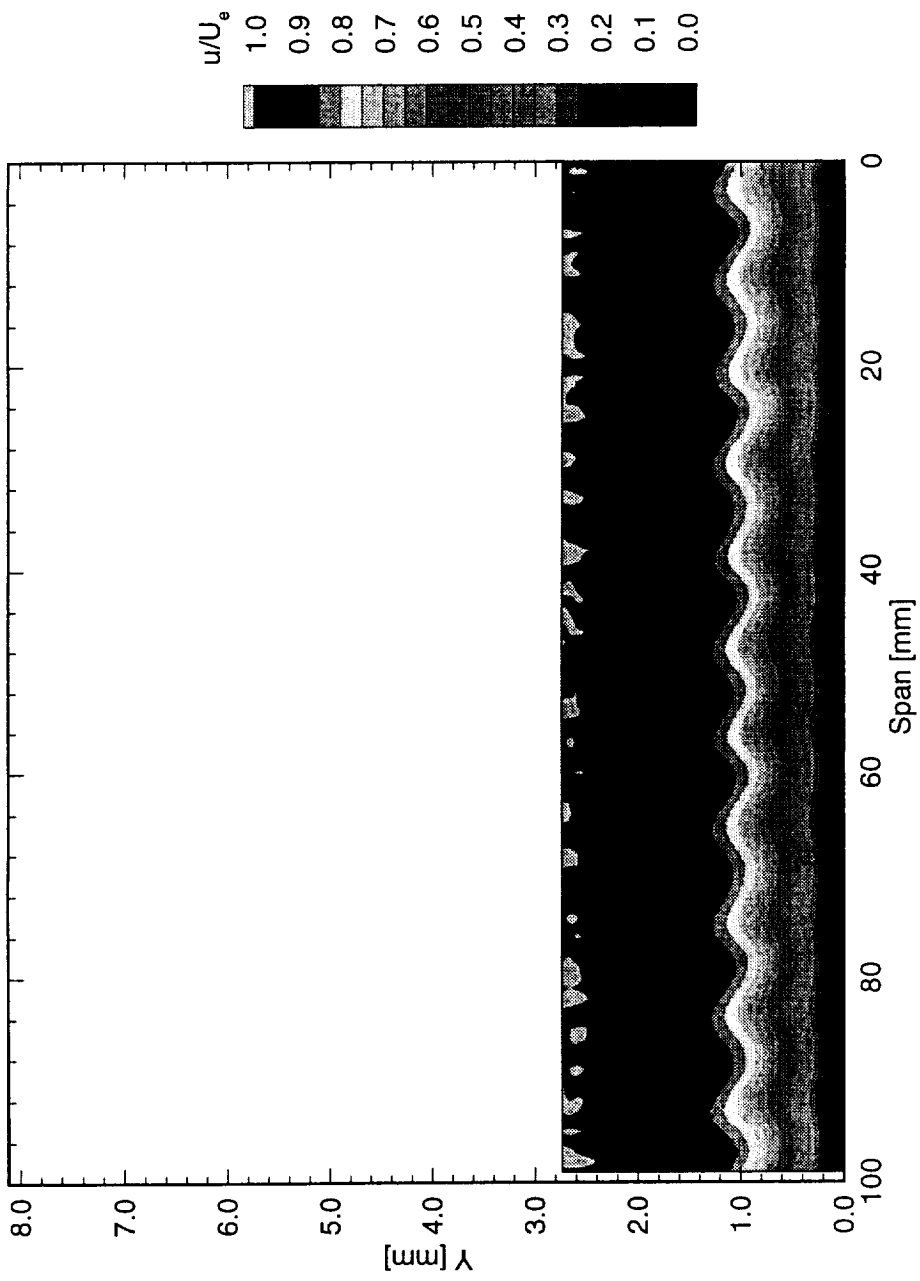

Figure 5.73: Normalized boundary-layer velocity contours at $x/c = 0.20$. $Re_c = 2.4 \times 10^6$, [6|18] roughness.

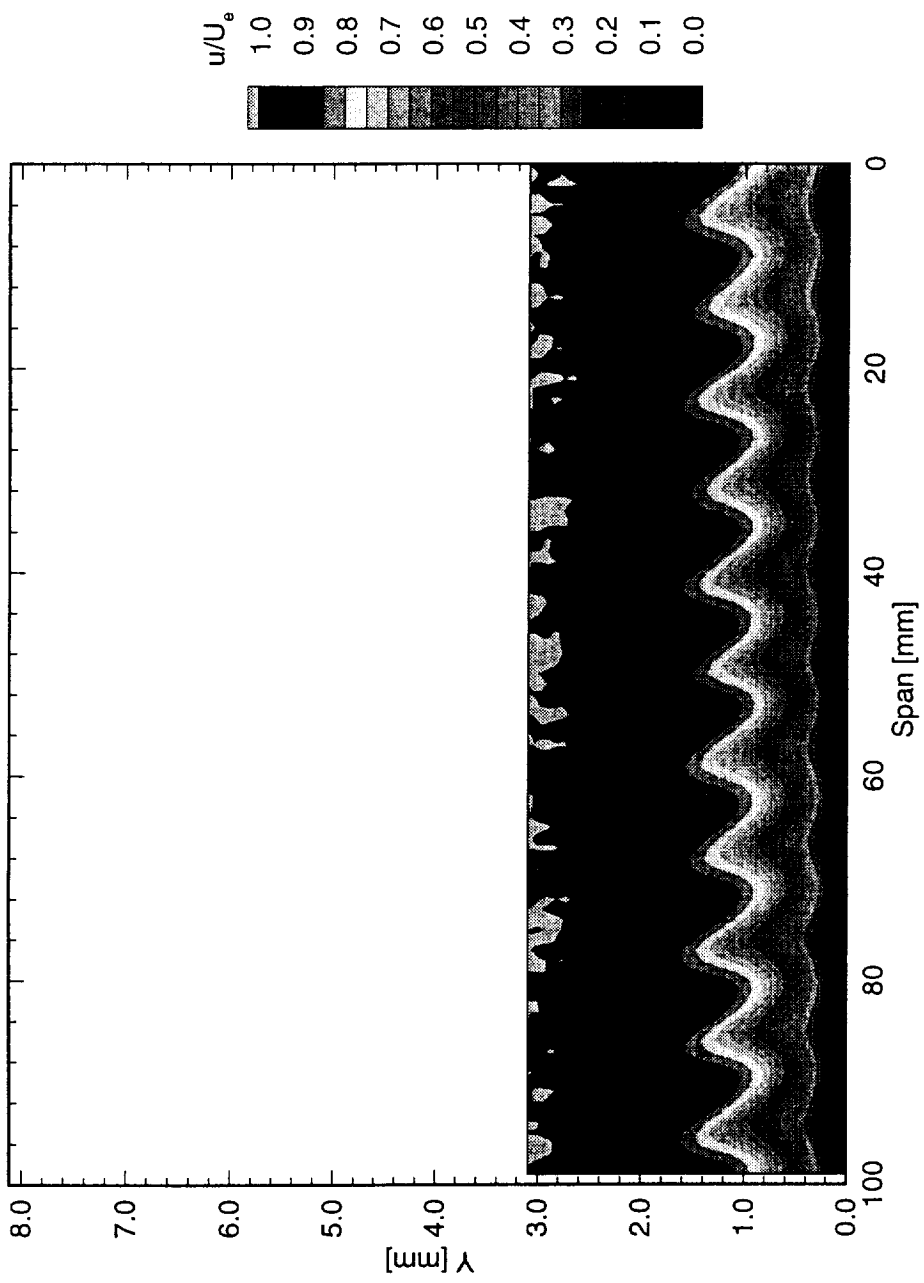

Figure 5.74: Normalized boundary-layer velocity contours at $x/c = 0.25$. $Re_c = 2.4 \times 10^6$, [6|18] roughness.

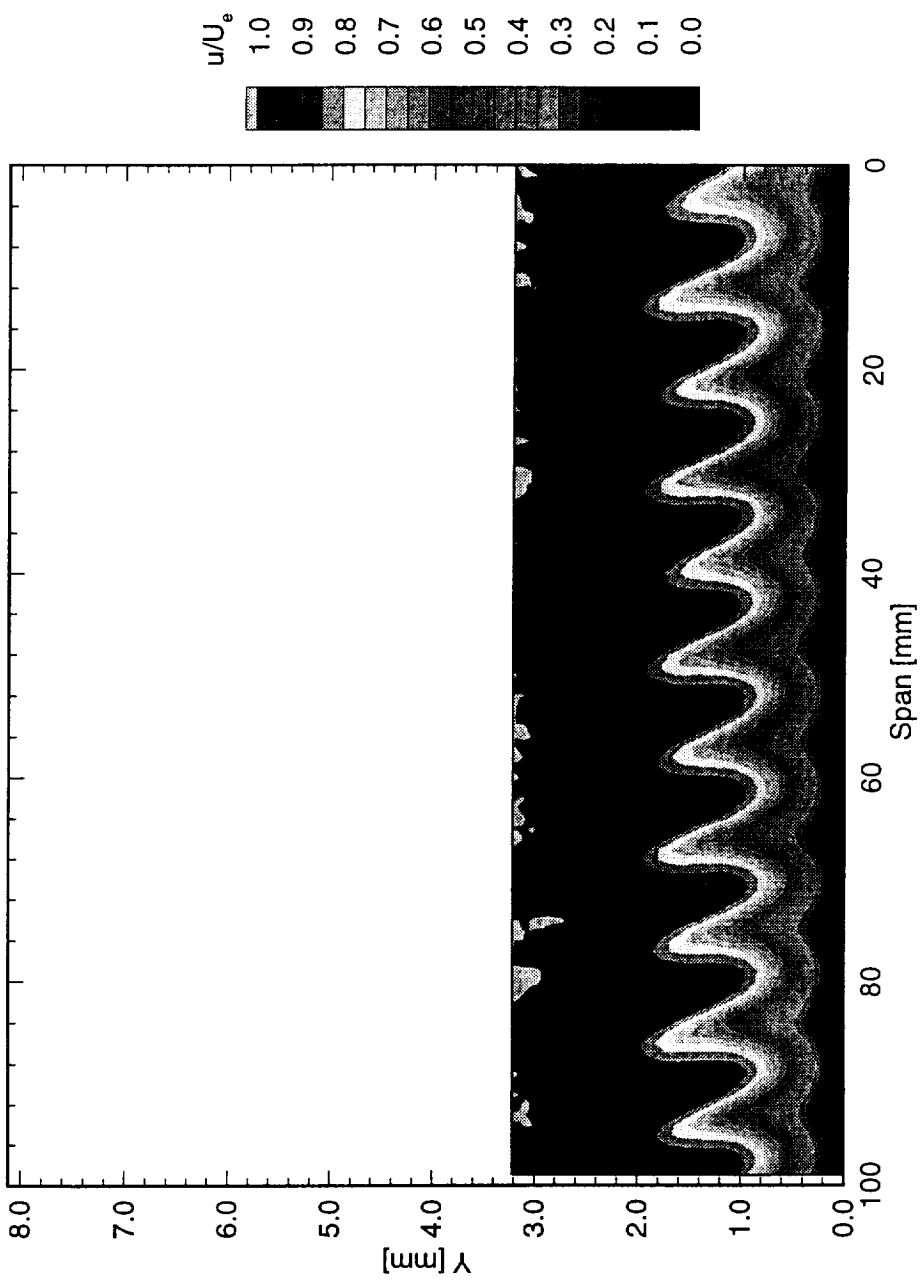

Figure 5.75: Normalized boundary-layer velocity contours at $x/c = 0.30$. $Re_c = 2.4 \times 10^6$, [6|18] roughness.

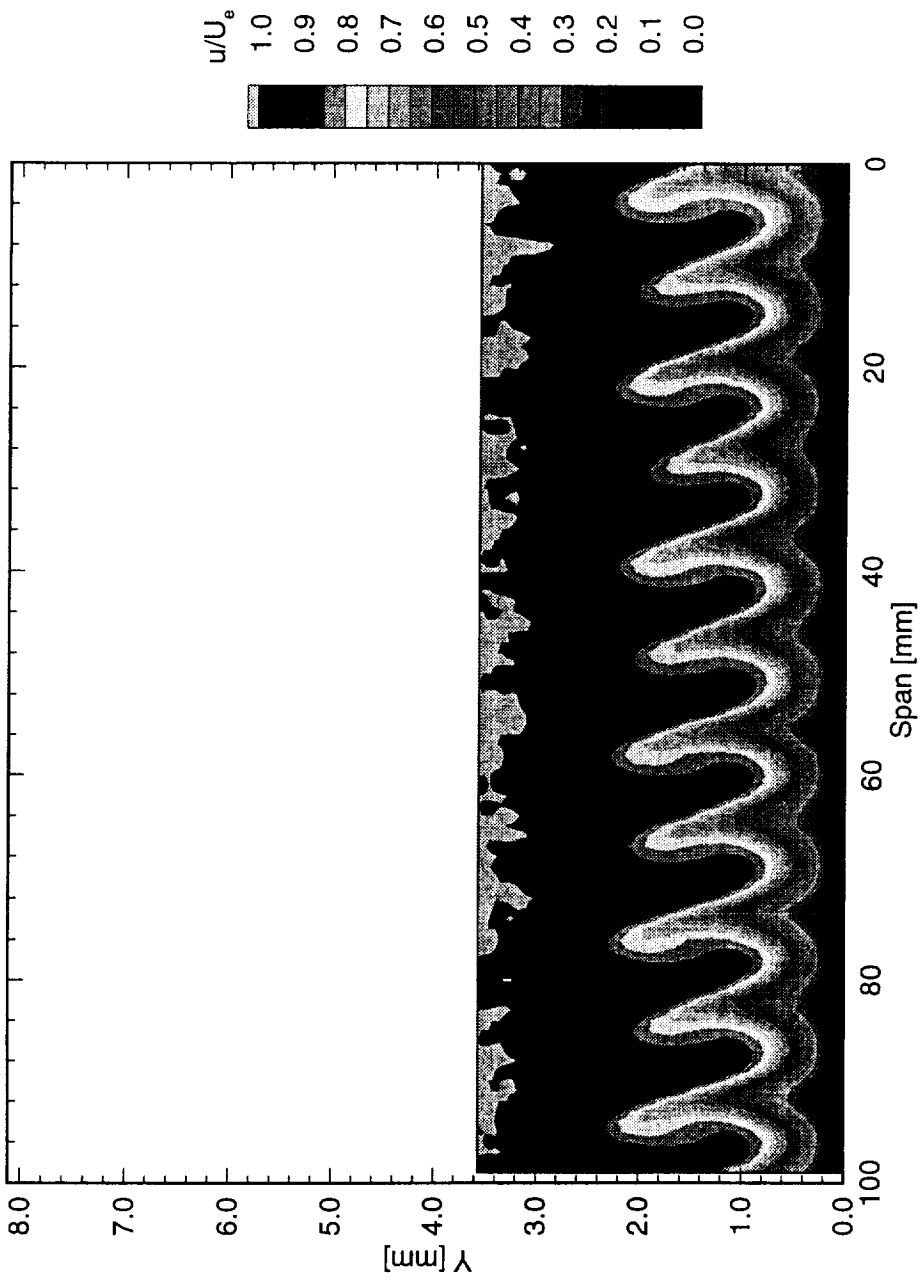

Figure 5.76: Normalized boundary-layer velocity contours at $x/c = 0.35$. $Re_c = 2.4 \times 10^6$, [6|18] roughness.

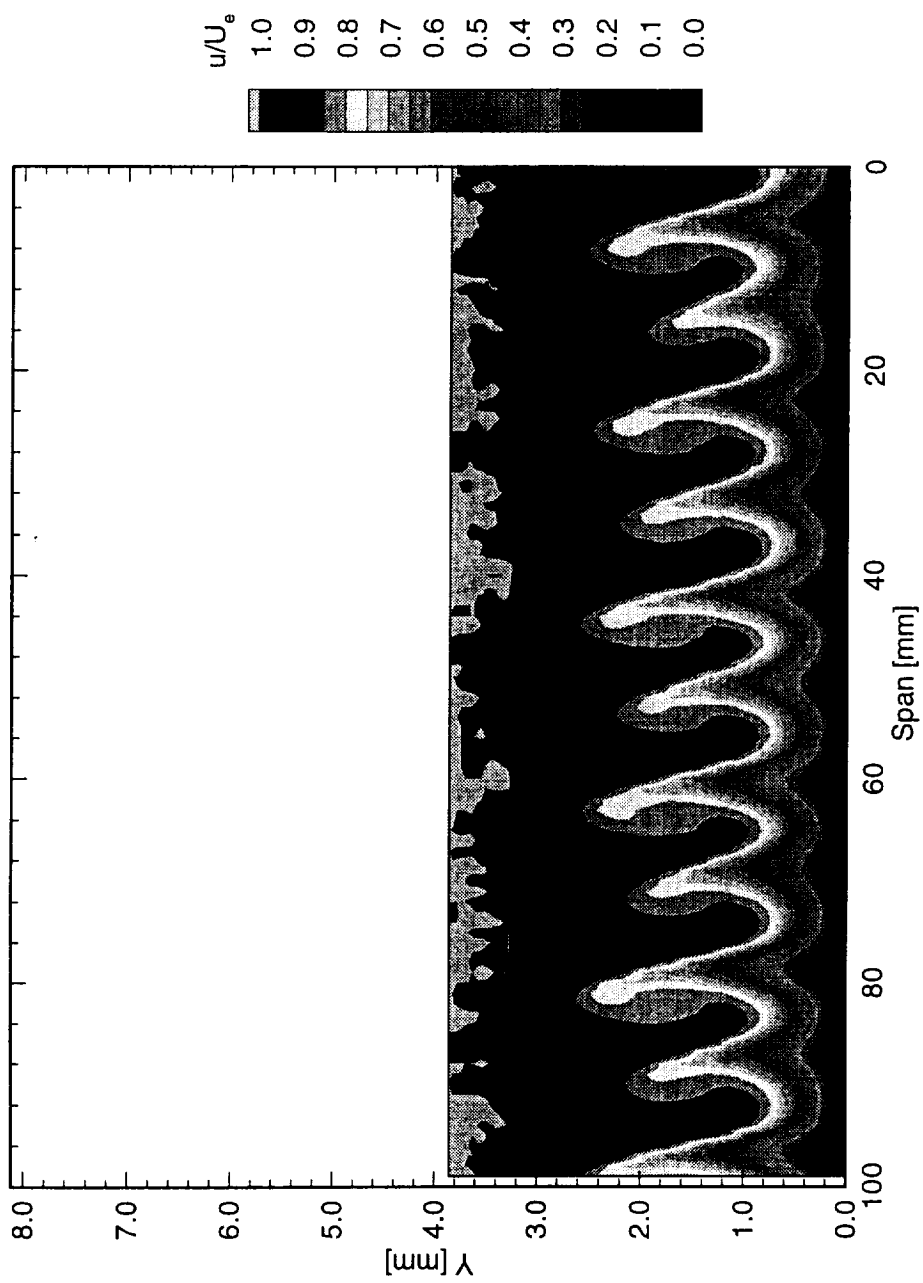

Figure 5.77: Normalized boundary-layer velocity contours at $x/c = 0.40$. $Re_c = 2.4 \times 10^6$, [6|18] roughness.

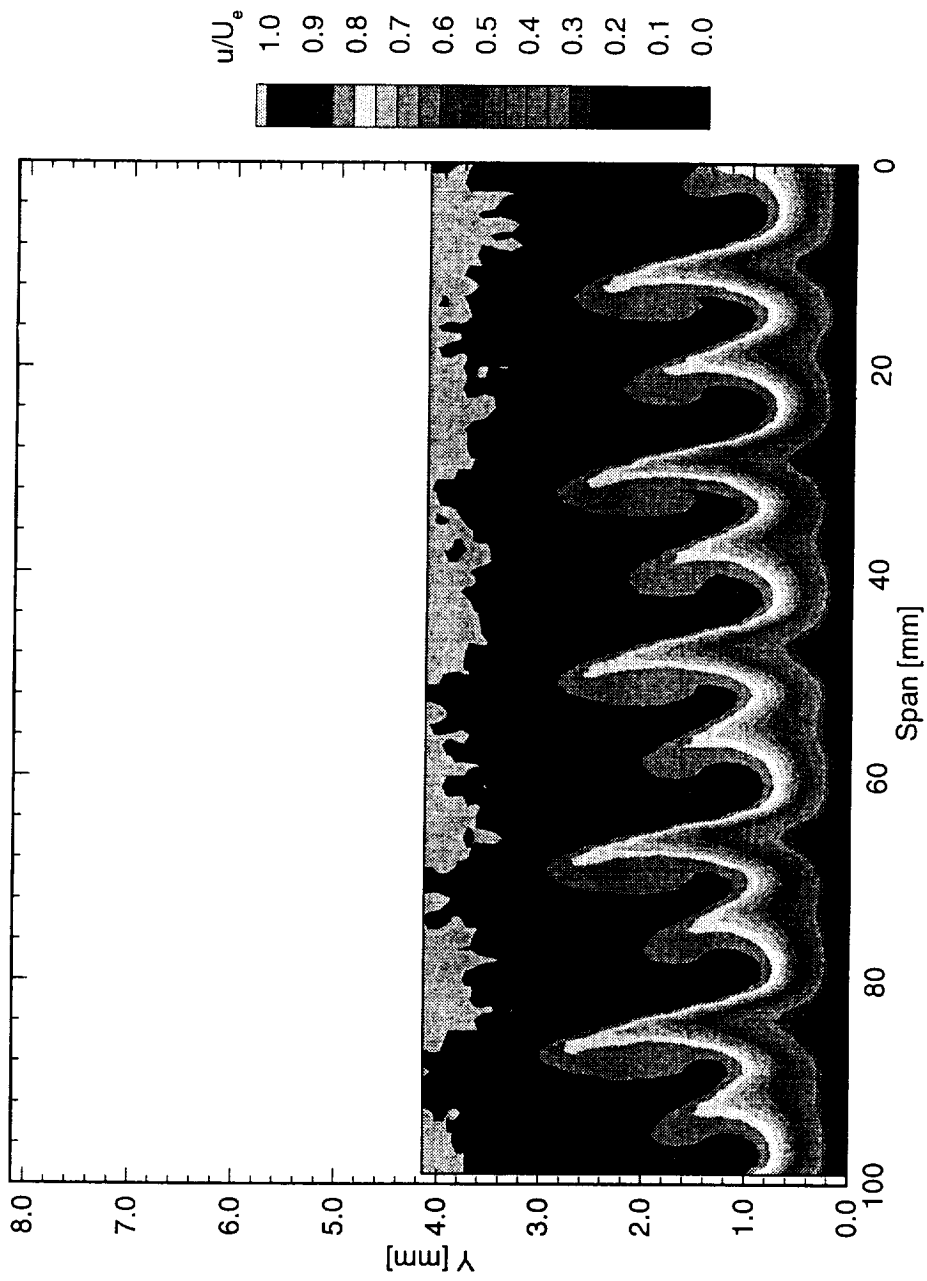

Figure 5.78: Normalized boundary-layer velocity contours at $x/c = 0.45$. $Re_c = 2.4 \times 10^6$, [6|18] roughness.

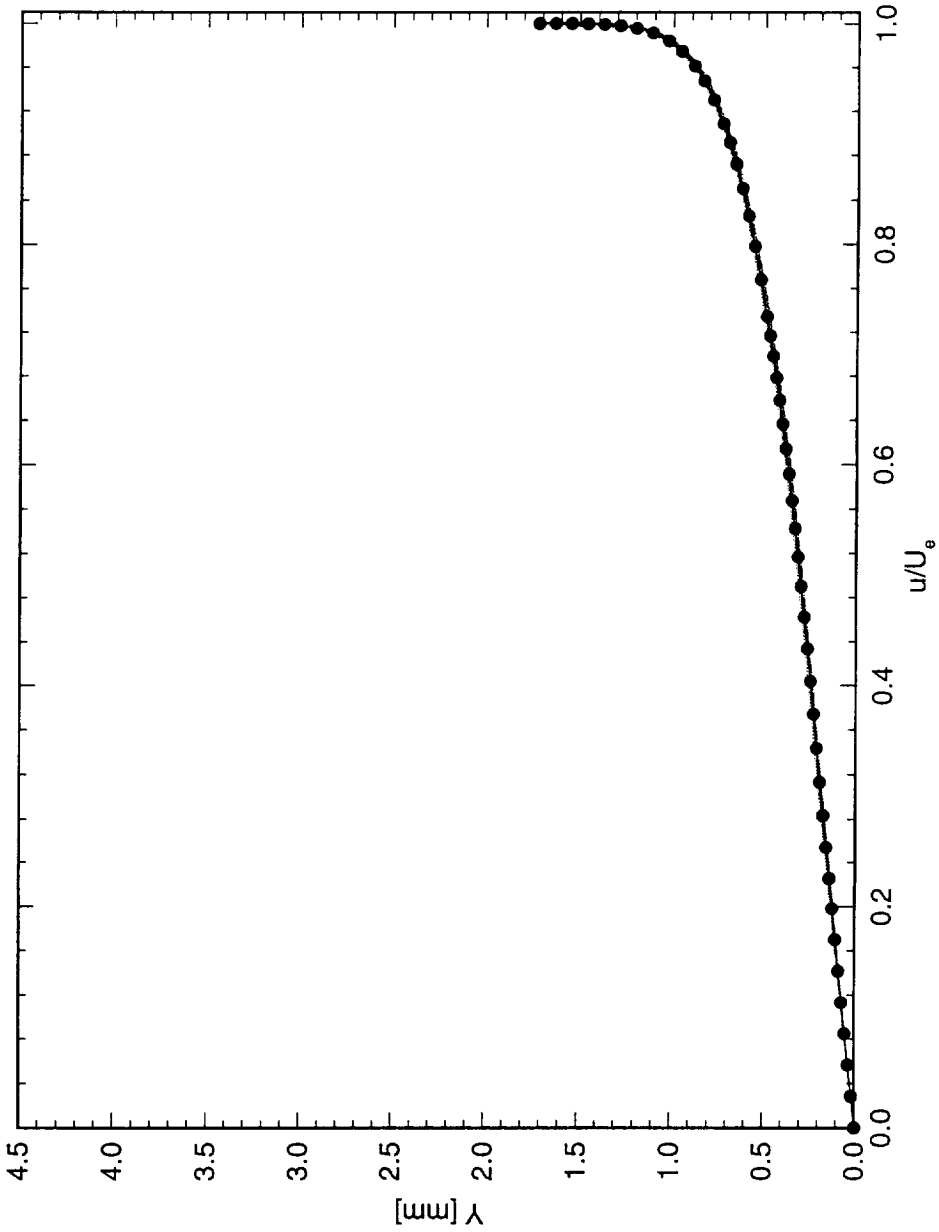

Figure 5.79: Spanwise array of 100 boundary-layer profiles spaced 1 mm apart in span at $x/c = 0.05$. $Re_c = 2.4 \times 10^6$, [6|18] roughness. The dots represent the spanwise average of the profiles.

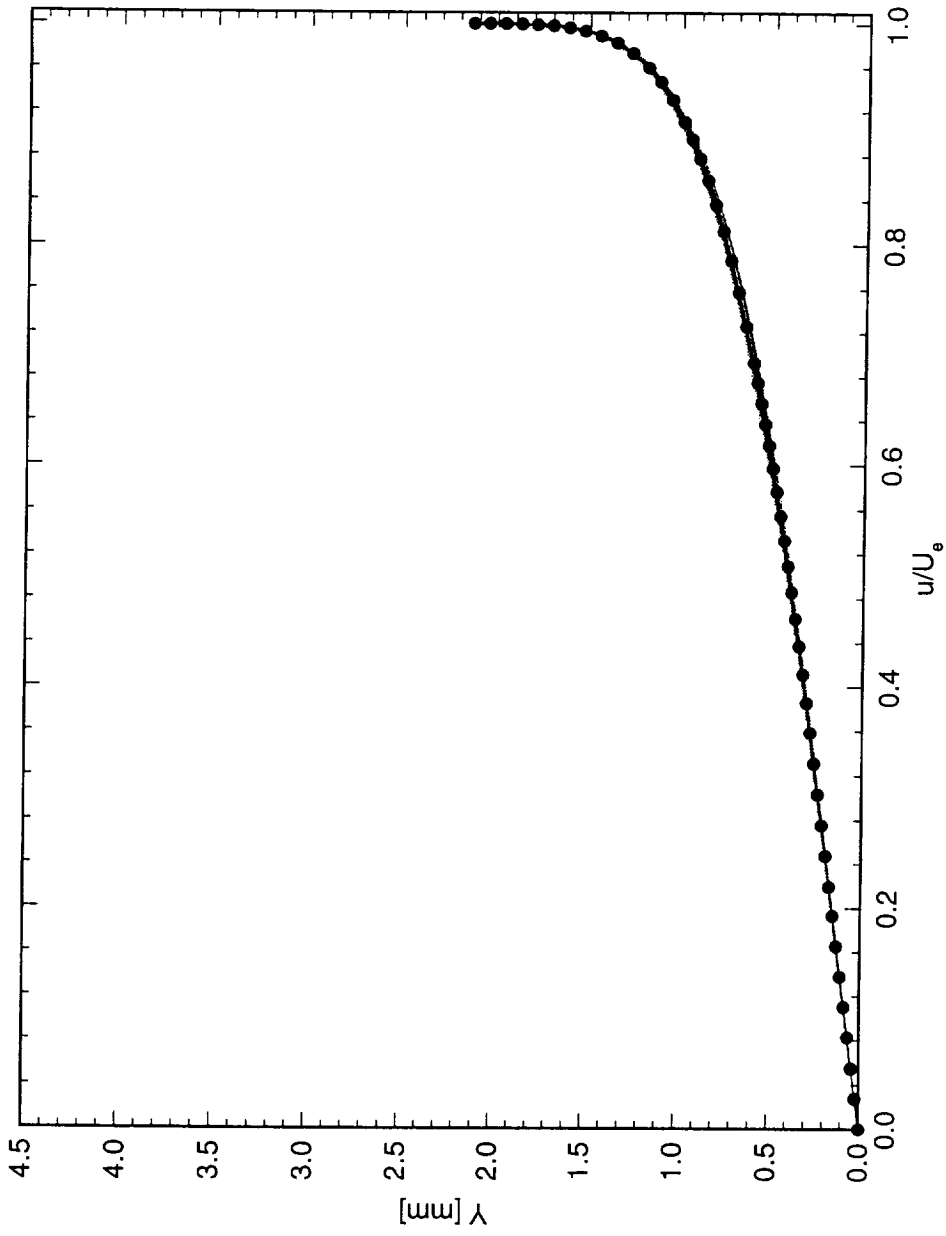

Figure 5.80: Spanwise array of 100 boundary-layer profiles spaced 1 mm apart in span at $x/c = 0.10$. $Re_c = 2.4 \times 10^6$, [6|18] roughness. The dots represent the spanwise average of the profiles.

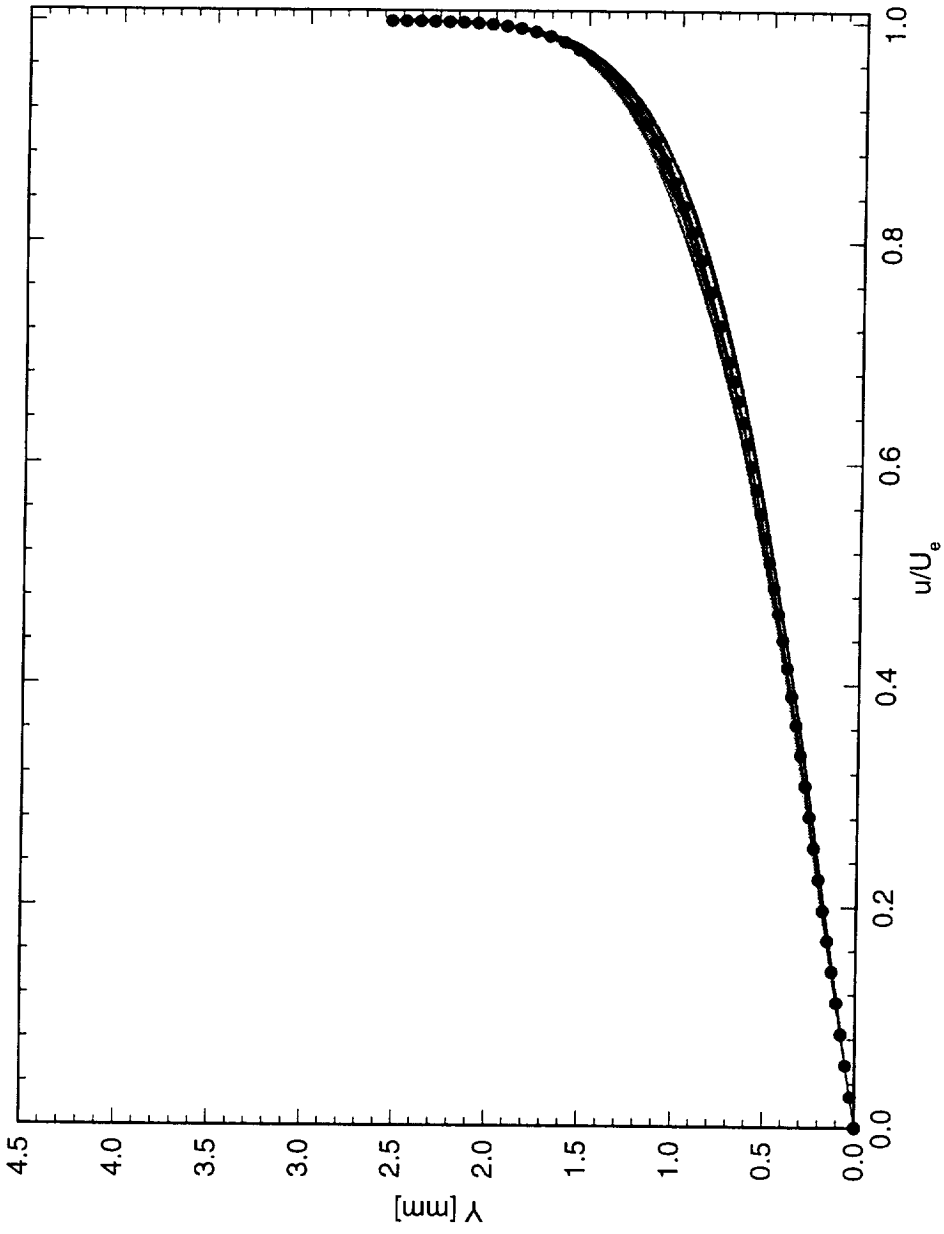

Figure 5.81: Spanwise array of 100 boundary-layer profiles spaced 1 mm apart in span at $x/c = 0.15$. $Re_c = 2.4 \times 10^6$, [6|18] roughness. The dots represent the spanwise average of the profiles.

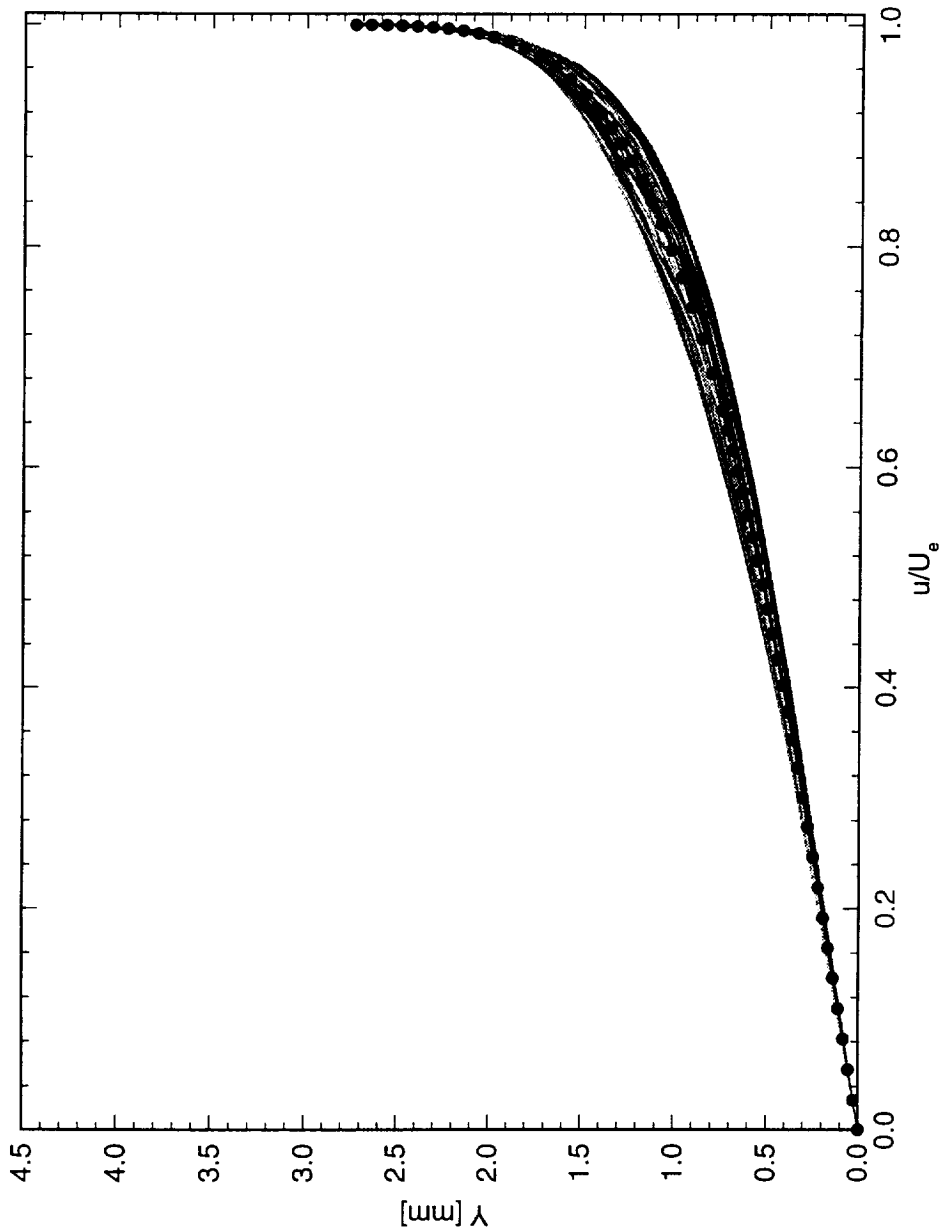

Figure 5.82: Spanwise array of 100 boundary-layer profiles spaced 1 mm apart in span at $x/c = 0.20$. $Re_c = 2.4 \times 10^6$, [6|18] roughness. The dots represent the spanwise average of the profiles.

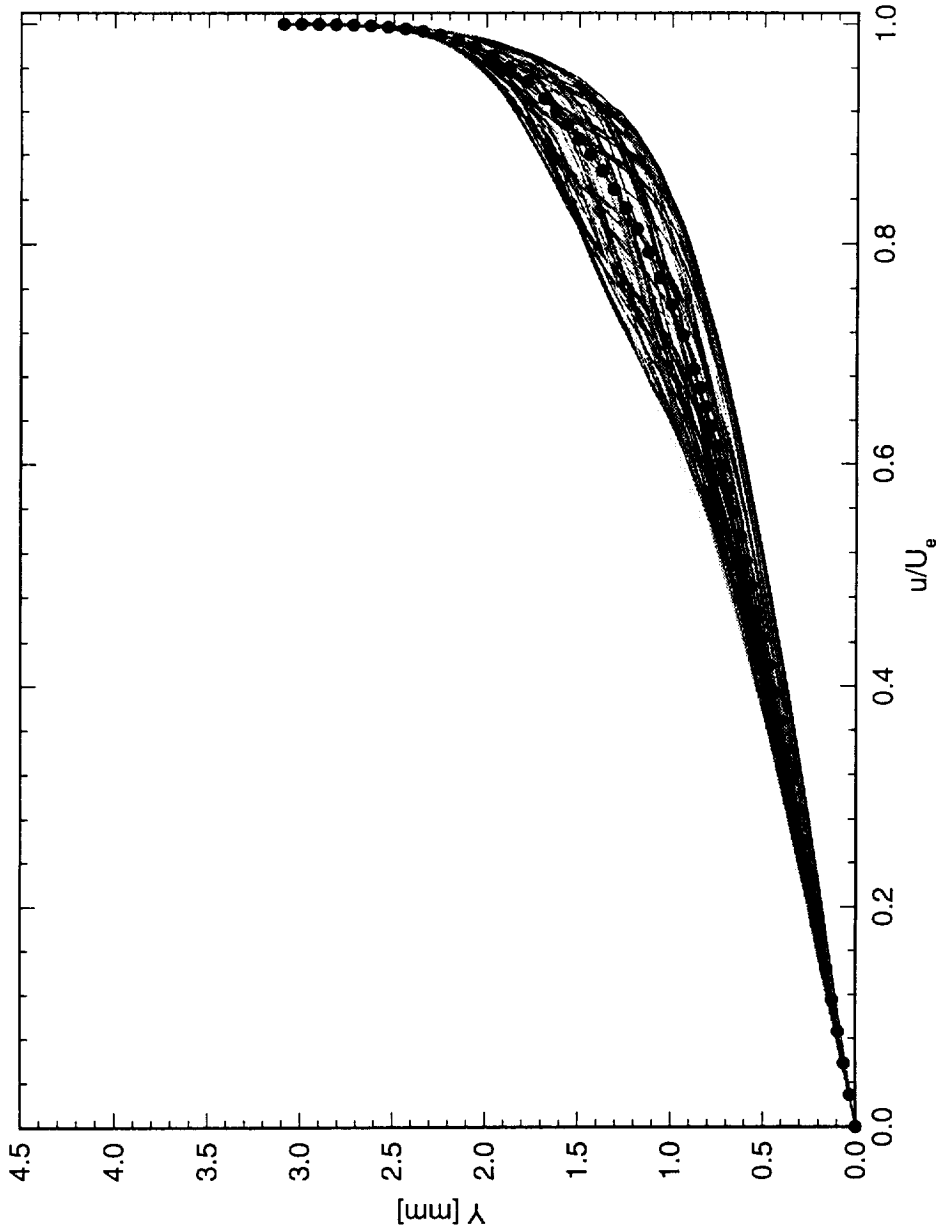

Figure 5.83: Spanwise array of 100 boundary-layer profiles spaced 1 mm apart in span at $x/c = 0.25$. $Re_c = 2.4 \times 10^6$, [6|18] roughness. The dots represent the spanwise average of the profiles.

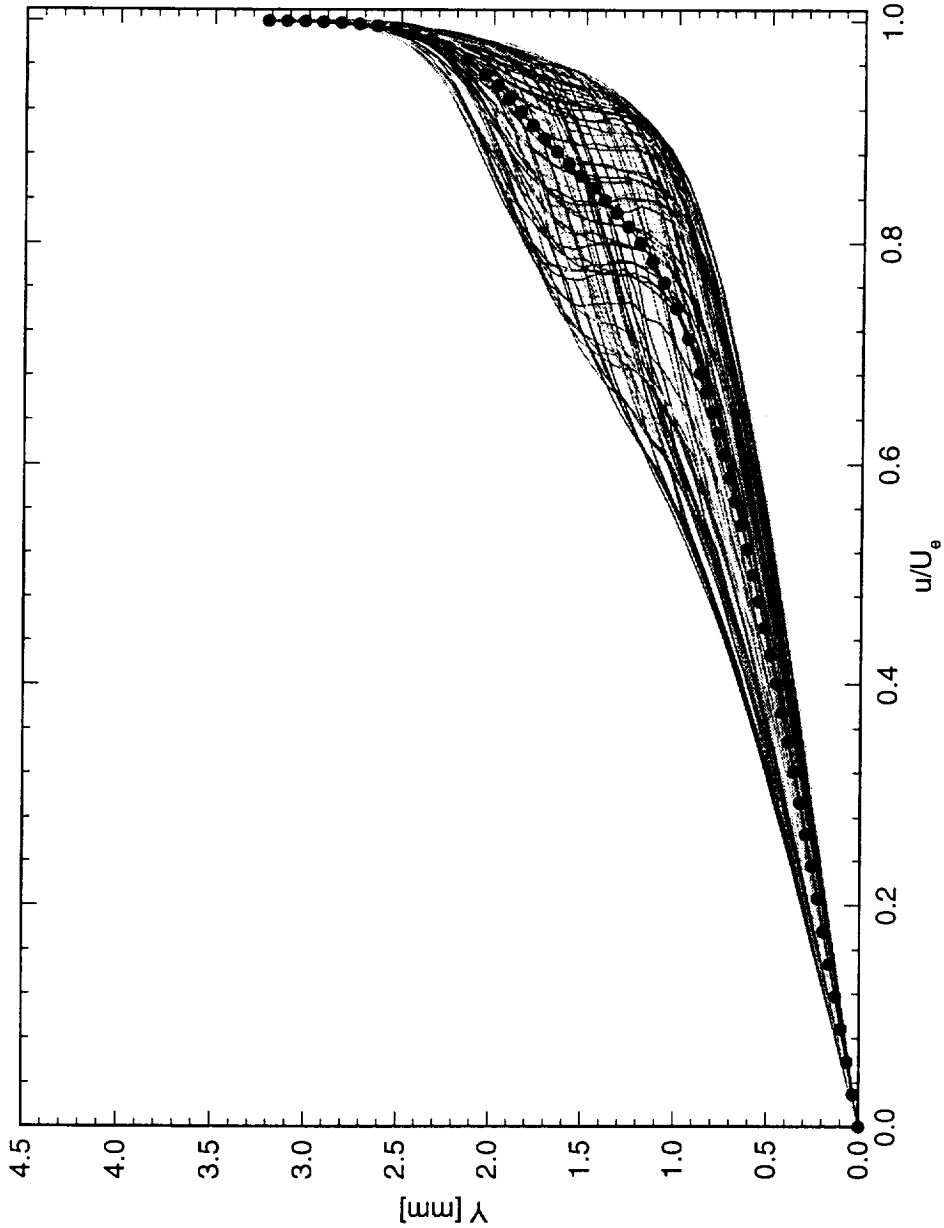

Figure 5.84: Spanwise array of 100 boundary-layer profiles spaced 1 mm apart in span at $x/c = 0.30$. $Re_c = 2.4 \times 10^6$, [6|18] roughness. The dots represent the spanwise average of the profiles.

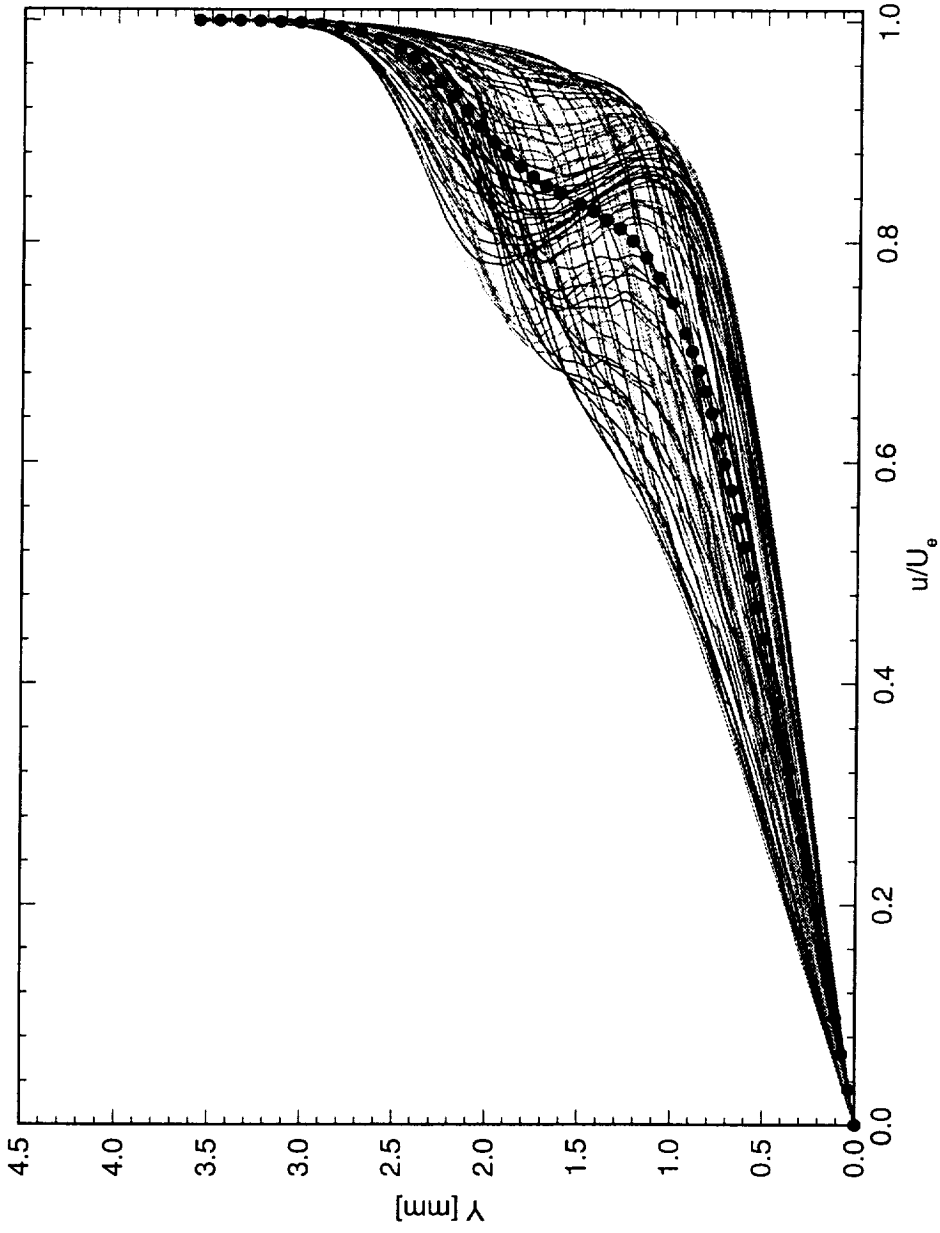

Figure 5.85: Spanwise array of 100 boundary-layer profiles spaced 1 mm apart in span at $x/c = 0.35$. $Re_c = 2.4 \times 10^6$, [6|18] roughness. The dots represent the spanwise average of the profiles.

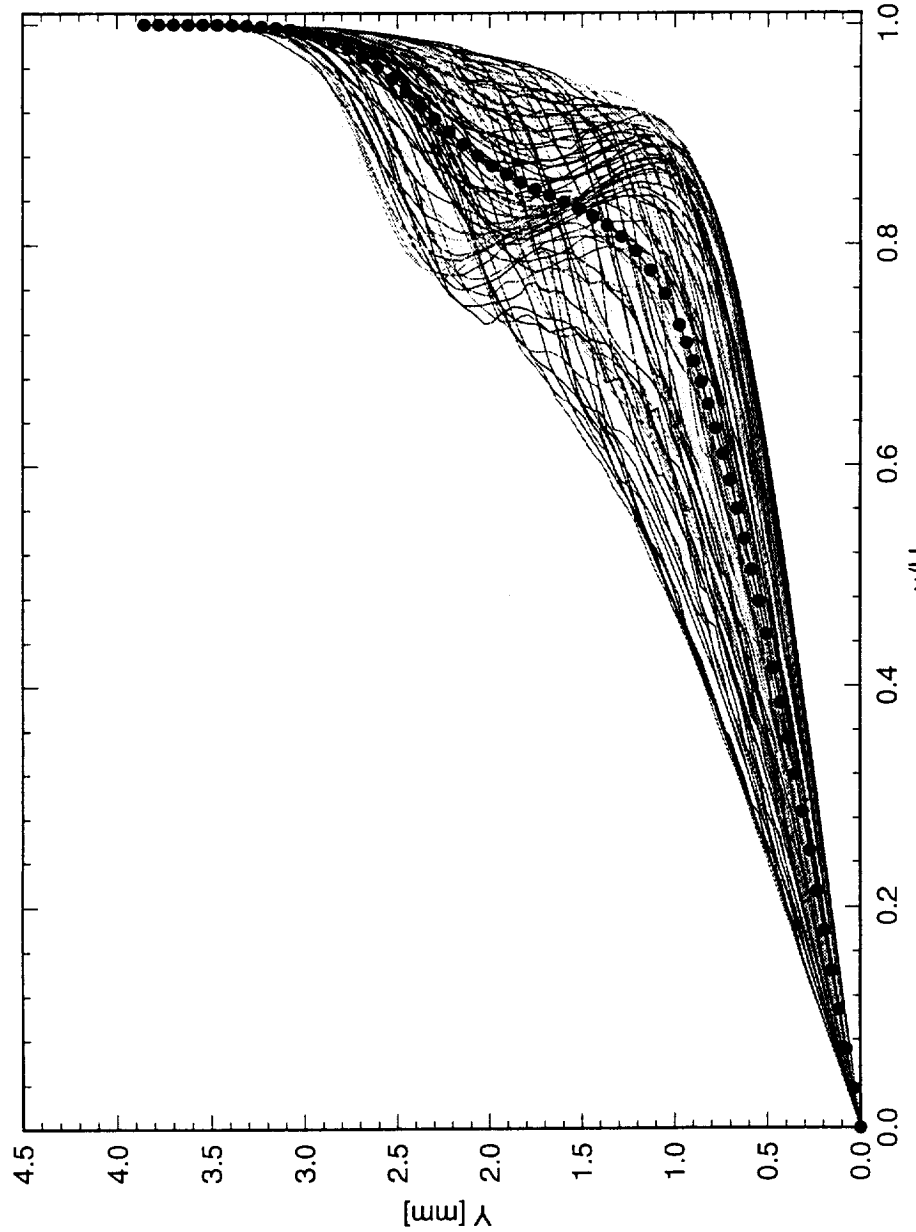

Figure 5.86: Spanwise array of 100 boundary-layer profiles spaced 1 mm apart in span at $x/c = 0.40$. $Re_c = 2.4 \times 10^6$, [6|18] roughness. The dots represent the spanwise average of the profiles.

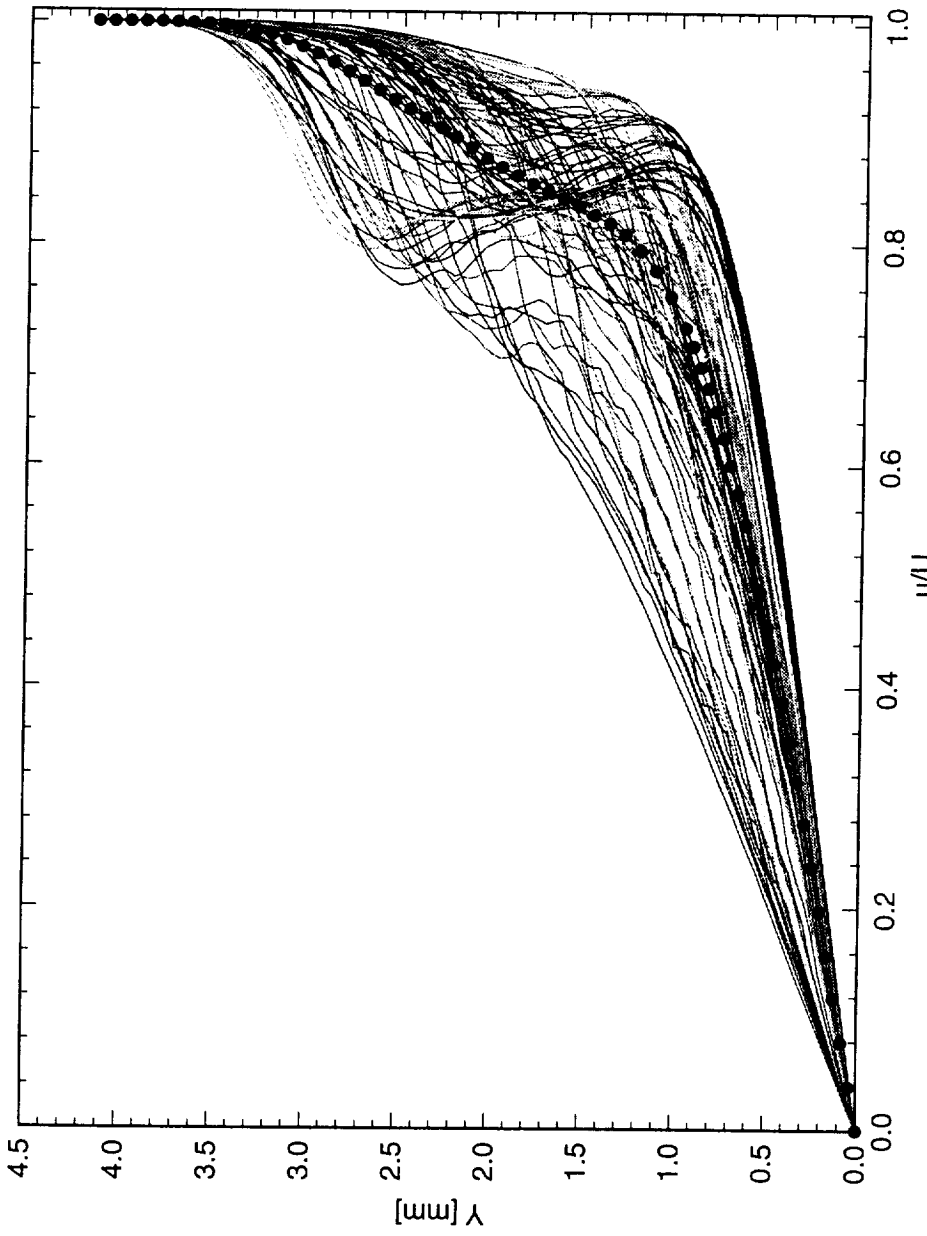

Figure 5.87: Spanwise array of 100 boundary-layer profiles spaced 1 mm apart in span at $x/c = 0.45$. $Re_c = 2.4 \times 10^6$, [6|18] roughness. The dots represent the spanwise average of the profiles.

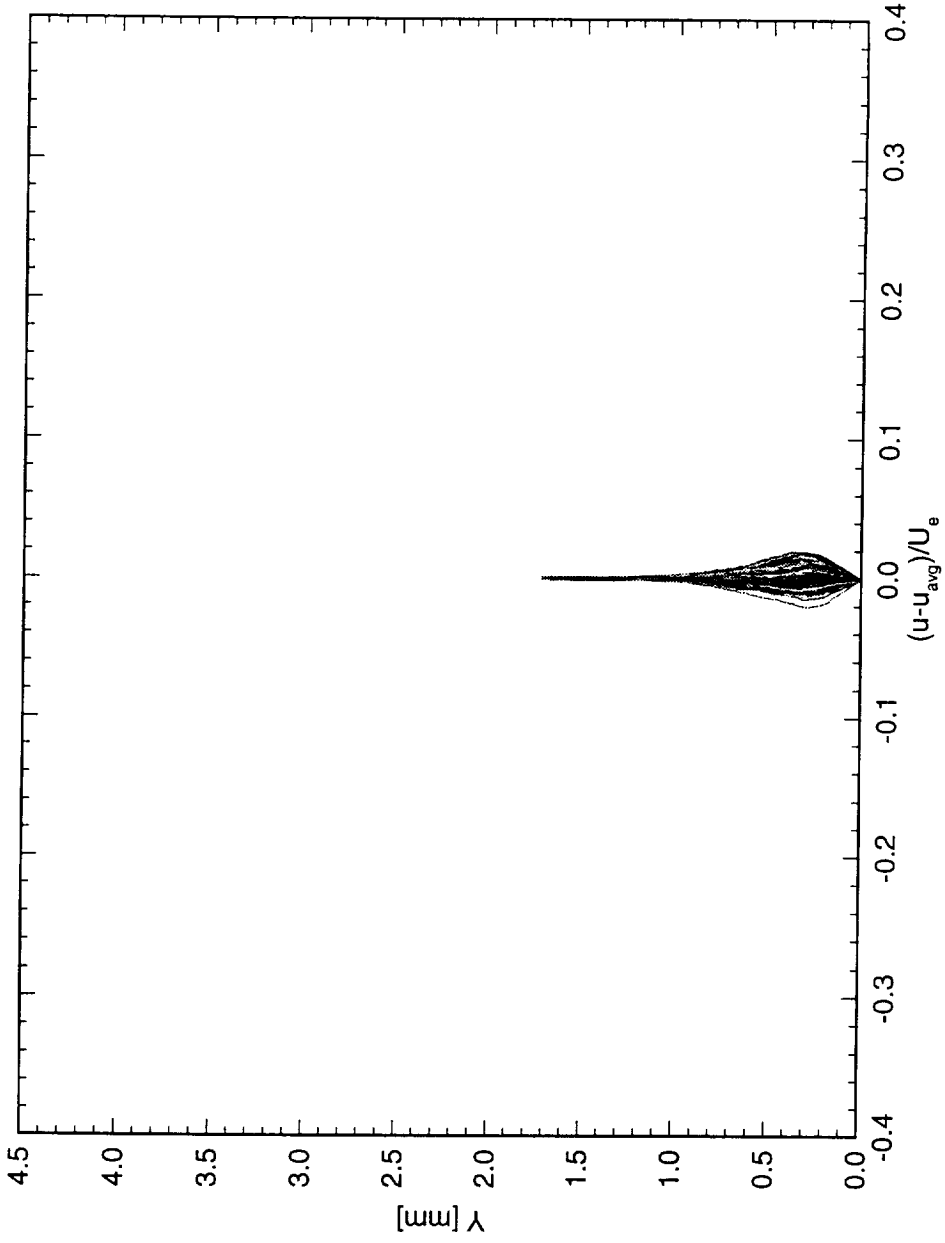

Figure 5.88: Spanwise array of 100 disturbance profiles spaced 1 mm apart in span at $x/c = 0.05$. $Re_c = 2.4 \times 10^6$, [6|18] roughness.

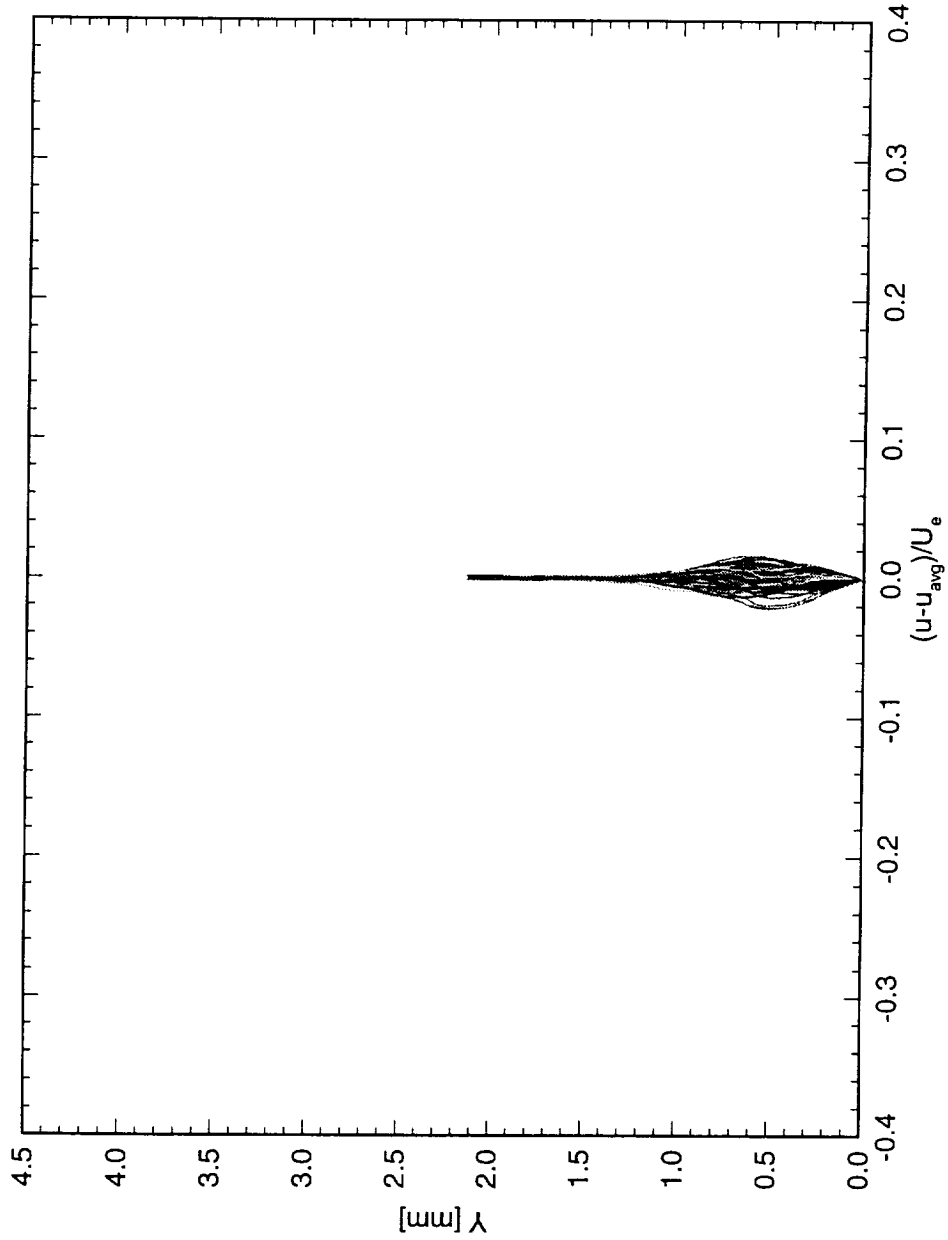

Figure 5.89: Spanwise array of 100 disturbance profiles spaced 1 mm apart in span at $x/c = 0.10$. $Re_c = 2.4 \times 10^6$, [6|18] roughness.

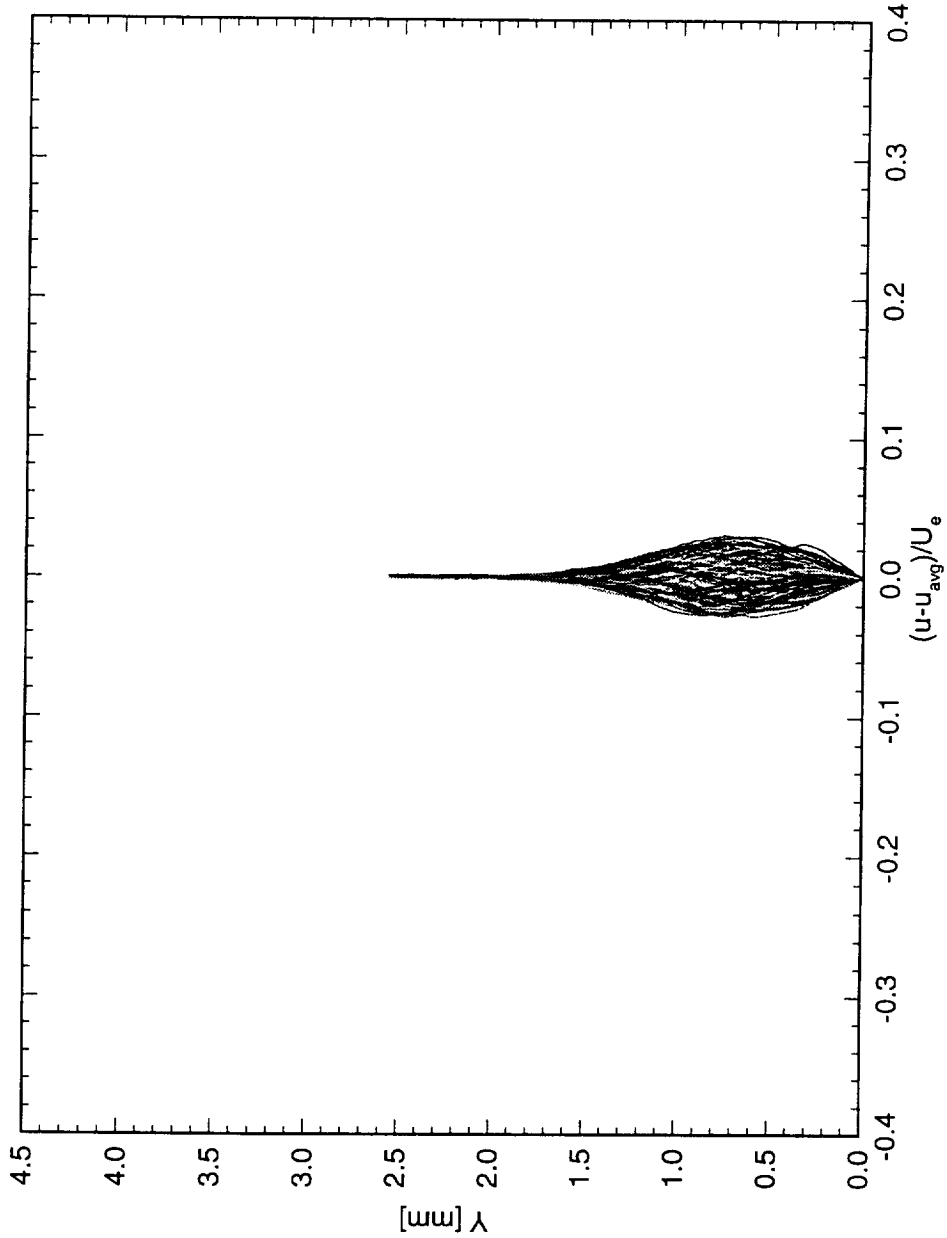

Figure 5.90: Spanwise array of 100 disturbance profiles spaced 1 mm apart in span at $x/c = 0.15$. $Re_c = 2.4 \times 10^6$, [6|18] roughness.

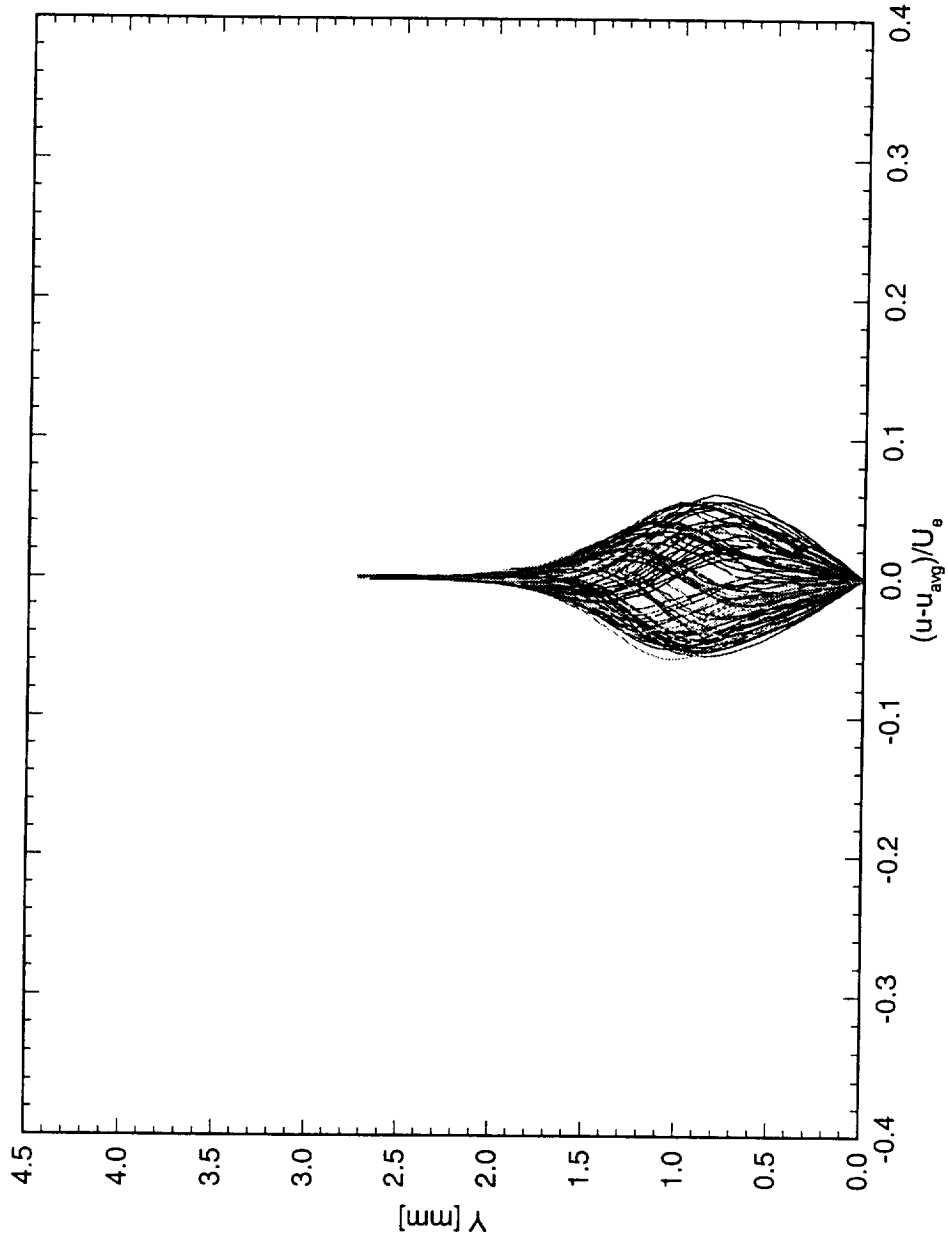

Figure 5.91: Spanwise array of 100 disturbance profiles spaced 1 mm apart in span at $x/c = 0.20$. $Re_c = 2.4 \times 10^6$, [6|18] roughness.

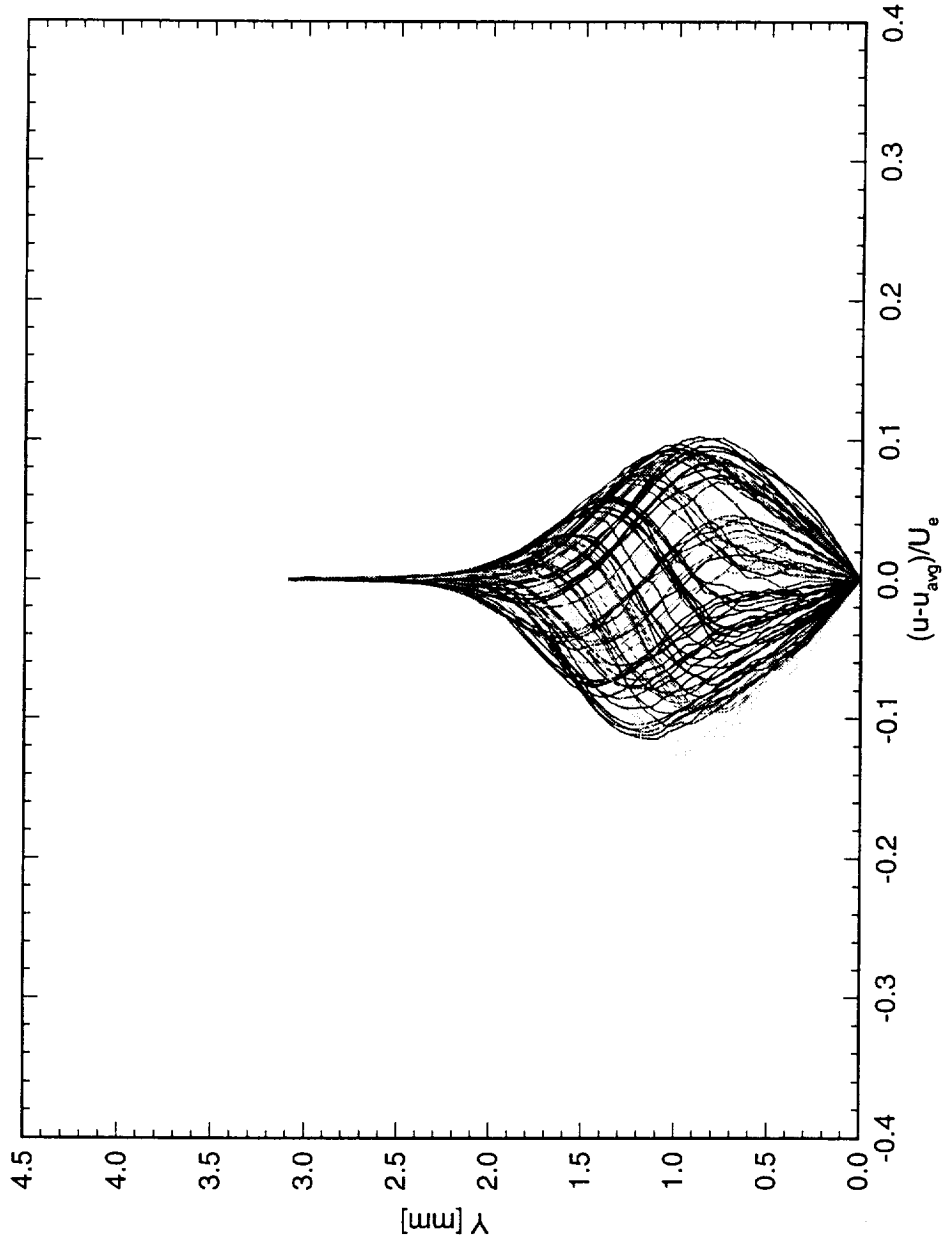

Figure 5.92: Spanwise array of 100 disturbance profiles spaced 1 mm apart in span at $x/c = 0.25$. $Re_c = 2.4 \times 10^6$, [6|18] roughness.

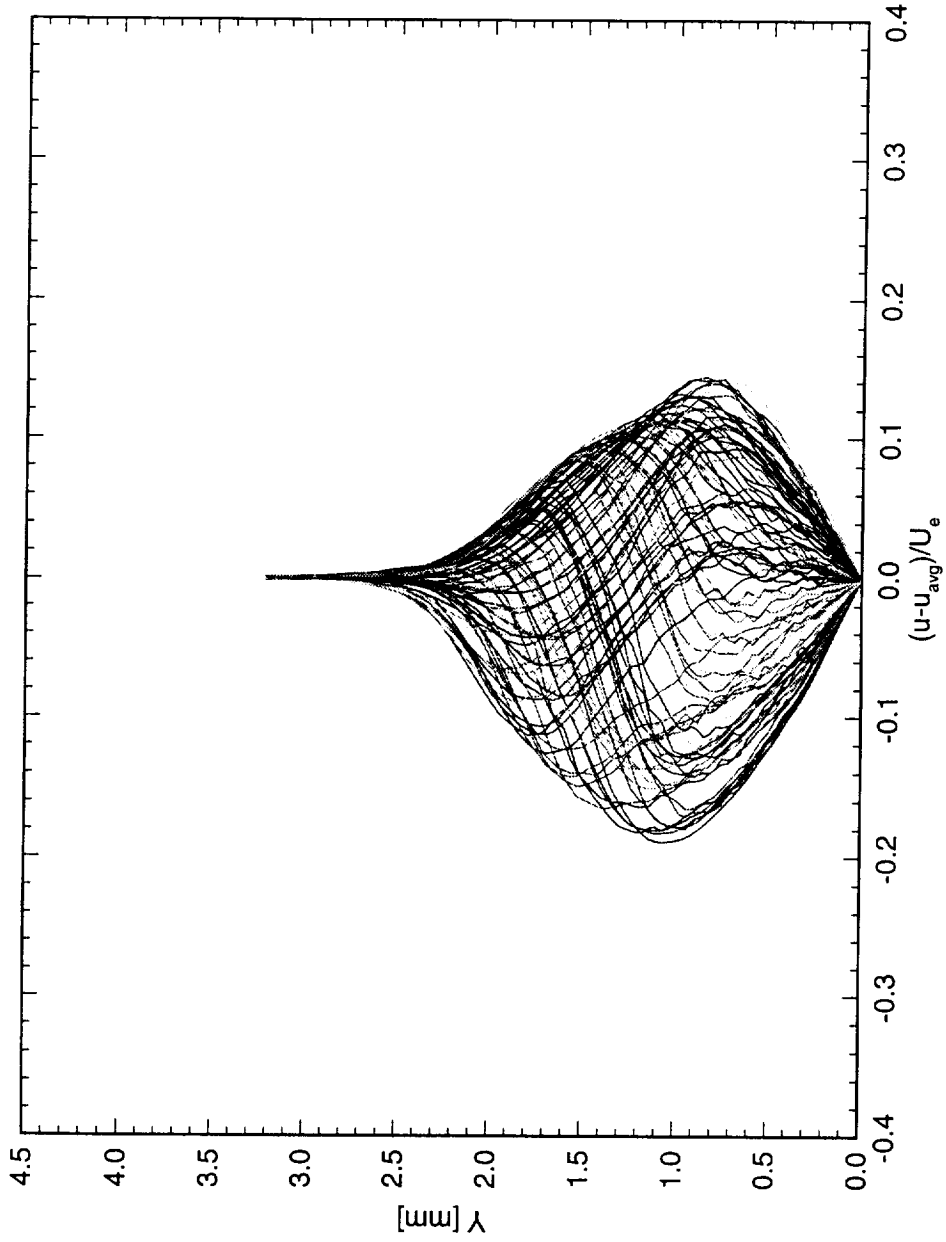

Figure 5.93: Spanwise array of 100 disturbance profiles spaced 1 mm apart in span at $x/c = 0.30$. $Re_c = 2.4 \times 10^6$, [6|18] roughness.

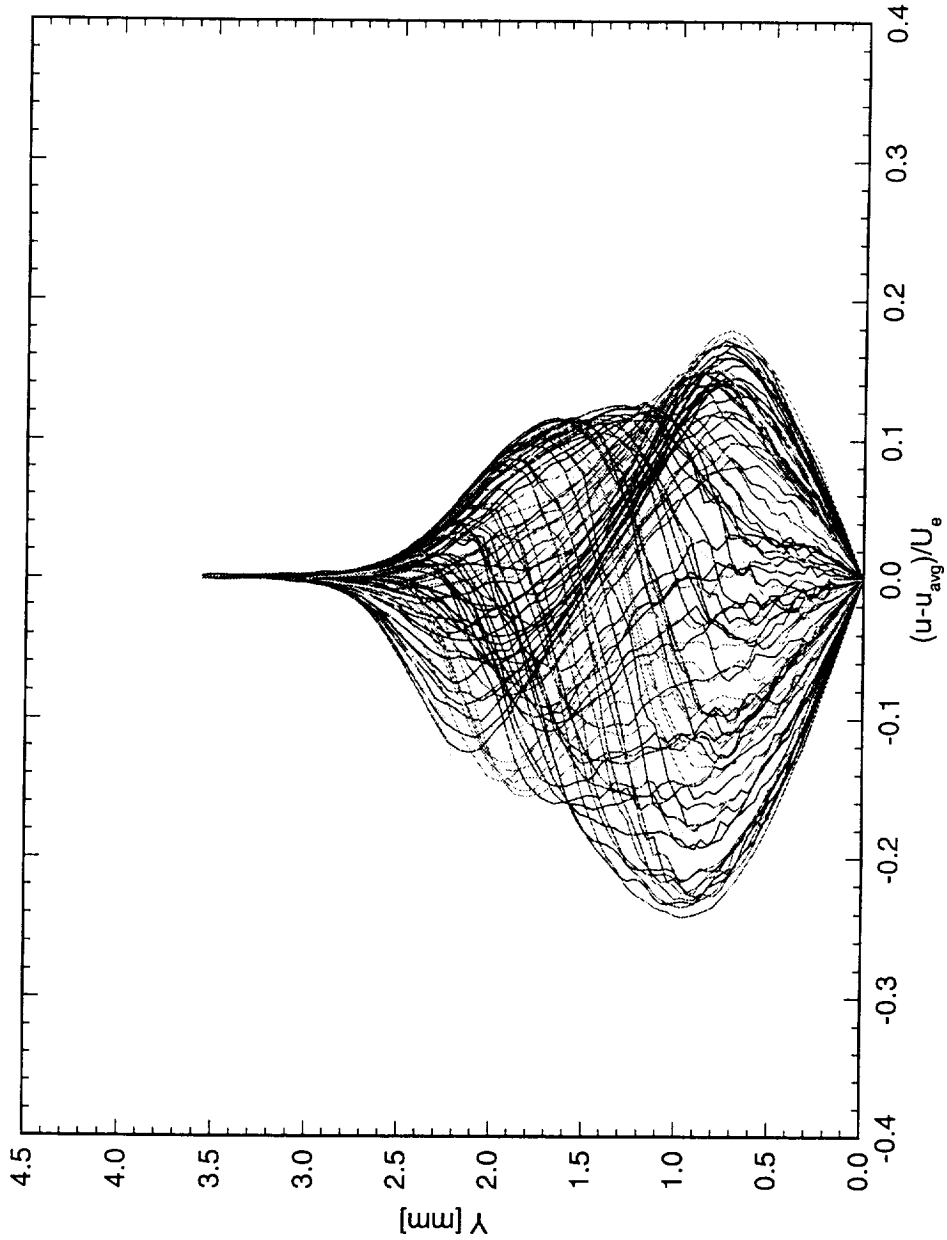

Figure 5.94: Spanwise array of 100 disturbance profiles spaced 1 mm apart in span at $x/c = 0.35$. $Re_c = 2.4 \times 10^6$, [6|18] roughness.

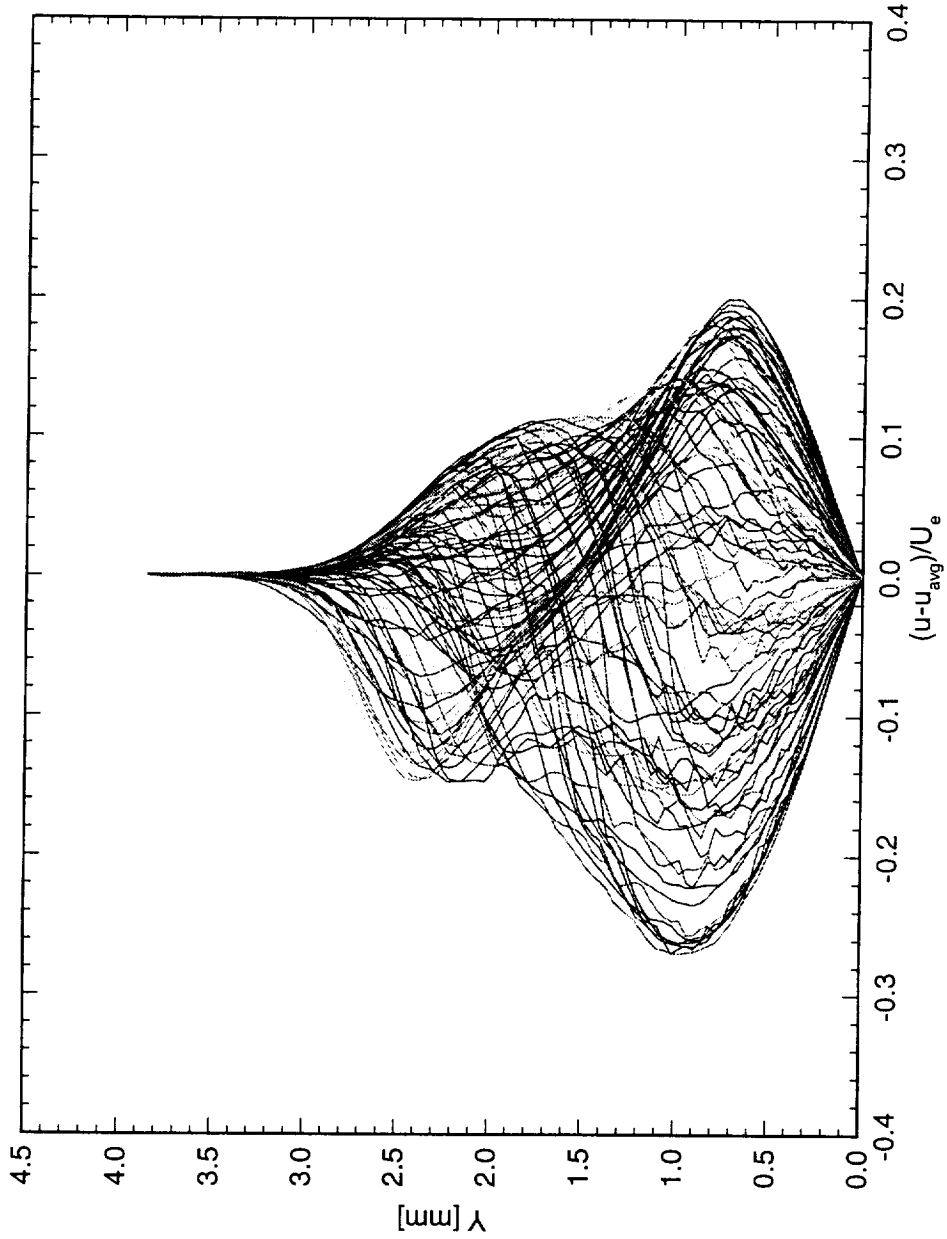

Figure 5.95: Spanwise array of 100 disturbance profiles spaced 1 mm apart in span at $x/c = 0.40$. $Re_c = 2.4 \times 10^6$, [6|18] roughness.

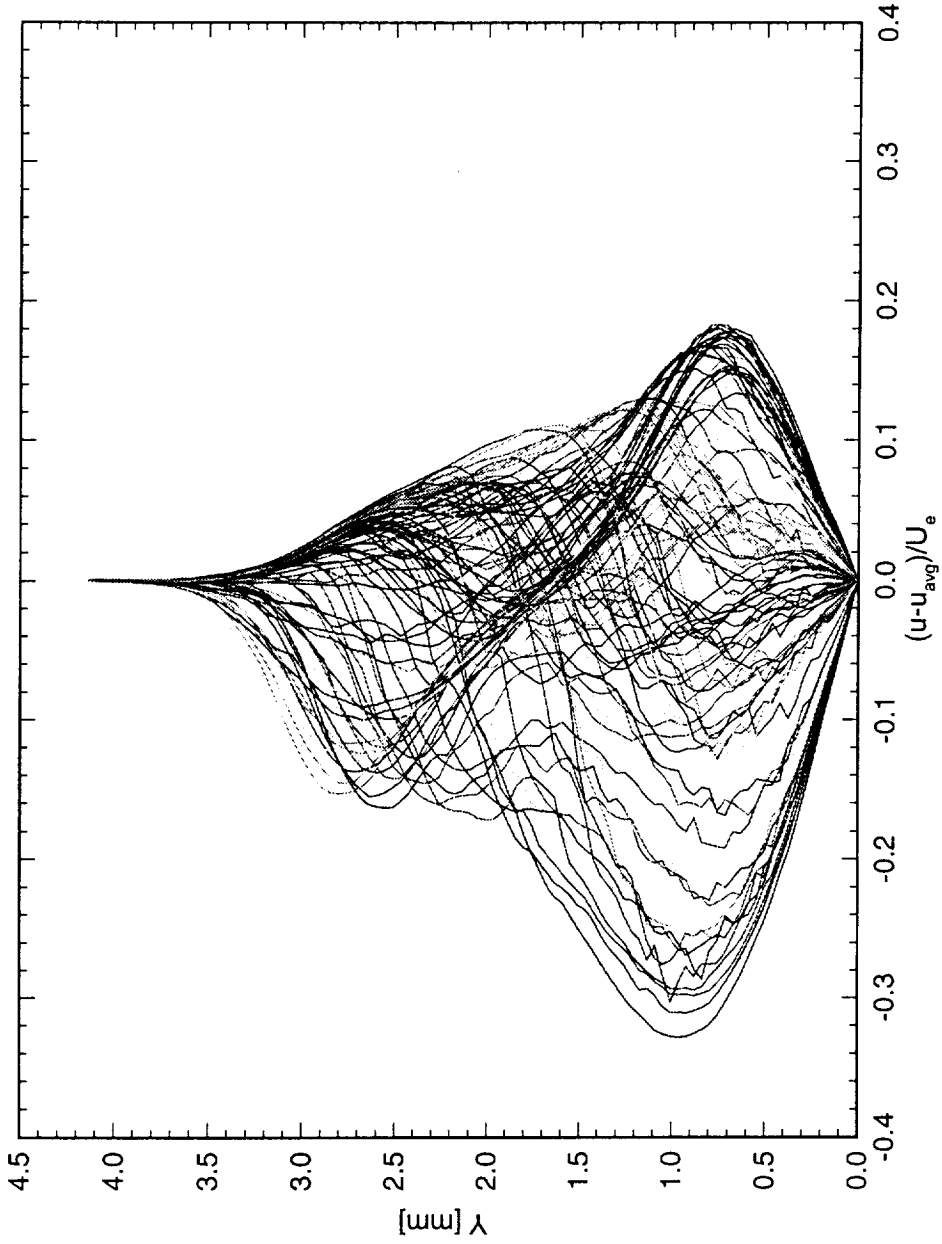

Figure 5.96: Spanwise array of 100 disturbance profiles spaced 1 mm apart in span at $x/c = 0.45$. $Re_c = 2.4 \times 10^6$, [6|18] roughness.

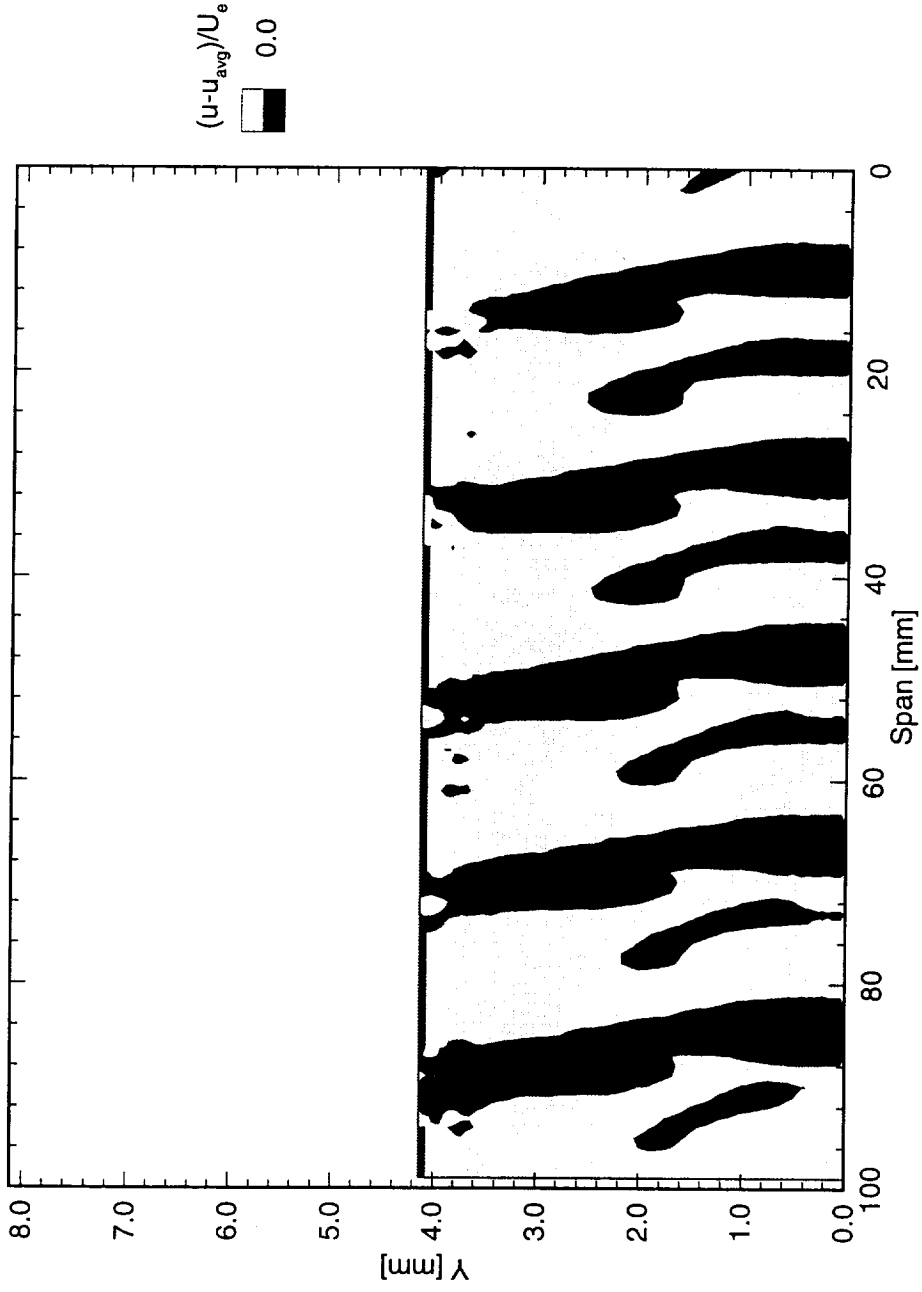

Figure 5.97: Normalized disturbance velocity contours at $x/c = 0.45$. $Re_c = 2.4 \times 10^6$, [6|18] roughness.

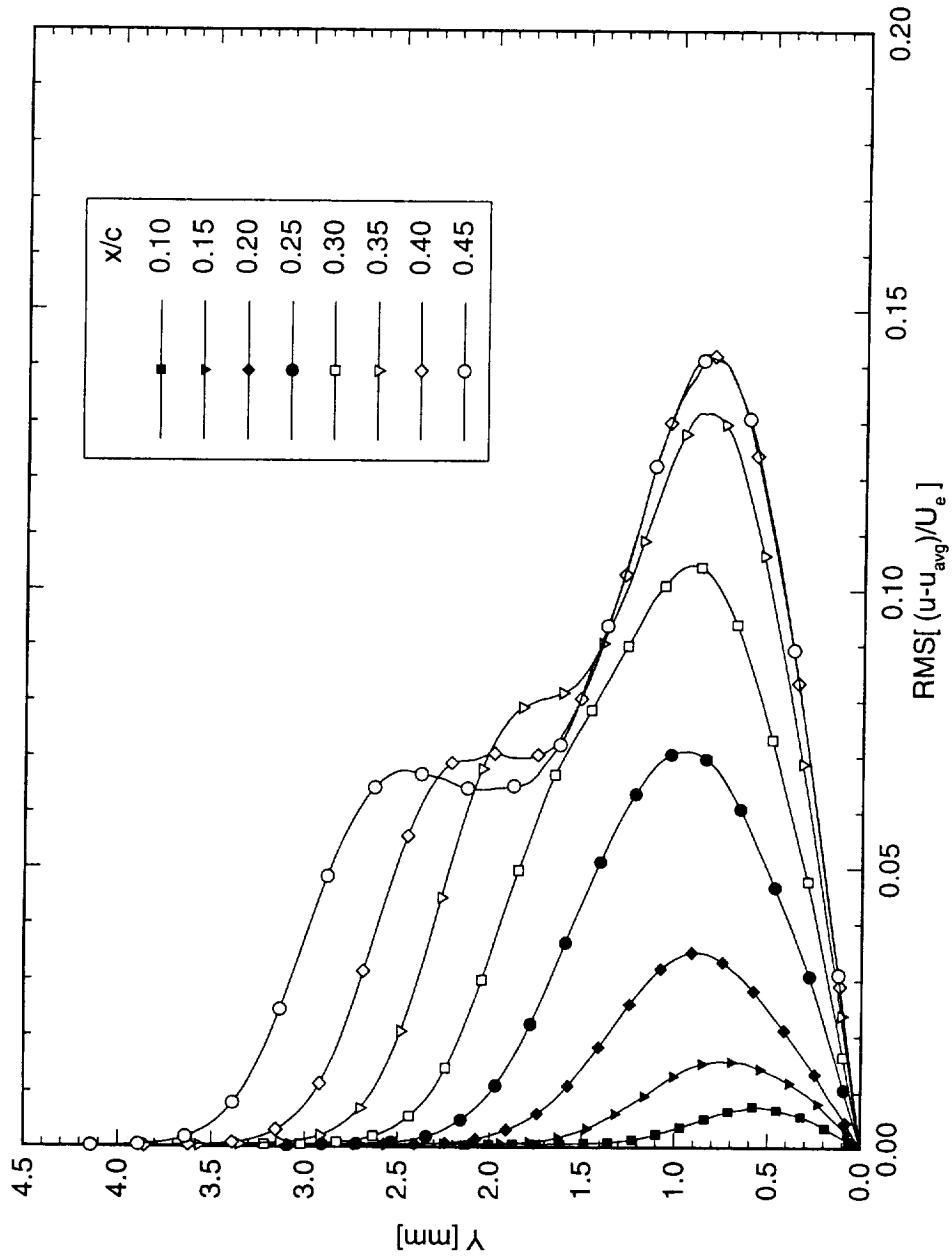

Figure 5.98: Stationary crossflow mode shapes for $Re_c = 2.4 \times 10^6$ and [6|18] roughness. The symbols are merely indicators and do not indicate measurement points

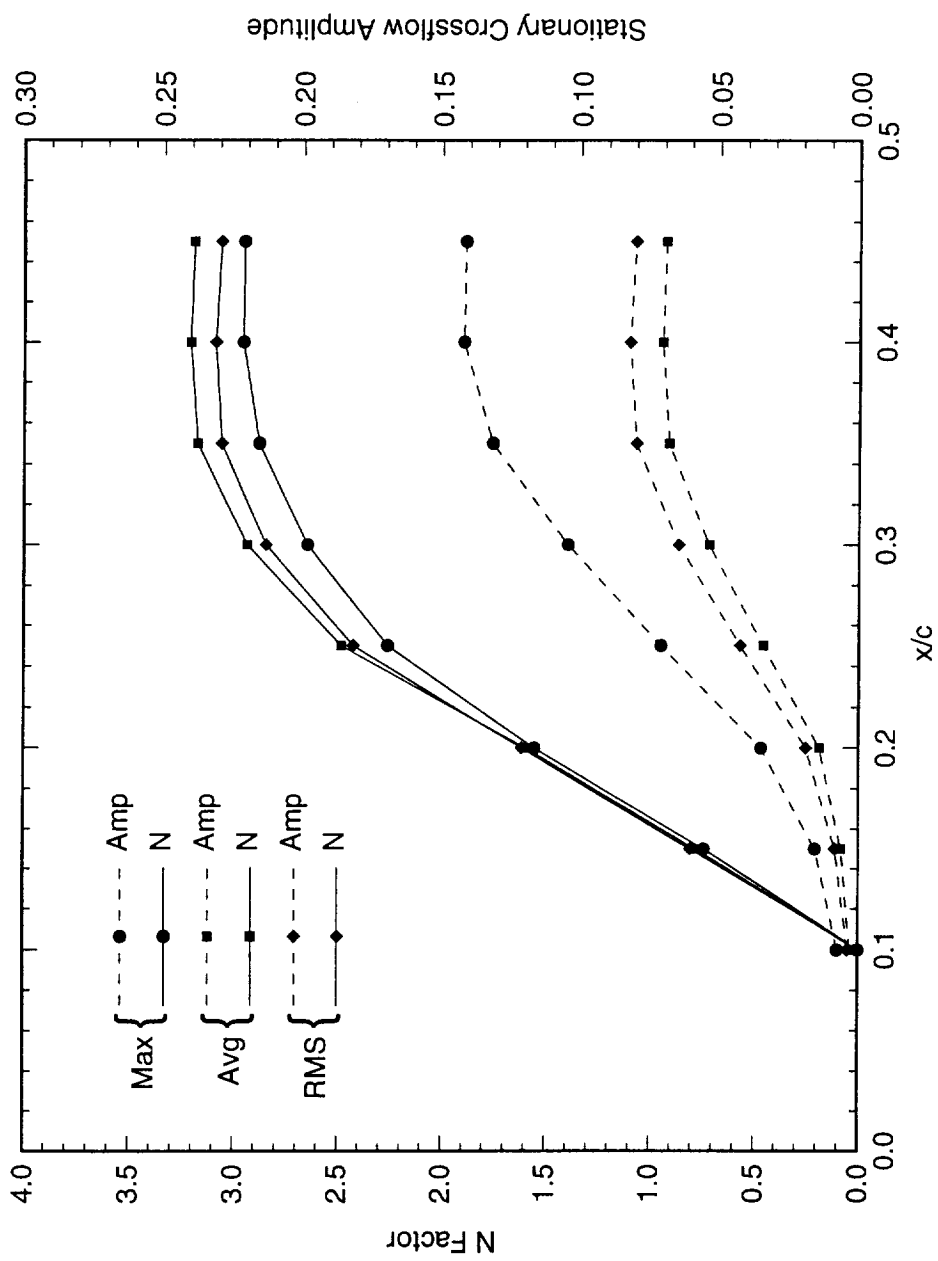

Figure 5.99: Total disturbance amplitude and relative N-factor for $Re_c = 2.4 \times 10^6$ and [6|18] roughness. N-factor calculations are relative to $x/c = 0.10$.

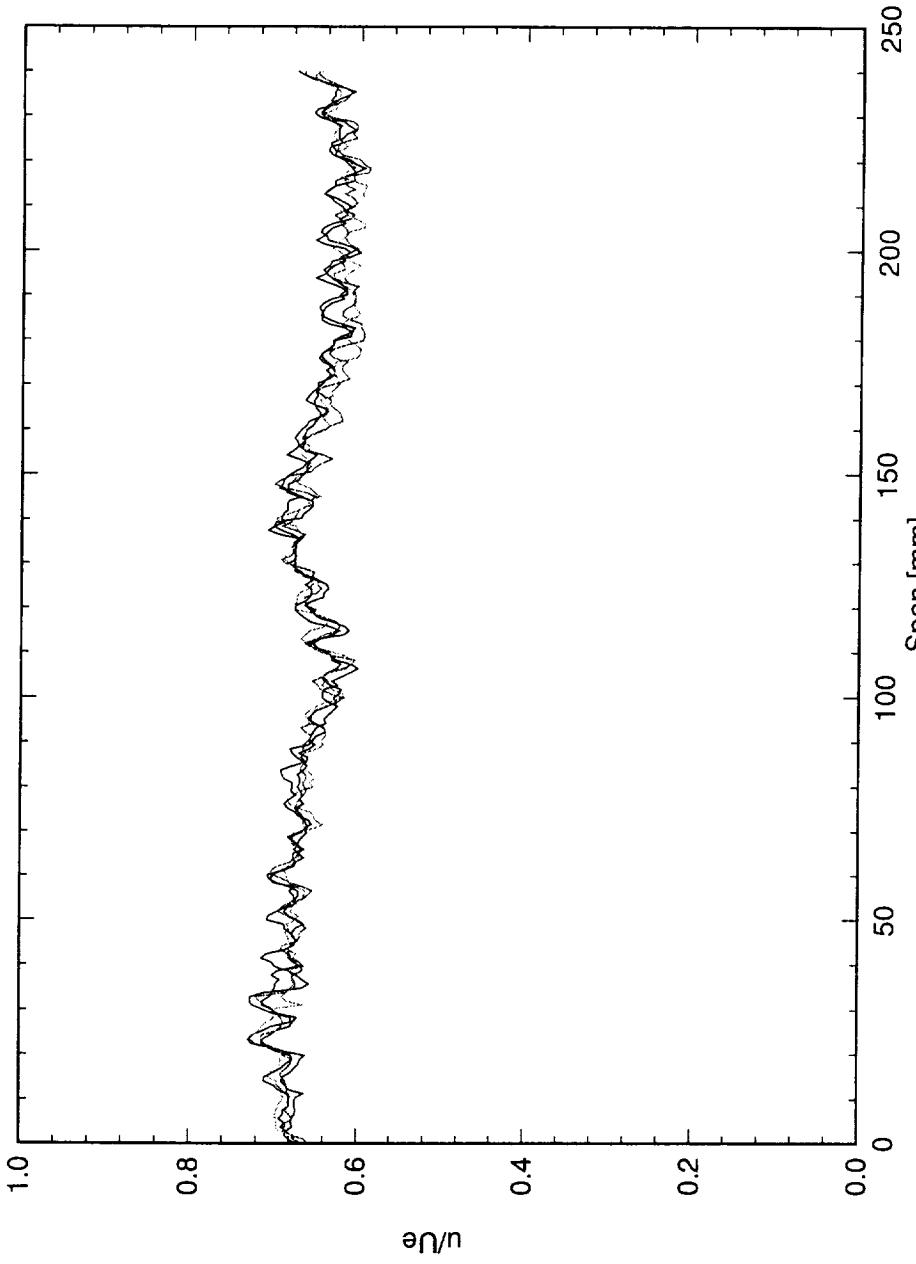

Figure 5.100: Spanwise hot-wire scan at $x/c = 0.10$ and $Y = 0.60$ mm. $Re_c = 2.4 \times 10^6$, [6|18] roughness.

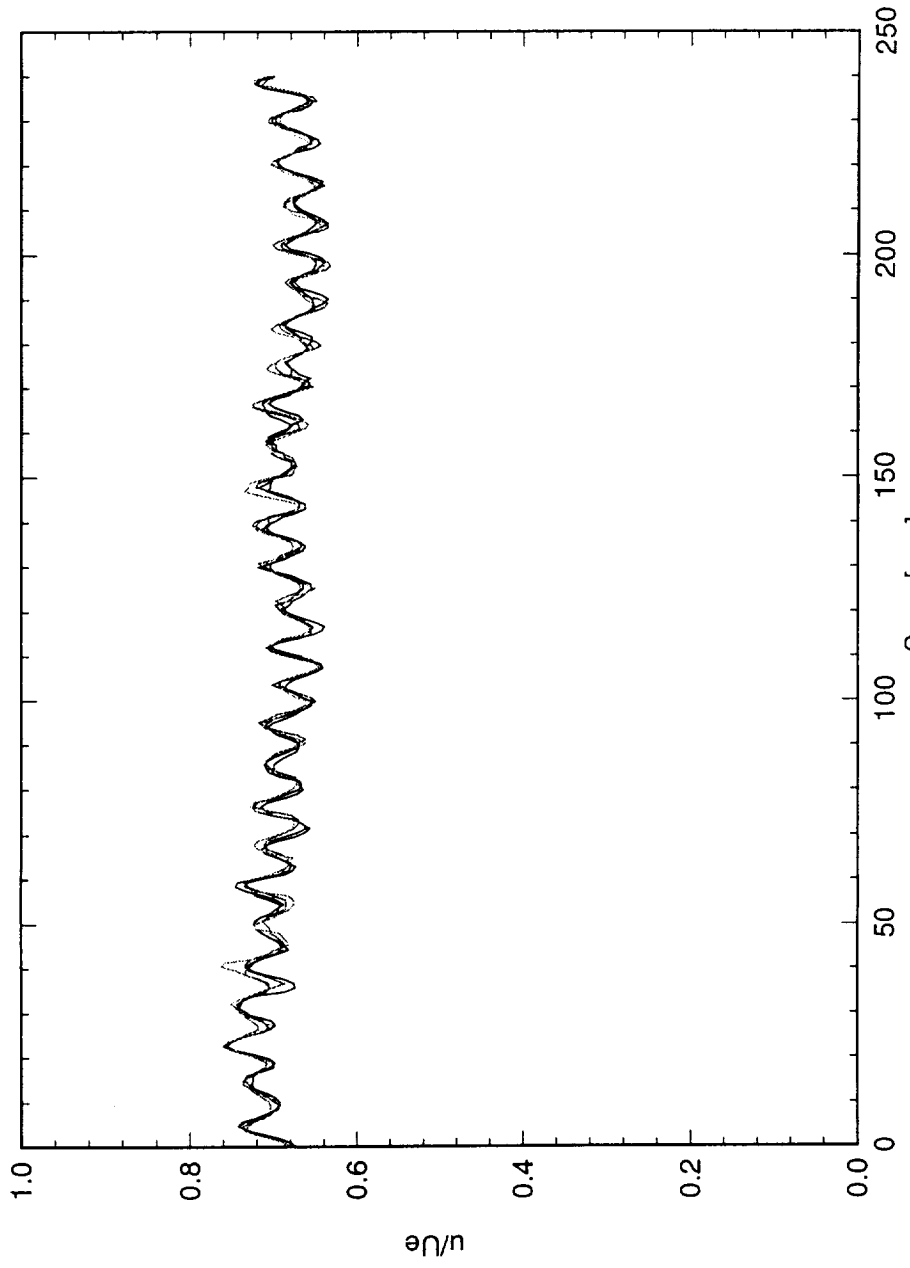

Figure 5.101: Spanwise hot-wire scan at $x/c = 0.15$ and $Y = 0.75$ mm. $Re_c = 2.4 \times 10^6$, [6|18] roughness.

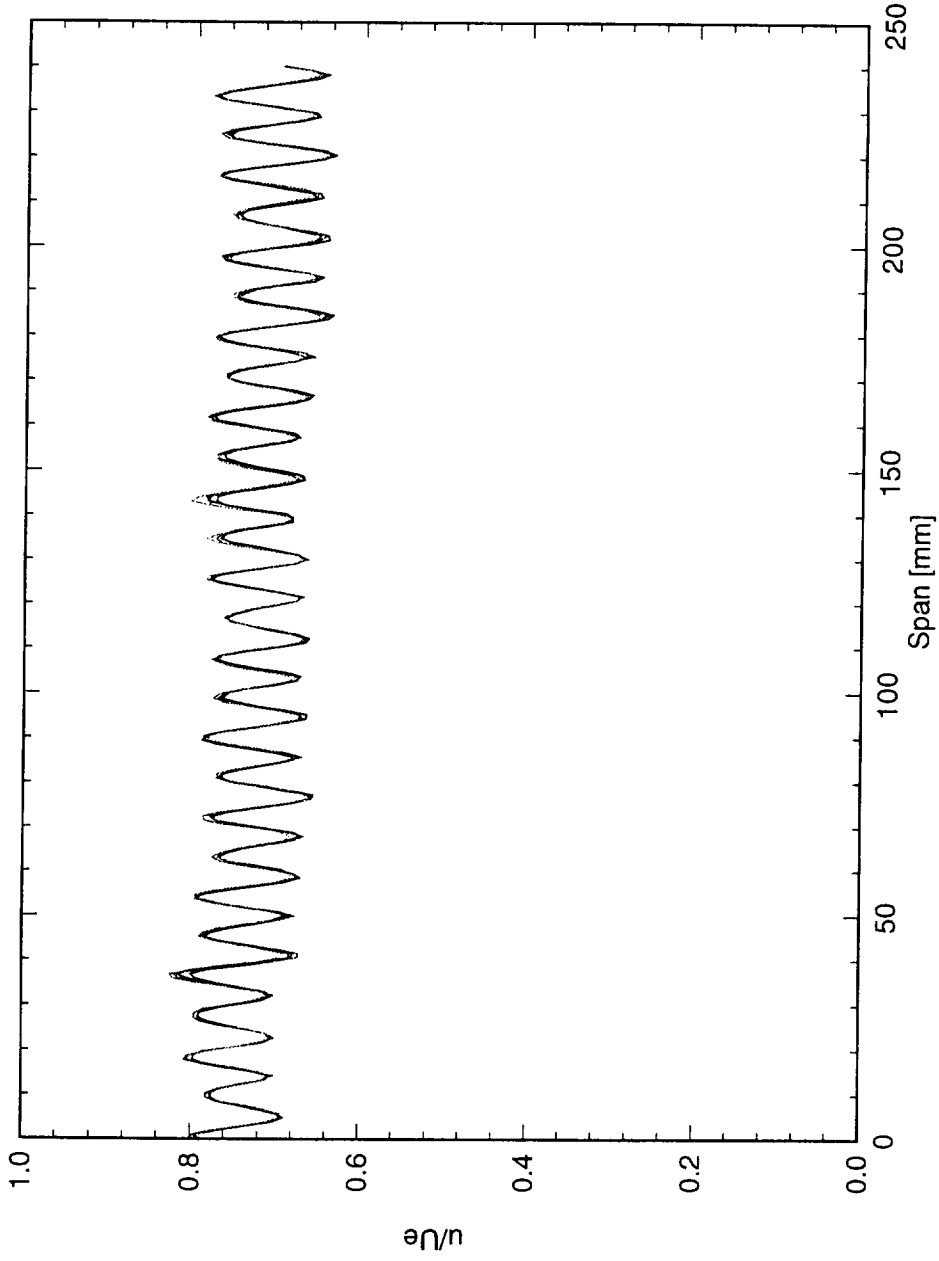

Figure 5.102: Spanwise hot-wire scan at $x/c = 0.20$ and $Y = 0.90$ mm. $Re_c = 2.4 \times 10^6$, [6|18] roughness.

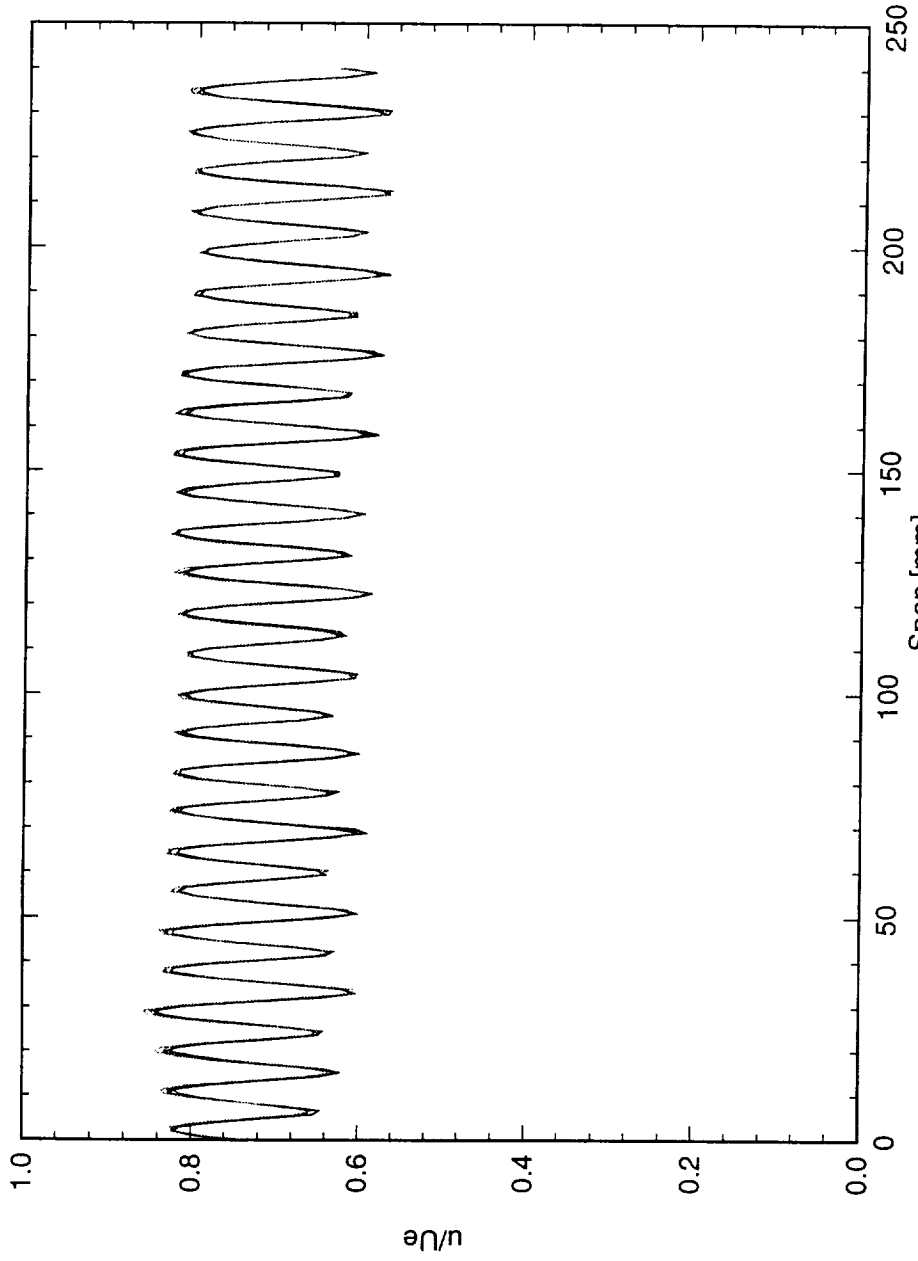

Figure 5.103: Spanwise hot-wire scan at $x/c = 0.25$ and $Y = 0.95$ mm. $Re_c = 2.4 \times 10^6$, [6|18] roughness.

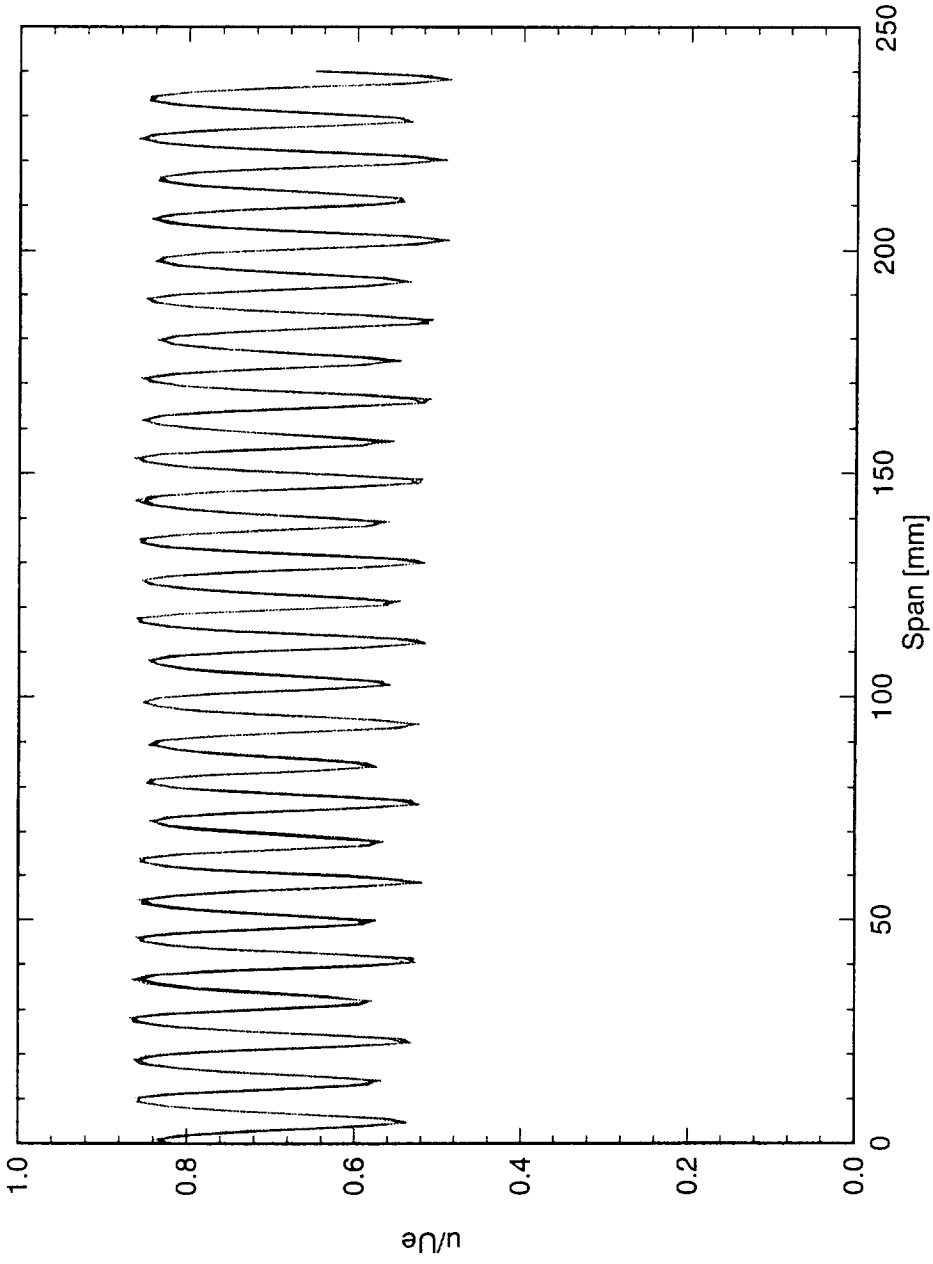

Figure 5.104: Spanwise hot-wire scan at $x/c = 0.30$ and $Y = 0.95$ mm. $Re_c = 2.4 \times 10^6$, [6|18] roughness.

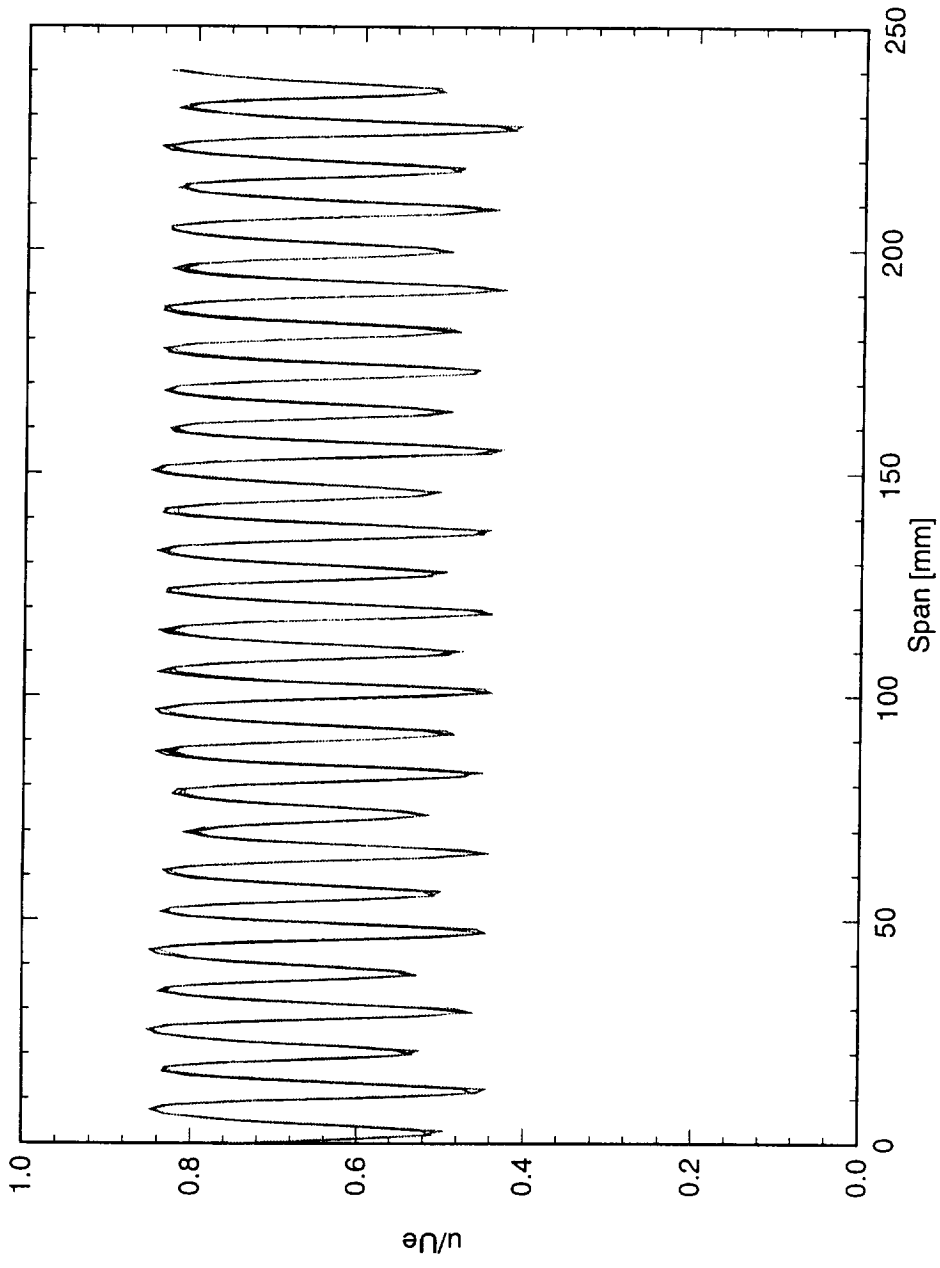

Figure 5.105: Spanwise hot-wire scan at $x/c = 0.35$ and $Y = 0.85$ mm. $Re_c = 2.4 \times 10^6$, [6|18] roughness.

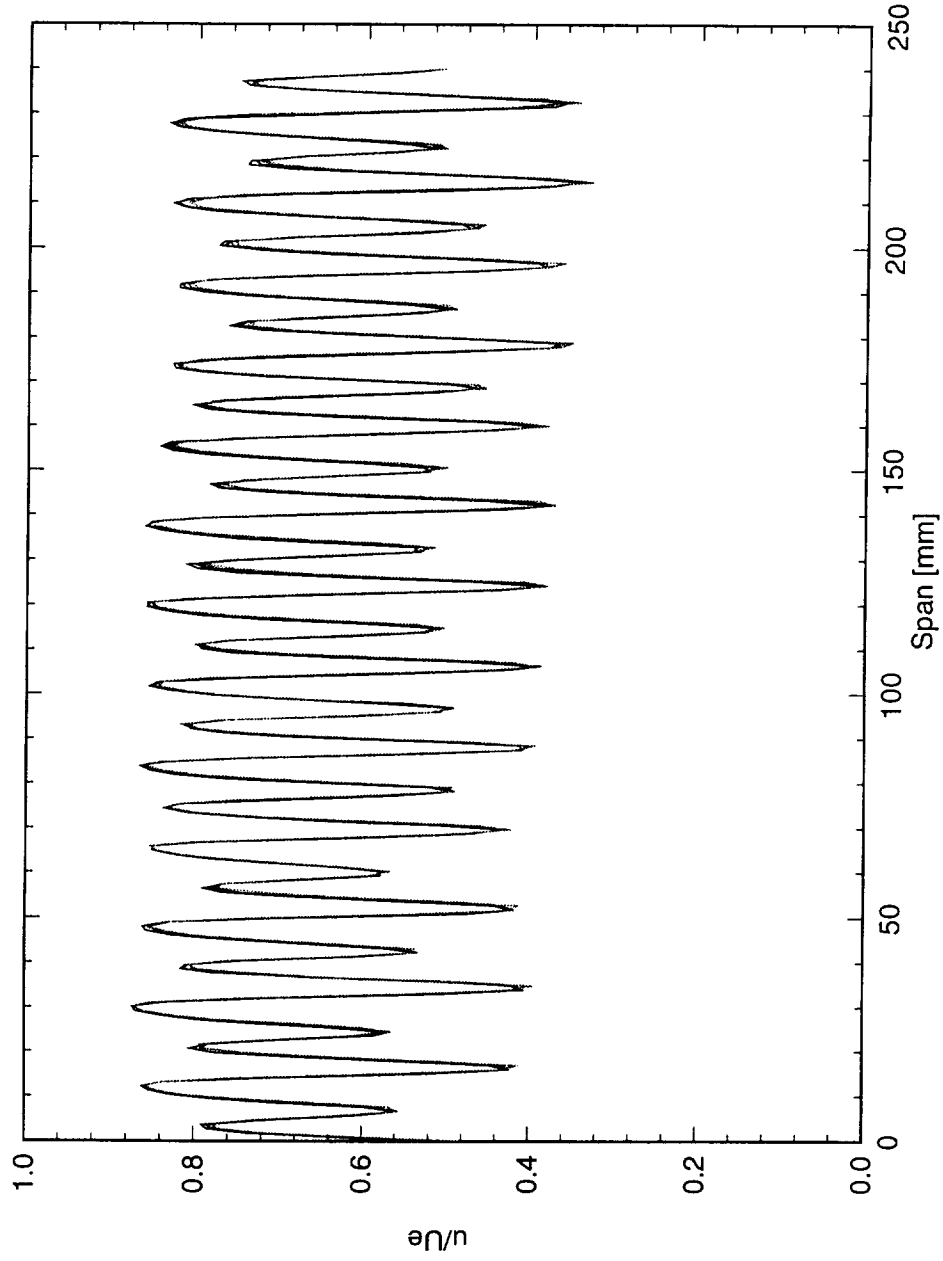

Figure 5.106: Spanwise hot-wire scan at $x/c = 0.40$ and $Y = 0.85$ mm. $Re_c = 2.4 \times 10^6$, [6|18] roughness.

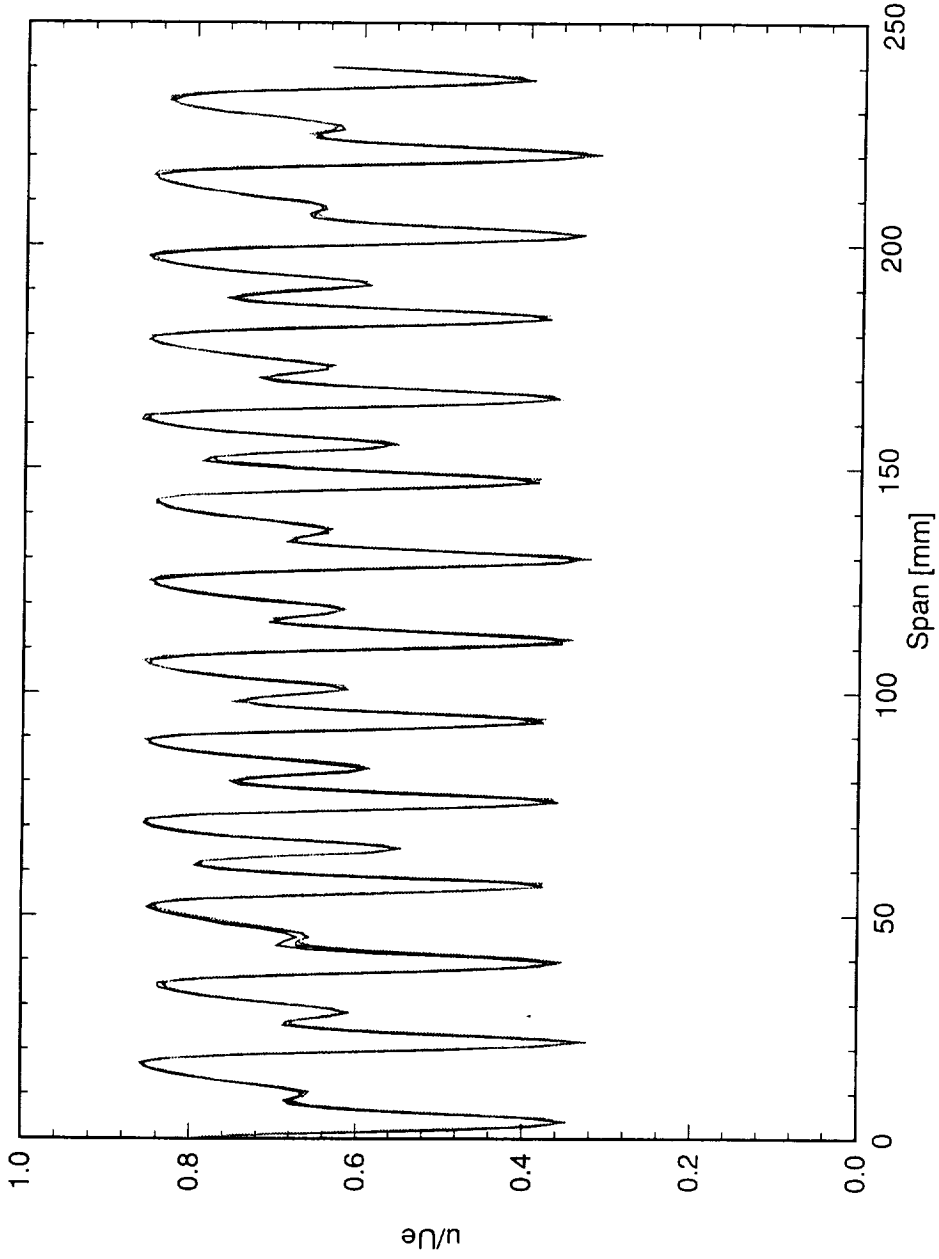

Figure 5.107: Spanwise hot-wire scan at $x/c = 0.45$ and $Y = 0.85$ mm. $Re_c = 2.4 \times 10^6$, [6|18] roughness.

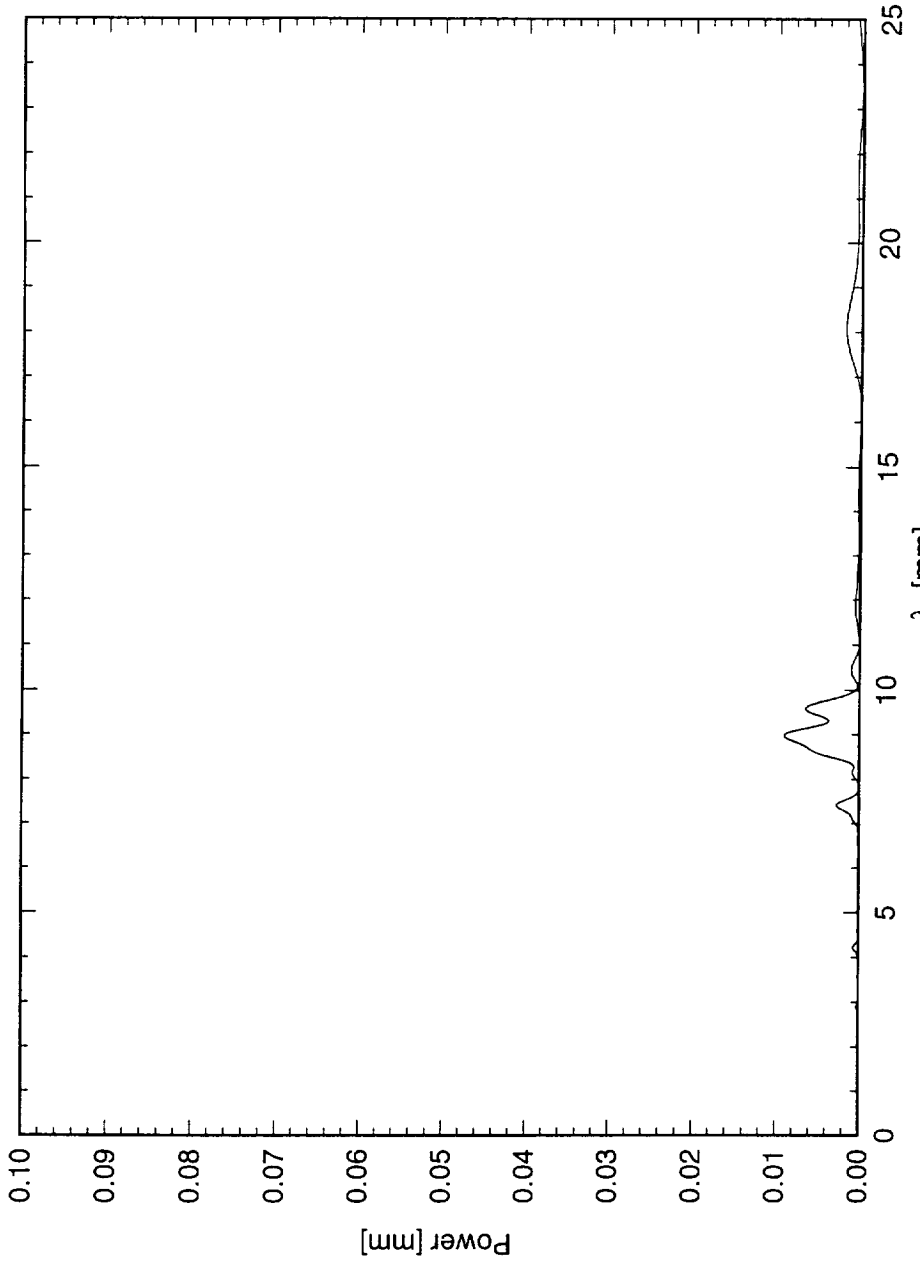

Figure 5.108: Power spectral density of constant-Y scan at $x/c = 0.10$ and $Y = 0.60$ mm. $Re_c = 2.4 \times 10^6$, [6|18] roughness.

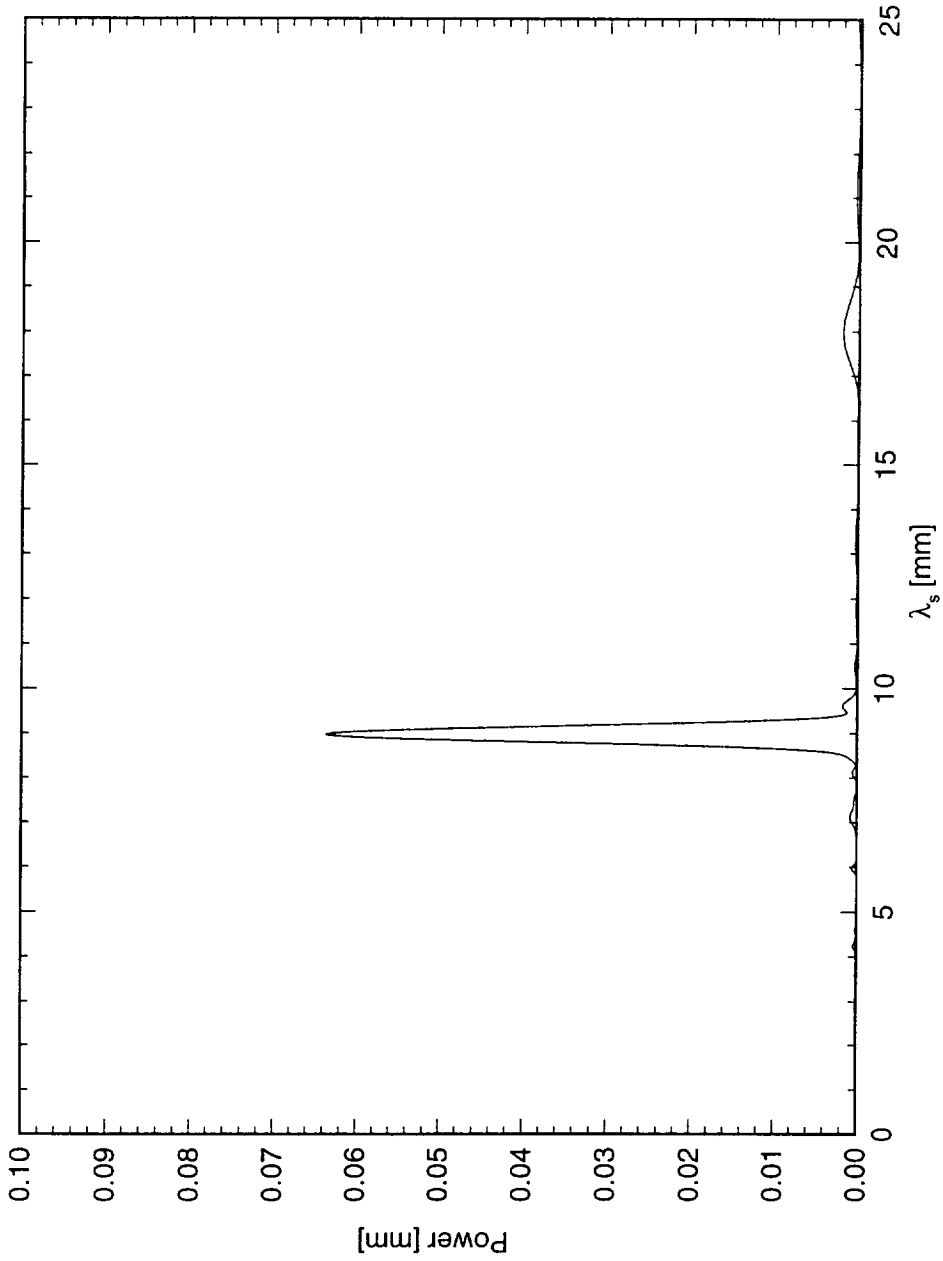

Figure 5.109: Power spectral density of constant-Y scan at $x/c = 0.15$ and $Y = 0.75$ mm. $Re_c = 2.4 \times 10^6$, [6|18] roughness.

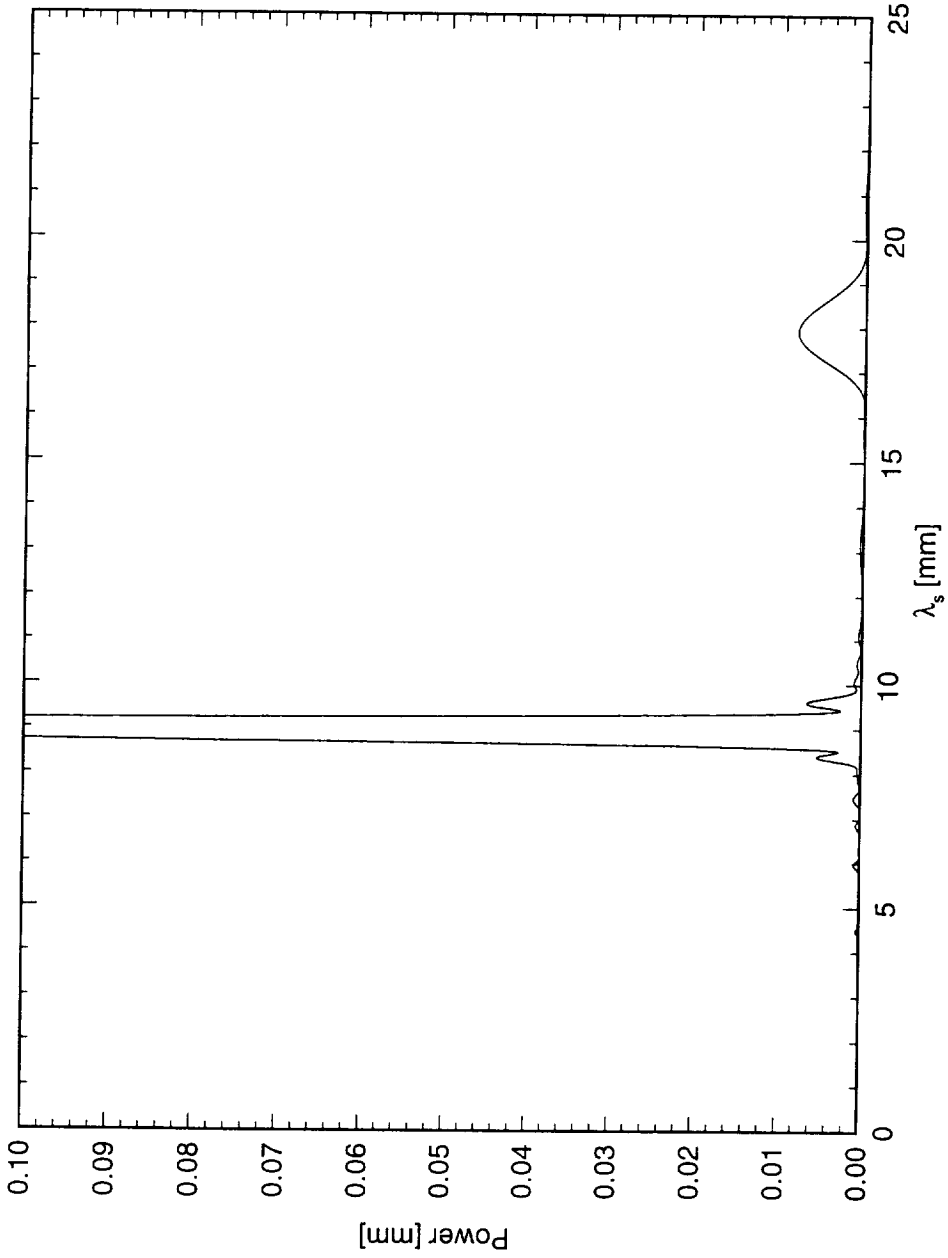

Figure 5.110: Power spectral density of constant-Y scan at $x/c = 0.20$ and $Y = 0.90$ mm. $Re_c = 2.4 \times 10^6$, [6|18] roughness.

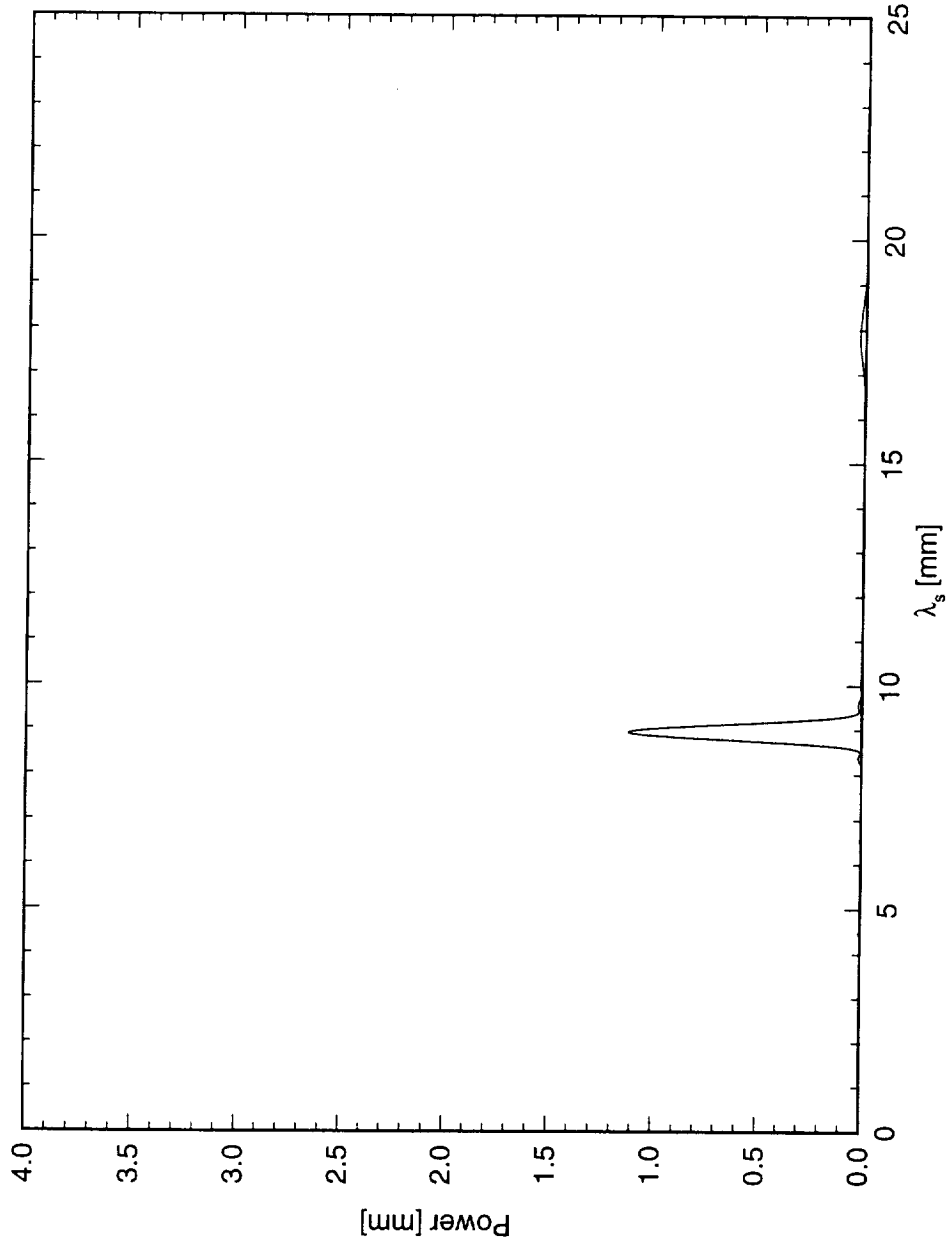

Figure 5.111: Power spectral density of constant-Y scan at $x/c = 0.25$ and $Y = 0.95$ mm. $Re_c = 2.4 \times 10^6$, [6|18] roughness.

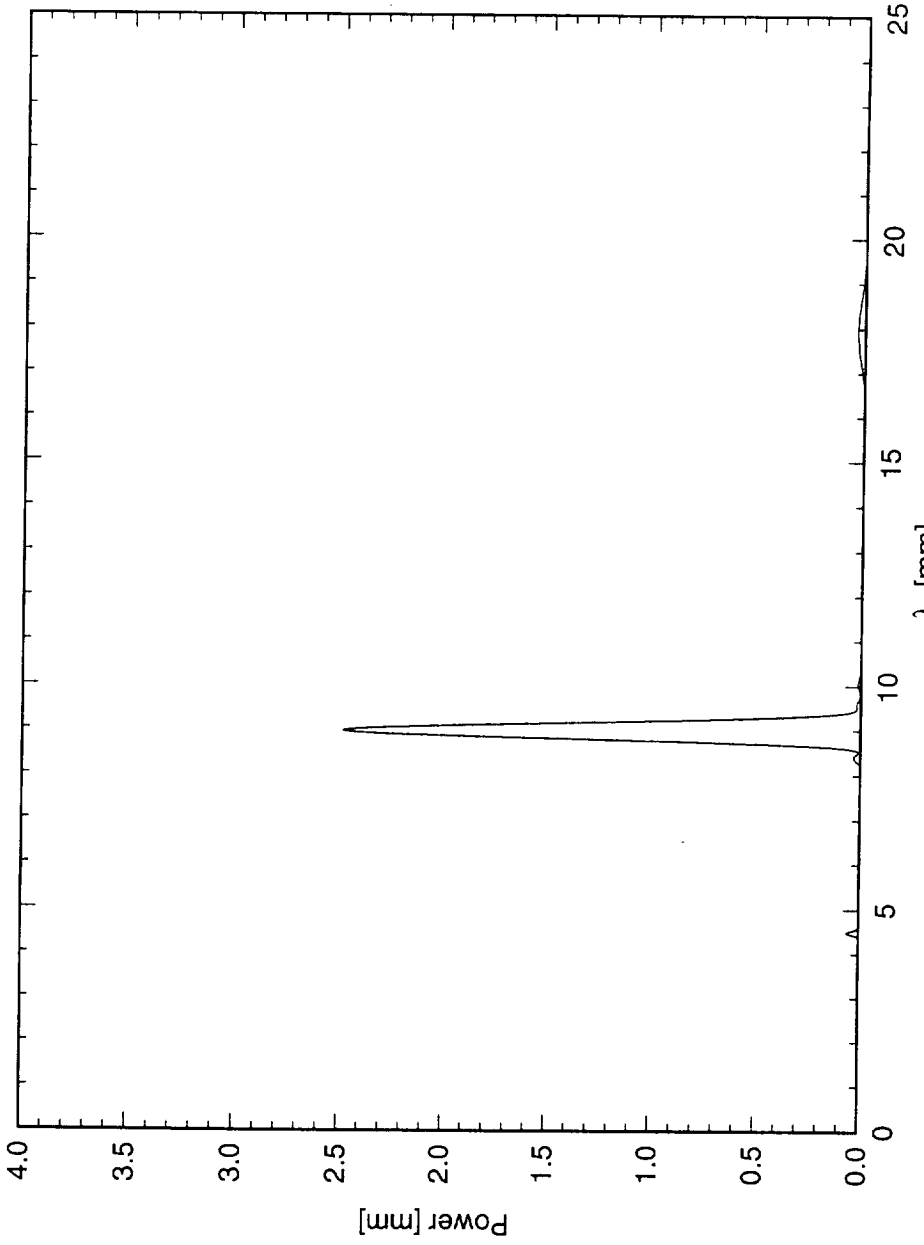

Figure 5.112: Power spectral density of constant-Y scan at $x/c = 0.30$ and $Y = 0.95$ mm. $Re_c = 2.4 \times 10^6$, [6|18] roughness.

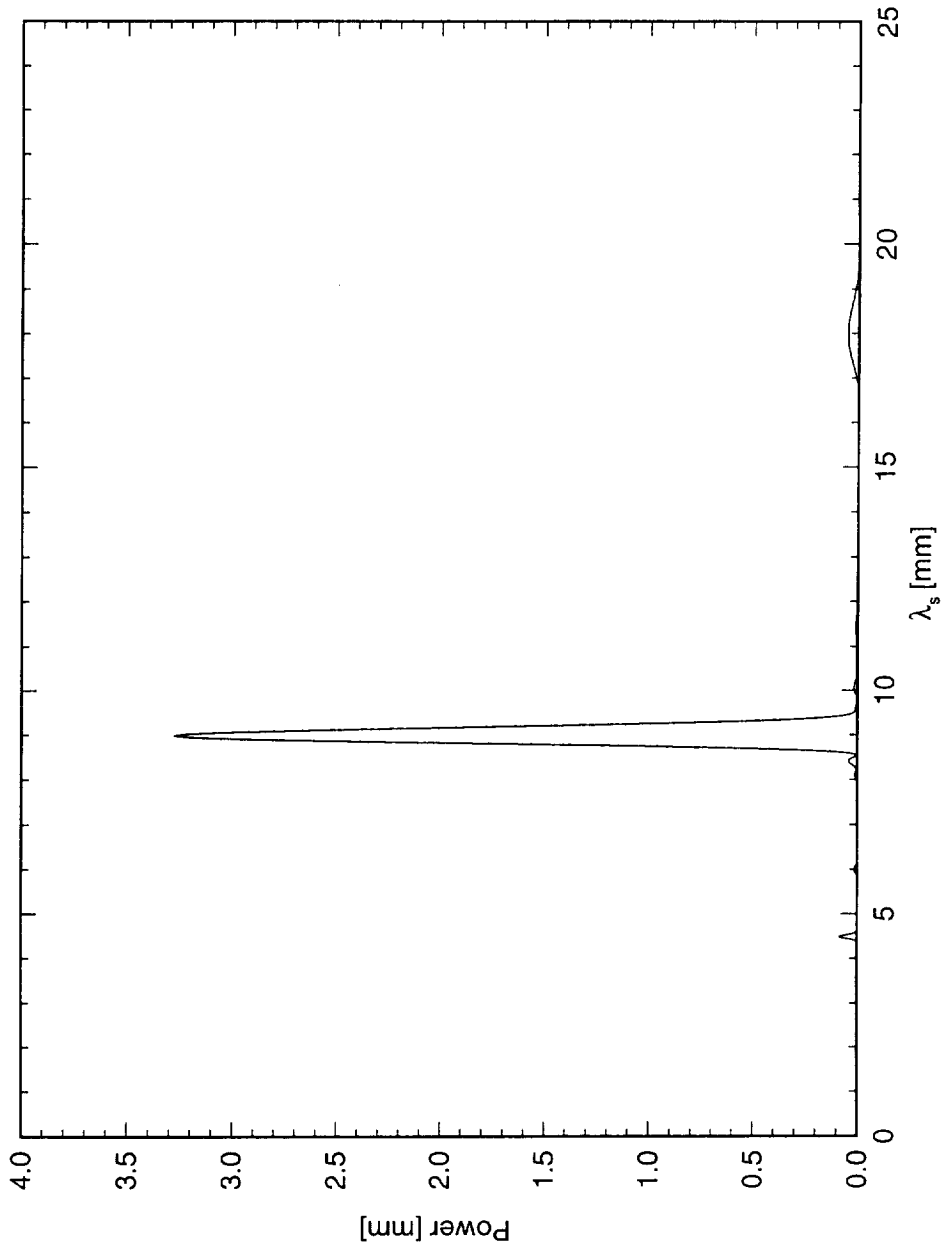

Figure 5.113: Power spectral density of constant-Y scan at $x/c = 0.35$ and $Y = 0.85$ mm. $Re_c = 2.4 \times 10^6$, [6|18] roughness.

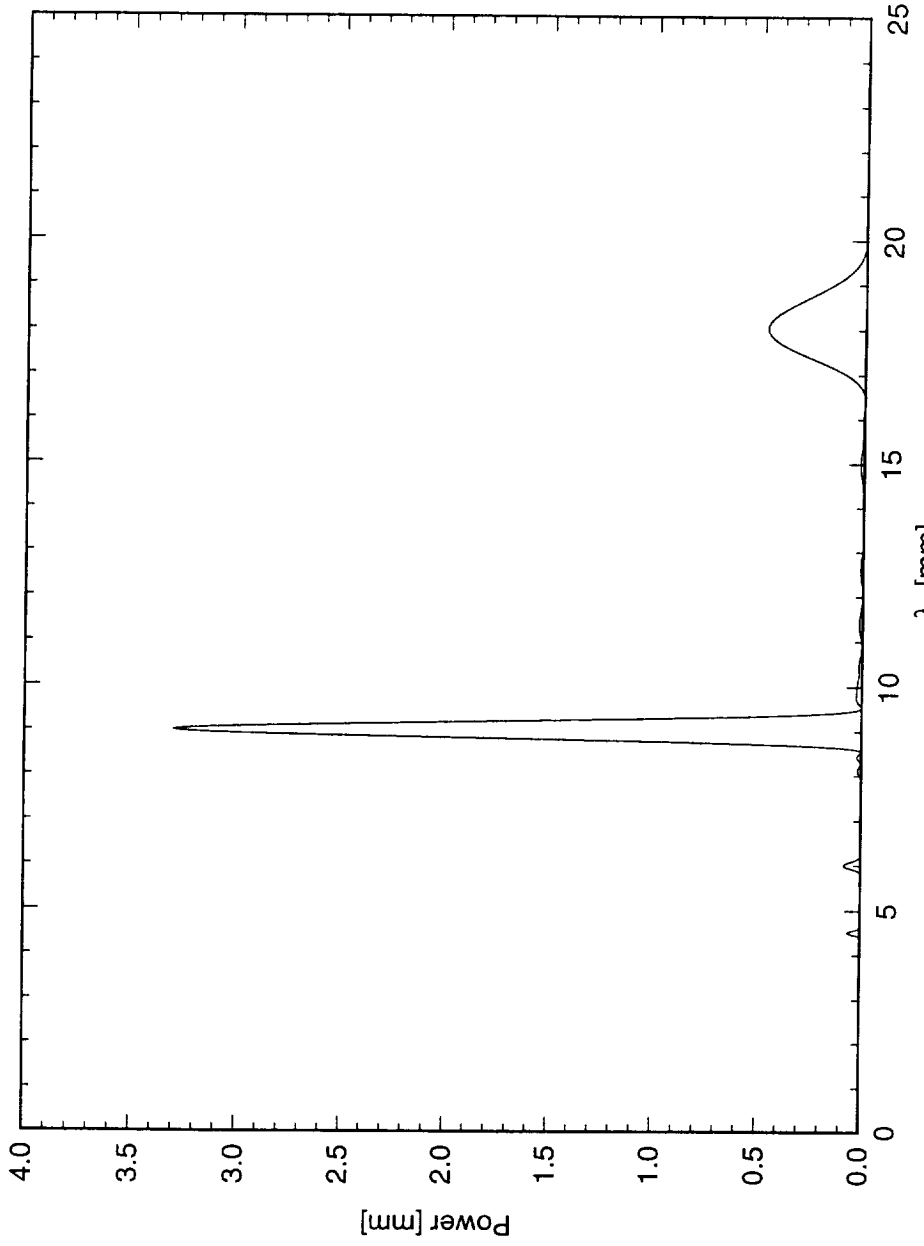

Figure 5.114: Power spectral density of constant-Y scan at $x/c = 0.40$ and $Y = 0.85$ mm. $Re_c = 2.4 \times 10^6$, [6|18] roughness.

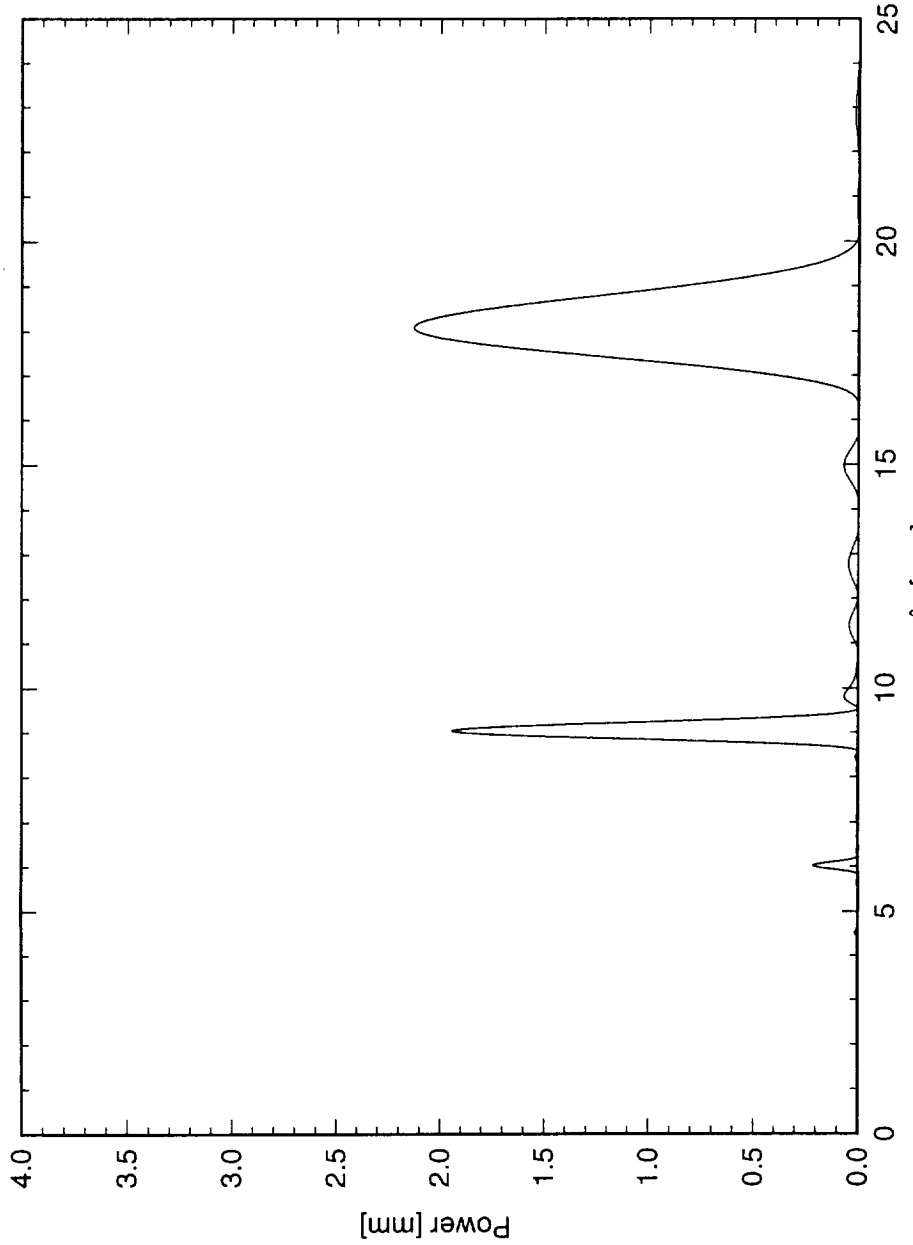

Figure 5.115: Power spectral density of constant-Y scan at $x/c = 0.45$ and $Y = 0.85$ mm. $Re_c = 2.4 \times 10^6$, [6|18] roughness.

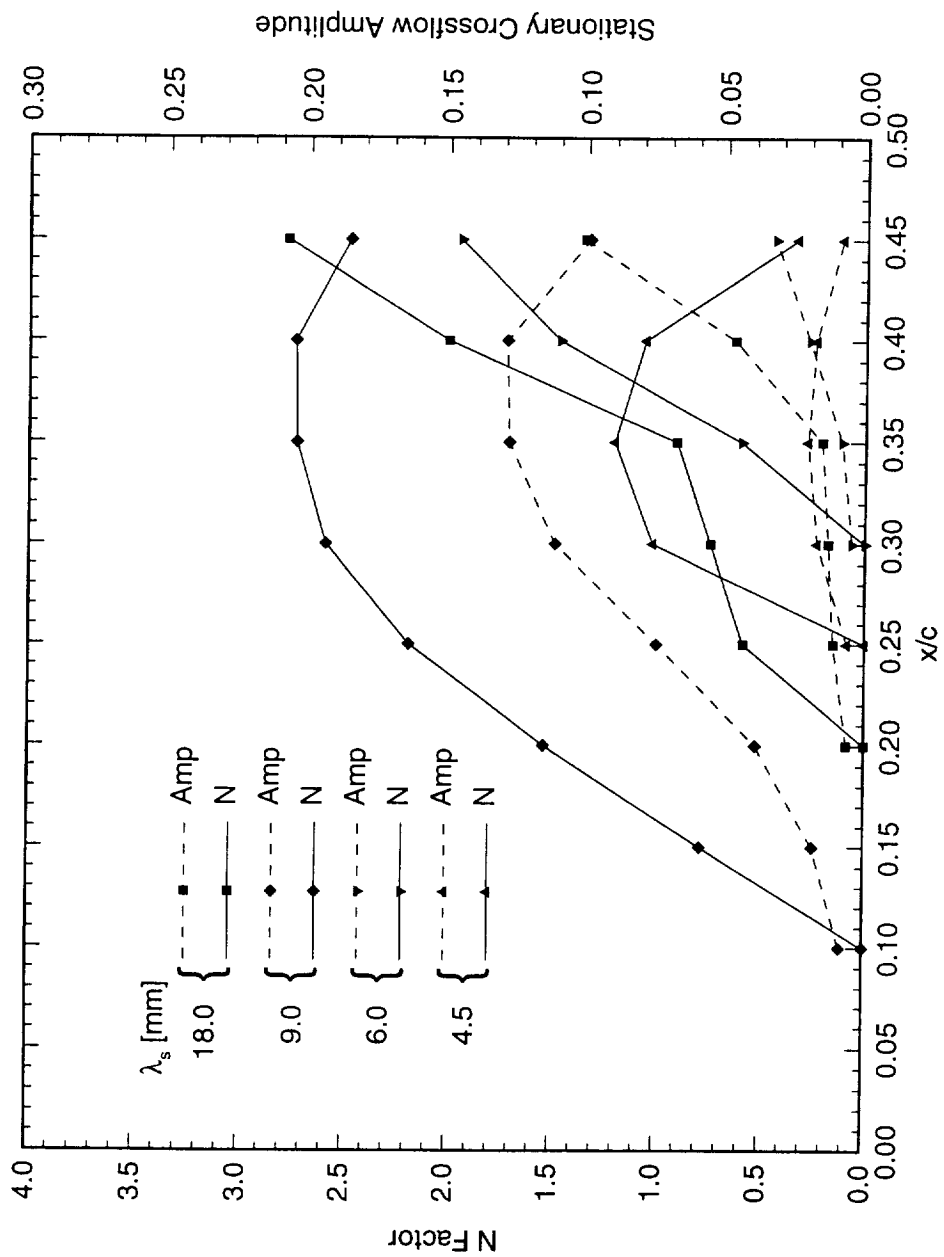

Figure 5.116: Single-mode disturbance amplitude and N-factors. $Re_c = 2.4 \times 10^6$, [6|18] roughness. N-factor calculations are relative to the location where the disturbance is first detected.

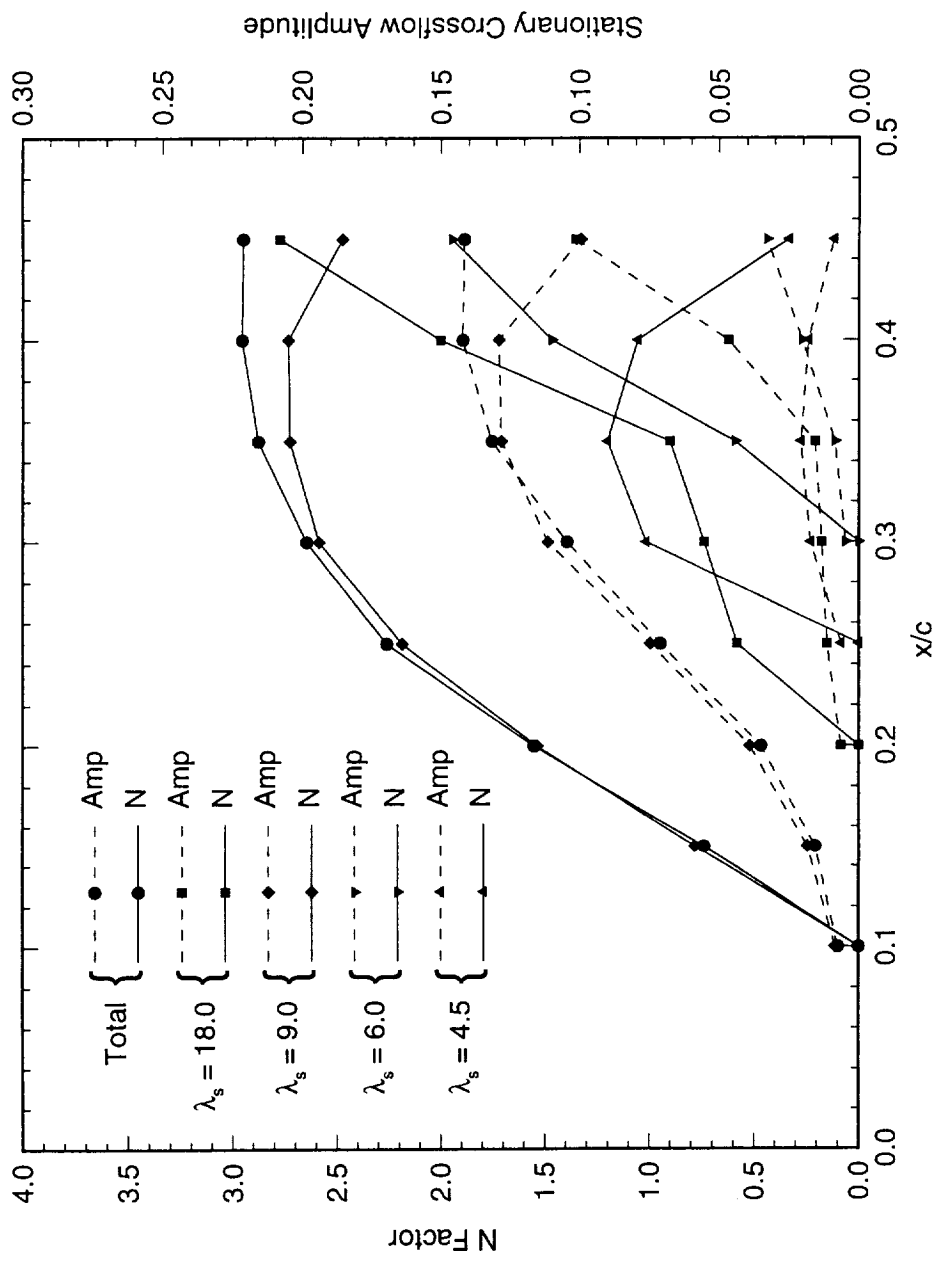

Figure 5.117: Total and single-mode disturbance amplitude and N-factors. $Re_c = 2.4 \times 10^6$, [6|18] roughness. N-factor calculations are relative to the location where the disturbance is first detected.

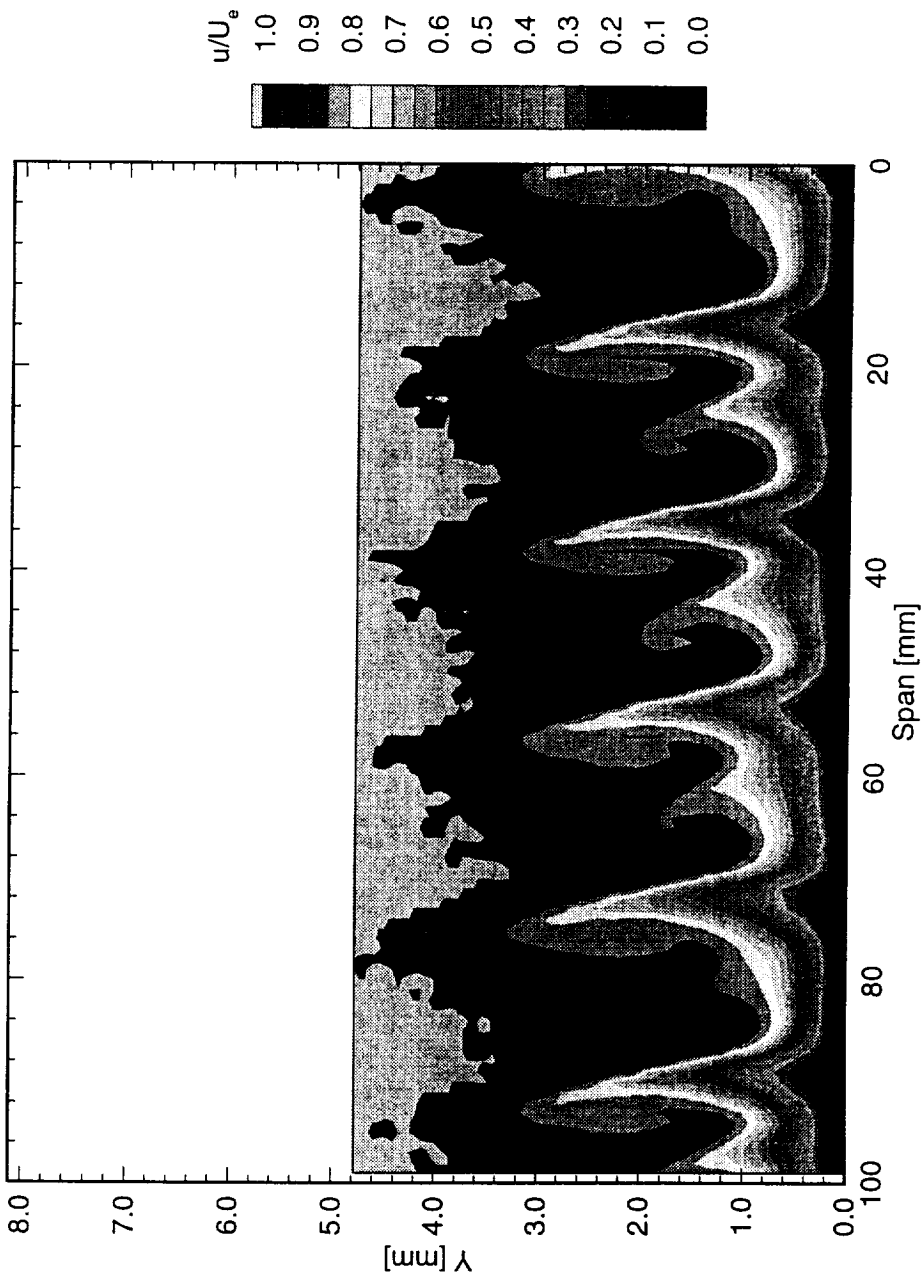

Figure 5.118: Normalized boundary-layer velocity contours at $x/c = 0.45$. $Re_c = 2.4 \times 10^6$, [12|18] roughness.

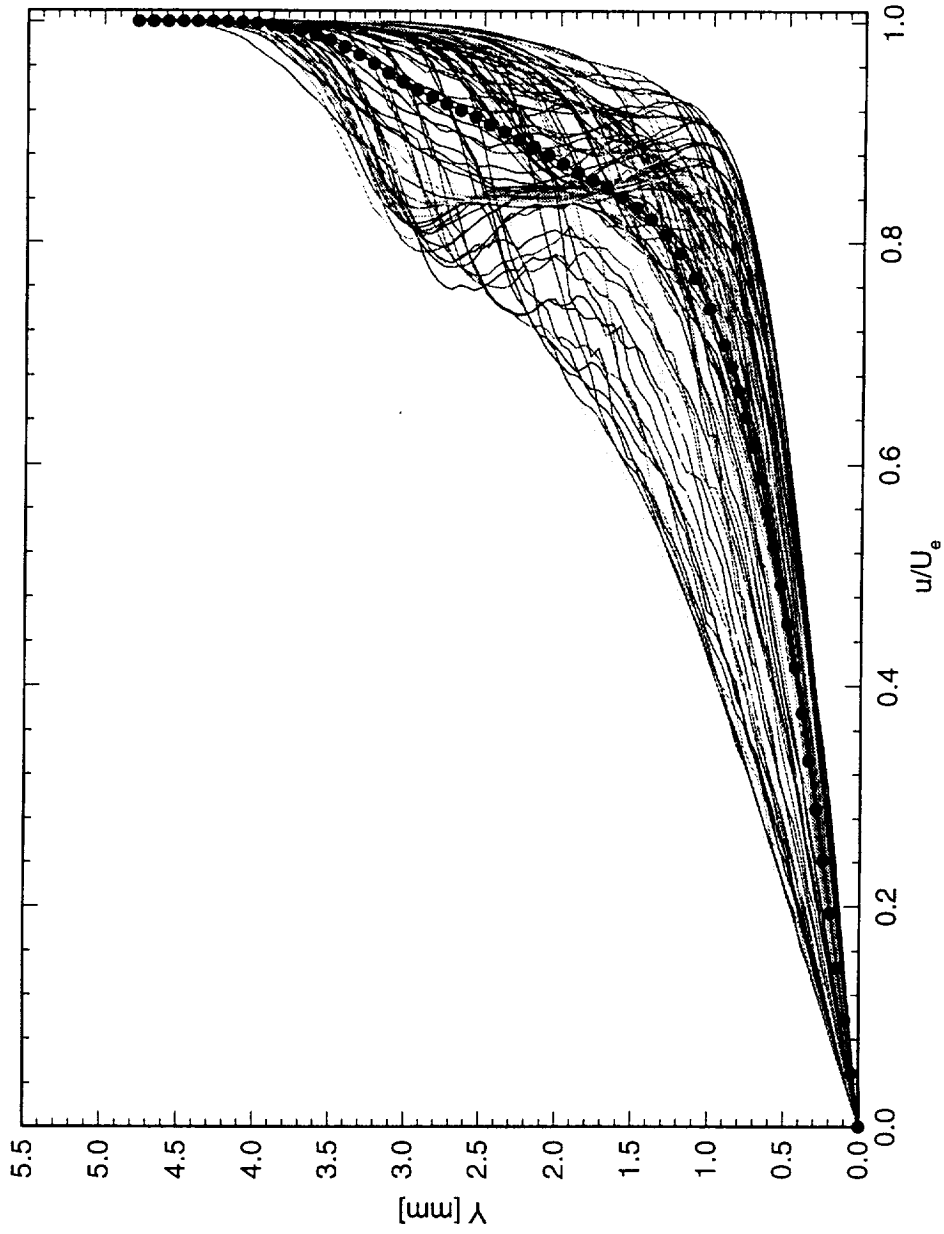

Figure 5.119: Spanwise array of 100 boundary-layer profiles spaced 1 mm apart in span at $x/c = 0.45$. $Re_c = 2.4 \times 10^6$, [12|18] roughness. The dots represent the spanwise average of the profiles.

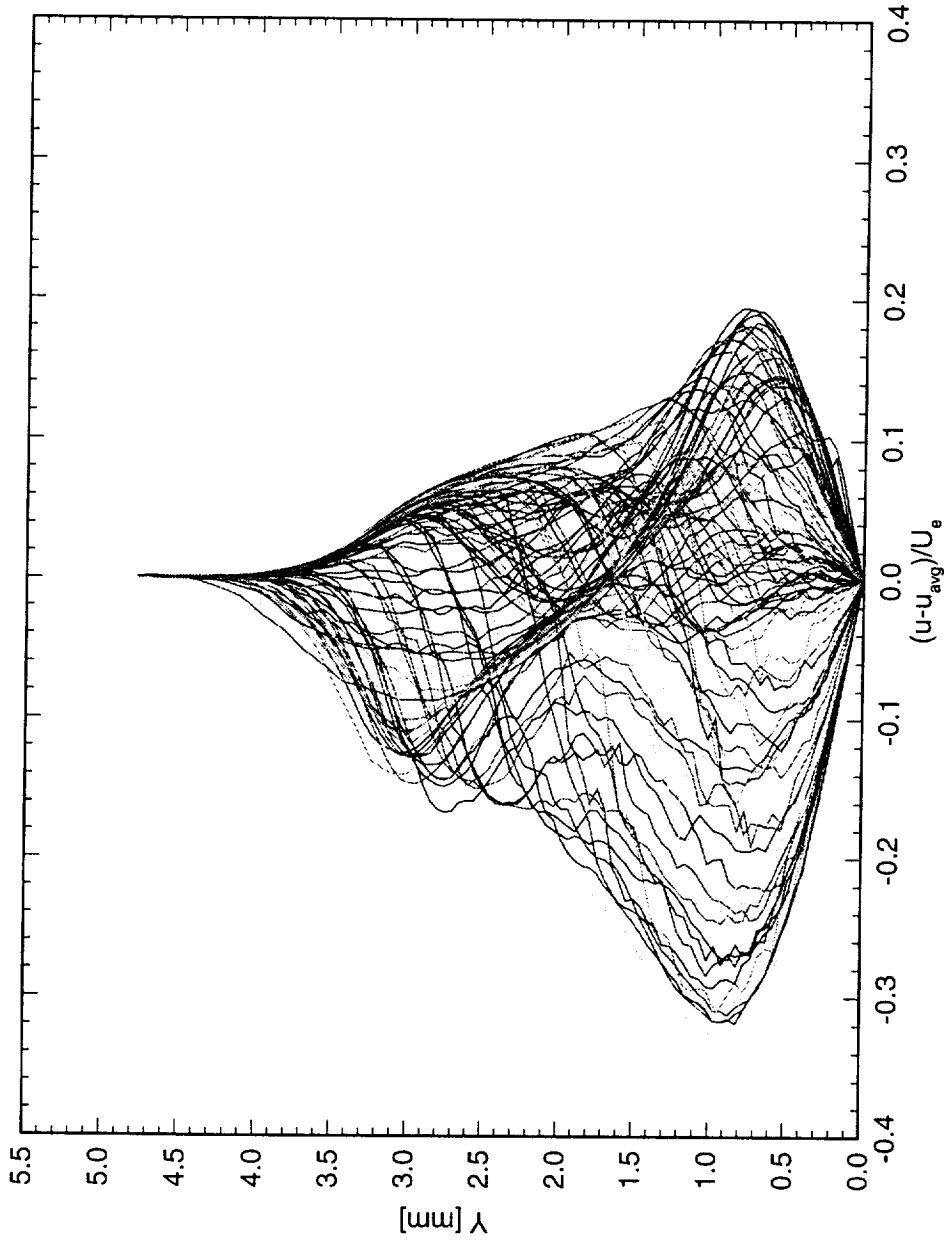

Figure 5.120: Spanwise array of 100 disturbance profiles spaced 1 mm apart in span at $x/c = 0.45$. $Re_c = 2.4 \times 10^6$, [12|18] roughness.

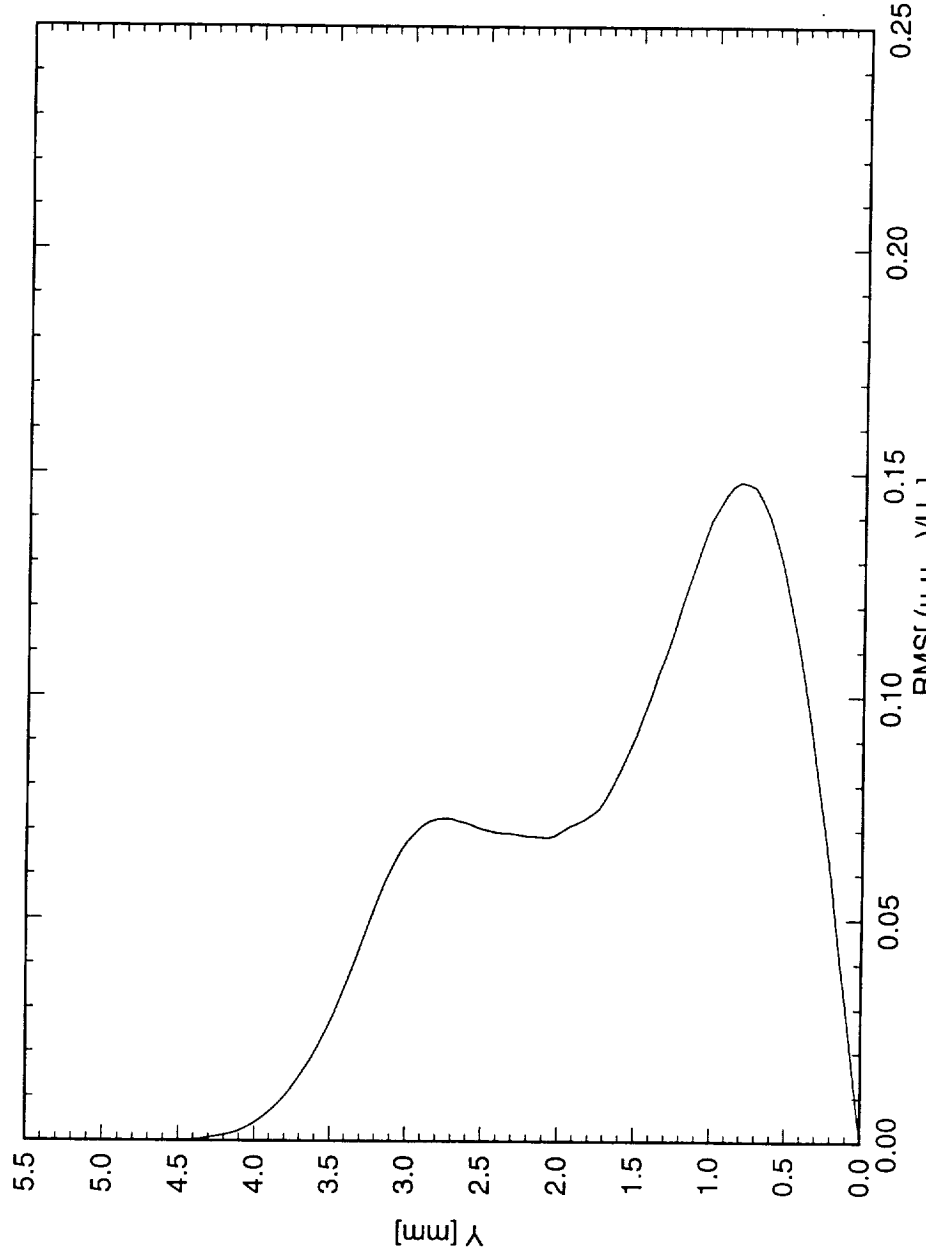

Figure 5.121: Stationary crossflow mode shape at $x/c = 0.45$. $Re_c = 2.4 \times 10^6$, [12|18] roughness.

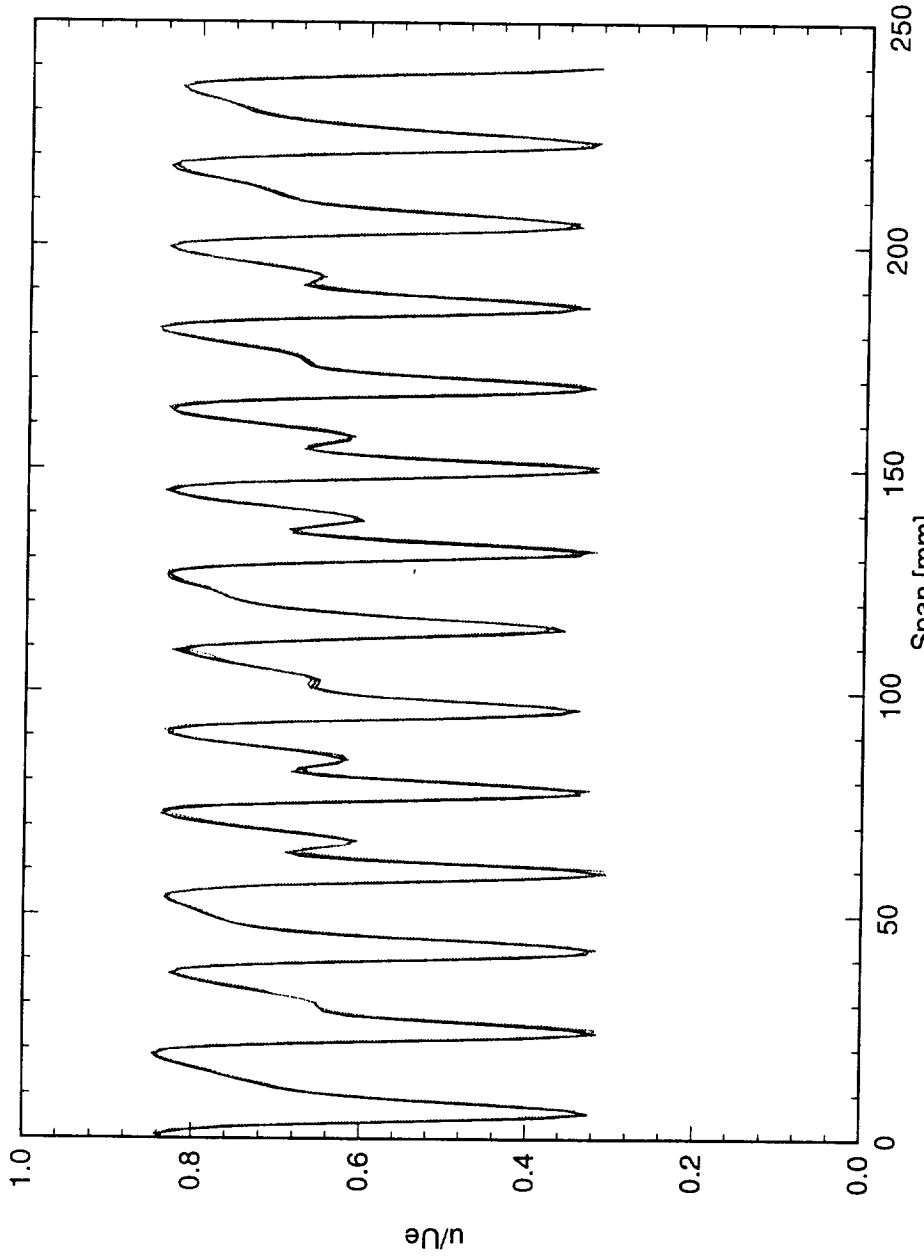

Figure 5.122: Spanwise hot-wire scan at $x/c = 0.45$ and $Y = 0.80$ mm. $Re_c = 2.4 \times 10^6$, [12|18] roughness.

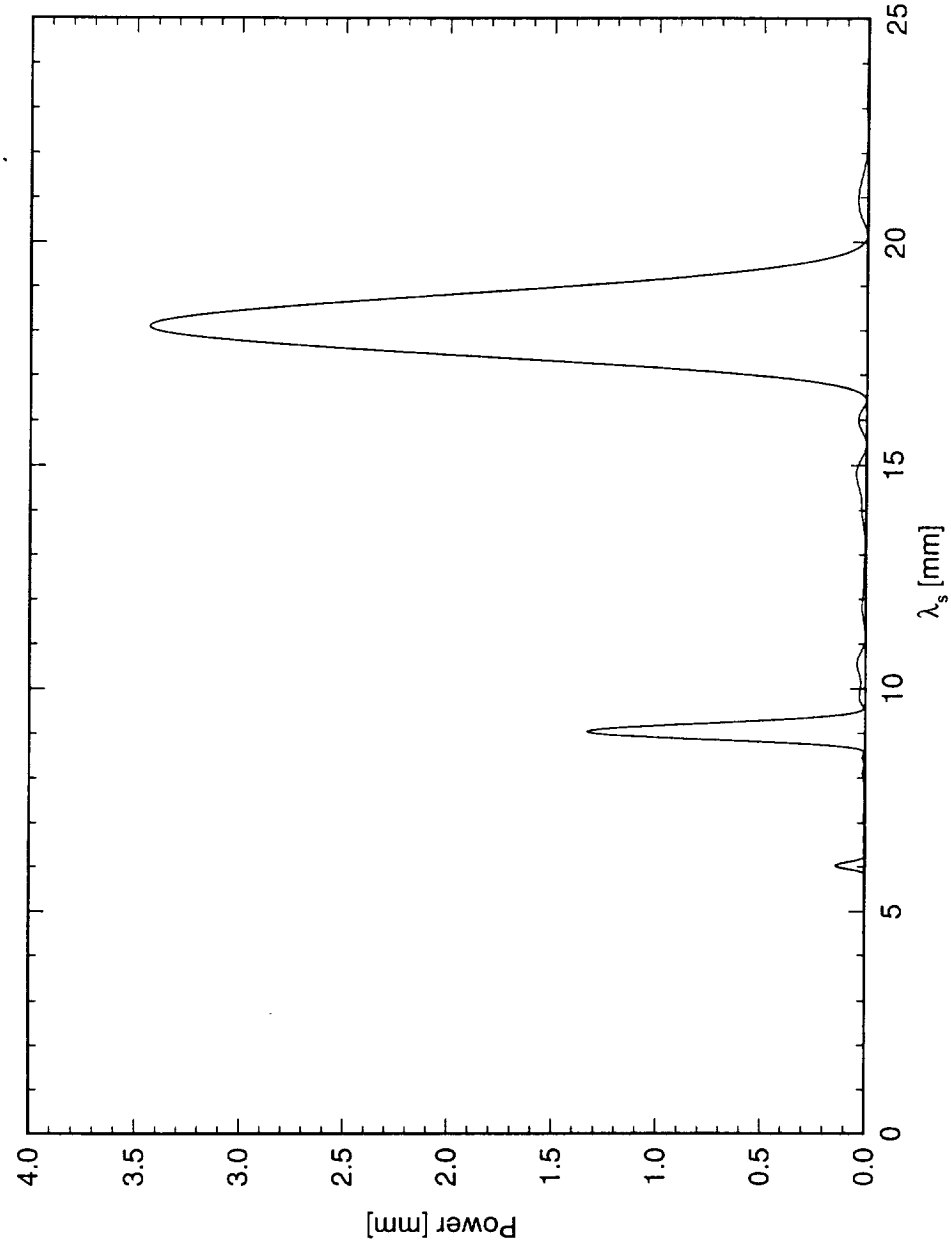

Figure 5.123: Power spectral density of constant-Y scan at $x/c = 0.45$ and $Y = 0.80$ mm. $Re_c = 2.4 \times 10^6$, [12|18] roughness.

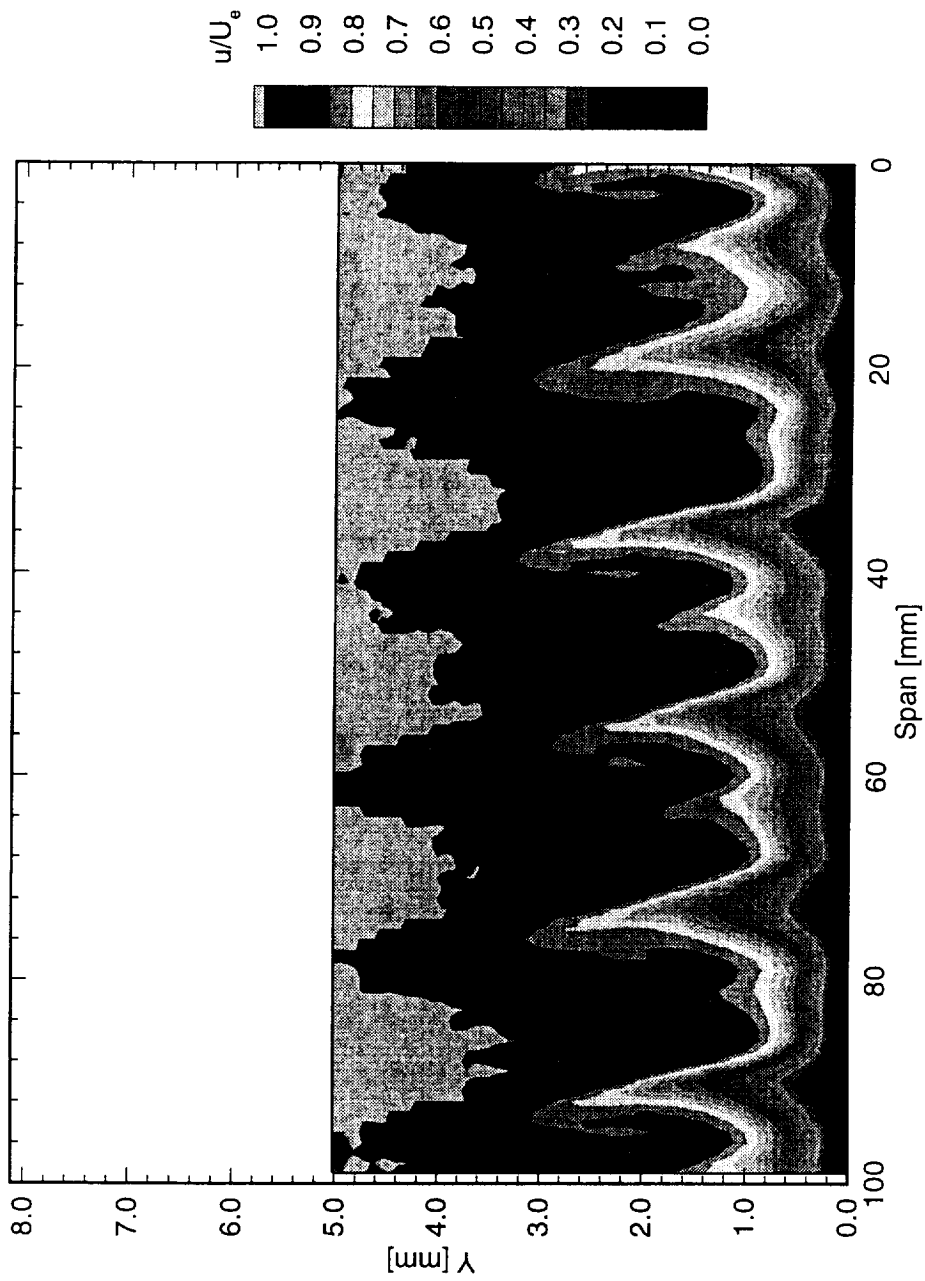

Figure 5.124: Normalized boundary-layer velocity contours at $x/c = 0.45$. $Re_c = 2.4 \times 10^6$, [18|18] roughness.

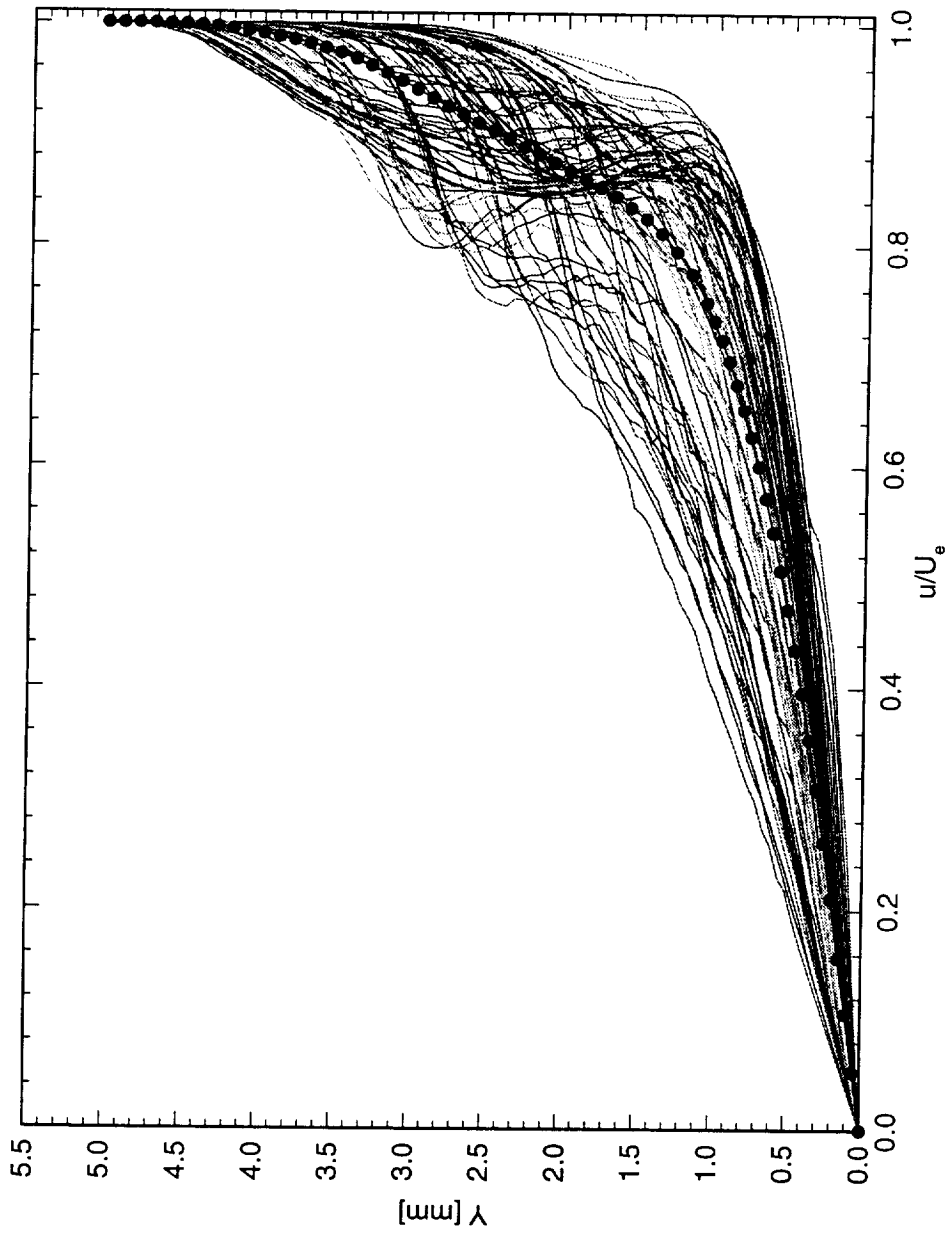

Figure 5.125: Spanwise array of 100 boundary-layer profiles spaced 1 mm apart in span at $x/c = 0.45$. $Re_c = 2.4 \times 10^6$, [18|18] roughness. The dots represent the spanwise average of the profiles.

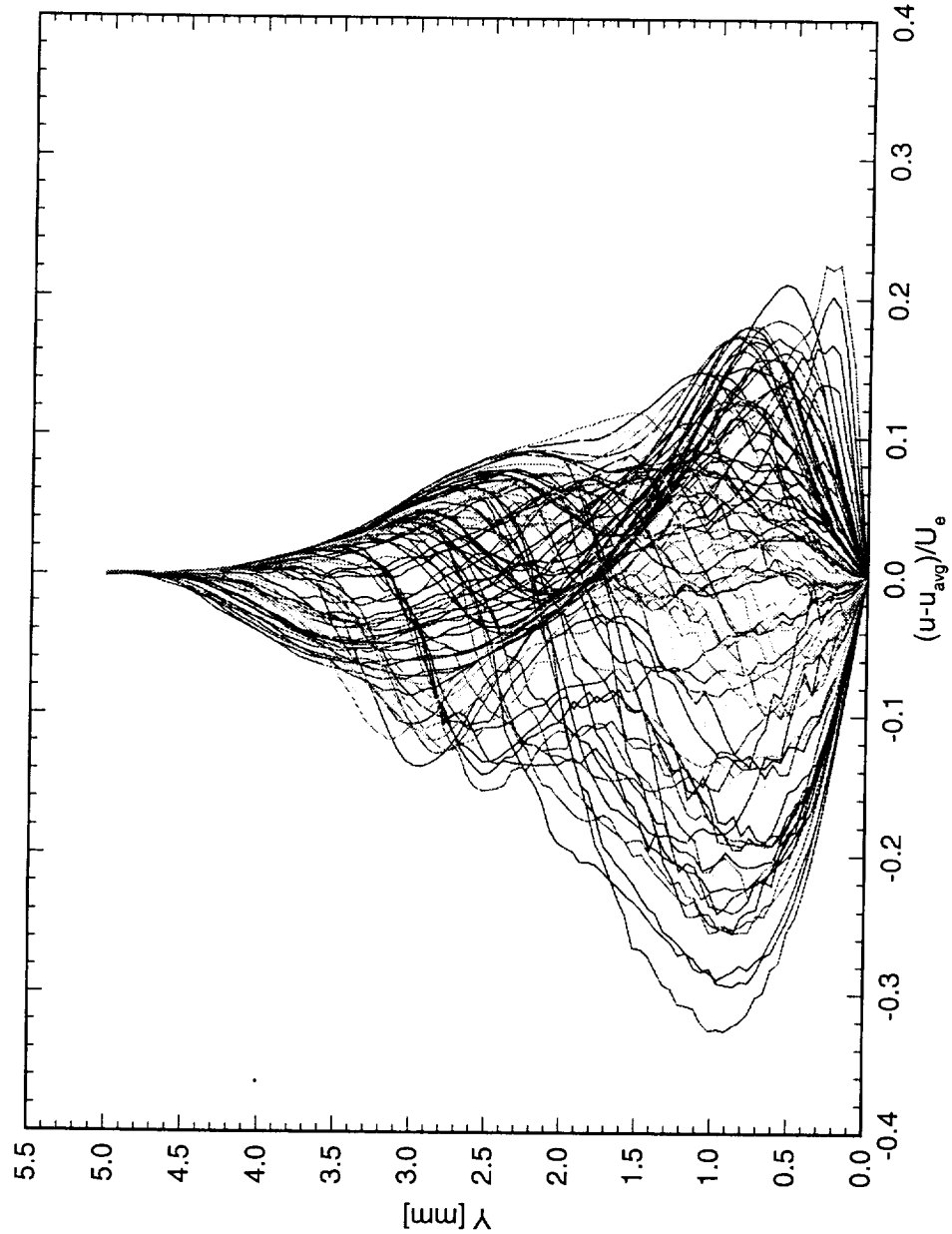

Figure 5.126: Spanwise array of 100 disturbance profiles spaced 1 mm apart in span at $x/c = 0.45$. $Re_c = 2.4 \times 10^6$, [18|18] roughness.

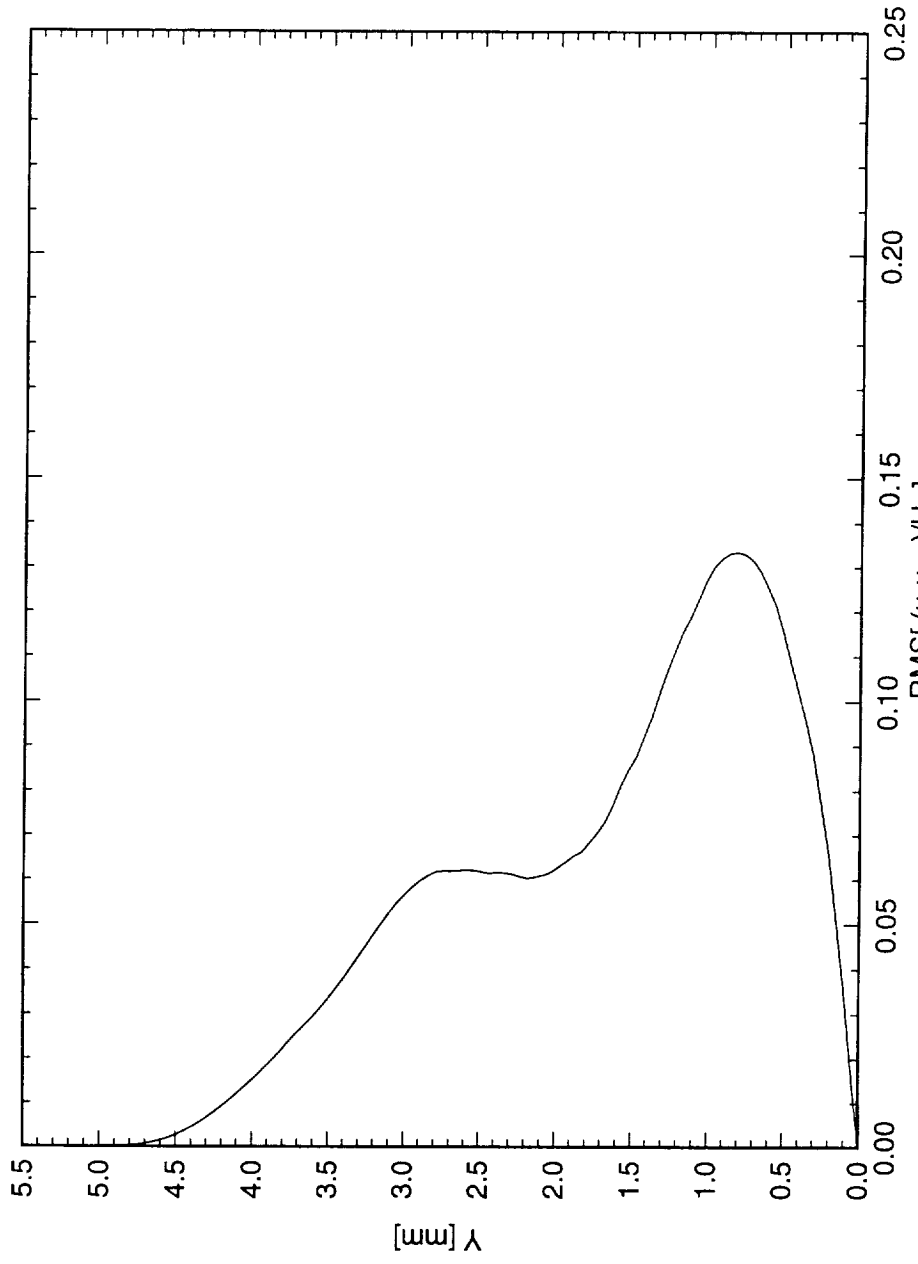

Figure 5.127: Stationary crossflow mode shape at $x/c = 0.45$. $Re_c = 2.4 \times 10^6$, [18|18] roughness.

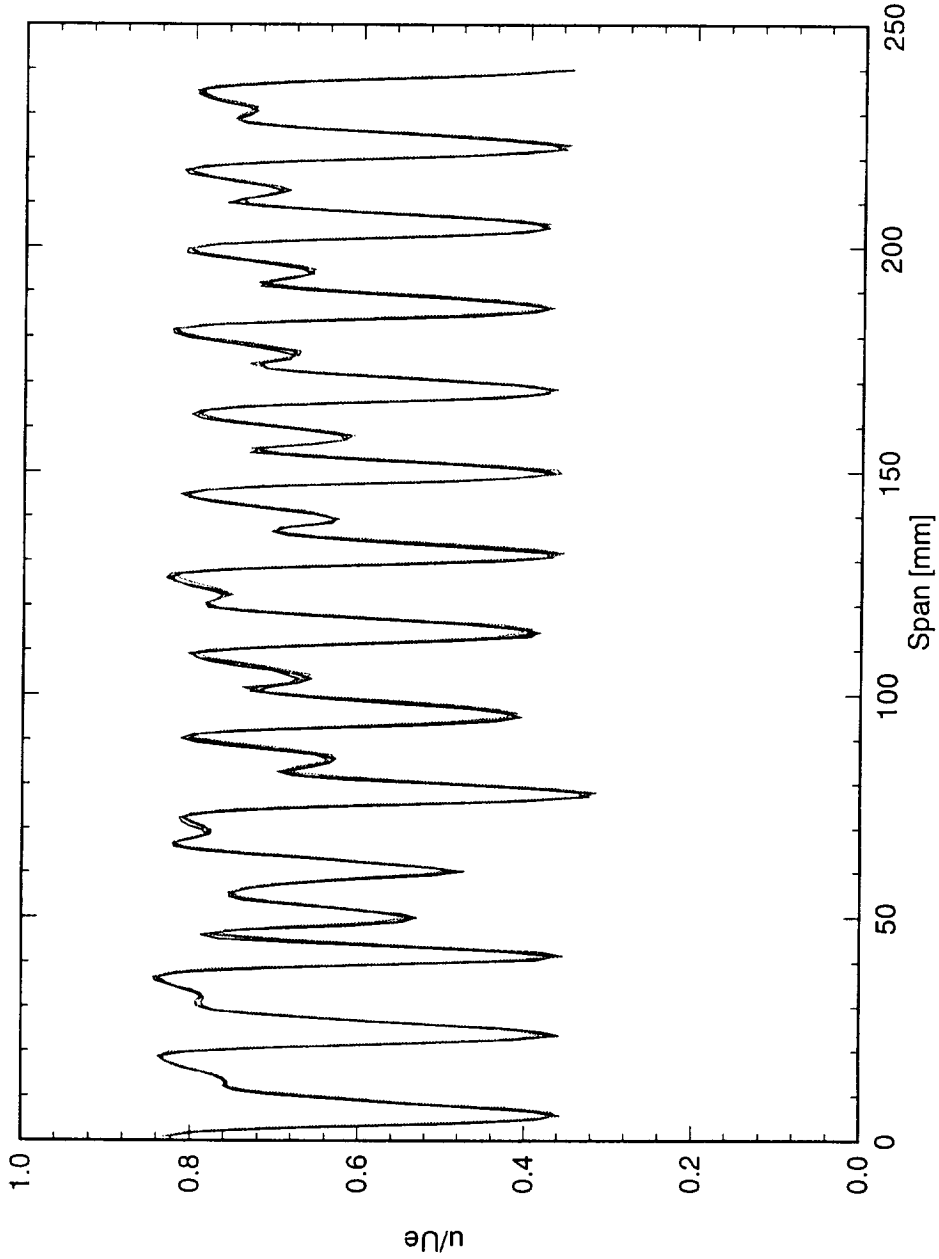

Figure 5.128: Spanwise hot-wire scan at $x/c = 0.45$ and $Y = 0.80$ mm. $Re_c = 2.4 \times 10^6$, [18|18] roughness.

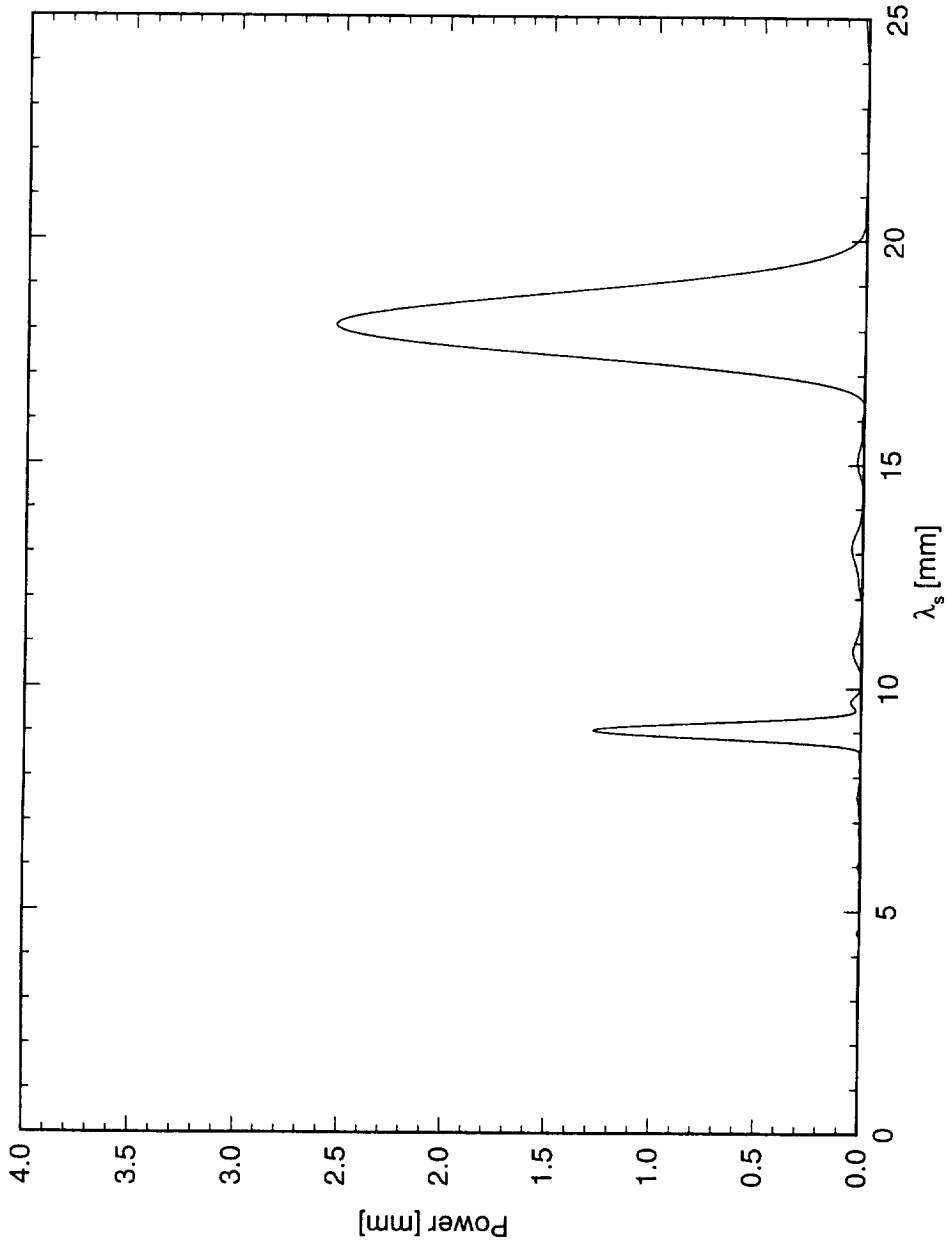

Figure 5.129: Power spectral density of constant-Y scan at $x/c = 0.45$ and $Y = 0.80$ mm. $Re_c = 2.4 \times 10^6$, [18|18] roughness.

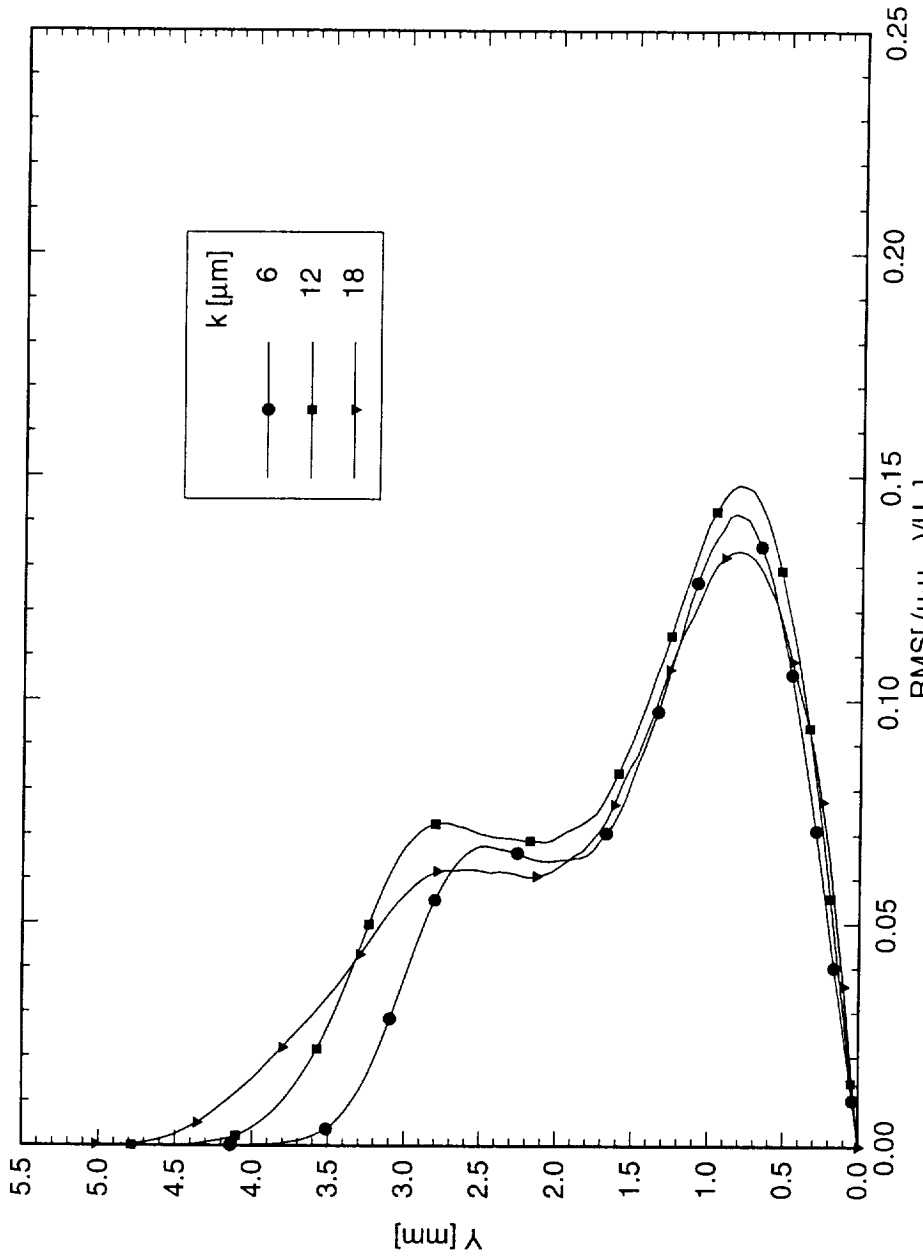

Figure 5.130: Stationary crossflow mode shapes at $x/c = 0.45$ for $Re_c = 2.4 \times 10^6$ and $[k|18]$ roughness. The symbols are merely indicators and do not represent measurement points.

Figure 5.131: Naphthalene flow visualization for $Re_c = 2.4 \times 10^6$, [6|8] roughness.

Figure 5.132: Naphthalene flow visualization for $Re_c = 2.6 \times 10^6$, [6|8] roughness.

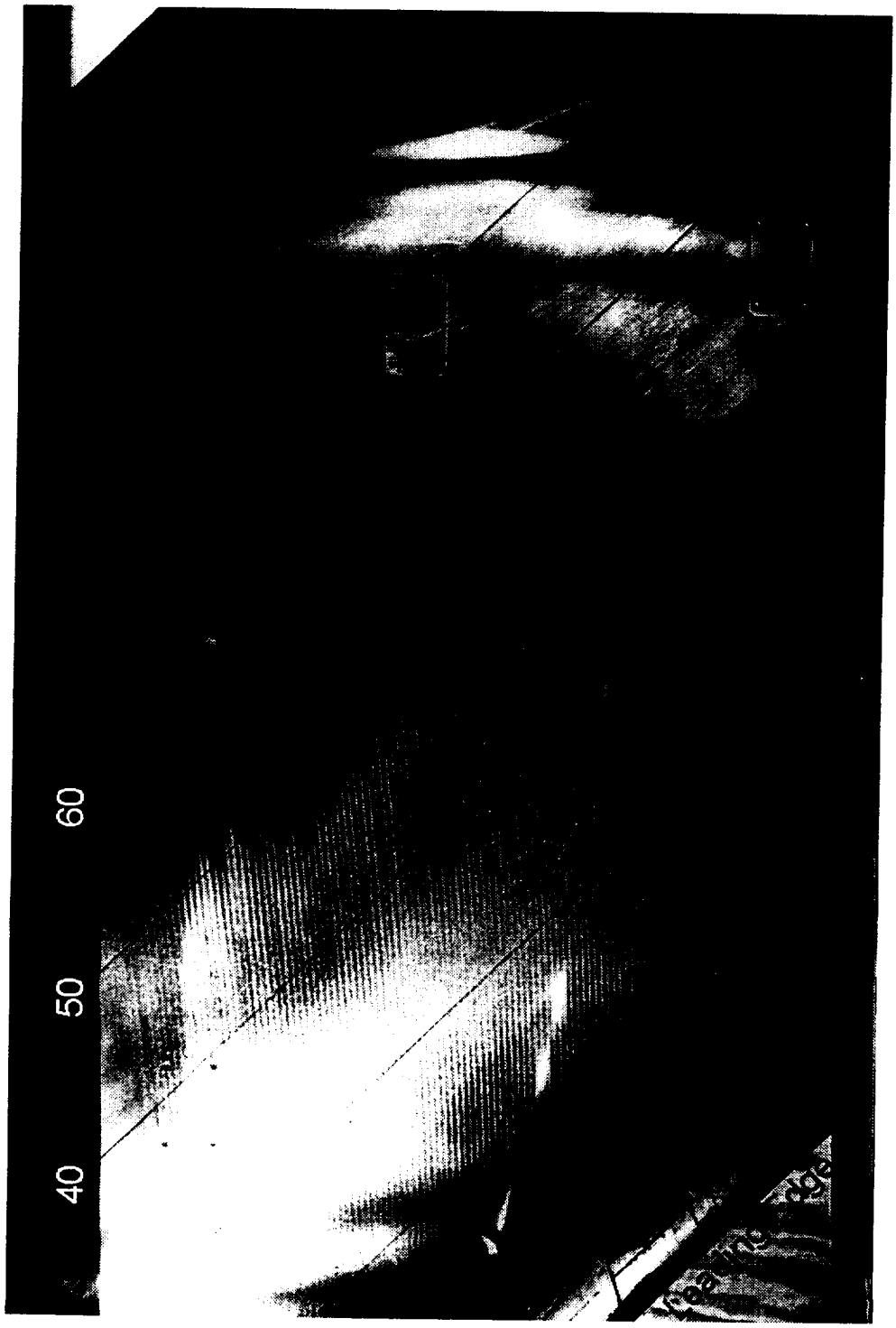

Figure 5.133: Naphthalene flow visualization for $Re_c = 2.8 \times 10^6$, [6|8] roughness.

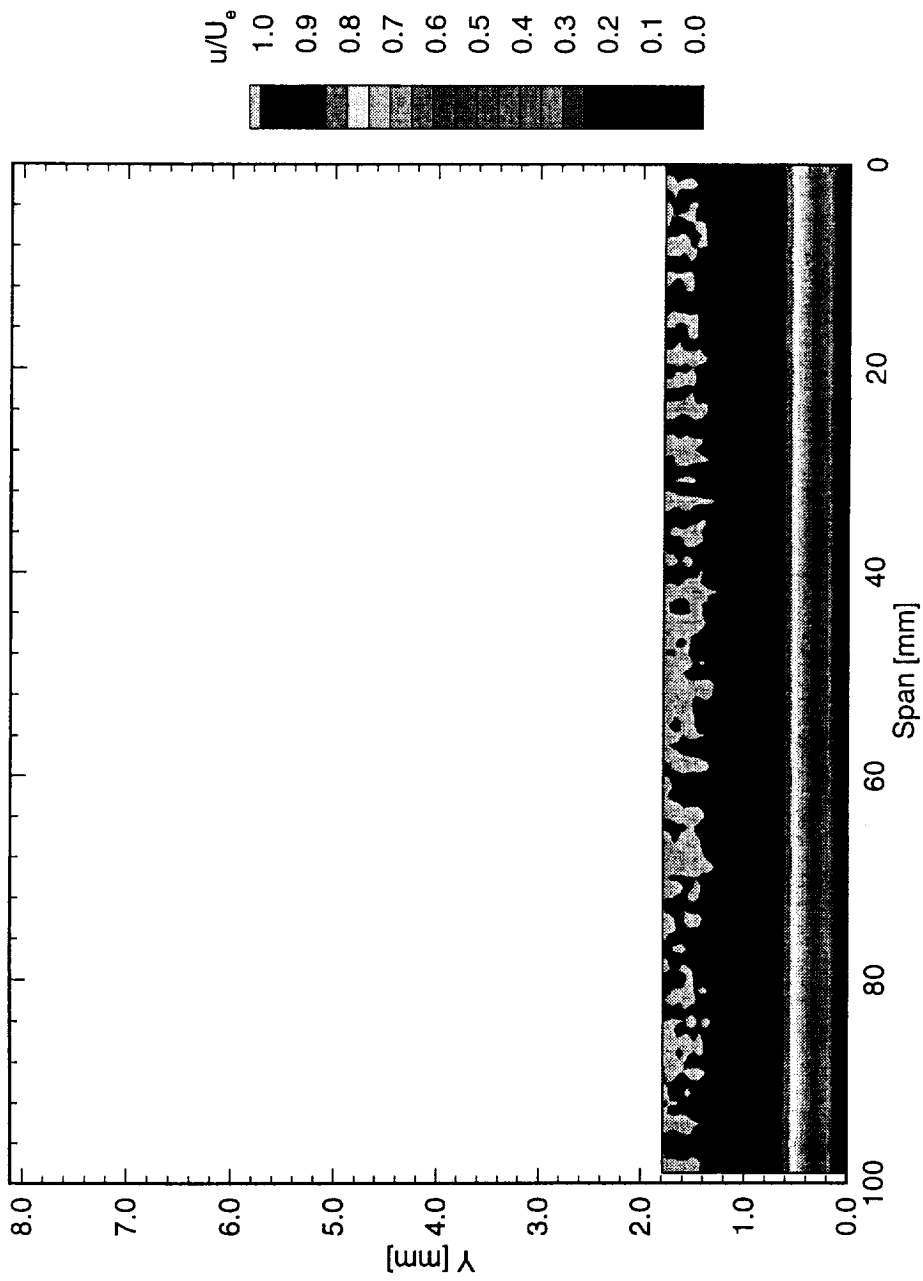

Figure 5.134: Normalized boundary-layer velocity contours at $x/c = 0.05$. $Re_c = 2.4 \times 10^6$, [6|8] roughness.

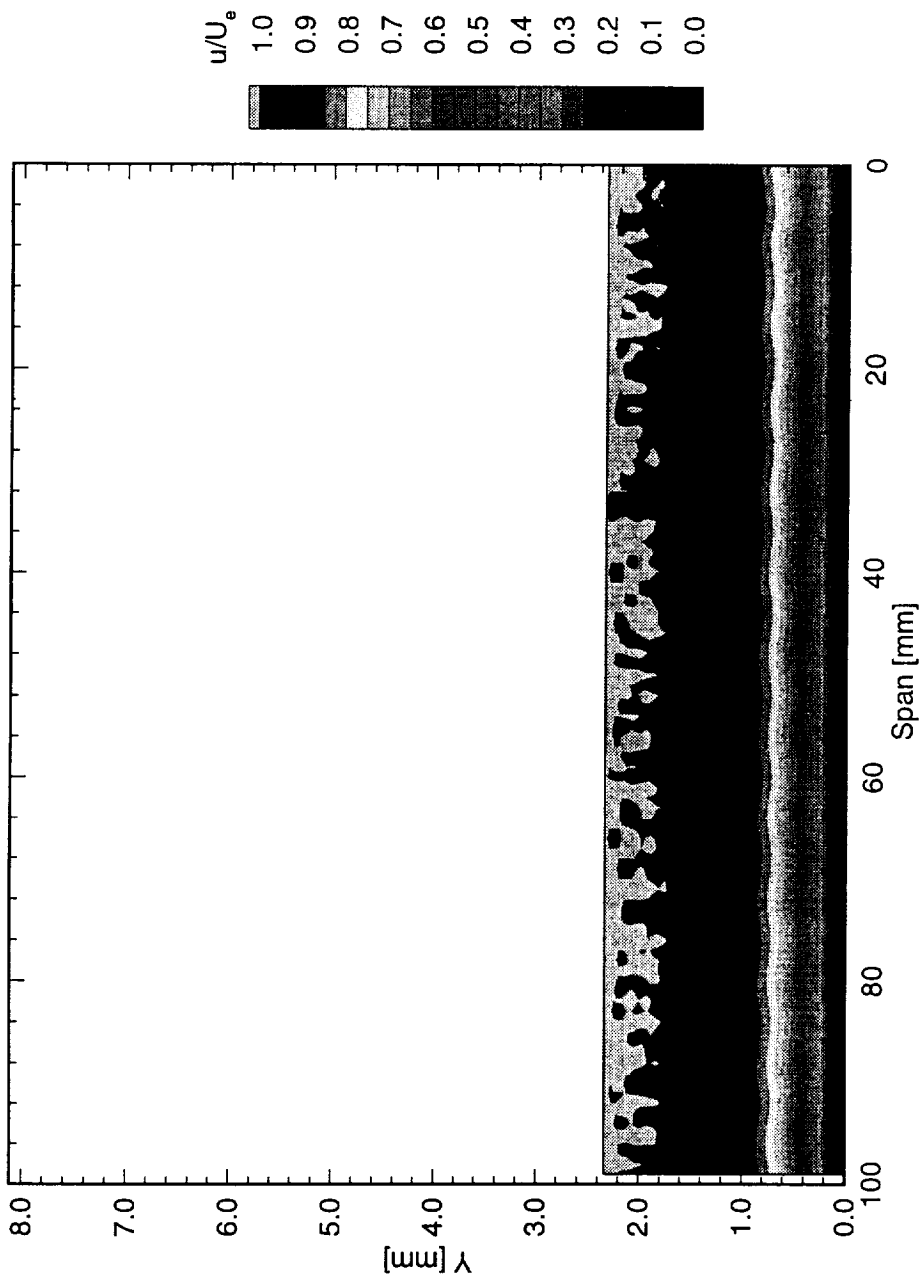

Figure 5.135: Normalized boundary-layer velocity contours at $x/c = 0.10$. $Re_c = 2.4 \times 10^6$, [6|8] roughness.

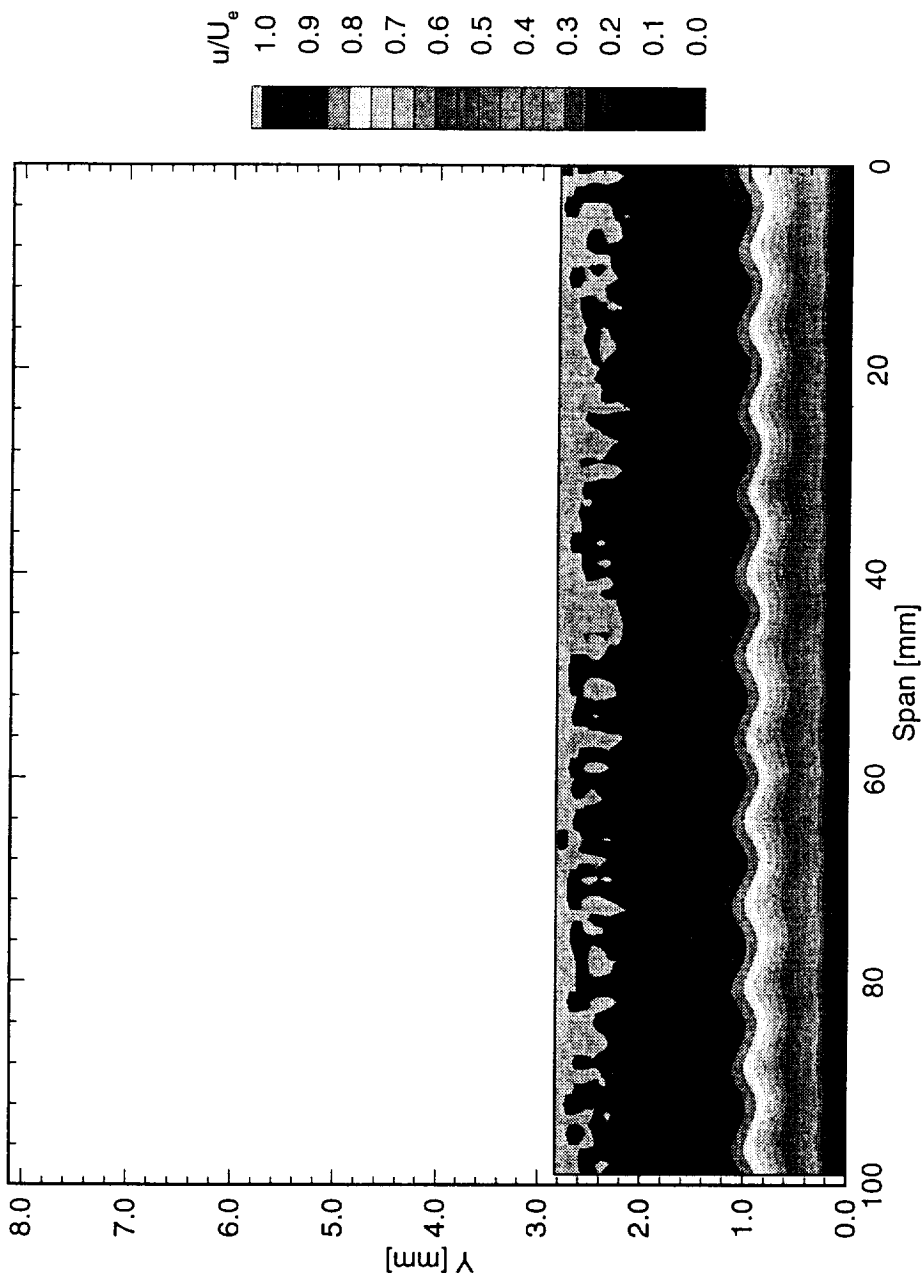

Figure 5.136: Normalized boundary-layer velocity contours at $x/c = 0.15$. $Re_c = 2.4 \times 10^6$, [6|8] roughness.

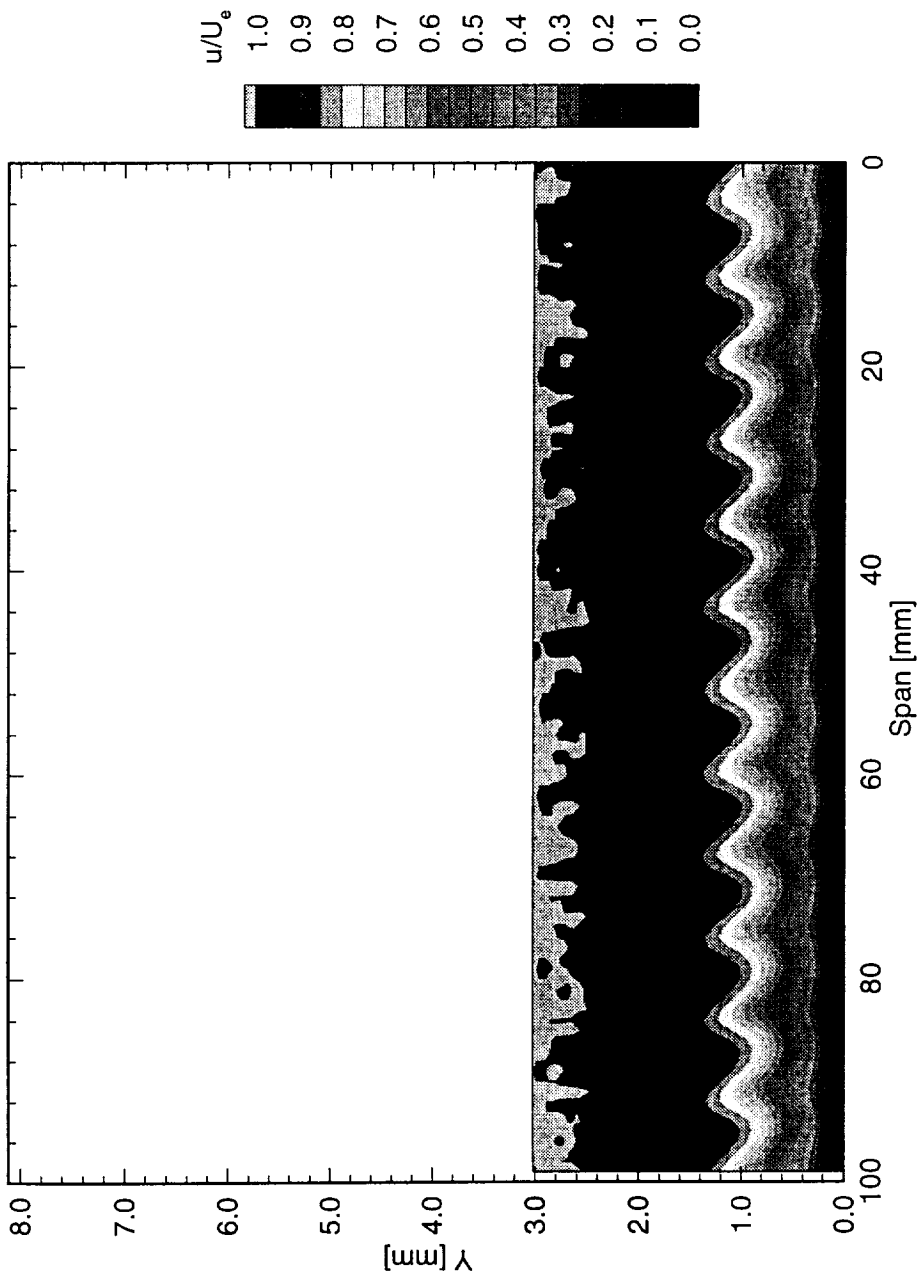

Figure 5.137: Normalized boundary-layer velocity contours at $x/c = 0.20$. $Re_c = 2.4 \times 10^6$, [6|8] roughness.

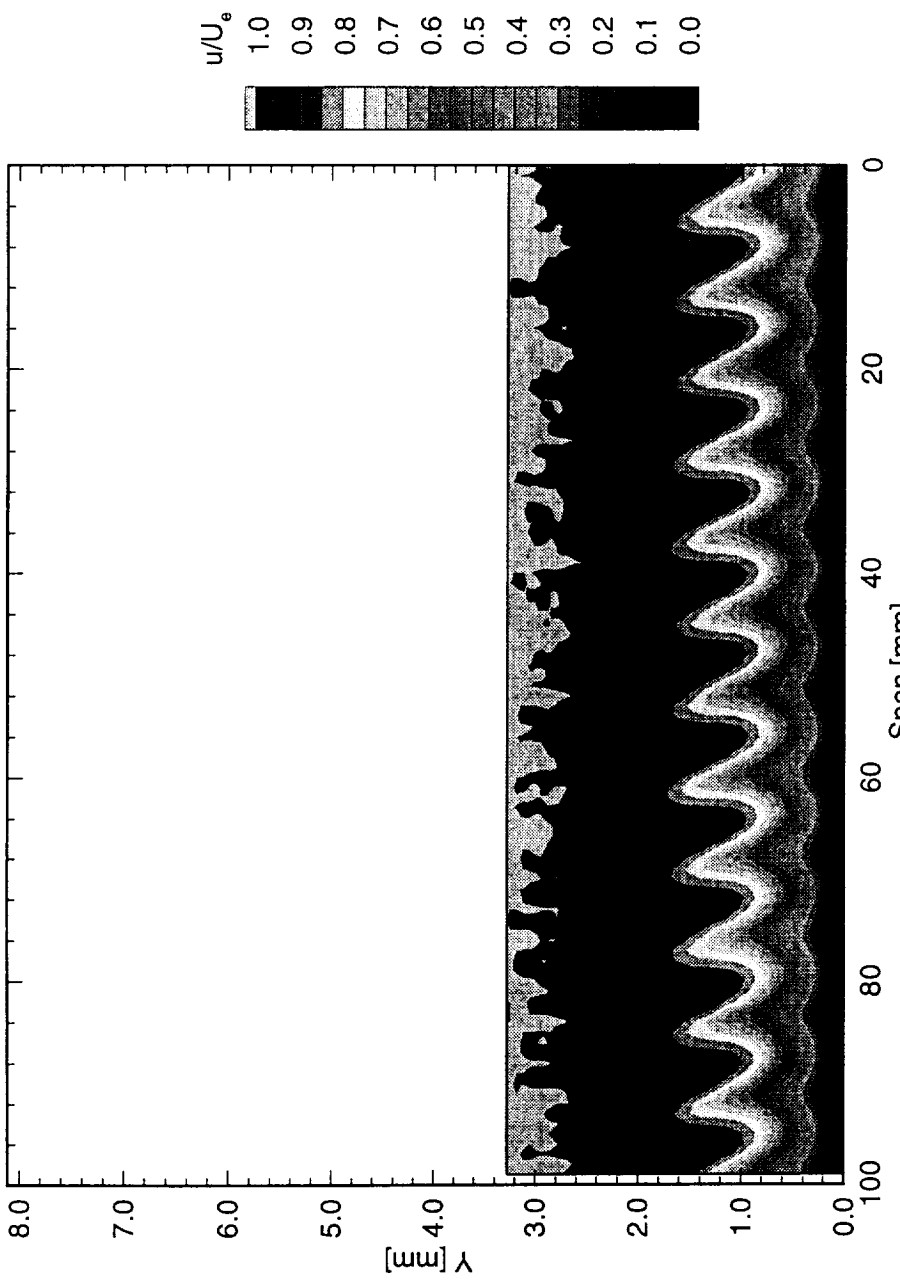

Figure 5.138: Normalized boundary-layer velocity contours at $x/c = 0.25$. $Re_c = 2.4 \times 10^6$, [6|8] roughness.

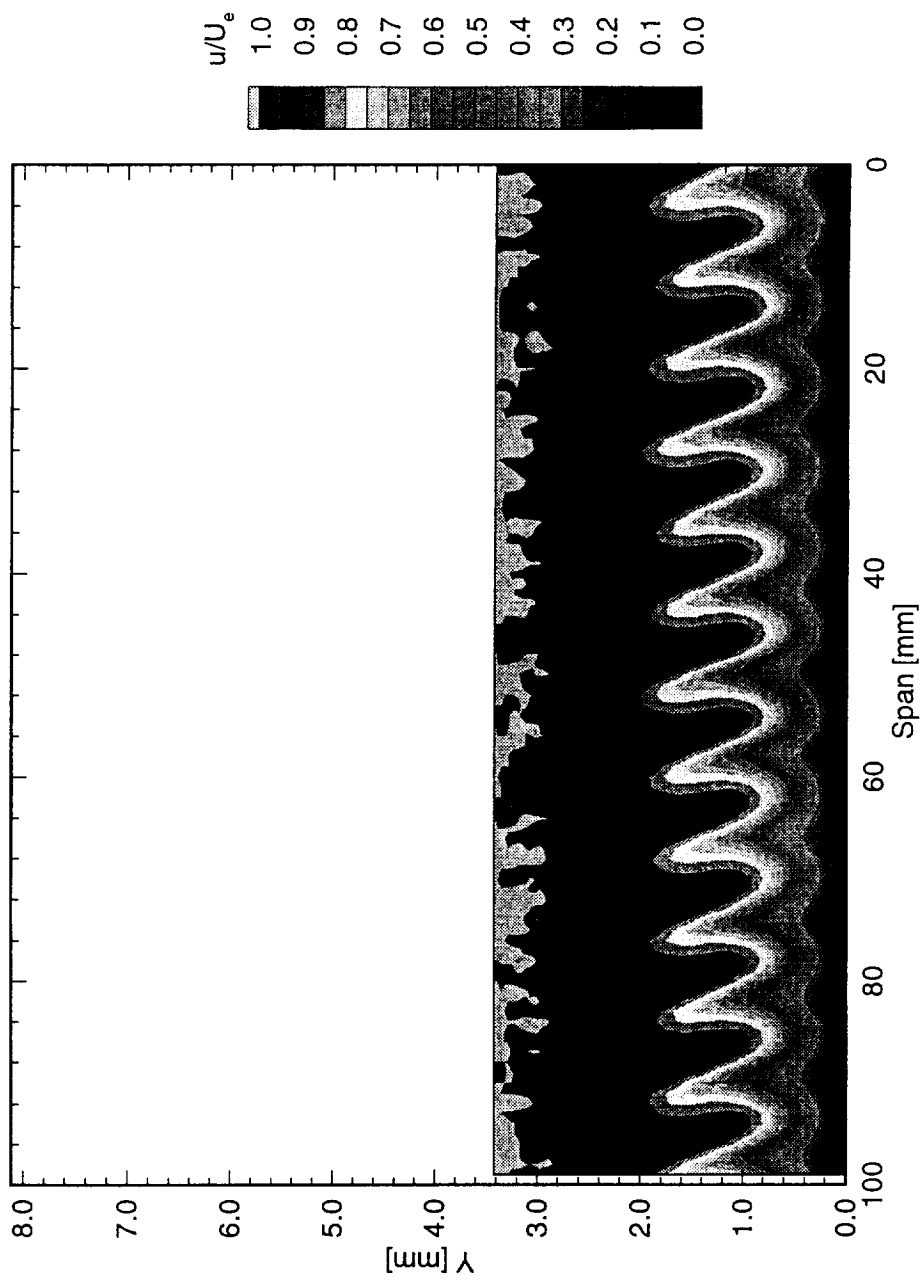

Figure 5.139: Normalized boundary-layer velocity contours at $x/c = 0.30$. $Re_c = 2.4 \times 10^6$, [6|8] roughness.

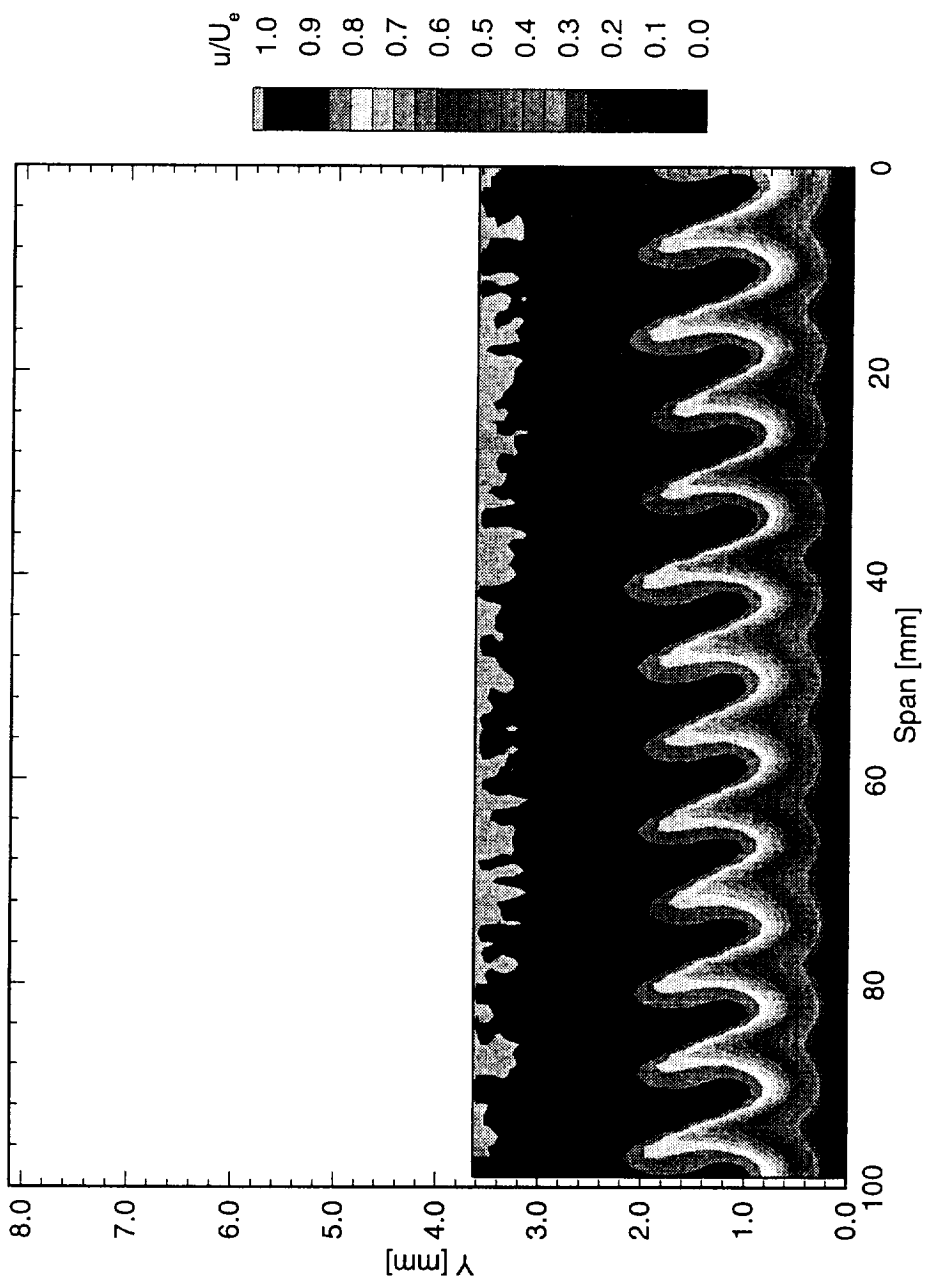

Figure 5.140: Normalized boundary-layer velocity contours at $x/c = 0.35$. $Re_c = 2.4 \times 10^6$, [6|8] roughness.

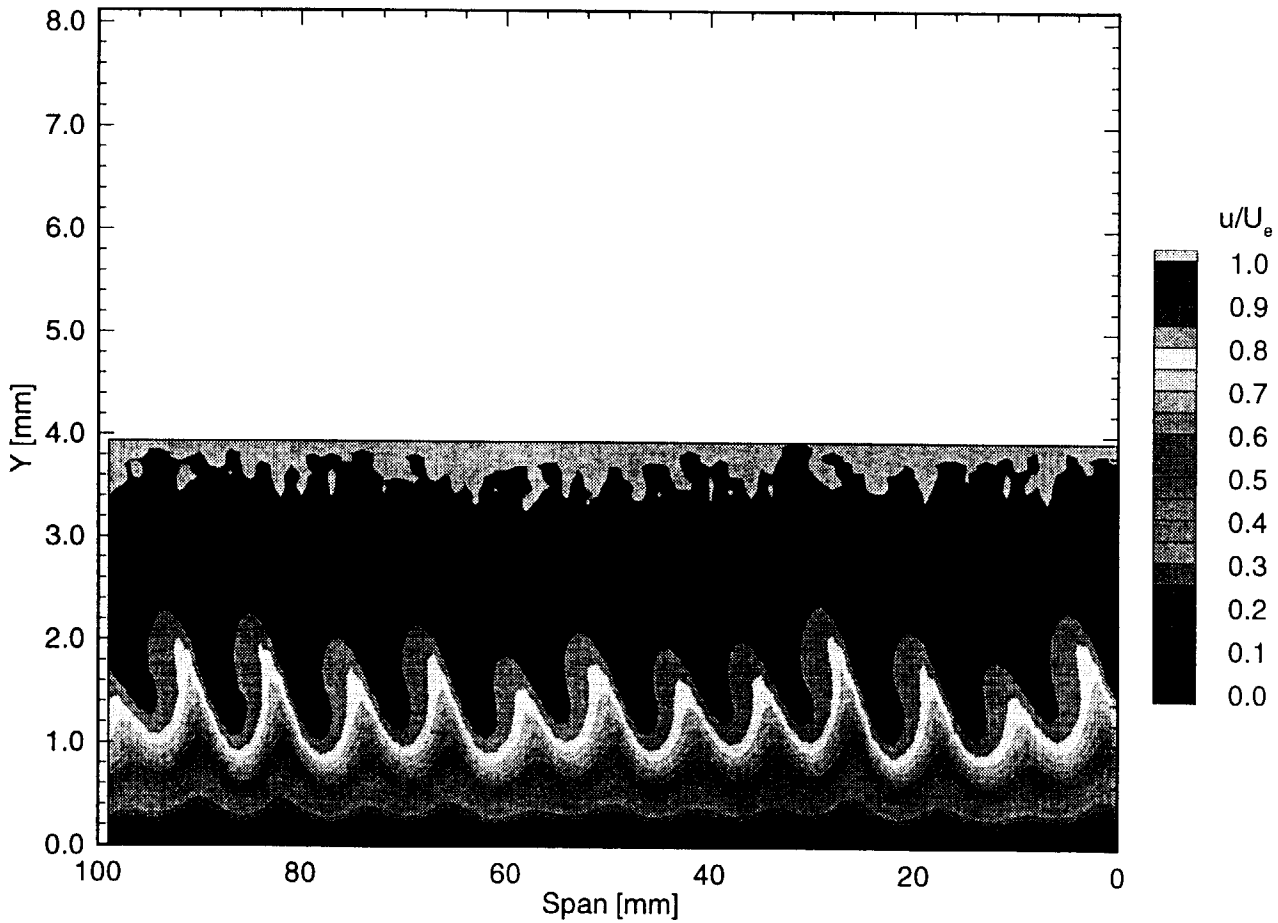

Figure 5.141: Normalized boundary-layer velocity contours at $x/c = 0.40$. $Re_c = 2.4 \times 10^6$, [6|8] roughness.

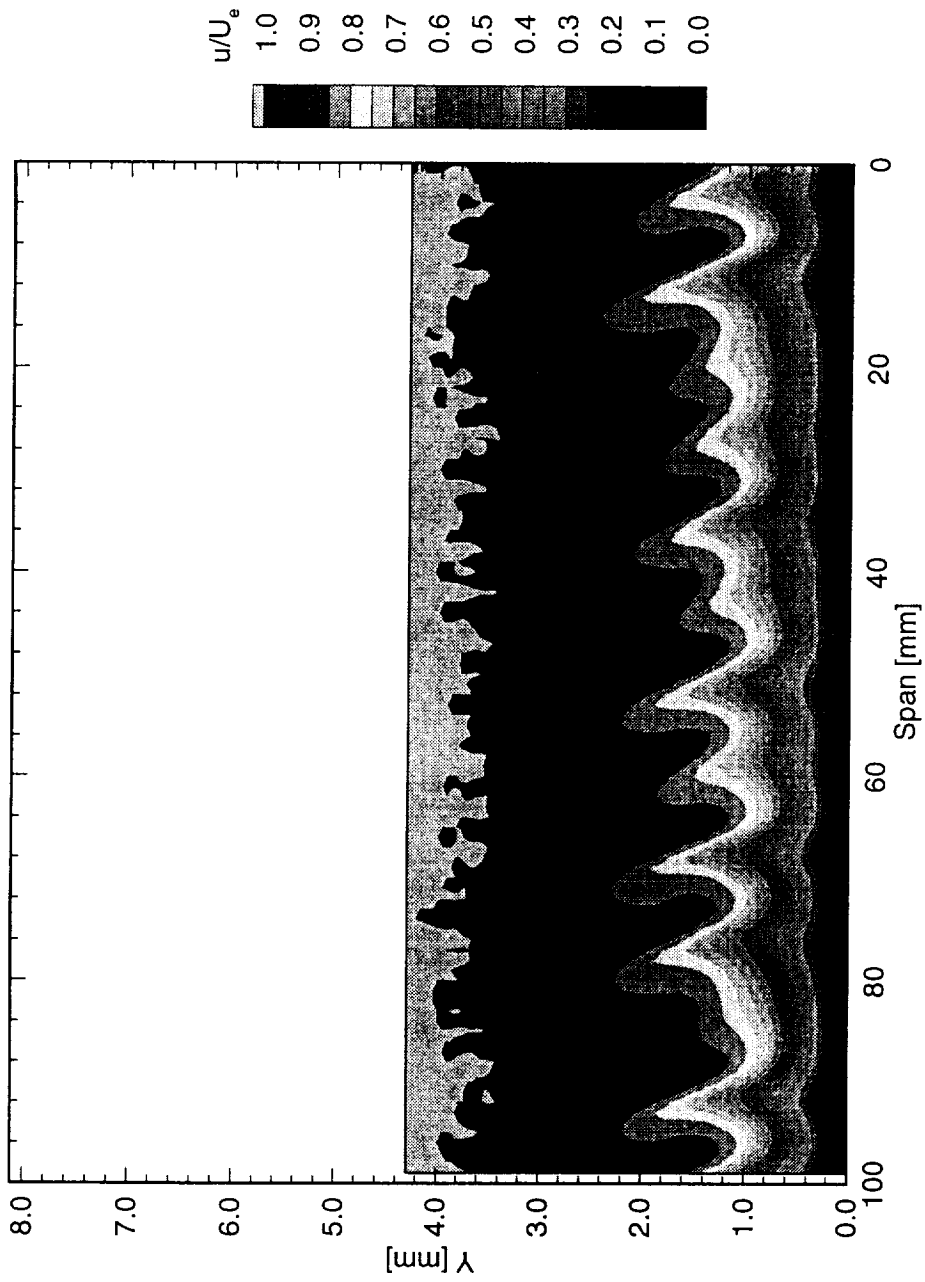

Figure 5.142: Normalized boundary-layer velocity contours at $x/c = 0.45$. $Re_c = 2.4 \times 10^6$, [6|8] roughness.

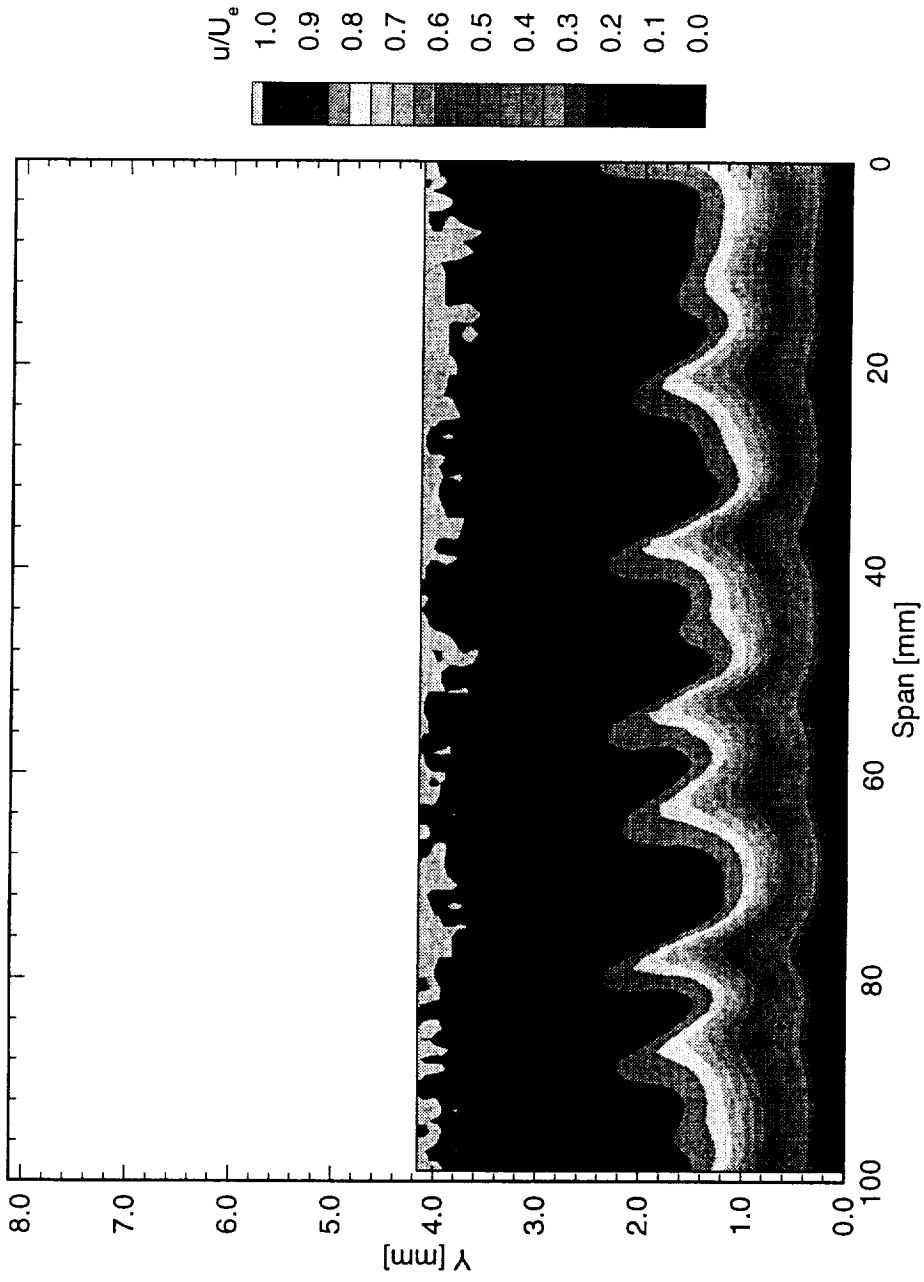

Figure 5.143: Normalized boundary-layer velocity contours at $x/c = 0.50$. $Re_c = 2.4 \times 10^6$, [6|8] roughness.

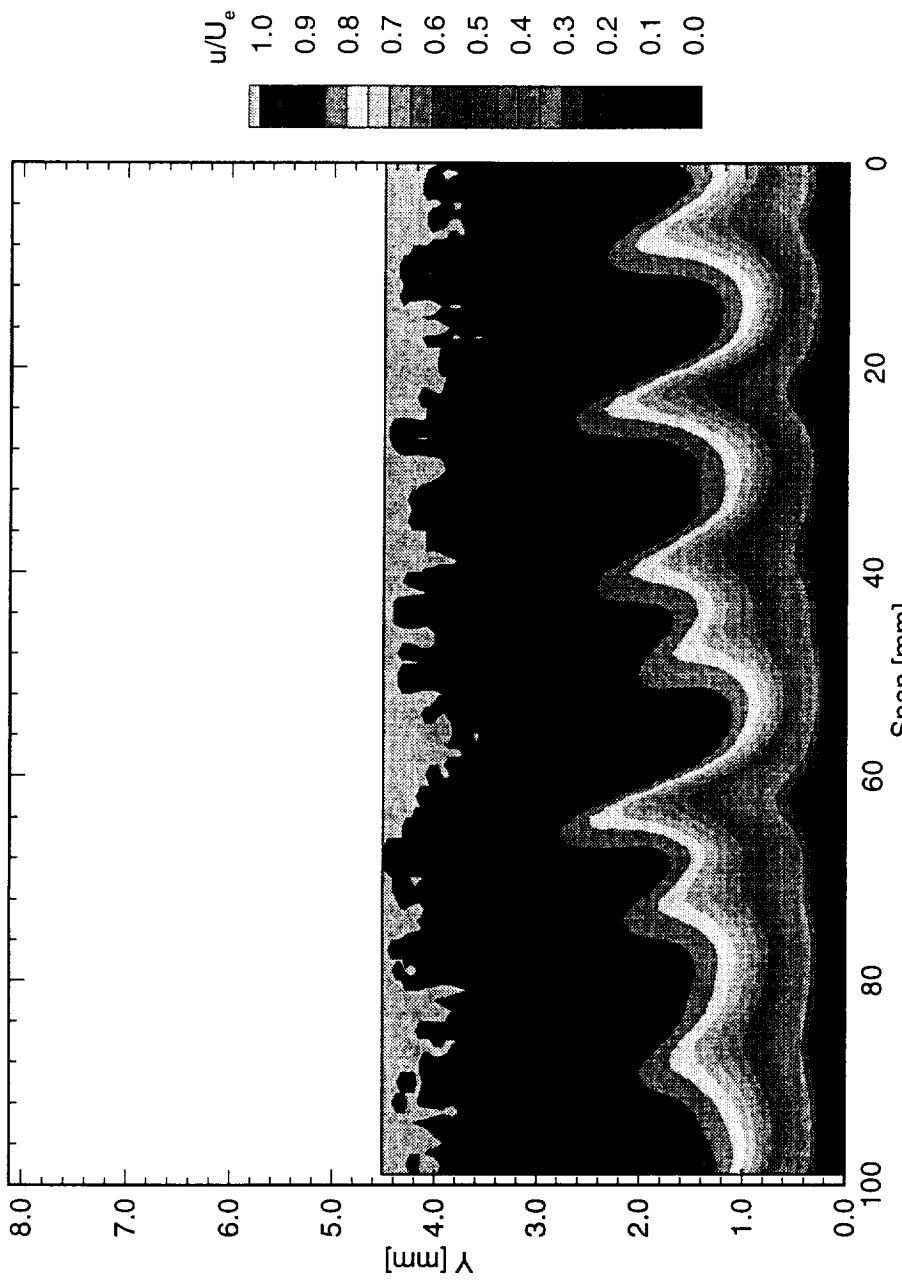

Figure 5.144: Normalized boundary-layer velocity contours at $x/c = 0.55$. $Re_c = 2.4 \times 10^6$, [6|8] roughness.

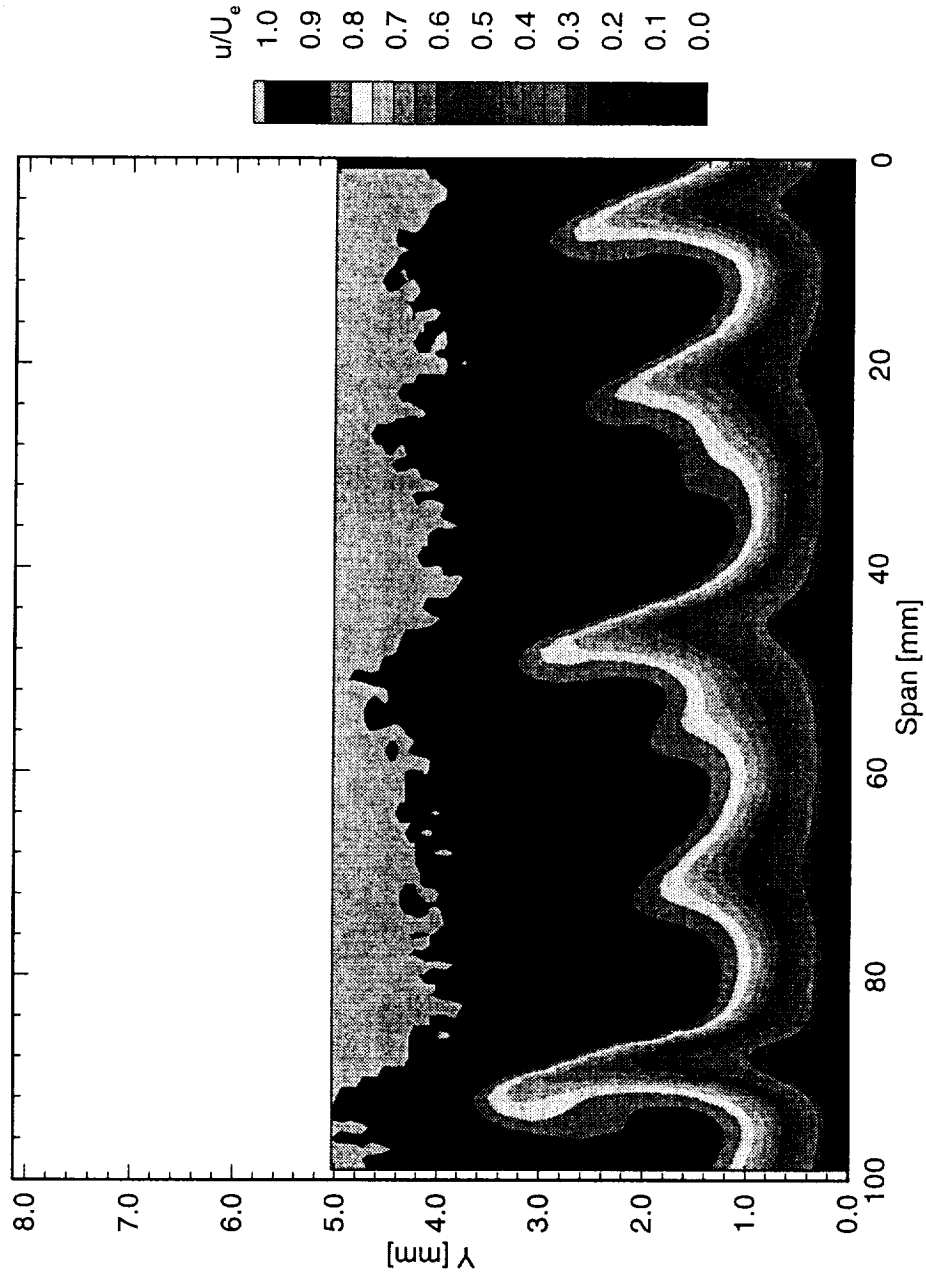

Figure 5.145: Normalized boundary-layer velocity contours at $x/c = 0.60$. $Re_c = 2.4 \times 10^6$, [6|8] roughness.

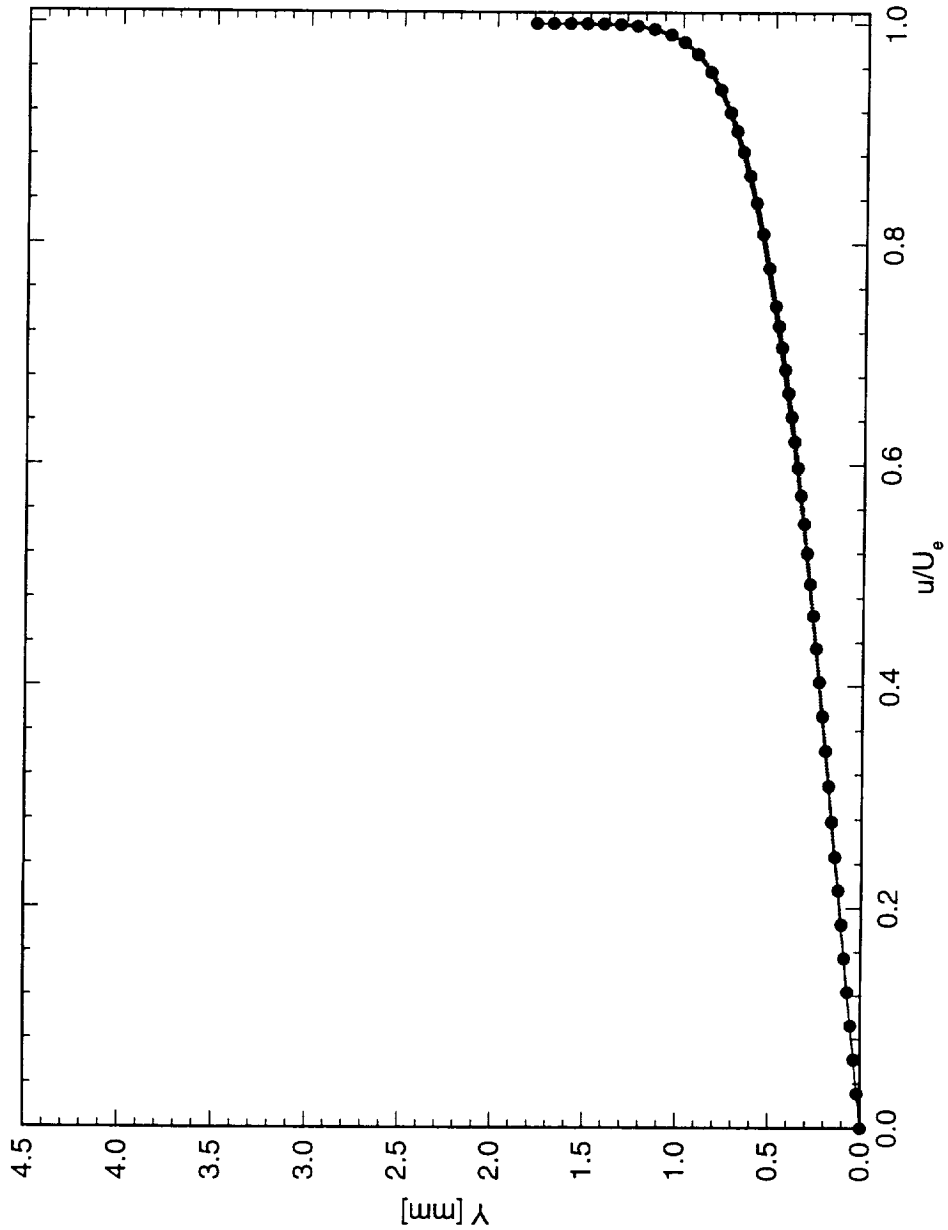

Figure 5.146: Spanwise array of 100 boundary-layer profiles spaced 1 mm apart in span at $x/c = 0.05$. $Re_c = 2.4 \times 10^6$, [6|8] roughness. The dots represent the spanwise average of the profiles.

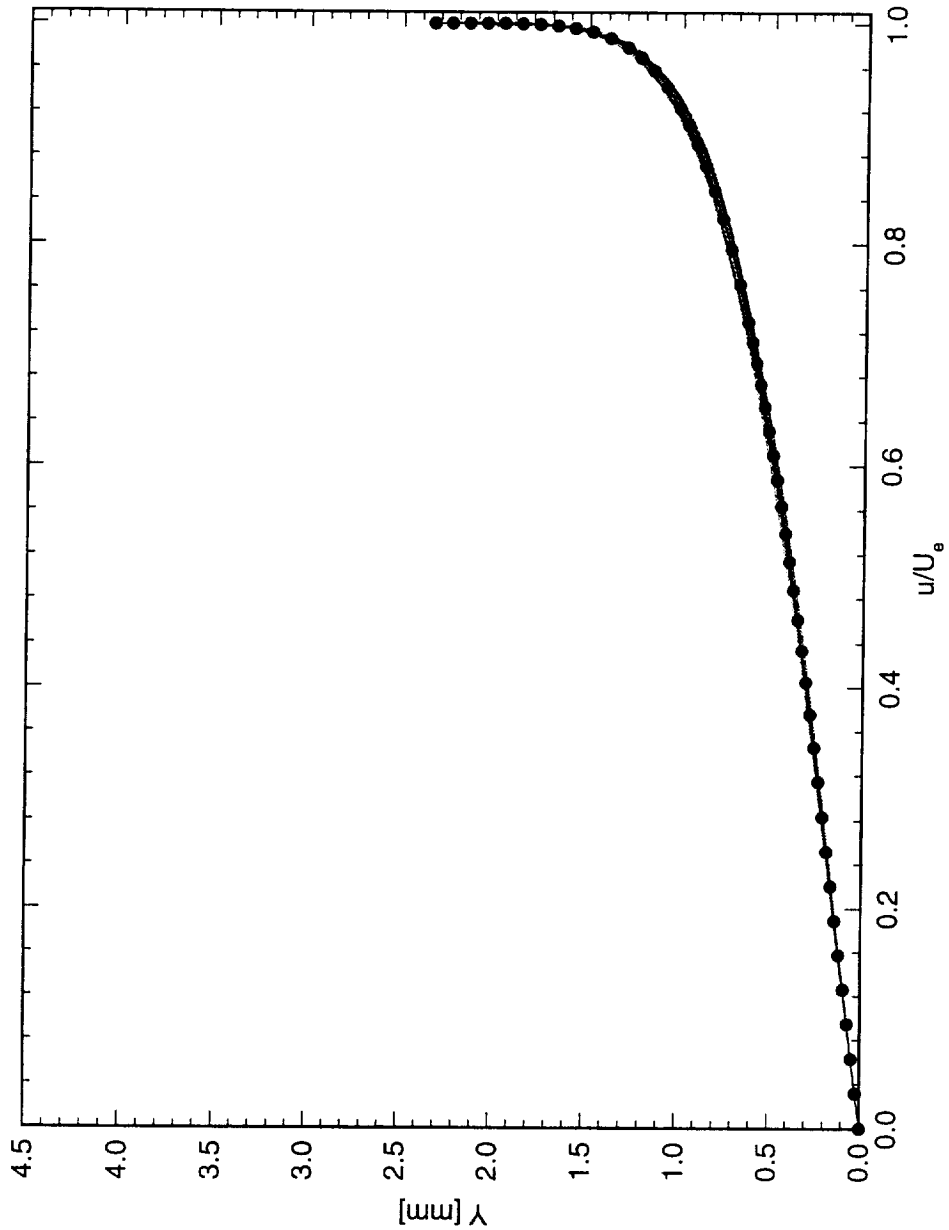

Figure 5.147: Spanwise array of 100 boundary-layer profiles spaced 1 mm apart in span at $x/c = 0.10$. $Re_c = 2.4 \times 10^6$, [6|8] roughness. The dots represent the spanwise average of the profiles.

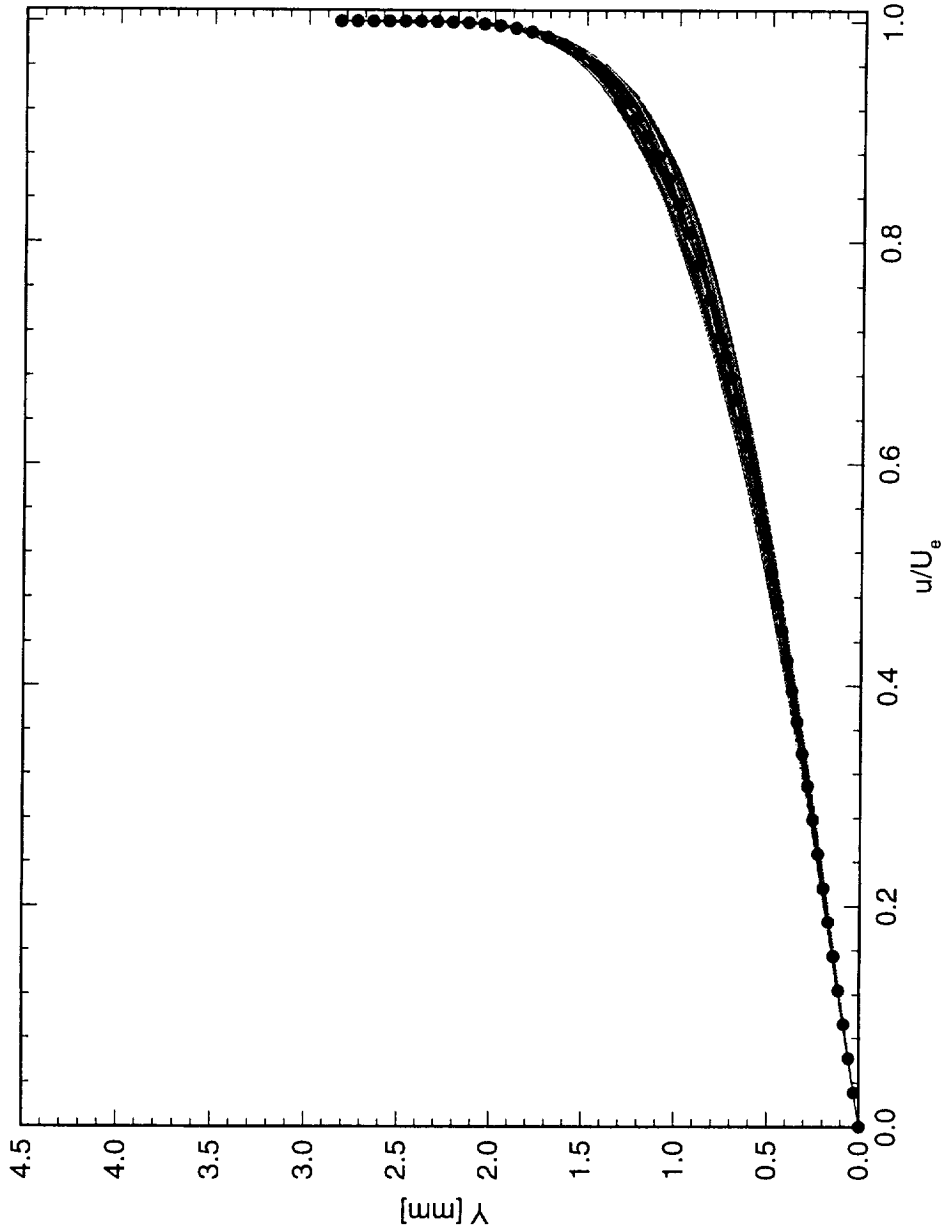

Figure 5.148: Spanwise array of 100 boundary-layer profiles spaced 1 mm apart in span at $x/c = 0.15$. $Re_c = 2.4 \times 10^6$, [6|8] roughness. The dots represent the spanwise average of the profiles.

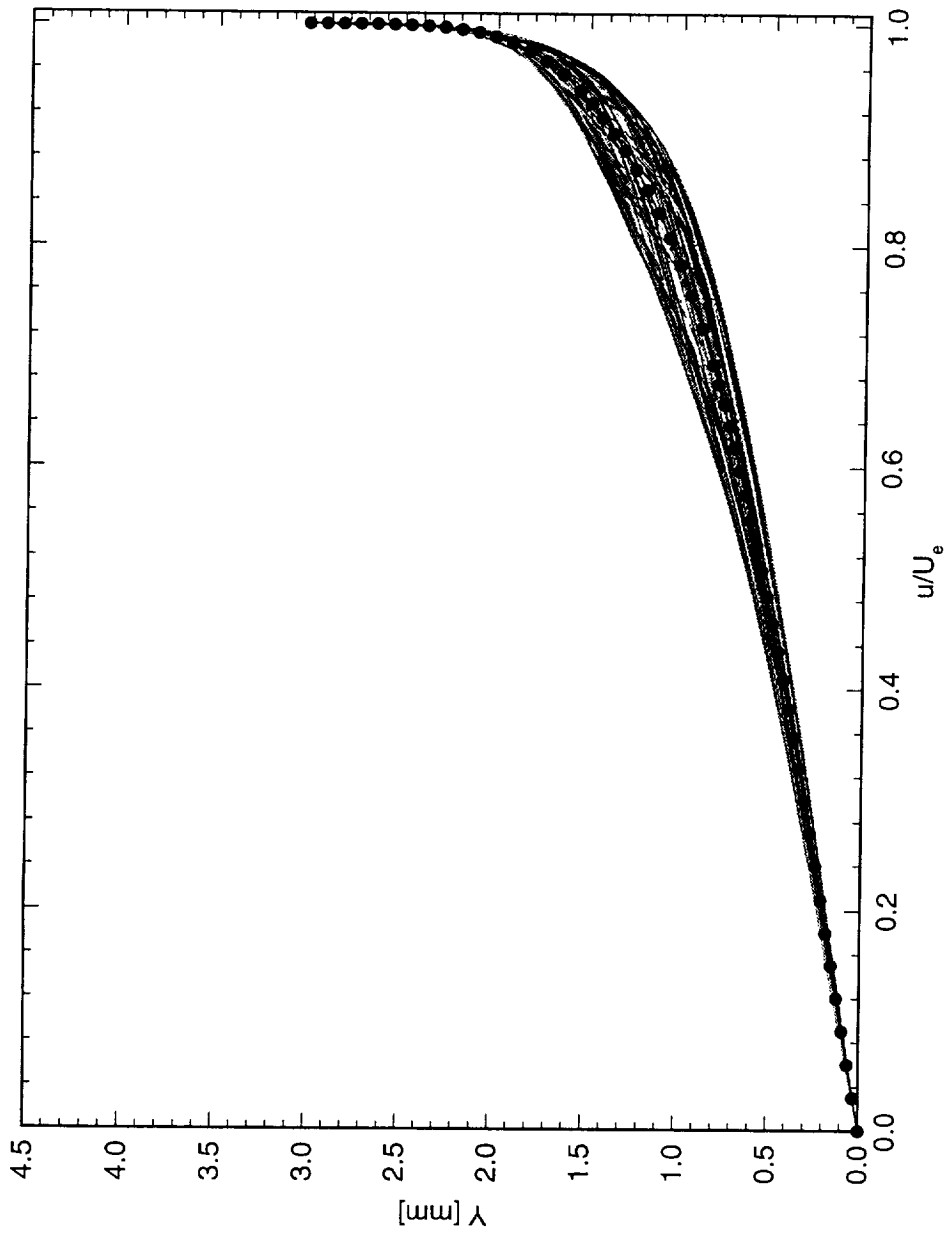

Figure 5.149: Spanwise array of 100 boundary-layer profiles spaced 1 mm apart in span at $x/c = 0.20$. $Re_c = 2.4 \times 10^6$, [6|8] roughness. The dots represent the spanwise average of the profiles.

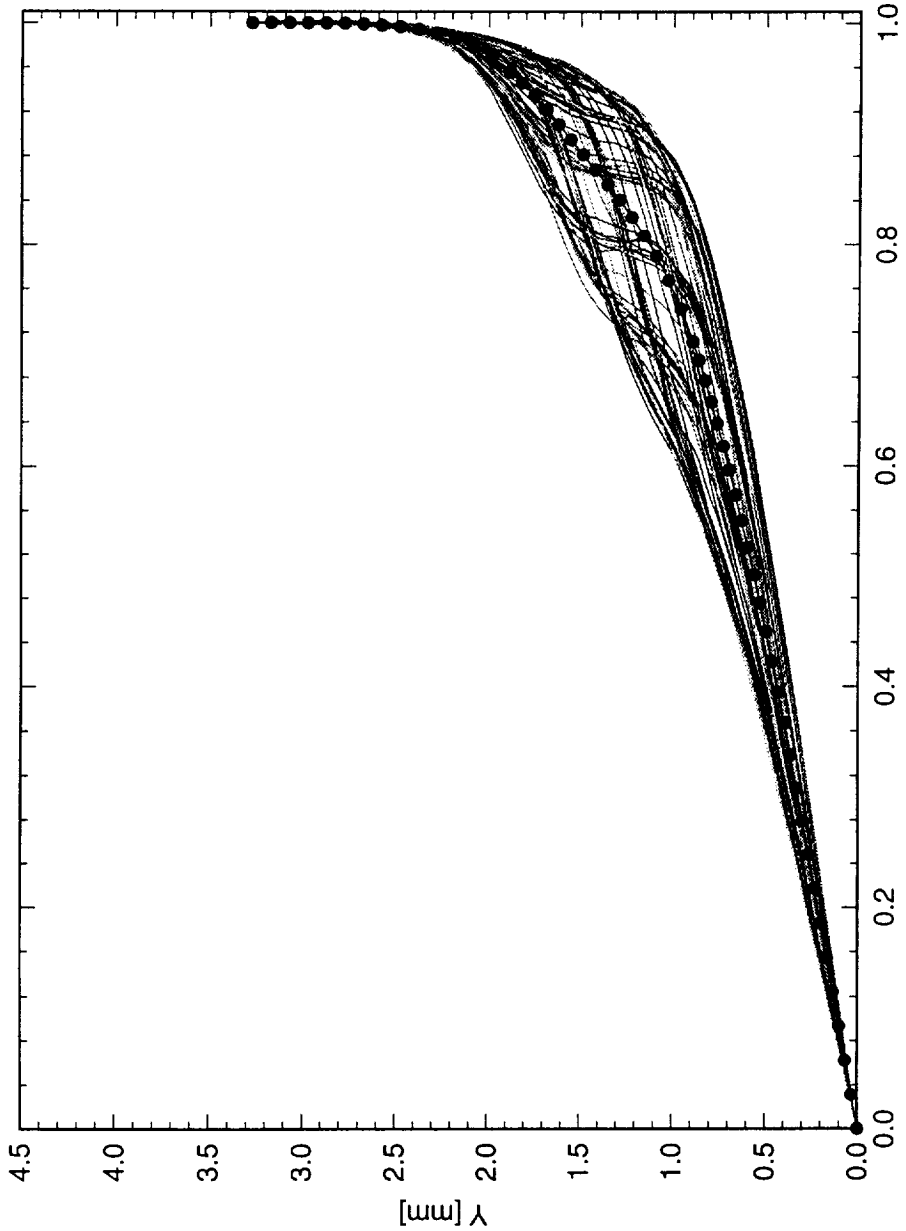

Figure 5.150: Spanwise array of 100 boundary-layer profiles spaced 1 mm apart in span at $x/c = 0.25$. $Re_c = 2.4 \times 10^6$, [6|8] roughness. The dots represent the spanwise average of the profiles.

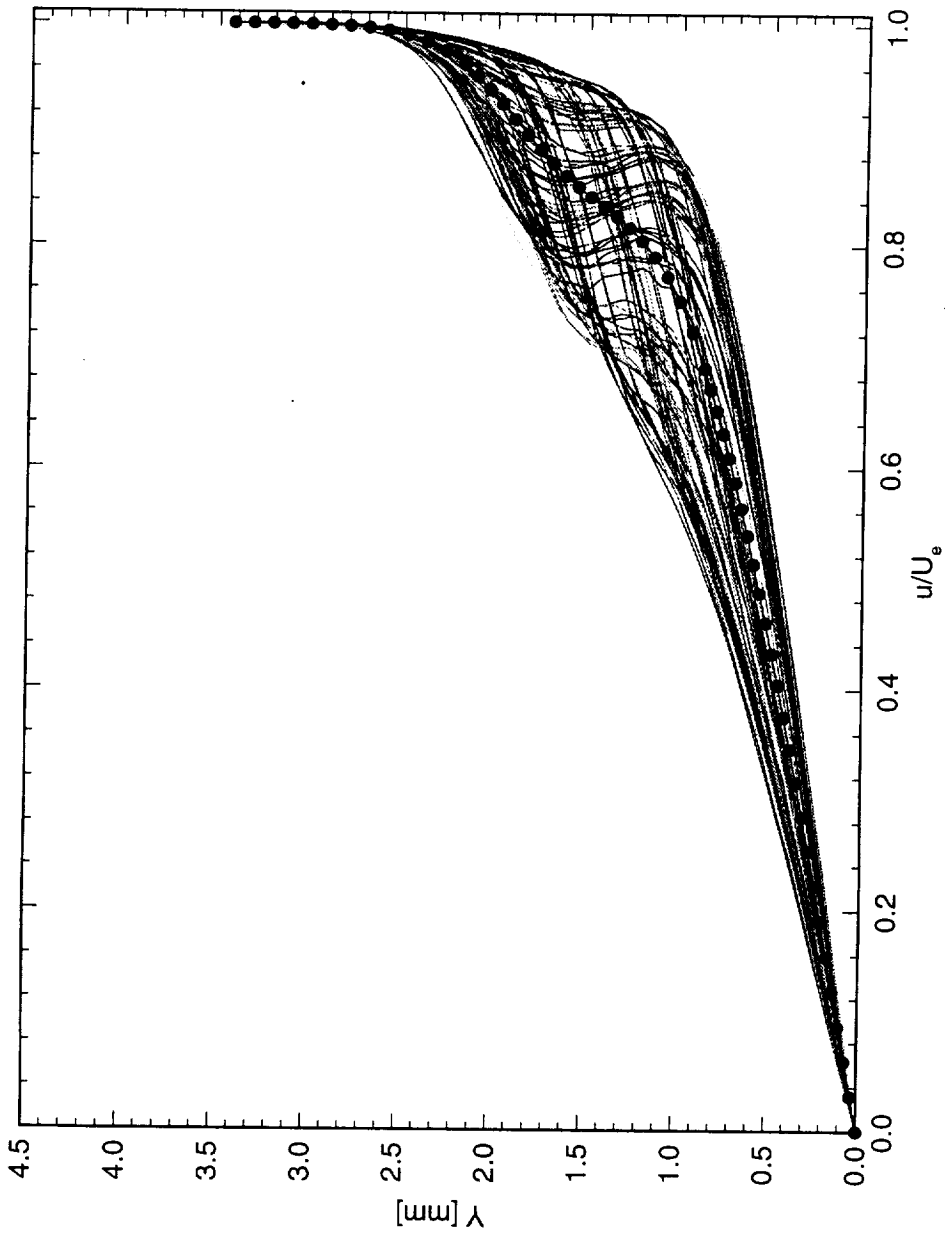

Figure 5.151: Spanwise array of 100 boundary-layer profiles spaced 1 mm apart in span at $x/c = 0.30$. $Re_c = 2.4 \times 10^6$, [6|8] roughness. The dots represent the spanwise average of the profiles.

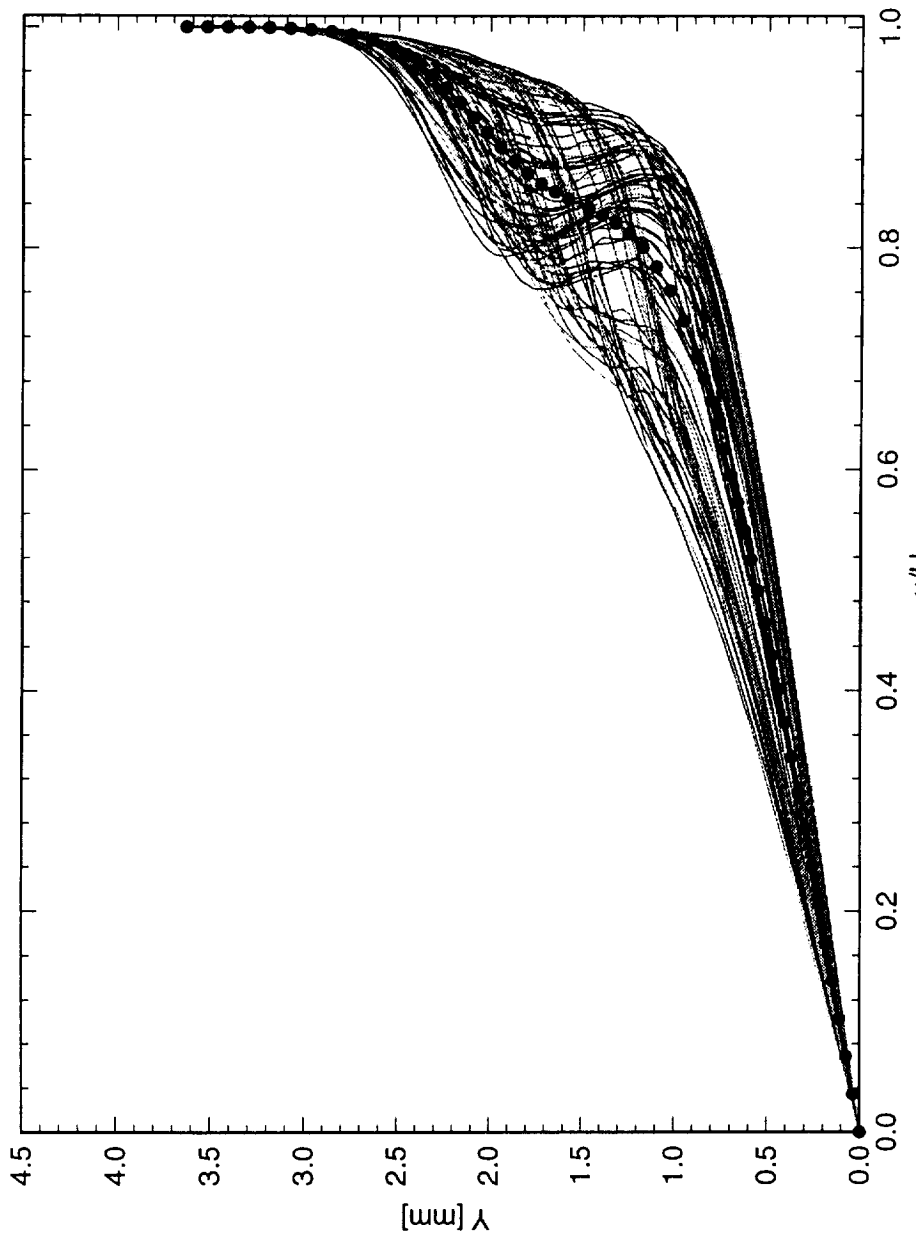

Figure 5.152: Spanwise array of 100 boundary-layer profiles spaced 1 mm apart in span at $x/c = 0.35$. $Re_c = 2.4 \times 10^6$, [6|8] roughness. The dots represent the spanwise average of the profiles.

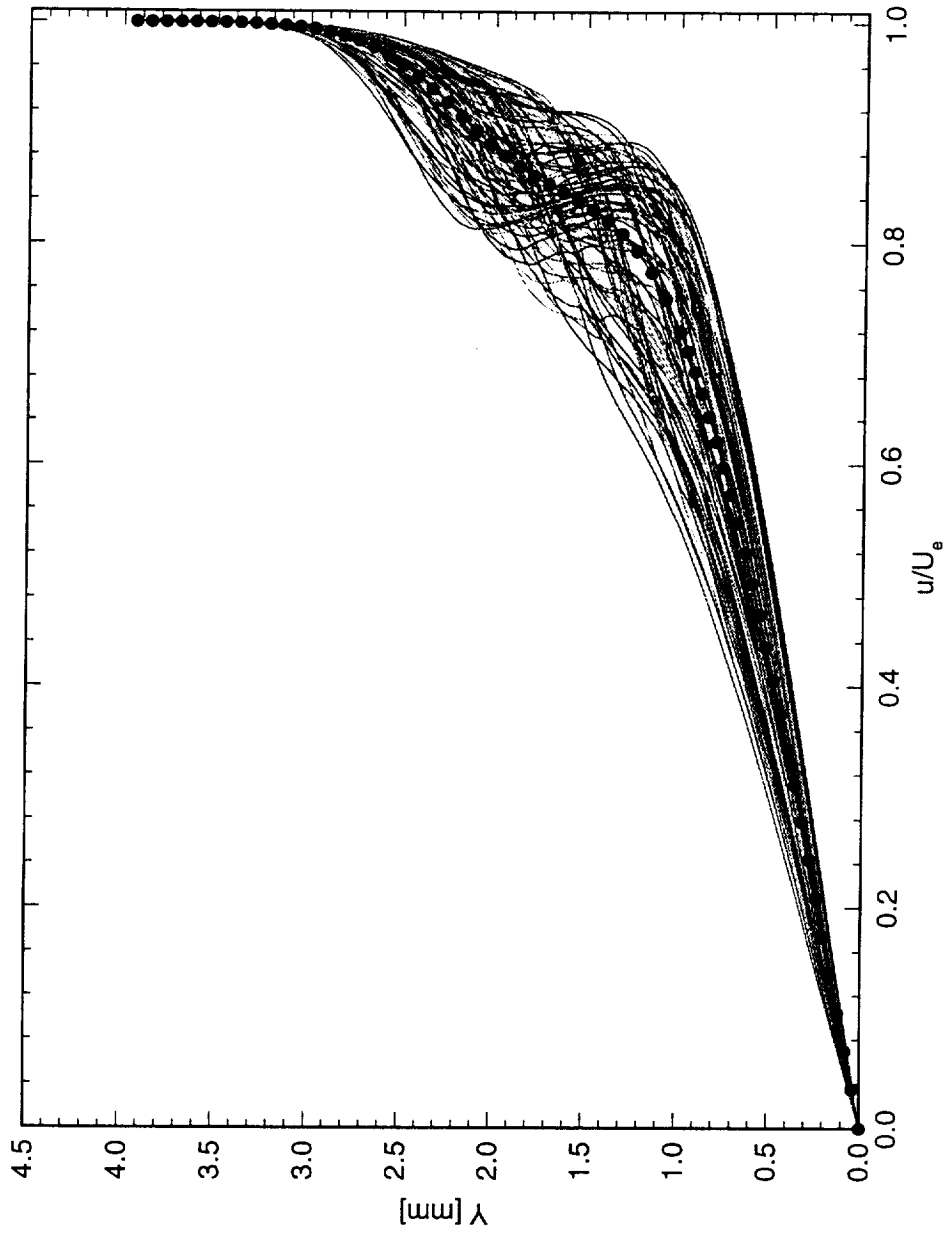

Figure 5.153: Spanwise array of 100 boundary-layer profiles spaced 1 mm apart in span at $x/c = 0.40$. $Re_c = 2.4 \times 10^6$, [6|8] roughness. The dots represent the spanwise average of the profiles.

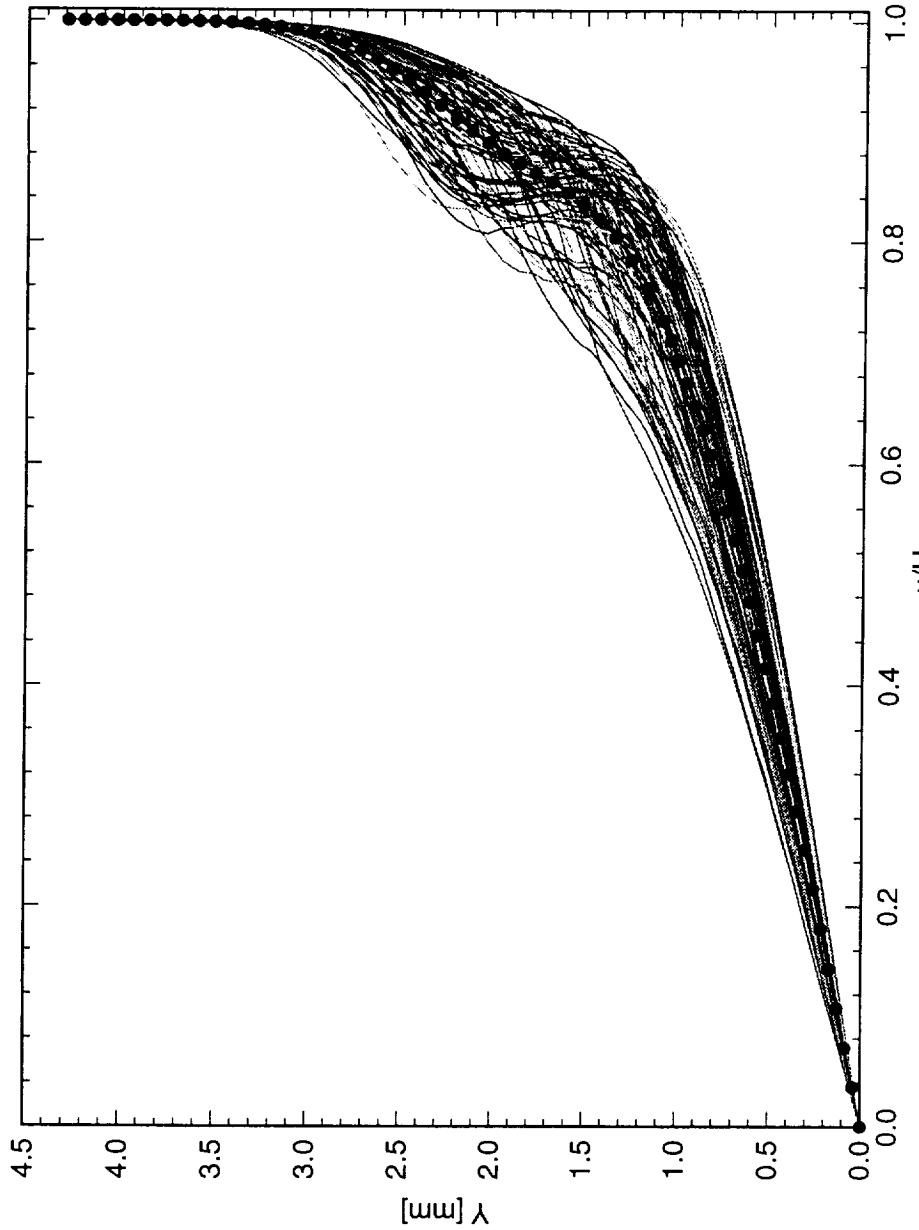

Figure 5.154: Spanwise array of 100 boundary-layer profiles spaced 1 mm apart in span at $x/c = 0.45$. $Re_c = 2.4 \times 10^6$, [6|8] roughness. The dots represent the spanwise average of the profiles.

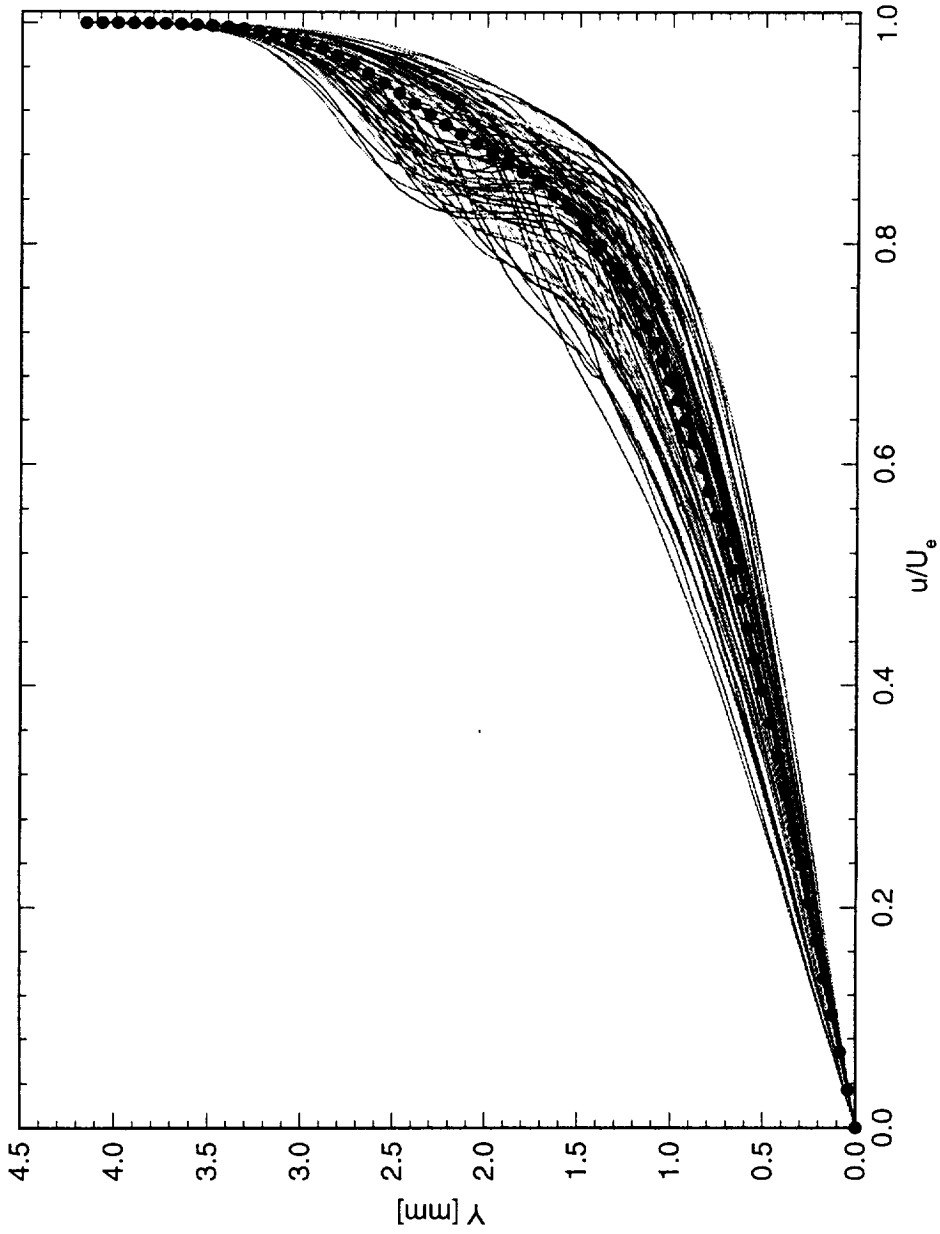

Figure 5.155: Spanwise array of 100 boundary-layer profiles spaced 1 mm apart in span at $x/c = 0.50$. $Re_c = 2.4 \times 10^6$, [6|8] roughness. The dots represent the spanwise average of the profiles.

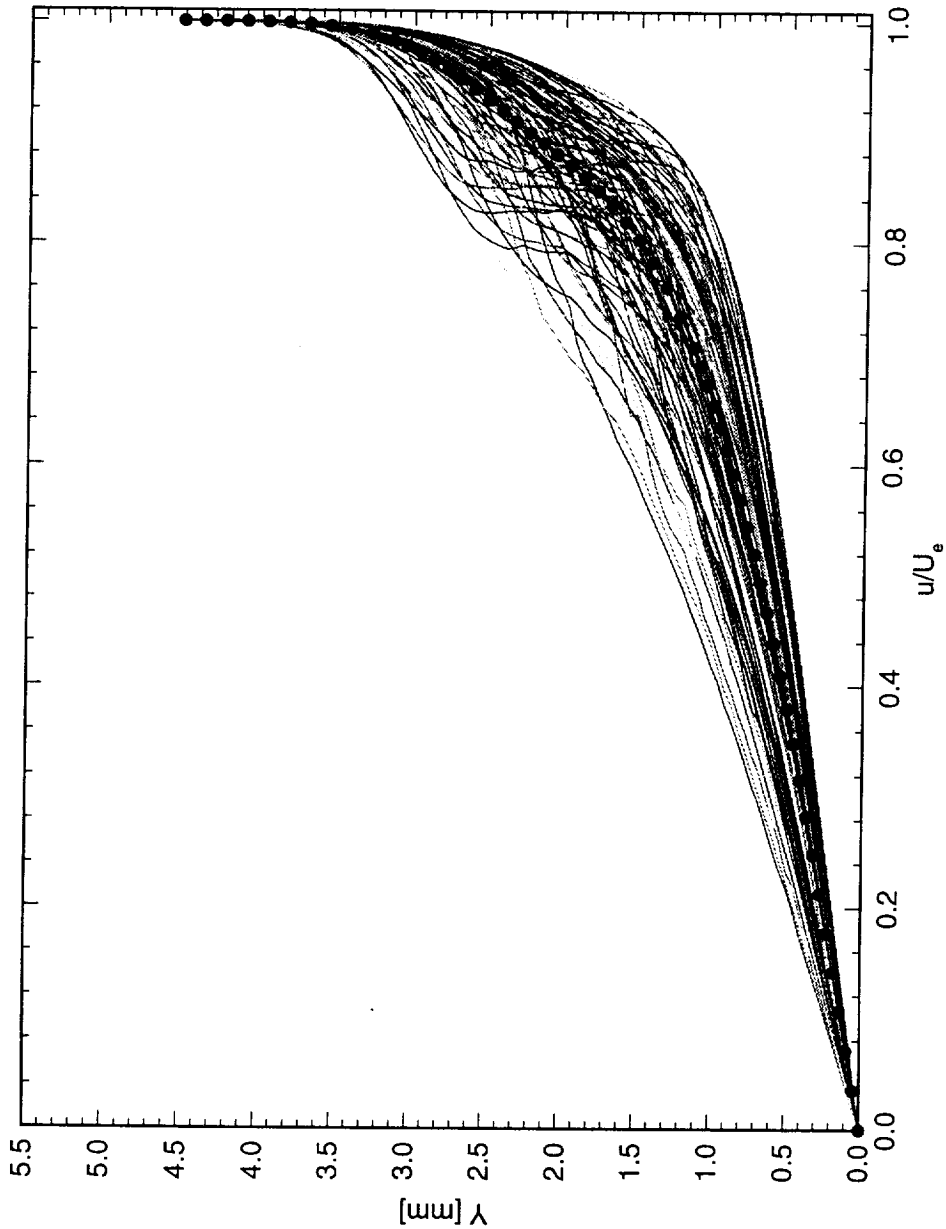

Figure 5.156: Spanwise array of 100 boundary-layer profiles spaced 1 mm apart in span at $x/c = 0.55$. $Re_c = 2.4 \times 10^6$, [6|8] roughness. The dots represent the spanwise average of the profiles.

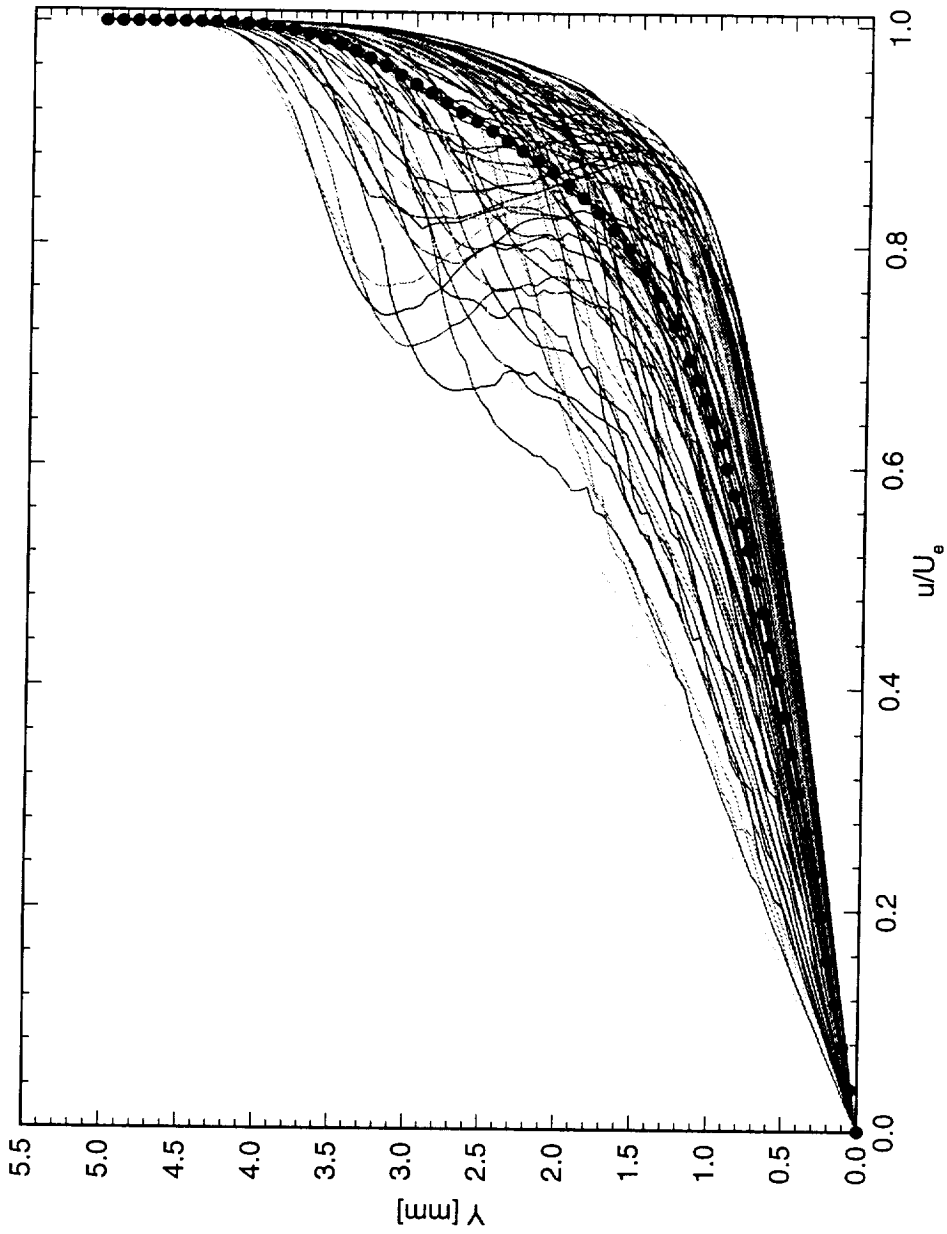

Figure 5.157: Spanwise array of 100 boundary-layer profiles spaced 1 mm apart in span at $x/c = 0.60$. $Re_c = 2.4 \times 10^6$, [6|8] roughness. The dots represent the spanwise average of the profiles.

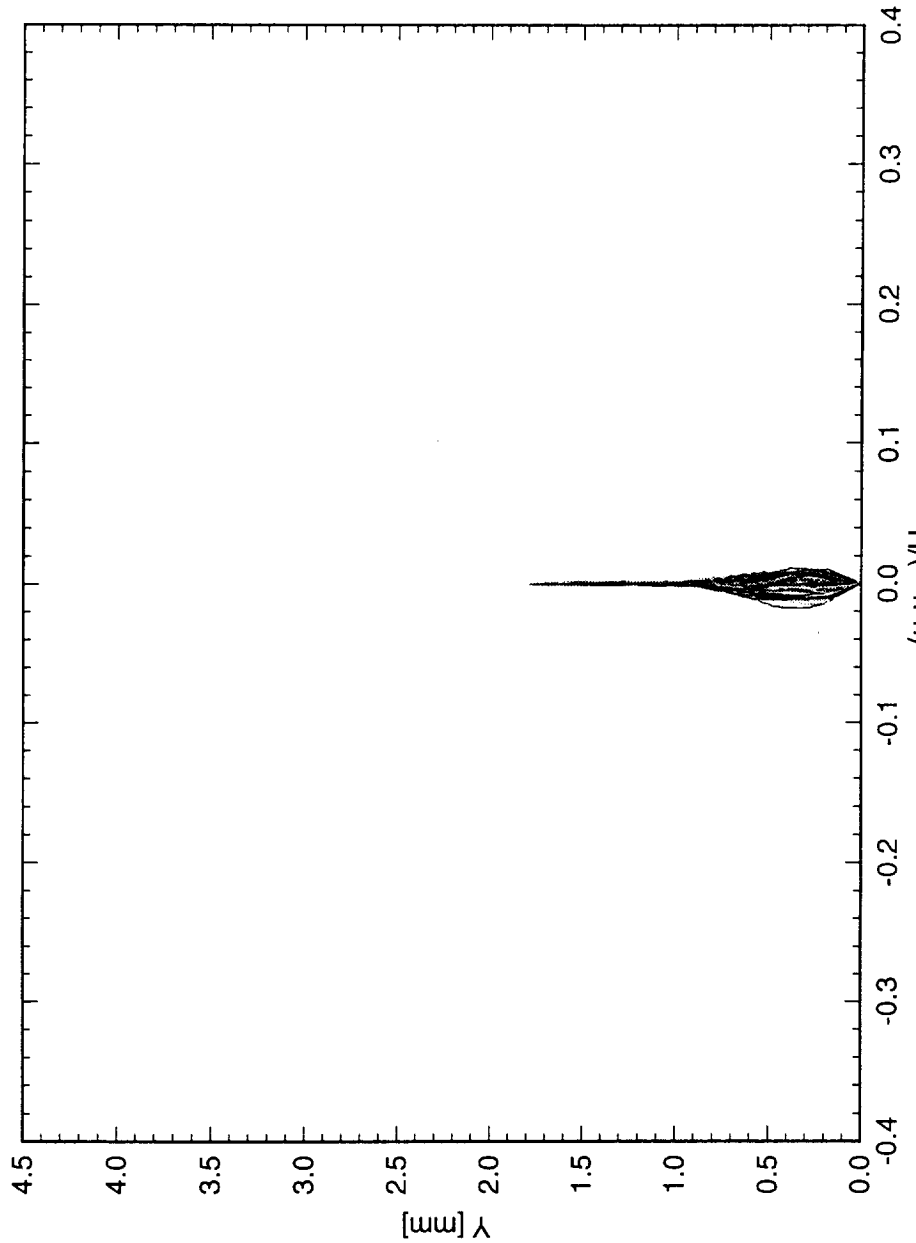

Figure 5.158: Spanwise array of 100 disturbance profiles spaced 1 mm apart in span at $x/c = 0.05$. $Re_c = 2.4 \times 10^6$, [6|8] roughness.

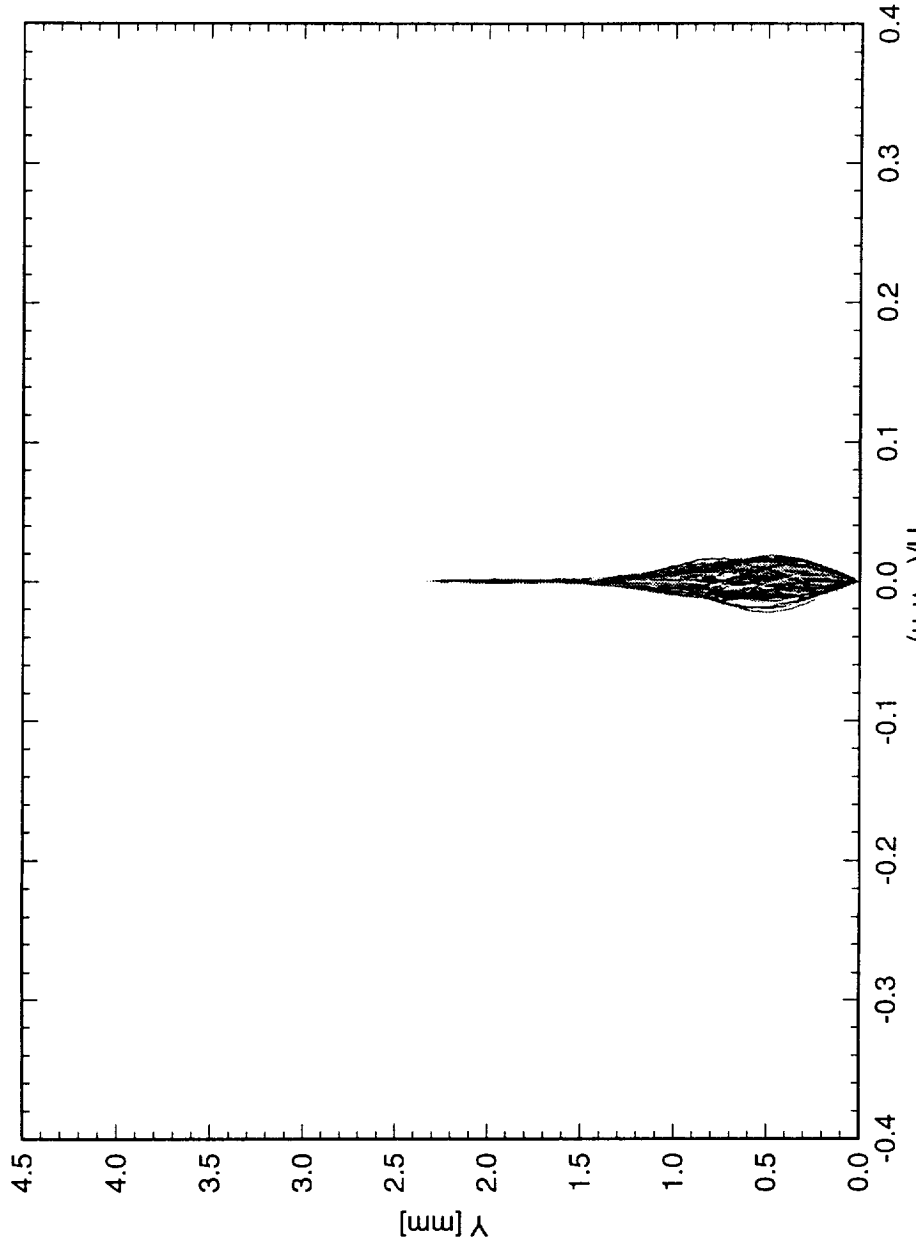

Figure 5.159: Spanwise array of 100 disturbance profiles spaced 1 mm apart in span at $x/c = 0.10$. $Re_c = 2.4 \times 10^6$, [6|8] roughness.

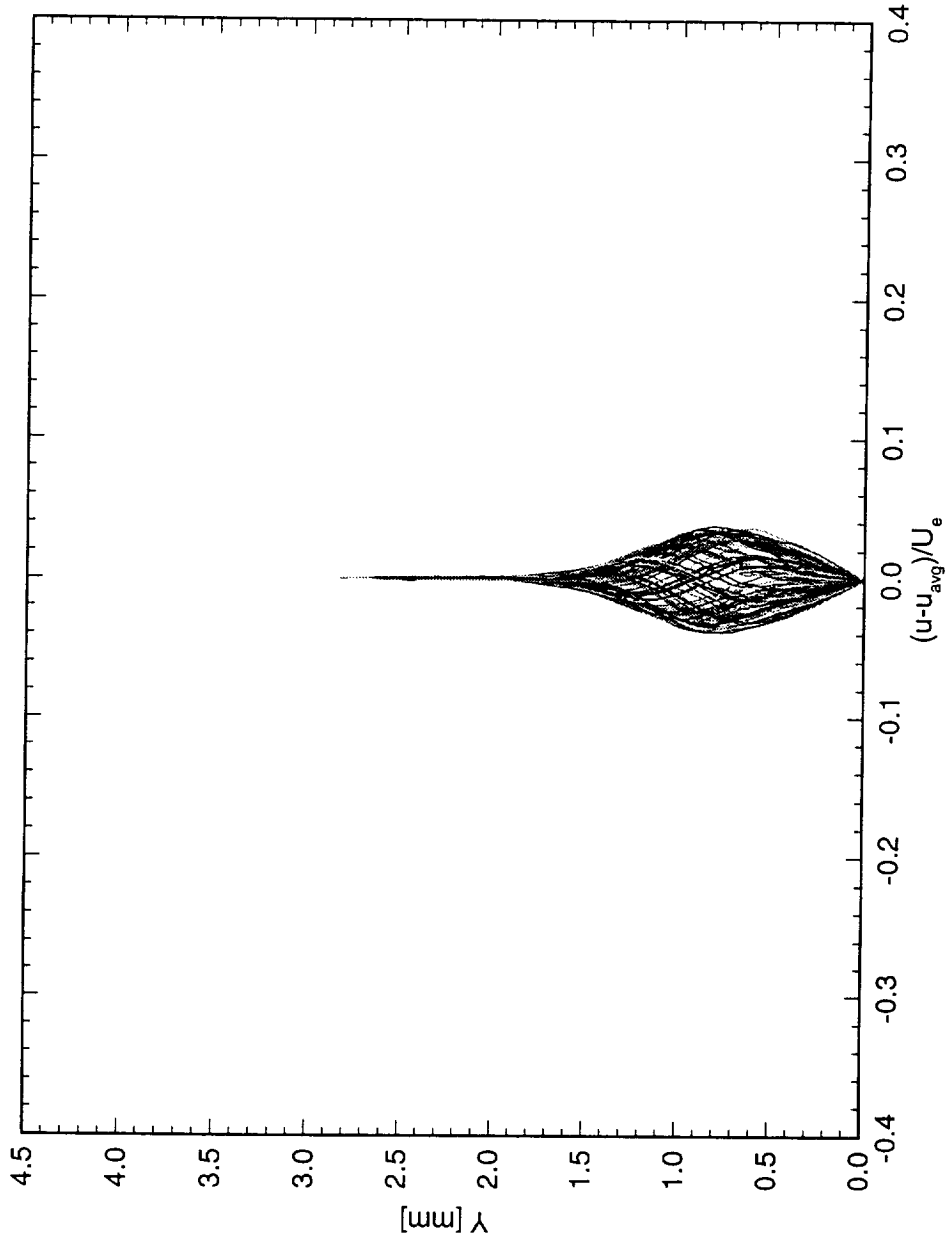

Figure 5.160: Spanwise array of 100 disturbance profiles spaced 1 mm apart in span at $x/c = 0.15$. $Re_c = 2.4 \times 10^6$, [6|8] roughness.

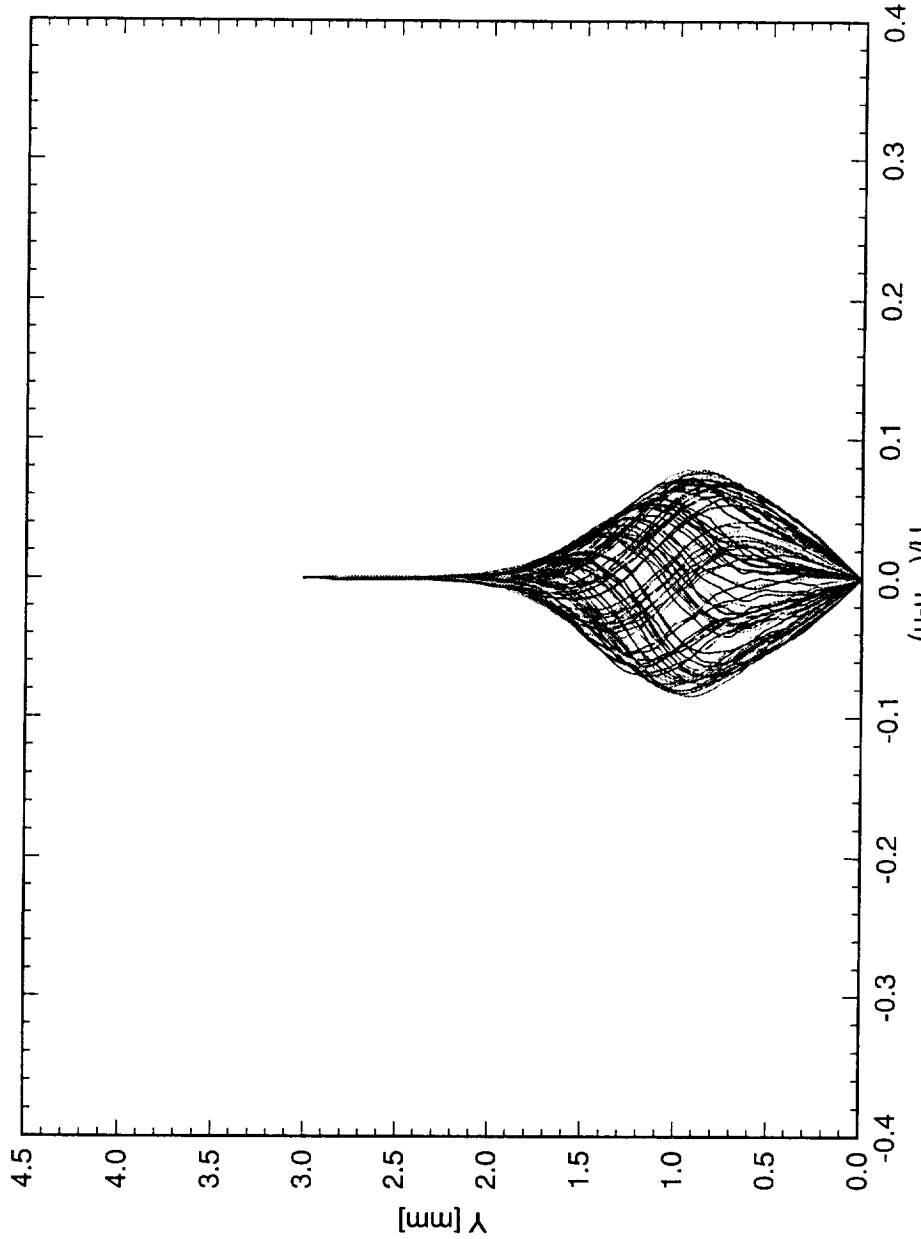

Figure 5.161: Spanwise array of 100 disturbance profiles spaced 1 mm apart in span at $x/c = 0.20$. $Re_c = 2.4 \times 10^6$, [6|8] roughness.

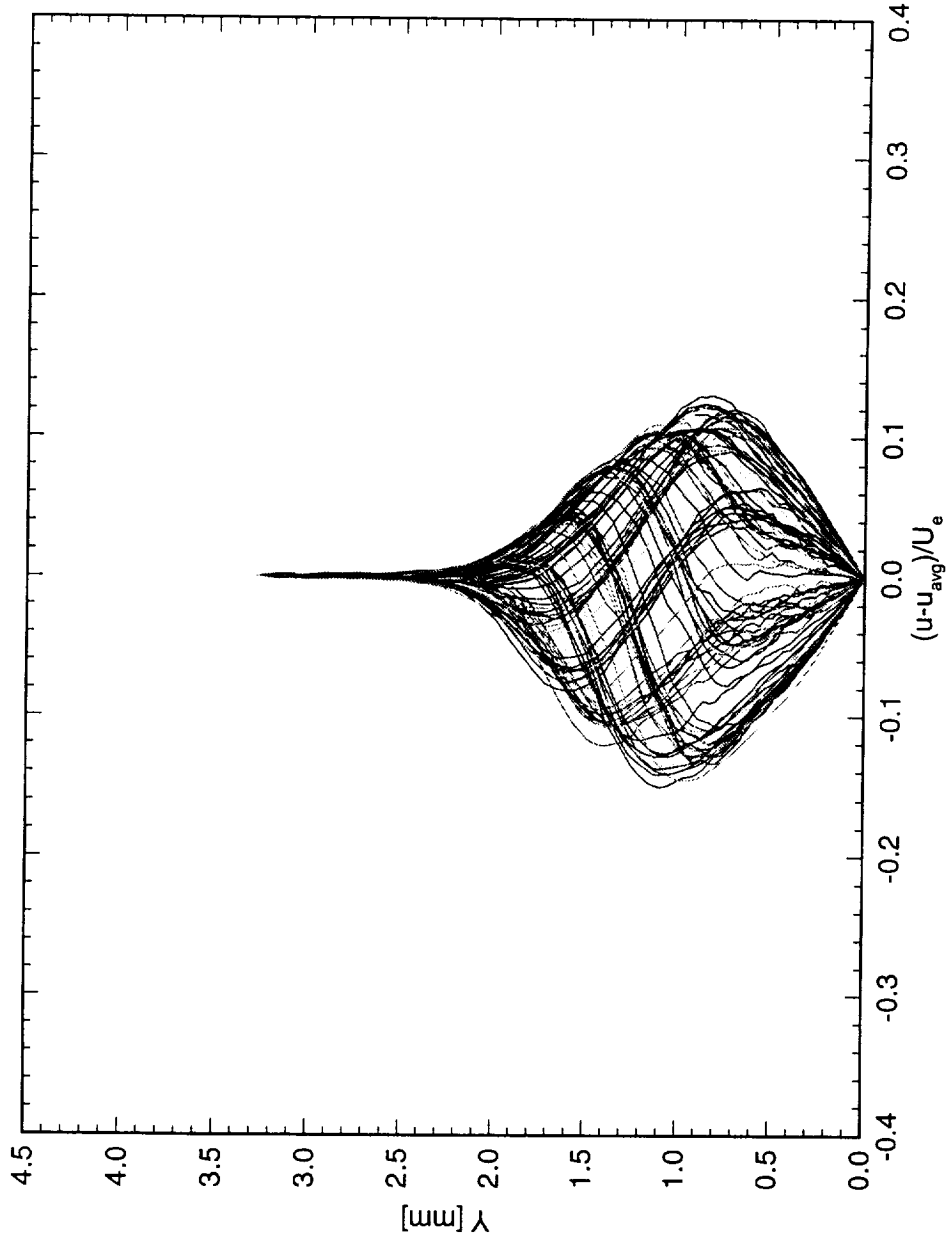

Figure 5.162: Spanwise array of 100 disturbance profiles spaced 1 mm apart in span at $x/c = 0.25$. $Re_c = 2.4 \times 10^6$, [6|8] roughness.

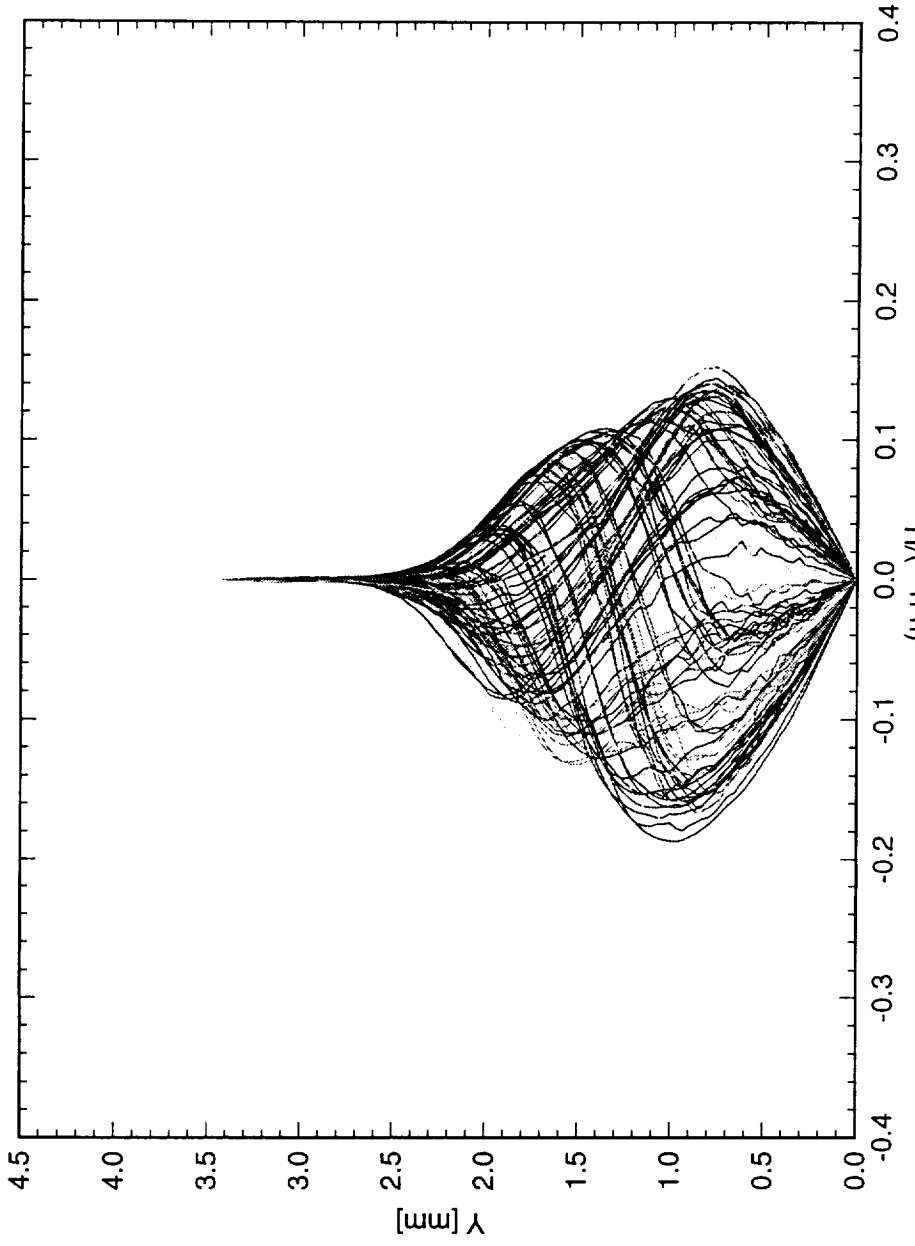

Figure 5.163: Spanwise array of 100 disturbance profiles spaced 1 mm apart in span at $x/c = 0.30$. $Re_c = 2.4 \times 10^6$, [6|8] roughness.

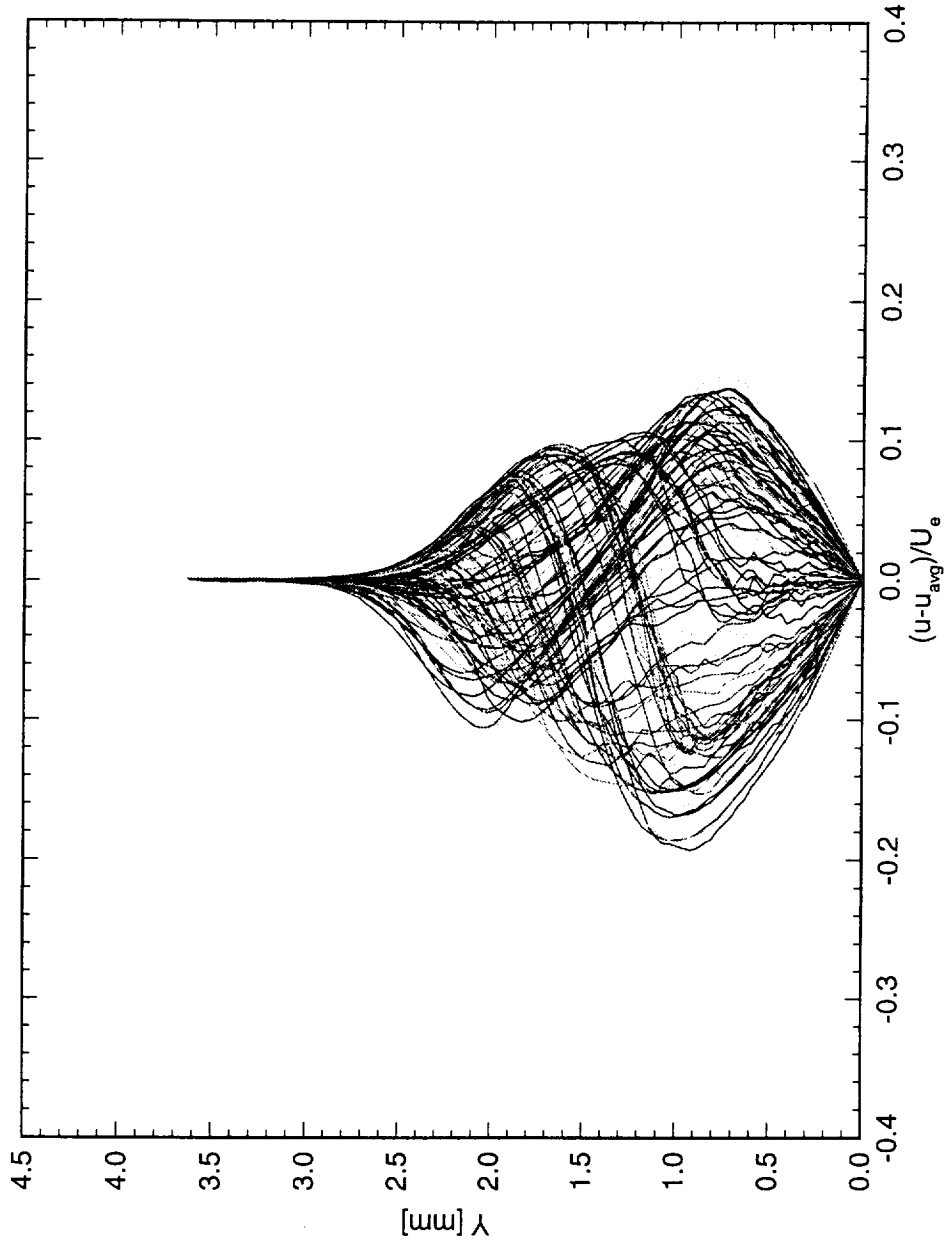

Figure 5.164: Spanwise array of 100 disturbance profiles spaced 1 mm apart in span at $x/c = 0.35$. $Re_c = 2.4 \times 10^6$, [6|8] roughness.

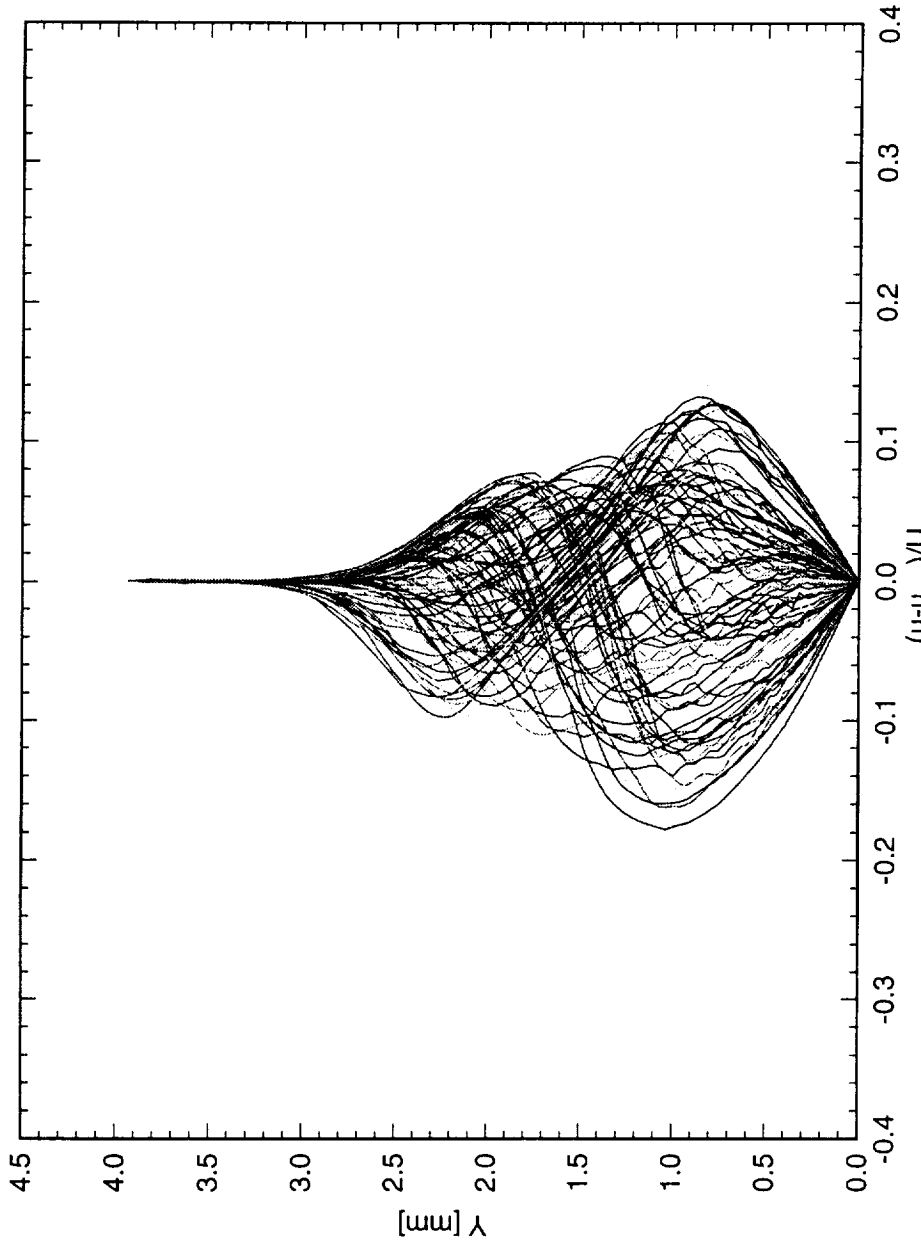

Figure 5.165: Spanwise array of 100 disturbance profiles spaced 1 mm apart in span at $x/c = 0.40$. $Re_c = 2.4 \times 10^6$, [6|8] roughness.

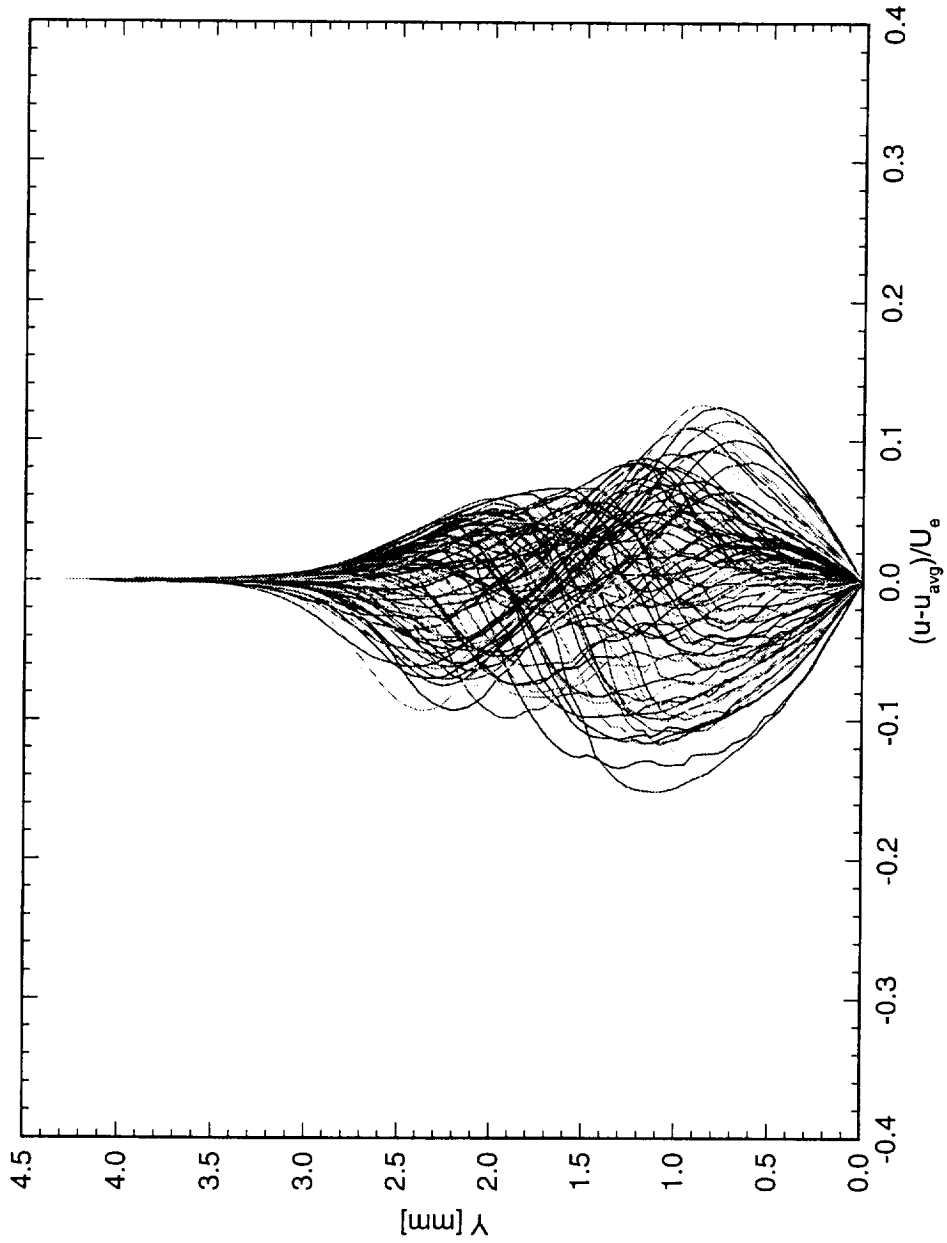

Figure 5.166: Spanwise array of 100 disturbance profiles spaced 1 mm apart in span at $x/c = 0.45$. $Re_c = 2.4 \times 10^6$, [6|8] roughness.

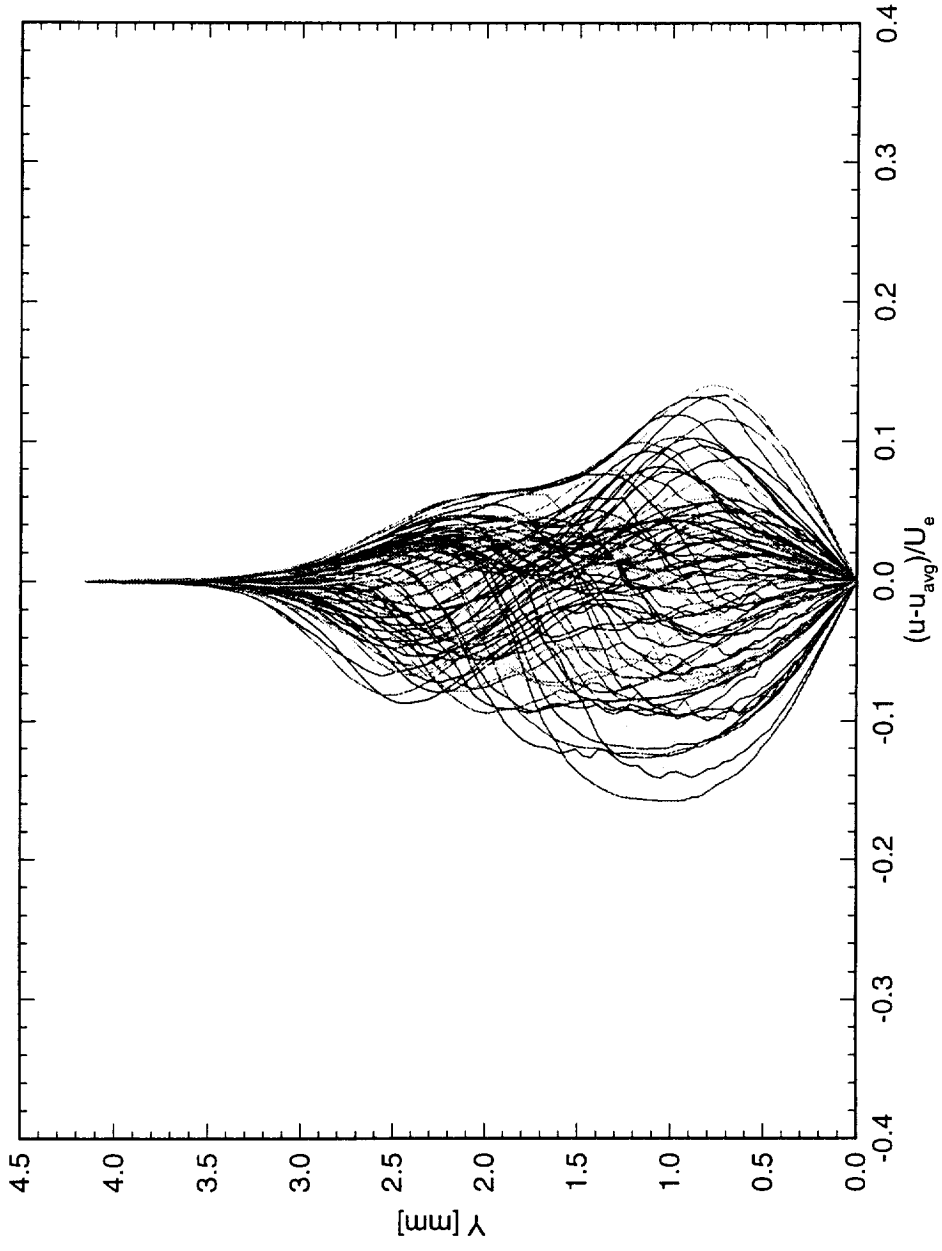

Figure 5.167: Spanwise array of 100 disturbance profiles spaced 1 mm apart in span at $x/c = 0.50$. $Re_c = 2.4 \times 10^6$, [6|8] roughness.

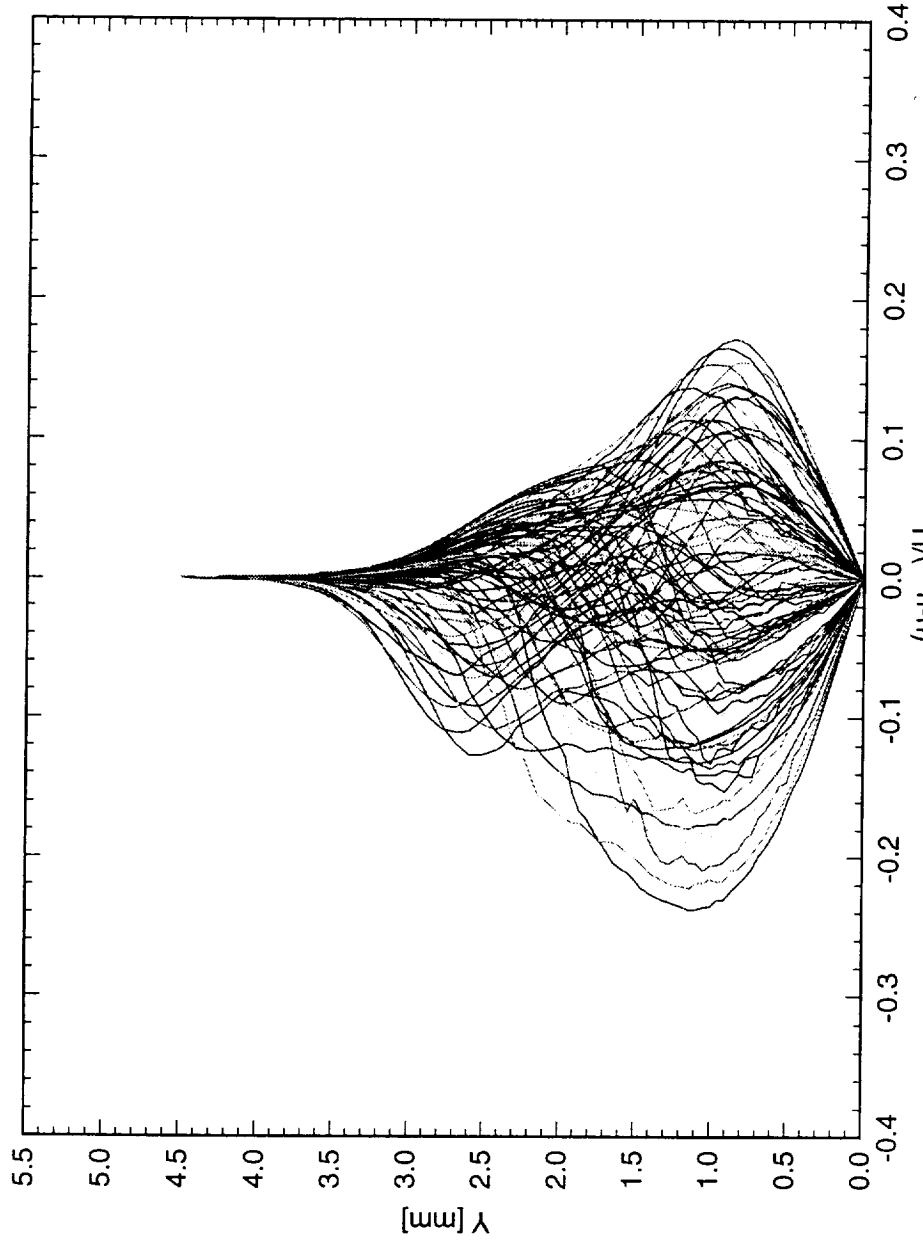

Figure 5.168: Spanwise array of 100 disturbance profiles spaced 1 mm apart in span at $x/c = 0.55$. $Re_c = 2.4 \times 10^6$, [6|8] roughness.

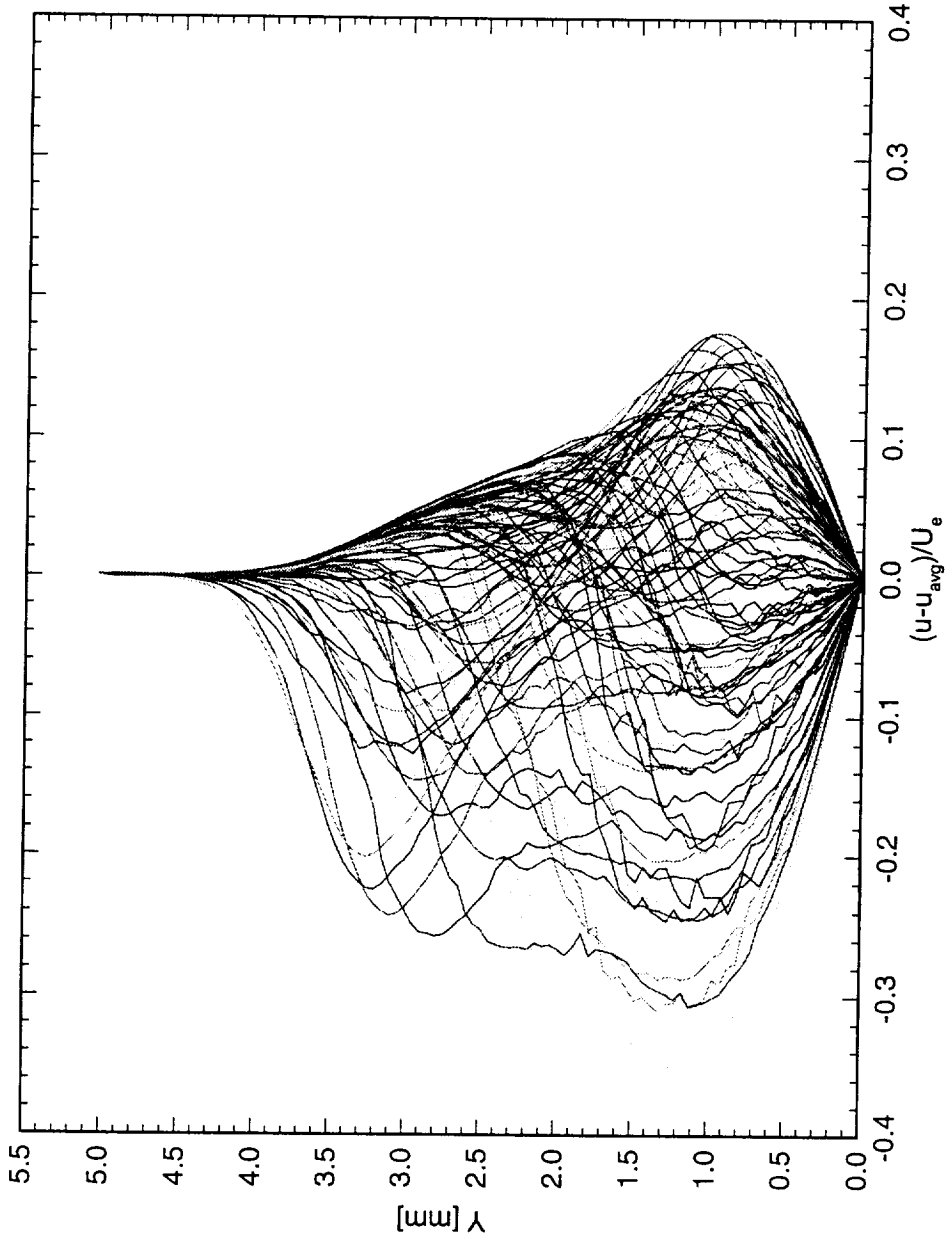

Figure 5.169: Spanwise array of 100 disturbance profiles spaced 1 mm apart in span at $x/c = 0.60$. $Re_c = 2.4 \times 10^6$, [6|8] roughness.

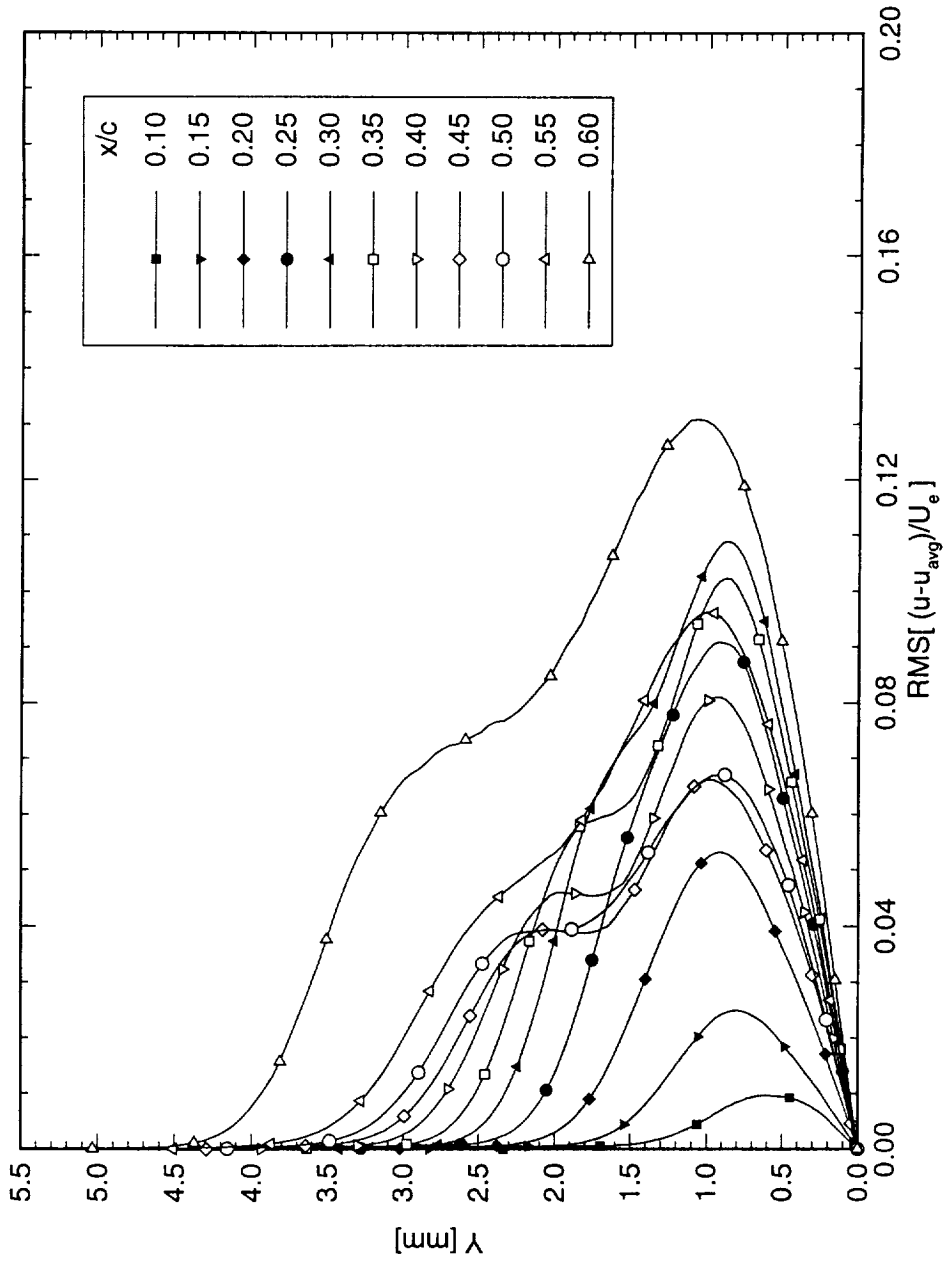

Figure 5.170: Stationary crossflow mode shapes for $Re_c = 2.4 \times 10^6$ and [6|8] roughness. The symbols are merely indicators and do not indicate measurement points

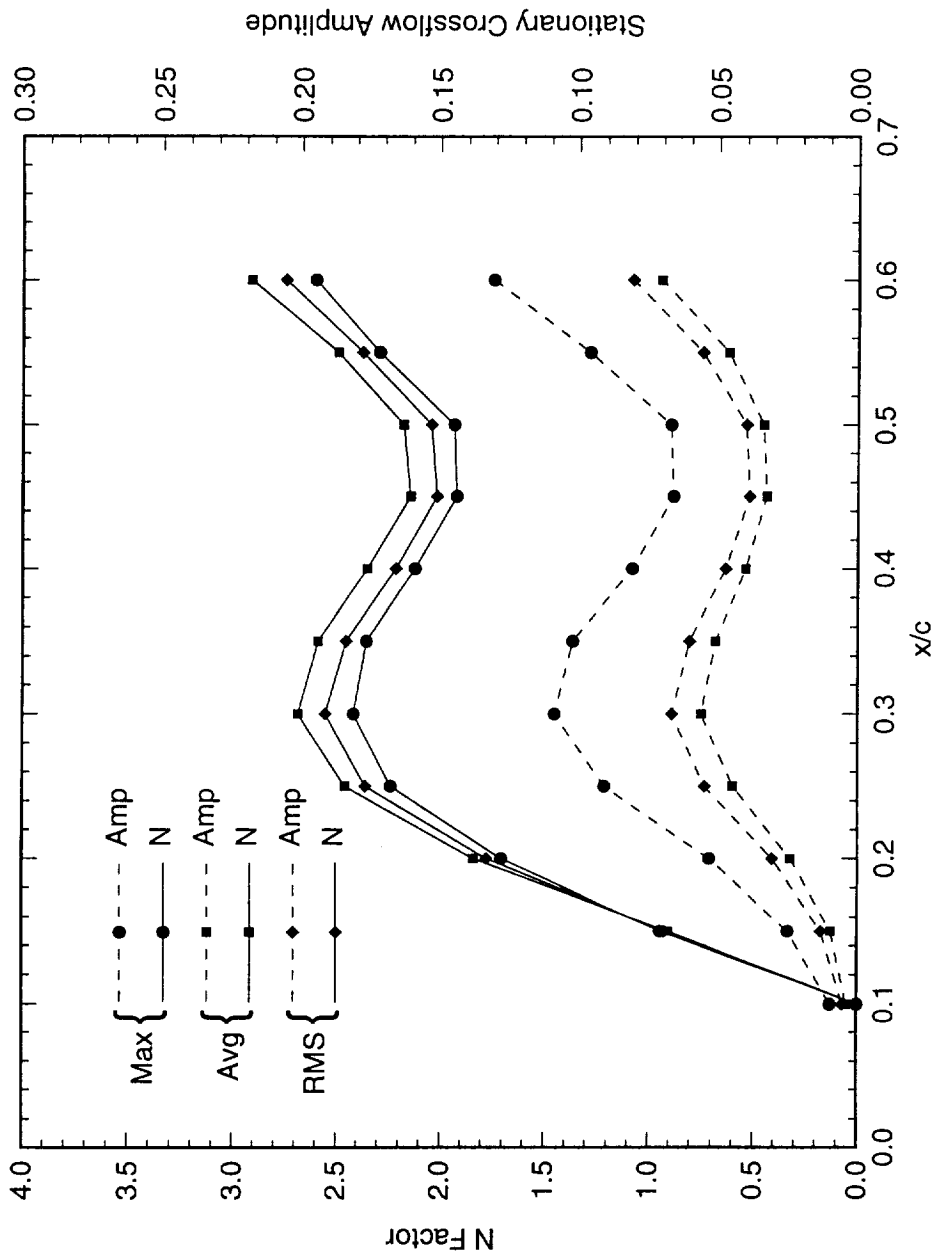

Figure 5.171: Total disturbance amplitude and relative N-factor for $Re_c = 2.4 \times 10^6$ and [6|8] roughness. N-factor calculations are relative to $x/c = 0.10$.

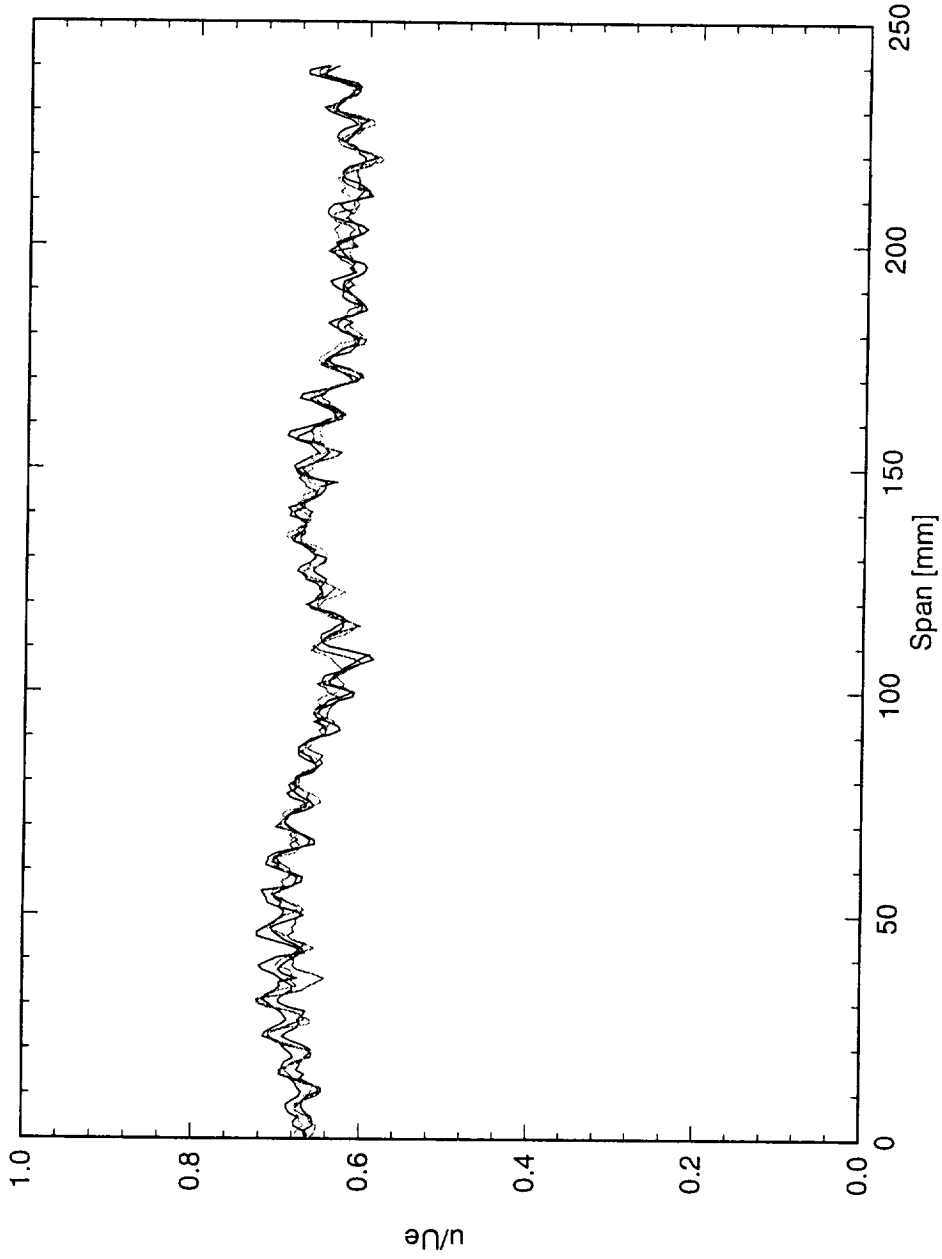

Figure 5.172: Spanwise hot-wire scan at $x/c = 0.10$ and $Y = 0.60$ mm. $Re_c = 2.4 \times 10^6$, [6|8] roughness.

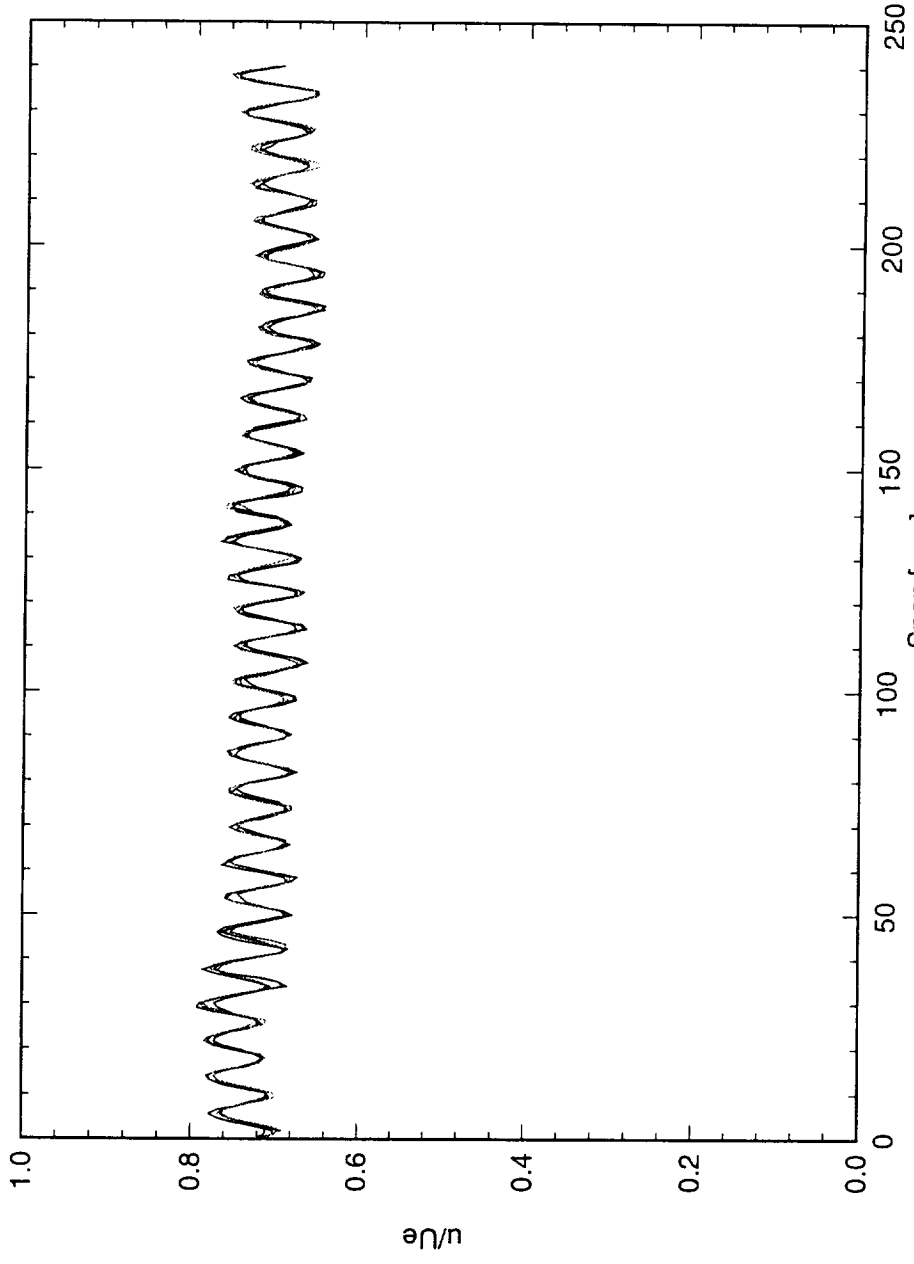

Figure 5.173: Spanwise hot-wire scan at $x/c = 0.15$ and $Y = 0.80$ mm. $Re_c = 2.4 \times 10^6$, [6|8] roughness.

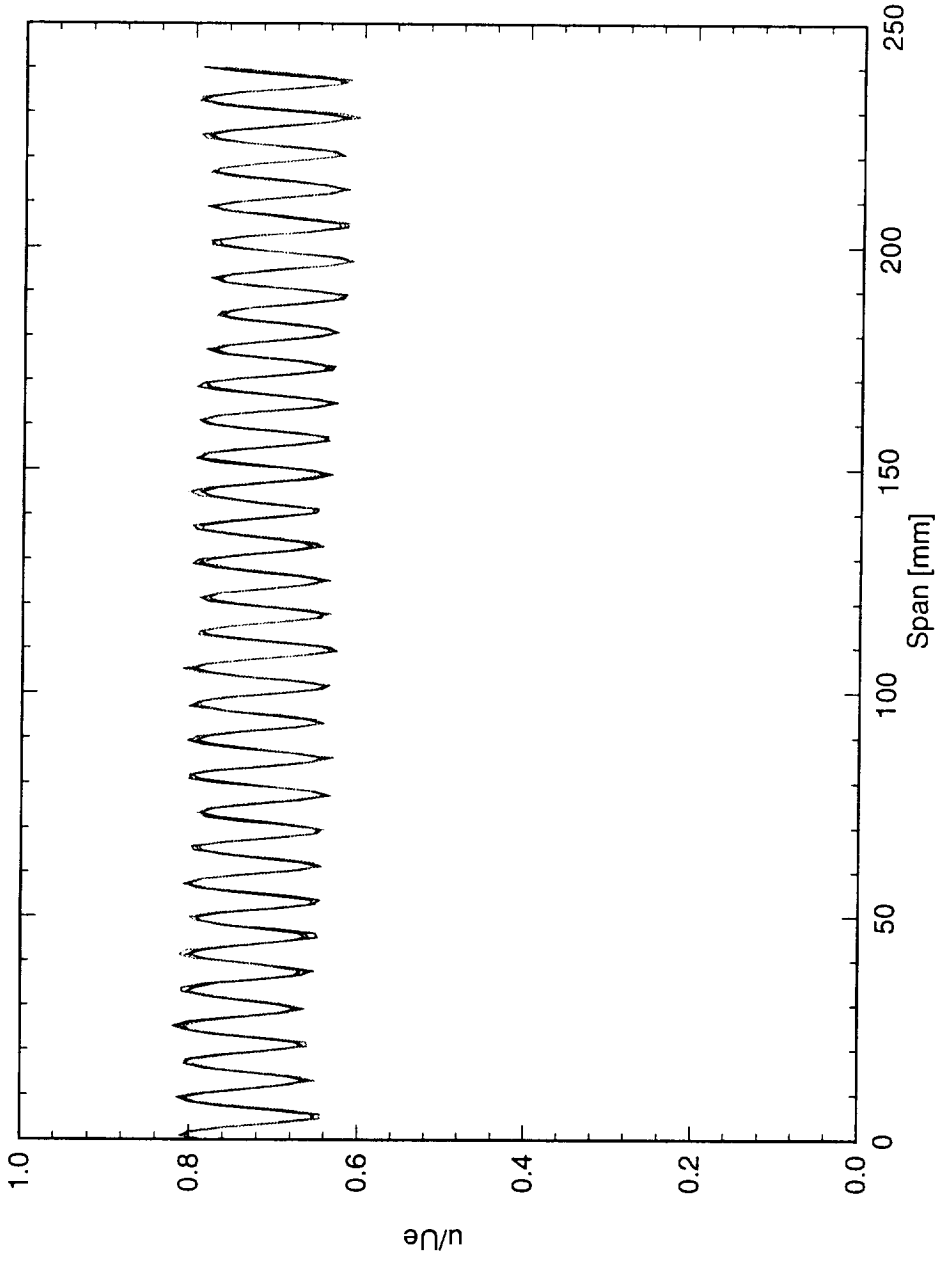

Figure 5.174: Spanwise hot-wire scan at $x/c = 0.20$ and $Y = 0.90$ mm. $Re_c = 2.4 \times 10^6$, [6|8] roughness.

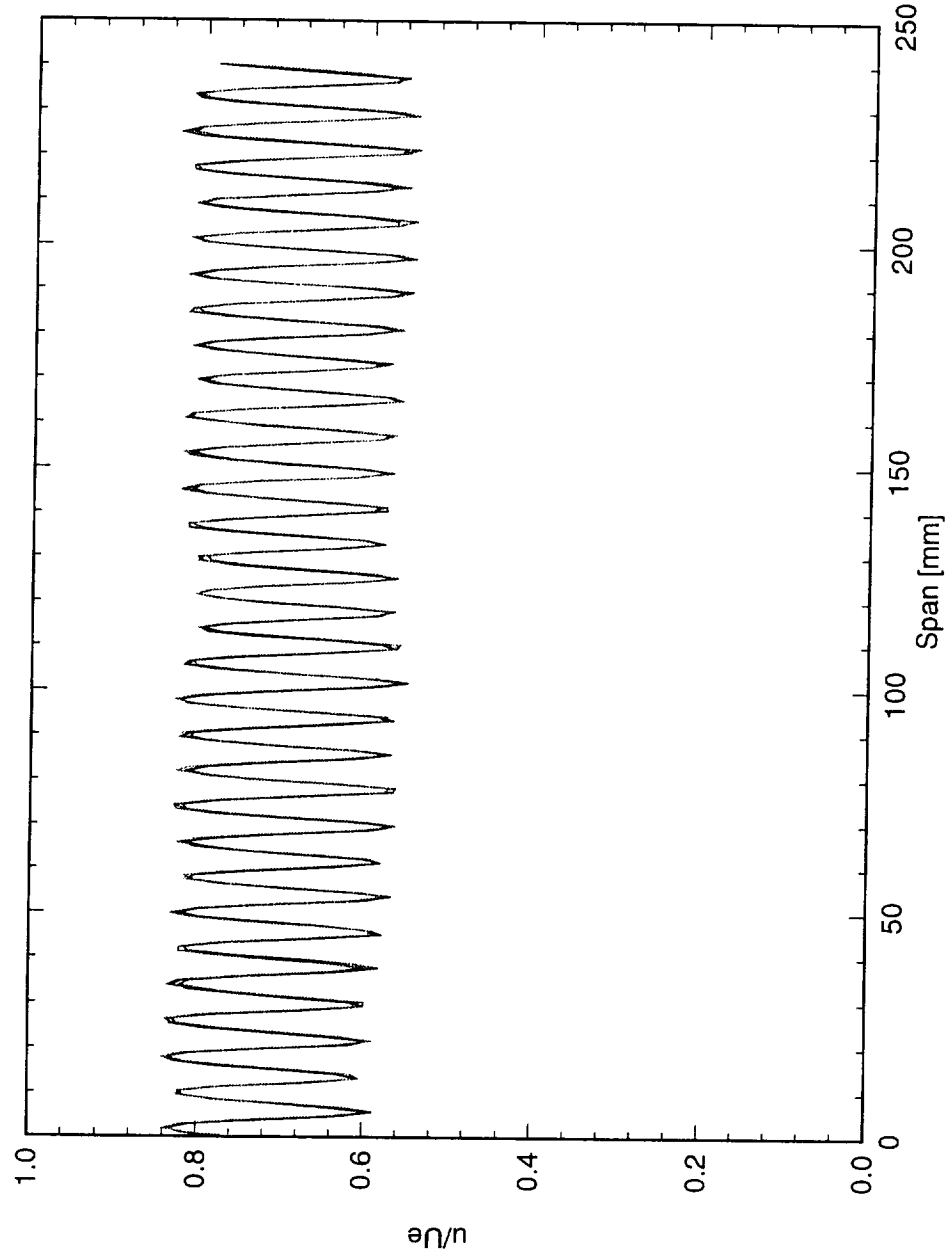

Figure 5.175: Spanwise hot-wire scan at $x/c = 0.25$ and $Y = 0.90$ mm. $Re_c = 2.4 \times 10^6$, [6|8] roughness.

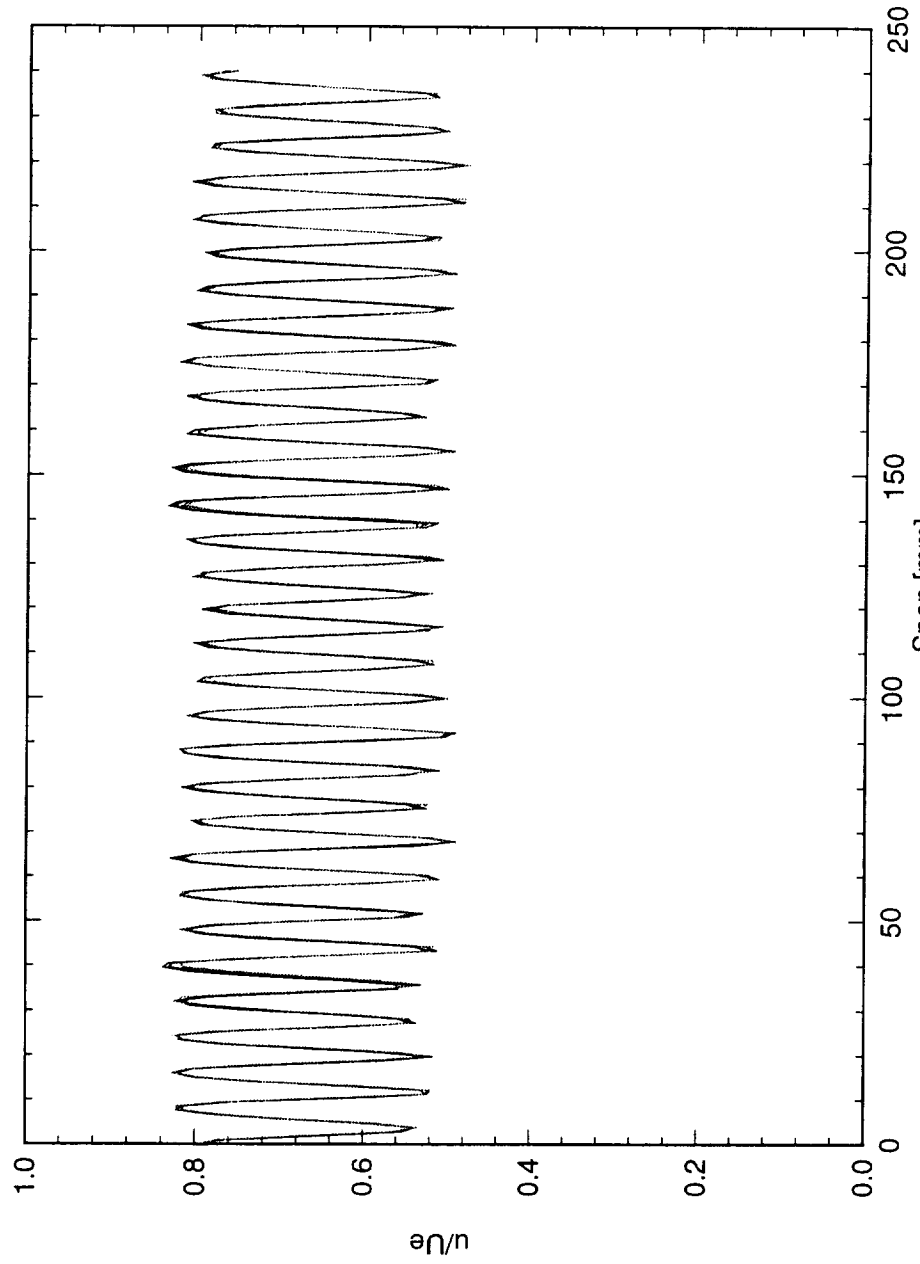

Figure 5.176: Spanwise hot-wire scan at $x/c = 0.30$ and $Y = 0.85$ mm. $Re_c = 2.4 \times 10^6$, [6|8] roughness.

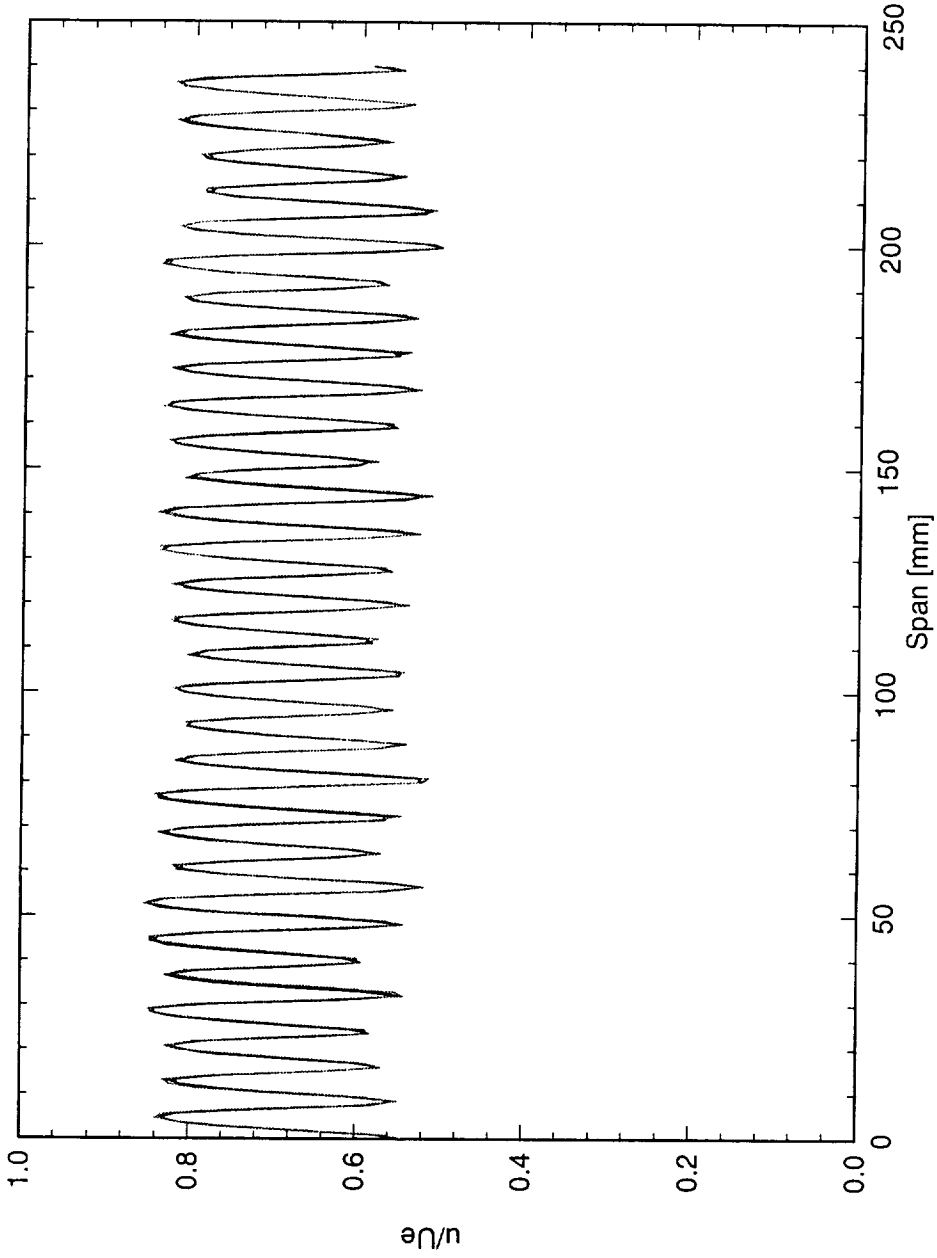

Figure 5.177: Spanwise hot-wire scan at $x/c = 0.35$ and $Y = 0.90$ mm. $Re_c = 2.4 \times 10^6$, [6|8] roughness.

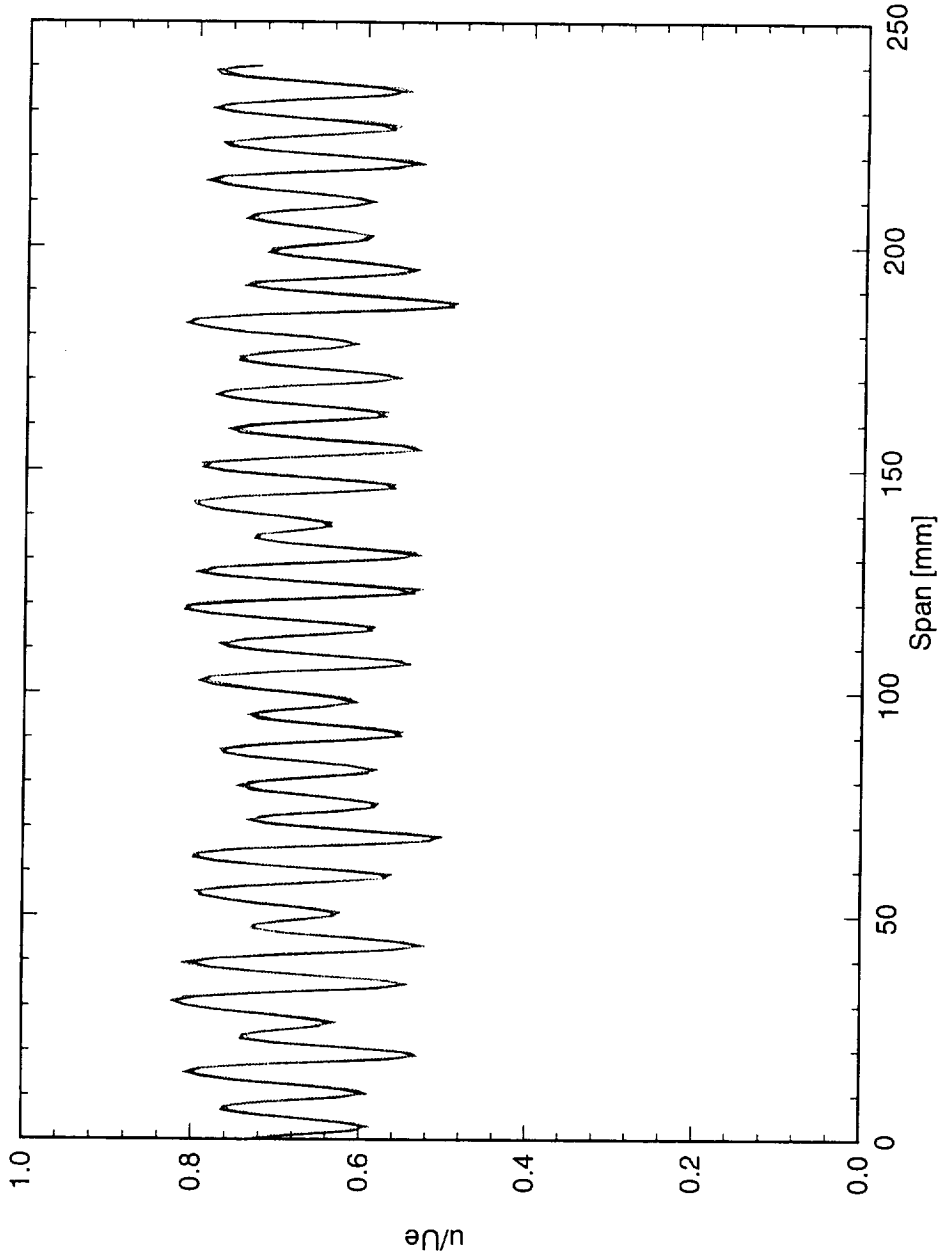

Figure 5.178: Spanwise hot-wire scan at $x/c = 0.40$ and $Y = 0.90$ mm. $Re_c = 2.4 \times 10^6$, [6|8] roughness.

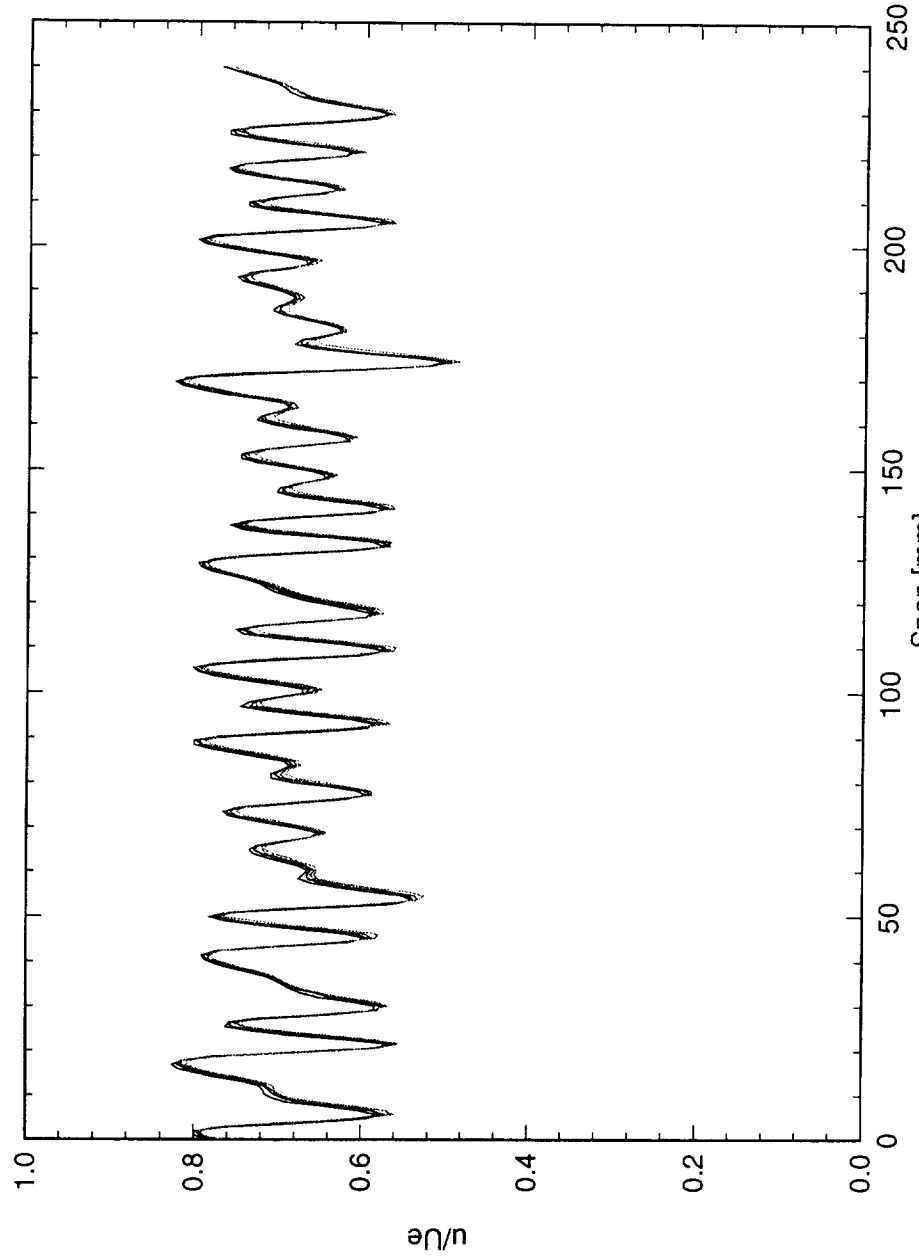

Figure 5.179: Spanwise hot-wire scan at $x/c = 0.45$ and $Y = 1.0$ mm. $Re_c = 2.4 \times 10^6$, [6|8] roughness.

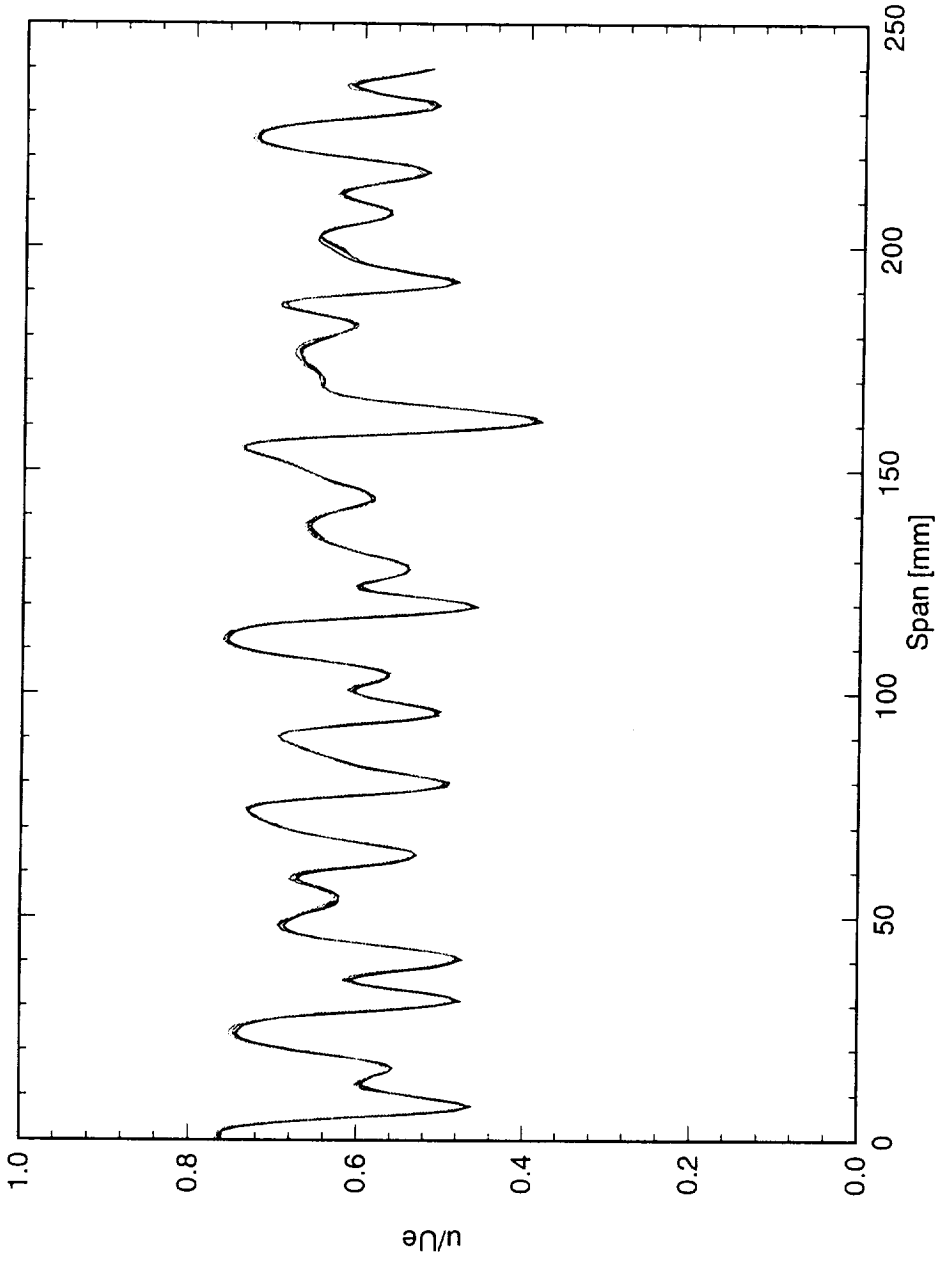

Figure 5.180: Spanwise hot-wire scan at $x/c = 0.50$ and $Y = 0.90$ mm. $Re_c = 2.4 \times 10^6$, [6|8] roughness.

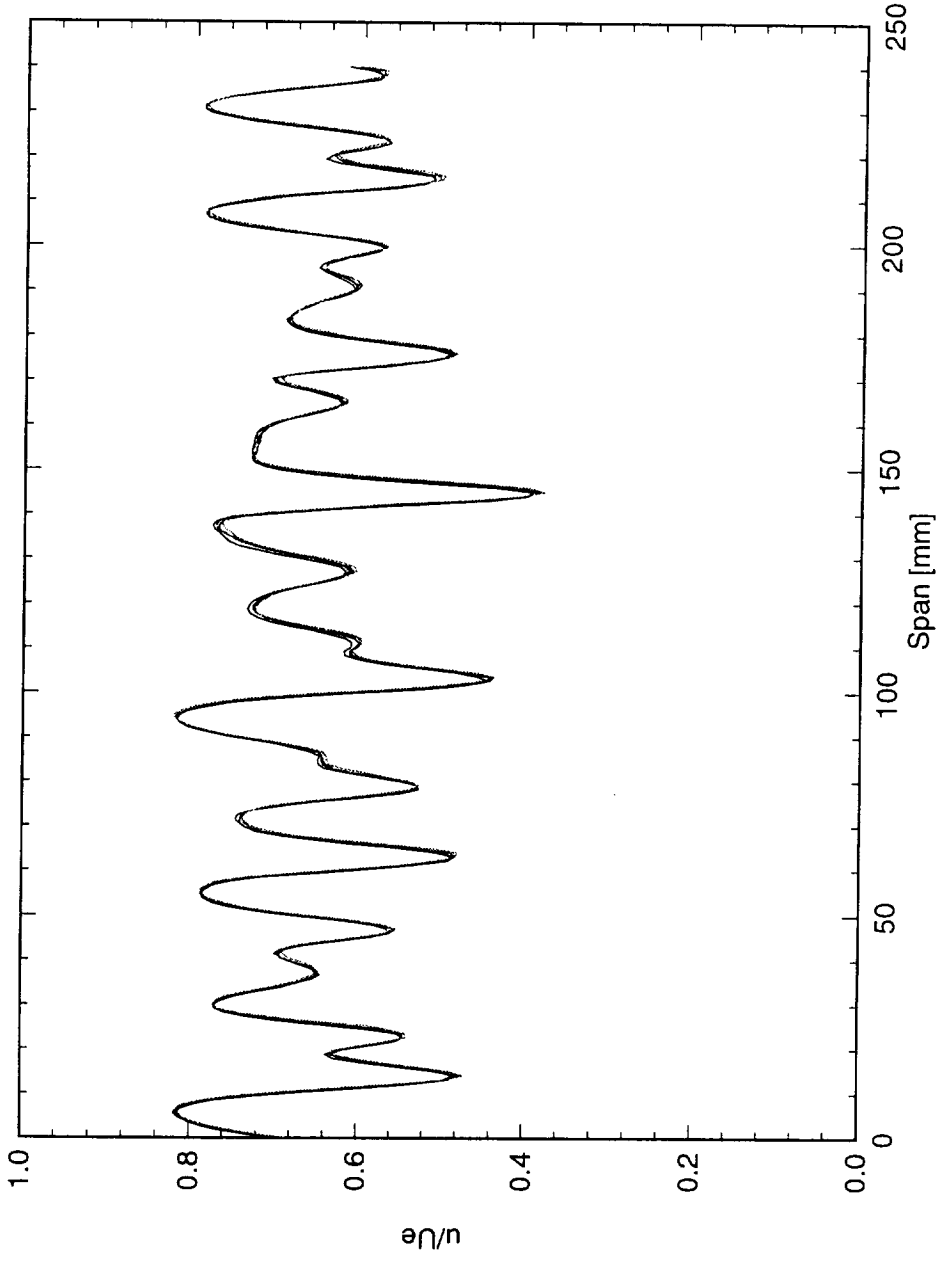

Figure 5.181: Spanwise hot-wire scan at $x/c = 0.55$ and $Y = 1.0$ mm. $Re_c = 2.4 \times 10^6$, [6|8] roughness.

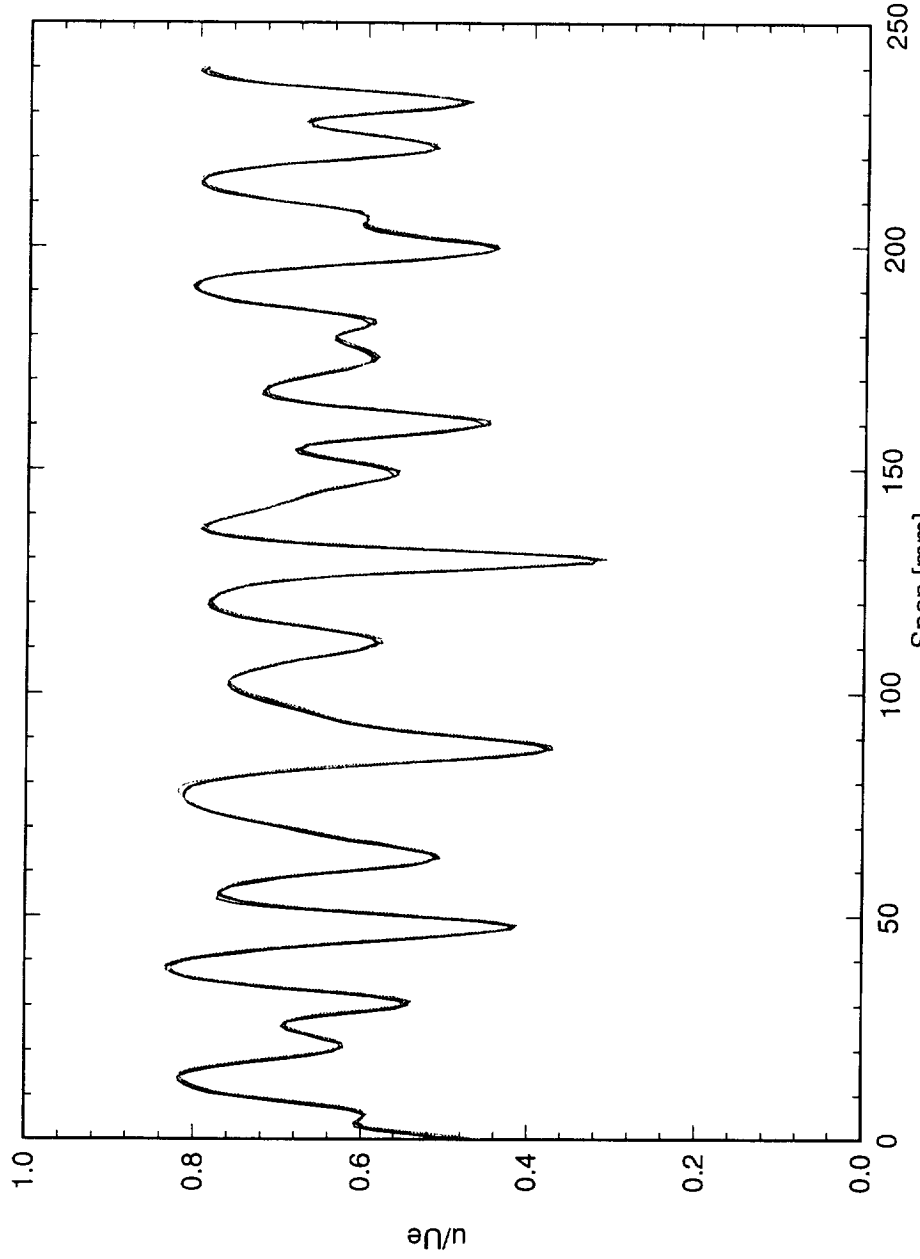

Figure 5.182: Spanwise hot-wire scan at $x/c = 0.60$ and $Y = 1.0$ mm. $Re_c = 2.4 \times 10^6$, [6|8] roughness.

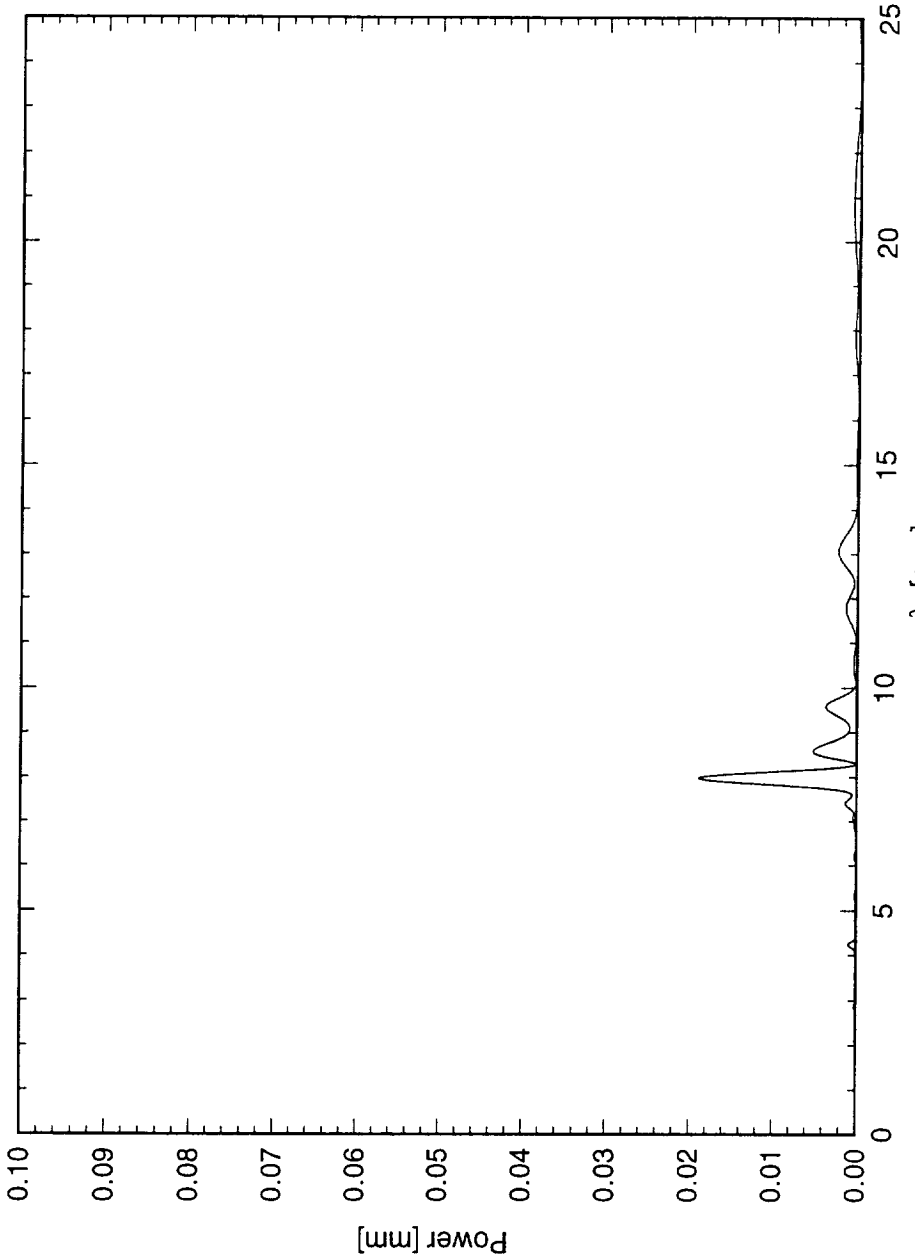

Figure 5.183: Power spectral density of constant-Y scan at $x/c = 0.10$ and $Y = 0.60$ mm. $Re_c = 2.4 \times 10^6$, [6|8] roughness.

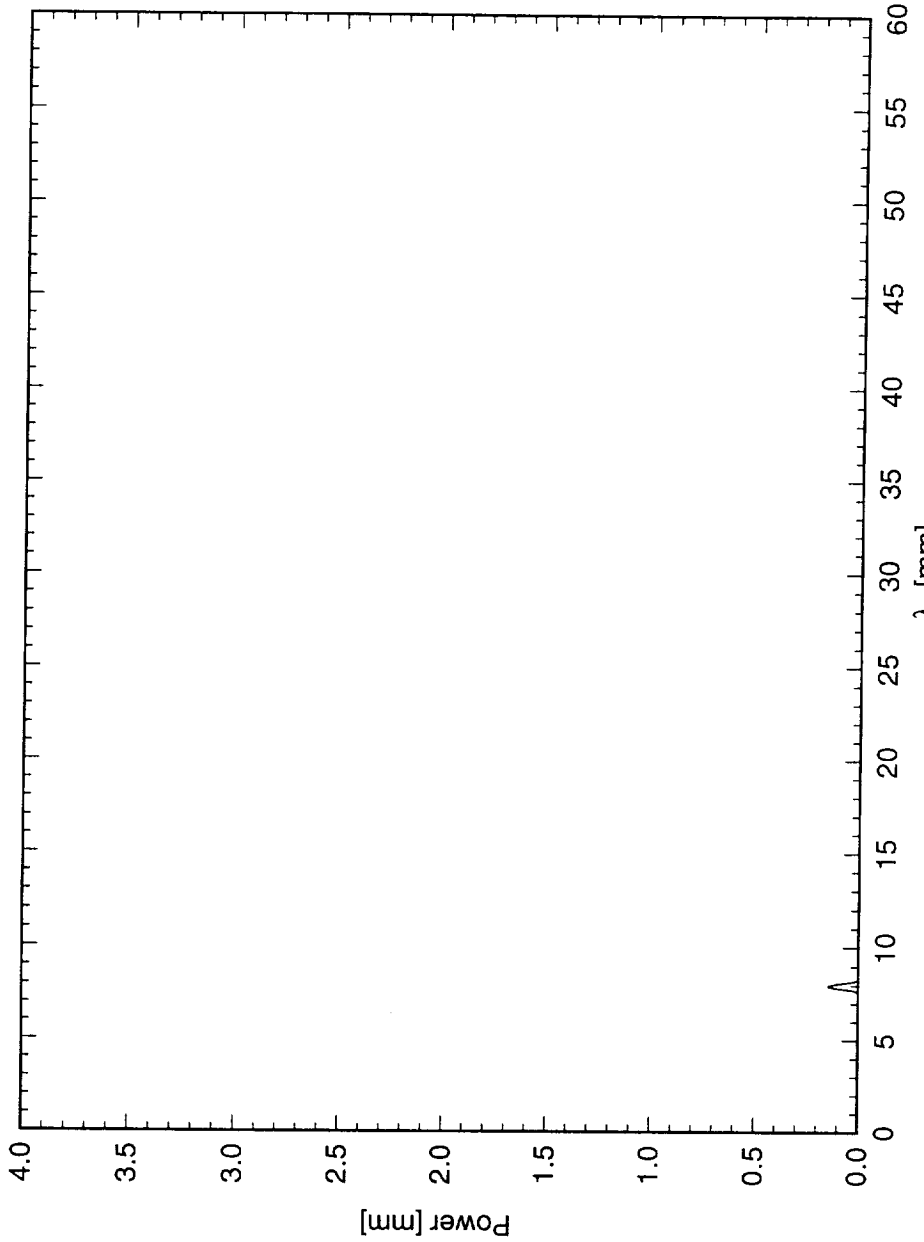

Figure 5.184: Power spectral density of constant-Y scan at $x/c = 0.15$ and $Y = 0.80$ mm. $Re_c = 2.4 \times 10^6$, [6|8] roughness.

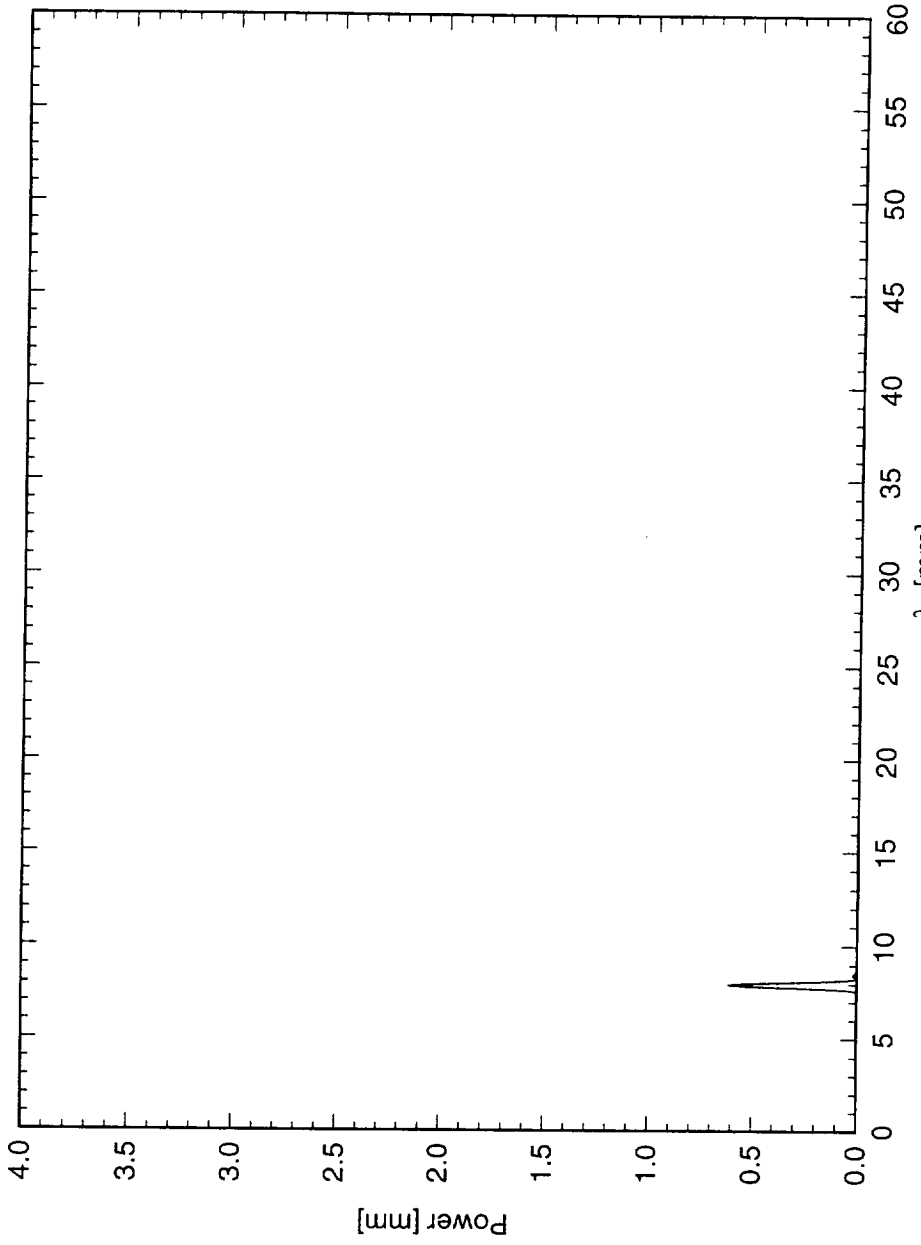

Figure 5.185: Power spectral density of constant-Y scan at $x/c = 0.20$ and $Y = 0.90$ mm. $Re_c = 2.4 \times 10^6$, [6|8] roughness.

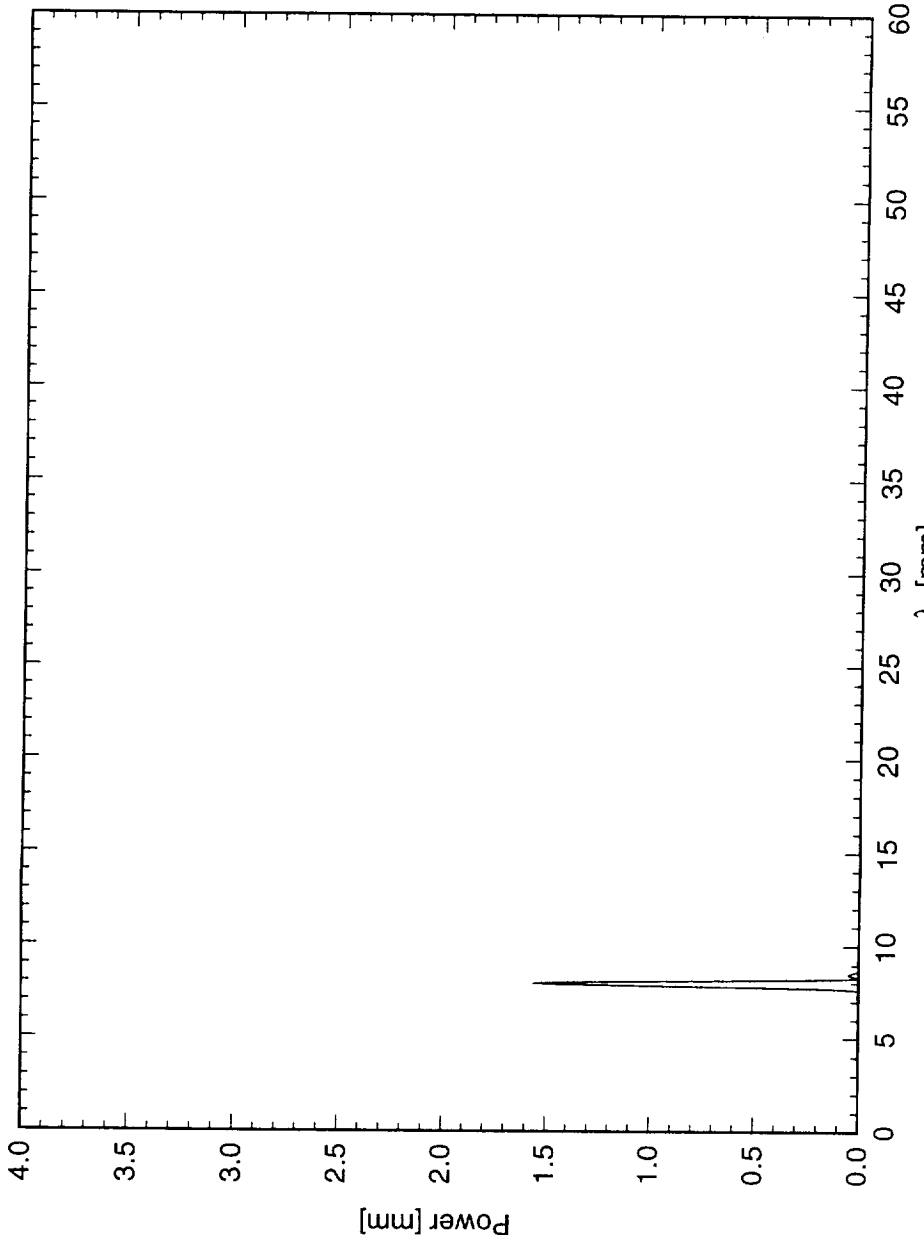

Figure 5.186: Power spectral density of constant-Y scan at $x/c = 0.25$ and $Y = 0.90$ mm. $Re_c = 2.4 \times 10^6$, [6|8] roughness.

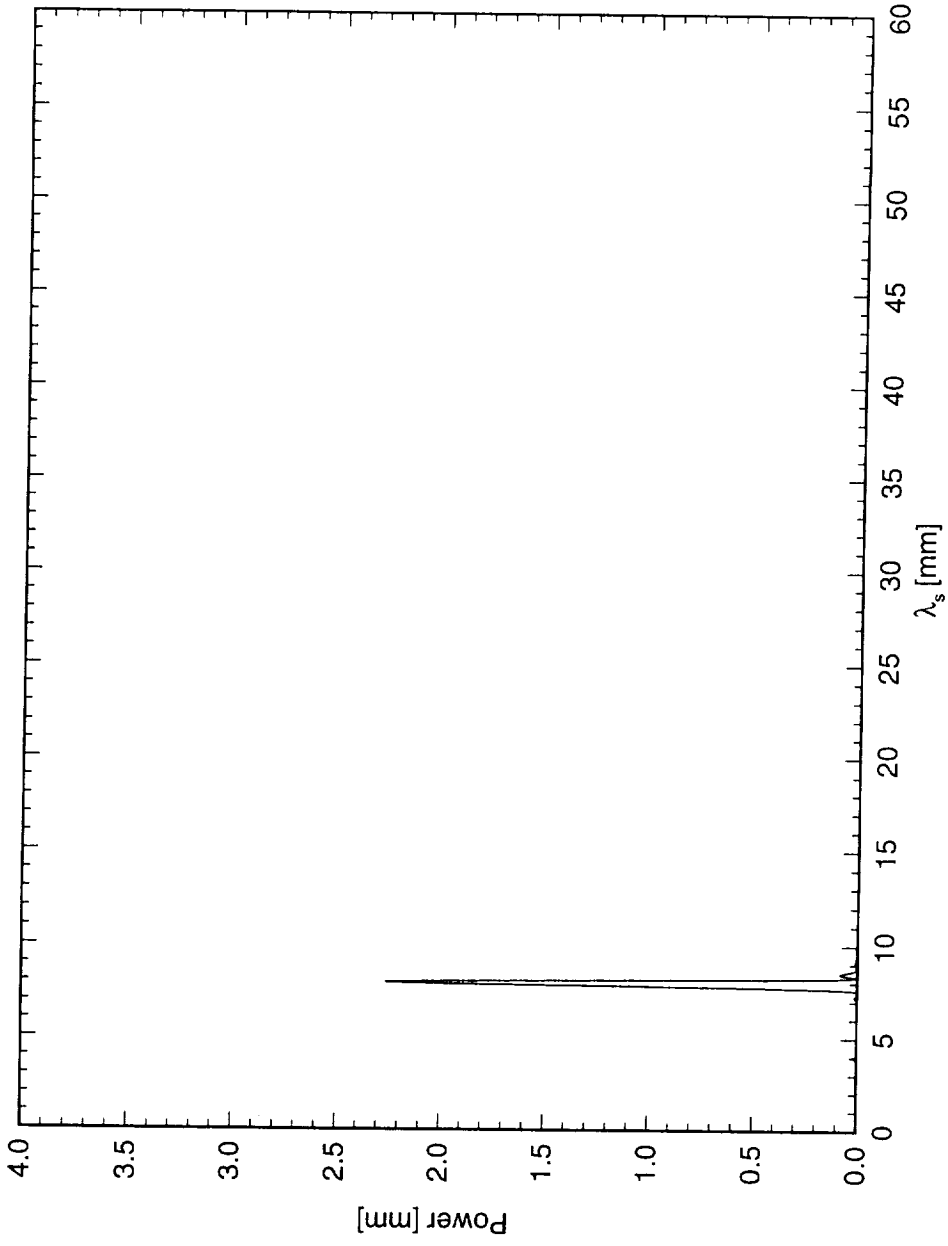

Figure 5.187: Power spectral density of constant-Y scan at $x/c = 0.30$ and $Y = 0.85$ mm. $Re_c = 2.4 \times 10^6$, [6|8] roughness.

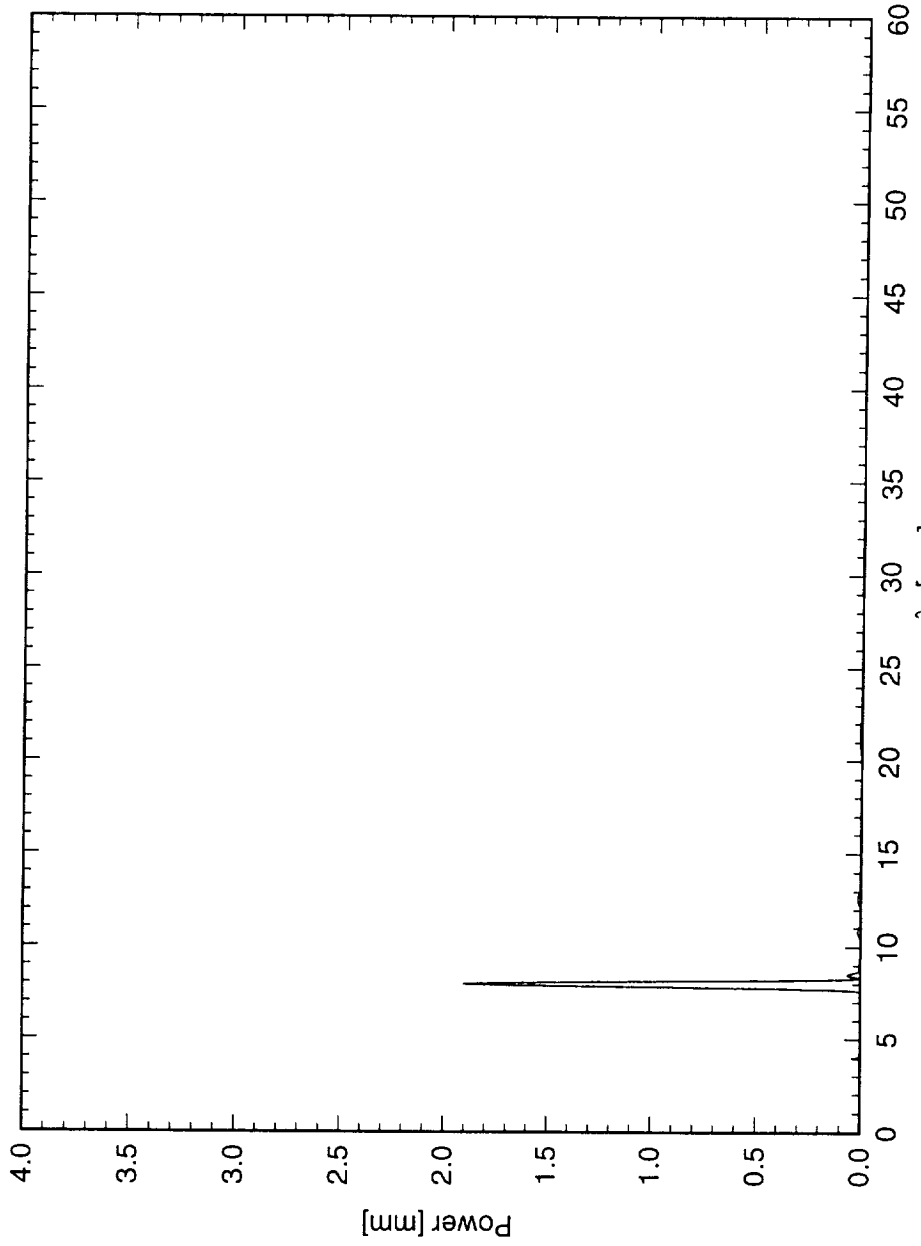

Figure 5.188: Power spectral density of constant-Y scan at $x/c = 0.35$ and $Y = 0.90$ mm. $Re_c = 2.4 \times 10^6$, [6|8] roughness.

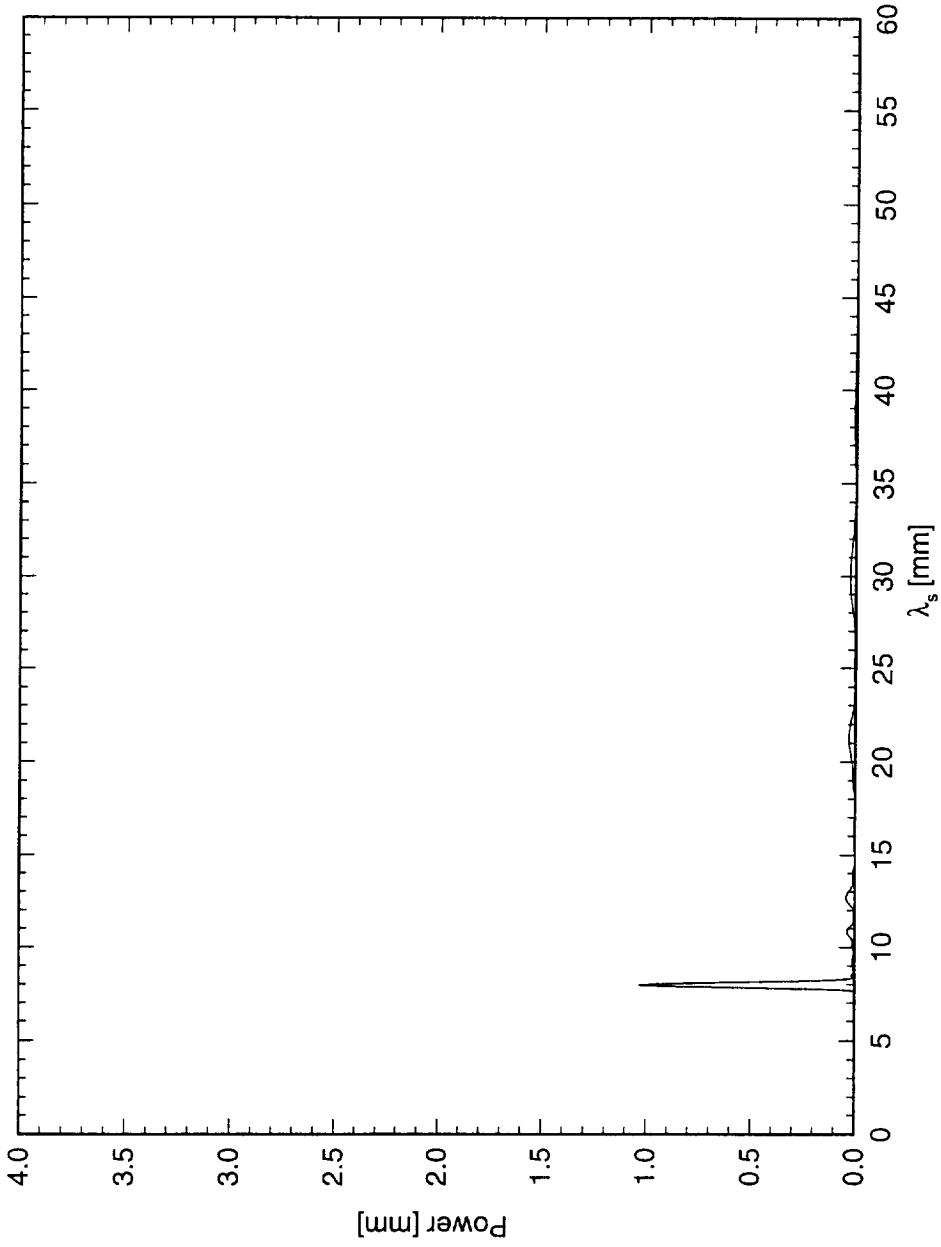

Figure 5.189: Power spectral density of constant-Y scan at $x/c = 0.40$ and $Y = 0.90$ mm. $Re_c = 2.4 \times 10^6$, [6|8] roughness.

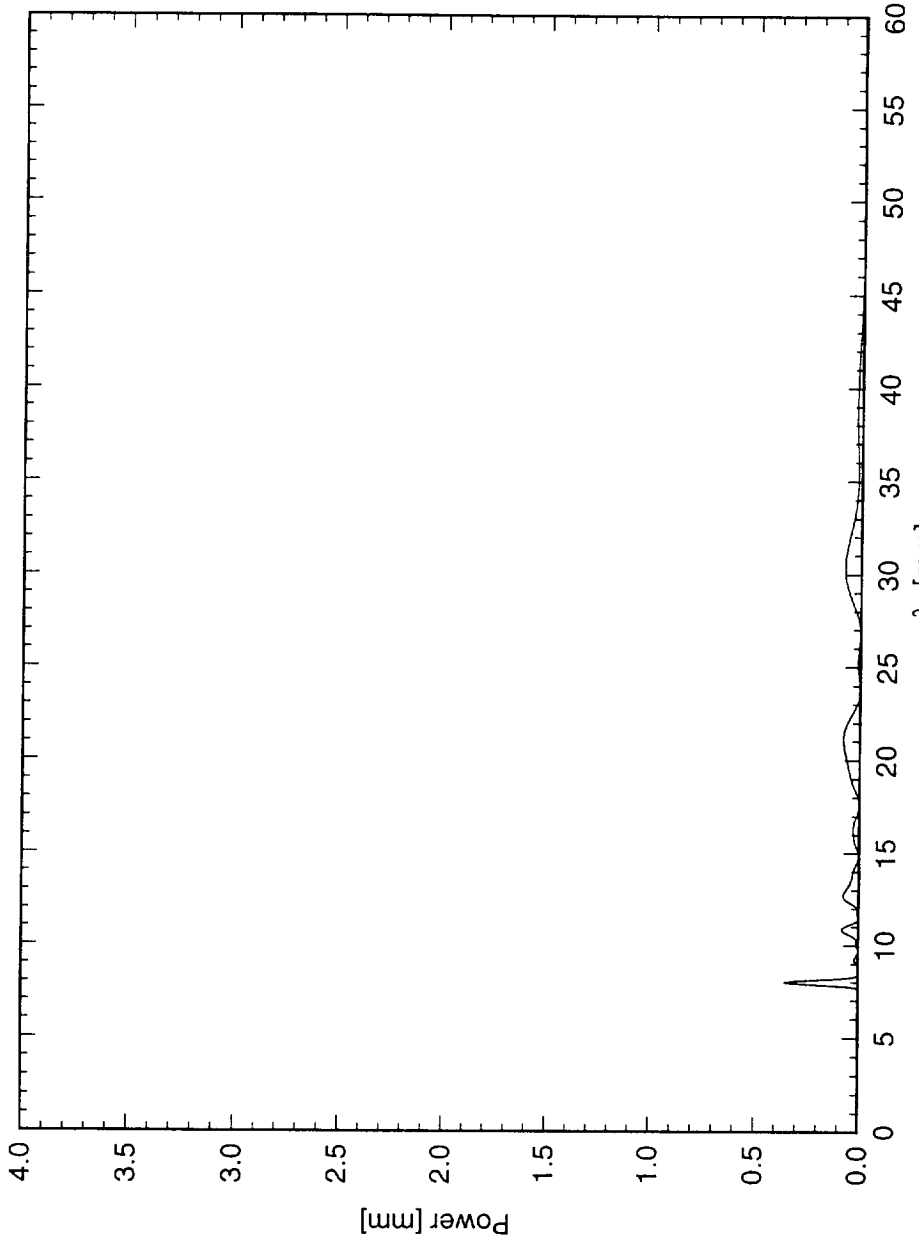

Figure 5.190: Power spectral density of constant-Y scan at $x/c = 0.45$ and $Y = 1.0$ mm. $Re_c = 2.4 \times 10^6$, [6|8] roughness.

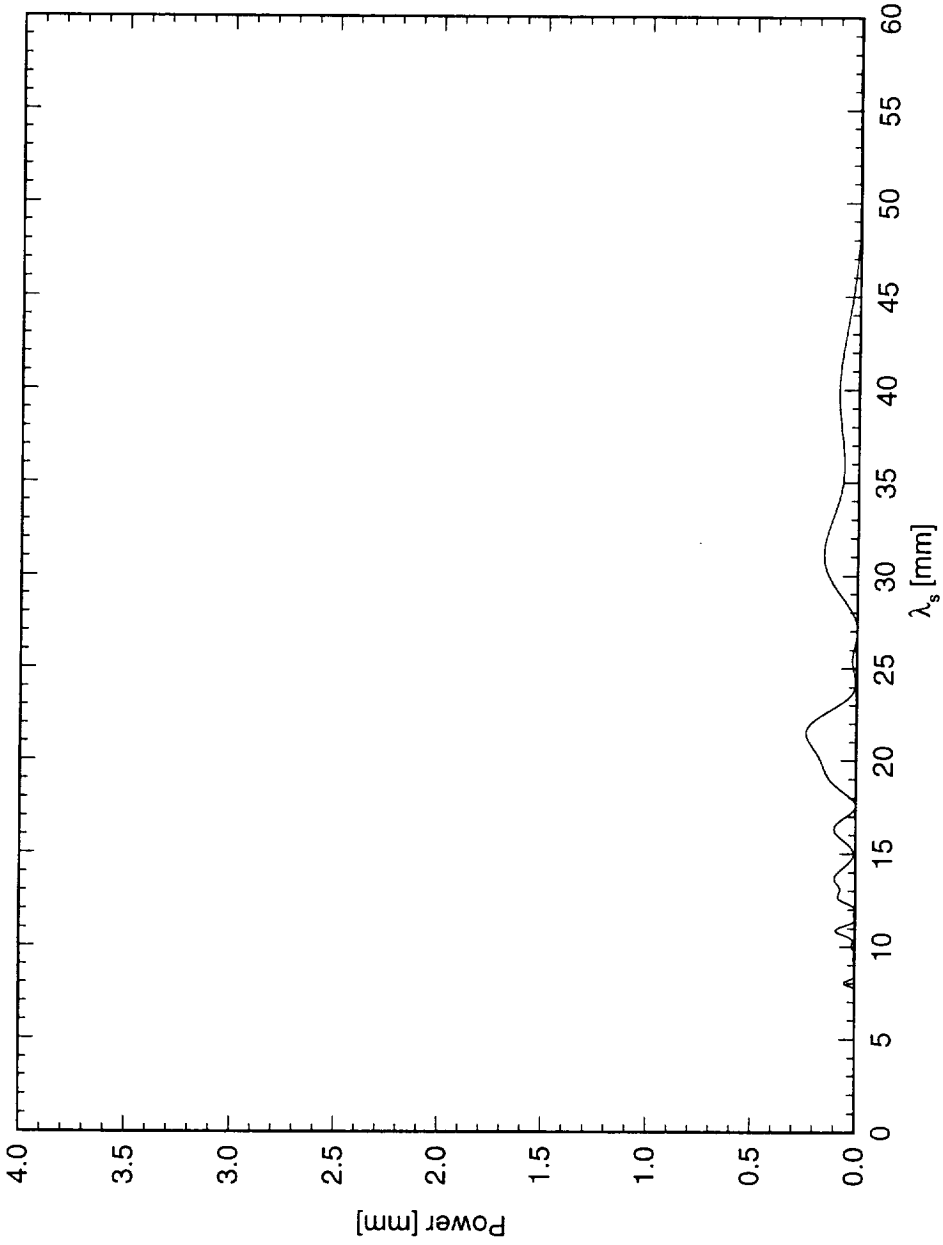

Figure 5.191: Power spectral density of constant-Y scan at $x/c = 0.50$ and $Y = 0.90$ mm. $Re_c = 2.4 \times 10^6$, [6|8] roughness.

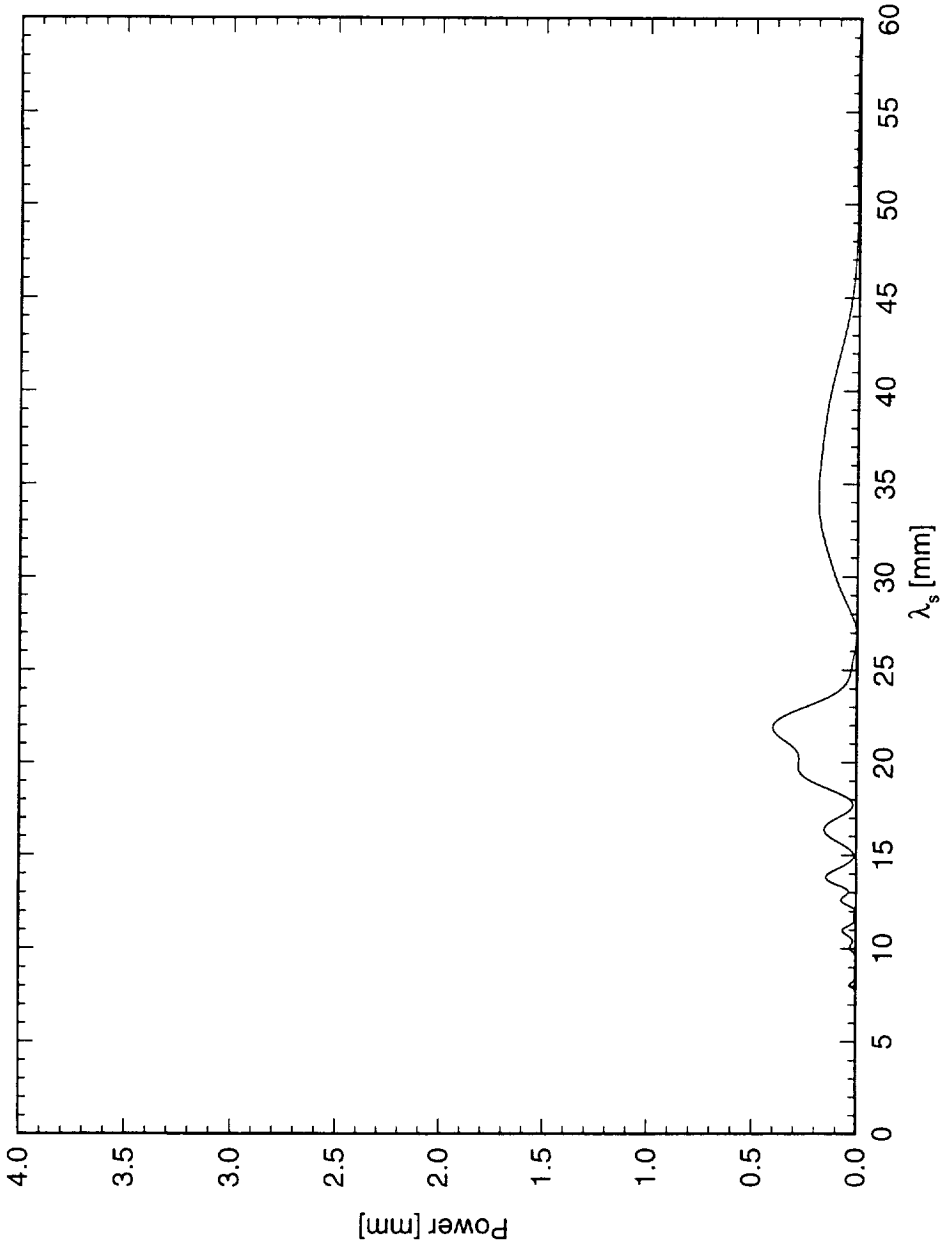

Figure 5.192: Power spectral density of constant-Y scan at $x/c = 0.55$ and $Y = 1.0$ mm. $Re_c = 2.4 \times 10^6$, [6|8] roughness.

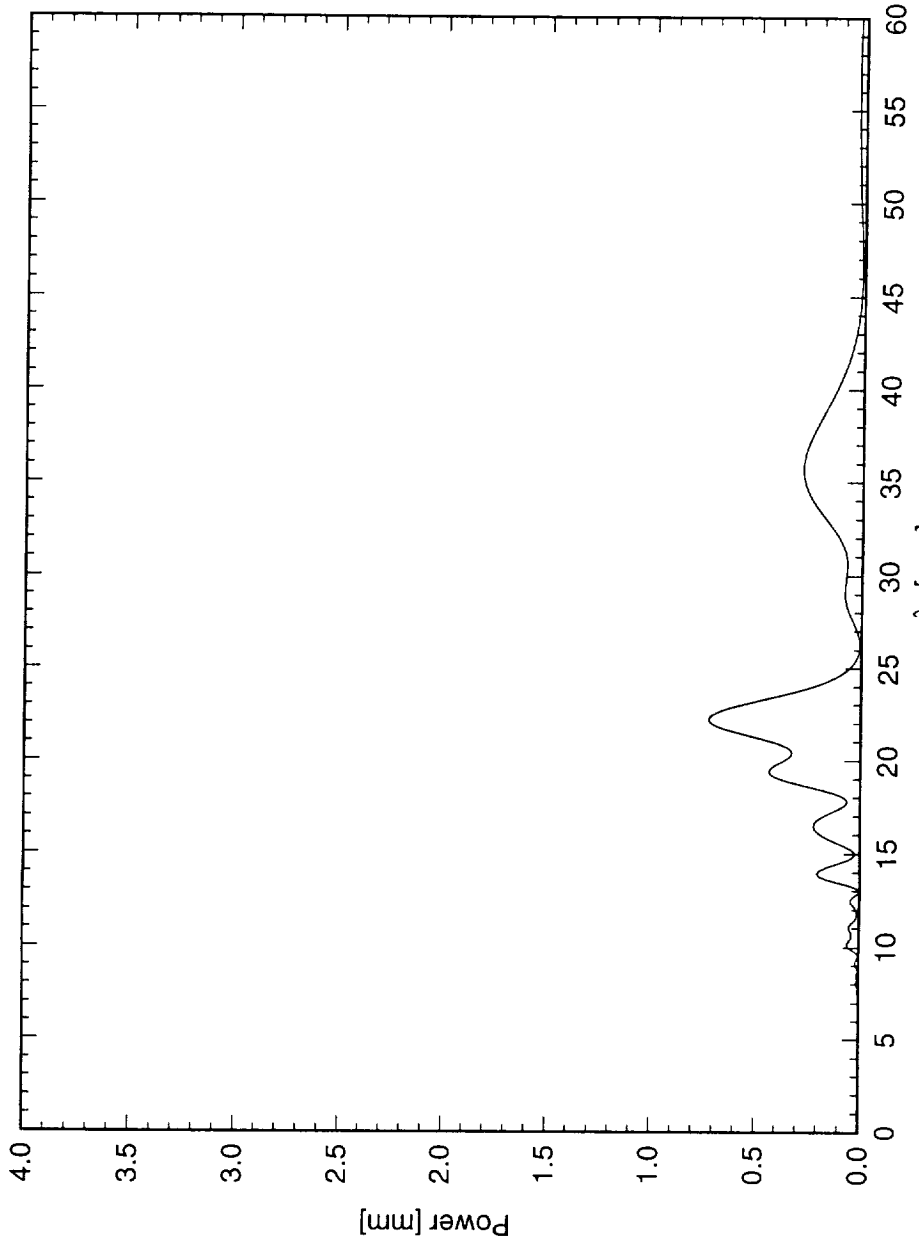

Figure 5.193: Power spectral density of constant-Y scan at $x/c = 0.60$ and $Y = 1.0$ mm. $Re_c = 2.4 \times 10^6$, [6|8] roughness.

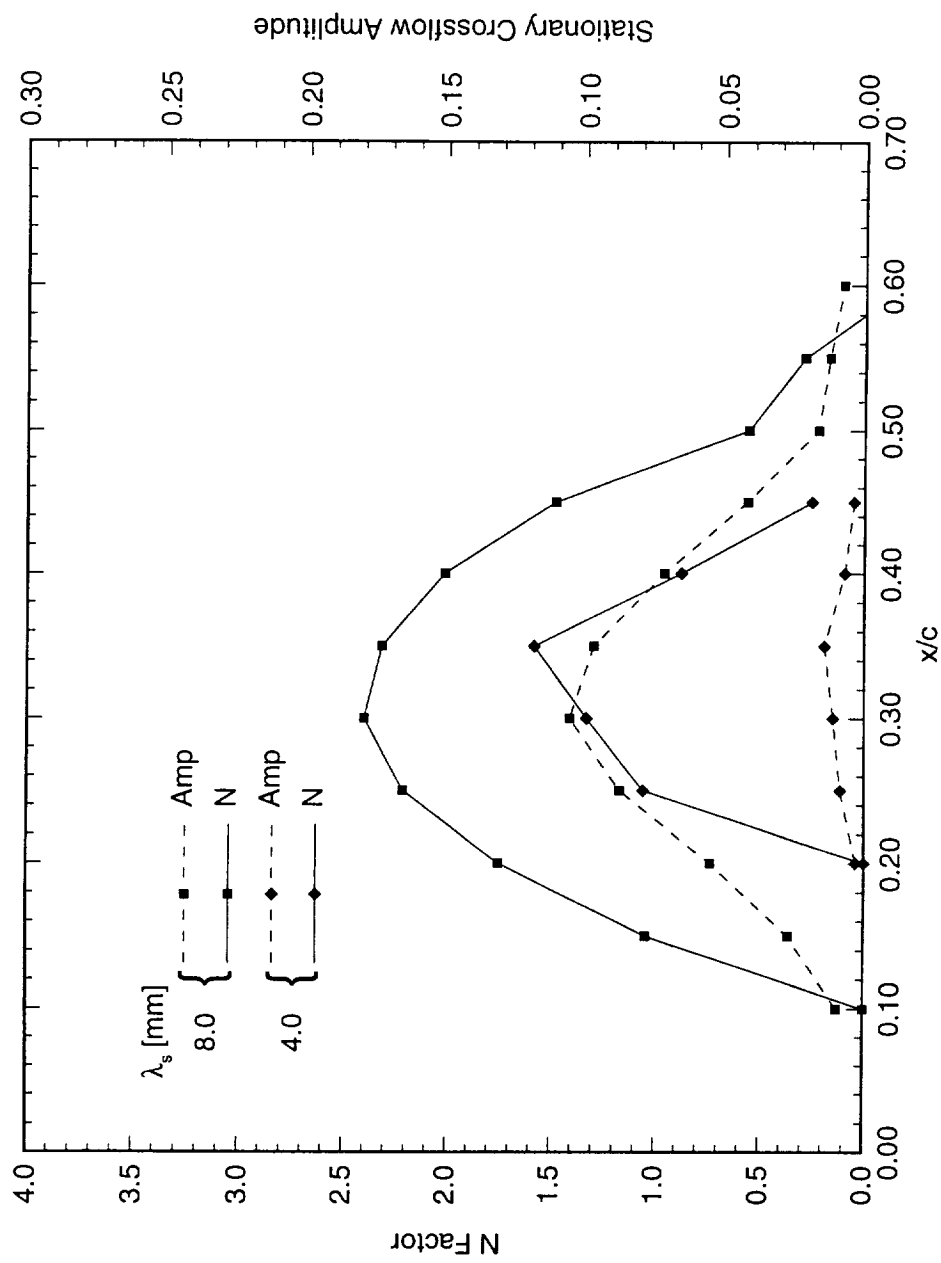

Figure 5.194: Single-mode disturbance amplitude and N-factors. $Re_c = 2.4 \times 10^6$, [6|8] roughness. N-factor calculations are relative to the location where the disturbance is first detected.

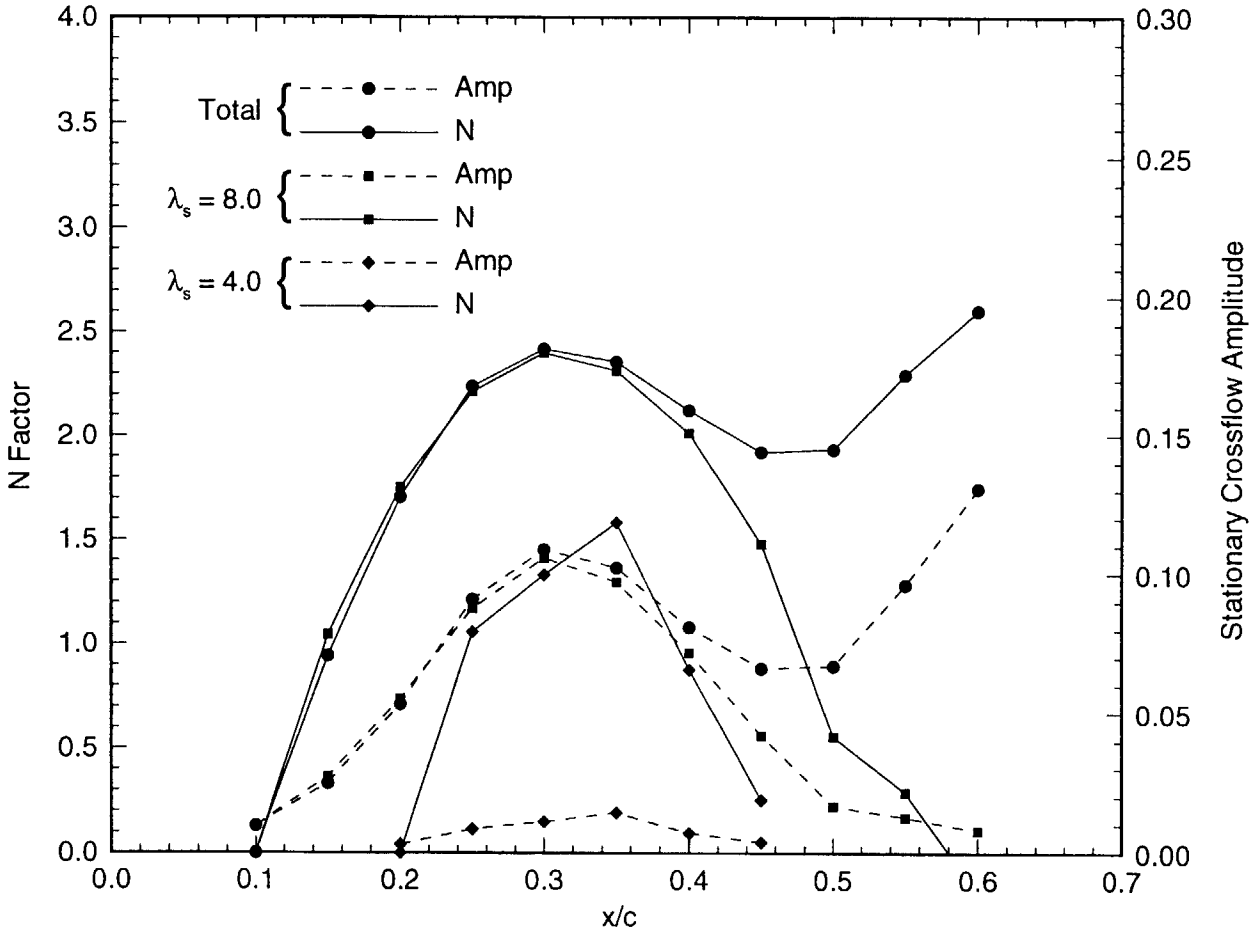

Figure 5.195: Total and single-mode disturbance amplitude and N-factors. $Re_c = 2.4 \times 10^6$, [6|8] roughness. N-factor calculations are relative to the location where the disturbance is first detected.

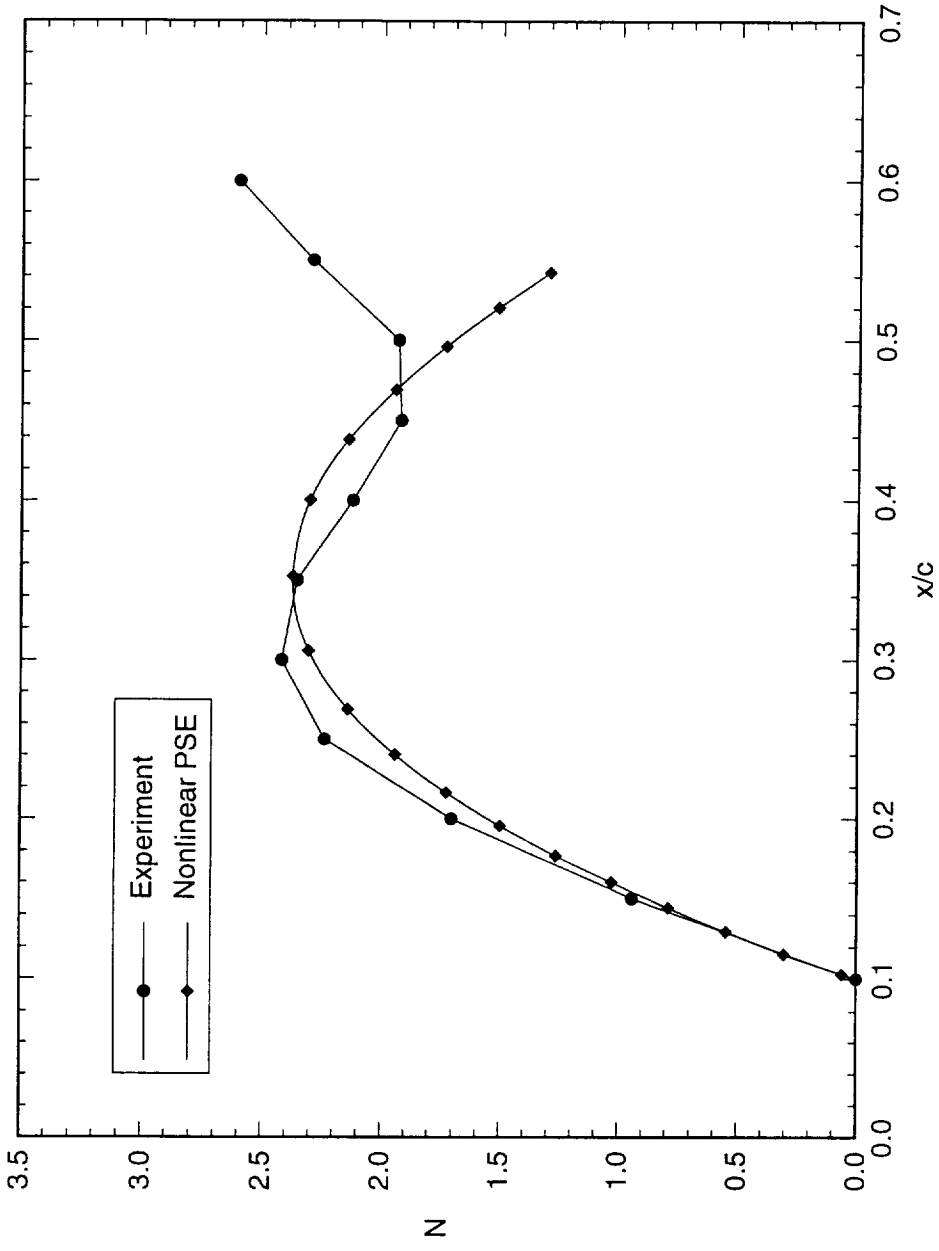

Figure 5.196: Comparison of experimental and theoretical total disturbance amplification factor N for $Re_c = 2.4 \times 10^6$ and [6|8] roughness. N-factor calculations are relative to $x/c = 0.10$.

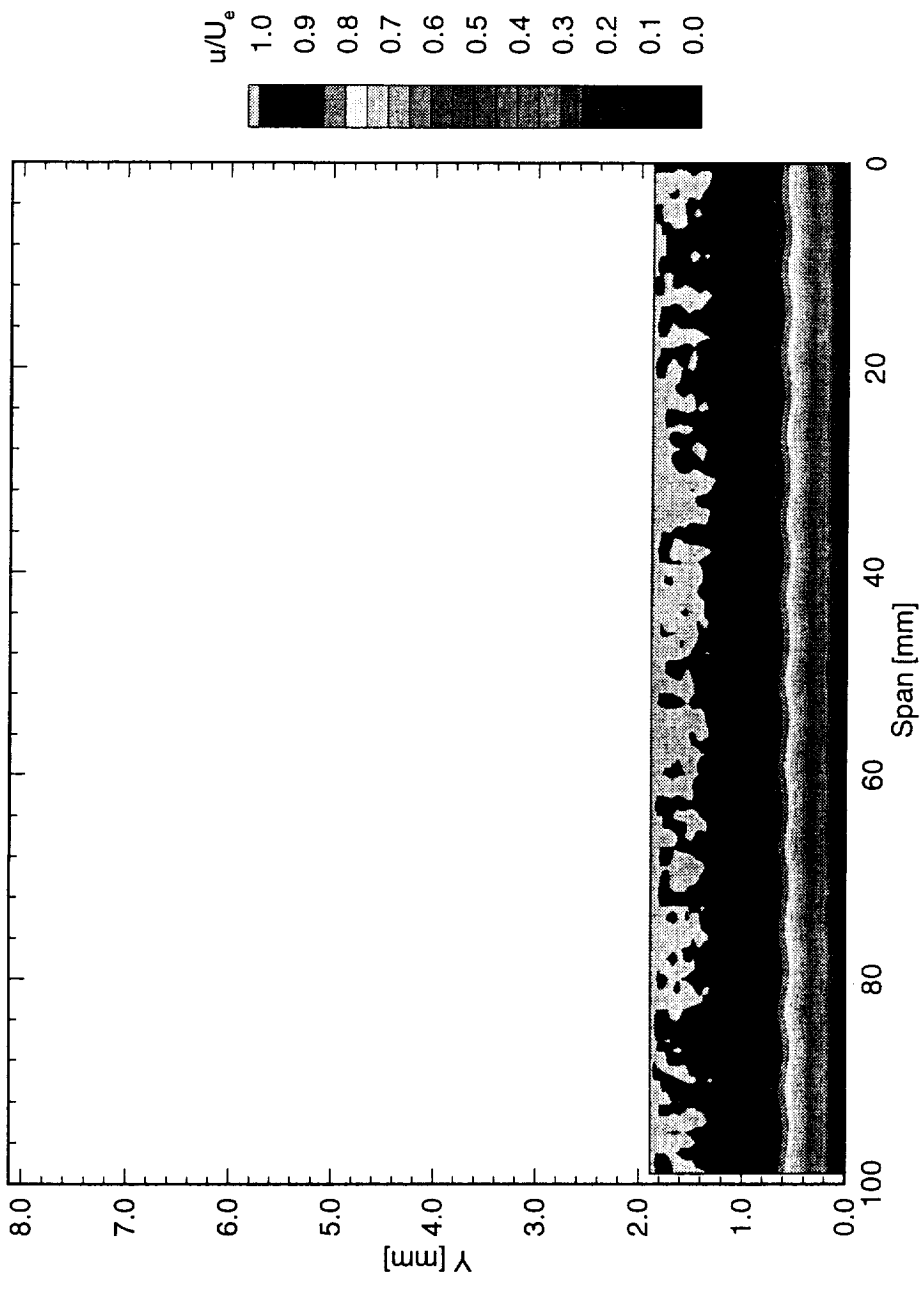

Figure 5.197: Normalized boundary-layer velocity contours at $x/c = 0.05$. $Re_c = 2.4 \times 10^6$, [48|8] roughness.

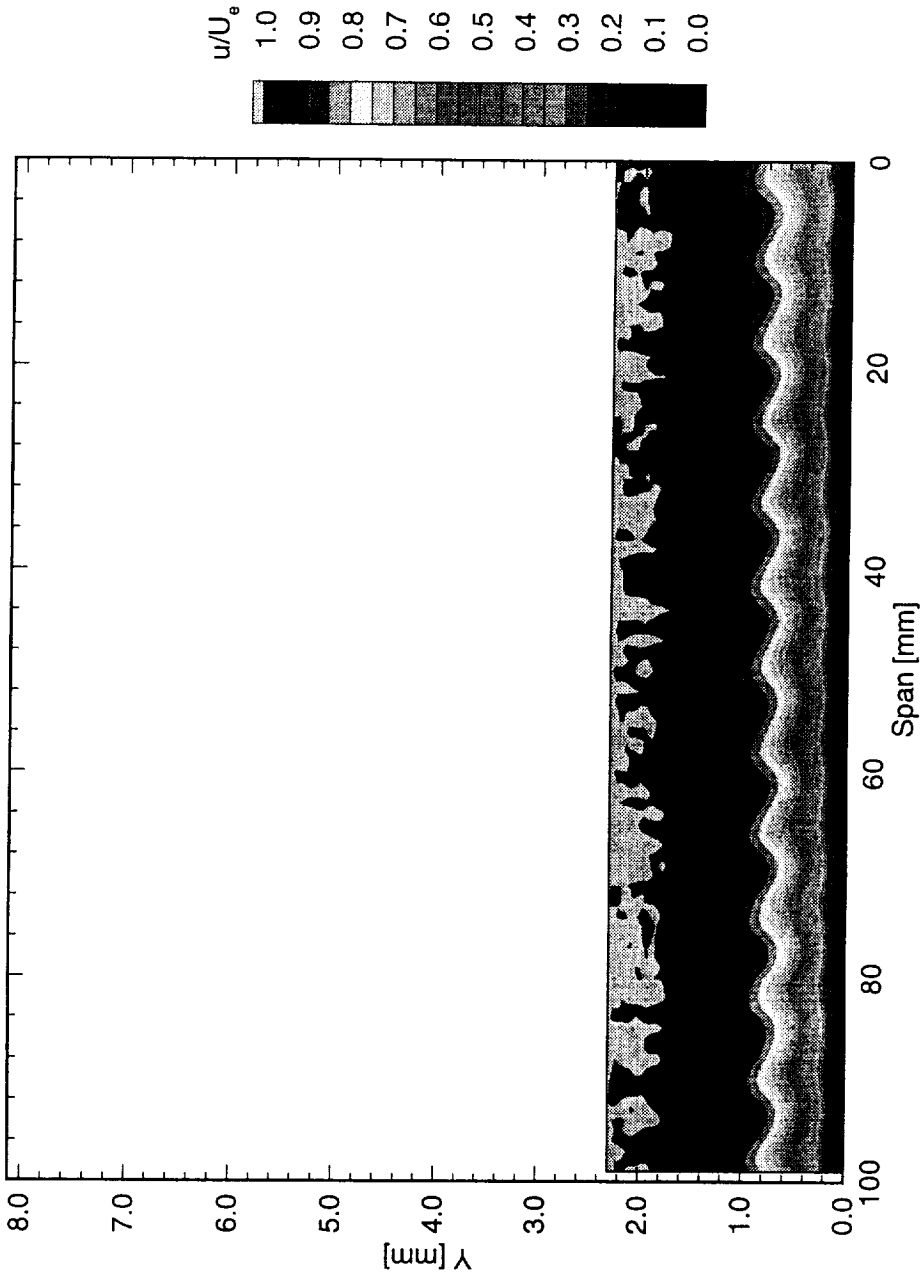

Figure 5.198: Normalized boundary-layer velocity contours at $x/c = 0.10$. $Re_c = 2.4 \times 10^6$, [48|8] roughness.

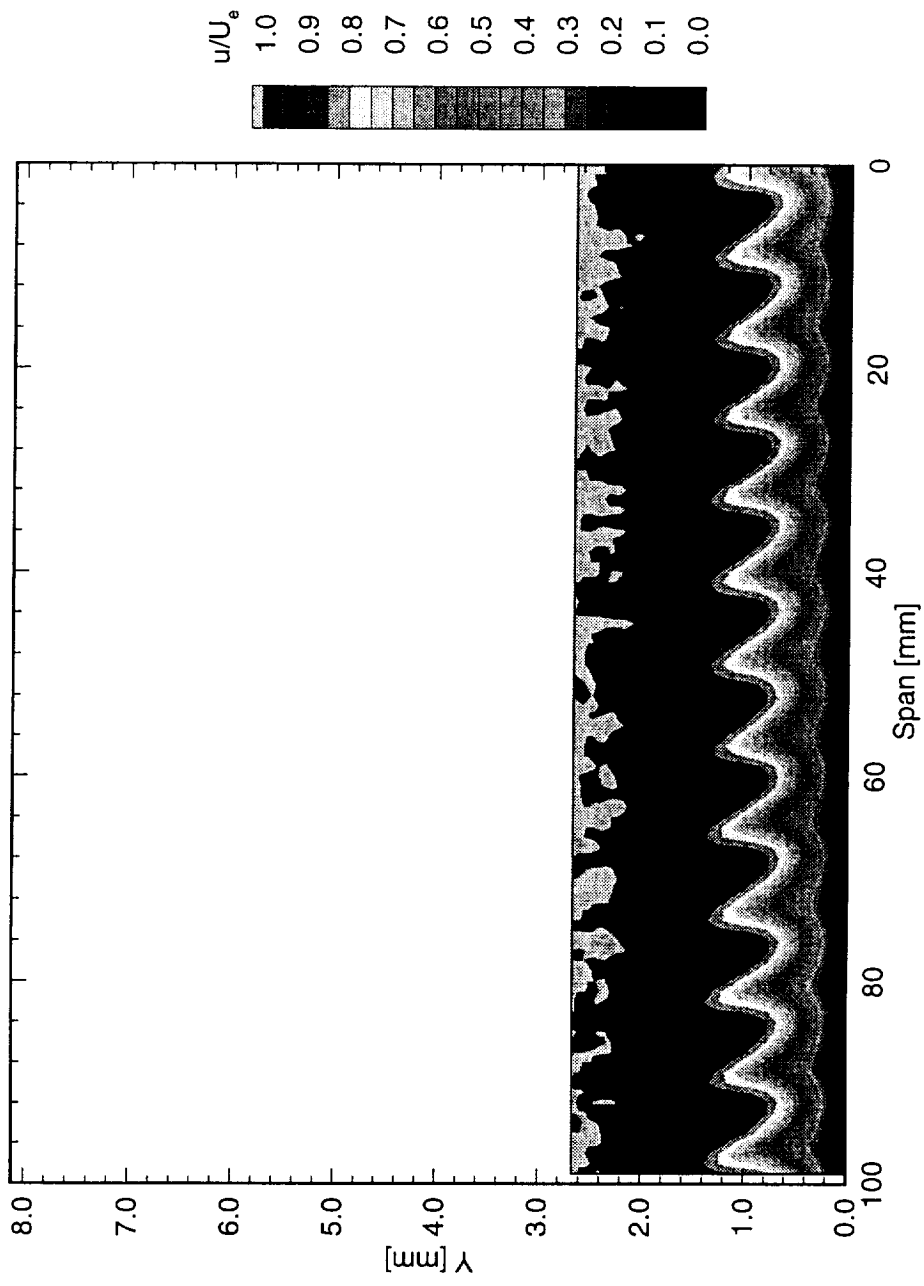

Figure 5.199: Normalized boundary-layer velocity contours at $x/c = 0.15$. $Re_c = 2.4 \times 10^6$, [48|8] roughness.

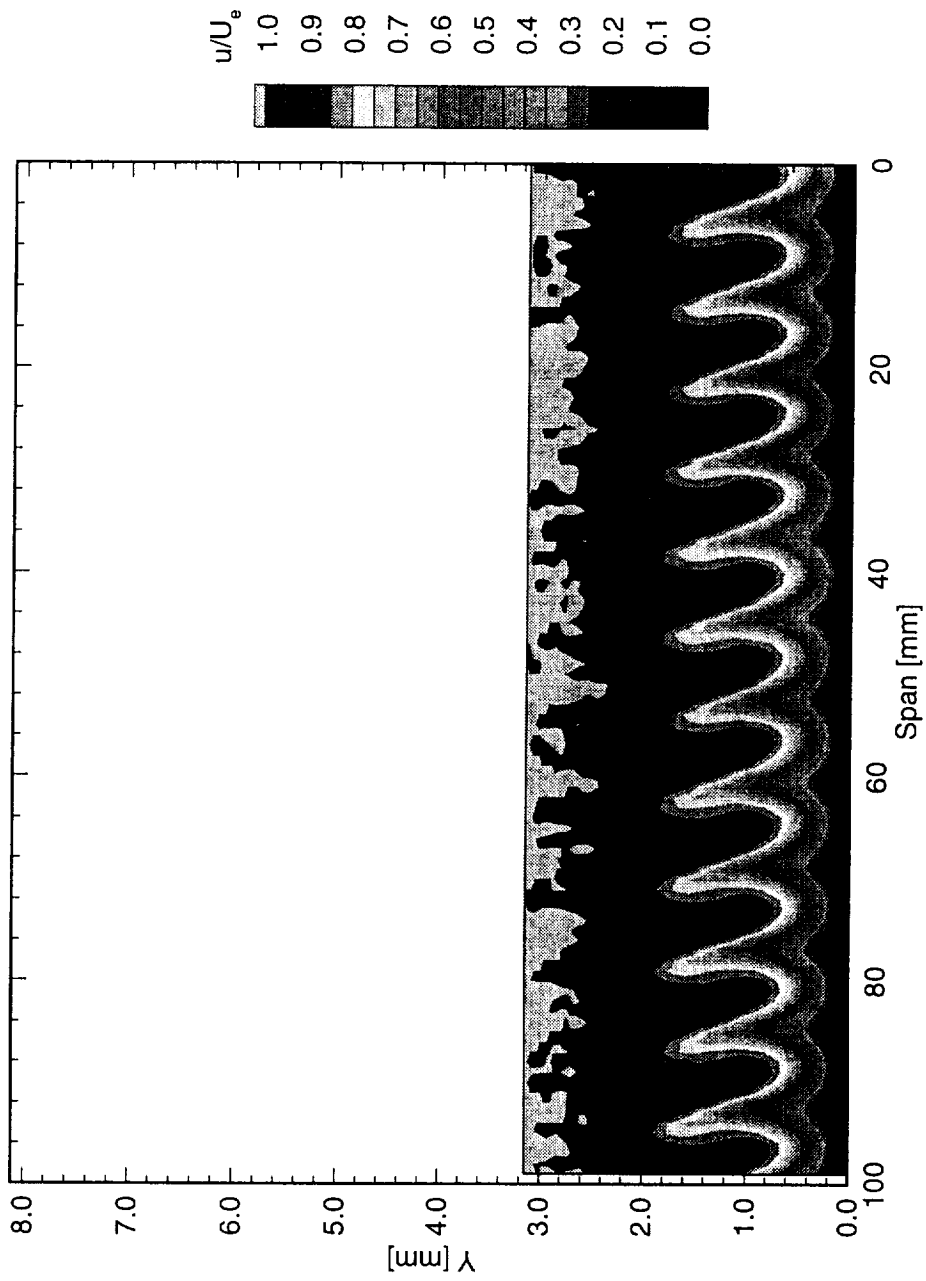

Figure 5.200: Normalized boundary-layer velocity contours at $x/c = 0.20$. $Re_c = 2.4 \times 10^6$, [48|8] roughness.

Figure 5.201: Normalized boundary-layer velocity contours at $x/c = 0.25$. $Re_c = 2.4 \times 10^6$, [48|8] roughness.

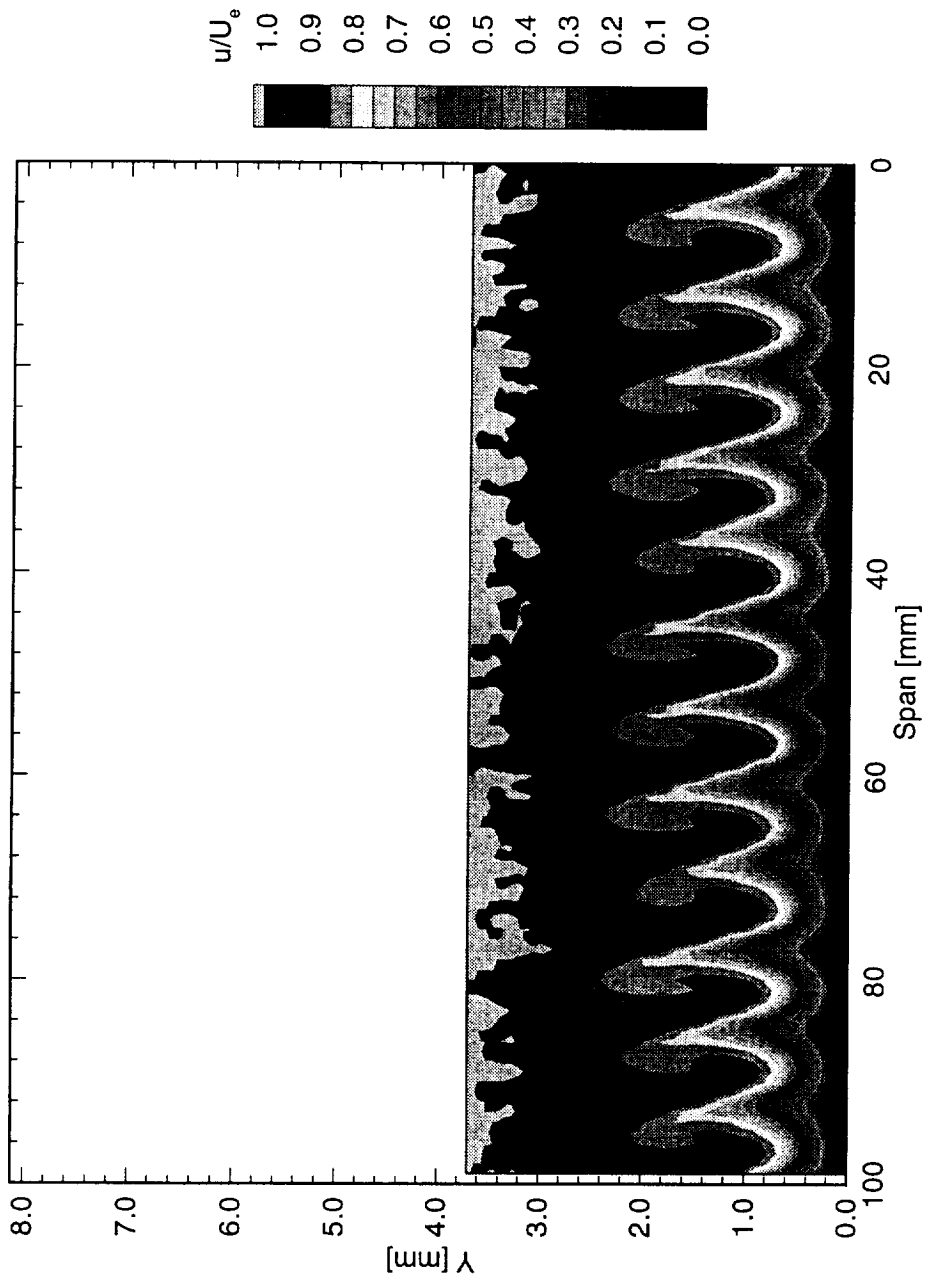

Figure 5.202: Normalized boundary-layer velocity contours at $x/c = 0.30$. $Re_c = 2.4 \times 10^6$, [48|8] roughness.

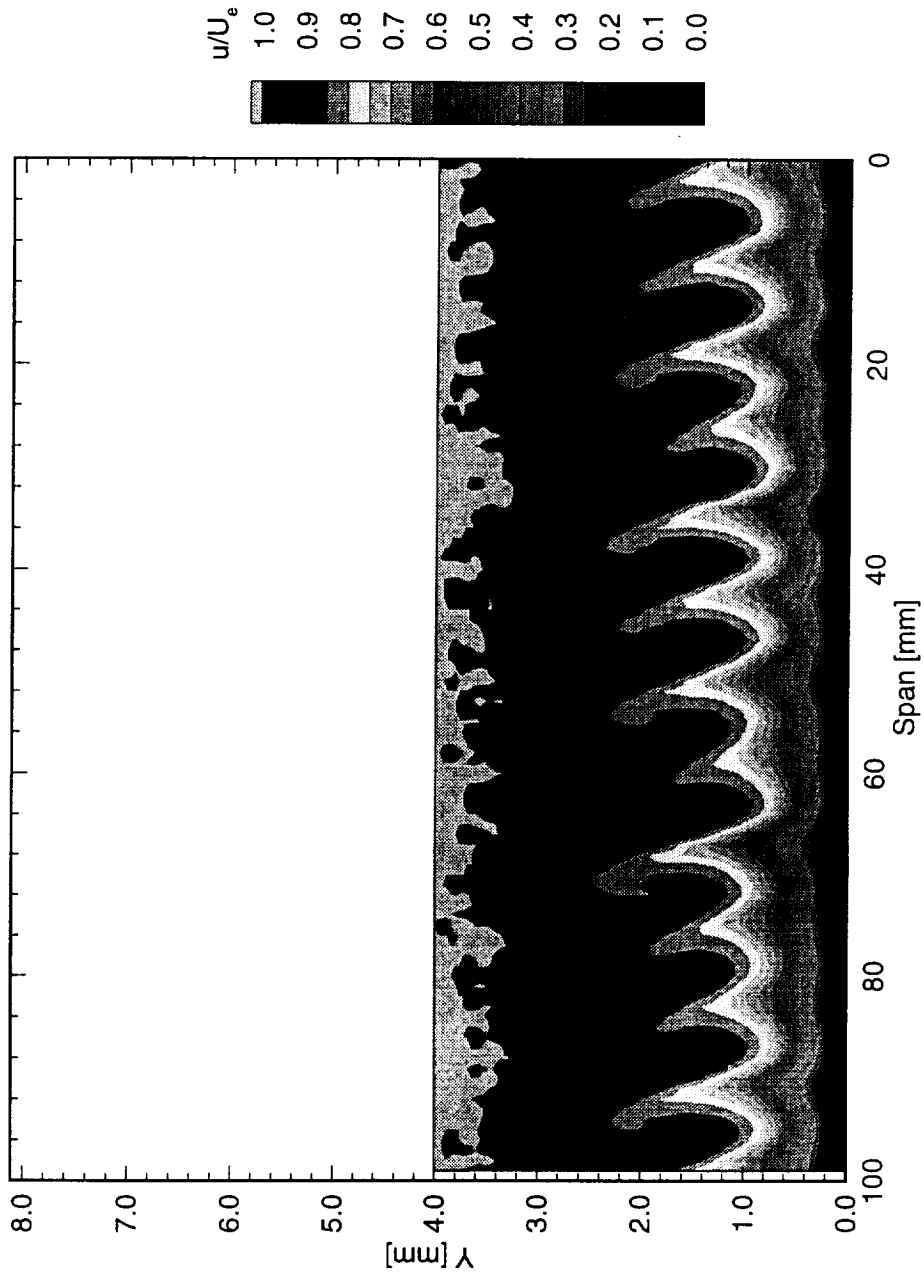

Figure 5.203: Normalized boundary-layer velocity contours at $x/c = 0.35$. $Re_c = 2.4 \times 10^6$, [48|8] roughness.

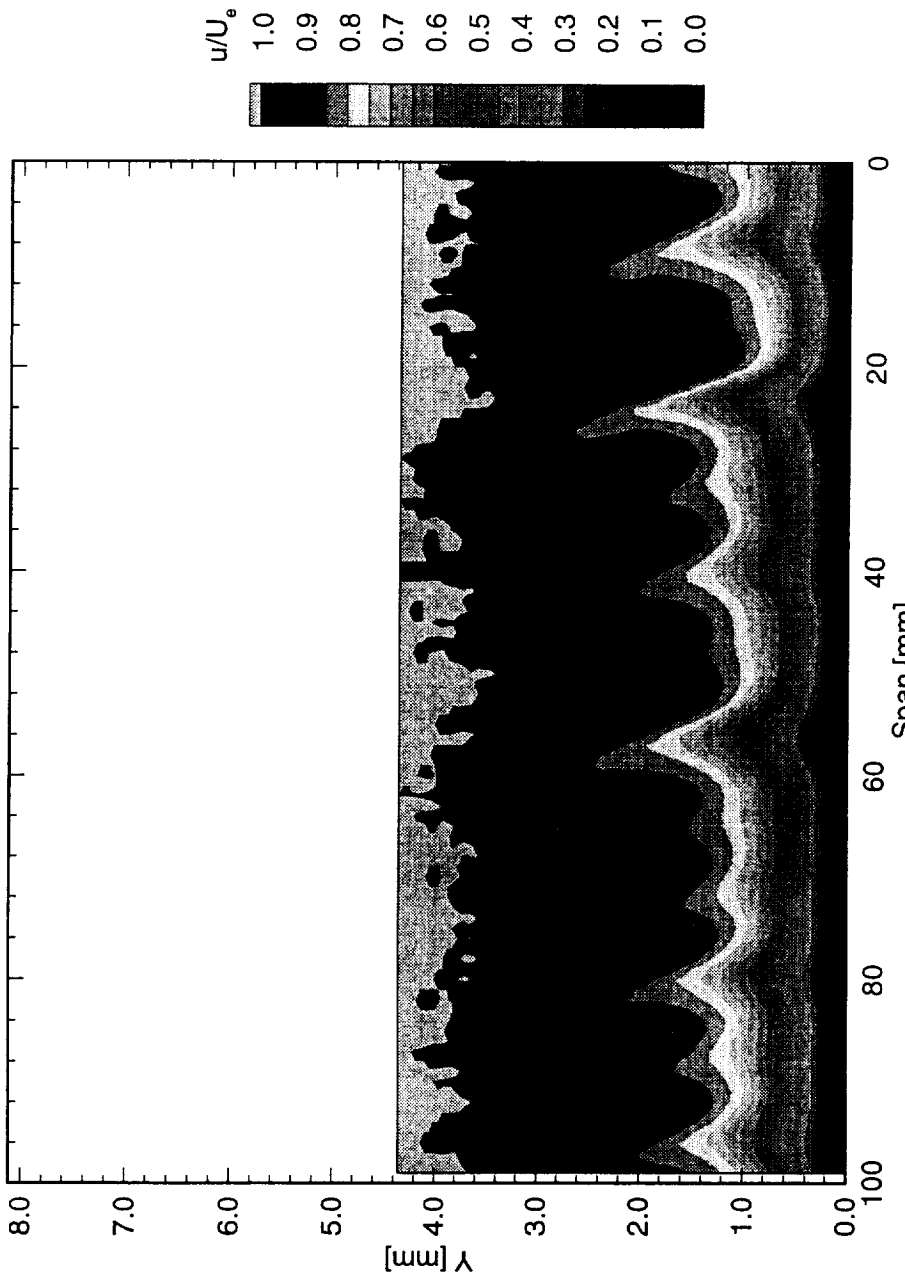

Figure 5.204: Normalized boundary-layer velocity contours at $x/c = 0.40$. $Re_c = 2.4 \times 10^6$, [48|8] roughness.

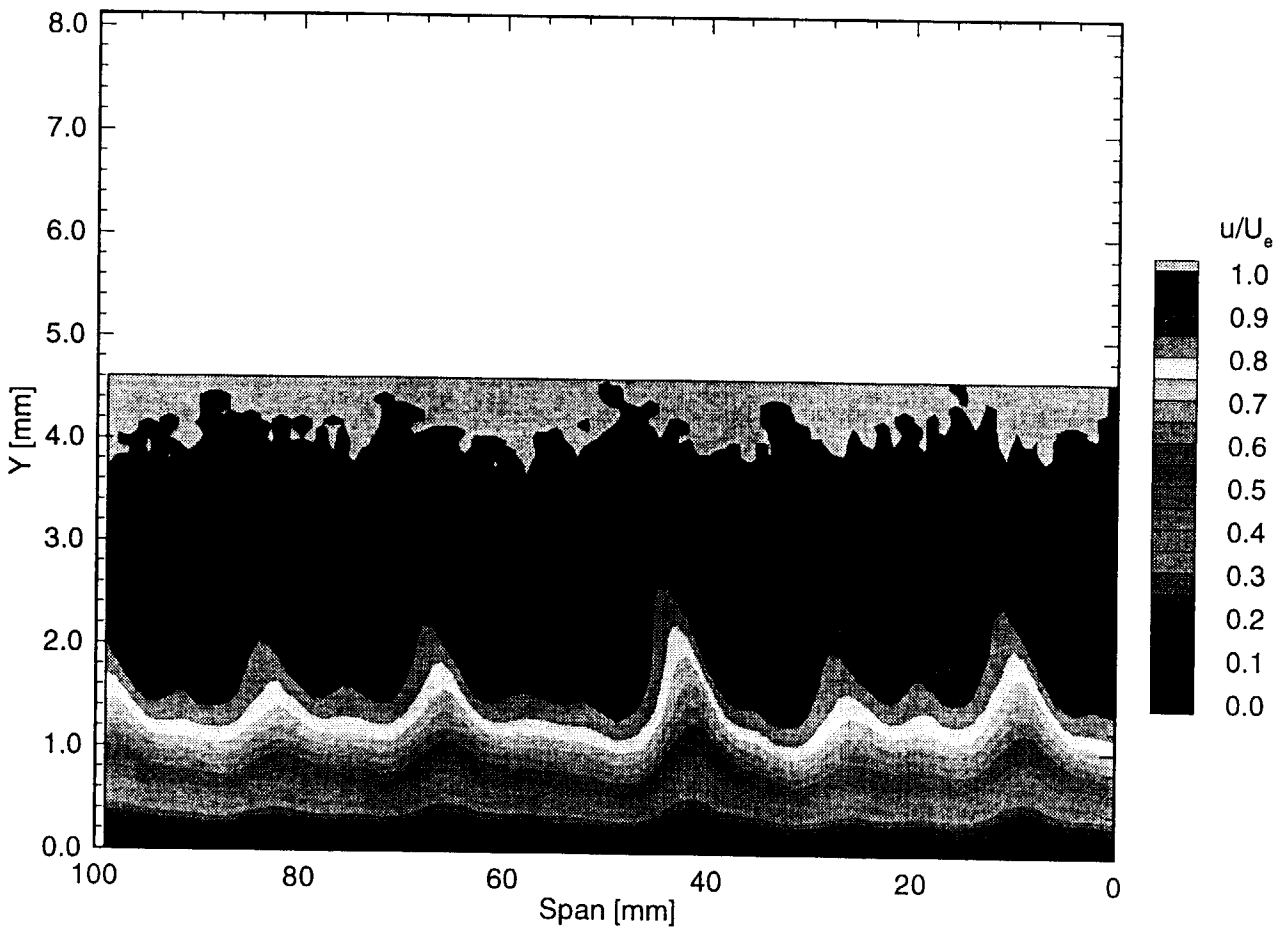

Figure 5.205: Normalized boundary-layer velocity contours at $x/c = 0.45$. $Re_c = 2.4 \times 10^6$, [48|8] roughness.

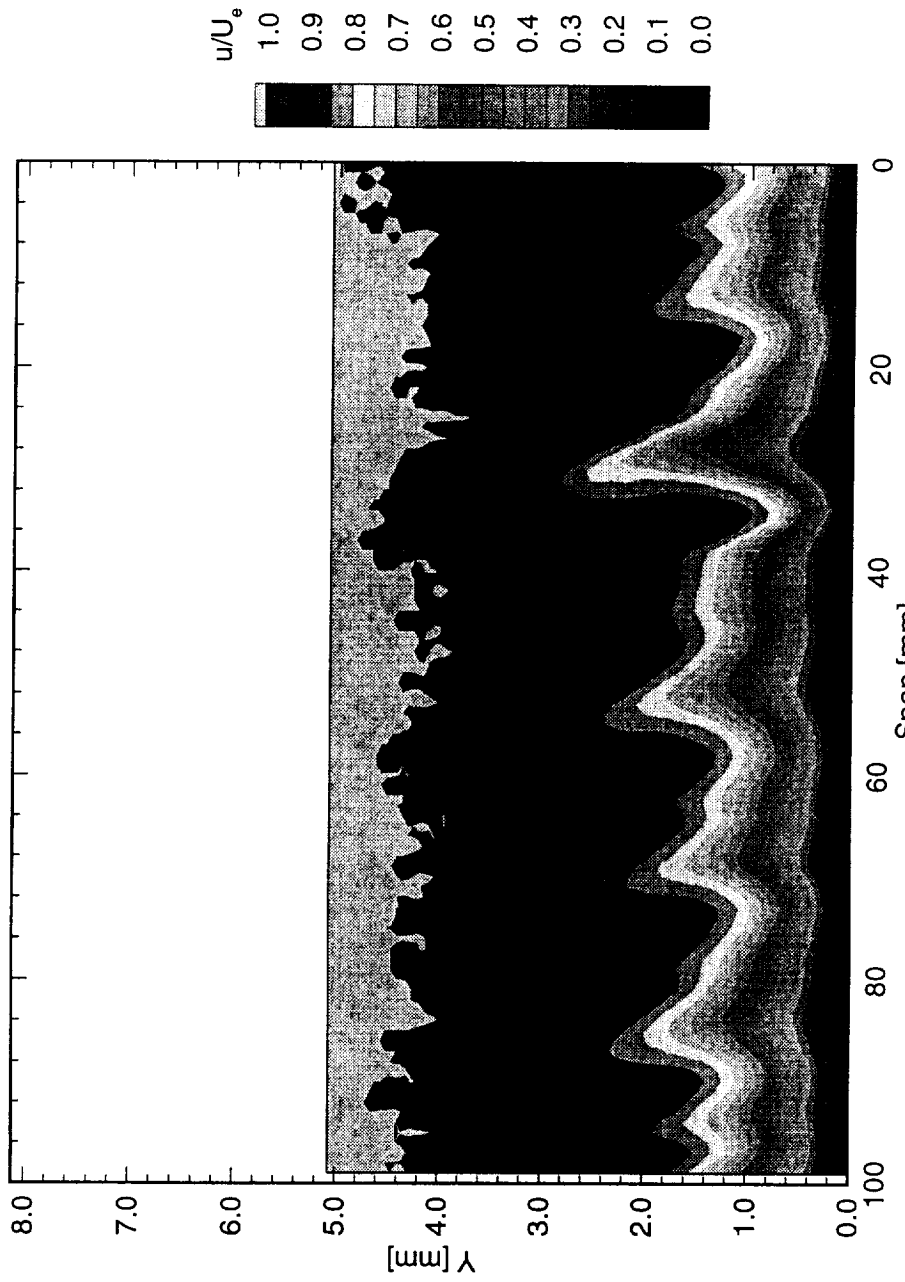

Figure 5.206: Normalized boundary-layer velocity contours at $x/c = 0.50$. $Re_c = 2.4 \times 10^6$, [48|8] roughness.

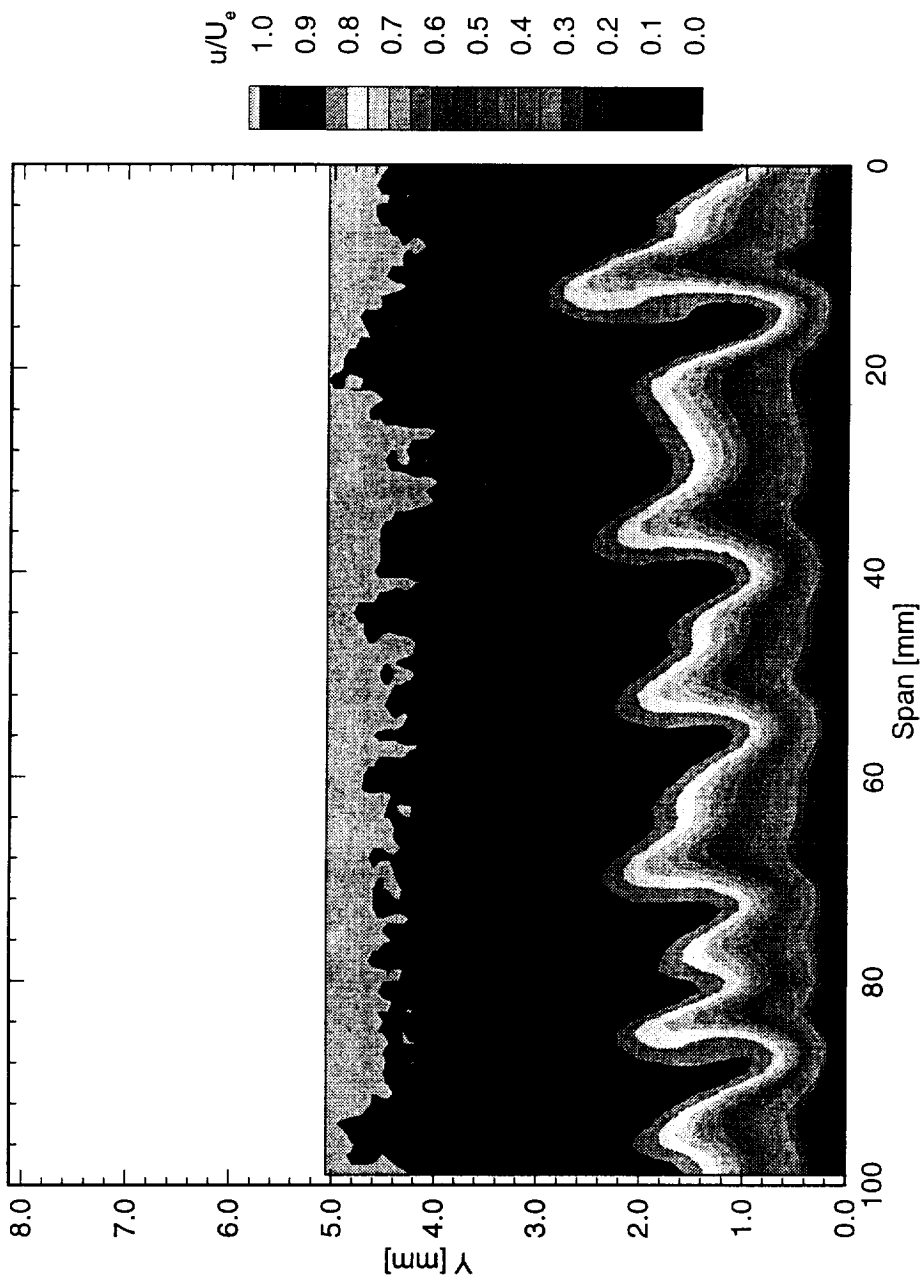

Figure 5.207: Normalized boundary-layer velocity contours at $x/c = 0.55$. $Re_c = 2.4 \times 10^6$, [48|8] roughness.

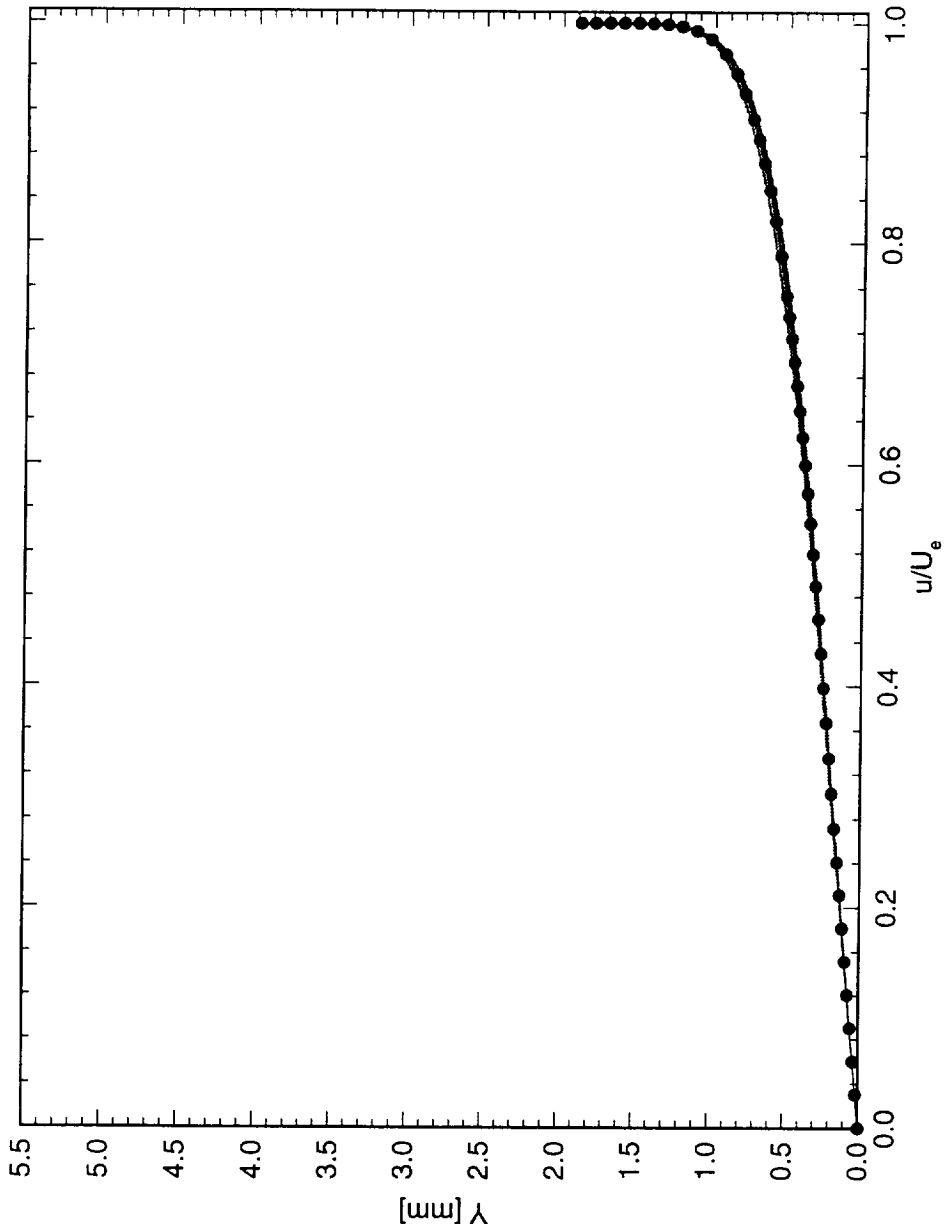

Figure 5.208: Spanwise array of 100 boundary-layer profiles spaced 1 mm apart in span at $x/c = 0.05$. $Re_c = 2.4 \times 10^6$, [48|8] roughness. The dots represent the spanwise average of the profiles.

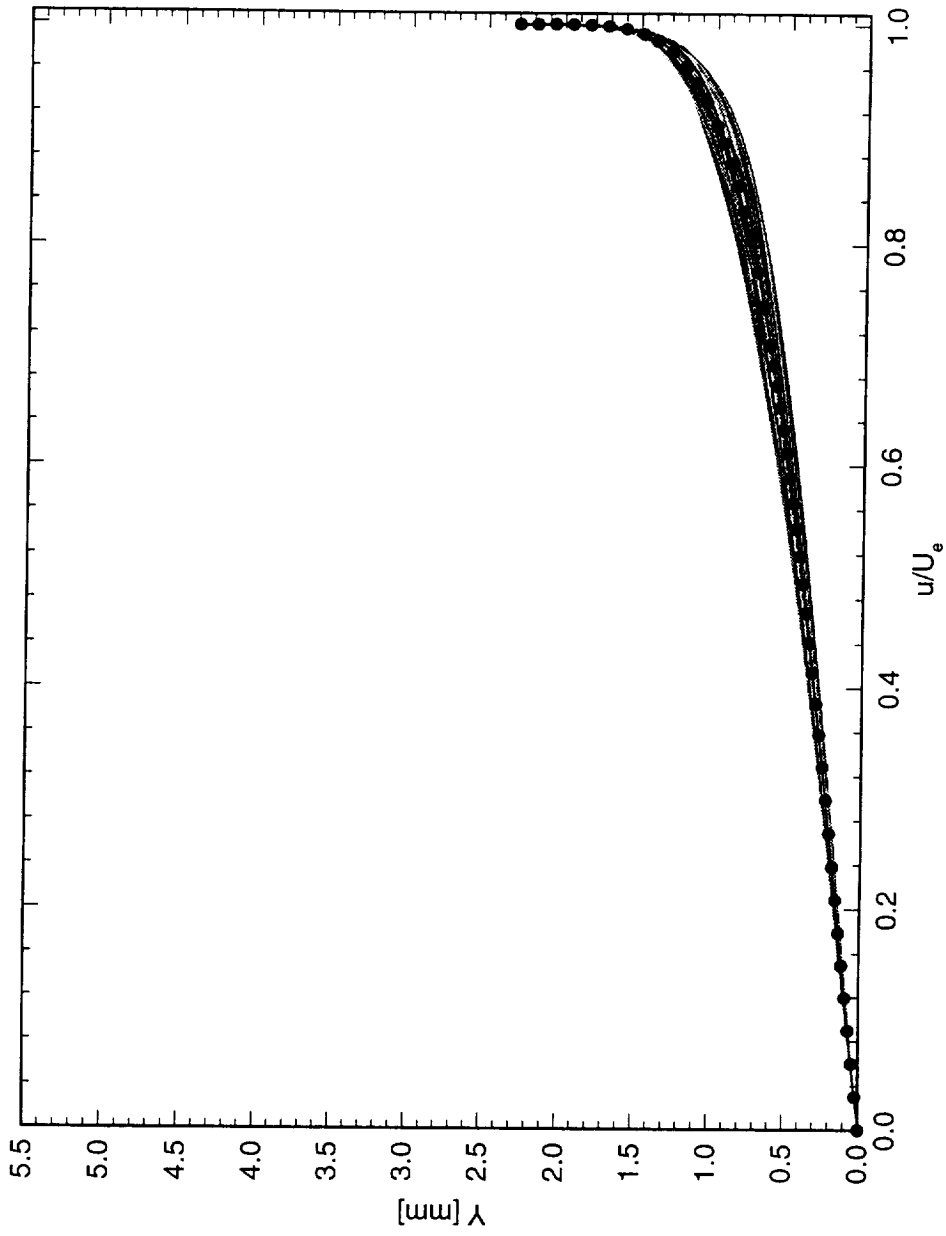

Figure 5.209: Spanwise array of 100 boundary-layer profiles spaced 1 mm apart in span at $x/c = 0.10$. $Re_c = 2.4 \times 10^6$, [48|8] roughness. The dots represent the spanwise average of the profiles.

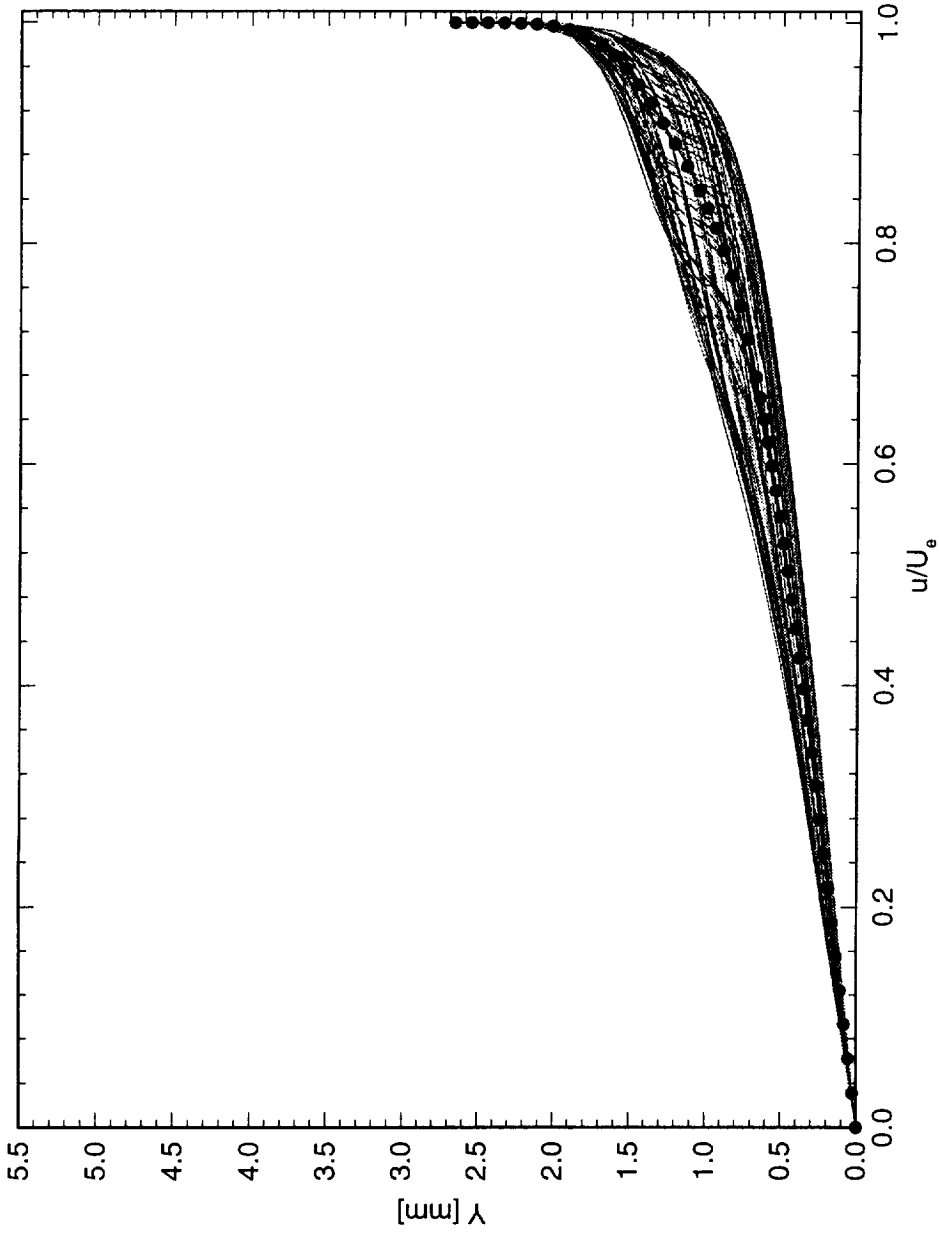

Figure 5.210: Spanwise array of 100 boundary-layer profiles spaced 1 mm apart in span at $x/c = 0.15$. $Re_c = 2.4 \times 10^6$, [48|8] roughness. The dots represent the spanwise average of the profiles.

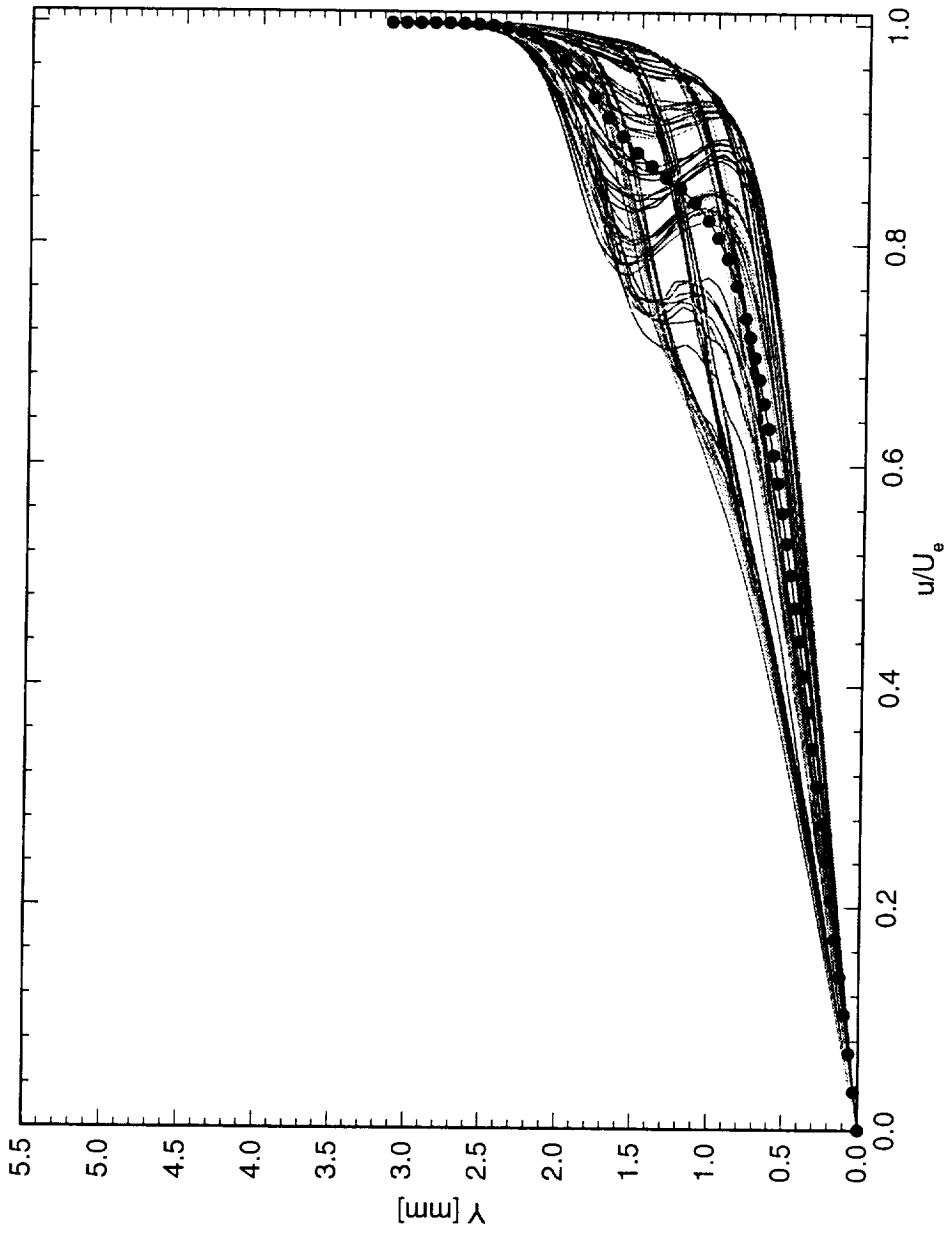

Figure 5.211: Spanwise array of 100 boundary-layer profiles spaced 1 mm apart in span at $x/c = 0.20$. $Re_c = 2.4 \times 10^6$, [48|8] roughness. The dots represent the spanwise average of the profiles.

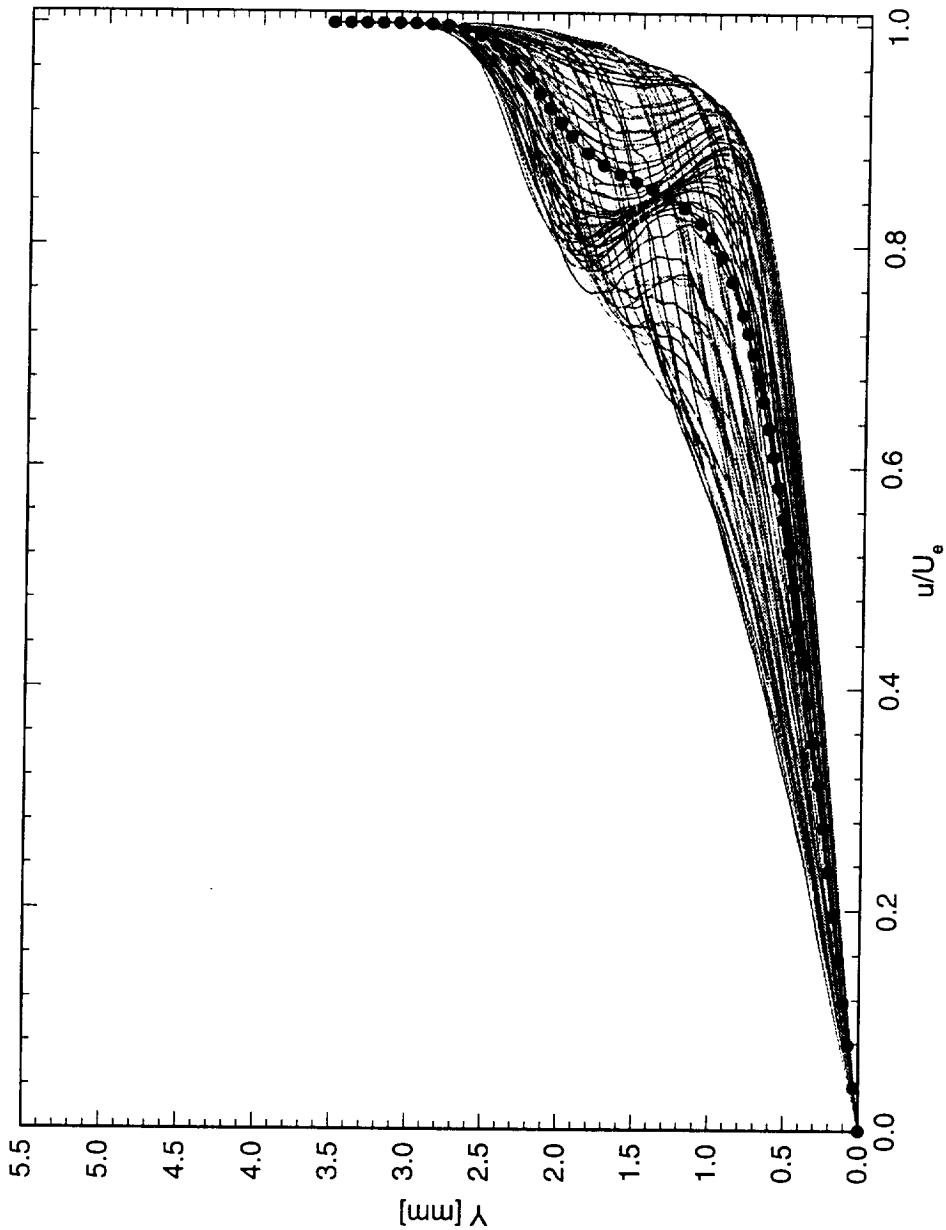

Figure 5.212: Spanwise array of 100 boundary-layer profiles spaced 1 mm apart in span at $x/c = 0.25$. $Re_c = 2.4 \times 10^6$, [48|8] roughness. The dots represent the spanwise average of the profiles.

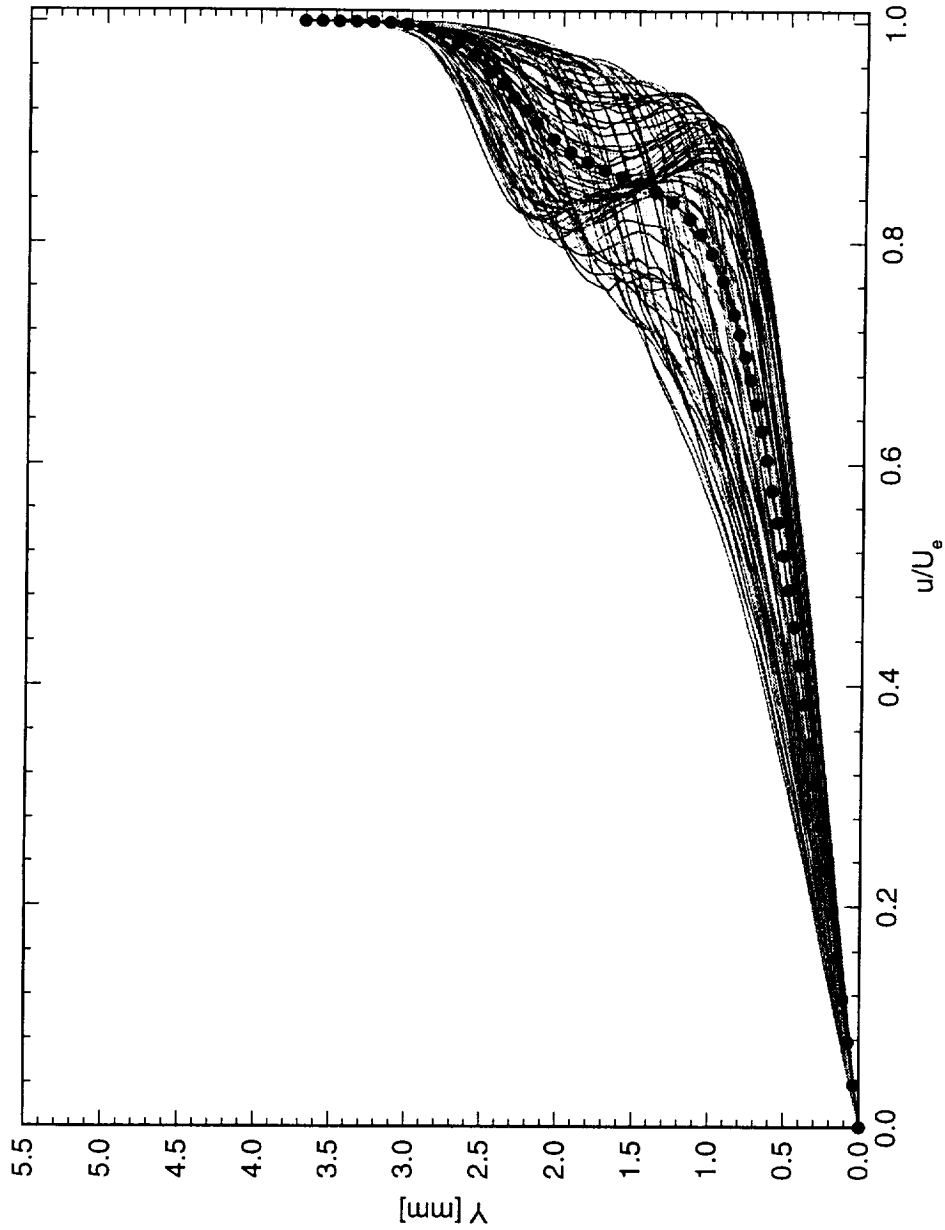

Figure 5.213: Spanwise array of 100 boundary-layer profiles spaced 1 mm apart in span at $x/c = 0.30$. $Re_c = 2.4 \times 10^6$, [48|8] roughness. The dots represent the spanwise average of the profiles.

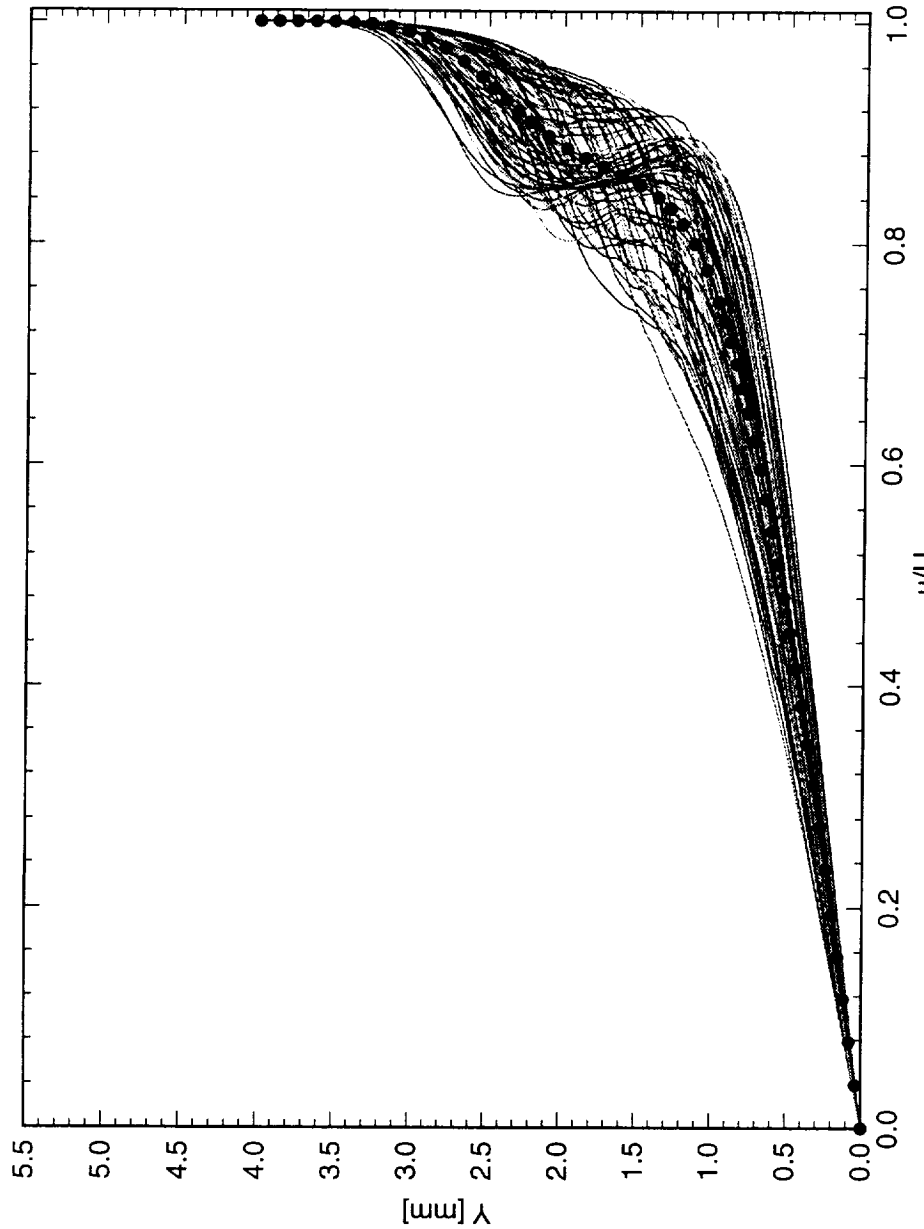

Figure 5.214: Spanwise array of 100 boundary-layer profiles spaced 1 mm apart in span at $x/c = 0.35$. $Re_c = 2.4 \times 10^6$, [48|8] roughness. The dots represent the spanwise average of the profiles.

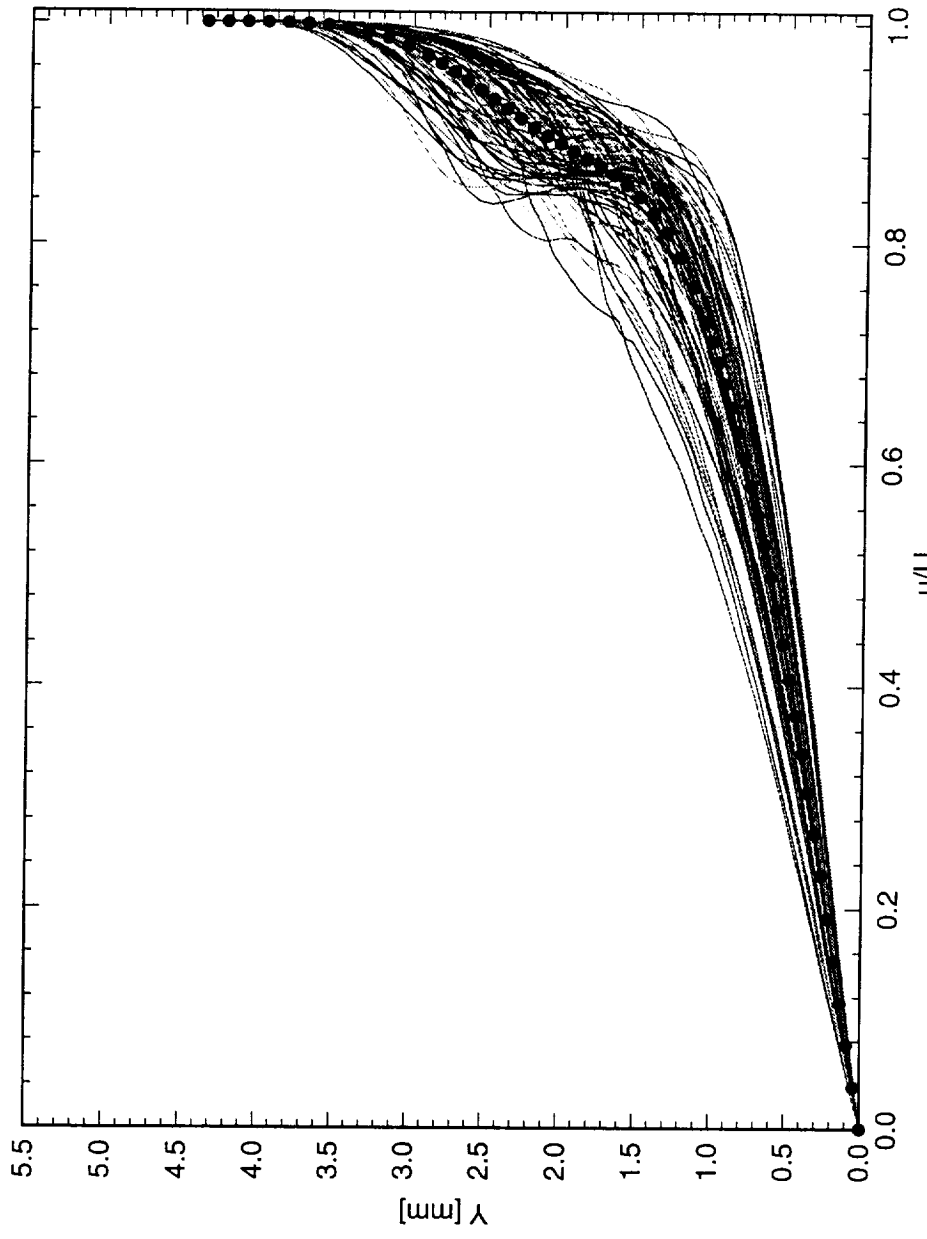

Figure 5.215: Spanwise array of 100 boundary-layer profiles spaced 1 mm apart in span at $x/c = 0.40$. $Re_c = 2.4 \times 10^6$, [48|8] roughness. The dots represent the spanwise average of the profiles.

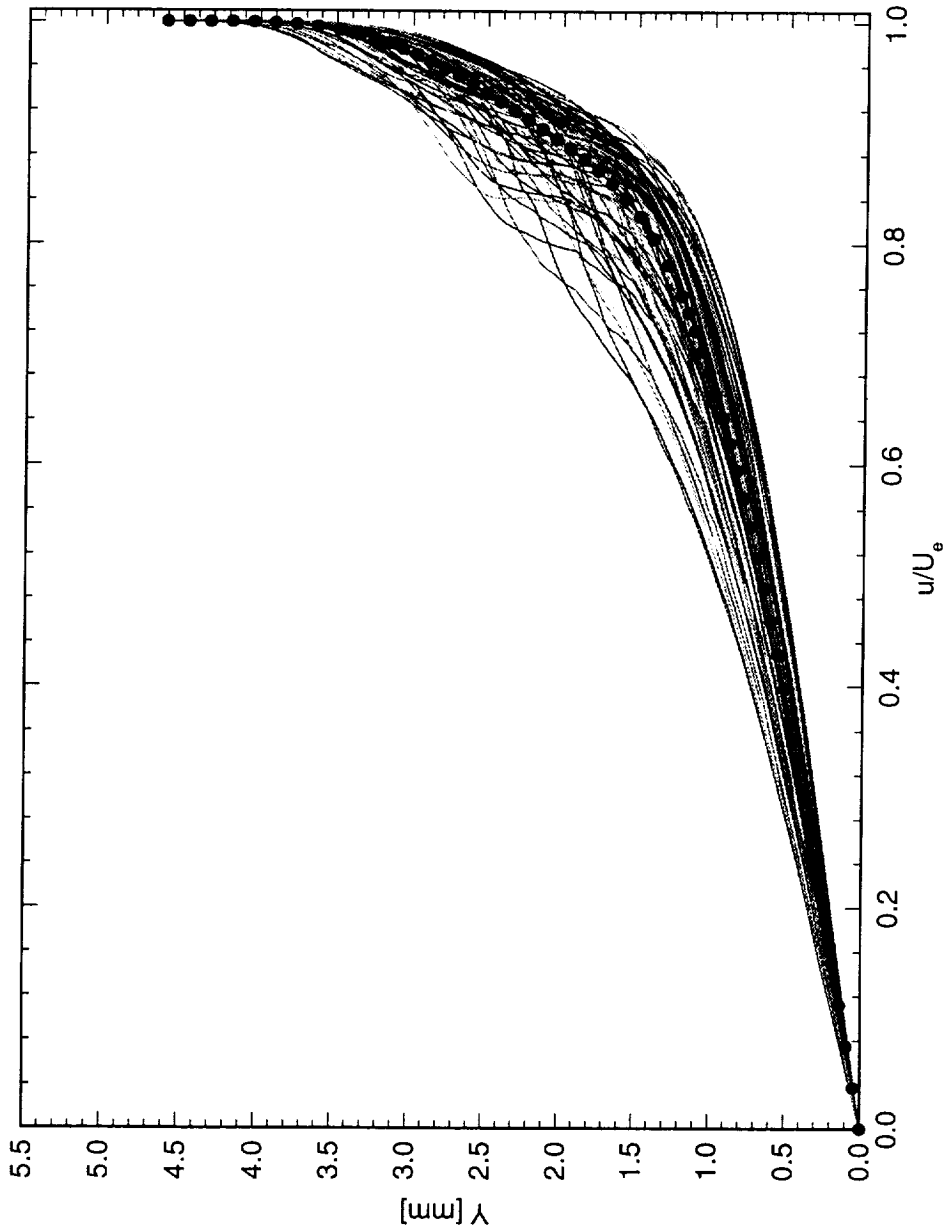

Figure 5.216: Spanwise array of 100 boundary-layer profiles spaced 1 mm apart in span at $x/c = 0.45$. $Re_c = 2.4 \times 10^6$, [48|8] roughness. The dots represent the spanwise average of the profiles.

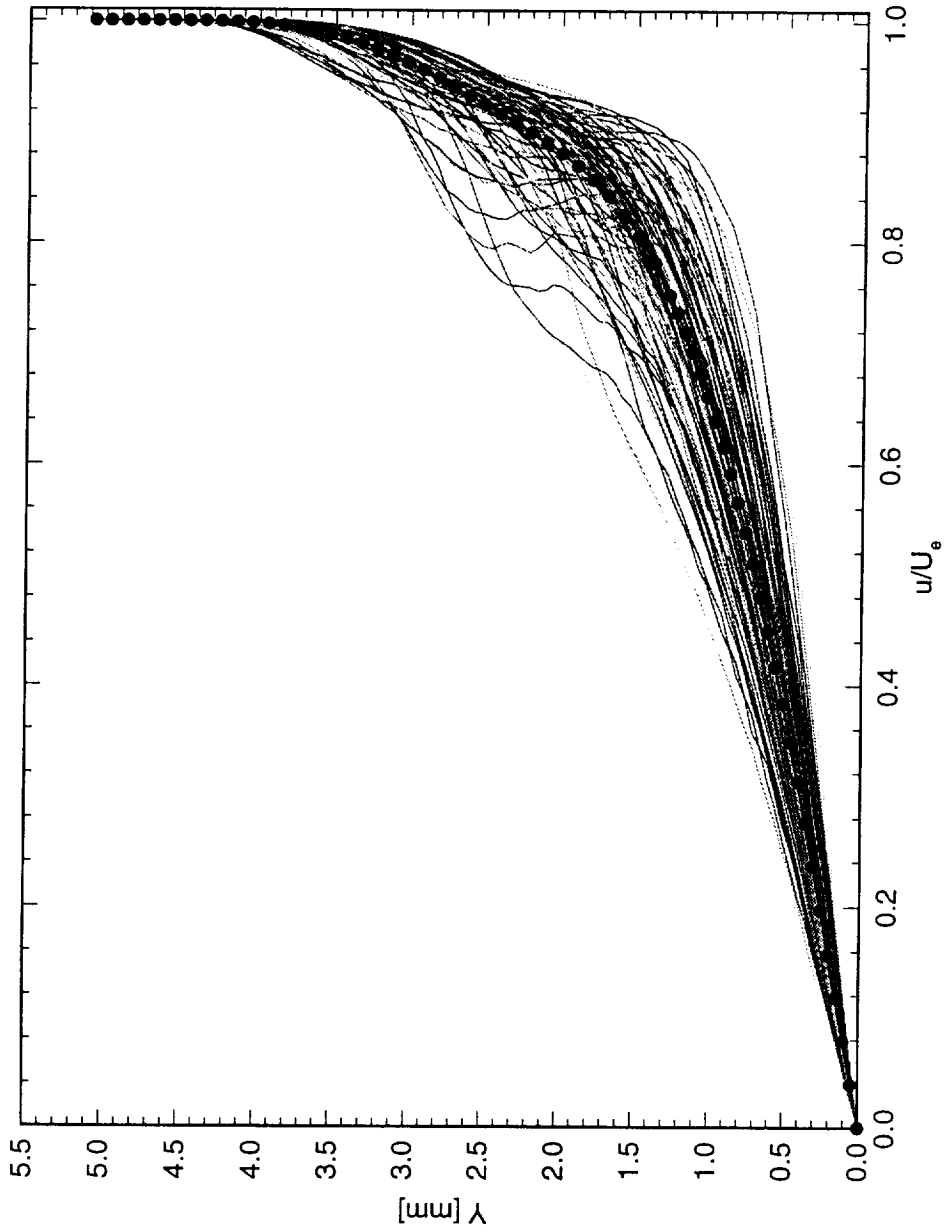

Figure 5.217: Spanwise array of 100 boundary-layer profiles spaced 1 mm apart in span at $x/c = 0.50$. $Re_c = 2.4 \times 10^6$, [48|8] roughness. The dots represent the spanwise average of the profiles.

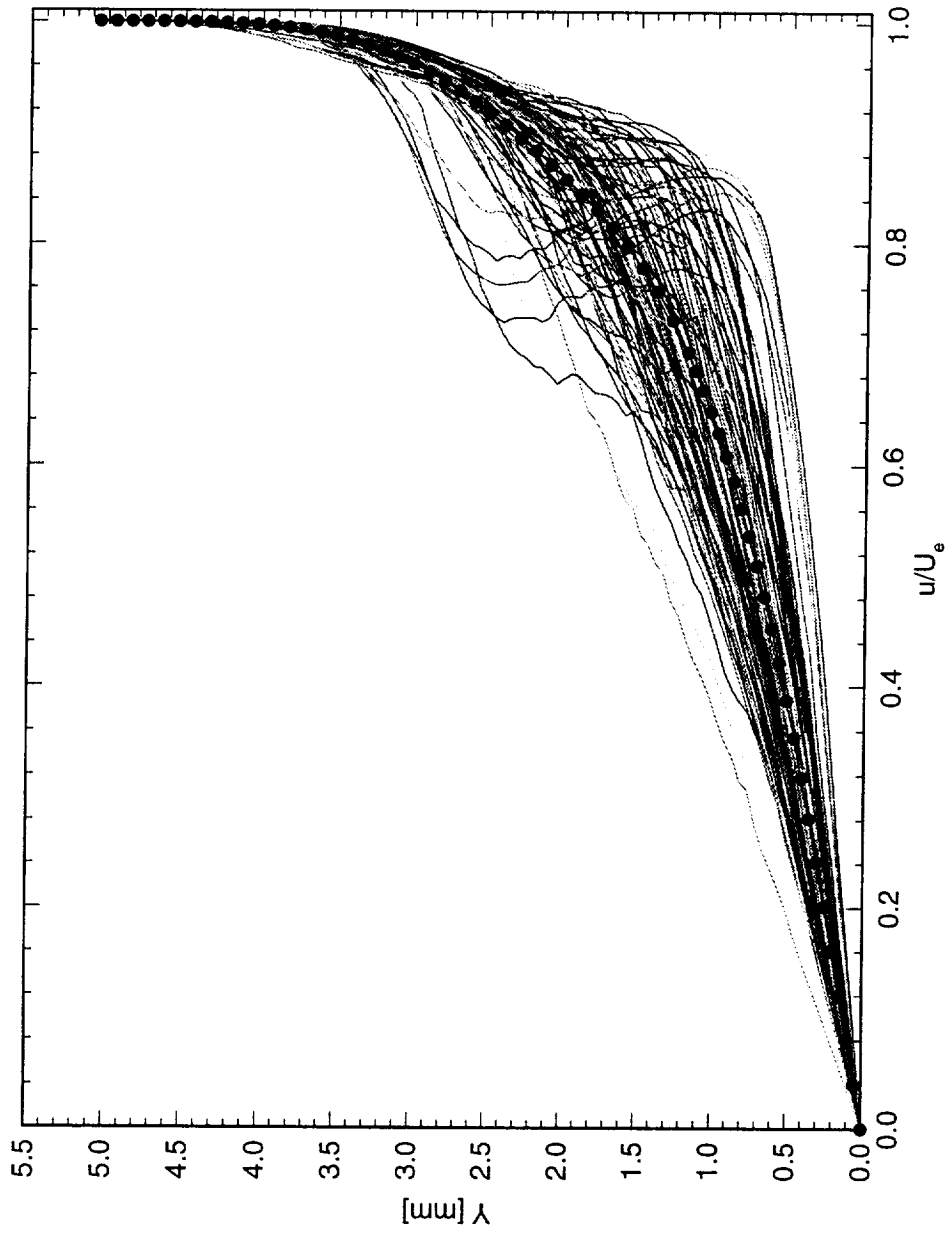

Figure 5.218: Spanwise array of 100 boundary-layer profiles spaced 1 mm apart in span at $x/c = 0.55$. $Re_c = 2.4 \times 10^6$, [48|8] roughness. The dots represent the spanwise average of the profiles.

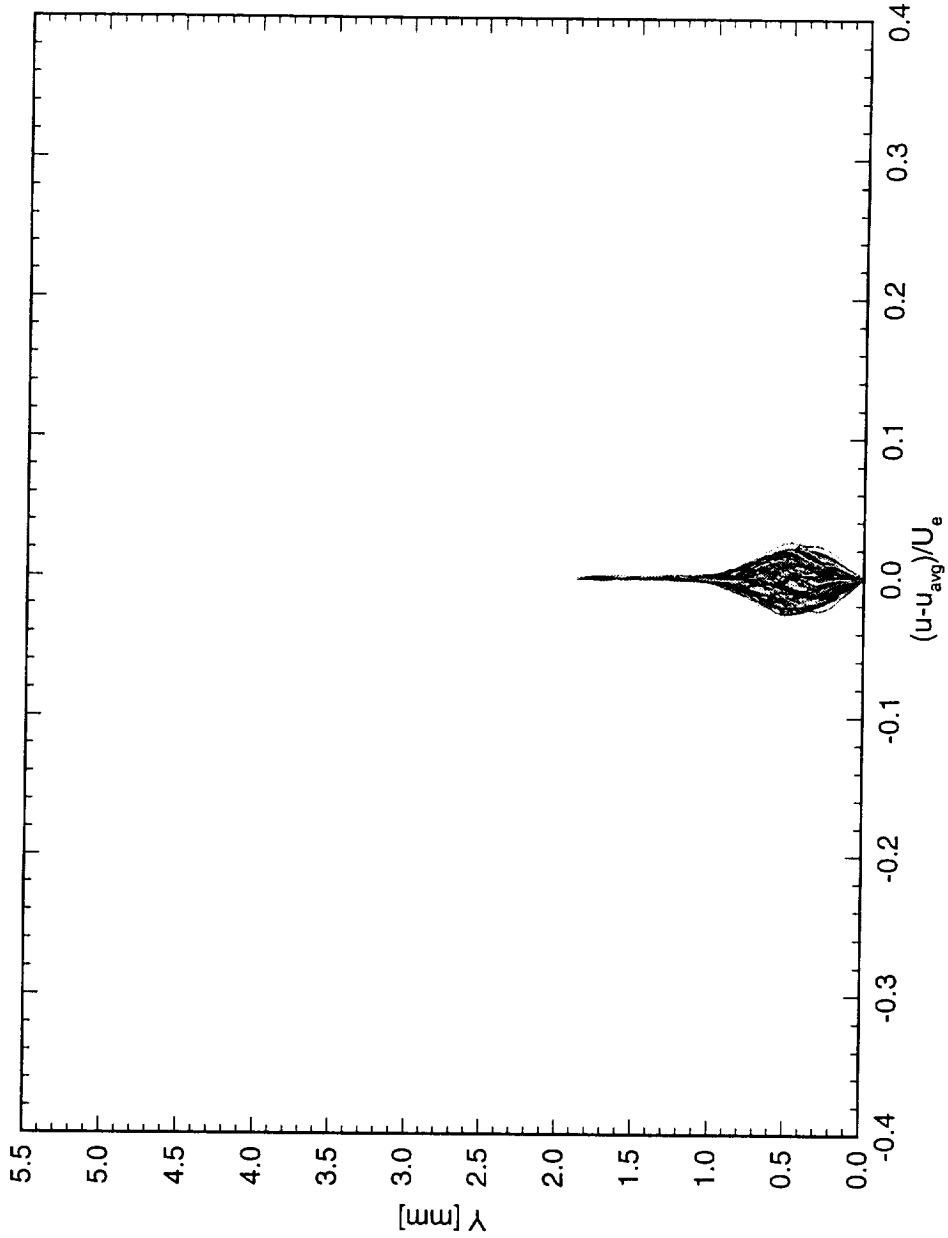

Figure 5.219: Spanwise array of 100 disturbance profiles spaced 1 mm apart in span at $x/c = 0.05$. $Re_c = 2.4 \times 10^6$, [48|8] roughness.

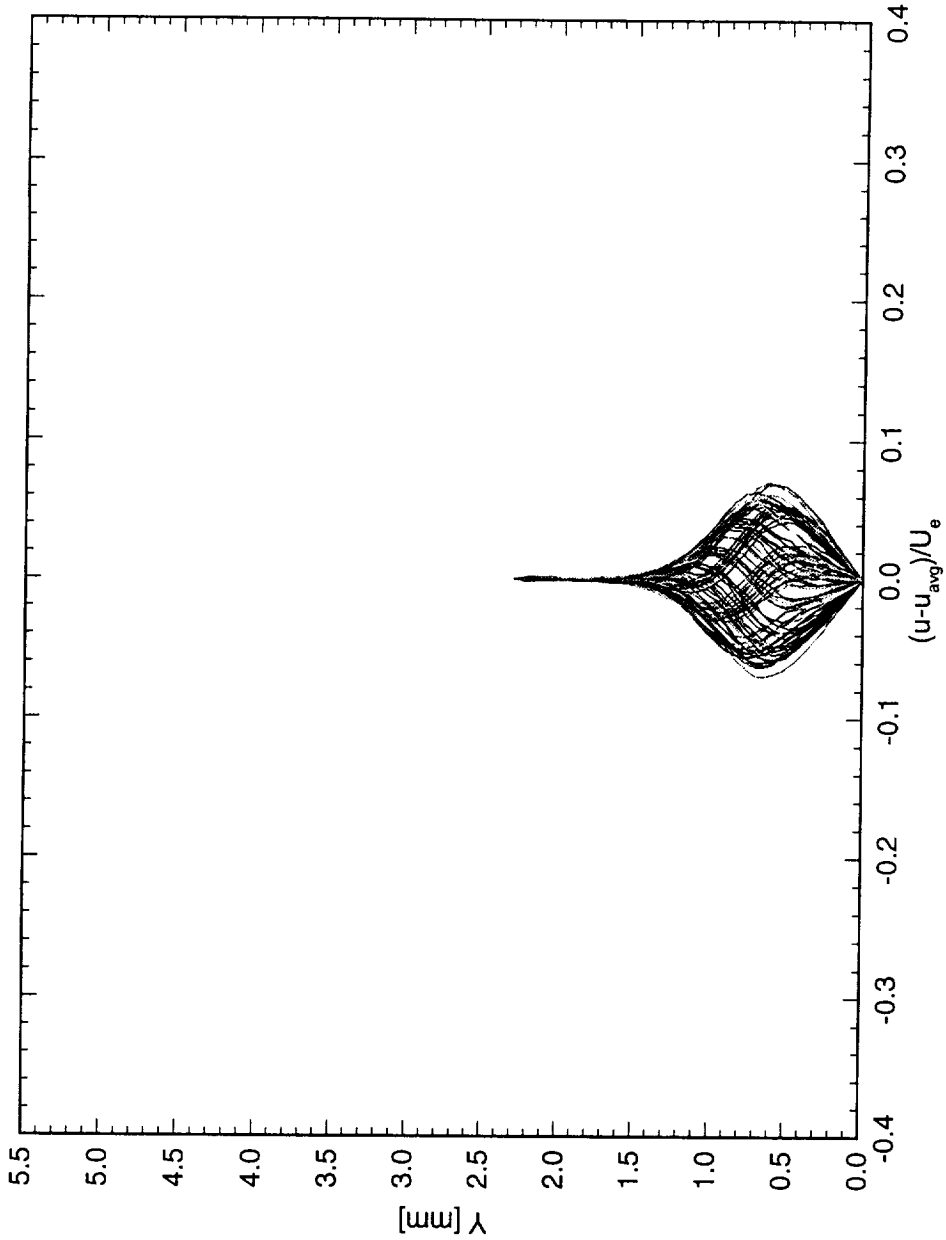

Figure 5.220: Spanwise array of 100 disturbance profiles spaced 1 mm apart in span at $x/c = 0.10$. $Re_c = 2.4 \times 10^6$, [48|8] roughness.

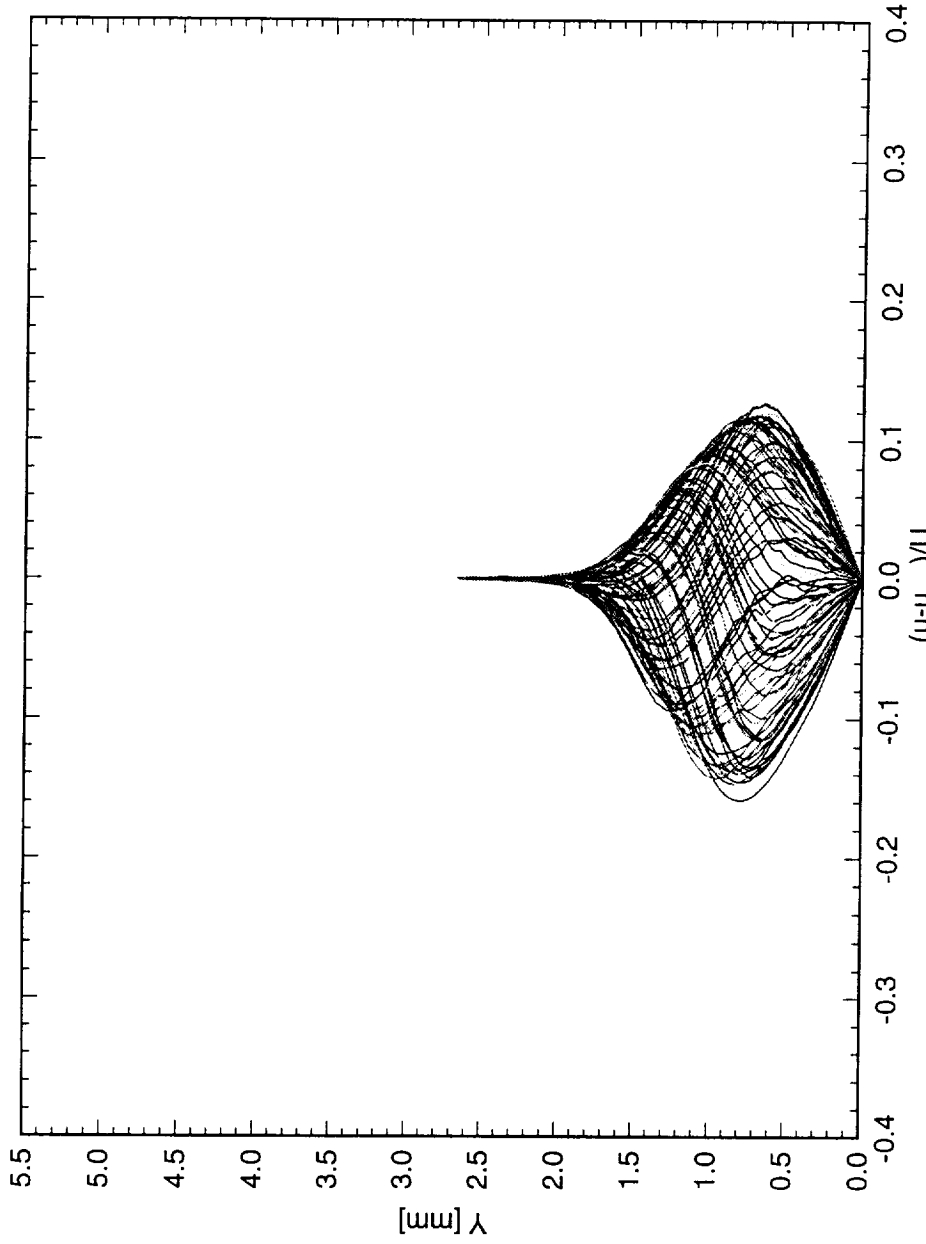

Figure 5.221: Spanwise array of 100 disturbance profiles spaced 1 mm apart in span at $x/c = 0.15$. $Re_c = 2.4 \times 10^6$, [48|8] roughness.

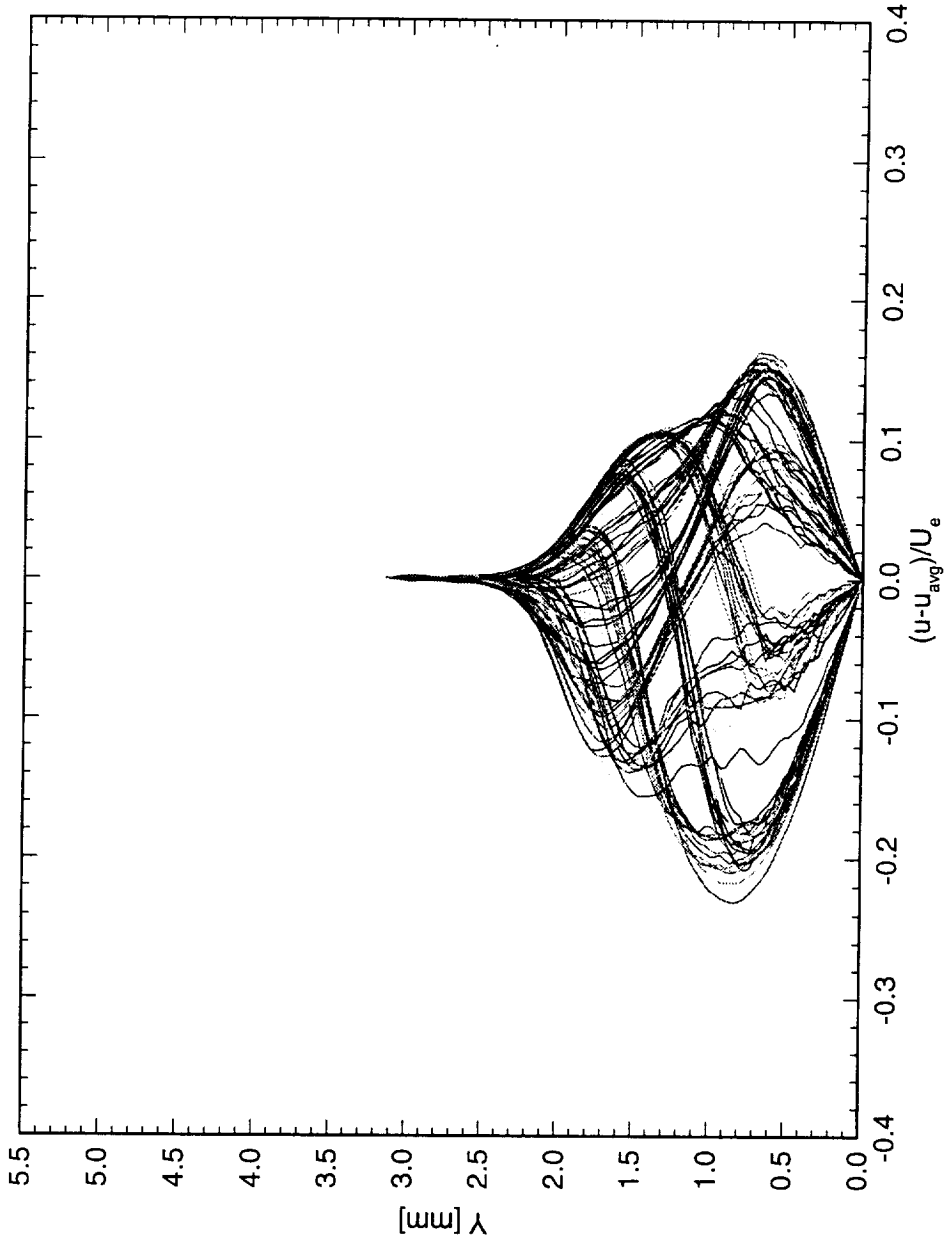

Figure 5.222: Spanwise array of 100 disturbance profiles spaced 1 mm apart in span at $x/c = 0.20$. $Re_c = 2.4 \times 10^6$, [48|8] roughness.

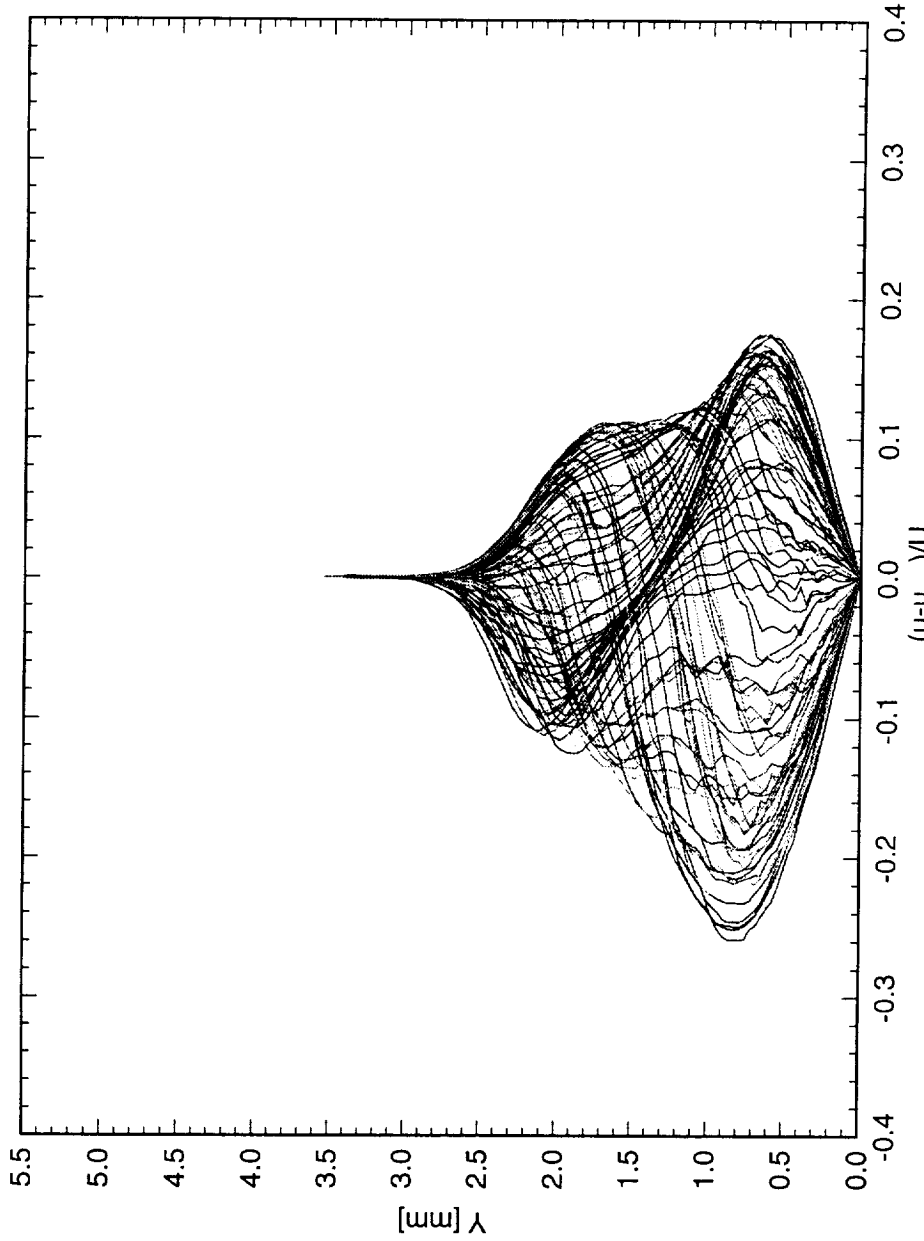

Figure 5.223: Spanwise array of 100 disturbance profiles spaced 1 mm apart in span at $x/c = 0.25$. $Re_c = 2.4 \times 10^6$, [48|8] roughness.

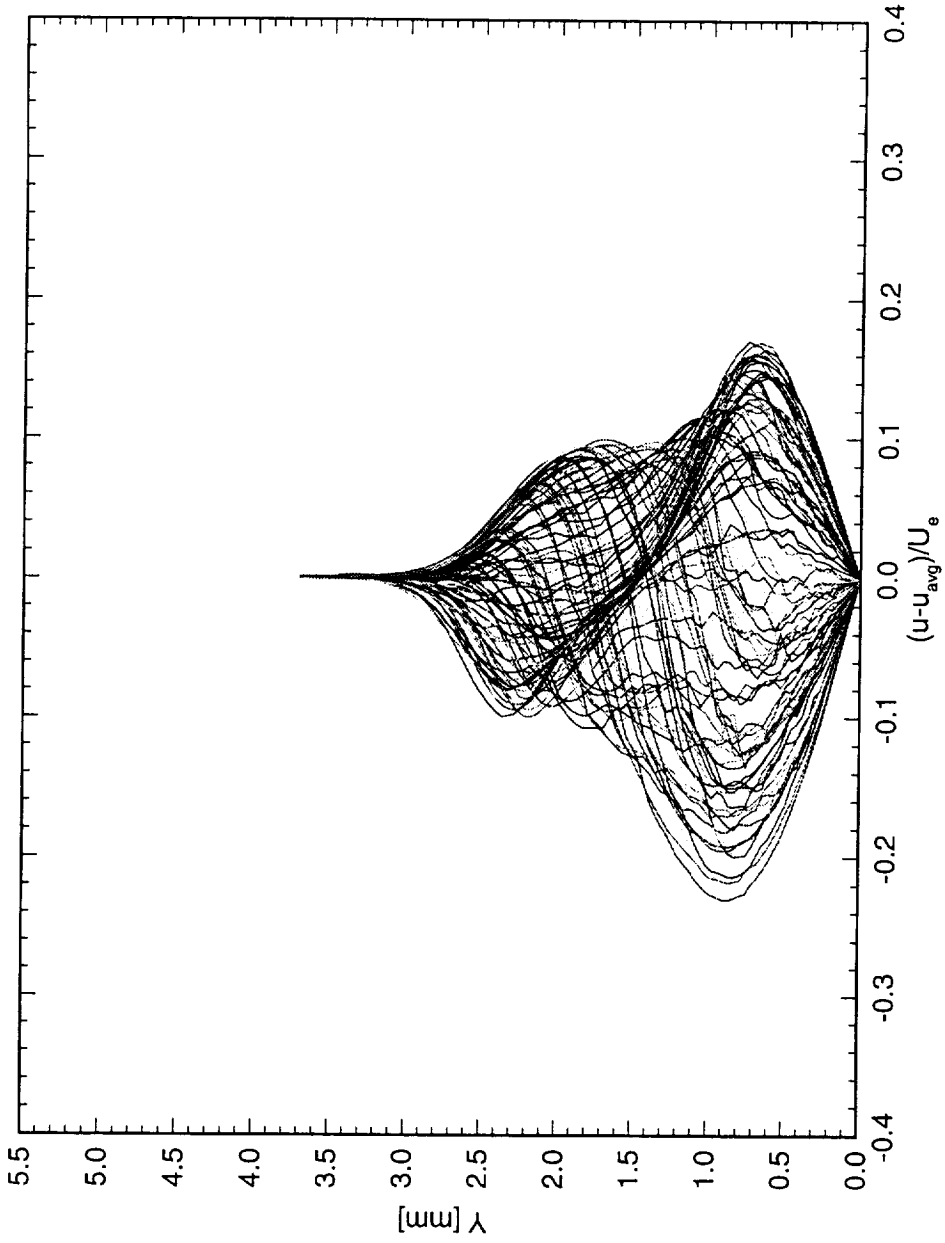

Figure 5.224: Spanwise array of 100 disturbance profiles spaced 1 mm apart in span at $x/c = 0.30$. $Re_c = 2.4 \times 10^6$, [48|8] roughness.

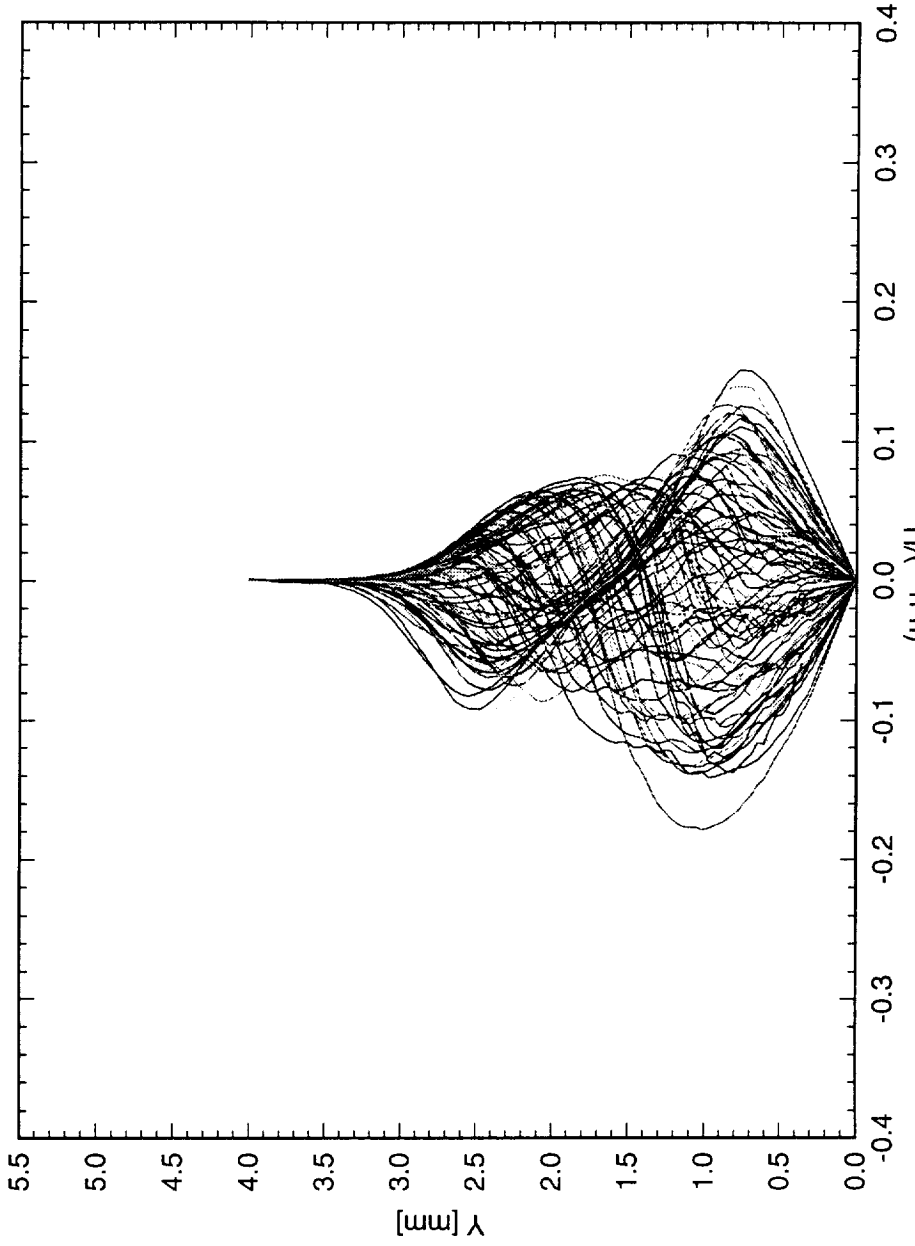

Figure 5.225: Spanwise array of 100 disturbance profiles spaced 1 mm apart in span at $x/c = 0.35$. $Re_c = 2.4 \times 10^6$, [48|8] roughness.

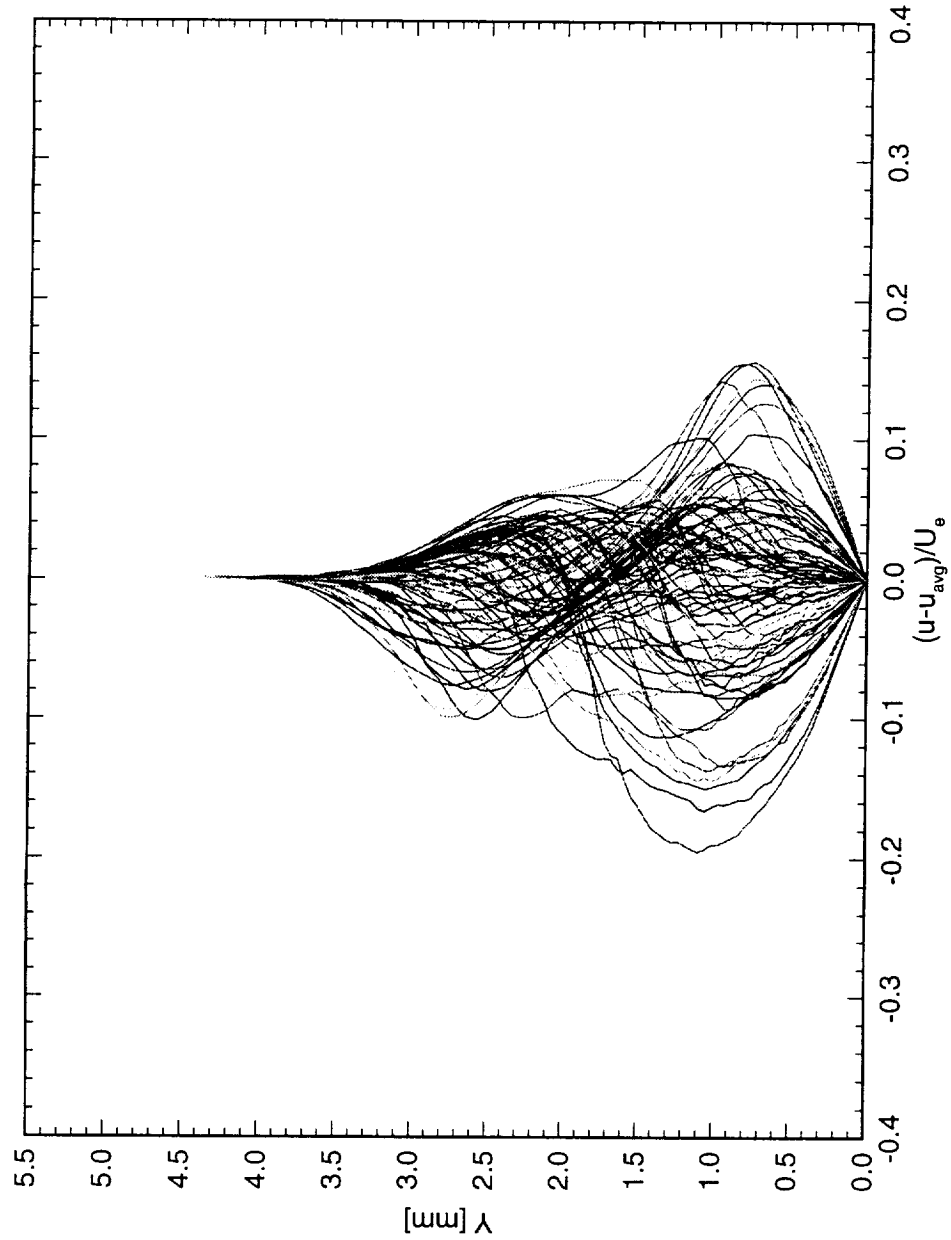

Figure 5.226: Spanwise array of 100 disturbance profiles spaced 1 mm apart in span at $x/c = 0.40$. $Re_c = 2.4 \times 10^6$, [48|8] roughness.

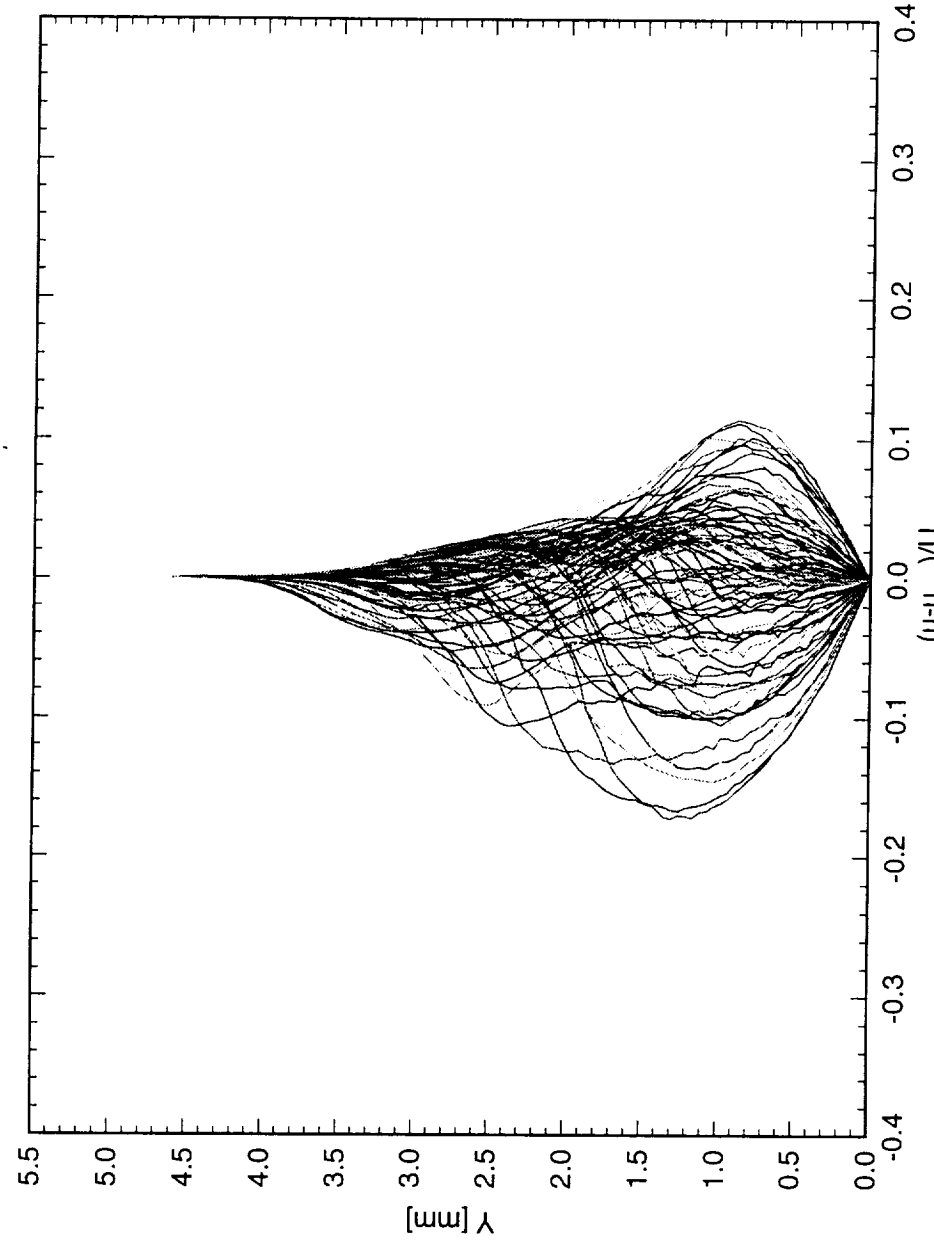

Figure 5.227: Spanwise array of 100 disturbance profiles spaced 1 mm apart in span at $x/c = 0.45$. $Re_c = 2.4 \times 10^6$, [48|8] roughness.

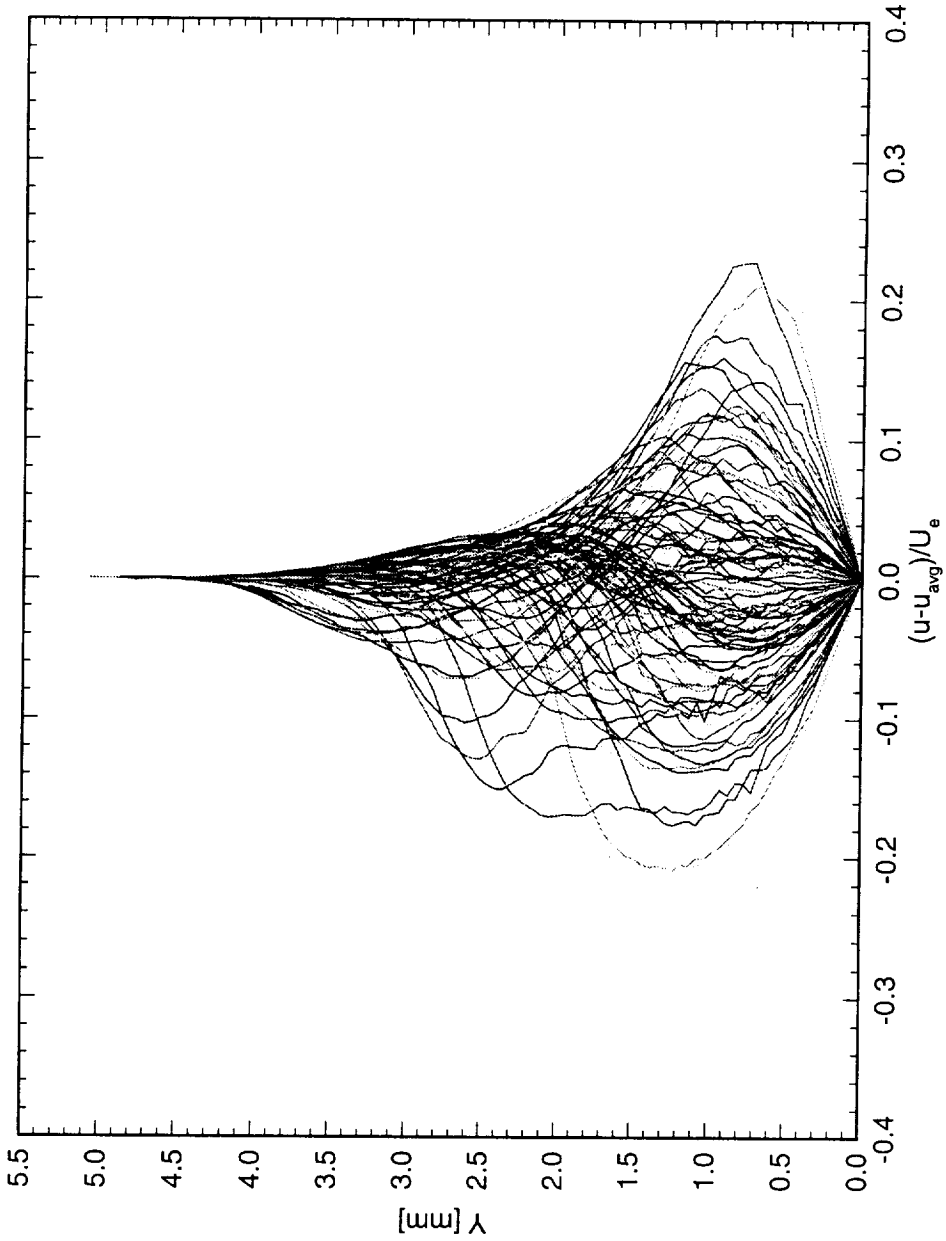

Figure 5.228: Spanwise array of 100 disturbance profiles spaced 1 mm apart in span at $x/c = 0.50$. $Re_c = 2.4 \times 10^6$, [48|8] roughness.

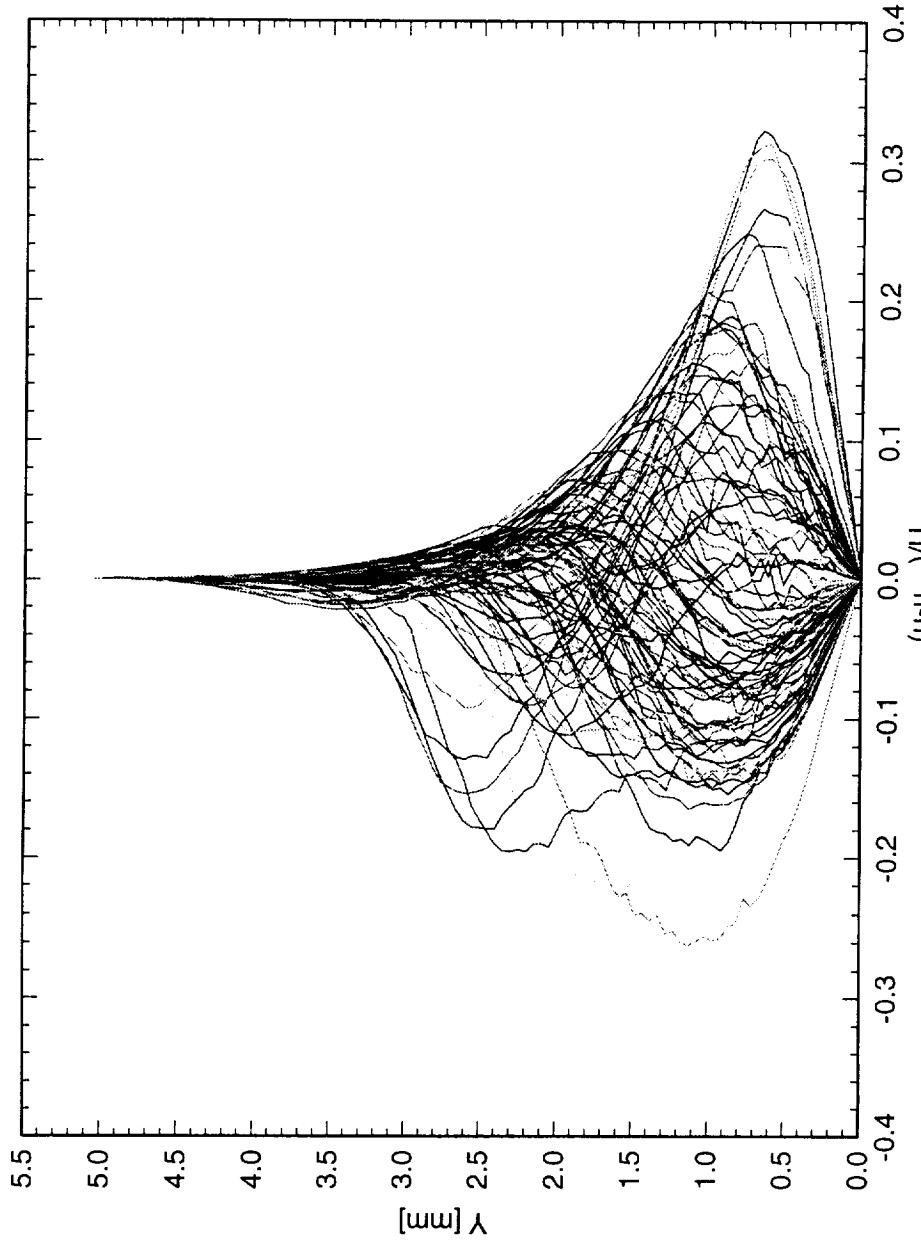

Figure 5.229: Spanwise array of 100 disturbance profiles spaced 1 mm apart in span at $x/c = 0.55$. $Re_c = 2.4 \times 10^6$, [48|8] roughness.

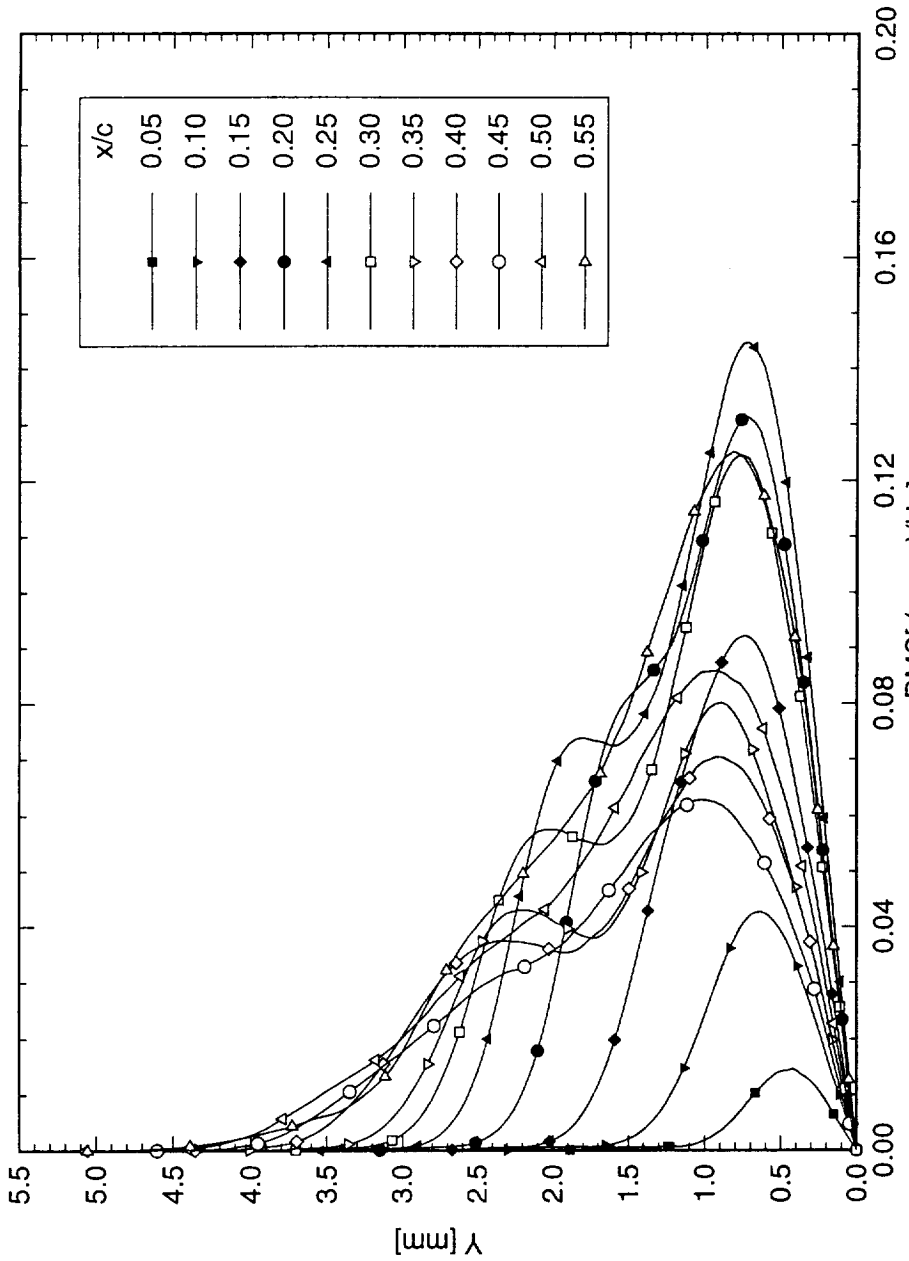

Figure 5.230: Stationary crossflow mode shapes for $Re_c = 2.4 \times 10^6$ and [48|8] roughness. The symbols are merely indicators and do not indicate measurement points

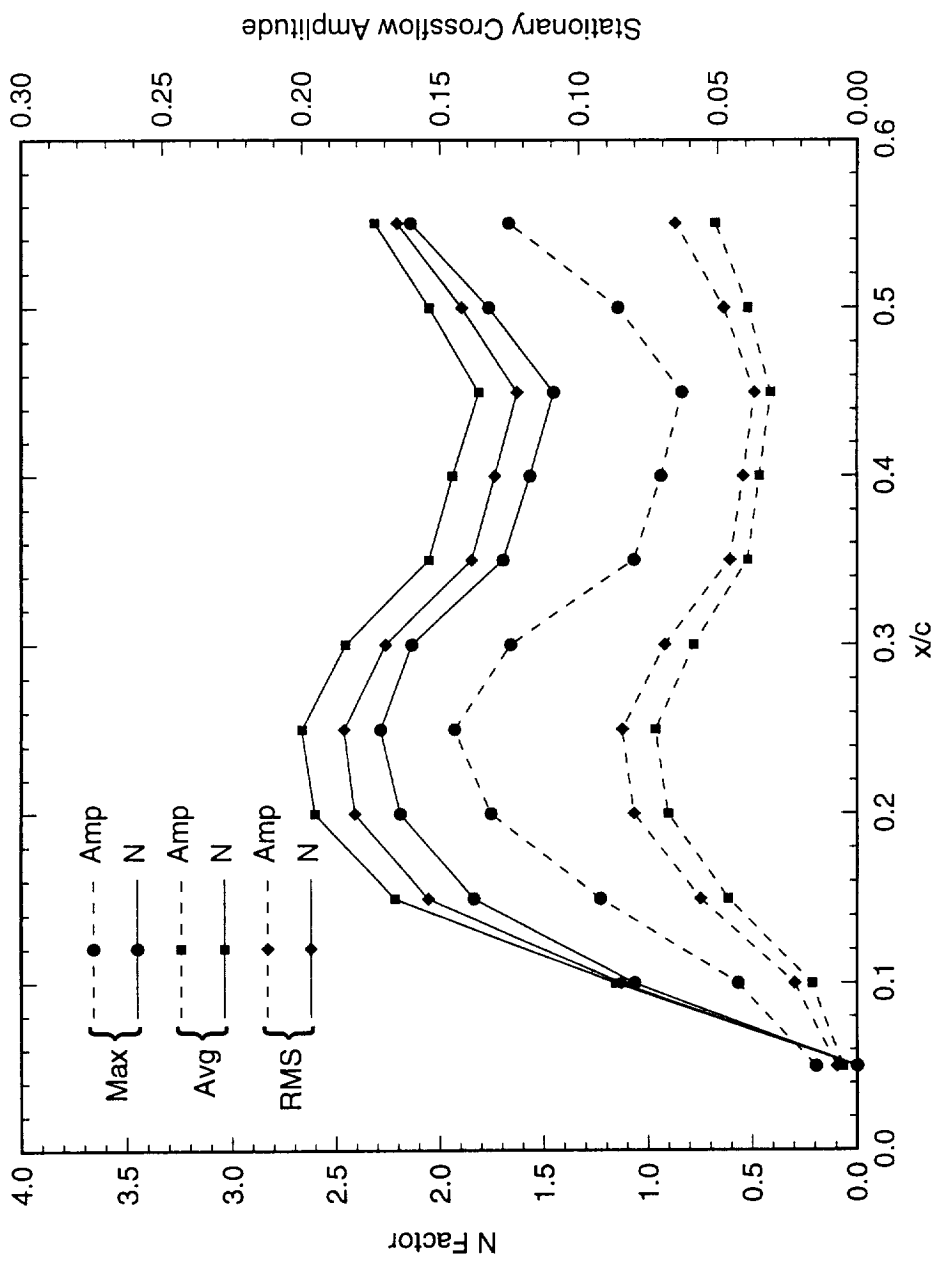

Figure 5.231: Total disturbance amplitude and relative N-factor for $Re_c = 2.4 \times 10^6$ and [48|8] roughness. N-factor calculations are relative to $x/c = 0.05$.

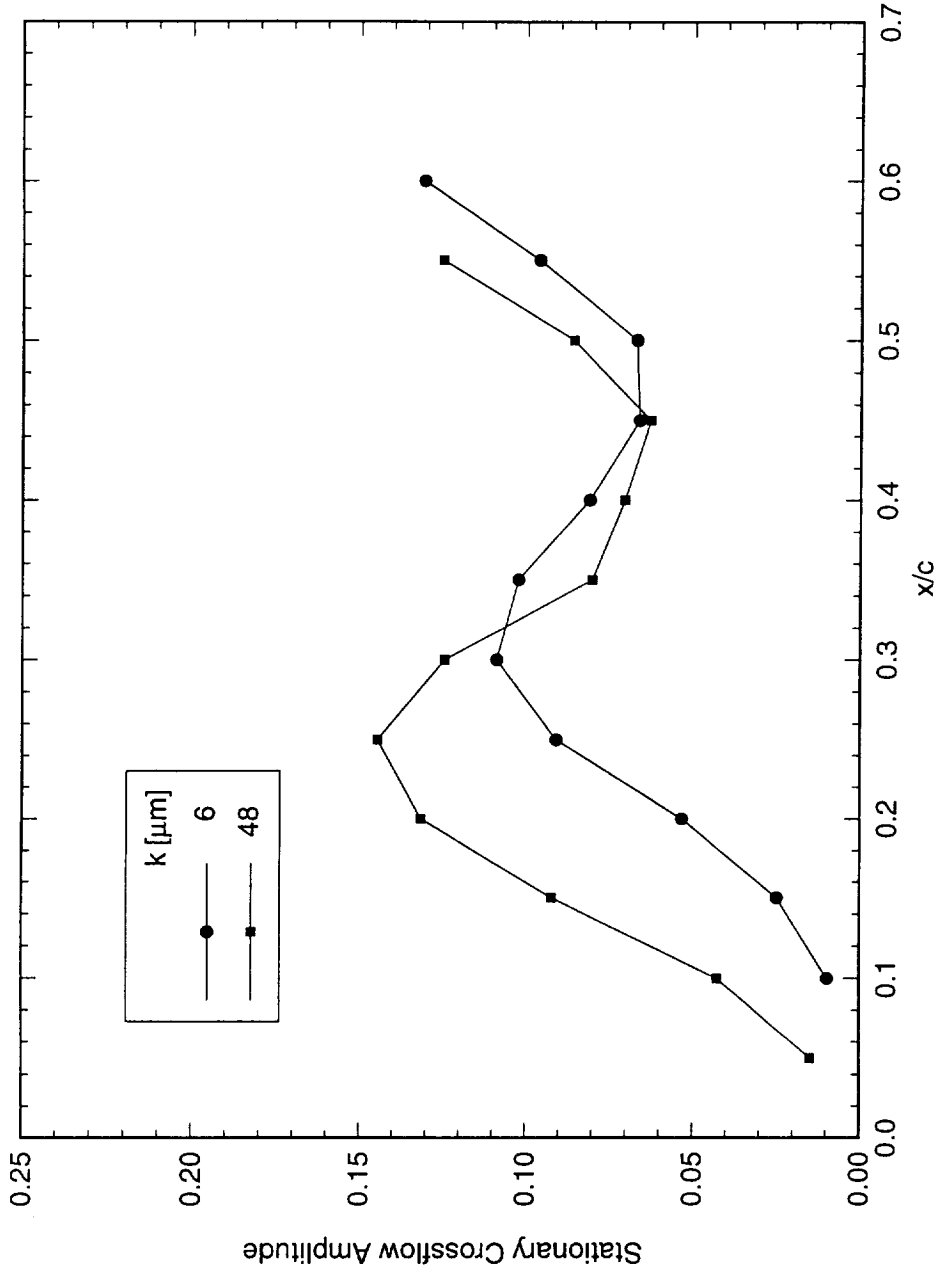

Figure 5.232: Total disturbance amplitude for $Re_c = 2.4 \times 10^6$ and $[k|8]$ roughness. The amplitudes are from the maximum of the mode-shape profiles.

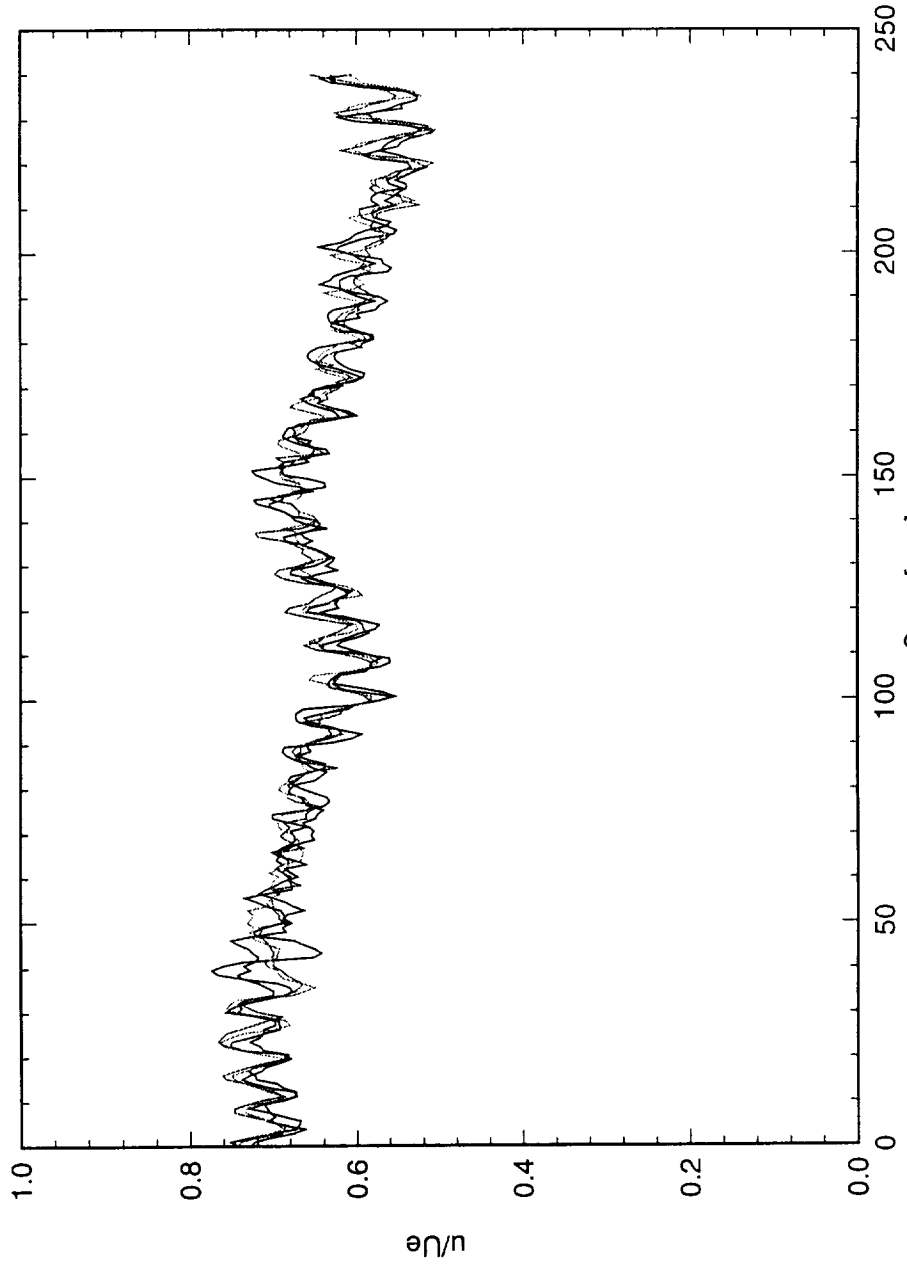

Figure 5.233: Spanwise hot-wire scan at $x/c = 0.05$ and $Y = 0.45$ mm. $Re_c = 2.4 \times 10^6$, [48|8] roughness.

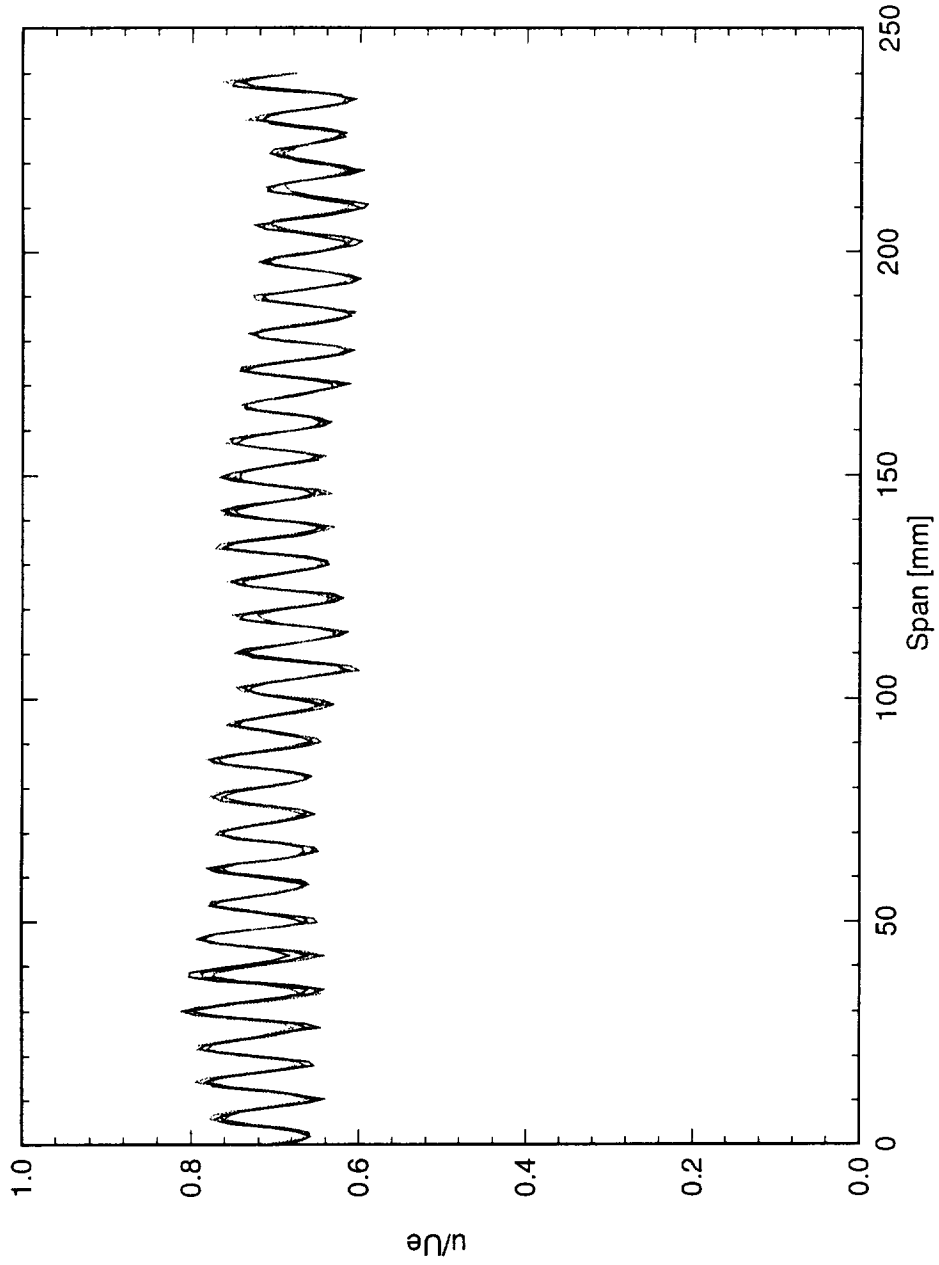

Figure 5.234: Spanwise hot-wire scan at $x/c = 0.10$ and $Y = 0.65$ mm. $Re_c = 2.4 \times 10^6$, [48|8] roughness.

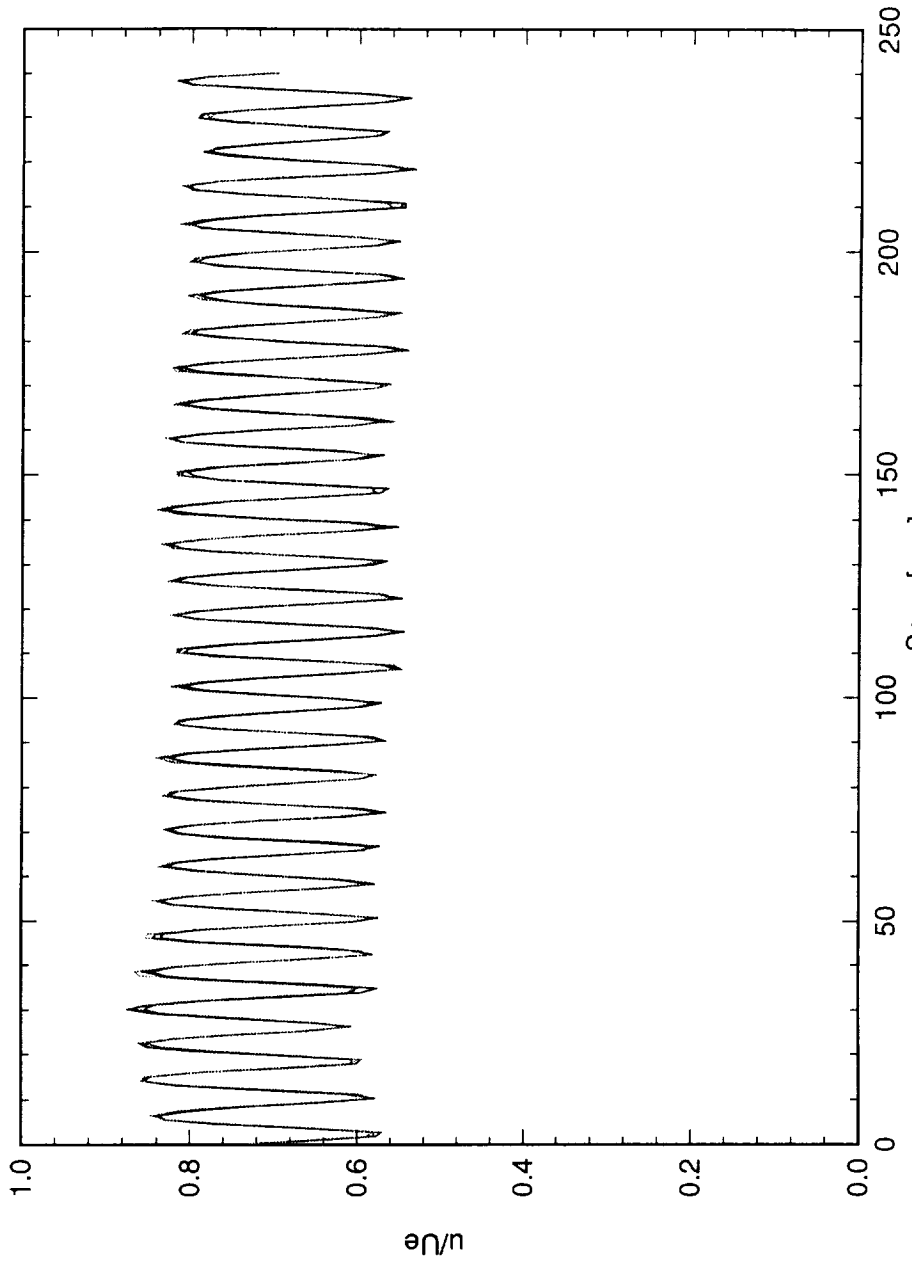

Figure 5.235: Spanwise hot-wire scan at $x/c = 0.15$ and $Y = 0.75$ mm. $Re_c = 2.4 \times 10^6$, [48|8] roughness.

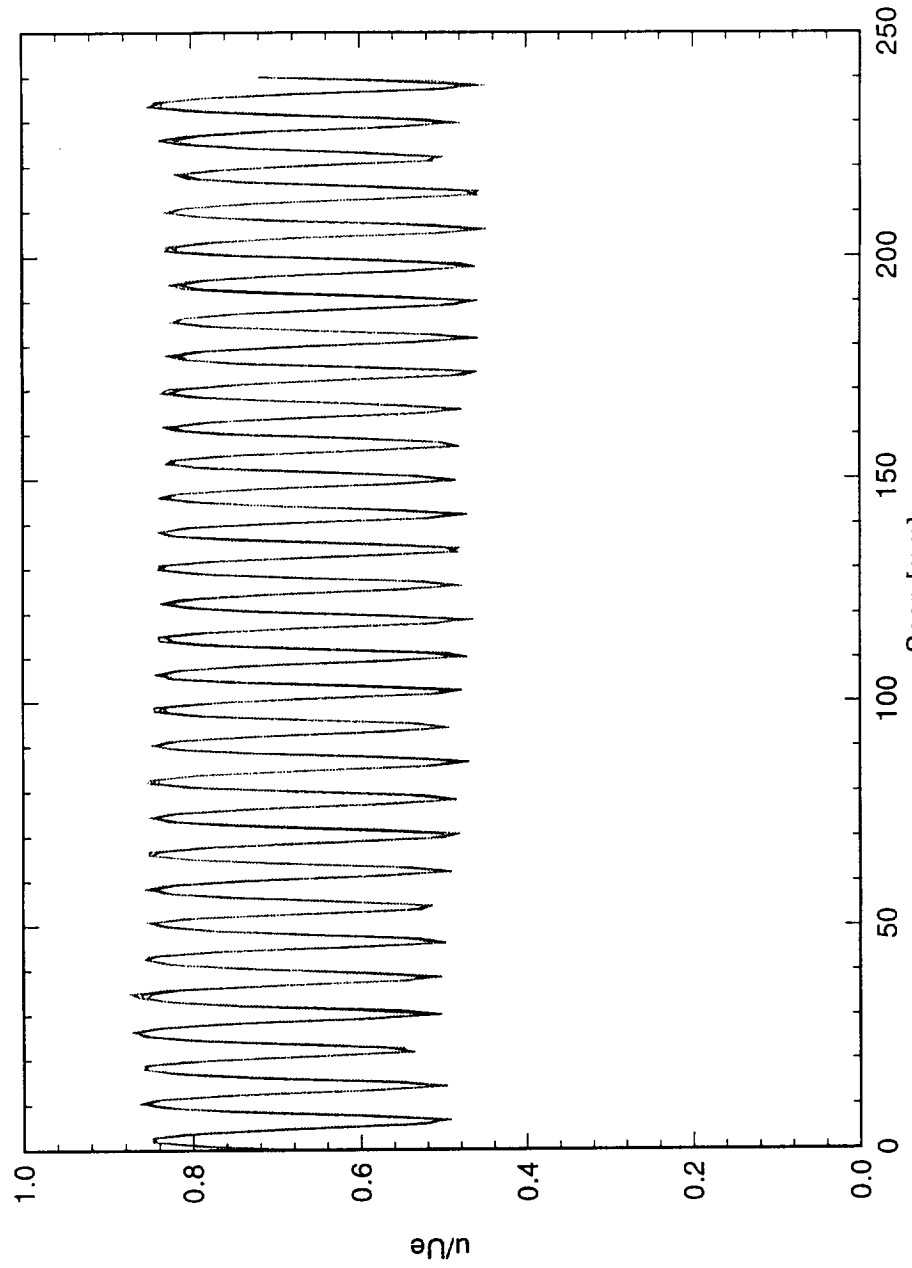

Figure 5.236: Spanwise hot-wire scan at $x/c = 0.20$ and $Y = 0.75$ mm. $Re_c = 2.4 \times 10^6$, [48|8] roughness.

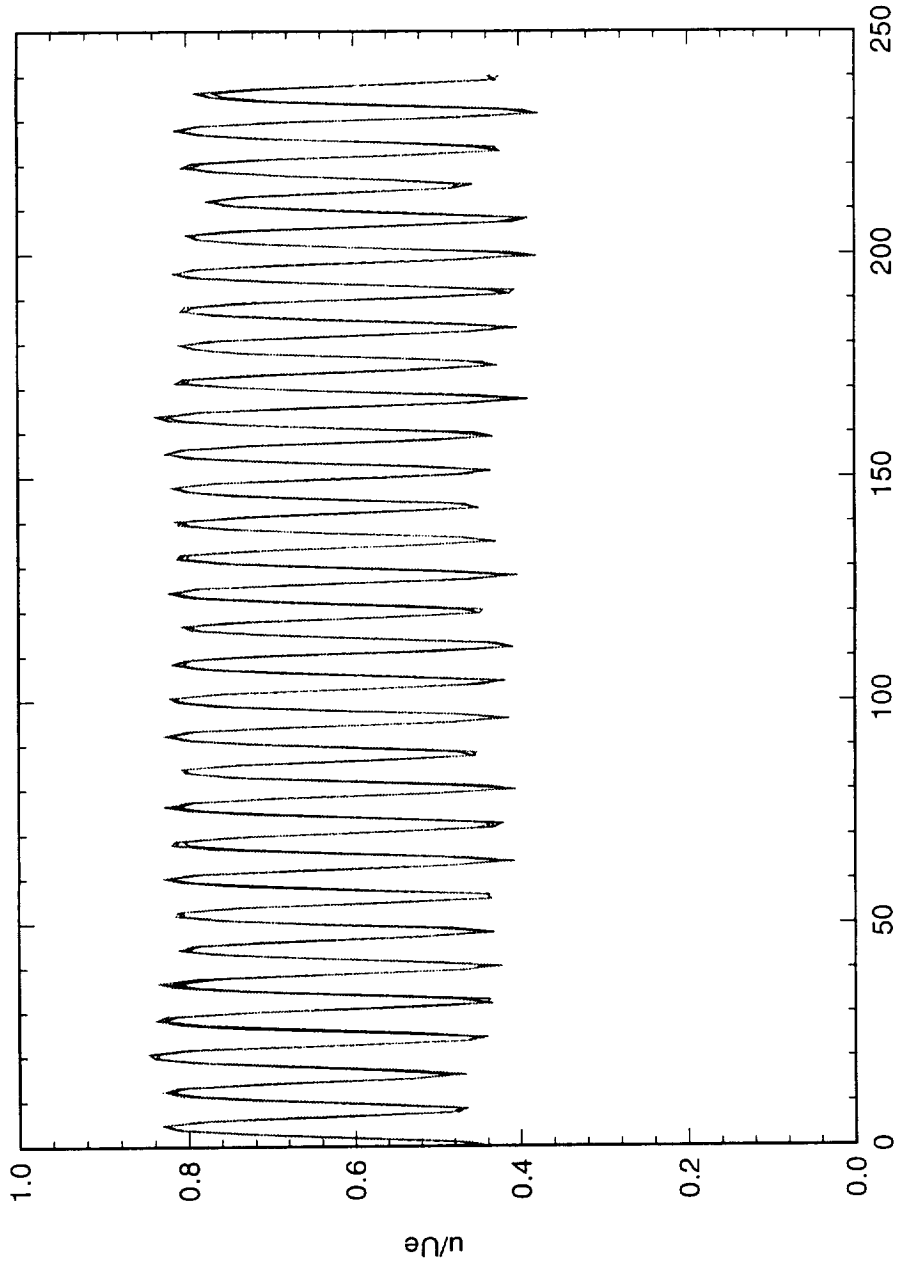

Figure 5.237: Spanwise hot-wire scan at $x/c = 0.25$ and $Y = 0.70$ mm. $Re_c = 2.4 \times 10^6$, [48|8] roughness.

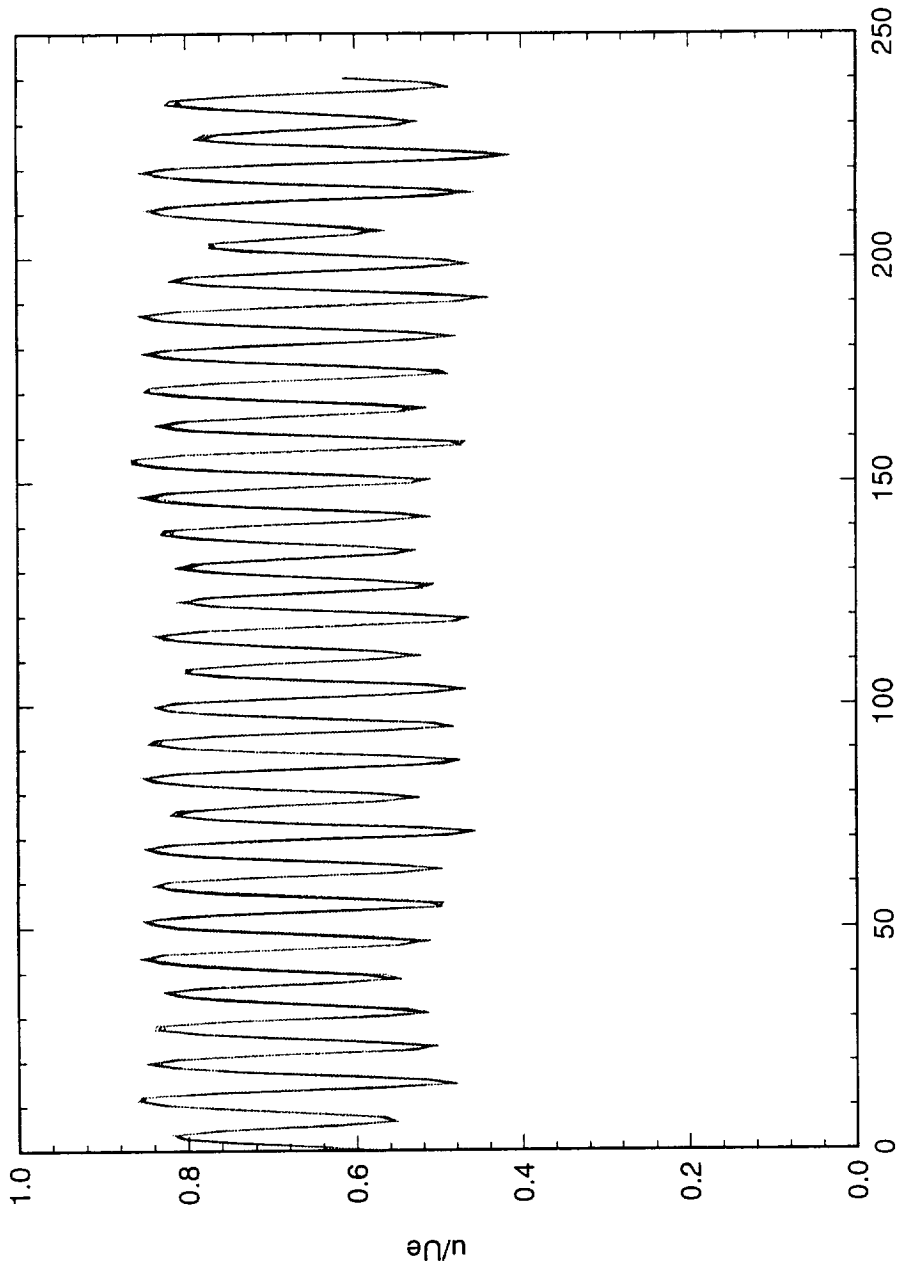

Figure 5.238: Spanwise hot-wire scan at $x/c = 0.30$ and $Y = 0.80$ mm. $Re_c = 2.4 \times 10^6$, [48|8] roughness.

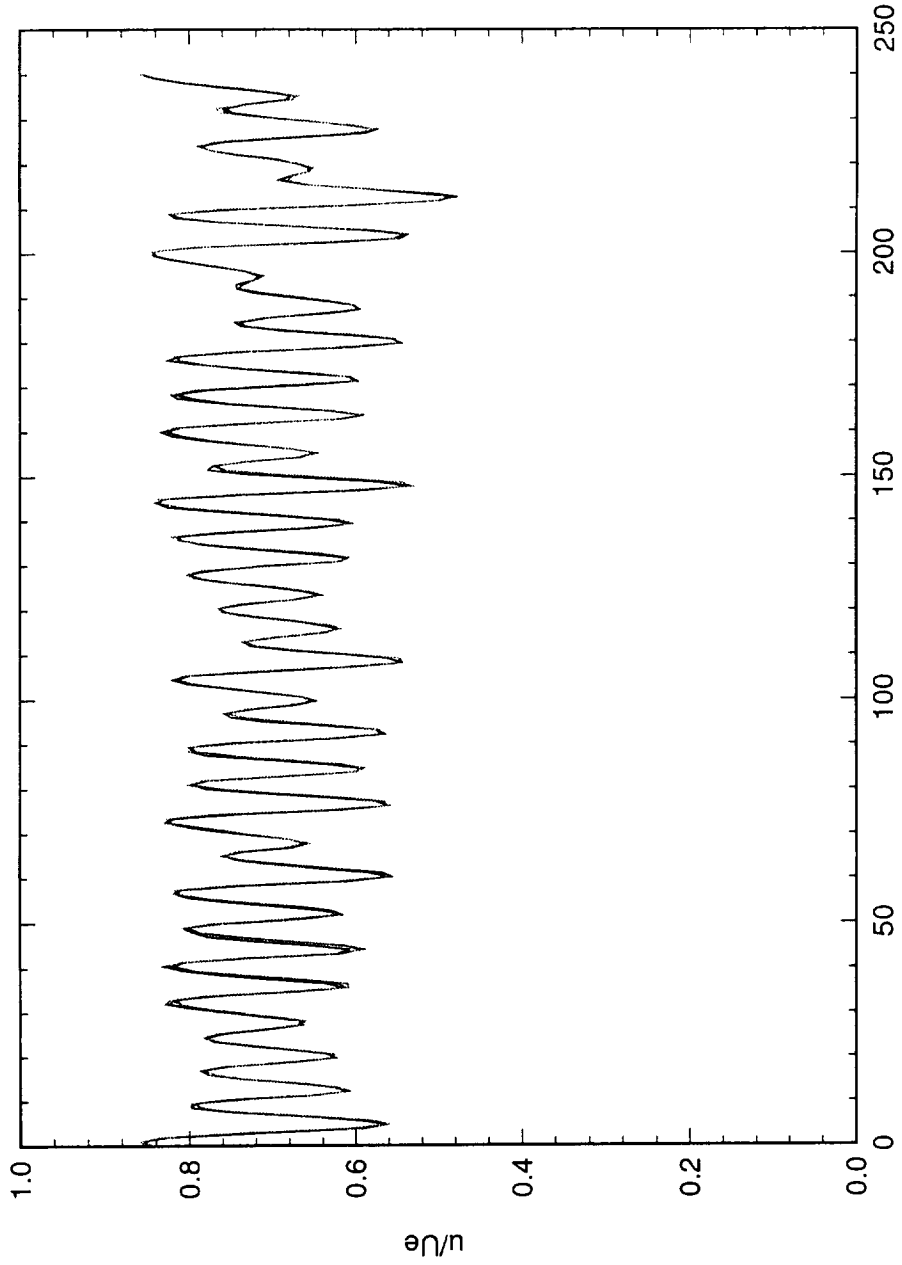

Figure 5.239: Spanwise hot-wire scan at $x/c = 0.35$ and $Y = 0.90$ mm. $Re_c = 2.4 \times 10^6$, [48|8] roughness.

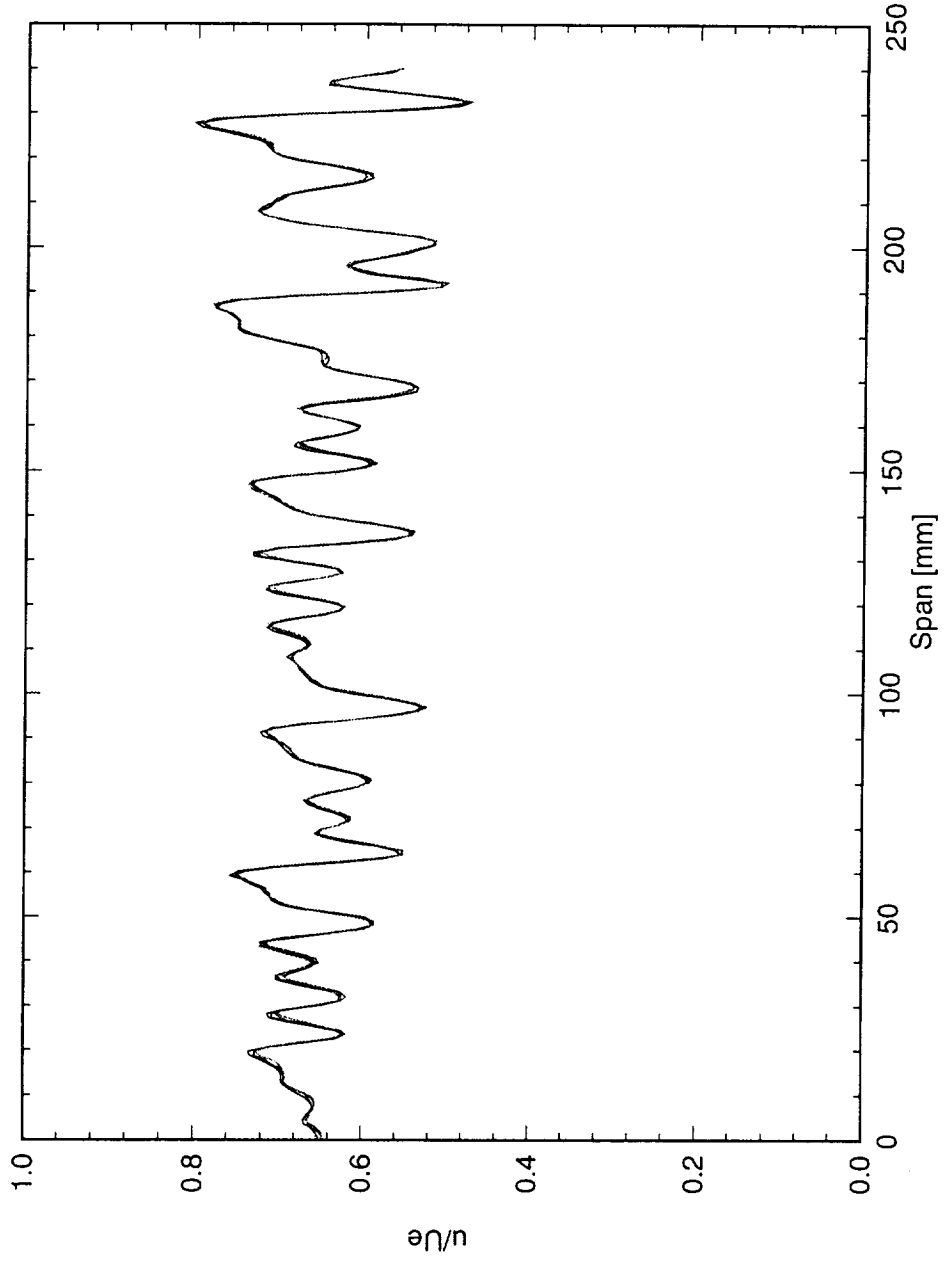

Figure 5.240: Spanwise hot-wire scan at $x/c = 0.40$ and $Y = 0.90$ mm. $Re_c = 2.4 \times 10^6$, [48|8] roughness.

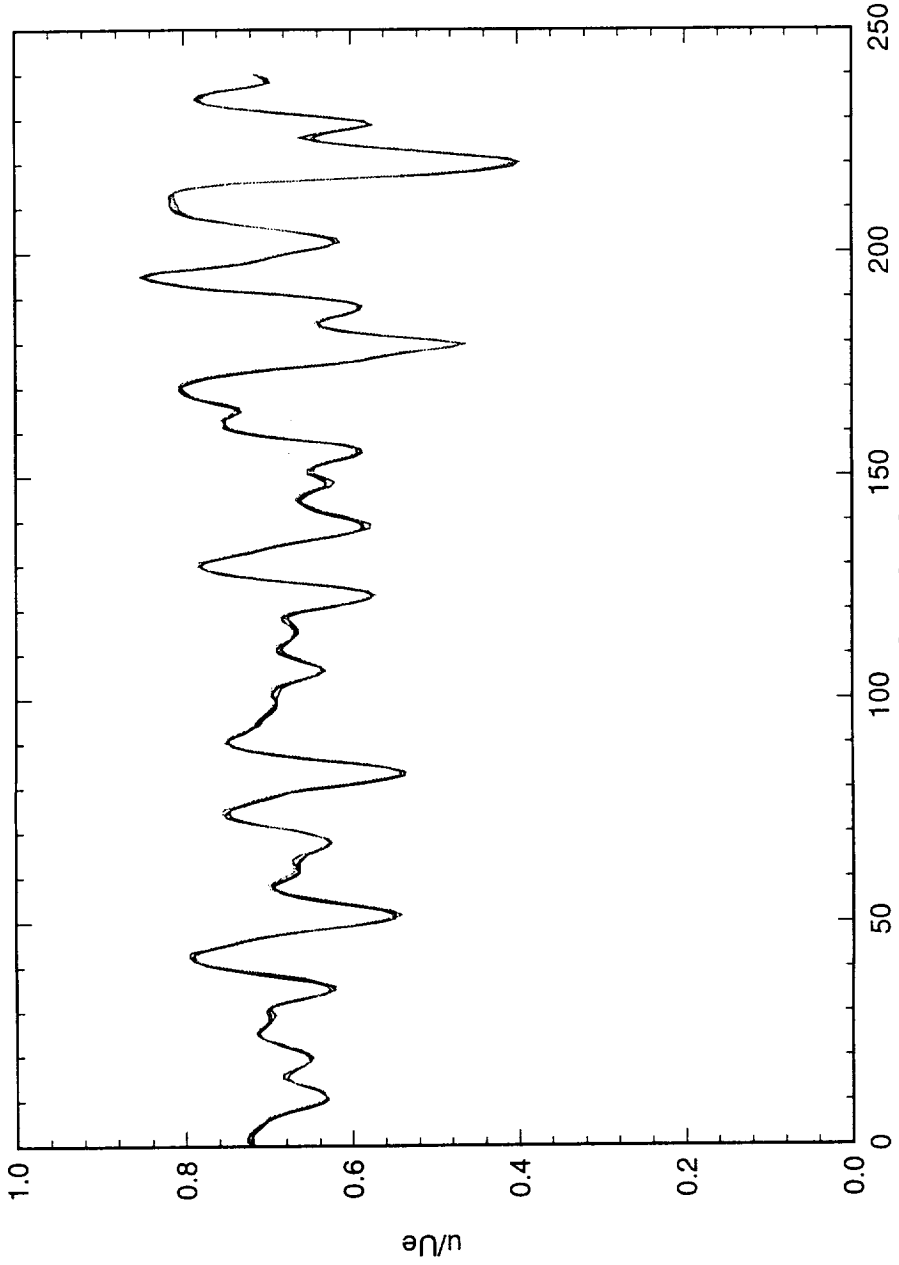

Figure 5.241: Spanwise hot-wire scan at $x/c = 0.45$ and $Y = 1.0$ mm. $Re_c = 2.4 \times 10^6$, [48|8] roughness.

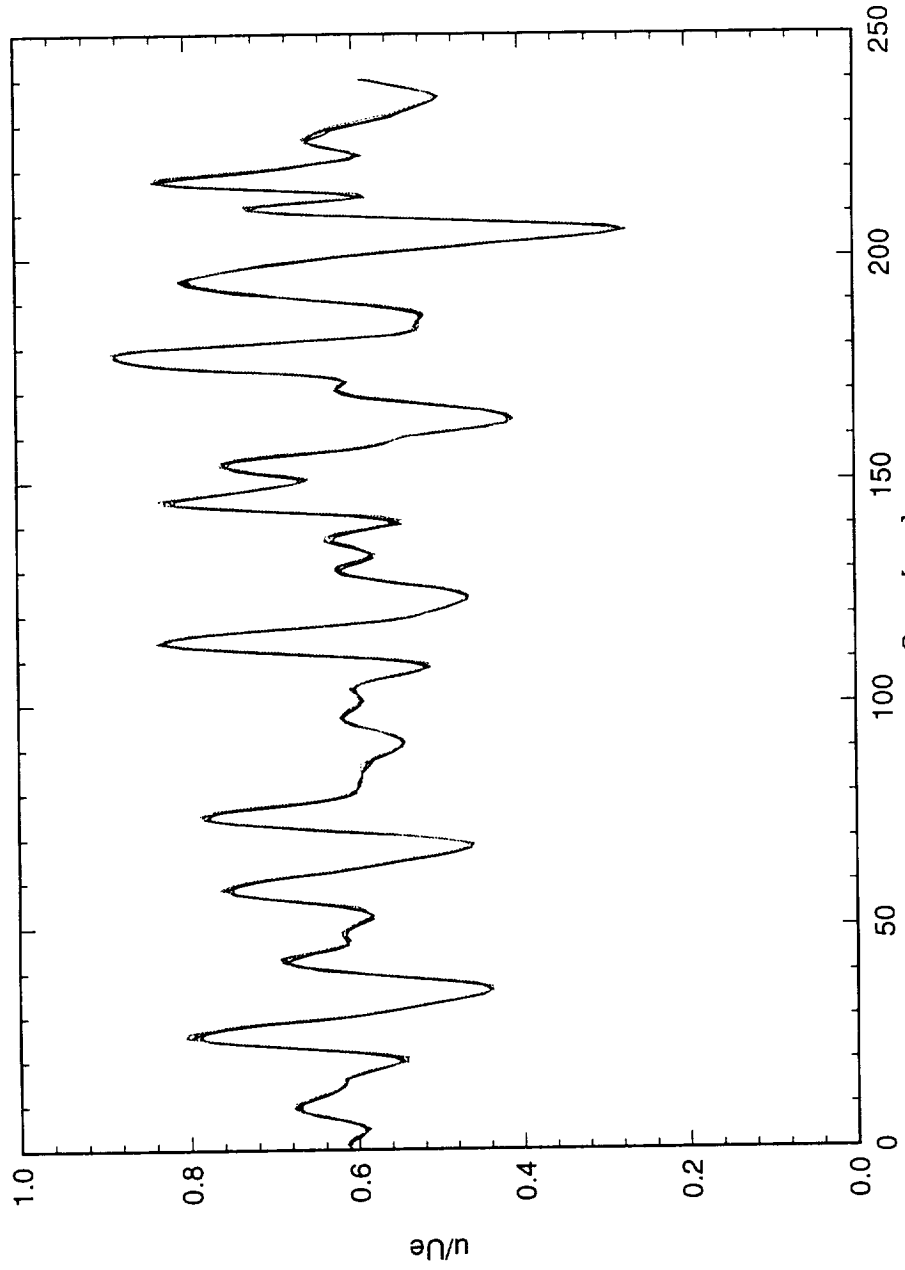

Figure 5.242: Spanwise hot-wire scan at $x/c = 0.50$ and $Y = 0.90$ mm. $Re_c = 2.4 \times 10^6$, [48|8] roughness.

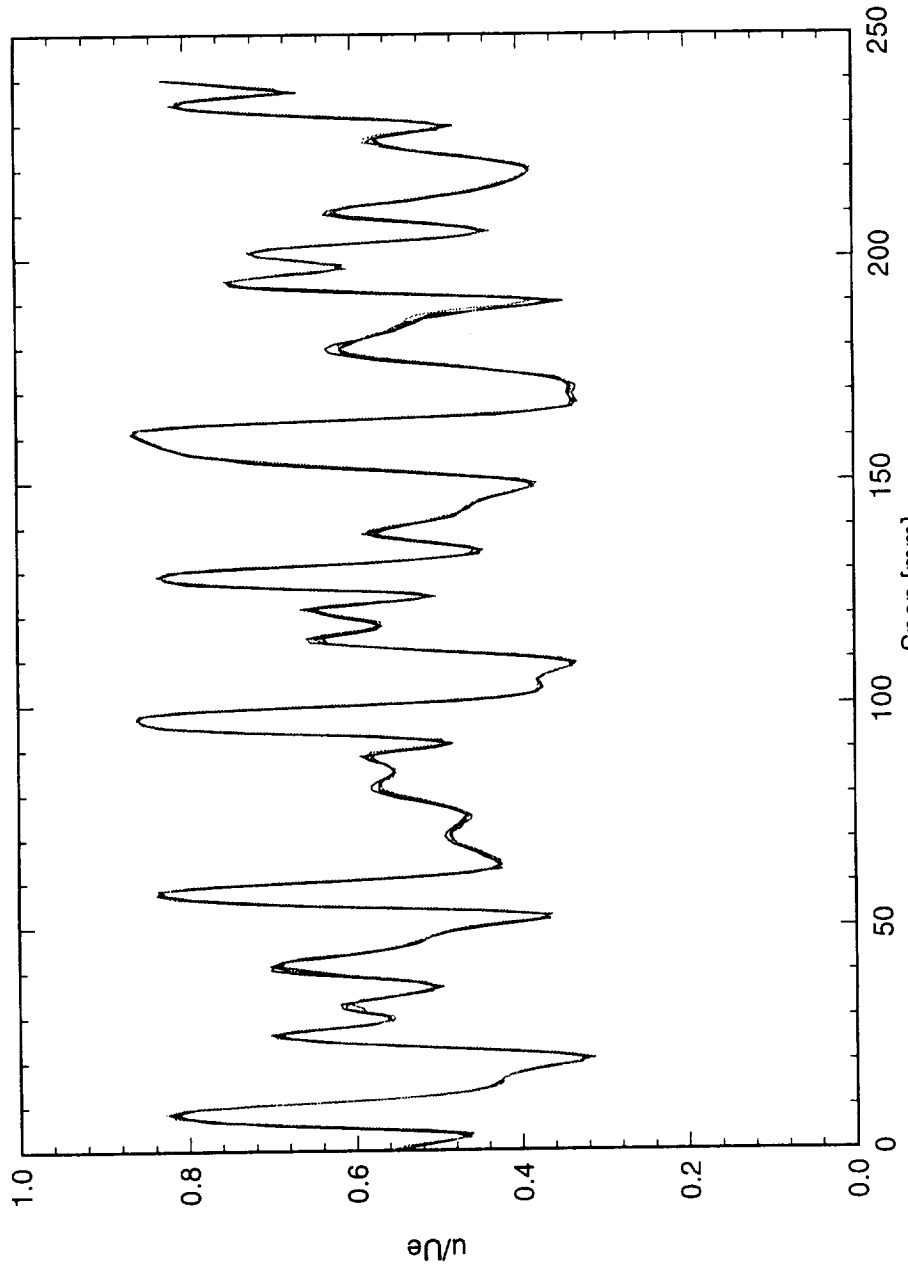

Figure 5.243: Spanwise hot-wire scan at $x/c = 0.55$ and $Y = 0.80$ mm. $Re_c = 2.4 \times 10^6$, [48|8] roughness.

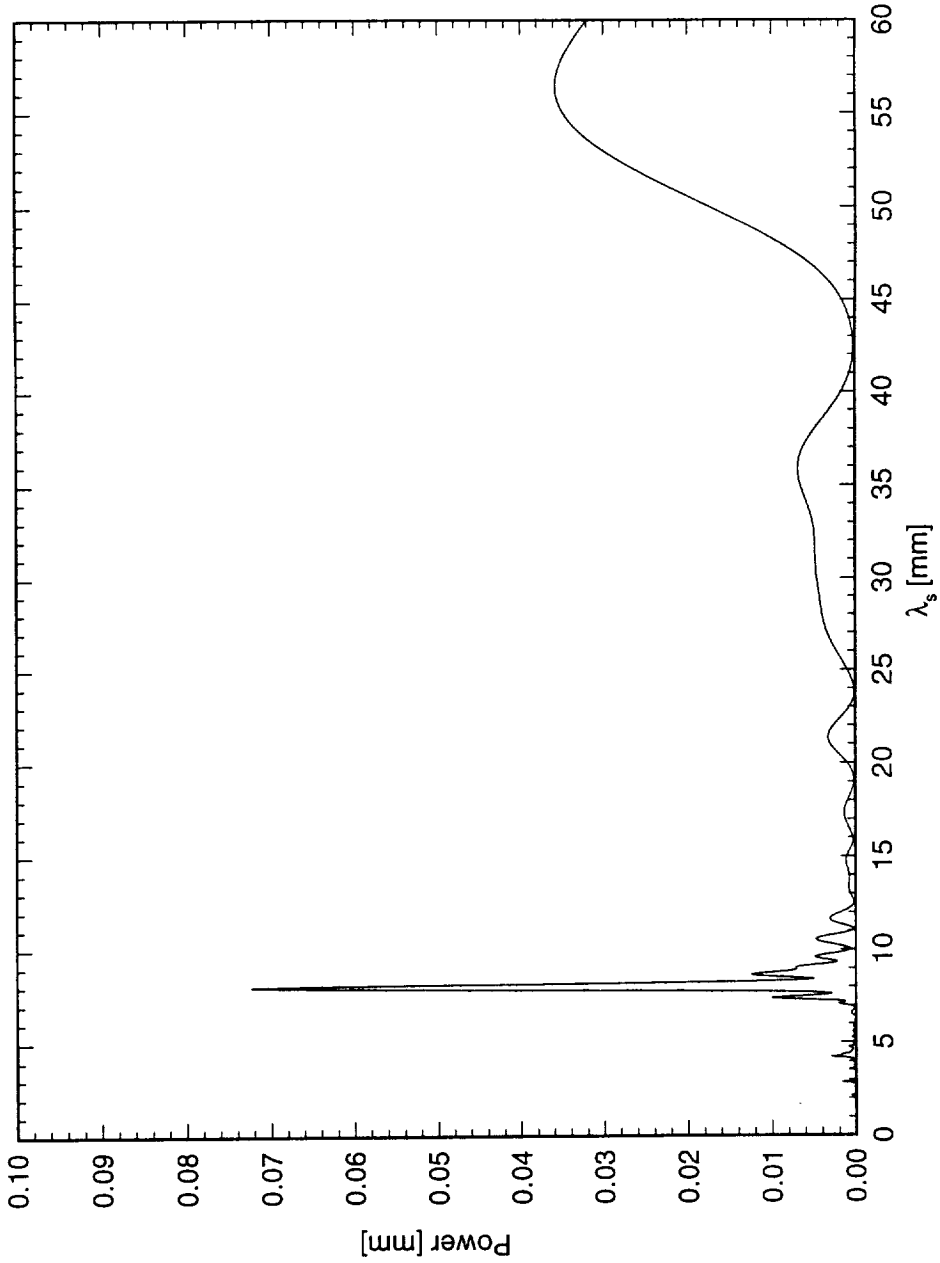

Figure 5.244: Power spectral density of constant-Y scan at $x/c = 0.05$ and $Y = 0.45$ mm. $Re_c = 2.4 \times 10^6$, [48|8] roughness.

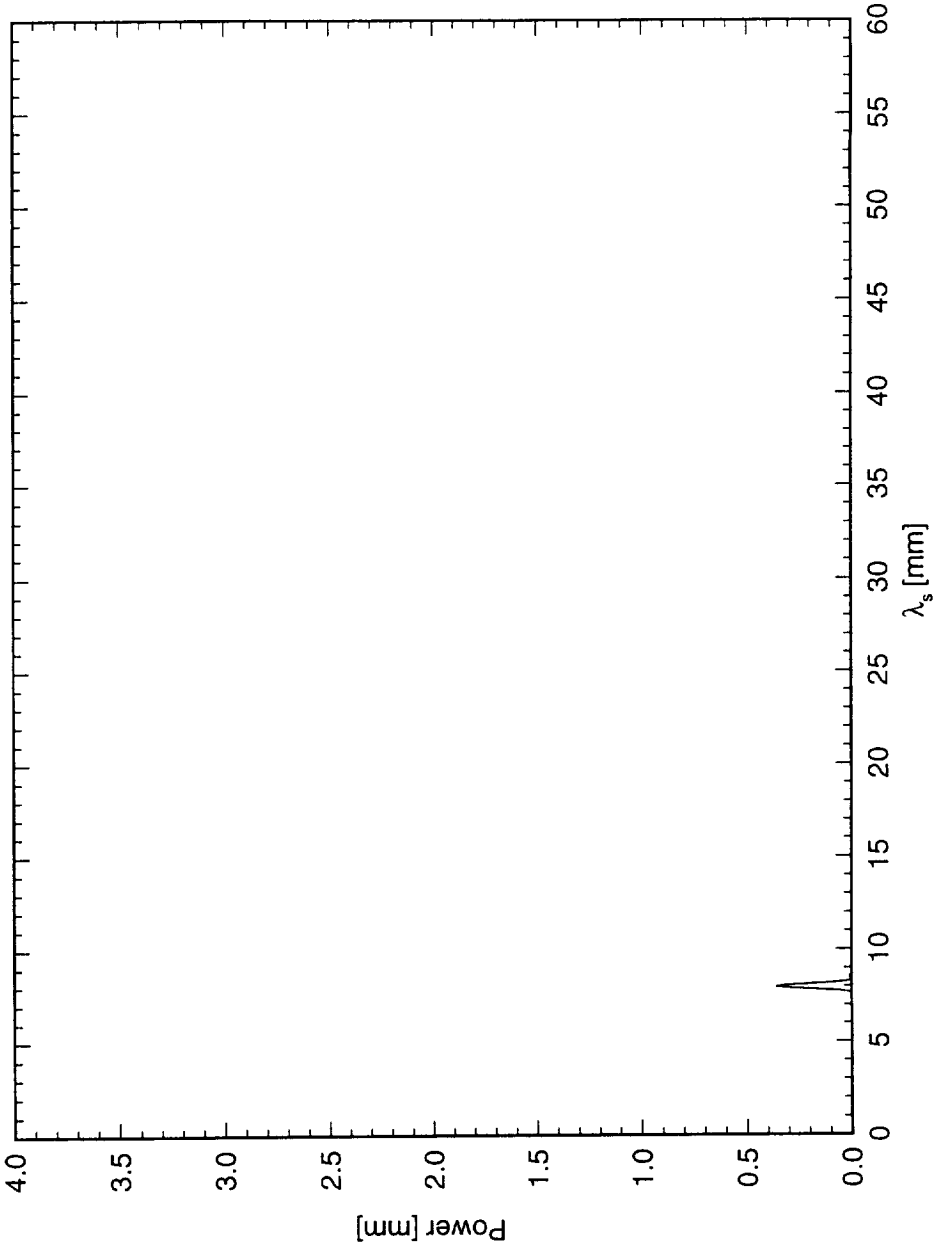

Figure 5.245: Power spectral density of constant-Y scan at $x/c = 0.10$ and $Y = 0.65$ mm. $Re_c = 2.4 \times 10^6$, [48|8] roughness.

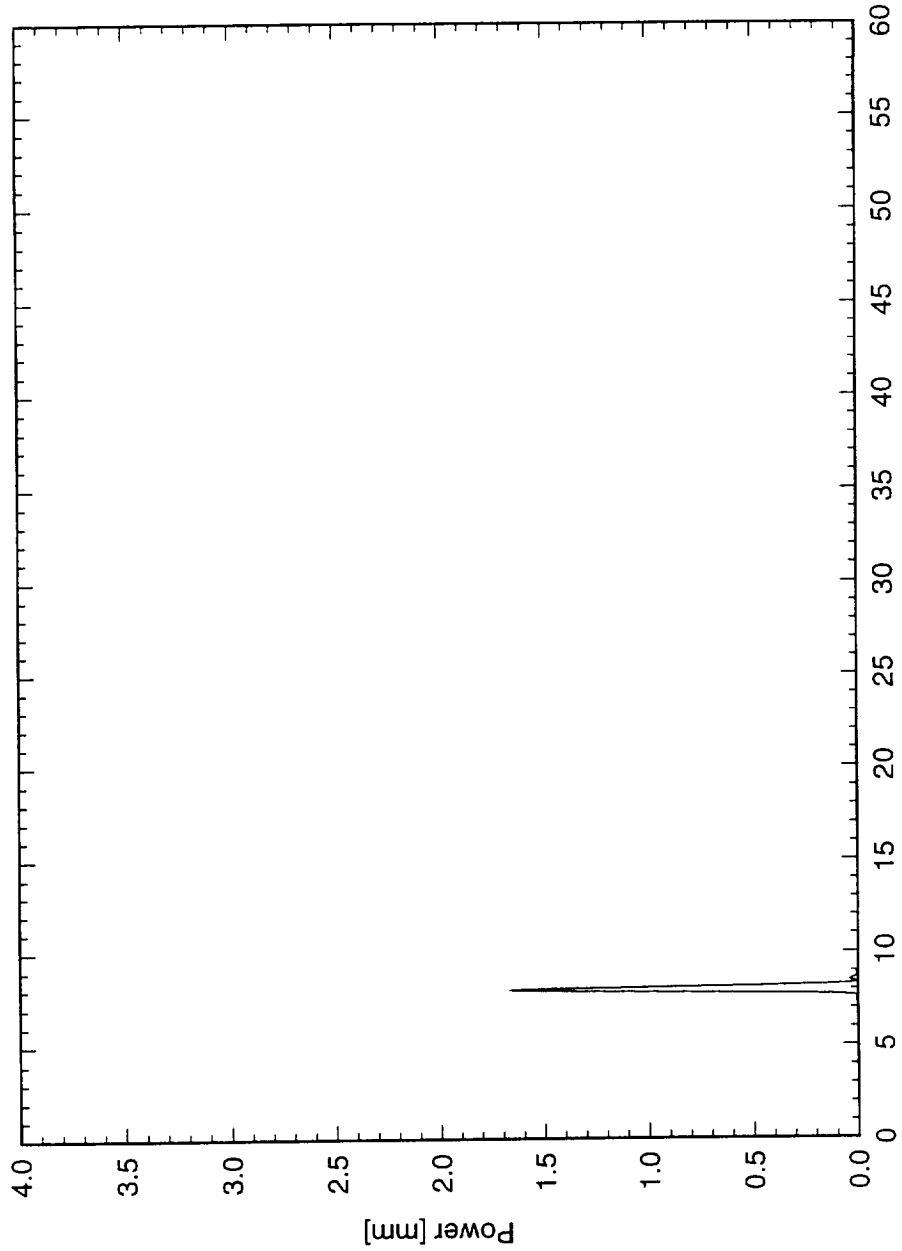

Figure 5.246: Power spectral density of constant-Y scan at $x/c = 0.15$ and $Y = 0.75$ mm. $Re_c = 2.4 \times 10^6$, [48|8] roughness.

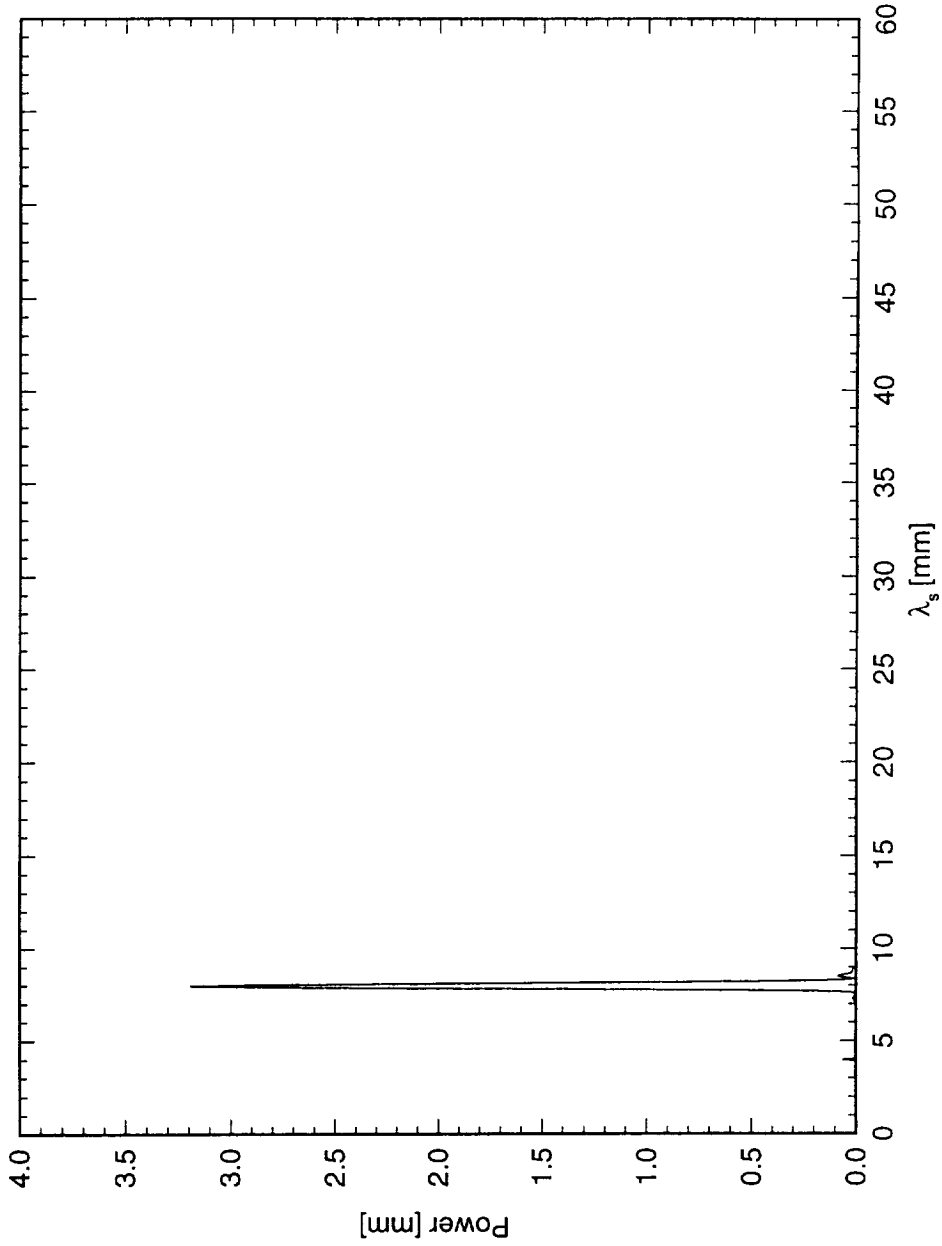

Figure 5.247: Power spectral density of constant-Y scan at $x/c = 0.20$ and $Y = 0.75$ mm. $Re_c = 2.4 \times 10^6$, [48|8] roughness.

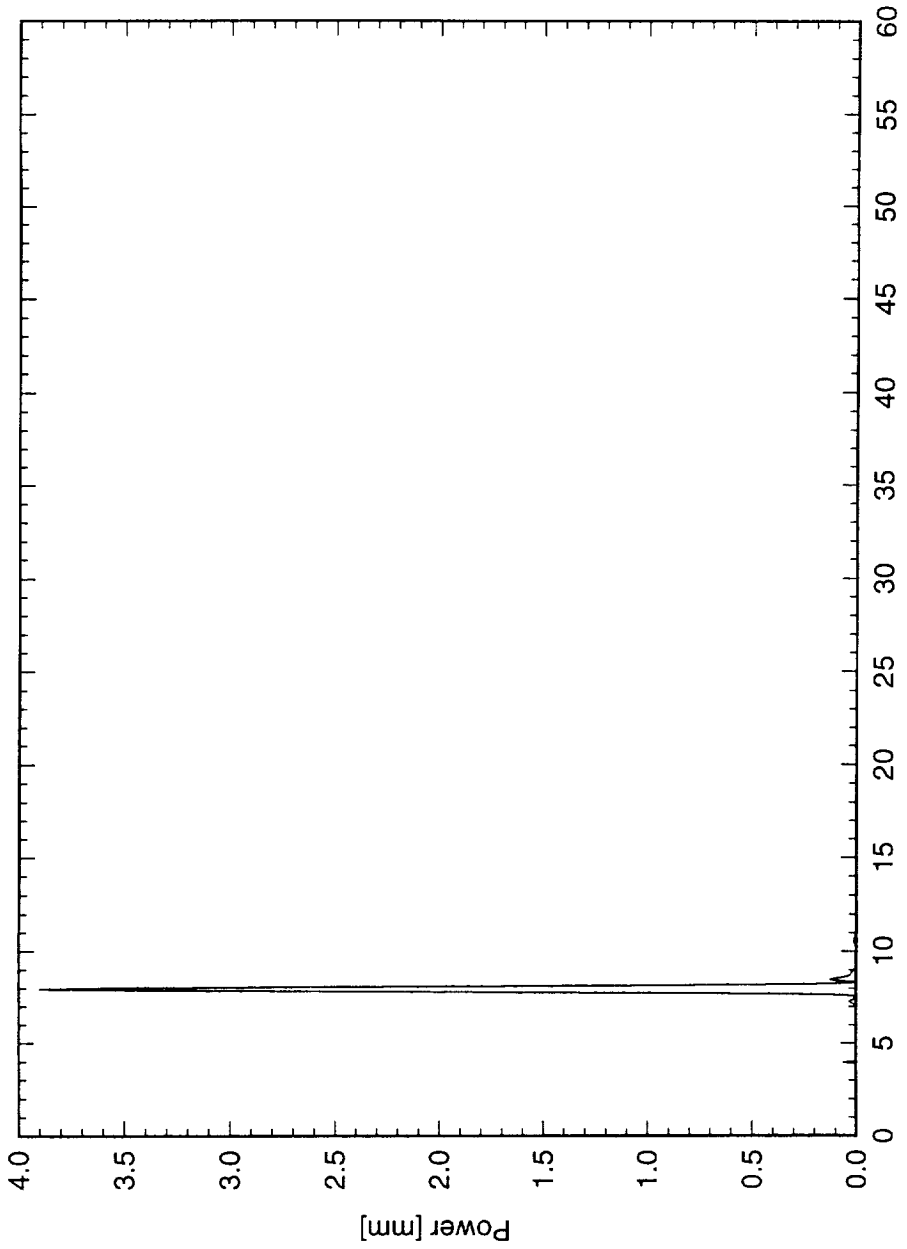

Figure 5.248: Power spectral density of constant-Y scan at $x/c = 0.25$ and $Y = 0.70$ mm. $Re_c = 2.4 \times 10^6$, [48|8] roughness.

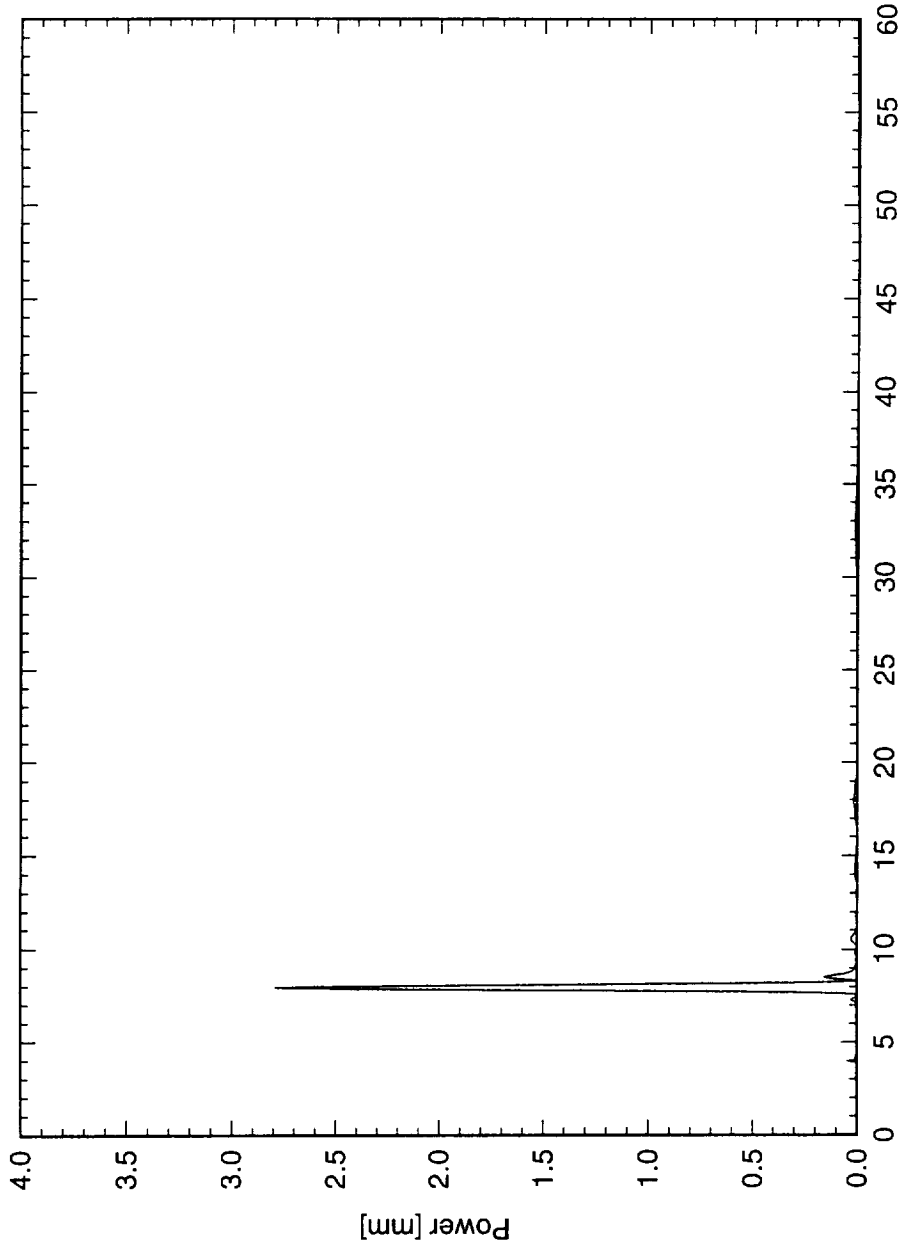

Figure 5.249: Power spectral density of constant-Y scan at $x/c = 0.30$ and $Y = 0.80$ mm. $Re_c = 2.4 \times 10^6$, [48|8] roughness.

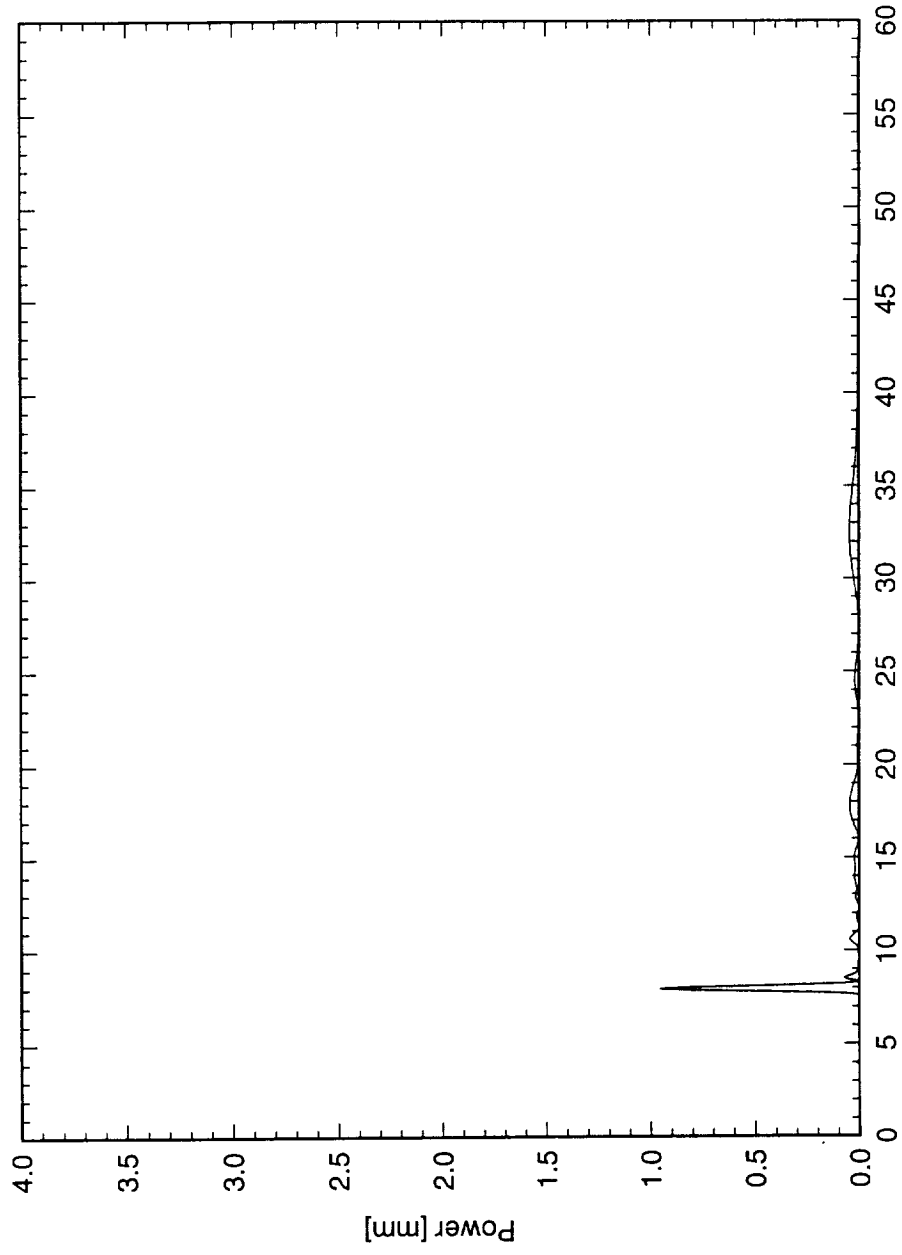

Figure 5.250: Power spectral density of constant-Y scan at $x/c = 0.35$ and $Y = 0.90$ mm. $Re_c = 2.4 \times 10^6$, [48|8] roughness.

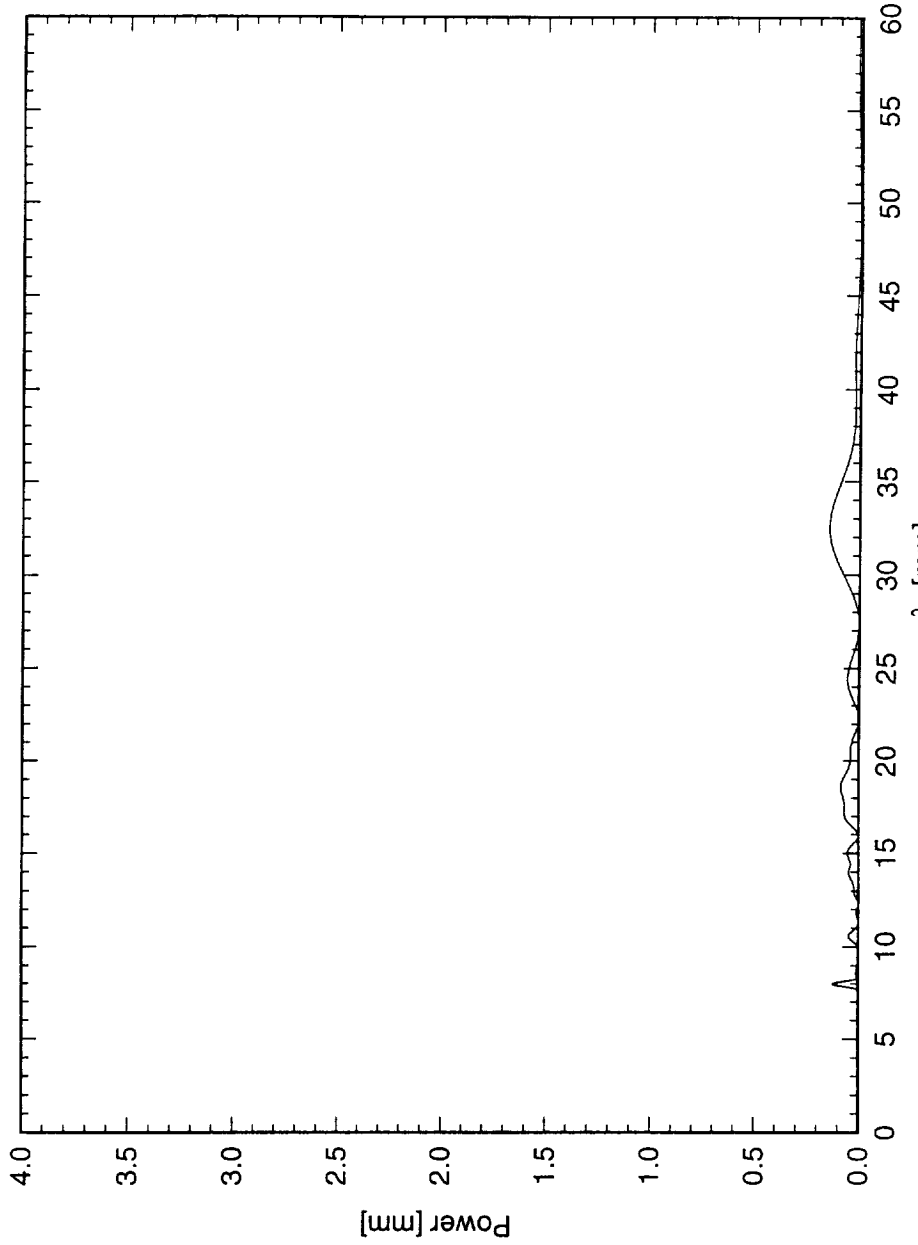

Figure 5.251: Power spectral density of constant-Y scan at $x/c = 0.40$ and $Y = 0.90$ mm. $Re_c = 2.4 \times 10^6$, [48|8] roughness.

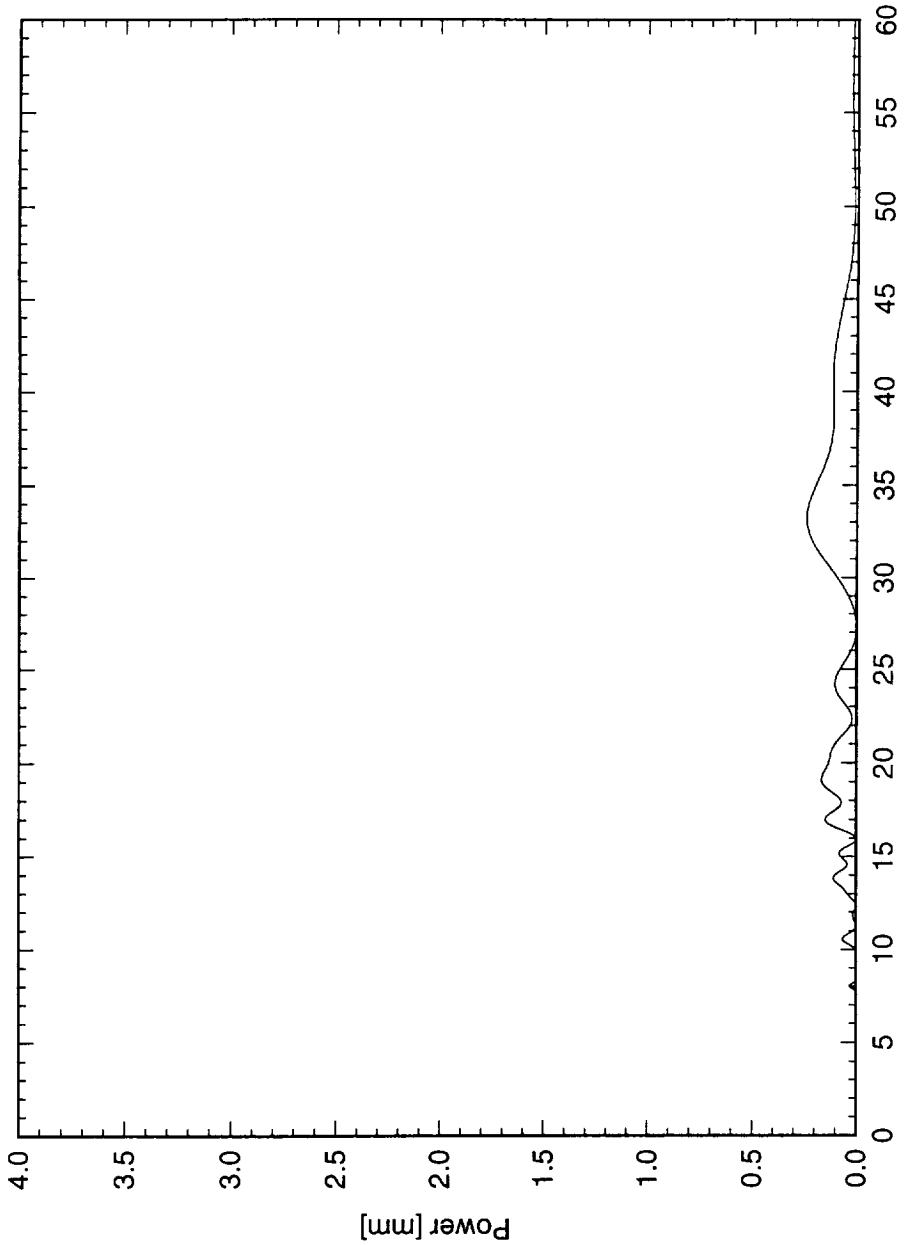

Figure 5.252: Power spectral density of constant-Y scan at $x/c = 0.45$ and $Y = 1.0$ mm. $Re_c = 2.4 \times 10^6$, [48|8] roughness.

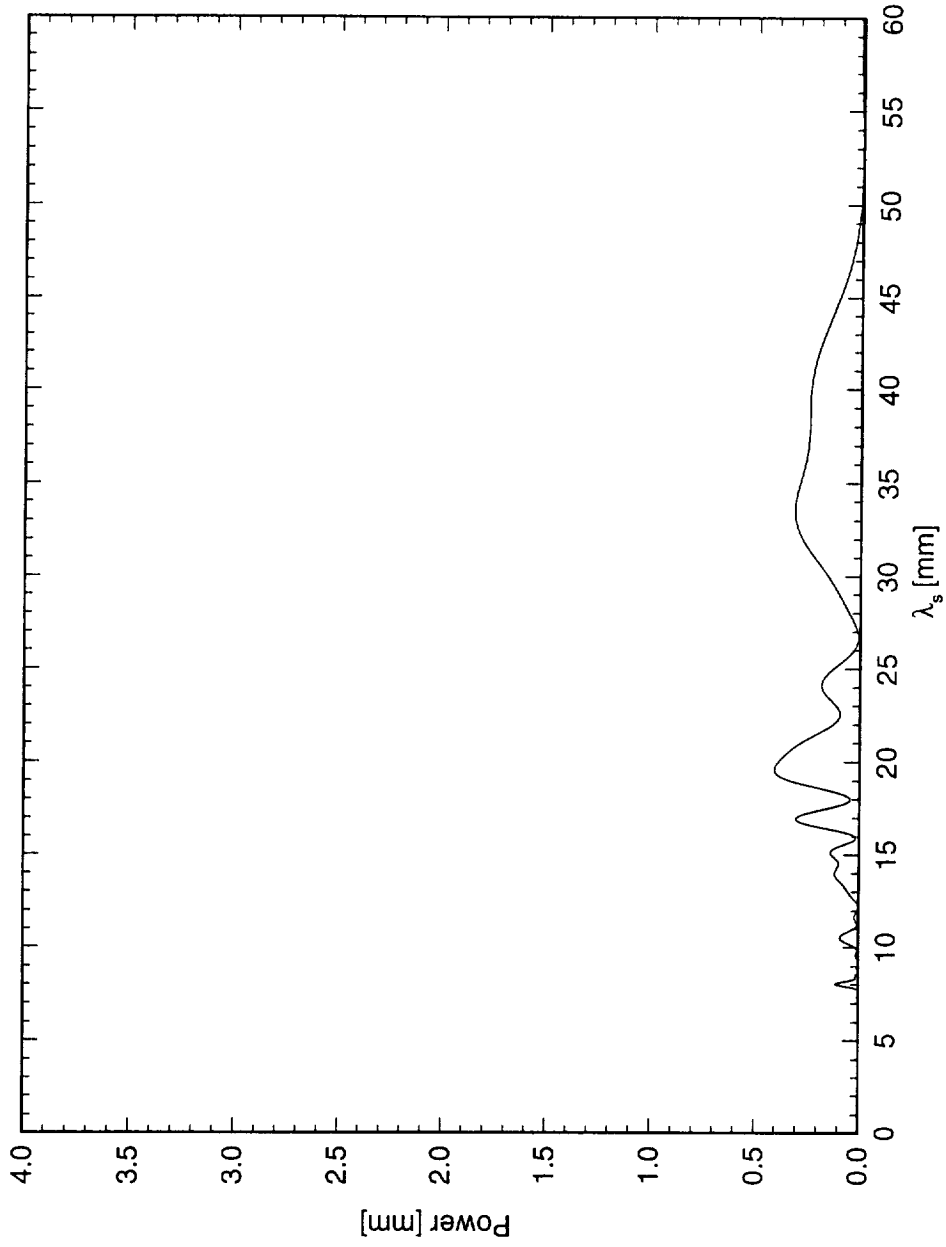

Figure 5.253: Power spectral density of constant-Y scan at $x/c = 0.50$ and $Y = 0.90$ mm. $Re_c = 2.4 \times 10^6$, [48|8] roughness.

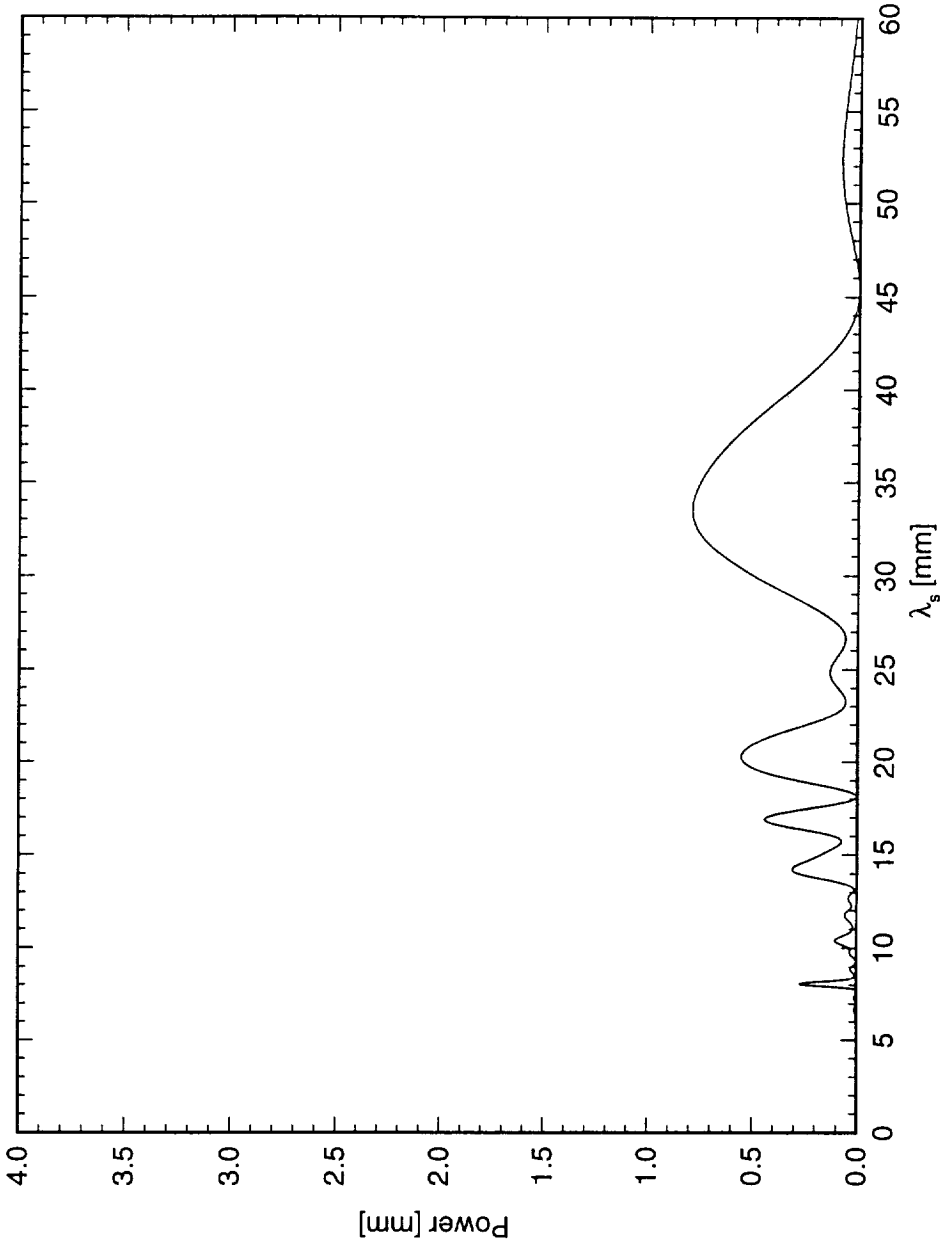

Figure 5.254: Power spectral density of constant-Y scan at $x/c = 0.55$ and $Y = 0.80$ mm. $Re_c = 2.4 \times 10^6$, [48|8] roughness.

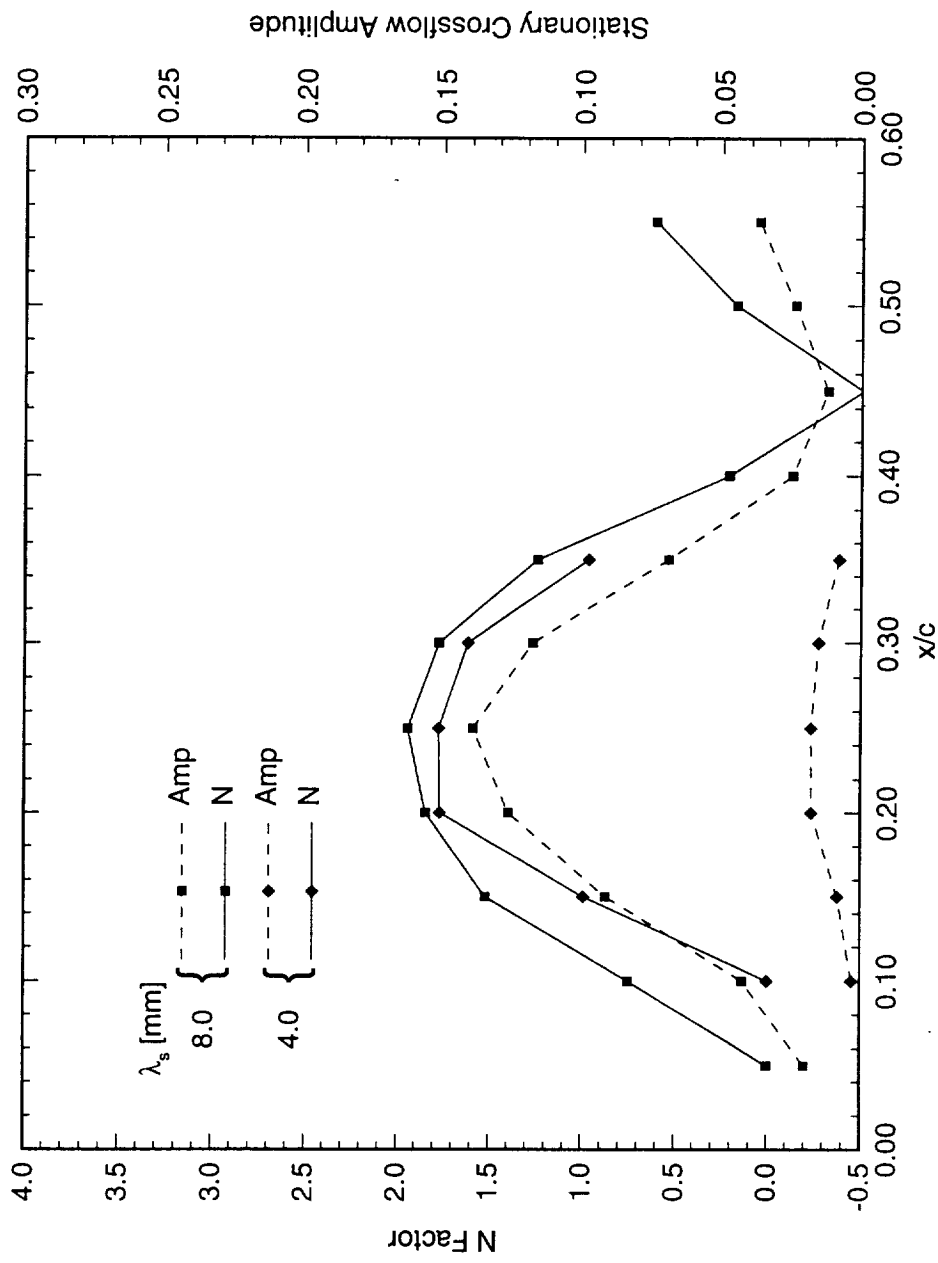

Figure 5.255: Single-mode disturbance amplitude and N-factors. $Re_c = 2.4 \times 10^6$, [48|8] roughness. N-factor calculations are relative to the location where the disturbance is first detected.

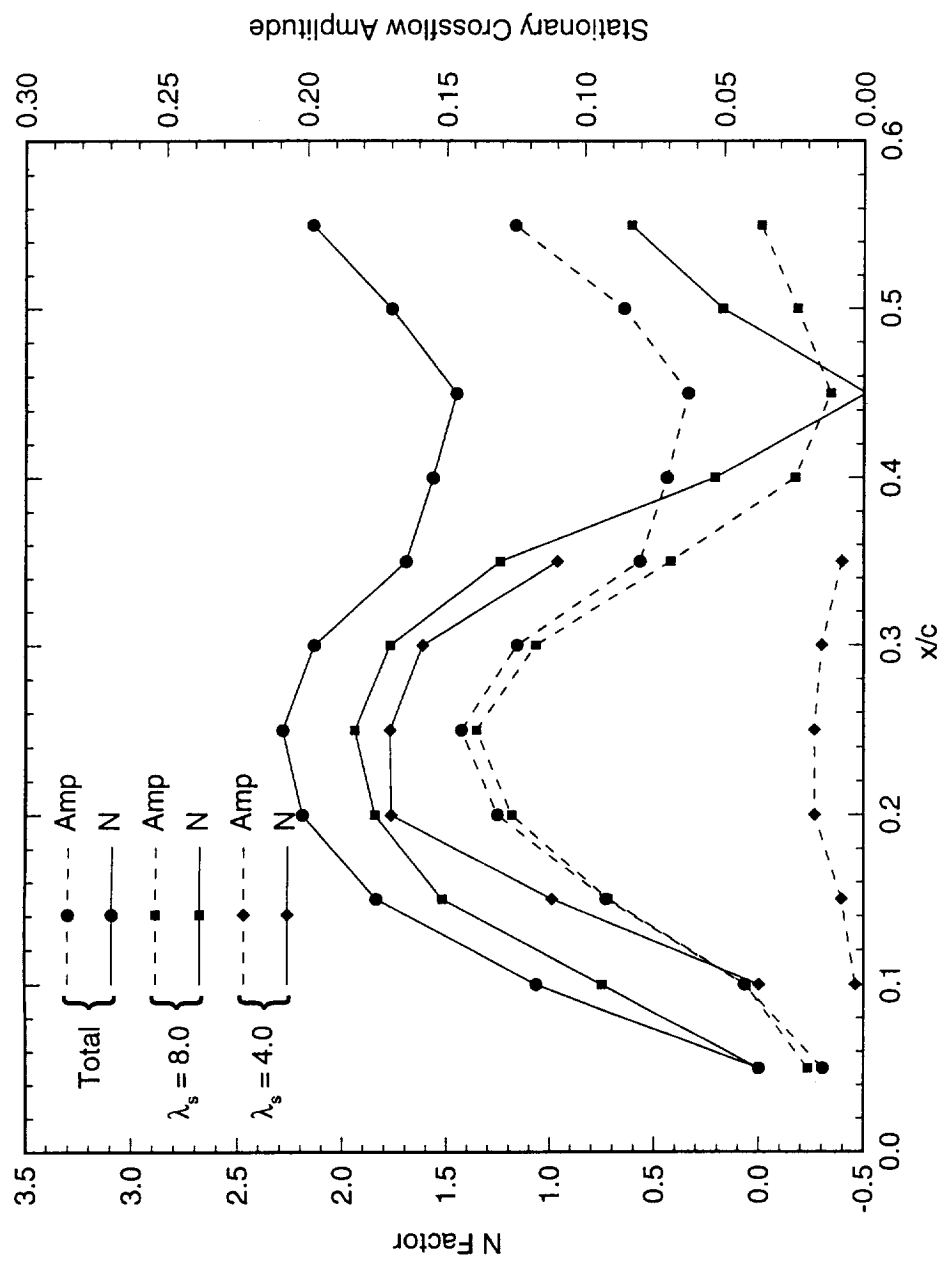

Figure 5.256: Total and single-mode disturbance amplitude and N-factors. $Re_c = 2.4 \times 10^6$, [48|8] roughness. N-factor calculations are relative to the location where the disturbance is first detected.